META'14 - Singapore

The 5th International Conference on Metamaterials, Photonic Crystals and Plasmonics

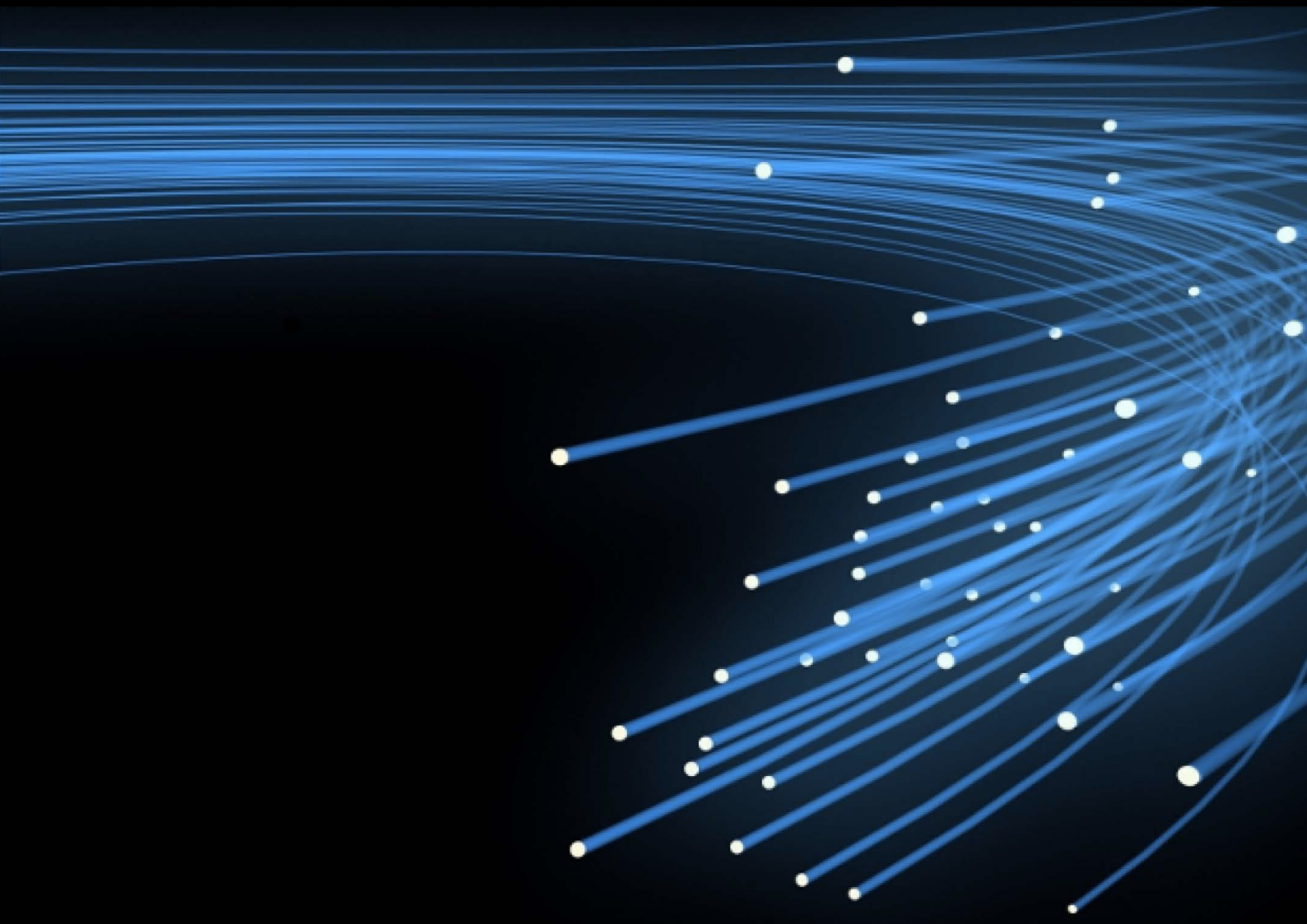

Proceedings

ISBN : 978-2-9545460-4-9

www.metaconferences.org

ISBN: 978-2-9545460-4-9
ISSN: 2429-1390

META'14 - Singapore

The 5th International Conference on Metamaterials, Photonic Crystals and Plasmonics

Edited by

Said Zouhdi | Paris-Sud University, France
Nikolay Zheludev | NTU, Singapore & Southampton University, United Kingdom
Jing Hua Teng | A*STAR, Singapore

Contents

META'14 ORGANIZATION 1

SPONSORS AND SUPPORTERS 3

TABLE OF CONTENTS 4

META'14 ORGANIZATION

META General Chair

Said Zouhdi, Paris–Sud University, France

META'14 General Co-Chairs

Nikolay Zheludev, NTU, Singapore
&
Southampton University, United Kingdom

Jinghua Teng, A*STAR, Singapore

Organizing Committee

Volkan Demir Hilmi, Singapore
Er Ping Li, Singapore
Ai Qun Liu, Singapore
Boris Luk'yanchuk, Singapore
Dan Pickard, Singapore
Cheng-Wei Qiu, Singapore
Laurent Santandrea, France
Ze Xiang Shen, Singapore
Cesare Soci, Singapore
Eric Verney, France
Baile Zhang, Singapore
Hua Zhang, Singapore

International Advisory Committee

Nader Engheta, USA
Mathias Fink, France
Sailing He, Sweden
Tatsuo Itoh, USA
Yuri Kivshar, Australia
Graeme W. Milton, USA
Raj Mittra, United States
Susumu Noda, Japan
Masaya Notomi, Japan
Yahya Rahmat-Samii, USA
Vladimir Shalaev, USA
Ari Sihvola, Finland
David R. Smith, USA
Sergei Tretyakov, Finland
J(Yiannis) Vardaxoglou, UK
Alexey Vinogradov, Russia
Martin Wegener, Germany

Technical Program Committee

J. Aizpurua, Spain
T. Akalin, France
A. Alu, USA
W. L. Barnes, UK
X. Begaud, France
S. I. Bozhevolnyi, Denmark
K. Busch, Germany
C. T. Chan, Hong Kong
A. Chipouline, Germany
C. Craeye, Belgium
J. Christensen, Spain
A. Dmitriev, Sweden
D. Felbacq, France
W. Fritzsche, Germany
F. J. Garcia, Spain

J. Krenn, Austria
O. Hess, UK
R. Hillenbrand, Spain
D. Kim, Korea
K. Leosson, Iceland
J. Li, Hong Kong
S. Maier, UK
M. McCall, UK
L. M. Moreno, Spain
P. Nordlander, USA
T. Odom, USA
D. Pawlak, Poland
C. E. Jason Png, Singapore
C.-W. Qiu, Singapore
M. Qiu, Sweden
T. Tanaka, Japan
A. Urbas, USA
J. K. W. Yang, Singapore
A. V. Zayats, UK
X. Zhang, USA
L. Zhou, China

Special Session Organizers

I. Ahmed, Singapore
T. Akalin, France
G. Alagappan, Singapore
S. Arslanagic, Denmark
P. Belov, Russia
H. Benisty, France
A. Boardman, UK
S. N. Burokur, France
P.-Y. Chen, USA
A. Chipouline, Germany
C. Couteau, France
A. de Lustrac, France
M. Farhat, Saudi Arabia
V. Fedotov, UK
D. Felbacq, France
I. Gabitov, USA
S. Gaponenko, Belarus
R. Gordon, Canada
A. Govorov, USA
R. Hao, China
K. E. Huat, Singapore
A. Kavokin, UK
Y. Y. Kim, UK
V. Klimov, Russia
I. Kurochkin, Russia
M. Kuzuoglu, Turkey
N. Lazarides, Greece
D. Li, Singapore
Z. Liu, Singapore
A. Lupu, France
K. MacDonald, UK
R. Malureanu, Denmark
S. Maier, UK
F. Moreno, Spain
M. Naruse, Japan
I. Nazarenko, Germany
A. Neogi, USA
M. Nieto-Vesperinas, Spain
S.-H. Oh, USA
M. Ohtsu, Japan
O. Ozgun, Turkey
W. (Won) Park, USA
D. Pawlak, Poland
C. E. Jason Png, Singapore
D. Qingguo, Singapore
M. Qiu, China
K. Sakoda, Japan
I. Shadrivov, Australia
A. Sihvola, Finland
Y. Sivan, Israel
C. Hong Son, Singapore
Y. Sonnefraud, France
P. Verma, Japan
A. Vinogradov, Russia
H. Volkan Demir, Turkey
J. Wang, China
D. Wilkowski, Singapore
V. Yannopapas, Greece
Y. Yu, Singapore
A. Zagoskin, UK

SPONSORS AND SUPPORTERS

We wish to thank the following institutions, exhibitors and sponsors for their contribution to the success of this conference :

TABLE OF CONTENTS

Metamaterials and negative index materials

Complementary electric-LC resonator antenna for WLAN applications (pp. 15)
Bashir D. Bala, Mohamad Kamal B. A. Rahim, Noor Asniza Murad,

Antenna optimization using metamaterial cover (pp. 18)
Surabhi Dwivedi, Vivekanand Mishra, Yogesh Kosta,

Electromagnetic characteristics of Hilbert curve based metamaterials (pp. 24)
Ruirui Chen, Sucheng Li, Chendong Gu, Shahzad Anwar, Bo Hou, Yun Lai,

Scattering by a cylindrical dielectric Shell with DNG metamaterial (pp. 29)
Mousa Hussein,

Interaction of Bessel light beams with epsilon-near-zero metamaterials (pp. 33)
Svetlana Kurilkina, Mohammed A. Binhussain, Vladimir Belyi, Nikolai Kazak,

Left handed mode propagating in coplanar isolator based on Yittrium Iron Garnet (YIG) (pp. 39)
Ouzer-Nabil Adam, Eric Verney, Souad Kirouane, Bruno Sauviac, Soultan Malloum,

Application of teaching learning based optimization in antenna designing (pp. 43)
Surabhi Dwivedi, Vivekanand Mishra, Yogesh Kosta,

Finite element simulation for cylindrical invisibility cloaking using linear transformation optics (pp. 49)
Karim Atallah, Kareem El Assy, Xue-Feng Zhu, Mohamed Badr, Nourhan Rasheed, Khaled Galal, Eslam Magdy,

Superposing Lorentzian resonance functions towards engineering target responses (pp. 53)
Christopher Dirdal, Johannes Skaar,

Distinction of opto-electronic properties between random and ordered nano-holed layers (pp. 59)
Mikita Marus, Aliaksandr Hubarevich, Wang Hong, Eugeny Muha, Aliaksandr Smirnov, Sun Xiaowei, Fan Weijun,

Plasmon coupling in three-dimensional magnetic SRR metamolecules (pp. 63)
Wei-Lun Hsu, Wei-Yi Tsai, Pin Chieh Wu, Wei Ting Chen, Yao-Wei Huang, Chun Yen Liao, Ai Qun Liu, Greg Sun, Din Ping Tsai,

Plasmonics and nanophotonics

Doped metal-LiNbO3-metal plasmonic waveguides (pp. 67)
Montasir Qasymeh,

A CMOS-compatible platform based on metal-dielectric-Si hybrid plasmonic waveguide for integrated plasmonic circuits (pp. 72)
Shiyang Zhu, Guo-Qiang Lo, Dim-Lee Kwong,

Tuning the dispersion relation of a plasmonic waveguide via graphene contact (pp. 80)
Yu Zhou, Cheng Wang, Di-Hu Xu, Ren-Hao Fan, Ru-Wen Peng, Qing Hu, Mu Wang,

Retroreflection of light from nanoporous InP: Correlation with high absorption (pp. 85)
Sergey Prislopski, Elena Naumenko, Ion Tiginyanu, Lidia Ghimpu, Eduard Monaico, Lilian Sirbu, Sergey Gaponenko,

SERS scaling rules (pp. 89)
Yoshiaki Nishijima, Yoshiakazu Hashimoto, Lorenzo Rosa, Jacob Khurgin, Saulius Juodkazis,

Engineering gold alloys for plasmonics (pp. 93)
Yoshiaki Nishijima, Yoshiakazu Hashimoto, Gediminas Seniutinas, Lorenzo Rosa, Saulius Juodkazis,

Propagation characteristics of Plasmonic waveguides (pp. 98)
Padmaja Bhanu Bandaru, R. Shevgoankar, A. Chandorkar,

Impact of process factors on the performance of hole-array metallic filters (pp. 101)
Romain Girard Desprolet, Sandrine Lhostis, Charlotte Beylier, Vincent Farys, Guy Vitrant, Salim Boutami,

Plasmon-enhanced photovoltaics, photocatalysis, and solar fuels

CuInS2 solar cell absorber plasmonically modified by gold nanoparticles (pp. 108)
Taavi Repan, Leonid Dolgov, Atanas Katerski, Ilona Oja Acik, Erki Karber, Arvo Mere, Valdek Mikli, Malle Krunks, Ilmo Sildos,

Nanobiophotonics

Volatile Organic Compounds (VOCs) detection with surface enhanced Raman scattering (SERS) based on plasmonic bimetallic nanogap substrate (pp. 113)
Chi Lok Wong, U. S. Dinish, Kavitha Devi Buddharaju, Malini Olivo,

Near-field optics and nano-optics

Far-field flat lens based on multilayered metal- dielectric structure (pp. 119)
Vladimir Belyi, Mohammed A. Binhussain, Nikolai Khilo, Nikolai Kazak,

Transformational electromagnetics

Asymmetric cloaking theory based on effective electromagnetic field for photon (pp. 125)
Masato Taki, Tomo Amemiya,

Photonic crystals

Study on modulating properties of magnetic defect in photonic crystal in terahertz region (pp. 131)
Hui Zhang, Xian-feng Xu, Shengjiang Chang, Cuiping Jia, Zhiyong Jiao,

Two dimension photonic crystal Y-branch beam splitter with variation of splitting ratio based on hybrid defect controlled (pp. 136)
Teanchai Chantakit, Keerayoot Srinuanjan, Preecha P. Yupapin,

Non-reciprocal transmission of terahertz waves through a photonic crystal cavity with graphene (pp. 142)
Yu Zhou, Ye-Qing Dong, Ru-Wen Peng, Qing Hu, Mu Wang,

Optical properties of metamaterial based devices modulated by a liquid crystal (pp. 147)
Filiz Karaomerlioglu, Amirullah Mamedov, Ekmel Ozbay,

Numerical study on the structural color of blue birds by a disordered porous photonic crystal model (pp. 153)

Tsuyoshi Ueta, Garuda Fujii, Gen Morimoto, Kiyoshi Miyamoto, Akinori Kosaku,

FSS, HIS and Extraordinary transmission

Analysis of periodic strong chiral - metamaterial structures as frequency selective surfaces and polarization rotators using transfer matrix method (pp. 158)
M. J. Mughal, S. K. Marwat, N. Amin, M. Omar,

Analytical and numerical modelling

A Bloch mode expansion approach for analyzing quasi-normal modes in open nanophotonic structures (pp. 164)
Jakob Rosenkrantz de Lasson, Philip Trost Kristensen, Jesper Mork, Niels Gregersen,

Equivalent circuit model of Jerusalem cross FSS using vector fitting (pp. 167)
Payal Majumdar, Zhiya Zhao, Ruopeng Liu, Chunlin Ji,

Electromagnetic small-scale modeling of composite panels involving periodic arrays of circular fibers (pp. 170)
Changyou Li, Dominique Lesselier, Yu Zhong,

Scattering characteristics of structures of lossy metamaterial-semiconductor cylinders (pp. 176)
Juozas Bucinskas, Liudmila Nickelson, Romanas Martavicius,

Level set-based topology optimization for whispering gallery mode resonator circuits incorporating surface effects (pp. 182)
Garuda Fujii, Tsuyoshi Ueta, Mamoru Mizuno, Masayuki Nakamura,

Characterization of blade bragg grating modeling with different incident angle profiles for strain sensor applications (pp. 187)
Niparat Cheamanunkul, Keerayoot Srinuanjan, Preecha P. Yupapin,

Improved analytical model for short-wire metamaterials (pp. 191)
Zahra Mostajabi, Jalil-Agha Rashed-Mohassel, Leila Yousefi,

Electromagnetic field and dispersion characteristic analysis of absorbing onion-like carbon tube waveguides (pp. 195)
Liudmila Nickelson, Arturas Bubnelis, Romanas Martavicius, Steponas Asmontas,

Investigation of surface roughness influence on hyperbolic metamaterial performance (pp. 200)
Serge Kozik, Mohammed Binhussain, Andrei Smirnov, Nikolai Khilo, Vladimir Agabekov,

Technologies and applications: micro and nanofabrication, active plasmonic components, cloaking, absorption, plasmon

NiZn ferrite/Fe hybrid epoxy-based composites: Extending magnetic properties to high frequency (pp. 205)
Yunqi Wang, Patrick Grant,

A study of metamaterial absorber based on circular ring structure with and without copper lines (pp. 211)
Osman Ayop, Mohamad Kamal A. Rahim, Noor Asniza Murad,

Compact wideband antenna above a wideband non-uniform artificial magnetic conductor (pp. 214)
Lana Damaj, Anne Claire Lepage, Xavier Begaud,

Keynote presentations

Light harvesting with metasurfaces: Applications to sensors and energy generation (pp. 221)
David Crouse, Eli Lansey, Isroel Mandel, Ian Hooper,

Metasurfaces at Terahertz, Infrared and Optical Frequencies

Programmable terahertz metamaterials through V-beam electrothermal devices (pp. 229)
Antonios Lalas, Nikolaos Kantartzis, Theodoros Tsiboukis,

Transformation Electromagnetics concepts and applications

Antipodal radiation pattern of a patch antenna combined with superstrate using transformation electromagnetics (pp. 236)
Mark Clemente Arenas, Anne Lepage, Xavier Begaud,

Metamaterial-based radiating and absorbing structures

On-metal UHF-RFID tags based on non-bianisotropic complementary split ring resonators (pp. 242)
Simone Zuffanelli, Gerard Zamora, Ferran Paredes, Pau Aguila, Ferran Martin, Jordi Bonache,

Resistive high-impedance surfaces (RHIS) as absorbers for oblique Incidence electromagnetic waves (pp. 247)
Yenny Pinto, Julien Sarrazin, Anne Claire Lepage, Xavier Begaud, Nicolas Capet,

Design and model of wideband absorber made of ultrathin metamaterial structures (pp. 252)
Alexandre Sellier, Tatiana Teperik, Shah Nawaz Burokur, Guy Sabanowski, Gerard-Pascal Piau, A. de Lustrac,

Hyperbolic metamaterials

Tailoring radiation patterns in planar RF metamaterials (pp. 260)
Polina Kapitanova, Alena Shchelokova, Dmitry Filonov, Alexander Poddubny, Pavel Ginzburg, Anatoly Zayats, Pavel Belov, Yuri Kivshar,

New Materials for Plasmonics and Photonic Metamaterials

Design of ultracompact electroabsorption based on novel CMOS-compatible plasmonic materials (pp. 264)
Shiyang Zhu, Guo-Qiang Lo, Dim-Lee Kwong,

PT-symmetry in photonics, metamaterials and plasmonic systems

Practical limitation on operation of nonlinear parity-time Bragg gratings (pp. 270)
Sendy Phang, Ana Vukovic, Hadi Susanto, Trevor Benson, Phillip Sewell,

Parity-time symmetric cloak with one-way invisibility (pp. 276)
Xue-Feng Zhu, Liang Feng, Peng Zhang, Xiaobo Yin, Xiang Zhang,

Bionanoplasmonics

New SERS-active junction based on cerium dioxide facet dielectric films for biosensing (pp. 281)
Ilya Kurochkin, Ilya Ryzhikov, Andrey Sarychev, Konstantin Afanasiev, Igor Budashov, Marina Sedova, Irina Boginskaya, Sergey

Amitonov, Andrey Lagarkov,

New horizons for NTA: scattering labelling of soft particles (pp. 285)
Evgeniy Evtushenko,

Superconducting and Quantum Metamaterials

Wide-Band tuneability, nonlinear transmission, and dynamic multistability in SQUID metamaterials (pp. 289)
George Tsironis, Nikos Lazarides, I. Margaris,

Numerical Modeling Techniques for Metamaterials

Approximation of transformation media-based reshaping action by genetic optimization (pp. 300)
Ozlem Ozgun, Mustafa Kuzuoglu,

Automated synthesis of transmission lines loaded with complementary split ring resonators (CSRRs) and open complementary split ring resonators (OCSRRs) through aggressive space mapping (ASM) (pp. 305)
Jordi Selga, Ana Rodriguez, Marco Orellana, Vicente Boria, Ferran Martin,

Design of 2D and 3D isotropic transformation media for light management (pp. 313)
Carlos GarciaÂ-a-Meca, Alejandro Martinez,

Photonic Crystals (Theory and Applications)

A band structure calculation method for one-dimensional photonic crystals based on time integration and matrix-exponential decomposition (pp. 321)
Xiao-Xing Su, Chuanzeng Zhang, Yue-Sheng Wang,

Flexible Ag electrode for quantum dot light-emitting diode (pp. 327)
Jing Chen, Zhi Li, Jiangyong Pan, Qingguo Du, Wei Lei,

Active and Tunable Metamaterials

Tunable terahertz metamaterials by means of piezoelectric MEMS actuators (pp. 331)
Antonios Lalas, Nikolaos Kantartzis, Theodoros Tsiboukis,

Graphene-based electrically reconfigurable deep-subwavelength metamaterials for active control of THz light propagation (pp. 336)
Sara Arezoomandan, Kai Yang, Berardi Sensale-Rodriguez,

Resonant dielectric nanostructures and metamaterials

A sensitive sensor with a double U-shaped rings-based metamaterial (pp. 341)
An Yang, Changchun Yan, Jie-Bing Tian, Cheng Wang, Ying Han, Dao Hua Zhang, Dongdong Li, Zhengji Xu,

Metamaterials and negative index materials

Complementary electric-LC resonator antenna for WLAN applications

Bashir D. Bala, Mohamad Kamal B. A. Rahim, Noor Asniza Murad,

Communication Engineering Department, Faculty of Electrical Engineering,
Universiti Teknologi Malaysia (UTM), 81310, Johor Bahru, Malaysia

bashirdbala@yahoo.com, mkamal@fke.utm.my, asniza@fke.utm.my

Abstract

In this paper, a metamaterial antenna based on complementary electric-LC (CELC) resonator is proposed. The antenna consists of slot loaded ELC on the ground plane as the main antennas radiating element and excited by a microstrip line. The peak realized gain and efficiency of 2.63 dB and 86% are obtained respectively at resonance frequency. Simulation and measurement results are presented to validate the design. The antenna is suitable for WLAN applications (2.39 GHz-2.48 GHz).

1. Introduction

Recently, metamaterials with both double negative (DNG) and single negative (SNG) constitutive parameters have been widely used in antenna designs [1]. Resonant structures such as electric inductive-capacitive loaded resonator (ELC) and its complementary counterpart (CELC) are the main building blocks of the metamaterials. ELC and CELC has been known to have electric and magnetic response respectively when used to design periodic structures such as photonic band gap, absorbers, phase shifters [2] and defected ground planes [3]. Several studies shows the ELC and CELC can be used to design single and multiband antennas when excited by a monopole or patch antenna or when employ as a parasitic element to enhanced antennas performance [4], [5]. In [4] a triple band antenna was obtained by loading ELC as a parasitic element at the back of a printed monopole, the response is due to the monopole itself and the ELC loading. In [5] the CELC resonator is excited by monopole. However, it is very difficult to obtain their accurate equivalent circuit models since the antenna response is dependent on parasitic and the main radiating element.

In this paper, a CELC resonator is employed as the main antenna radiating element excited by a microstrip feed line. The equivalent circuit model of the CELC is obtained based on its physical dimensions. Circuit and electromagnetic simulations are compared. The antenna is designed to operate at 2.42 GHz for WLAN operation (2.39 GHz- 2.48 GHz.

2. Antenna Design

The geometry of the proposed slot metamaterial antenna is shown in Figure 1. The antenna consists of CELC resonator loaded on the ground plane and feed by a 50Ω microstrip line at the top. The antenna is fabricated on Taconic substrate of permittivity 3.5, tangential loss of 0.0018 and thickness of 1.52 mm. The size of the antenna is Lg = 40mm x Wg = 40 mm. Table 1 shows the geometrical dimensions of the CELC resonator. Figure 2 shows the equivalent circuit model of the CELC resonator. The CELC resonator can be modeled by a shunt resonant tank (L_m x C_m) in series with inductance (L) of the ground plane and gap capacitance (C) between the outer and inner slot of the ground plane. L_m is the inductance of the stub L1 connecting the upper and lower arm of CELC and C_m is the gap capacitance due to slot g1between upper and the lower arm. L is the inductance of the outer ground plane and C is the capacitance due to g2. The determined values from the equivalent elements are C_m = 0.965 pF, L_m = 6.05 nH, L = 10.1 nH, and C =2.5 pF. The resonance frequency of the CELC resonator is given by:

$$f_r = \frac{1}{2\pi\sqrt{L_m C_m}} \tag{1}$$

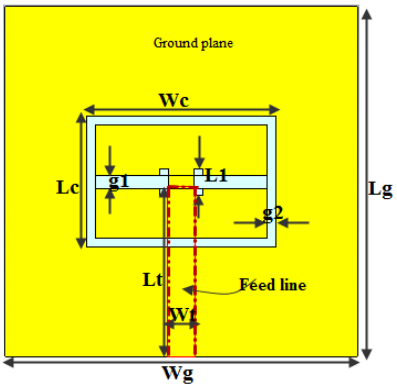

Figure 1: Geometry of the proposed MTM antenna.

Table 1: Geometrical dimension of CELC resonator

Geometrical Parameters of CELC (mm)						
Lt	Wt	Lc	Wc	L1	g1	g2
19.5	3.2	15	21.5	3.0	1.5	1.0

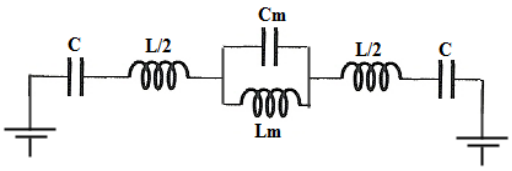

Figure 2: Equivalent circuit model of the CELC resonator.

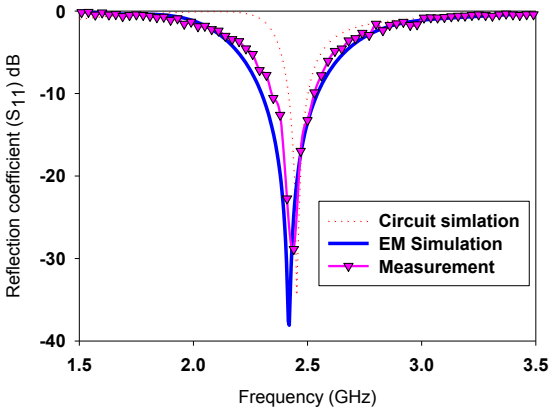

Figure 3: Reflection coefficient (S_{11}) dB

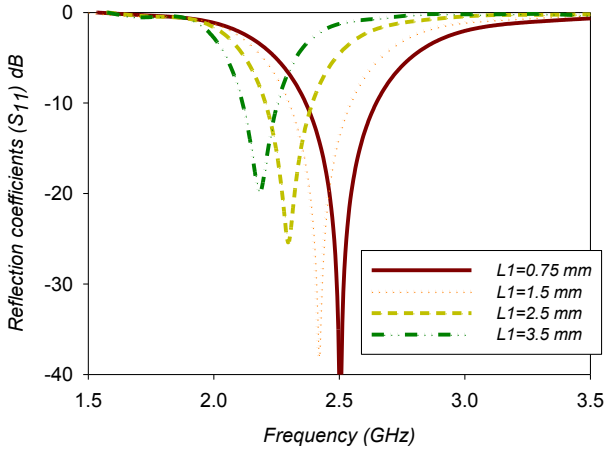

Figure 4: Effect of shunt inductance Lm on resonance frequency

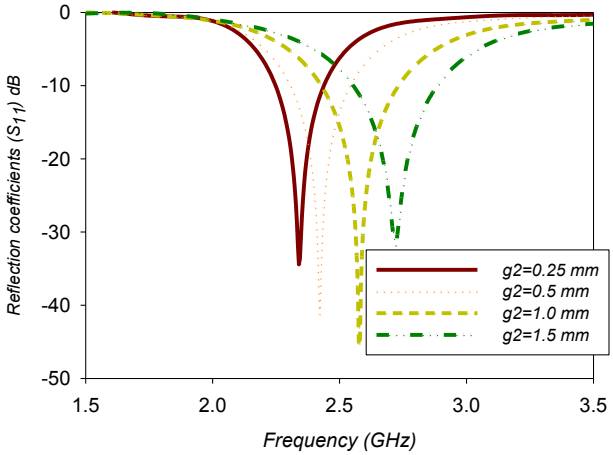

Figure 5: Effect of the capacitance C on resonance frequency

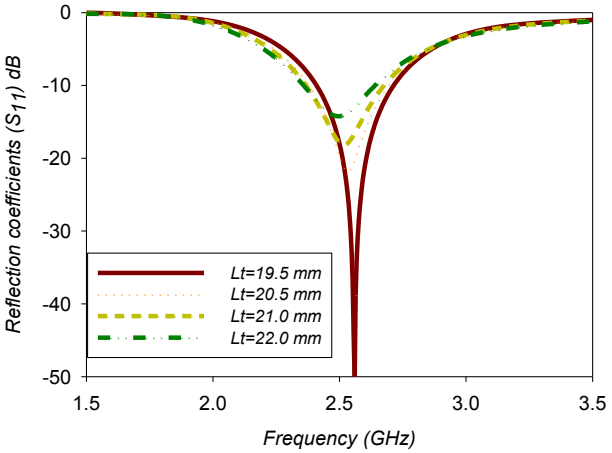

Figure 6: Effect of the length Lt of the feed line on impedance matching

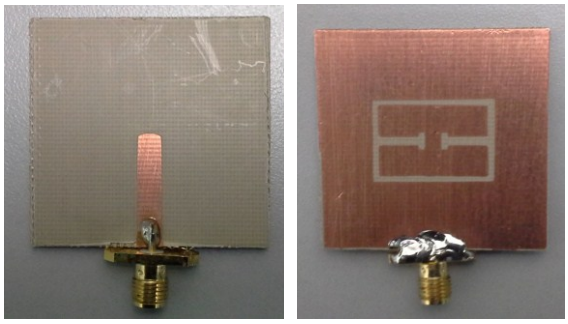

(a) (b)

Figure 7: Fabricated antenna (a) Front view (b) Back view

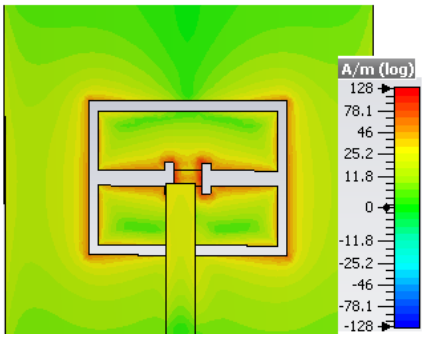

Figure 8: Surface current distribution

3. Discussion

The reflection coefficient of the proposed antenna is shown in Figure 3. The antenna resonates at 2.42 GHz. There is good agreement between the circuit simulation, electromagnetic simulation and measured results. The design is optimized and parametric studies have been conducted. Figure 4 shows the effect of shunt inductance Lm on the resonance frequency. The resonance frequency

decreases with increase in the length L1 of the shunt inductor while the effect of the capacitance C on the resonance frequency is shown in Figure 5. For a good impedance matching the size of the feed line is optimized as shown in Figure 6. The fabricated prototype is shown in Figure 7. Surface current distribution is shown in Figure 8 with strong current distribution around the CELC resonator indicating it is main antennas resonating element. Simulated and measured radiation patterns for both E- and H-plane are shown in Figure 9. Directional and omnidirectional patterns are obtained for E and H-plane respectively. Figure 10 show the peak realized gain and radiation efficiency. The gain is low due to the slots on the ground plane. A reflector is put at a quarter wavelengths from the ground plane to reflect back incidence wave and hence the gain of the antenna improved from 2.63 dB to 6.48 dB at 2.42 GHz. A radiation efficiency of 86% is also obtained at resonance frequency.

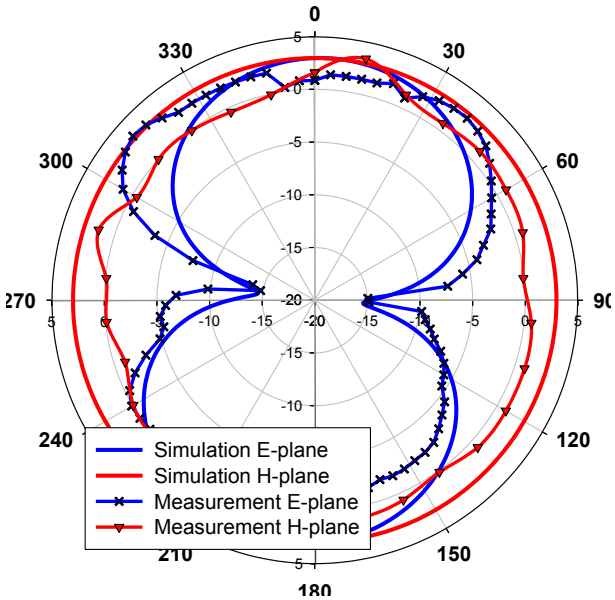

Figure 9: Radiation patterns

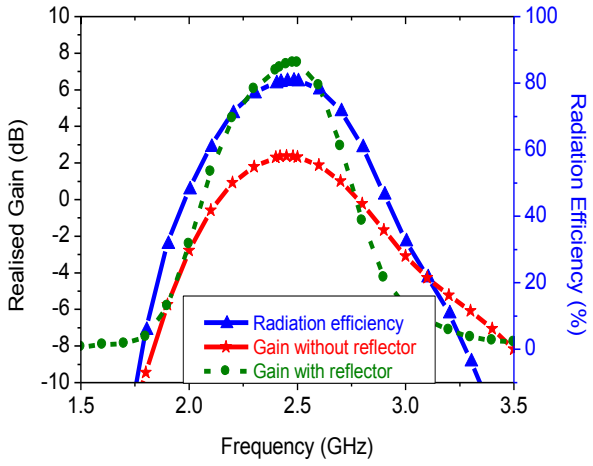

Figure 10: Realized gain and efficiency

4. Conclusions

A metamaterial antenna based on complementary electric-LC (CELC) resonator is presented. The antenna consists of slot loaded ELC on the ground plane as the main antennas radiating element and excited by a microstrip line. A peak realized gain of 6.48 dB is obtained when a reflector is put at a quarter wavelength distance from the ground plane. A radiation efficiency of 86% is obtained at 2.42 GHz. Simulation and measurement results are presented to validate the design. The antenna is suitable for WLAN applications (2.39 GHz-2.42 GHz).

Acknowledgements

This work was supported by Ministry of Higher education (MOHE), Research Management Centre (RMC), Universiti Teknologi Malaysia (UTMJB) Johor Bahru, under research grant no R.J130000.7923.4S007, 04H38 and 4L811

References

[1] Y. H. Xie, C. Zhu, L. Li, and C. H. Liang, "A novel dual-band metamaterial antenna based on complementary split ring resonators," *Microwave and Optical Technology Letters*, vol. 54, no. 4, pp. 1007–1009, 2012.

[2] M. Lu, J. Y. Chin, R. Liu, and T. J. Cui, "A microstrip phase shifter using complementary metamaterials," in *2008 International Conference on Microwave and Millimeter Wave Technology*, 2008, vol. 2, no. c, pp. 1569–1571.

[3] J.-I. Park, C.-S. Kim, J. Kim, J.-S. Park, Y. Qian, and T. Itoh, "Modeling of a photonic bandgap and its application for the low-pass filter design," in *Asia-Pacific Conference on Microwave (APMC 1999)*, pp. 331–334.

[4] K. Li, C. Zhu, L. Li, and Y. Cai, "Design of electrically small metamaterial antenna with ELC and EBG loading," *IEEE Antennas and Wireless Propagation Letters*, vol. 12, pp. 678–681, 2013.

[5] H. Odabasi, F. L. Teixeira, and D. O. Guney, "Electrically small, complementary electric-field-coupled resonator antennas," *Journal of Applied Physics*, vol. 113, no. 8, p. 084903, 2013.

Antenna optimization using metamaterial cover

Surabhi Dwivedi*[1], Vivekanand Mishra[1], Yogesh P. Kosta[2],

[1]Sardar Vallabhbhai National Institute Of Technology, Surat, Gujarat, India
[2]Marwadi Education Foundations Group of Institutions,Rajkot, Gujarat
*corresponding author, E-mail: sur_2310@yahoo.co.in

Abstract

Metamaterials are materials typically engineered with artificial structures to produce electromagnetic properties that are difficult to obtain in nature. They provide engineerable permittivity, permeability, and index of refraction, and hence have drawn broad interest in the field of overall antenna size miniaturization. They have also led to possible utilization in many electromagnetic applications from the microwave to optical regime. Microstrip patch antenna suffers from the limitations like low gain and low directivity. Metamaterial cover which acts as a lens can effectively enhance the directivity of the microstrip patch antenna.

1. Introduction

Metamaterial are exotic composite materials that display properties beyond those available in naturally occurring materials. Instead of constructing materials at the chemical level, these are constructed with two or more materials at the macroscopic level. One of their defining characteristics is that the electromagnetic response results from combining two or more distinct materials in a specified way which extends the range of electromagnetic patterns because of the fact that they are not found in nature [1]. Metamaterials gain their properties not from their composition, but from their exactingly-designed structures. Their precise shape, geometry, size, orientation and arrangement can affect the waves of light or sound in an unconventional manner, creating material properties which are unachievable with conventional materials.

In 1968, V. G. Veselago put forward the concept of a medium having simultaneously negative permittivity and permeability [2]. In his article, he believed that such medium was allowed by Maxwell equations, and would have an interesting and unusual electrodynamics property: negative refraction ($n < 0$). The medium with such property is also called Negative Index Materials (NIM). There is no known material with simultaneously negative permittivity and permeability existing in nature.

In a conventional medium, traveling planar wave can be described by electric field intensity vector E, magnetic field intensity vector H, and wave vector k, which follow a right-handed triplet, so conventional medium is also called Right-Handed Medium (RHM). However, in DNG medium, E, H, and k form a left-handed triplet. Though, E, H, and k follow left-hand rule in NIM, the Poynting vector s, which describes the energy flow direction maintains right hand relationship with E and H. In NIM, the wave vector k is anti-parallel to the Poynting vector s.

2. Retrieval of negative parameters

J. B. Pendry proposed a Split-Ring Resonators (SRRs) design [3], which can provide negative permeability (μ) around its resonance frequency (w_m). Together, with a continuous wires array [4] which gives negative permittivity (ϵ) up to the plasma frequency (w_p), due to the plasmas response, the composite structure, SRRs plus wires give a negative refractive index (n).

2.1. Negative permittivity medium

All the metals, have negative permittivity up to the plasma frequency. However, the usage of solid metal in metamaterials is limited by the fact that the absolute value of the negative is too large at the target frequency, i.e., from microwave to optical frequency. So, one must determine a method to scale the value of ϵ to a reasonable value of the order of -1. Usually the permittivity of a metal can be described by the Drude model [5],

$$\epsilon(w) = 1 - \frac{w_p^2}{w(w + iw_c)} \tag{1}$$

where w_c is the damping frequency, and w_p is the plasma frequency given by

$$w_p^2 = \frac{n_e^2}{\epsilon_0 m_{eff}} \tag{2}$$

where w_p corresponds to the typical electrostatic oscillation frequency in response to a small charge seperation, n_e is the electron density, e is the electric charge, ϵ_0 is the permittivity of free space and m_{eff} is the effective mass of free electrons. Plasma frequency is extremely high in metals, e.g., silver has $w_p = 2\pi \times 2184$ THz and $w_c = 2\pi \times 4.35$ THz. As a result, the absolute value of permittivity is extremely large, $Re(\epsilon) < -10^8$, and, therefore, not suitable for metamaterials.

Pendry proposed a wire array design, which can significantly decrease the plasma frequency and realize negative permittivity $\epsilon \approx -1$ at microwave frequencies. Moreover, the value of ϵ and the frequency are completely controllable via the geometrical parameters [4]. The wire array structure

consists of periodically arranged "infinite" long wires with separation, a, and radius, r. The effective permittivity of wire arrays is similar to the permittivity in bulk metal, except the plasma frequency is much lower.

$$w_p^2 = \frac{2\pi c_0^2}{a^2 \ln(a/r)} \tag{3}$$

One can see that the plasma frequency, w_p, only depends on the radius of wire, r, and the lattice constant, a, as c_0 i.e. speed of light is the constant quantity. By changing these geometric parameters, one can control the plasma frequency and therefore control the value of the permittivity.

2.2. Negative permeability medium

Pendry proposed a split ring resonator (SRR) design [3], which can provide a narrow frequency band with negative permeability under certain polarization of incident EM wave. The SRR arrays consist of periodically arranged arrays of double split ring structures, made from good conductors such as copper, with the lattice constant, a. If we apply an incident EM wave with a magnetic field, H, perpendicular to the plane of SRR, circular currents will be induced on both the inner and outer rings, and also charges will accumulate across the gaps in both the inner and outer rings, respectively. Thus, each individual SRR acts as a series LRC circuits with the inductance, L, of the rings and the capacitance, C, between the two rings [6]. With combines LC effect, Pendry showed that the effective permeability, μ_{eff}, can be approximated as,

$$\mu_{eff} = 1 - \frac{\pi r^2/a^2}{1 + \frac{2\sigma i}{wr\mu_0} - \frac{3dc_0^2}{\pi^2 w^2 r^3 \epsilon_r}} \tag{4}$$

where w is angular frequency, σ is conductivity, μ_0 is the permeability in vacuum ,c_0 is the speed of light, ϵ_r is the permittivity of substrate , r is the radius of split ring, a is the spacing distance between rings, and d is distance between inner and outer rings.

2.3. Retrieval method

The retrieval method used here is based on the approach used by Xudong Chen et al in [7], where the S-parameters are defined in terms of the reflection and transmission coefficients as $S_{11} = R$ and $S_{21} = Te^{ik_0 d}$.

where k_0 is the wave number in free space and d is the thickness of the material being examined. The impedance Z and the refractive index n are,

$$z = \sqrt{\frac{(1+S_{11})^2 - S_{21}^2}{(1-S_{11})^2 - S_{21}^2}} \tag{5}$$

$$n = \frac{1}{k_0 d}\{[Im[\ln(e^{ik_0 d})] + 2m\pi] - j[Re[\ln(e^{ik_0 d})]]\} \tag{6}$$

The permittivity (ε) and permeability (μ) are then directly calculated from $\mu = nz$ and $\varepsilon = n/z$.

3. Antenna design with metamaterial cover

Negative parameters are retrieved by inserting unit cell within a waveguide structure as shown in Figure 1. The values of reflection and transmission parameters can be obtained from the model shown in Figure 1 and permittivity and permeability values can be found out by the above mentioned formulae by calculating the values of impedance and refractive index from Equations 5 and 6, respectively.

In order to study the metamaterial properties in a waveguide, a unit cell is identified from the full size structure and placed in a waveguide to collect the S-parameters . The unit cell for the LHM is shown in Figure 1. The unit cell here is modeled with PEC material, and the background as air. The top and bottom surface has PMC boundary conditions, whereas the left and right has perfect electric conductor (PEC) boundary conditions and front and back as open boundary condition. A waveguide port is placed at the open boundaries.

The S parameters for the unit cell are computed using HFSS Ansoft, a commercial finite-element-based electromagnetic mode solver. Both the S parameters and the retrieved material parameters are presented below. Figure 2 and Figure 3 show the magnitude and phase of the computed S parameters respectively. The dip in the phase of S_{21}, which indicates the presence of a negative index band.

The permittivity (ε) and permeability (μ) are then directly calculated from $\mu = nz$ and $\varepsilon = n/z$. Hence, the plot for negative refraction and impedance obtained from these formulae are depicted in Figure 4 and Figure 5. Finally, Figure 6 shows the permittivity and Figure 7 shows the permeability which, when both are negative at a given frequency, results in a negative refractive index for that given frequency.

The retrieved refractive index in Figure 4 confirms the negative index band that lies between roughly 2.5 to 3 GHz. This material condition is desirable for many applications because it represents a matched case. In other words, if the wave is traveling from a material with a refractive index of one into a medium with a refractive index of negative one, then there will be no reflections and also it has focusing effect. Reflections are generally undesirable because we normally want as much power as possible to be delivered from the transmitting antenna to the receiving antenna.

Now as depicted from the plots shown above that the proposed structure behaves as metamaterial, as it shows negative refraction in the frequency band of 2.5 to 3 GHz. Hence, an array of unit cell is developed as a cover over the patch as shown in Figures 8 and Figure 9 to improve performance parameters of the microstrip patch antenna mainly directivity.

4. Simulation and results

Ansoft HFSS software is used to model and simulate the microstrip patch antena. High frequency structure simulator (HFSS) has been widely used in design of patch antenna,

microwave filters and other microwave components. It can be used to calculate and plot S-Parameters (S11 and S22), Voltage Standing Wave Ratio(VSWR), bandwidth ,gain and directivity etc. Based on the simplified formulation that has been described, a design procedure is outlined which leads to design of rectangular microstrip patch antennas with coaxial feeding. The essential design parameters for the design are: f_0=2.5 GHz ,ϵ_r=4.4 , h=1.56 mm and thickness of copper layer is taken as 0.0175 mm.

Hence the improved return loss, VSWR and directivity patterns are shown in Figure 10, Figure 11 and Figure 12 respectively.

5. Applications and future prospects

Alu et al. had stated various applications of metamaterial and metamaterial cover [8, 9, 10, 11]. In 2005, he had given the very important concept of achieving transparency with plasmonic and metamaterial coatings [8, 9].Chen et al. in 2006 proposed controllable left-handed metamaterial and its application to a steerable antenna [12]. Silveirinha et al. developed parallel-plate metamaterials for cloaking structures [11]. The applications of microstrip patch with metamaterial cover includes aircraft, radar, navigation, missiles, telemetry, satellites, remote sensing radars, biomedical systems, intruder alarms and many more. Later in the year 2008, researchers have proposed metamaterial cloaking [10].

6. Conclusion

In this paper, thorough survey on metamaterial and metamaterial cover over the microstrip patch antenna is made and presented. Recent works in this area of antenna designing is reviewed using radome structure. We examined structural characteristics of metamaterial, concept of plasma frequency, relation of substrate and patch dimensions and retrieval of negative parameters in detail. A survey is made on theoretical, analytical, numerical analysis, designing and modeling of the metamaterial cover over the patch. Metamaterial cover opens the new gateway of research as it has compact size, convenient fabrication procedures and low cost. There are still some topics worthy to explore, such as fabrication procedures, characterizations etc.

Acknowledgement

The current team of authors would like to thank Dr. Ved Vyas Dwivedi for his technical guidance.

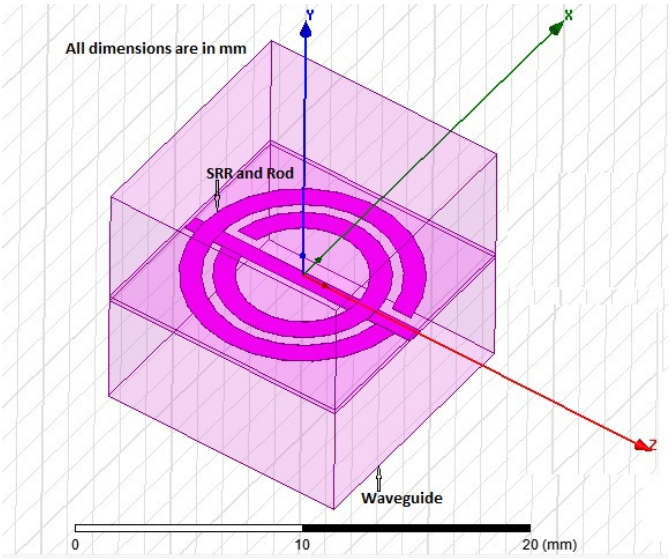

Figure 1: Unit cell within a waveguide structure

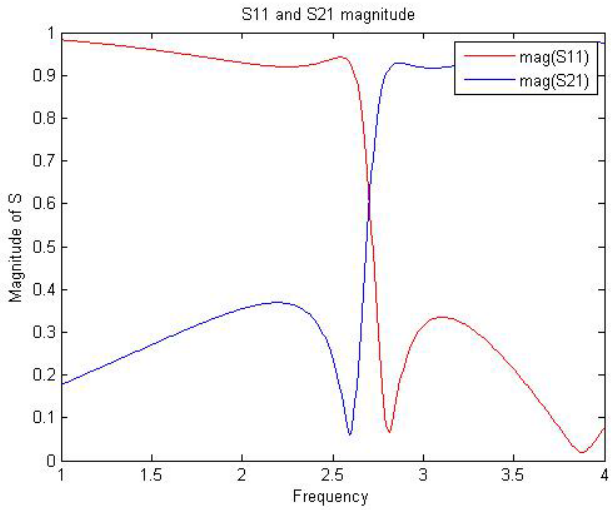

Figure 2: Magnitude of the simulated S parameters

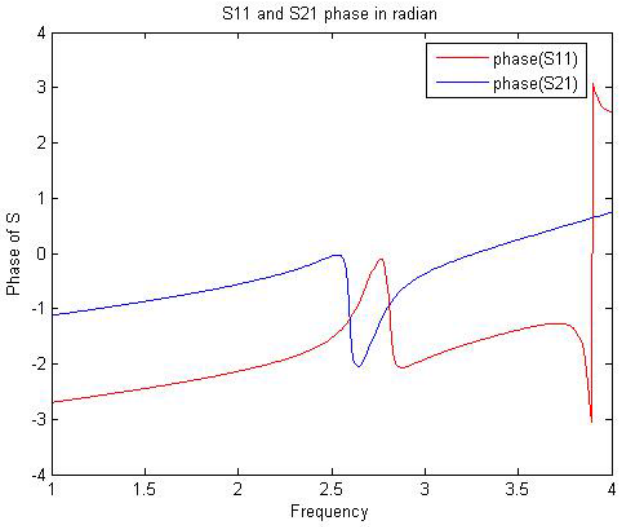

Figure 3: Phase of the simulated S parameters

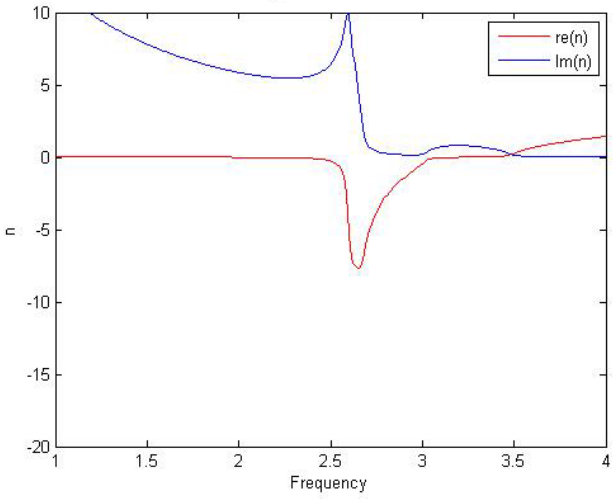

Figure 4: Retrieved negative refraction

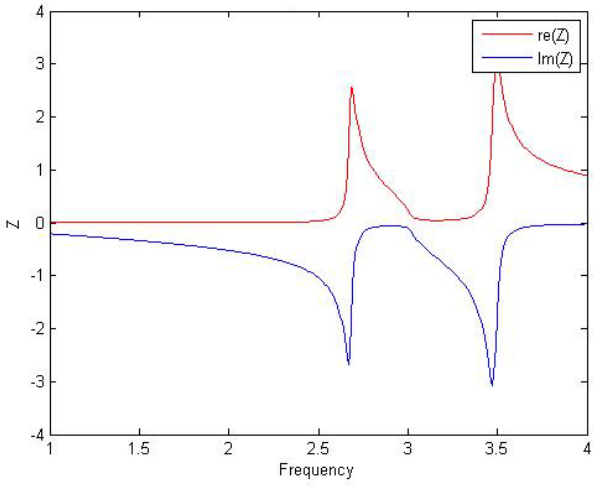

Figure 5: Impedance plot

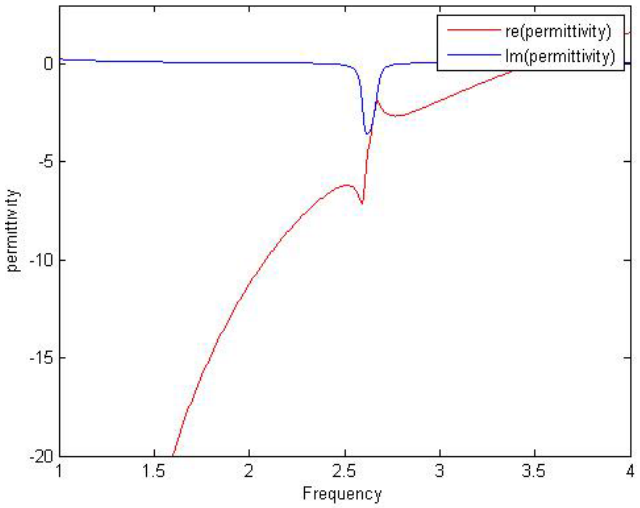

Figure 6: Effective permittivity

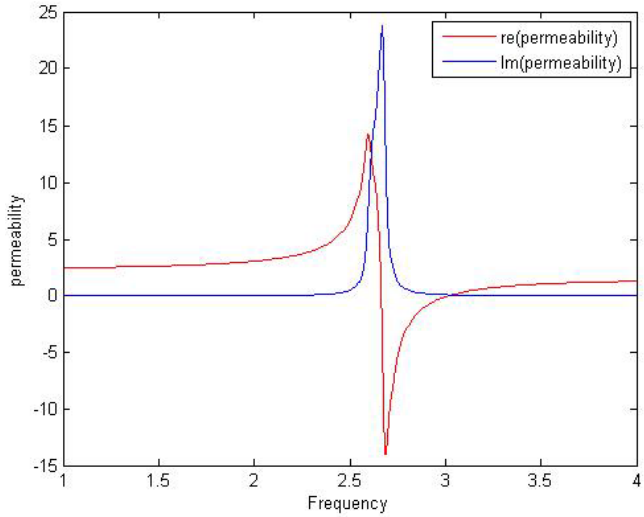

Figure 7: Effective Permeability

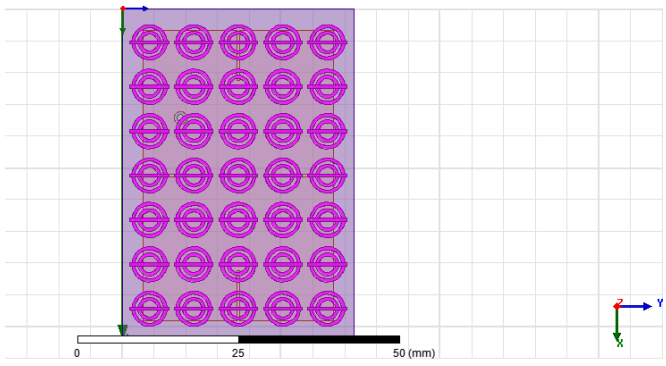

Figure 8: Radome Structure(Top View)

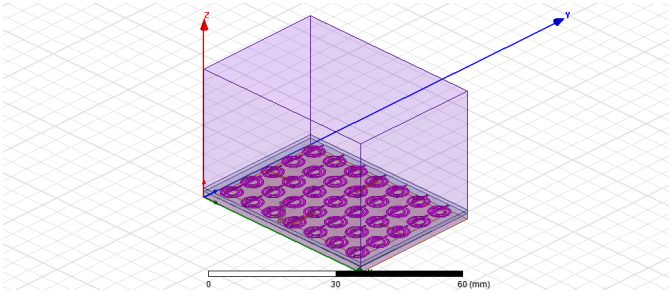

Figure 9: Array of SRR and Rod as patch cover(Isometric View)

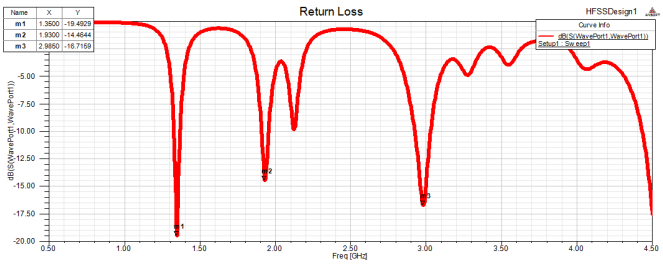

Figure 10: Return Loss of metamaterial cover

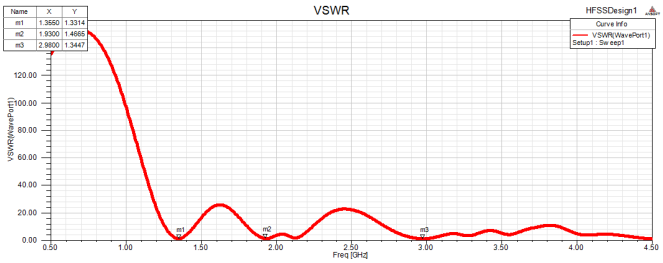

Figure 11: VSWR of metamaterial cover

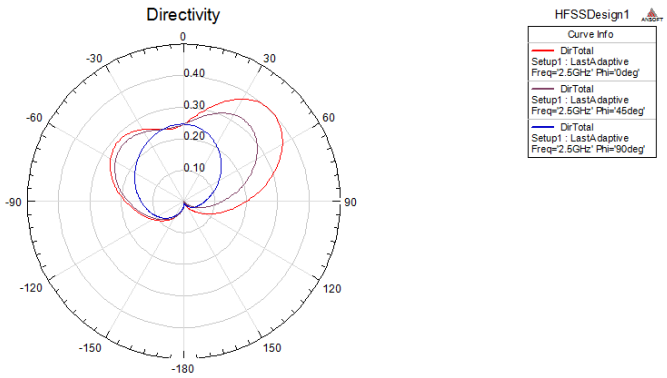

Figure 12: Improved directivity of metamaterial cover

References

[1] N. Engheta and R. W. Ziolkowski, *Metamaterials: physics and engineering explorations*. Wiley. com, 2006.

[2] V. G. Veselago, "The electrodynamics of substances with simultaneously negative values of ϵ and μ," *Physics-Uspekhi*, vol. 10, no. 4, pp. 509–514, 1968.

[3] J. B. Pendry, A. J. Holden, D. Robbins, and W. Stewart, "Magnetism from conductors and enhanced nonlinear phenomena," *Microwave Theory and Techniques, IEEE Transactions on*, vol. 47, no. 11, pp. 2075–2084, 1999.

[4] J. Pendry, A. Holden, W. Stewart, and I. Youngs, "Extremely low frequency plasmons in metallic mesostructures," *Physical review letters*, vol. 76, no. 25, p. 4773, 1996.

[5] J. D. Jackson and R. F. Fox, "Classical electrodynamics," *American Journal of Physics*, vol. 67, p. 841, 1999.

[6] C. Caloz and T. Itoh, *Electromagnetic metamaterials: transmission line theory and microwave applications*. John Wiley & Sons, 2005.

[7] X. Chen, T. M. Grzegorczyk, B.-I. Wu, J. Pacheco Jr, and J. A. Kong, "Robust method to retrieve the constitutive effective parameters of metamaterials," *Physical Review E*, vol. 70, no. 1, p. 016608, 2004.

[8] A. Alù and N. Engheta, "Achieving transparency with plasmonic and metamaterial coatings," *Physical Review E*, vol. 72, no. 1, p. 016623, 2005.

[9] A. Alù, F. Bilotti, N. Engheta, and L. Vegni, "Metamaterial covers over a small aperture," *Antennas and Propagation, IEEE Transactions on*, vol. 54, no. 6, pp. 1632–1643, 2006.

[10] A. Alù and N. Engheta, "Plasmonic and metamaterial cloaking: physical mechanisms and potentials," *Journal of Optics A: Pure and Applied Optics*, vol. 10, no. 9, p. 093002, 2008.

[11] M. G. Silveirinha, A. Alù, and N. Engheta, "Parallel-plate metamaterials for cloaking structures," *Physical Review E*, vol. 75, no. 3, p. 036603, 2007.

[12] H. Chen, B.-I. Wu, L. Ran, T. M. Grzegorczyk, and J. A. Kong, "Controllable left-handed metamaterial and its application to a steerable antenna," *Applied physics letters*, vol. 89, no. 5, pp. 053 509–053 509, 2006.

Electromagnetic Characteristics of Hilbert Curve Based Metamaterials

Ruirui Chen, Sucheng Li, Chendong Gu, Shahzad Anwar, Bo Hou,* and Yun Lai

School of Physical Science and Technology, Soochow University, Suzhou 215006, China
*corresponding author, E-mail: houbo@suda.edu.cn

Abstract

As the typical building blocks of metamaterials, the cut wire and the split ring resonator have been extensively studied in recent years. Besides them, the space-filling curve based metamaterials are receiving great attentions because of their intrinsic subwavelength and multi-bands characteristics. In this work, we have investigated experimentally and numerically the electromagnetic characteristics of such Hilbert curve metamaterial in the microwave frequency regime and found a deeply subwavelength magnetic resonances supported by the fractal pattern and featuring the wavelength-to-size ratio more than 20. The subwavelength electromagnetic properties of the Hilbert curve will be beneficial to realize high-performance metamaterials.

1. Introduction

Resonance is essential to a lot of wave phenomena and wave functional materials, for instance metamaterials [1,2]. Via elaborately designing electromagnetic (EM) resonances of the artificial meta-atoms and packing them into the periodic crystal structures, metamaterials have exhibited many exotic EM characteristics, such as negative index of refraction [3], optical magnetism [4,5], ultrahigh-index dielectrics [6,7], extremely anisotropy [8,9] and even cloaking/illusion [10,12], which have never been found in natural materials. As the typical building blocks of metamaterials, the cut wire and the split ring resonator (SRR) have been extensively studied in recent years [13], and the local resonances supported by both metallic structures endow them with the role of electric and magnetic meta-atoms in constructing metamaterials, respectively. In order to realize the high-performance metamaterials, these meta-atoms should be made as subwavelength tiny as possible.

Due to their intrinsic structures, the purely metallic building blocks cannot give rise to a significant ratio of the operative wavelength over their size (the typical ratio less than 10) without the addition of dielectric substrates. On the other hand, it is well known that a type of significantly subwavelength EM resonators has been employed in designing ultra-compact radio antennas which are from the fractal patterns like Koch curves and Sierpinski gaskets [14-16]. The subwavelength property of the fractal patterns is attributed to their peculiar geometrical structure which is featured by self-similarity or scaling invariance, and enables them as excellent building blocks for metamaterials and photonic applications. Recently the fractal based metamaterials and photonic structures have been investigated because of their appealing subwavelength and multi-bands characteristics and been shown to possess more features in dual-band or multi-band gaps than conventional photonic crystals [17-21].

In this study, we investigated the EM characteristics of metallic Hilbert fractal curves in the microwave frequency domain. The Hilbert curve is a unique type of fractal curve with space-filling property. Its resonant modes were generated by the interaction between electric field and magnetic field after the TEM wave incident normally on the Hilbert structures. We found that the fundamental resonance was induced by magnetic flux. Moreover, we summarized the subwavelength characteristics between the varying fractal order of the samples and the relevant localized resonances.

2. Two-dimensional Hilbert curve

The Hilbert fractal curve is one of the space-filling curves with the deterministic self-similarity features [22]. The first order Hilbert curve covers a unit cell by connecting every center of the square grids with 2×2 section. The center of the 2×2 section is connected between the left bottom and the right bottom in a clockwise direction. The side length of the first-order curve is half of the length in a unit cell. With the increase of the fractal order, the unit cell was divided into $2^N\times2^N$ section (N is the order of Hilbert curve). Draw a single curve with every center of the interval in certain rules until the curve fulfills the whole plane. As a result, the fractal Hausdorff dimension is given by $D_f = \log(n)/\log(1/s)$, where s is the scaling factor and n is the number of self-similar units generated after scaling. Therefore, the first order of the structure has a "Π" shape with three identical lines connected in the x-y plane, as shown in Fig. 1(a). The second order Hilbert curve replaces the first order curve by four "Π" shape, which is connected by three red lines as shown in Fig.1. The length of the shortest line in the second Hilbert curve is half of the first order (that is s=0.5). Note that as the number of orders N approaches infinity, the length of red line is close to zero, and thus the fractal Hasudorff dimension $D_f = \log(4)/\log(1/0.5)=2$. It is necessary to point out that we changed the side length of the curve for the convenience of the research in order to harmonize the unit cell size of the period lattice. Hence, the each order has the same physical size, *i.e.* the side length, equal to a. For the N-level structure, the length of the shortest line is $a/(2^N-1)$ and the number of the shortest

line is counted to be $4^N - 1$. Therefore, the Euclidean total length of Hilbert curve is $L = (2^N + 1)a$. Figure 1 shows the first four levels of geometrical pattern shapes.

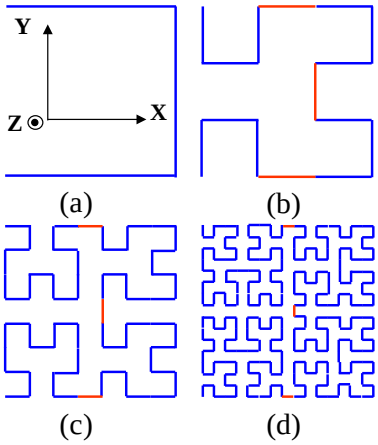

Figure 1: 1-4 orders of Hilbert curves

3. Sample and measurement

The experimental sample was 1-3 orders two dimension (2D) fractal curves with the side length a=30 mm, made of metallic wires with a diameter of 0.5 mm and the conductivity of 5.9×10^7 S/m . The characteristic shortest lines are a, $a/3$, $a/7$ and the total lengths are 90 mm, 150 mm, 270 mm for 1-order, 2-order and 3-order Hilbert curves, respectively. In order to increase the sample cross section so as to facilitate microwave measurements, a 7×7 square lattice comprising 49 fractal units was fabricated, with a lattice constant of 40 mm. Two identical horn antennas were connected with a network analyzer (Agilent N5230C) to generate and receive the electromagnetic waves. The sample was placed between the two antennas and the transmission spectra were detected at normal incidence within frequencies 0.1 GHz-10 GHz. All transmission data were normalized to the free space transmission value. Since the 2D fractal is anisotropic, the transmissions along three incident directions (*X*, *Y*, and *Z*, as shown Fig. 1(a)) were measured, respectively. For each transmission direction, the EM wave was incident normally on the sample array with two orthogonal polarization orientations by adjusting the horn antennas.

Figure 2: Photos of 1-3 orders of Hilbert-curve sample.

The experimental samples are shown in Fig. 2 and the corresponding results are plotted in Figs. 3-5. One can obtain a total of six spectra for all the incident directions and polarizations, but as long as the incident electric field (*E*-field) is oriented along the *Z* axis, the sample will be transparent to EM wave and the transmission is 100%. This is because there is neither electric polarization nor magnetic flux coupling of EM waves to the Hilbert curve. Hence we only plotted the other four transmissions spectra where open symbols denote the experimental results.

4. Results and discussion

The 1st-order fractal structure exhibits a total of four band gaps below the Wood's anomaly (7.5 GHz), as plotted in Fig. 3. In order to get a clear picture of stop band position, the band edge is identified as the frequency where the transmission value is 0.5, and consequently the middle frequency of a stop band can be defined as $f_c = (f_- + f_+)/2$ where f_- and f_+ are frequencies for the lower edge and upper edge, respectively. For the polarization of *E*-field parallel to the *Y*-axis, there are two stop bands at 1.7 GHz and 4.9 GHz, no matter which direction the wave is propagating. In contrast, for the polarization of *E*-field parallel to the *X*-axis, the transmissions differ a lot for two propagation directions. If the wave vector ***k*** is perpendicular to the curve which means the *H*-field is in plane, two stop bands at 3.6 GHz and 6.79 GHz are identified. While the wave vector ***k*** is in plane and the *H*-field is out of plane, we can observe four stop bands which positions coincide with the four frequencies 1.8 GHz, 3.6 GHz, 5.0 GHz, and 6.79 GHz.

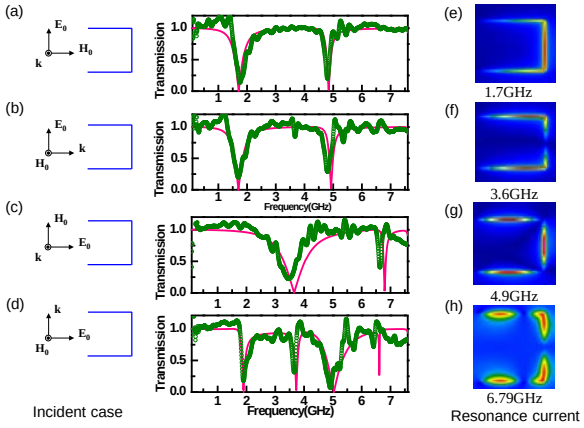

Figure 3: (a)-(d) The transmission spectra of the 1st-order Hilbert curve at four kinds of incidence configurations, as illustrated. (e)-(h) The simulated distributions of current intensity at four band gap frequencies 1.7 GHz, 3.6 GHz, 4.9 GHz, and 6.79 GHz. The red area indicates the maximum current intensity. These frequency values correspond to the minimum transmission positions of the band gaps in the simulation.

To understand such stop bands, the finite-difference time-domain simulation was employed, with periodic and perfect conductor boundary conditions. The simulated results are plotted as solid lines in Fig. 3, which shows good agreement between experiment and simulation results. The simulation results also reveals the distributions of the current intensity on the curve at the transmission dip frequencies for these stop bands, as illustrated in Fig. 3(e)-(h). The current patterns indicate the standing wave resonances on the curve are excited, and these stop bands

correspond to the resonance harmonics of order 1, 2, 3, and 4, featured by the current sections on the curve, respectively. In fact, the 1st-order Hilbert curve may be regarded as SRR and its transmission characteristics are almost identical to those of SRR. When the *E*-field is polarized perpendicular to the symmetric axis of the curve, the harmonics 1 (~1.7 GHz) and 3(~4.9 GHz) are always excited, regardless of the ***k*** direction, as shown in Figs. 3(a) and 3(b). When the *E*-field is polarized parallel to the symmetric axis, the harmonics 2 (~3.6 GHz) and 4 (~6.79 GHz) are always excited, as shown in Fig3(c), 3(d), regardless of the ***k*** direction. However, if ***k*** is in plane and *H*-field is out of plane, the harmonics 1 and 3 can be excited because of the magnetic flux coupling. Thus, all four harmonics are seen in Fig. 3(d) where the *H*-field induces the odd modes and the *E*-field excites the even modes.

Since the 1st-order Hilbert curve is essentially the SRR, these harmonics frequency, f_m may be predicted by the simple standing wave condition [23]

$$f_m = \frac{m}{2}\frac{c}{L}, \qquad (1)$$

where c is the speed of light in vacuum, L is the path length of the curve, and m is positive integer denoting the harmonics order. For the 1st-order curve, $L=3a$, and the four harmonics are predicted to be 1.67 GHz, 3.5 GHz, 5 GHz, and 6.7 GHz, respectively, agreeing well with the experiment and simulation results.

For comparing, we show that the simulation and experiment results of the 2-order curve in Fig. 4. The frequency values from Eq. (1) are 1 GHz, 2 GHz, 3 GHz, 4 GHz, 5 GHz, 6 GHz and 7 GHz below the wood's anomaly for the 2-order Hilbert curve. Comparing to the simulation and measurement results, these frequency values shift slightly, and the frequency difference might come from the ideal condition of half-wave resonance theory requiring the metallic wire is ideally thin or the diameter of the wire is negligible with respect to the length of wire. In the simulations and experiments of the 2-order and 3-order fractal structures, the ratios of the wire diameter over length are equal to 1/20 and 1/8.6, which implies the diameter is not thin enough to be neglected. It is seen that the lowest-frequency resonance mode occurs at the wavelength of 272 mm (at frequency 1.1 GHz in simulation), resulting in the ~2 ratio of the fundamental resonance wavelength over the total wire length (272 mm/150 mm=1.82).

At the same time, the 3-order Hilbert curve results have shown in Fig. 5. The resonance of lowest-frequency is 0.56 GHz and 0.7 GHz from the formula and the simulation, respectively. The ratio between the fundamental resonance wavelength and the wire length is 420 mm/270 mm=1.56.
On one hand, we have noticed that the fundamental resonance would shift towards the lower frequencies with increasing the fractal order. This is because the total length of resonance current path is increasing with the order. On the other hand, the ratio of the relevant wavelength to the total wire length would deviate away from the factor 2 which represents the fundamental resonance (m=1) from Eq. (1). The varying ratio should be related to the increasing structural complexity with the fractal order, which points out the unique EM characteristic of the fractal structure.

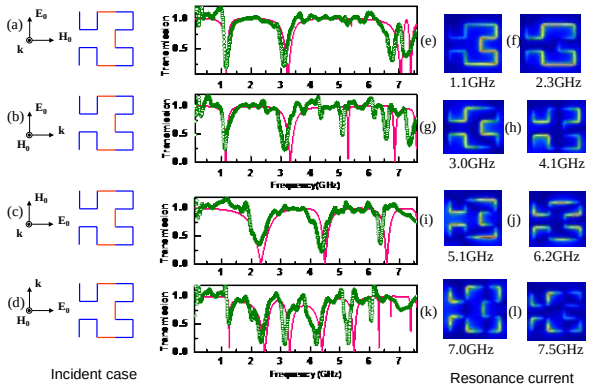

Figure 4: (a)-(d) The transmission spectra of the 2nd-order Hilbert curve at four kinds of incidence configurations, as illustrated. (e)-(l) The simulated distributions of current intensity at eight band gap frequencies 1.1GHz, 2.3GHz, 3.0GHz, 4.1GHz, 5.1GHz, 6.2GHz, 7.0GHz, and 7.5GHz. The red area indicates the maximum current intensity. These frequency values correspond to the minimum transmission positions of the band gaps in the simulation.

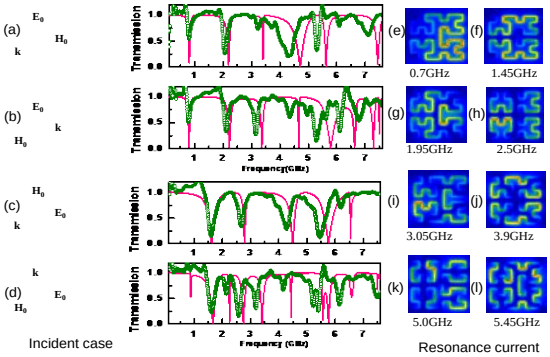

Figure 5: (a)-(d) The transmission spectra of the 3rd-order Hilbert curve at four kinds of incidence configurations, as illustrated. (e)-(l) The simulated distributions of current intensity at eight band gap frequencies 0.7 GHz, 1.45 GHz, 1.95 GHz, 2.5 GHz, 3.05 GHz, 3.9 GHz, 5.0 GHz, and 5.45 GHz. The red area indicates the maximum current intensity. These frequency values correspond to the minimum transmission positions of the band gaps in the simulation.

We are also particularly interested in the subwavelength feature of the fundamental mode from the two-order and higher orders, the side length of the fractal structure of which is much smaller than the relevant wavelength. It is easy to show the ratio $\lambda_N^{(1)}=2\times(2^N+1)$ for the fundamental resonance. The theoretical ratio indicates an exponentially increasing relationship with respective to the order N, as shown in Fig. 6. In the case of the 4th-order Hilbert structure, the fundamental resonance occurs at 666 mm (at frequency 0.45 GHz), which is 22 times larger than the sample size (see the dashed line in Fig. 6). Note that when

the *E*-field is polarized parallel to the symmetric axis of the curve and *H*-field is perpendicular to the plane of the curve the fundamental resonance is always excited, which reveals a magnetic resonance character. This magnetic response can also be identified by retrieving the effective permeability from the numerical transmission and reflection coefficients. Therefore, we can obtain the magnetic resonance of the wavelength over 20 times larger than the size of the resonant structure.

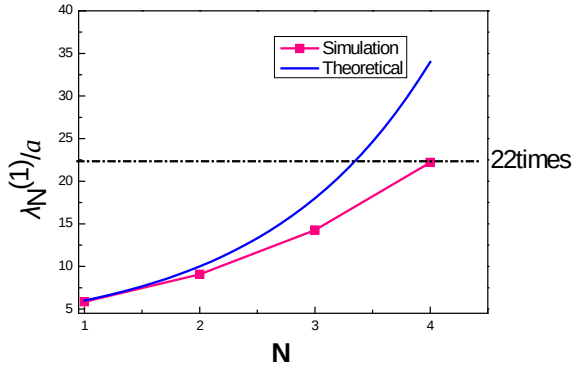

Figure 6: The ratio of the fundamental resonance wavelength $\lambda_N^{(1)}$ over the side length a is plotted with the increasing fractal order N.

5. Conclusions

We have found that the Hilbert curve patterns exhibit the resonance wavelength can be significantly larger than its physical size using pure metallic structures. Furthermore, the transmission spectra from the different polarizations of incidence reveal the fundamental resonance is of magnetic nature. The deeply subwavelength magnetic resonance supported by the Hilbert curves will be beneficial to realize high-performance metamaterials [24], for example those of less spatial dispersion.

Acknowledgements

This work was supported by the National Natural Science Foundation of China (Grant No. 11104198) and a Project Funded by the Priority Academic Program Development (PAPD) of Jiangsu Higher Education Institutions.

References

[1] W.J. Padilla, D.N. Basov, D.R. Smith. Negative refractive index metamaterials, *Materials Today* 9: 28-35, 2006.

[2] D.R. Smith, J.B. Pendry, M.C.K. Wiltshire, Metamaterials and negative refractive Index, *Science* 305: 788-792, 2006.

[3] R.A. Shelby, D.R. Smith, S. Schultz, Experimental verification of a negative index of refraction , *Science* 292: 77-79, 2000.

[4] A.N. Grigorenko, et al, Nanofabricated media with negative permeability at visible frequencies. *Nature* 438: 335–338, 2005.

[5] N. Liu, L. Fu, S. Kaiser, H. Schweizer, H. Giessen. Plasmonic building blocks for magnetic molecules in three dimensional optical metamaterials, *Adv Mater* 20: 3859–3865, 2008.

[6] M.S. Choi. H. Lee, Y. Kim, S. Kang, et al, A terahertz metamaterial with unnaturally high refractive index, *Nature*, 470: 369-373, 2011.

[7] J. Shin, J.T. Shen, S. Fan, Three-dimensional metamaterials with an ultrahigh effective refractive index over a broad bandwidth, *Phys Rev Lett* 102: 093903, 2009.

[8] J. Luo, P. Xu, H. Chen , B. Hou. Realizing almost perfect bending waveguides with anisotropic epsilon-near-zero metamaterials, *Appl Phys Lett* 100: 221903, 2012.

[9] P.B. Catrysse, S. Fan, Routing of deep-subwavelength optical beams and images without reflection and diffraction using infinitely anisotropic metamaterials, *Adv Mater* 25: 194-198, 2013.

[10] D. Schurig, J.J. Mock, B.J. Justice, et al, Metamaterials electromagnetic cloak at microwave frequencies, *Science* 314: 977-980, 2006.

[11] Y.Lai, J. Ng, H, Chen, et al, Illusion Optics: The optical transformation of an object into another object, *Phys Rev Lett* 102: 253902, 2009.

[12] C. Li, X. Meng, X, Liu, et al, Experimental realization of a circuit-based broadband illusion-optics analogue, *Phys Rev Lett* 105: 233906, 2010.

[13] L. Zhou, X. Huang, Z. Yi, S. Chui, Resonance properties of metallic ring systems, *Mater Today* 12: 52-59, 2009.

[14] D.H. Werner, R. Mittra. *Frontiers in electromagnetic*, NJ: IEEE press, Piscataway, pp. 96-200, 2000.

[15] K.J. Vinoy, K.A. Jose, V.K. Varadan, V.V. Varadan, Hilbert curve fractal antenna: A small resonant antenna for VHF/UHF applications, *Microwave Opt Technol Lett*, 29: 215-219, 2001.

[16] J. Romeu, S. Blanch, A three dimensional Hilbert antenna, *Antennas and Propagation Society International Symposium, 2002. IEEE*, IEEE, Vol4, pp. 550-553, 2002.

[17] W. Wen, L. Zhou, J. Li, W. Ge, C. T. Chan, P. Sheng, Subwavelength photonic band gaps from planar fractals, *Phys Rev Lett* 89: 223901, 2002.

[18] J. McVay, N. Engheta, A. Hoorfar, Three-dimensional Hilbert space-filling-curve plasmonics，*Antennas and Propagation Society International Symposium 2006*, IEEE, pp. 769-772, 2006.

[19] B. Hou, H. Xie, W. Wen, P. Sheng. Three-dimensional metallic fractals and their photonic crystal characteristics, *Phys Rev B* 77: 125113, 2008.

[20] M.W. Takeda, S. Kirihara, Y. Miyamoto, et al, Locallization of electromagnetic waves in Three-dimensional fractal Cavities, *Phys Rev Lett* 92: 093902, 2004.

[21] Wu Q, Feng X, Hou B, Chen H, Lai Y, Li Y, An Inside-out Eaton Lens Made of H-fractal Metamaterials, *Applied Physics Letters* 101: 031903, 2012.

[22] http://en.wikipedia.org/wiki/Hilbert_curve.

[23] Y. Qi, B. Hou, W. Wen, Band gaps from ring resonators and structural periodicity, *Journal of Physics D:*

Applied Physics 38: 590-595, 2005.

[24] L. Yousefi, O.M. Ramahi, New artificial magnetic materials based on fractal hilbert curves, *Antenna Technology: Small and Smart Antennas Metamaterials and Applications, 2007. IWAT'07, International Workshop on*. IEEE, pp. 237-240, 2007.

Scattering by a Cylindrical Dielectric Shell with DNG Metamaterial

M. I. Hussein[1],

[1]Electrical Engineering Department, UAE University, UAE; mihssein@uaeu.ac.ae

Abstract

The scattering by a plane wave incident on an infinitely long cylindrical shell loaded with DNG metamaterial is derived using the boundary-value method, and the exact series solution in terms of the Mathieu functions. The validity of the solution is verified by comparison with the circular cylindrical shell. Different types of DNG metamaterial are investigated and the resulting echo width as well as the scattered field pattern and results are presented.

1. Introduction

The use of dielectric materials for modifying the radiation characteristics of radiators and the eradication fields of the scatterer adds an additional degree of freedom because both the shape and dielectric permittivity are important parameters. So far, a number of theoretical and experimental investigations have been carried out to study the possible control of antenna characteristics by dielectrically loading conventional antennas and reflector surfaces. Knop [1] treats the dielectric-loaded aerial slot antenna on a circular cylinder, which he solved analytically, with certain simplifying assumptions, to obtain the external slot admittance. Nonetheless, analytical solutions of the problem of scattering by elliptical dielectric cylinders have applications in the field of fiber optics, acoustics, biomedical, and radio astronomy. Also they can be used to check the accuracy of approximate and numerical solutions of similar geometries. The analytical solution to the problem of a plane electromagnetic wave scattering by a lossless homogeneous dielectric elliptic cylinder was first obtained by Yeh using Mathieu functions of real arguments [2-3]. The scattering by different configurations of lossless dielectric elliptic cylinders was studied by many authors [4-8]. El Sherbeni had investigated the Scattering by a circular cylindrical dielectric shell with inhomogeneous Permittivity profile [9]. The scattering by a weakly lossy multilayer elliptic cylinder was obtained by Caorasi et al using a first order truncation of the Taylor expansion of each Mathieu function of real argument [10].

Metamaterials are artificial materials engineered to provide properties which "may not be readily available in nature". The different classes of metamaterial include single-negative (SNG) materials, such as epsilon-negative (ENG) and mu-negative (MNG) materials, and double-negative (DNG) materials.

Among all the double negative (DNG) materials [11]-[14] in which the real part of both the permittivity and permeability are negative is the most interesting. In such materials the electric and magnetic field intensity vectors of a plane wave form a left-handed set of vectors with its wave number vector. This is in contrast to double positive (DPS) materials, in which these vectors form a right-handed set.

It is known that DNG materials are not found in nature and therefore must be made artificially. At microwave frequency one possible realization of DNG materials is based on periodic arrangements of conducting wires and split-ring resonators (SRRs). The relative effective permittivity and the relative effective permeability of such realization were found to possess a negative real part and an imaginary part as follow [15]-[17],

$$\varepsilon_r(\omega) = 1 - \frac{\omega_{pe}^2}{\omega^2 - j\omega\Gamma_e} \tag{1}$$

$$\mu_r(\omega) = 1 - \frac{F\omega^2}{\omega^2 - \omega_{0m}^2 - j\omega\Gamma_m} \tag{2}$$

The strong interest in DNG materials is due to their unfamiliar electromagnetic properties and the potential applications due to these properties.

In this work the scattering properties of an elliptical cylinder shell loaded with DNG metamaterial will be investigated. The analysis is based on the well-known separation of variable and exact boundary value technique, in the elliptic cylindrical coordinates system and Mathieu functions. Electric and Magnetic fields in all regions are expressed in terms of Fourier series with unknown expansion coefficients. The formulation of the problem of TM case is introduced. The system of equations is solved using standard numerical techniques to generate numerical results. The far scattered field pattern is calculated after using the large argument approximation of Mathieu Hankel function. The results are compared against hose of circular cylindrical shell.

2. Problem Formulation and Solution

The electromagnetic wave interaction with elliptical cylinder is typically expressed in terms of the elliptic cylinder coordinates system (ξ, η, z). Consider the case of a linearly polarized electromagnetic plane wave incident at an angle φ_i with respect to the positive x axis on an elliptical cylindrical shell loaded by DNG metamaterials, and have negative real part, at certain frequency, as shown in Figure 1, with time dependence. The electric field component of the TM polarized plane wave of amplitude is given by,

$$E_z^i = E_0 e^{jk_o\rho\cos(\phi-\phi_i)} \tag{3}$$

Where k_0 is the wave number in free space. The incident electric field may be expressed as follows

$$E_z^i = \sum_{m=0}^{\infty} A_{em} R_{em}^{(1)}(c_0,\xi) S_{em}(c_0,\eta) + \sum_{m=1}^{\infty} A_{om} R_{om}^{(1)}(c_0,\xi) S_{om}(c_0,\eta) \tag{4}$$

Where,

$$A_{\substack{em\\om}} = E_0 j^m \frac{\sqrt{8\pi}}{N_{\substack{em\\om}}(c_0)} S_{\substack{em\\om}}(c_0,\cos\phi_i) \tag{5}$$

$$N_{\substack{em\\om}}(c) = \int_0^{2\pi} [S_{\substack{em\\om}}(c,\eta)]^2 \, dv \tag{6}$$

$c_0 = k_0 F$, F is the semi-focal length of the elliptical cross section, S_{em} and S_{om} are the even and odd angular Mathieu functions of order *m*, respectively, $R_{em}^{(1)}$ and $R_{om}^{(1)}$ are the even and odd radial Mathieu functions of the first kind with complex argument, and N_{em} and N_{om} are the even and odd normalized functions.

The scattered electric field outside the coated elliptic cylinder for ($\xi > \xi_2$) can be expressed in terms of Mathieu functions as follows

$$E_z^s = \sum_{m=0}^{\infty} B_{em} R_{em}^{(4)}(c_0,\xi) S_{em}(c_0,\eta) + \sum_{m=1}^{\infty} B_{om} R_{om}^{(4)}(c_0,\xi) S_{om}(c_0,\eta) \tag{7}$$

Where B_{em} and B_{om} are the unknown scattered field expansion coefficients, $R_{em}^{(4)}$ and $R_{om}^{(4)}$ are the even and odd Mathieu functions of the fourth kind. Similarly, the transmitted electric field inside the shell (region 1) for ($\xi_1 < \xi < \xi_2$) can be written as

$$E_z^1 = \sum_{m=0}^{\infty} \left[C_{em} R_{em}^{(1)}(c_1,\xi) + D_{em} R_{em}^{(2)}(c_1,\xi) \right] S_{em}(c_1,\eta) + \sum_{m=1}^{\infty} \left[C_{om} R_{om}^{(1)}(c_1,\xi) + D_{om} R_{om}^{(2)}(c_1,\xi) \right] S_{om}(c_1,\eta) \tag{8}$$

Where $c_1 = k_1 F$, $k_1 = \omega\sqrt{\mu_1\varepsilon_1}$, C_{em}, C_{om}, D_{em}, D_{em} are the unknown transmitted field expansion coefficients, $R_{em}^{(2)}$ and $R_{om}^{(2)}$ are the radial Mathieu functions of the second type.

Field expression in region 2 ($\xi < \xi_2$) is,

$$E_z^2 = \sum_{m=0}^{\infty} F_{em} R_{em}^{(1)}(c_1,\xi) S_{em}(c_1,\eta) + \sum_{m=1}^{\infty} F_{om} R_{om}^{(1)}(c_1,\xi) S_{om}(c_1,\eta) \tag{9}$$

The magnetic field component in all 3 regions can be obtained using Maxwell's equations. The unknown expansion coefficients given in equations (7)-(9) can be obtained by imposing the continuity of the tangential electric and magnetic fields first at $\xi = \xi_1$ and then at $\xi = \xi_2$ along with the orthogonality property of the angular Mathieu function, one gets the unknown scattering coefficients B_{em} and B_{om}

The scattered near and far fields for the TM can be calculated once the scattered fields' expansion coefficients are known. The far scattered field expressions can be obtained as follows

$$E_z^s = \sqrt{\frac{j}{k_0\rho}} e^{-jk_0\rho} \sum_m j^m \left[B_{em}^{TM} S_{em}(c_0,\eta) + B_{om}^{TM} S_{om}(c_0,\eta) \right] \tag{10}$$

Far Field data are usually expressed in terms of the scattering cross section per unit length, i.e., the echo width is defined as

$$\sigma_{TM} = 2\pi\rho \lim_{\rho\to\infty} \frac{\left|E_z^s\right|^2}{\left|E_z^i\right|^2} \tag{11}$$

Eq. (11) can take simpler form as follows,

$$\sqrt{\frac{\sigma_{TM}}{\lambda}} = \sum_m j^m \left[B_{em} S_{em}(c_0,\eta) + B_{om} S_{om}(c_0,\eta) \right] \tag{12}$$

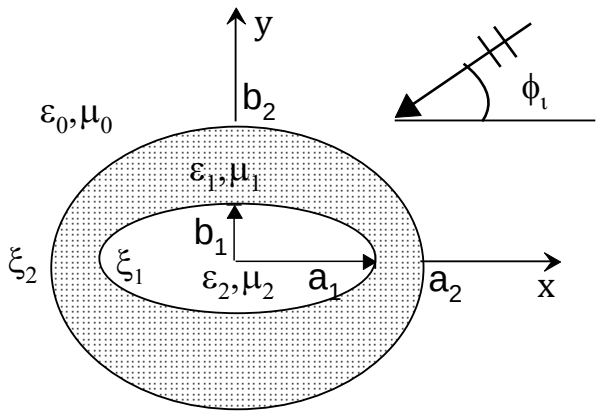

Figure 1: Geometry of the elliptical shell

3. NUMERICAL RESULTS AND DISCUSSION

The analytic solution of the electromagnetic scattering by a lossy dielectric elliptical shell is given in terms of two, uncoupled, linear system of equations for the even and odd ordered expansion scattered field coefficients for both even and odd functions. In order to solve these equations for the scattered field coefficients B_{em} and B_{om}, the infinite series are truncated to include only the first *N* terms, where *N*, in general, is a suitable truncation number proportional to the structure's electrical size.

Fig. 2 shows the echo width pattern for a dielectric shell with respect to the observation angle ϕ and incident angle $\phi_i = 0^o$. The numerical results are plotted for different real valued of permittivity and permeability. The electrical

dimensions of the scatterer major axis are and $k_o a = 1.0470$, $k_o a_1 = 2.094$, and an aspect ratio of 2. The numerical results show a significant reduction in the echo width pattern especially at the scattering angle 180 degrees while the reduction becomes insignificant for both epsilon and mu negative. Fig. 3 compares the effect of adding a loss component for the permittivity; it is evident that the double negative lossy shells, the most significant reduction with higher loss factor. The variation of scattering echo width as a function of real permittivity and with inserting a loss factor is shown in Fig. 4. The backscattering echo width pattern verses ka, for shell relative permittivity ($\varepsilon_r = -2 - j$) and permeability $\mu_r = 1, -2, and\ -4$, are given in Fig 5.

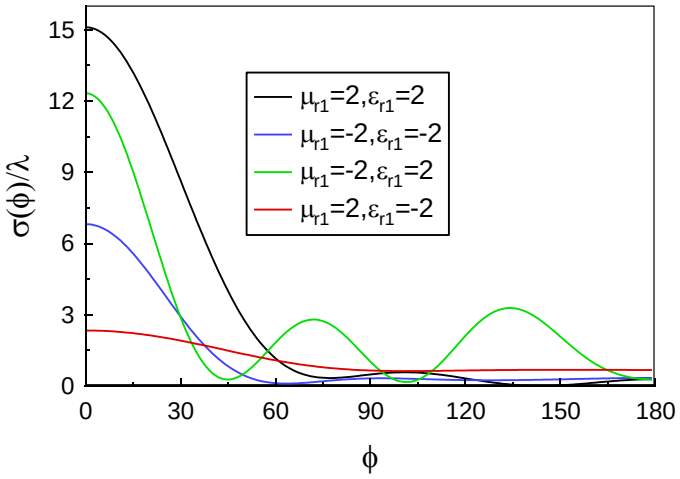

Figure 2: Figure 2: Echo width pattern for a dielectric shell with respect to the observation angle ϕ, for real ε and μ

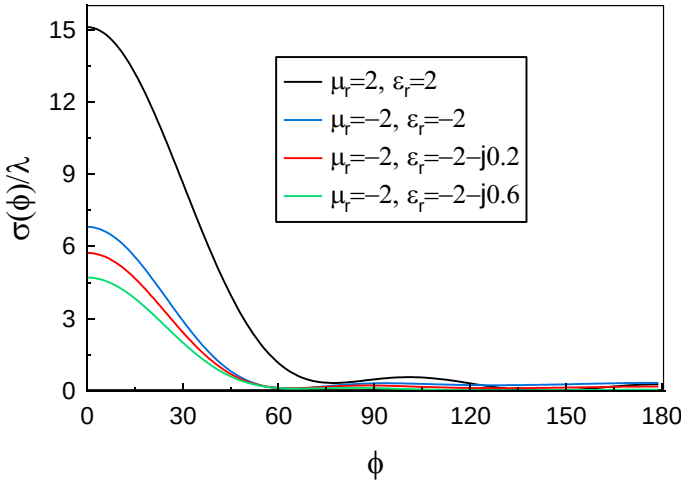

Figure 3: Echo width pattern with respect to the observation angle ϕ, for real negative perm

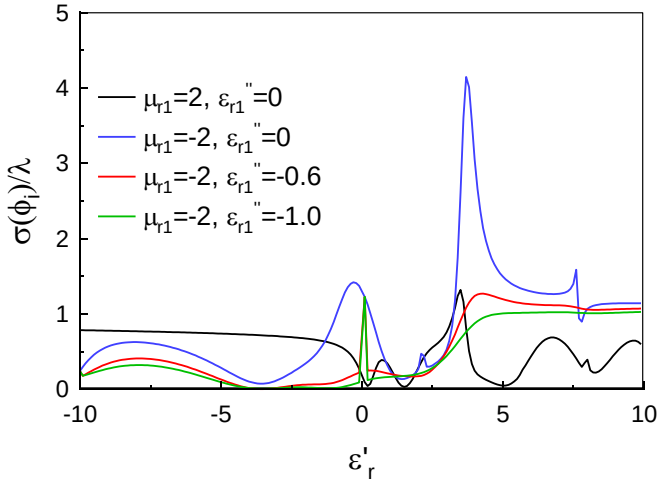

Figure 4: Echo width pattern with respect to the Re{ε_r}

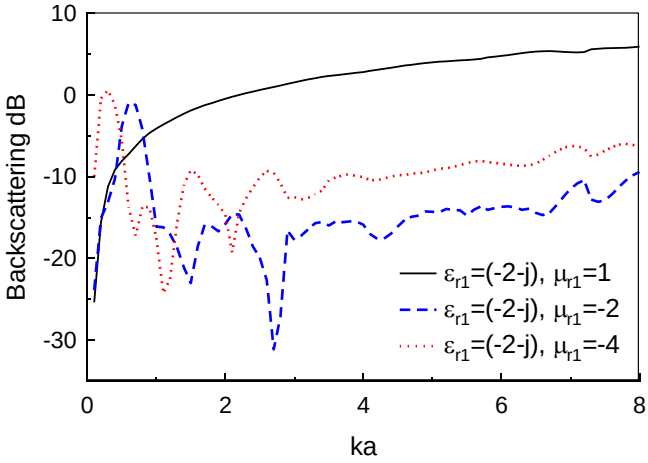

Figure 4: Backscattering width pattern with respect to the *ka*

4. Conclusions

An analytical solution of the electromagnetic scattering by a dielectric elliptical cylindrical shell loaded with DNG metamaterial is formulated and solved using boundary value method. Numerical results will be obtained for the TM polarization after developing a special code to compute Mathieu functions of nigative arguments. The validity and accuracy of the obtained numerical results will be verified against the limiting case of circular cylindrical shell using series solution. Finally, different cases of shell loading will be considered in addition to shell thickness.

Acknowledgements

The author wish to acknowledge the support provided by the United Arab Emirates University.

References

[1] Knop, C., "External admittance of an axial slot on a coated metal cylinder," Radio Sci.,new series, 3, 803-817, 1968

[2] Yeh, C., 'The diffraction of waves by a penetrable ribbon,' J. of Mathematical Phys., vol. 4, no.1, pp. 65-72, 1963.
[3] Yeh, C., 'Backscattering cross section of a dielectric elliptic cylinder,' J. Opt., Soc. Amer., vol.55, pp. 309-314, 1965.
[4] Richmond, J.H., 'Scattering by a dielectric conducting elliptic cylinder with dielectric coating,' Radio Sci, vol.23, pp. 1061-1066, 1988.
[5] Holand, R., Cable, V.P., 'Mathieu functions and their applications to scattering by a coated strip,' IEEE Trans. On Elect. Compt., vol. 34, no. 1, pp. 9-16, 1992.
[6] Sebak, A-R., Electromagnetic scattering by two parallel dielectric elliptic cylinders,' IEEE Trans. On Antenna and Prog., vol. 42, no. 11, pp. 1521-1527, 1994.
[7] Caorsi, S, Pastorino, M., and Raffetto, M., 'Electromagnetic scattering by a mutilayer elliptic cylinder under transverse-magnetic illumination: series solution in terms of Mathieu function,' IEEE Trans. On Antenna and Prog., vol. 45, no. 6, pp. 926-935, 1997.
[8] Li, L.W., Wee, H.G, Yeo, T.S, Leong, M.S., ' Analysis of scattering by a dielectric elliptical cylinder using radiation-to-scattering transform,' Proc. of IEEE AP-S/URSI Int. Symp., Salt Lake City, Utah, U.S.A., July 16-21, 2000.
[9] El Sherbeni, A. Z., Hamid, M., "Scattering by a circular cylindrical dielectric shell with inhomogeneous Permittivity profile," Int. J. Electronics, vol. 58, No. 6, pp 949-962, 1985.
[10] Caorsi, S, Pastorino, M., and Raffetto, M., 'Electromagnetic scattering by weakly lossy multilayer elliptic cylinders,' IEEE Trans. On Antenna and Prog., vol. 46, no. 11, pp. 1750-1751, 1998.
[11] V.G. Veselago, "The electrodynamics of substances with simultaneously negative values of ε and μ," Soviet Physics Usp., vol. 10, no. 4, pp. 509-514, Jan. 1968.
[12] R. A. Shelby, D. R. Smith, S. Schultz, "Experimental verification of a negative index of refraction," Science, vol. 292, pp. 77-79, 6 April 2001.
[13] J. Lu, T. M. Grzegorczyk, Y. Zhang, J. Pacheco, Jr., B.-I. Wu, J. A. Kong, and M. Chen, "Cerenkov, "radiation in materials with negative permittivity and permeability," Opt. Express, vol. 11, pp. 723–734, Apr. 2003.
[14] Al`u and N. Engheta, "Radiation from a traveling-wave current sheet at the interface between a conventional material and a material with negative permittivity and permeability," Microwave Opt. Tech. Lett., vol. 35, no. 6, pp. 460–463, Dec. 2002.
[15] J. B. Pendry, A. J. Holden, W. J. Stewart, and I. Youngs, "Extremely low frequency plasmons in metallic meso structures," Phys. Rev. Lett., vol. 76, no. 25, pp. 4773-4776, June 1996.
[16] J. B. Pendry, A. J. Holden, D. J. Robbins, and W. J. Stewart, "Low frequency plasmons in thin wire structures," J. Phys. Condens. Matter, vol. 10, pp. 4785-4809, 1998.
[17] J. B. Pendry, A. J. Holden, D. J. Robbins, and W. J. Stewart, "Magnetism from conductors and enhanced nonlinear phenomena," IEEE Trans. Microwave Theory Techniques, vol. 47, no. 11, pp. 2075-2084, Nov. 1999.

Interaction of Bessel Light Beams with Epsilon-near-zero Metamaterials

Svetlana Kurilkina[1]*, Mohammed A Binhussain[2], Vladimir Belyi[1], Nikolai Kazak[1]

[1]B.I.Stepanov Institute of Physics, National Academy of Sciences of Belarus, Minsk, Belarus
[2]The National Center for Building System KACST, Riyadh, Saudi Arabia
*corresponding author, E-mail: s.kurilkina@ifanbel.bas-net.by

Abstract

The article explores possibilities and conditions of generation of a new type of diffraction-free needle-like field Bessel plasmon polaritons (BPPs) with super narrow cone angle in an epsilon-near-zero metamaterial, surrounded by semi-infinite dielectric media. Correct analytical expressions are obtained and analyzed in detail for the electric and magnetic fields of BPPs formed inside and outside the metamateral slab.

1. Introduction

Recent advances in nanofabrication and developments in the theory of light-matter interaction have brought to life a new class of composite media, known as metamaterials (MMs). MMs offer new avenues for manipulation of light, lithography, lifetime engineering, high-resolution imaging [1-3]. One subclass of metamaterials is hyperbolic metamaterials (HMMs) in which one of the diagonal permittivity tensor components is negative [4-6]. This results in a hyperbolic dispersion instead of elliptic one as in conventional dielectrics. The reason for HMMs widespread interest is due to relative ease of nanofabrication, broadband non-resonant response, wavelength tunability and high figure of merit [7]. Hyperbolic metamaterials can be used for a variety of applications from negative index waveguides to nanoscale resonators [6,7].

In the approximation of the effective medium theory hyperbolic metamaterial can be considered as an uniaxial uniform medium characterizing by the effective permittivities which are dependent on parameters of HMM. The conditions can be fulfilled when one of the effective permittivities is very small (≈ 0). As established earlier [8, 9], such metamaterials, named as epsilon-near-zero metamaterials (ENZMs), display unique properties by interaction with a plane wave, for example, the possibility of canalization of radiation. Recently such media were experimentally realized [10].

In 1987 Durnin suggested a new type of waves, the so-called Bessel light beams (BLBs); they are also referred to as diffraction-free beams [11- 18]. The transverse profile of the amplitude of these beams is described by a Bessel function of the first kind. In the domain of spatial frequencies BLBs are represented as a superposition of plane waves with wave vectors which are wrapped around a conical surface having the cone angle 2γ . The main properties of Bessel light beams are the ability to keep the transverse size of the central lobe unchanged much longer than the Rayleigh range and to restore the wave front behind an obstacle. Owing to these features BLBs are promising for a number of applications, for example, for optical trapping and manipulation of microparticles and atoms, and for technical diagnostics of subjects with a sub-wave resolution [19-22].

The authors of Ref. [23-27] theoretically and experimentally investigated evanescent BLBs formed in the condition of the internal total reflection in an optically less dense dielectric medium. These beams exponentially decay while moving off the surface but retain their original transversal shape. In those investigations, of particular interest was the structure of the central lobe of evanescent BLBs. It is established that its diameter can be reduced to a nanosize value. This makes it possible to use evanescent Bessel beams in optical microscopy [28].

But the evanescent BLBs investigated before possess an essential disadvantage, namely, they are weak, which causes the necessity of application of strong laser fields for their generation. One of the ways of taking Bessel light field advantages for microscopy is the formation of Bessel plasmon polaritons (BPPs) [29, 30].

The present report considers the peculiarities of generation of Bessel plasmon polaritons in epsilon-near-zero metamaterials. Investigation of this problem attracts interest owing to a possibility to combine unusual features of BPPs and ENZMs.

The paper is structured as follows. In Section 2 the description is given of features of generation of Bessel plasmon polaritons in the symmetrical structure on the base of ENZM slab sandwiched between two semi-infinite dielectrics. The behavior of electric and magnetic vectors in the structure is analyzed in detail. A conclusion is given in Section 3.

2. Bessel plasmons in epsilon-near-zero metamaterials

We considered the hyperbolic metamaterial made of metallic nanocylinders periodically embedded in the

dielectric template matrix, having the thickness h (Fig.1), surrounded by an external isotropic medium with the dielectric permittivity ε_1 (for example, by air with $\varepsilon_1 = 1$). This composite can be made electrochemically.

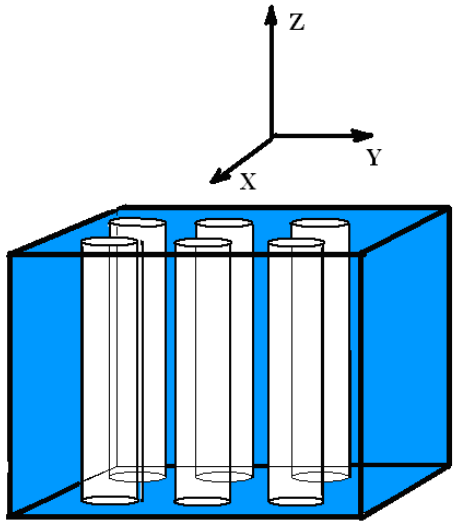

Figure 1: Metamaterial made of metallic nanocylinders periodically embedded in the dielectric template matrix.

At that, the controllable parameters are the metallic nanocylinder radius r, the metallic permittivity ε_m, the average distance between the centers of two adjacent cylinders D, and the membrane dielectric permittivity ε_d. It should be noted that permittivity of metallic nanocylinders is determined by the following correlation:

$$\varepsilon_m(\lambda) = \varepsilon_\infty - \lambda^2/[\lambda_p^2(1 + i\lambda\Gamma_1/2\pi c)], \qquad (1)$$

where ε_∞ is the dielectric permittivity of the bulk metal, λ is the wavelength of optical radiation, λ_p is the plasma wavelength, $\Gamma_1 \approx \Gamma + V_F/2r$, Γ is the damping constant, V_F is the Fermi velocity. For silver (Ag) nanocylinders, for example, we have $\varepsilon_\infty = 5$, $\lambda_p = 137\,nm$, $\Gamma = 32 \cdot 10^{12}\,s^{-1}$, $V_F = 1.4 \cdot 10^6\,ms^{-1}$ [31].

In the approximation of the effective medium theory neglecting nonlocal spatial dispersion effects this metamaterial can be considered as a uniaxial uniform medium characterizing by the following main effective permittivities [32]:

$$\varepsilon_x = \varepsilon_y = \frac{\beta\varepsilon_m N + \varepsilon_d(1-N)}{\beta N + (1-N)}, \qquad (2)$$

$$\varepsilon_z = \varepsilon_m N + \varepsilon_d(1-N),$$

where $N = \pi r^2/D^2$ is the inclusion factor $\beta = 2\varepsilon_d/(\varepsilon_m + \varepsilon_d)$. At that, $N << 1$ and $D, r << \lambda$. As follows from Eq.(2), if the inclusion factor is fulfilled by the condition

$$N = N_0 = \varepsilon_d/(\varepsilon_d - \mathrm{Re}\,\varepsilon_m), \qquad (3)$$

the real part of the component ε_z is equal to zero.

As it is known, the optical anisotropy of a uniaxial medium is characterized by the difference between two parameters: $\varepsilon_o = \varepsilon_x = \varepsilon_y$ and ε_e. At that:

$$\varepsilon_e = \frac{\varepsilon_o \varepsilon_z}{\varepsilon_o \sin^2\gamma_e + \varepsilon_z \cos^2\gamma_e}, \qquad (4)$$

$$\gamma_e = \arcsin\frac{\sqrt{\varepsilon_1}\sin\gamma_{inc}}{\sqrt{\varepsilon_o + (1 - \frac{\varepsilon_o}{\varepsilon_z})\varepsilon_1 \sin^2\gamma_{inc}}}, \qquad (5)$$

where γ_{inc} is the angle of incidence of light. It follows from Eq.(3) that if $\varepsilon_z = 0$, ε_e is not equal zero only for $\gamma_e = 0$. Moreover, from Eq. (5) one can see that for the case $\varepsilon_z = 0$ for the arbitrary γ_{inc} angle we have $\gamma_e = 0$.

But it is very difficult to realize in practice the condition when ε_z is exactly equal to zero. Fixing the value of permittivity ε_z to a nonzero but low value, let us study the interaction of TH polarized Bessel light beams having the wavelength λ and the half-cone angle γ_{inc} with ENZM. From the Maxwell's equations for a uniaxial crystal in the cylinder coordinate system with the unit vectors $\vec{e}_\rho, \vec{e}_\varphi$, and $\vec{e}_z$ ($\vec{e}_z$ is collinear to the propagation direction) and $z = 0$ at the entrance face of the metamaterial, one can obtain the formula for the longitudinal (z), radial (ρ) and azimuthal (φ) components of the electric $\vec{E}$ and magnetic $\vec{H}$ fields for extraordinary (e) type Bessel beams excited inside semi-infinite ENZM :

$$E_\rho^e = i\frac{k_{ze}}{\varepsilon_o}J'_m(q\rho), \quad H_\rho^e = k_0\frac{m}{q\rho}J_m(q\rho),$$

$$E_\varphi^e = -\frac{k_{ze}}{\varepsilon_o}k_{ze}\frac{m}{q\rho}J_m(q\rho), \quad H_\varphi^e = ik_0 J'_m(q\rho), \qquad (6)$$

$$E_z^e = q\frac{1}{\varepsilon_z}J_m(q\rho), \qquad H_z^e = 0.$$

Here the phase multiplier $\exp[i(k_e z + m\varphi)]$ is omitted; $k_0 = 2\pi/\lambda$; q and k_{ze} are transversal and longitudinal (in general case, complex) components of wave vectors forming BLB in the domain of spatial frequencies, respectively; $J_m(q\rho), J'_m(q\rho) = \partial J_m(q\rho)/\partial(q\rho)$ are the m-order Bessel functions and their derivatives, m is the integer. At that

$$k_{ze} = [k_0^2\varepsilon_o - (\varepsilon_o/\varepsilon_z)q^2]^{1/2}. \qquad (7)$$

Note that the formula for TH BLB inside the semi-infinite isotropic medium ε_1 can be obtained from Eqs.(6) where it should be replaced $\varepsilon_z \to \varepsilon_1$, $k_{ze} \to k_{z1} = [k_0^2\varepsilon_1 - q^2]^{1/2}$.

The electric and magnetic vectors of the field inside the ENZM slab (it is denoted by the symbol "2") of finite thickness h and outside it in our case are expressed as

$$\vec{E}_{1,3}(R) = \vec{E}^{tr}_{1,3}(R) + \vec{E}^{l}_{1,3}(R),$$
$$\vec{E}^{l}_{1}(R) = A_{inc}\frac{q}{\varepsilon_1}\exp i\left[m\varphi - k_{z1}z\right]J_m(q\rho)\vec{e}_z,$$
$$\vec{E}^{tr}_{1}(R) = -\frac{iA_{inc}k_{z1}}{\varepsilon_1\sqrt{2}}\exp i[(m-1)\varphi - k_{z1}z]\vec{F}^{-}_{m}, \quad (8)$$
$$\vec{E}^{l}_{3}(R) = A_{inc}\frac{q}{\varepsilon_1}t\exp i\left[m\varphi + k_{z3}(z-h)\right]J_m(q\rho)\vec{e}_z,$$
$$\vec{E}^{tr}_{3}(R) = \frac{iA_{inc}k_{z1}}{\varepsilon_1\sqrt{2}}\exp i[(m-1)\varphi + k_{z1}(z-h)]t\vec{F}^{-}_{m}.$$
$$\vec{H}_1(R) = \frac{k_0A_{inc}}{\sqrt{2}}\exp i[(m-1)\varphi - k_{z1}z]\vec{F}^{+}_{m}, \quad (9)$$
$$\vec{H}_3(R) = \frac{k_0A_{inc}}{\sqrt{2}}\exp i[(m-1)\varphi + k_{z3}(z-h)]t\vec{F}^{+}_{m}.$$
$$\vec{E}_2(R) = \vec{E}^{tr}_{2}(R) + \vec{E}^{l}_{2}(R),$$
$$\vec{E}^{l,tr}_{2}(R) = (\vec{E}^{l,tr}_{2})^{f} + (\vec{E}^{l,tr}_{2})^{b},$$
$$(\vec{E}^{l}_{2})^{f,b} = A_{inc}q\frac{1}{\varepsilon_z}s^{f,b}\exp i[m\varphi \pm$$
$$\pm k_{ze}\,|\,z - ph\,|]J_m(q\rho)\vec{e}_z, \quad (10)$$
$$(\vec{E}^{tr}_{2}(R))^{f,b} = \pm\frac{iA_{inc}k_{ze}}{\varepsilon_o\sqrt{2}}s^{f,b}\exp i[(m-1)\varphi \pm$$
$$\pm k_{ze}\,|\,z - ph\,|]\vec{F}^{-}_{m}.$$
$$\vec{H}_2(R) = (\vec{H}_2(R))^{f} + (\vec{H}_2(R))^{b},$$
$$(\vec{H}_2(R))^{f,b} = \frac{k_0A_{inc}}{\sqrt{2}}s^{f,b}\exp i[(m-1)\varphi \pm \quad (11)$$
$$\pm k_{ze}\,|\,z - ph\,|]\vec{F}^{+}_{m}.$$

Here $R = (\rho, \varphi, z)$ are the cylindrical coordinates; t is amplitude transmission coefficient of the slab, s^f, s^b are the amplitude coefficients for the forward and backward Bessel fields inside the ENZM slab, respectively; $\vec{F}^{\pm} = J_{m-1}(q\rho)\vec{e}_{+} \pm J_{m+1}(q\rho)\exp(2i\varphi)\vec{e}_{-}$; $\vec{e}_{\pm} = (\vec{e}_1 \pm i\vec{e}_2)/\sqrt{2}$ are the unit circular vectors which are orthogonal to the $\vec{e}_z$ vector; $p = 0$ for s^f and $p = 1$ for s^b; symbols "*tr*", "*l*" denote the transversal and longitudinal component of the electric (magnetic) vector, respectively; symbols "1" and "3" denote the media adjacent to the input and output surfaces of ENZM slab, respectively.

Using the boundary conditions of continuity of the tangential components of the electric and magnetic fields, which have to be satisfied at the planes $z = 0$ and $z = h$, as well as Eqs. (8), (9), (10), (11), we obtain the system of equations for the coefficients t, $s^{f,b}$ from which it follows:

$$t = \left[\cos(k_{ze}h) - i\sin c(k_{ze}h)\frac{(\varepsilon_o^2k_{z1}^2 + \varepsilon_1^2k_{ze}^2)h}{2\varepsilon_o\varepsilon_1k_{z1}}\right]^{-1}, \quad (12)$$

$$s^{f} = \frac{k_{z1}\varepsilon_o t\exp(-ik_{ze}h)}{\varepsilon_1k_{ze}(1+\vartheta)}, \quad (13)$$

$$s^{b} = -\frac{k_{z1}\varepsilon_o t\vartheta}{\varepsilon_1k_{ze}(1+\vartheta)}. \quad (14)$$

Here $\sin c(k_{ze}h) = \sin(k_{ze}h)/(k_{ze}h)$,
$\vartheta = \left[(k_{z1}/\varepsilon_1) - (k_{ze}/\varepsilon_o)\right]/\left[(k_{z1}/\varepsilon_1) + (k_{ze}/\varepsilon_o)\right]$.

From the boundary conditions for Eqs.(8), (9), (10), (11) one can find the dispersion equation determining the existence of Bessel surface plasmon polaritons in the structure shown in Fig. 1.

$$\exp(ik_{ze}h) = \pm 1/\vartheta \quad . \quad (15)$$

Note that Eq.(15) coincides with the condition of determining the poles of reflection coefficient:

$$r = \frac{\vartheta(1-\exp(2ik_{ze}h))}{1-\vartheta^2\exp(2ik_{ze}h)}. \quad (16)$$

It is conveniently to rewrite Eq.(15) as an equation for the unknown complex value k_{ze} taking into account that $k_{z1}^2 = k_0^2(\varepsilon_1 - \varepsilon_z) + (\varepsilon_z/\varepsilon_o)k_{ze}^2$. One can obtain from Eq. (15) that the condition of Bessel plasmon polariton generation in ENZM is fulfilled for $k_{ze} \approx 0$.

It follows from Eq.(7) that it is realized if the following condition is fulfilled:

$$q = k_0\sqrt{\varepsilon_z} \quad . \quad (17)$$

At that,

$$\mathrm{Re}\,q = \frac{k_0}{\sqrt{2}}\left[\mathrm{Re}\,\varepsilon_z + \sqrt{(\mathrm{Re}\,\varepsilon_z)^2 + (\mathrm{Im}\,\varepsilon_z)^2}\right]^{1/2}, \quad (18)$$

$$\mathrm{Im}\,q = \frac{k_0\,\mathrm{Im}\,\varepsilon_z}{\sqrt{2}}\left[\mathrm{Re}\,\varepsilon_z + \sqrt{(\mathrm{Re}\,\varepsilon_z)^2 + (\mathrm{Im}\,\varepsilon_z)^2}\right]^{-1/2} \quad (19).$$

If $\mathrm{Re}\,\varepsilon_z \to 0$ we have $\mathrm{Re}\,q \approx \mathrm{Im}\,q = k_0\sqrt{\mathrm{Im}\,\varepsilon_z}/\sqrt{2}$. Then, if the absorption of metal component of ENZM, determining the value of $\mathrm{Im}\,\varepsilon_z$, decreases, the parameter $\mathrm{Re}\,q$ decreases too. Note that $\mathrm{Re}\,q$ characterizes the half-cone angle of wave vectors γ_{inc} forming incident BLB in the domain of spatial frequencies.

If the condition $\mathrm{Im}\,\varepsilon_z \to 0$ is fulfilled, the generation of BPPs is observed at incidence on ENZM slab of Bessel light beam with the half-cone angle $\gamma_{inc} = \arcsin(\mathrm{Re}\,q/(k_0\sqrt{\varepsilon_1})) \to 0$.

We can represent dielectric permittivity ε_z in the form

$$\varepsilon_z = (\mathrm{Re}\,\varepsilon_m - \varepsilon_d)\alpha N_0 + i\,\mathrm{Im}\,\varepsilon_m(1+\alpha)N_0, \quad (20)$$

where $\alpha = \Delta N/N_0$, ΔN is deviation of inclusion factor from N_0. As follows from Eqs. (17), (20), parameter $\mathrm{Re}\,q$ is dependent on the deviation of inclusion factor ΔN. The $\gamma_{inc}(\Delta N)$ for the case of ENZM slab made on the base of alumina oxide with periodically embedded silver nanocylinders is represented in Fig.2 It is seen that in real situation (when $\mathrm{Im}\,\varepsilon_z \neq 0$) the value of γ_{inc} is not equal zero too and decreases with increasing ΔN.

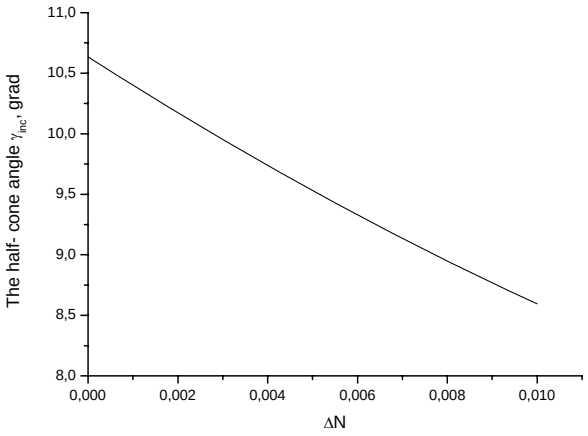

Figure 2: The dependence on the deviation of inclusion factor ΔN of the half-cone angle of incident Bessel light beam for which Bessel plasmon polariton is excited in ENZM slab made of alumina oxide with periodically embedded silver nanocylinders ($r = 25$ nm) and surrounded by air. Here $\lambda = 633$ nm.

It is interesting to physically interpret Bessel plasmon polariton. As it mentioned above, Bessel beam can be considered as a superposition of *p*-polarized plane monochromatic waves having the wavelength λ and wave vectors lying on the surface of a cone. Every *p*-polarized plane-wave component of the incident BLB in conditions of the plasmon resonance excites the surface plasmon polariton (SPP) propagating along the interface of external medium and ENZM slab. Here the phase of every SPP is determined by the phase of the plane-wave component of the incident BLB. Thus, in the ENZM slab an array of propagating SPPs arises, wave vectors of which are being oriented in the direction of the center determining the intersection of the incident BLB axis with the surface of the epsilon-near-zero metamaterial. As a result there occurs the generation of pairs of two counter-propagating SPP waves with the wave vectors $\pm\vec{q}$. The generated SPPs will propagate in all the possible radial directions to form a localized SPP field. This results in a complex high-symmetric interference light structure emerging in sections parallel to the dielectric-metamaterial surface.

For the case where the longitudinal components of the electric field $\vec{E}$ for every radially propagating SPP has the same phase, in the center of such a standing light structure a maximum appears, i.e. the shape of the $\vec{E}$ component of localized Bessel plasmon polariton is described by zero-order Bessel function $J_0(q\rho)$. In a special case, each pair of counter propagating SPPs is in counter-phase and the local plasmonic field appears with a minimum in the center, i.e. the so-called vortex localized BPP is formed. In this case the electric field $\vec{E}$ of vortex BPP is described by $J_m(q\rho)$ Bessel function.

One of most important characteristics of Bessel plasmon polariton is the first ring radius $R_1 \approx 2.4/(\mathrm{Re}\, q)$ in transversal section of intensity distribution. It follows from Eq.(18) that if $\mathrm{Im}\,\varepsilon_z \to 0$ then $R_1 \to \infty$. But existence of absorption of metal component of ENZM limits the value of R_1 .

The problem of attenuation of the BPP should be studied now. Let us consider this field outside the ENZM layer (at the interface between air and ENZM). With this aim the limited narrow Bessel light beam of radius r_0 in the transversal section should be considered. As follows from Eq. (8), the transversal distribution of the longitudinal component of the electric field of Bessel SPP is determined by the $J_m(q\rho)$ Bessel function which can be represented as a sum of the cylindrical Hankel functions of the first $H_m^{(1)}(q\rho)$ (outgoing) and second $H_m^{(2)}(q\rho)$ (incoming) kinds [33]:

$$J_m(q\rho) = \left(H_m^{(1)}(q\rho) + H_m^{(2)}(q\rho)\right)/2 . \qquad (21)$$

According to Eq.(21), in the region $\rho < r_0$ the BPPs are formed by converging and diverging conical beams described by appropriate Hankel functions. Outside the area $\rho > r_0$ there exists only a diverging conical beam, and that is why in the decomposition Eq. (21) it is supposed that $H_m^{(2)} = 0$. Using the asymptotic approximation of Hankel function [34], we obtain that the intensity of the longitudinal component of Bessel SPP electric vector $\left|\vec{E}^{\,l}\right|^2 \sim \left|J_m(q\rho)\right|^2$ is determined by the expression:

$$\left|\vec{E}^{\,l}\right|^2 \sim \frac{1}{|q|^2\rho^2}\exp[-2(\mathrm{Im}\, q)\rho]. \qquad (22)$$

Thus, from Eq. (22) it follows that beyond the boundary of the exciting source the BPP decays exponentially in the radial direction. The 1/e energy-attenuation radius R_{BSSP} is determined by the expression

$$R_{BSSP} = 1/(2\,\mathrm{Im}\, q) . \qquad (23)$$

Let us analyze in detail the features of Bessel plasmon polariton generating in the structure represented in Fig.1. As it follows from Eq. (8) the electric (magnetic) vector of the field of BPP in dielectric medium near the exit surface of ENZM slab is dependent on the transmission coefficient t determining by the following expression at $k_{ze} \approx 0$:

$$t = \left[1 - i\frac{\varepsilon_o k_{z1} h}{2\varepsilon_1}\right]^{-1} . \qquad (24)$$

It is evident from Eq. (24) that the value t (and hence, the longitudinal and transversal components of electric vector of BPP inside the external medium "3") is not equal to zero and dependent on the optical properties of ENZM and its thickness.

Much interest is attracted to investigate the features of BPP inside the ENZM slab. As it follows from Eqs. (10), (13), (14) in the conditions of plasmon resonance $k_{ze} \approx 0$

the longitudinal component of electric vector of BPP inside the ENZM slab is determined by the expression:

$$\vec{E}_2^{\,l}(R) \approx iA_{inc}\frac{q}{\varepsilon_z}\frac{k_{z1}\varepsilon_o t}{\varepsilon_1}(z-h)\times$$
$$\times \sin c[k_{ze}(z-h)]\exp i[m\varphi]J_m(q\rho)\vec{e}_z \approx \quad (25)$$
$$\approx (-1+i)A_{inc}\frac{k_0}{\sqrt{2\,\mathrm{Im}\,\varepsilon_z}}\frac{k_{z1}\varepsilon_o t}{\varepsilon_1}(z-h)J_m(q\rho)\vec{e}_z.$$

Here $0 < z < h$. It follows from Eq. (25) that the longitudinal component of electric vector of Bessel plasmon polariton decreases linearly with increasing the distance inside the slab. The intensity of longitudinal component is found from the expression

$$I^l \sim \frac{k_0^2}{\mathrm{Im}\,\varepsilon_z}\frac{k_{z1}^2\varepsilon_o^2|t|^2}{\varepsilon_1^2}(h-z)^2|J_m(q\rho)|^2 . \quad (26)$$

The value I^l is equal to zero at $z = h$. Note that I^l is greater for the case of ENZM with small absorption (small value of $\mathrm{Im}\,\varepsilon_z$) of the metal nanocylinders.

One can see from Eq. (26) that the transversal distribution of I^l is described by the Bessel function. Then the size of the central lobe of intensity pattern is not changed moving off the entrance surface of the ENZM slab.

The transversal component of the electric vector of BPP inside the ENZM slab is given by

$$\vec{E}_2^{\,tr}(R) \approx -A_{inc}\frac{k_{z1}t}{\sqrt{2\varepsilon_1}}\sin[k_{ze}(z-h)]\exp i[(m-1)\varphi]\vec{F}_m^-, \quad (27)$$

and it is very small.

As it follows from Eq. (11), the transversal component of magnetic vector can be expressed as

$$\vec{H}_2(R) \approx \frac{ik_0A_{inc}k_{z1}\varepsilon_o t(z-h)}{\sqrt{2\varepsilon_1}}\times$$
$$\times \sin c[k_{ze}(z-h)]\exp i[(m-1)\varphi]\vec{F}_m^+ \approx \quad (28)$$
$$\approx \frac{ik_0A_{inc}k_{z1}\varepsilon_o t(z-h)}{\sqrt{2\varepsilon_1}}\exp i[(m-1)\varphi]\vec{F}_m^+.$$

One can see from Eq. (28) that $\vec{H}_2(R)$ has essential value.

It is important to emphasize that in opposite to the case of generation of Bessel plasmon polariton in metal film [35] in considered case only single BPP is formed inside the ENZM slab. The full field of Bessel plasmon polariton inside and outside the ENZM slab is described by the Eqs. (8), (9), (26), (27), (28).

3. Conclusions

Thus, in this paper a theory is developed of generation of Bessel plasmon polaritons in the structure including a epsilon-near-zero metamaterial layer separating semi-infinite dielectrics.

The comparison was made of Bessel plasmon polaritons investigated in this paper and traditional surface plasmon polaritons. The traditional SPP is a propagating wave on the ENZM/dielectric surface. Unlike it, BPP is a superposition of counter propagating SPPs in all the possible radial directions. It is a complex high-symmetric interference light structure in sections parallel to the ENZM /dielectric interface. It should be noted as opposed to the propagating surface plasmon polariton, the Bessel one is a standing light structure.

The problem is studied of attenuation of the Bessel plasmon polariton excited by a limited narrow Bessel beam. It is shown that outside the region of the exciting source the BPP decays exponentially in the radial direction.

We have analyzed the cases of symmetric “dielectric – ENZM slab – dielectric” structure. A dispersion equation has been derived and analyzed for this case. The possibility is shown of excitation of the single type of Bessel plasmon polariton independently on the thickness of the ENZM slab. It is established that this BPP is characterized by essential transversal component of magnetic vector and longitudinal component of electric vector. The magnitude of the latter component is substantially dependent on the absorption in the metal nanocylinders.

The intensity distribution of the longitudinal component of the electric vector of Bessel plasmon polariton inside the ENZM layer is analyzed. It is shown that the large central lobe of the intensity pattern is not changed in its transversal size when moving off the entrance surface of the epsilon-near-zero metamaterial slab. So, it is established the possibility to form the diffraction-free needle-like standing plasmon field inside the ENZM layer.

The results obtained can be used for the development and optimization of techniques and devices for testing the quality of the surface of various substrates by Bessel plasmon polaritons.

Acknowledgements

The authors would like to thank King Abdul-Aziz City for Science and Technology (KACST) for Research Grant No. 814-33.

References

[1] J.B. Pendry, Negative refraction makes a pefraction makes a perfect lens, *Phys. Rev. Lett.* 85: 3966-3969, 2000.

[2] N. Fang, H. Lee, C. Sun, X. Zhang, Sub-diffraction-limited optical imaging with a silver superlens, *Science*. 308: 534-537, 2005.

[3] J.B. Pendry, D. Schurig, D.R. Smith, Controlling Electromagnetic Fields, Science 312: 1780-1782, 2006.

[4] D.R. Smith, P. Kolinko, D. Schurig, Negative refraction in indefinite media, *J. Opt. Soc. Am.* B21: 1032-1043, 2004.

[5] P.A. Belov, Y. Hao, Subwavelength imaging at optical frequences using a transmission device formed by a periodic layered metal-dielectric structure operating in the canalization regime, *Phys. Rev.* B73: 113110, 2006.

[6] V. P. Drachev, V. A. Podolsky, A.V.Kildishev, Hyperbolic metamaterials: new physics behind a

classical problem, *Opt. Express.* 21: 15048-15064, 2013.

[7] A. J. Hoffman, L. Alekseyev, C.Gmachl, Negative refraction in semiconductor metamaterials, *Nature Materials* 6: 946-950, 2007.

[8] G. Castaldi, S. Savoia, V. Galdi, Analytical study of subwavelength imaging by uniaxial epsilon-near-zero metamaterial slabs, *Phys. Rev.* B86: 115123, 2012.

[9] B. Wang, K.M. Huang, Shaping the radiation pattern with Mu and epsilon-near-zero metamaterials, *PIER.* 106:107-119, 2010.

[10] J. Gao *et al*, Experimental realization of epsilon-near-zero metamaterial slabs with metal-dielectric multilayers, *Appl. Phys. Lett.* 103: 051111 (2013).

[11] J. Durnin, Exact solutions for nondiffracting beams. I. The scalar theory, *J.Opt.Soc.Am*. A4: 651-654, 1987.

[12] J. Durnin, J.J. Muceli, J.H. Eberly, Diffraction-free beams, *Phys. Rev. Lett*. 58: 1499-1501, 1987.

[13] P. Sprangle, B. Hafizi, Comment on nondiffracting beams , *Phys. Rev. Lett.*: 66: 837-839, 1991.

[14] Z. Bouchal, J. Wagner, M. Chlup, Self-reconstruction of a distorted nondiffracting beam, *Opt. Commun*. 151: 207-211, 1998.

[15] Y. Lin *et al*, Experimental investigation of Bessel beam characteristics, *Appl. Opt*., 31: 2708-2713, 1992.

[16] D. McGloin, K. Dholakia, Bessel beams: diffraction in a new light, *Contemp. Phys*. 46: 15-28, 2005.

[17] J. Turunen, A.T. Friberg, Self-imaging and propagation-invariance in electromagnetic fields, *Pure Appl. Opt*. 2: 51-60, 1993.

[18] R. Horak, Z. Bouchal, J. Bajer, Nondiffracting stationary electromagnetic field, *Opt. Commun.* 133: 315-327, 1997.

[19] G. Milne, K. Dholakia, D. McGloin, K. Volke-Sepulveda, P. Zemanek, Particle dynamics in a Bessel beam, *Opt. Express.* 15: 13 972- 13 987, 2007.

[20] V. Garcés-Chavéz, D. Roskey, M.D. Summers, H. Melville, D. McGloin, E.M. Wright, K. Dholakia, Optical levitation in a Bessel light beam, *Appl. Phys. Lett.* 8: 4001-4003, 2004.

[21] L. Paterson, E. Papagiakoumou, G. Milne, V.Garcés-Chavéz, T. Briscoe, W. Sibbett, L. Dholakia, A. Riches, Passive optical separation with a 'nondiffracting' light beam, *J. Biomed. Opt*. 12: 054017, 2007.

[22] T. Cižmár, V. Garcés – Chávez, K. Dholakia, P. Zemánek, Optical conveyor belt for delivery of submicron objects, *Appl. Phys. Lett.* 86: 101-1-174 – 101-3, 2005.

[23] S. Rushin, A. Leizer, Evanescent Bessel beams, *J. Opt. Soc. Am.*.A15: 1139-1143, 1998.

[24] S. N. Kurilkina, V.N. Belyi, N.S. Kazak, Features of evanescent Bessel light beams formed in structures containing a dielectric layer, *Opt. Comm.* 283: 3860-3868, 2010.

[25] Q.Zhan, Evanescent Bessel beam generation via surface plasmon resonance excitation by a radially polarized beam, *Opt.Lett.* 31: 1726-1728, 2006.

[26] Muhanna K Al-Muhanna, S. N. Kurilkina, V. N. Belyi, N. S. Kazak, Energy flow patterns in an optical field formed by a superposition of evanescent Bessel light beams, *J.Opt*. 13: 105703, 2011.

[27] H.Kano, D. Nomura, H. Shibuya, Excitation of surface-plasmon polaritons by use of a zeroth-order Bessel beam, *Appl. Opt.* .43: 2409-2411, 2004.

[28] T. Grosjean, D. Courjon, D. Van Labeke, Bessel beams as virtual tips for near-field optics, *J. Microscopy*. 210: 319-323, 2003.

[29] H.Kano, D. Nomura, H. Shibuya, Excitation of surface-plasmon polaritons by use of a zeroth-order Bessel beam, *Appl. Opt.* 43: 2409-2411, 2004.

[30] J. Zapata-Rodriguez et al, Nondiffracting Bessel plasmons, Opt. Express. 19: 19572-19581, 2011.

[31] W. Cai, V. Shalaev, *Optical Metamaterials. Fundamentals and Applications*, Springer, New York, 2010.

[32] R.Atkinson *et al*, Anisotropic optical properties of arrays of gold nanorods embedded in alumina, *Phys. Rev*. B73: 235402-1 – 235402-8, 2006.

[33] G.N. Watson, *A Threatise on the theory of Bessel functions*, Cambridge University Press, Cambridge, 1966.

[34] G. B. Arfken, H.J.Weber, F.E.Harris, *Mathematical methods for physicists*, Academic Press, Orlando FL., 1985.

[35] S. N. Kurilkina, V. N. Belyi, N. S. Kazak, Features of vortex Bessel plasmons generated in metal–dielectric layered structures, *J. Opt.* 15: 044017, 2013.

Left Handed Mode Propagating In Coplanar Isolator Based on Yittrium Iron Garnet (YIG)

Adam Ouzer-Nabil[1,2], Eric Verney[1], Souad Kirouane[1], Bruno Sauviac[1], Soultan Malloum[2]

[1]Laboratory Telecom Claude Chappe, University of St-Etienne, France
[2]Universitary Institute of Sciences and Technics of Abéché, Tchad
*corresponding author, E-mail: eric.verney@univ-st-etienne.fr

Abstract

A hybrid structure of coplanar isolator, based on a YIG substrate with a bottom ground plane, shows a left-handed propagation around 10 GHz. The dependence of this effect to the dimensions of the device and the appearance of magneto-static waves in the thin magnetic layer is explored.

1. Introduction

Growing needs in telecommunications induced an undeniable revolution in the dimensions of the components. The miniaturization of the devices and the increase of operating frequencies are two important solutions for communication system development

One of the most useful microwave ferrite components is the isolator, which is a two port device with an unidirectional transmission, the common application of the isolator being the sources protection to prevent damages from possible reflections in the transmission lines.

The first isolators were made from waveguide loaded with a slab of ferrite, one advantage of this structure being that the full-height slab is easy to bias with an external permanent field, and they have been used for high frequency power, due to their size incompatible with integration.

To design isolators compatible with monolithic integration circuits, the preferred structure is the coplanar one, because of its simpler connection with the other components. The first coplanar isolator with ferrite rods was proposed in 1969 by C.P. Wen [1]. This device was operating near gyromagnetic resonance, and even if the isolation seemed to have been reached, insertion loss was still too high for a commercial application.

This paper proposes a new isolator design, operating in the X-band, composed of an asymmetrical [3-4] coplanar waveguide on a ferrite substrate and a bottom ground plane in the asymmetrical side of the structure.

This new coplanar isolator operates outside gyromagnetic frequency band, in the magneto-static waves frequency zone. At the operating frequency, the apparition of complex modes in this hybrid structure generates a left-handed mode in the asymmetrical side of the structure, that recombines destructively thanks to a 180° phase shift with the right-handed one propagating in the symmetrical side.

2. Physical and geometrical properties of the isolator

As shown in Fig. 1, the structure is based on a coplanar guide, with a ground plane on the bottom of the substrate, not connected to the upper ground planes. A gap is designed in one of the upper ground plane (or both, see Fig. 2), and a bias magnetic field is applied normally to the structure.

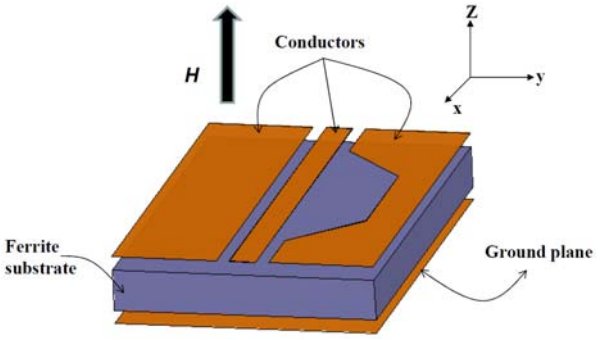

Figure 1: Structure of coplanar-based isolator.

The ferrite substrate (made of YIG) is 1mm thick, and a normal bias field is applied to saturate it. The lateral gap in the upper ground plane is necessarily in the same order of width as the thickness of the layer, around 1mm, for the structure to isolate. The CPW guide has a signal line width of 400 µm and a gap width of 200 µm. The isolator is 10mm long, and one of the final practical goals of this study is to minimize this length as well as the thickness of the magnetic layer, while keeping the same electromagnetical performances.

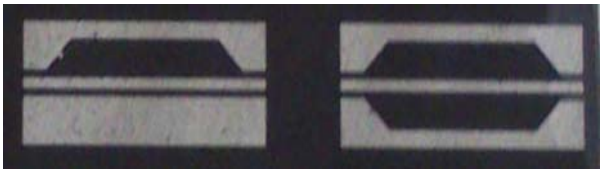

Figure 2: 10mm long coplanar isolator samples.

These electromagnetical properties are shown in Fig. 3, where one can see the isolation peak at 10.8 GHz, appearing

in the magneto-static band [2], right to the gyro-resonance frequency zone (between 6 and 9 GHz).

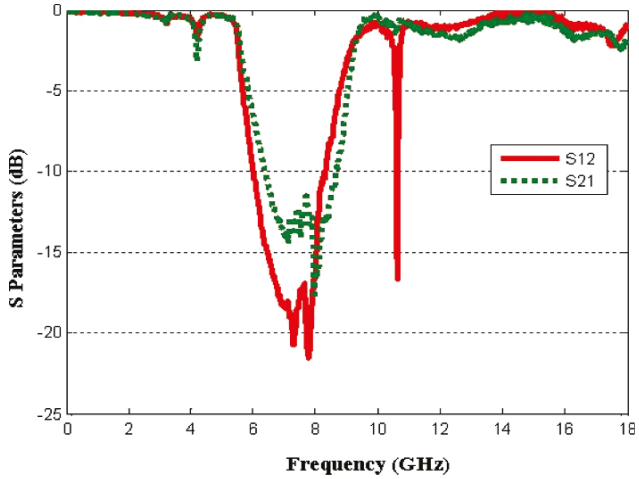

Figure 3: Response of the isolator under a 225mT bias field.

In this first and not optimized version of the isolator, the non-reciprocal effect is about 16 dB, and the insertion losses in the passing sense are about 1.5 dB. The S11 and S22 coefficients are about -20 dB at the resonance frequency. These performances are very interesting, and we'll then try to improve them.

3. Electromagnetic modes at the resonance

This component was developed with HFSS before being fabricated and measured. The accordance between measures and simulations is pretty good [4], and therefore HFSS was considered as a good mean to start analyzing the modes in the waveguide.
The bias magnetic field induces a field displacement in the asymmetric gap of the upper ground plane. The energy propagates in this hybrid structure, both coplanar and microstrip-like, and the modes in this guide are complex, with a strong ellipticity, both in *x* and *y* directions. The isolation effect still occurs if the bottom ground plane is fabricated only under the asymmetrical part, but absolutely no isolation is observed if it is totally suppressed (as well, of course, if we suppress the bias magnetic field).

The resonance occurs in the magneto-static waves band, close to the gyro-resonance band, and the permittivity tensor of the ferrite slab is still strongly asymmetric in this frequency band. The simulation clearly shows that at the resonance a left-handed propagation occurs in the asymmetric branch, while right-handed mode propagates in the symmetric one (Fig. 4). At the wave ports of the guide, both waves interact destructively, while reflection coefficients are close to -10dB (this value is better in measurements than in simulations) and the simulation shows that the energy is not dissipated by the material as we can observe it in the gyro-resonance frequency band.
Ferrite slabs show left-handed propagation in some cases [5], and the analytic demonstration of their apparition in our structure is still to be done, but one hypothesis to explain what we observe is a coupling between different modes in the structure, propagative and magneto-static.

As our analysis is based on simulations, let discuss how confident we can be with these results.
A preliminary parametric study in simulation showed that the frequency of resonance of the isolator was not dependent on lengths of the device (guide length, upper ground plane gap length), with a difference less than 1% on the resonance frequency between the different version (length varying between 10 mm and 6 mm). The study also showed that the thickness of the substrate and the upper ground plane gap had to be on the same order of size to get an important isolation effect. In facts, when we measured the different prototypes (see section 4), we noticed that if the gap width actually only has an influence on the peak depth, according to simulations, its length has an influence on the frequency of resonance, in proportions of 10%. So HFSS seems not to be completely able to simulate physical effects occurring in the magnetic slab. To confirm the validity of the observed modes in the simulation, it would be interesting to measure the propagating fields along the guide with a near-field probe.

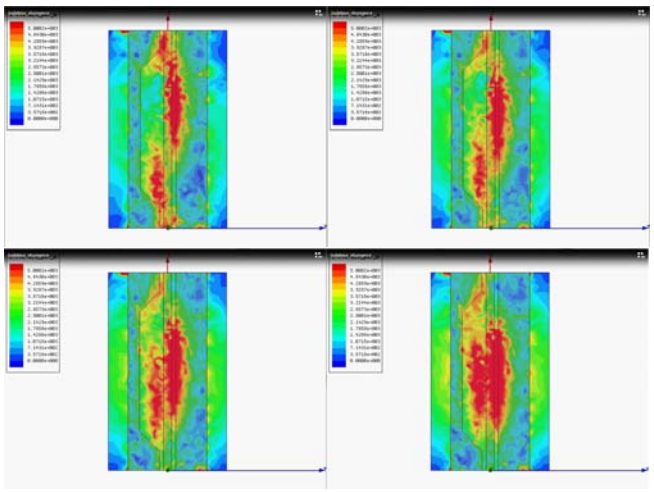

Figure 4: Simulation of the time evolution (from left to right, and from top to bottom) of the maximum of the electric field module, collocated with the maximum of the module of the Poynting's vector. Phase velocities in each branches of the guide are of opposite signs, when group velocities are of same signs (Poynting vector has the same direction in both branches of the guide).

4. Evolution and optimization of the structure

In order to understand the physics of this component, we simulated and fabricated a second structure with 2 gaps in the upper ground plane (see Fig. 2). All the dimensions and magnetic bias remain the same, we only added a second gap in the upper ground plane to the structure. We initially attempted to have no isolation anymore or a second isolation peak in the other sense of propagation at a different frequency. But the result is more complex than expected, and as with the first structure with a single gap in the ground

plane, simulation predictions are not completely verified. Anyway, in accordance with simulations, the result confirmed with this second version with two gaps, is that a change in the width of the gap only affects the depth of the isolation peak (correlated with a better reflection coefficient).

On the other hand, regarding to the influence of the length of the gaps of the ground plane, measurements show different kinds of evolutions of the electromagnetic response for the 1-gap or the 2-gaps versions. Keeping constant the total length of the device (10 mm), we varied the length of the gap of upper ground plane, from 8 to 6 mm, and this for both types of isolators.

For a gap of 8 mm, which correspond to results of Fig. 3 for the 1-gap structure, and to results of Fig. 5 for the 2-gaps structure, we get a deeper peak, from -16 dB to -20 dB, while keeping equivalent insertion losses around -1.5 dB. On the other hand, the frequency of resonance is shifted from 10.8 GHz to 9.8 GHz (in contradiction with simulation results, as seen in section 3). A second peak, with the isolation sense inversed, appear around 8.7 GHz, which seem to confirm or hypothesis that non-diagonal asymmetric parameters of the permittivity tensor of YIG layer take part in the definition of the frequency of resonance. On the other hand, the smaller depth of this peak may indicate that in that case the modes in the structure are not producing two waves with equal amplitudes in both branches, so the destructive interaction doesn't lead to a strong annihilation.

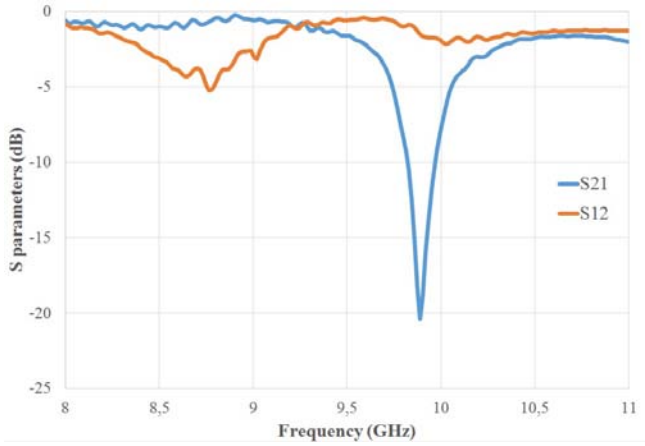

Figure 5: Response of the 2-gaps isolator with 8 mm gaps, under a 200mT bias field.

For a gap of 6 mm (Fig. 6), the 2-gaps isolator shows an isolation peak enhanced of 5 dB compared to the 1-gap version, which confirm the positive influence of the second gap on the performances of the device. The insertion losses keep the same between the two versions, around -4 dB, but of course this value is not sufficient for an application.

We also observe, as on Fig. 5, a second inversed non-reciprocal peak, around 8.5 GHz, this time for both structures, as predicted by simulations, with 4 dB of non-reciprocal effects. In the 1-gap version with 8 mm gap this effect seemed negligible (1.3 dB at 9.25 GHz), but it shows that the parametric study reveals a greater complexity in the distribution of the fields in the structure than initially expected.

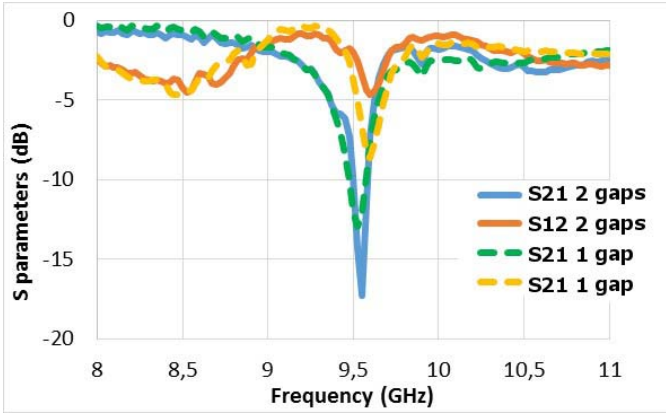

Figure 6: Comparison of the measurements of the response of the 1-gap and 2-gaps isolators with 6 mm gaps, under a 200 mT bias field.

The best performances obtained at that point of the study were obtained for a 10 mm long demonstrator, with a gap length of 8 mm and a gap width of 1.3 mm. The YIG substrate is 1mm thick with a 200 mT bias field. At 9.8 GHz the structure has a S21 of -19 dB, with S11 equal to -16.9 dB, and a S12 of -1.1 dB with a S22 equal to -11 dB.

5. Conclusion and perspectives

From an applicative point of view, this new structure of coplanar isolator shows a good potential, with around -20 dB of isolation, and -1.11 dB of insertion losses around 10 GHz. The development of a 2-gaps version, which despite its physical symmetry keeps the benefit brought by the asymmetrical permittivity tensor of the magnetic substrate layer, showed that an optimization could be done on its performances. From this version of demonstrator, the objective to compact the device for integration goals in telecommunication chains should be pursued. Different possibilities can be explored to achieve these goals, like shorten the device or lower the ferrite substrate thickness.

From the point of view of physics of the device, both complex and interesting, simulation softwares showing limitations, developing a model is necessary to understand how the resonances take place, and which parameters influence their frequencies and amplitudes. It also seems interesting to measure the fields along the guide with a near-field probe to confirm that a left-handed mode is propagating in one of its part. To help optimization, the analyze of the coupling modes and the conditions of their appearance is necessary.

References

[1] C.P. Wen, *IEEE Trans. Microwave. Theor. Technol.*, 17, 12, 1969.

[2] H.V.D. Vaart, *Electron. Lett.* 6, 601602, 1970.

[3] S. Kirouane, E. Verney, D. Vincent, A. Chaabi, Simulation results on a new non symmetrical coplanar isolator structure using magnetic thin

film, *Progress in Electromagnetic Research (PIER)*, Vol. 8, pp. 161-170, 2009.

[4] S. Kirouane, D. Vincent, E. Verney, O. Zahwe, B. Payet and A. Chaabi, Design of a new coplanar isolator made from YIG film operating in the X-frequency band, *The European Physical Journal Applied Physics*, 57, 01, 10602, 2011.

[5] D. D. Stancil, Theory of magnetostatic waves, Springer-Verlag New York, Inc., 1993.

Application of Teaching Learning Based Optimization in antenna designing

Surabhi Dwivedi[1*], Vivekanand Mishra[1], Yogesh Kosta[2],

[1]Sardar Vallabhbhai National Institute Of Technology, Surat, Gujarat, India
[2]Marwadi Education Foundations Group of Institutions,Rajkot, Gujarat
*corresponding author, E-mail: sur_2310@yahoo.co.in

Abstract

Numerous optimization techniques are studied and applied on antenna designs to optimize various performance parameters. Authors used many Multiple Attributes Decision Making(MADM) methods, which include, Weighted Sum Method (WSM), Weighted Product Method (WPM), Technique for Order Preference by Similarity to Ideal Solution (TOPSIS), Analytic Hierarchy Process (AHP), ELECTRE, etc. Of these many MADM methods, TOPSIS and AHP are more widely used decision making methods. Both TOPSIS and AHP are logical decision making approaches and deal with the problem of choosing an alternative from a set of alternatives which are characterized in terms of some attributes. Analytic Hierarchy Process (AHP) is explained in detail and compared with WSM and WPM. Authors finally used Teaching-Learning-Based Optimization (TLBO) technique; which is a novel method for constrained antenna design optimization problems.

1. Introduction

Multiple Criterion Decision Making (MCDM) refers to making decisions from multiple conflicting criteria. MCDM is broadly classified into two categories: multiple attribute decision making (MADM) and multiple objective decision making (MODM). The choice of selecting the best method depends on whether the problem is a selection problem or a design problem. MODM methods have decision variable values with a large number of choices and select the best that should satisfy the decision maker's constraints and preference priorities. Teaching Learning Based Optimization(TLBO) method is a kind of MODM technique. MADM methods, on the other hand, are generally discrete, with a limited number of predetermined alternatives. MADM is an approach employed to solve problems involving selection from among a finite number of alternatives. A MADM method specifies how attribute information is to be processed in order to arrive at the best choice. MADM methods require both inter- and intra-attribute comparisons, and involve appropriate explicit tradeoffs[1].

Each decision table (or decision matrix) in MADM methods has four main parts, namely: (a) alternatives, (b) attributes, (c) weight , and (d) measures of performance of alternatives w.r.t. the attributes. The decision table is shown in Table 1. The decision table shows alternatives, A_i (for i = 1, 2, .. , N), attributes, B_j (for j = 1, 2, .. , M), weights of attributes, w_j (for j=1, 2, .., M) and the measures of performance of alternatives, m_{ij} (for i= 1, 2, .., N; j=1, 2, .., M) [1].

2. MADM Methods

Following are the different types of MADM methods used by the present team of authors for their specific application of antenna designing.

2.1. Simple Additive Weighting (SAW) Method

This is also called the Weighted Sum Method (Fishburn, 1967) and is the simplest and widest used MADM method. Each attribute is given a weight and the sum of all weights must be 1. The overall or composite performance score of an alternative is given by Equation 1.

$$P_i = \sum_{j=1}^{M} w_j m_{ij} \tag{1}$$

A beneficial attribute (e.g. Peak Gain(PG), Directivity(D), Radiation Efficiency(RE), Front to Back Ratio(FBR)) means its higher values are desirable for the given decision-making problem. By contrast, non-beneficial attribute (e.g. Return Loss(RL), Voltage Standing Wave Ratio(VSWR), Loss Tangent(LT)) is that for which the lower values are desirable.

$$P_i = \left[\sum_{j=1}^{M} w_j \left(m_{ij}\right)_{normal}\right] / \sum_{j=1}^{M} w_j \tag{2}$$

2.2. Weighted Product Method (WPM)

This method is similar to SAW. The main difference is that, instead of addition in the model, there is multiplication (Miller and Starr, 1969). The overall or composite performance score of an alternative is given by Equation 3.

$$P_i = \prod_{j=1}^{M} \left[\left(m_{ij}\right)_{normal}\right]^{w_j} \tag{3}$$

2.3. Analytic Hierarchy Process (AHP) Method

One of the most popular analytical techniques for complex decision-making problems is the analytic hierarchy process

(AHP). In 1980, Saaty developed AHP, which decomposes a decision-making problem into a system of hierarchies of objectives, attributes and alternatives.
An AHP hierarchy can have as many levels as needed to fully characterize a particular decision situation of designing. A number of functional characteristics make AHP a useful methodology. These include the ability to handle decision situations involving subjective judgments, multiple decision makers, and the ability to provide measures of consistency of preference [2]. AHP can efficiently deal with tangible (i.e., objective) as well as non-tangible (i.e., subjective) attributes, especially where the subjective judgments of different individuals are required[1].

2.4. Comparison of SAW, WPM and AHP

Table 2 is drawn for selecting materials for substrate:
where, DC: Dielectric Constant, LT: Loss Tangent, RF: Radio Frequency, RL: Return Loss, VSWR: Voltage Standing Wave Ratio, PG: Peak Gain, D: Directivity, RE: Radiation Efficiency, FBR: Front to Back Ratio.
All the steps of AHP method are explained in detail in below mentioned Tables 3, Table 4 and Table 5.
In the Table 6 below, hierarchy generation using all the three methods is shown.

3. Teaching Learning Based Optimization in Antenna Designing

Teaching-Learning-Based Optimization algorithm (TLBO) is a teaching-learning process inspired algorithm proposed by Rao et al. [3] which is based on the effect of influence of a teacher on the result of learners in a class. The algorithm replicates the teaching-learning ability of teacher and learners in a class room. Teacher and learners are the two important components of the algorithm and describes two basic modes of the learning, through teacher (known as teacher phase) and interacting with the other learners (known as learner phase). The output in TLBO algorithm is considered in terms of grades of the learners which depend on the quality of teacher. In the entire population the best solution is considered as the teacher[4].

The working of TLBO is divided into two parts, Teacher phase and Learner phase.

i) Teacher phase
It is first part of the algorithm where learners learn through the teacher [3].

ii) Learner phase
It is second part of the algorithm where learners increase their knowledge by interaction among themselves. A learner interacts randomly with other learners for enhancing his or her knowledge[4].
The implementation steps of the TLBO are summarized below:
Step 1: Initialize the population (i.e. learners) and design variables of the optimization problem (i.e number of subjects offered to the learner) with random generation and evaluate them. In the case of antenna designing, different subjects are anonymous to the performance parameters DC, LT, RF, RL, VSWR, PG, D, RE and FBR)
Step 2: Select the best learner of each subject as a teacher for that subject and calculate mean result of learners in each subject.Different learners in this case are different dielectric materials chosen as antenna substrate; Bakelite, Diamond, RT Duroid 5880, FR4 epoxy, Rogers RT/ duroid 6006, Teflon.
Step 3: Evaluate the difference between current mean result and best mean result by utilizing the teaching factor (TF) which is taken as 1.
Step 4: Update the learners knowledge with the help of teachers knowledge.
Step 5: Update the learners knowledge by utilizing the knowledge of some other learner.
Step 6: Repeat the procedure from step 2 to 5 till the termination criterion is met.

4. Design and simulation

. The negative parameters are extracted by placing the unit cell of metamaterial design within the waveguide as shown in fig 1. The retrieval method used in this paper is based on the approach used by Xudong Chen et. al. in [5]. The negative values of impedance(refer fig 2), refractive index(refer fig 3), permittivity(refer fig 4) and permeability (refer fig 5) are plotted using matlab coding of Drude model.

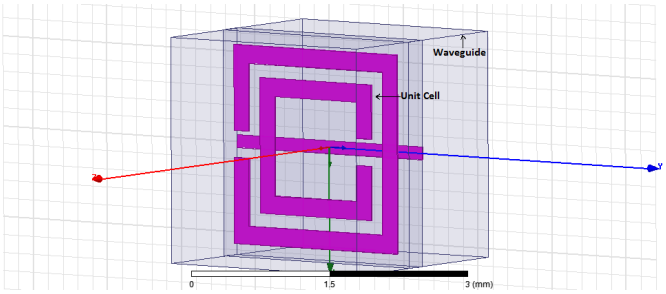

Figure 1: Unit cell in waveguide

Extracted negative parameters are shown in the figures drawn below:

Hence, it is proved that the unit cell behaves as MTM under desired band of frequency region. Then array of unit cells are placed over a patch to improve its directivity as shown in fig 6 and the spacing height is optimized using the above mentioned optimization techniques. The dielectric constant of the substrate is chosen by using TLBO algorithm as stated in section 3.

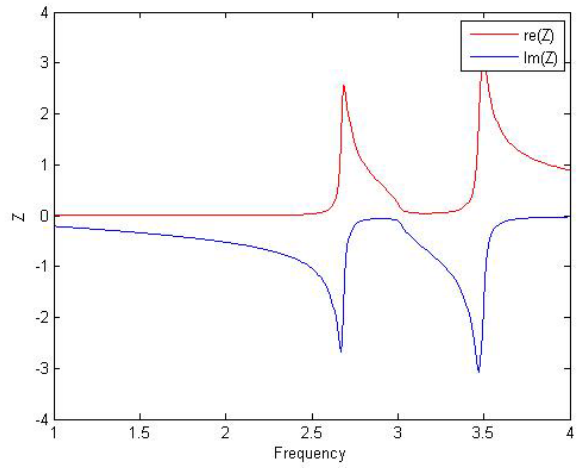

Figure 2: Impedance of unit cell

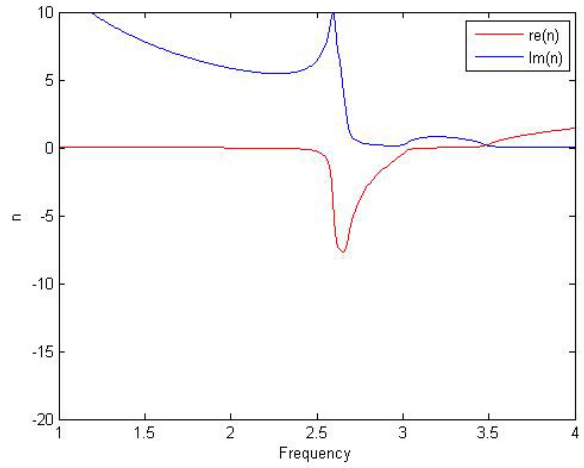

Figure 3: Refractive Index of Unit Cell

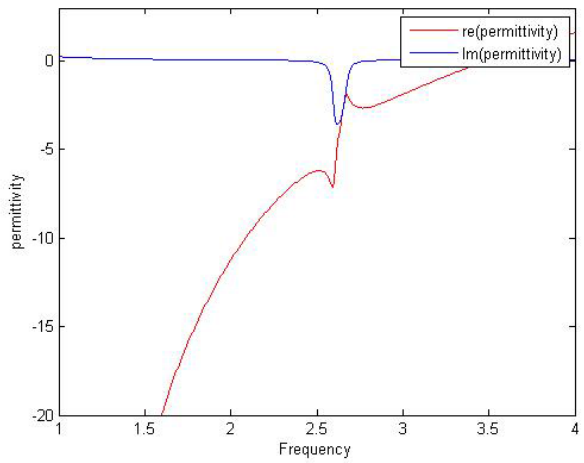

Figure 4: Permittivity of unit cell

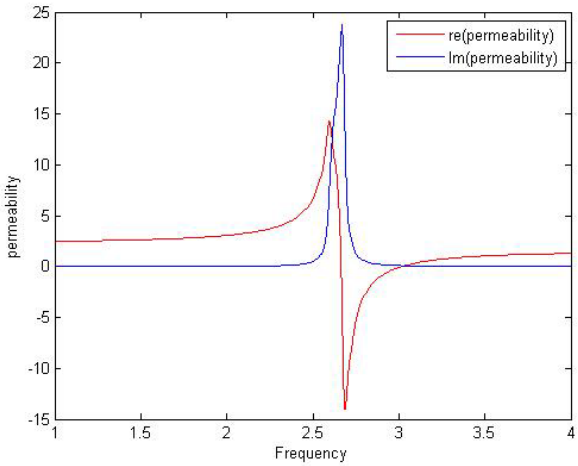

Figure 5: Permeability of unit cell

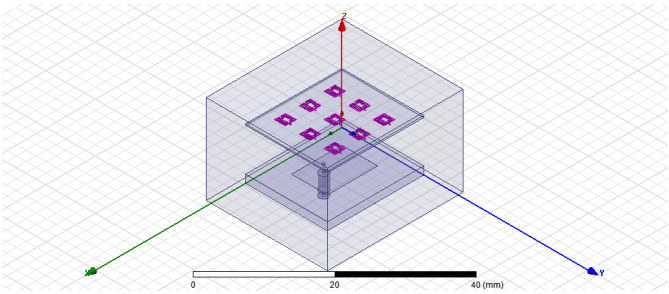

Figure 6: Patch cover

5. Applications of radome structure

As the LHM have negative refractive index it can be used to realize a focusing flat lens [6], whereas positive refractive index materials always require curved surfaces to focus EM waves [7].

Negative refraction by a slab of material bends a ray of light back toward the axis and thus has a focusing effect at the point where the refracted rays meet the axis as shown in fig 7. It was recently observed that a negative index lens exhibits an entirely new type of focusing phenomenon, bringing together not just the propagating rays but also the finer details of the electromagnetic near fields that are evanescent and do not propagate [8] as shown in fig 8.

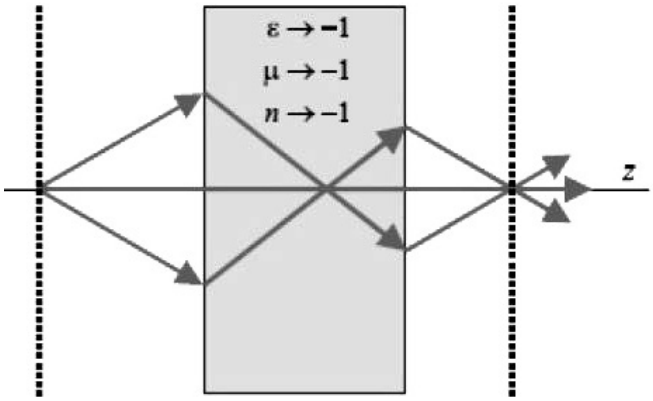

Figure 7: LHM slab as focusing lens [8]

6. Conclusion

The extracted result parameters obtained by using optimization algorithms are shown to be in excellent agreement with simulation results. It is concluded that numerous optimization techniques can be considered for antenna designing. And the selection of the best optimization method depends upon the designer's perspectives and his requirements. Proposed miniaturized structures is used to characterize and improve the directivity of microstrip patch antenna for the required frequency of operation of 1 to 4GHz. Comparative result analysis is obtained for three different types of optimization techniques. Directivity is improved by optimizing the spacing height at 8.4mm. The designed antenna is very useful for triband operation for several wireless applications in L and S band communication. They possess inherent advantages like reduced sizes. Ultimately Teaching-Learning Based Optimization Technique has been used to enhance the performance parameters of the antenna.The author looks forward to the implementation of TLBO concept for radome structure, which can further improve the present status of microstrip patch antenna performance. The proposed structure has compact size, convenient fabrication procedures and low cost.

Acknowledgement

The current team of authors would like to thank Dr. Ved Vyas Dwivedi for his technical guidance.

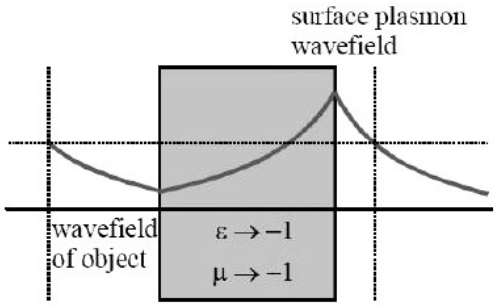

Figure 8: Near-field enhancement using a metamaterial [8]

Table 1: Decision table in MADM methods

Alternatives	Attributes					
	B1 (w1)	B2 (w2)	B3 (w3)	- - (-)	- - (-)	BM (wM)
A1	m11	m12	m13	- -	- -	m1M
A2	m21	m22	m23	- -	- -	m2M
A3	m31	m32	m33	- -	- -	m3M
- - - - - - -	- -	- -	- -	- -	- -	- -
- - - - - - -	- -	- -	- -	- -	- -	- -
AN	mN1	mN2	mN3	- -	- -	mNM

Table 2: Selection of Substrate Material

Material	DC	LT	RF (GHz)	RL (dB)	VSWR	PG (dB)	D (dB)	RE (%)	FBR
Vacuum	1	0	2.44	-10.1958	1.8951	4.1967	4.2046	99.81	6.92
Air	1.0006	0	2.44	-9.8920	1.9948	4.1586	4.1553	100.08	6.82
Bakelite	4.8	0.002	2.41	-7.5913	2.4322	1.9922	2.2439	88.78	8.2
Diamond	16.5	0	2.43	-3.1708	5.5394	1.0889	1.108	98.27	2.88
RT Duroid 5880	2.2	0.0009	2.42	-7.8571	2.3890	3.3201	3.4473	96.31	14.77
FR4 epoxy	4.4	0.2	2.43	-18.08	1.34	1.1296	2.3311	48.45	9.55
Rogers RT / duroid 6006	6.15	0.0019	2.42	-6.4392	2.9276	1.7019	1.927	88.32	6.28
Teflon	2.1	0.001	2.43	-9.4656	2.0134	3.3219	3.5047	94.78	15.93

Table 3: AHP: Step1

Materials	RF	RL	VSWR	PG	D	RE	FBR	Index/Score
Bakelite	0.2608	0.0934	0.0747	0.0472	0.0479	0.0230	0.0006	0.5480
Diamond	0.2208	0.0237	0.0190	0.0245	0.0080	0.0013	0	0.2976
RT Duroid 5880	0.1351	0.0342	0.0419	0.0255	0.0013	0	0	0.2381
FR4 epoxy	0.0781	0.0748	0.0255	0.0004	0	0	0	0.1789
Rogers RT/ duroid 6006	0.0745	0.0090	0.0006	0	0	0	0	0.0842
Teflon	0.0253	0.0006	0	0	0	0	0	0.0260

Table 4: AHP: Step2

	RF	RL	VSWR	PG	D	RE	FBR	Geometric mean	weightage	percentage
RF	1	3	3	5	5	7	5	2.6272	0.2608	26.0844
RL	0.33	1	3	5	5	7	5	2.2425	0.2226	22.2651
VSWR	0.33	0.33	1	3	3	5	3	1.3666	0.1356	13.5684
PG	0.2	0.2	0.33	1	1	5	3	0.7935	0.0787	7.87862
D	0.2	0.2	0.33	1	1	5	3	0.7541	0.0748	7.48738
RE	0.14	0.14	0.2	0.2	0.2	1	0.33	0.2570	0.0255	2.55238
FBR	0.2	0.2	0.33	0.33	0.33	3	1	0.0133	0.0013	0.13237
								8.0544		

Table 5: AHP: Step3

	RF	RL	VSWR	PG	D	RE	FBR	Index/Score
RF	0.2608	0.6679	0.4070	0.3939	0.3743	0.1786	0.0066	2.2894
RL	0.0734	0.1356	0.2363	0.3743	0.1276	0.0092	0	0.9567
VSWR	0.0447	0.0259	0.07487	0.0765	0.0039	0	0	0.2261
PG	0.0157	0.0149	0.0084	0.0013	0	0	0	0.0404
D	0.0149	0.0051	0.0004	0	0	0	0	0.0205
RE	0.0035	0.0001	0	0	0	0	0	0.0037
FBR	0.0002	0	0	0	0	0	0	0.0002
								2.2894

Table 6: Comparison of all the three methods of decision making

Materials	AHP	Materials	WPM	Materials	SAW
6	0.0260	2	0.6295	6	0.0260
5	0.0842	1	0.7038	5	0.0842
4	0.1789	3	0.8962	4	0.1789
3	0.2381	5	0.9726	3	0.2381
2	0.2976	4	0.9979	2	0.2976
1	0.5480	6	0.9989	1	0.5480

References

[1] R. V. Rao, *Decision Making in Manufacturing Environment Using Graph Theory and Fuzzy Multiple Attribute Decision Making Methods: Volume 2*. Springer, 2012, vol. 2.

[2] E. Triantaphyllou, *Multi-criteria decision making methods*. Springer, 2000.

[3] R. Rao, V. Savsani, and D. Vakharia, "Teaching–learning-based optimization: A novel method for constrained mechanical design optimization problems," *Computer-Aided Design*, vol. 43, no. 3, pp. 303–315, 2011.

[4] R. V. Rao and V. J. Savsani, *Mechanical design optimization using advanced optimization techniques*. Springer, 2012.

[5] X. Chen, T. M. Grzegorczyk, B.-I. Wu, J. Pacheco Jr, and J. A. Kong, "Robust method to retrieve the constitutive effective parameters of metamaterials," *Physical Review E*, vol. 70, no. 1, p. 016608, 2004.

[6] J. B. Pendry, "Negative refraction makes a perfect lens," *Physical review letters*, vol. 85, no. 18, p. 3966, 2000.

[7] K. Aydin, I. Bulu, and E. Ozbay, "Focusing of electromagnetic waves by a left-handed metamaterial flat lens," *Opt. Express*, vol. 13, no. 22, pp. 8753–8759, 2005.

[8] D. Smith, J. Pendry, and M. Wiltshire, "Metamaterials and negative refractive index," *Science*, vol. 305, no. 5685, pp. 788–792, 2004.

Finite Element Simulation for Cylindrical Invisibility Cloaking using Linear Transformation Optics

Karim Atallah[1*], Kareem El Assy[1], Xue-feng Zhu[2], Mohamed Badr[1], Nourhan Rasheed[1], Khaled Galal[1], Eslam Magdy[1]

[1]Department of Electronics Engineering, Arab Academy for Science and Technology and Maritime Transport, Egypt
[2]Department of Physics, Huazhong University of Science and Technology, Wuhan 430074, China

*Corresponding author: karim_18892@hotmail.com

Nowadays, the ability of achieving invisibility cloaks has become as reality, all because of the breakthrough in the world of metamaterials. A few papers are considered the groundwork for research in the area of metamaterials and cloaking, starting from Veselago in 1968, to the first experimental demonstration by Smith et al. through Pendry's work on a perfect lens. In this paper we will shed the light on the different cloaking techniques, specially the Transformation Optics (TO). There will be a comparison between linear and high-order TO; especially third order and fifth order, physically in terms of impedance mismatch, with FEM simulation and mathematical derivation. [1]

[1] Cloaking techniques

There are many techniques to achieve invisibility cloaks; some need metamaterials in the system, others do not. The three techniques we are discussing are: Mei Scattering, Transformation Optics and Quasi-conformal Mapping.

1.1 Mei Scattering

The Mei Scattering technique is based on the scattering cancellation technique (Figure 1). The key idea is to use polari-tonic spheres around the object to be cloaked in order to match the impedance of the surrounding media by cancelling the scattering response of that object.

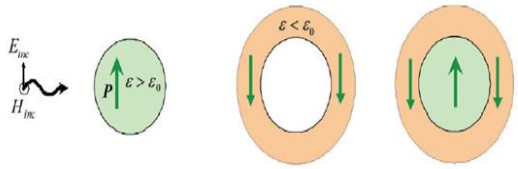

Figure 1: The dipole moments induced in the object to be made invisible and the s hell covering this object cancels each other [2]

1.2 Transformation Optics

The Transformation optics (TO) is based on coordinate transformation or mapping (Figure 2). This technique makes use of the amazing property of Maxwell's equations being invariant to changes in the coordinate system used to express them. It uses metamaterials to induce a profile of permittivity and permeability together with anisotropy in the transformed media. [1]

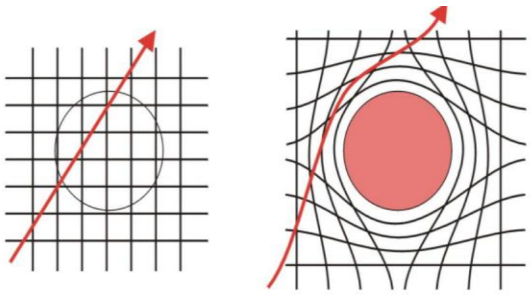

Figure 2: An undistorted coordinate system with a light ray trajectory (left). The distorted coordinate system with the ray trajectory being deflected around the protected zone, red circle in the center (right)

1.3 Quasi-conformal Mapping

Quasiconformal mapping is a type of transformation optics that does not require the extreme values of permittivity and permeability. When we work at frequencies near the visible frequencies, scaling down conventional metamaterials causes severe absorption because its resonating nature and also fabrication becomes more difficult. Quasiconformal mapping solves these problems as the principle axes of the tensors align with the coordinate lines (Figure 3). [3]

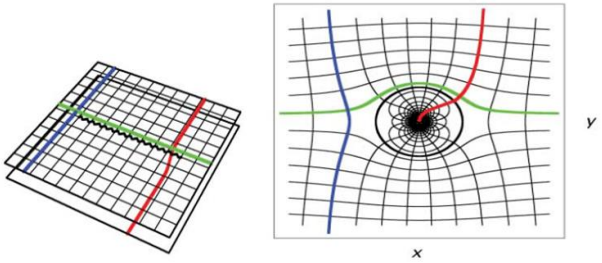

Figure 3: (a) An ordinary coordinate system; (b) A transformed coordinate system using conformal mapping [4]

[2] Transformation Optics Solutions

2.1 Linear Transformation Optics

In linear TO, the relation between the coordinate system (virtual system) and the transformed one (physical system) is linear (Figure 4).

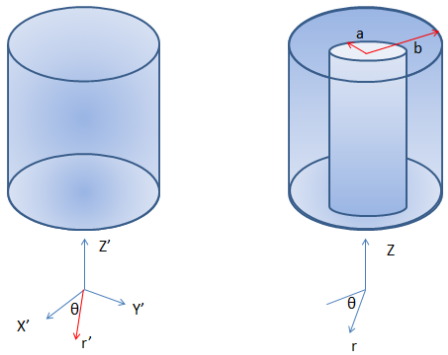

Figure 4: The coordinate transformation that compresses a cylindrical region r' ≤ b in the old coordinate system (r', θ', z') into a concentric cylindrical shell of a ≤ r ≤ b in the new coordinate system (r, θ, z)

Although linear TO be straightforward, it results in impedance mismatching and undesired scattering when using the reduced parameters below. [1]

$$\varepsilon_r = \mu_r = \frac{r-a}{r} \tag{1}$$

$$\varepsilon_\theta = \mu_\theta = \frac{r}{r-a} \tag{2}$$

$$\varepsilon_z = \mu_z = \left(\frac{b}{b-a}\right)^2 . \frac{r-a}{r} \tag{3}$$

2.1.1 Simulation Results

A simulation for a cylindrical cloak using linear (first order) TO was made on COMSOL is shown below.

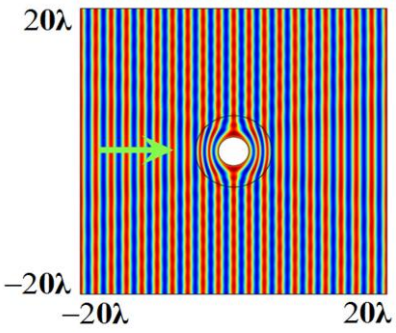

Figure 5: Cylindrical cloak using Linear TO technique

A simulation was made using MATLAB to show the material property tensors values needed to complete the spatial transformation based on linear TO.

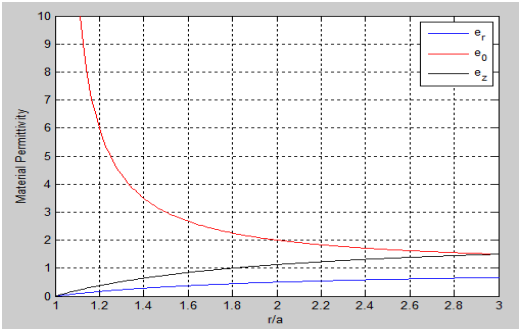

Figure 6: The required material properties based on Linear TO. The permittivity values at inner radius (a=1) approach 0, while at outer radius (b=3) approach 1.

2.1.2 Mathematical derivation

A step-by-step mathematical derivation for Linear TO for Cylindrical cloak was made and we came up with the same equation results for the parameters.

We start by deriving the Jacobian coordinate transformation matrix that describes the conversion from the Cartesian space to the cylindrical one.

$$\Lambda_{x'r'} = \begin{bmatrix} \cos\theta' & -r'\sin\theta' & 0 \\ \sin\theta' & r'\cos\theta' & 0 \\ 0 & 0 & 1 \end{bmatrix} \tag{4}$$

After that, we derive the Jacobian coordinate transformation matrix that describes the transformation from the *virtual* system to the *physical* one, as shown in Figure 4. This transformation is represented by the following relations: $r' = b\frac{r-a}{b-a}$, $\theta' = \theta$ and $z' = z$. Hence, the Jacobian matrix is as follows.

$$\Lambda_{r'r} = \begin{bmatrix} \frac{b}{b-a} & 0 & 0 \\ 0 & 1 & 0 \\ 0 & 0 & 1 \end{bmatrix} \tag{5}$$

The relationship between the electromagnetic system in the initial coordinates and the final ones is characterized by the global Jacobian coordinate transformation matrix which is the result of multiplying the individual matrices together. [5]

$$\Lambda_{x'r} = \begin{bmatrix} \frac{b}{b-a}\cos\theta & -b\frac{r-a}{b-a}\sin\theta & 0 \\ \frac{b}{b-a}\sin\theta & b\frac{r-a}{b-a}\cos\theta & 0 \\ 0 & 0 & 1 \end{bmatrix} \tag{6}$$

Now, since the permittivity and permeability in the original Cartesian coordinate system are isotropic ($\varepsilon' = \mu' = 1$), the newly obtained parameters that

will describe the new coordinate system are stated as follows. [6]

$$\bar{\bar{\varepsilon}} = \det(\Lambda)\, g^{-1}\varepsilon' \tag{7}$$

$$\bar{\bar{\mu}} = \det(\Lambda)\, g^{-1}\mu' \tag{8}$$

where $\bar{\bar{\varepsilon}}$ and $\bar{\bar{\mu}}$ are 3x3 permittivity and permeability tensors, respectively.

From these relations, we can calcite the new non-normalized parameter tensors.

$$\varepsilon_r = \mu_r = r - a \tag{9}$$

$$\varepsilon_\theta = \mu_\theta = \frac{1}{r-a} \tag{10}$$

$$\varepsilon_z = \mu_z = \left(\frac{b}{b-a}\right)^2 (r-a) \tag{11}$$

However, in the new coordinate system, we must use renormalized values of the permittivity and permeability. [7]

$$\varepsilon_r^s = \varepsilon_r \frac{Q_r}{Q_\theta Q_z} \tag{12}$$

$$\varepsilon_\theta^s = \varepsilon_\theta \frac{Q_\theta}{Q_r Q_z} \tag{13}$$

$$\varepsilon_z^s = \varepsilon_z \frac{Q_z}{Q_r Q_\theta} \tag{14}$$

where

$$Q_r^2 = \left(\frac{\partial x}{\partial r}\right)^2 + \left(\frac{\partial x}{\partial r}\right)^2 + \left(\frac{\partial x}{\partial r}\right)^2 = 1 \tag{15}$$

$$Q_\theta^2 = \left(\frac{\partial x}{\partial \theta}\right)^2 + \left(\frac{\partial x}{\partial \theta}\right)^2 + \left(\frac{\partial x}{\partial \theta}\right)^2 = r^2 \tag{16}$$

$$Q_z^2 = \left(\frac{\partial x}{\partial z}\right)^2 + \left(\frac{\partial x}{\partial z}\right)^2 + \left(\frac{\partial x}{\partial z}\right)^2 = 1 \tag{17}$$

Therefore, the final normalized parameters are

$$\varepsilon_r = \mu_r = \frac{r-a}{r} \tag{18}$$

$$\varepsilon_\theta = \mu_\theta = \frac{r}{r-a} \tag{19}$$

$$\varepsilon_z = \mu_z = \left(\frac{b}{b-a}\right)^2 \left(\frac{r-a}{r}\right) \tag{20}$$

We note that the final values of the parameters are the same as mentioned in a previous section, and this concludes this section.

2.2 High-Order Transformation Optics

In High-order TO, the relation between the coordinate system and the transformed system is high order (not linear). High-order TO has more smooth graduation in the effective values of the tensors at the outer boundary. This modification completely eliminates the scattering within the limits of the cloak and reduces the impedance mismatch significantly. The parameters obtained by linear TO are modified according to the transformation order *n* as follows. In this paper, we are working on third order TO (n=3) and fifth order TO (n=5).

$$\varepsilon_r = \mu_r = \frac{r-a}{nr} \tag{21}$$

$$\varepsilon_\theta = \mu_\theta = \frac{nr}{r-a} \tag{22}$$

$$\varepsilon_z = \mu_z = \frac{nb^2(r-a)^{2n-1}}{r(b-a)^{2n}} \tag{23}$$

2.2.1 Simulation Results

A simulation for a cylindrical cloak using third order TO was made on COMSOL is shown below

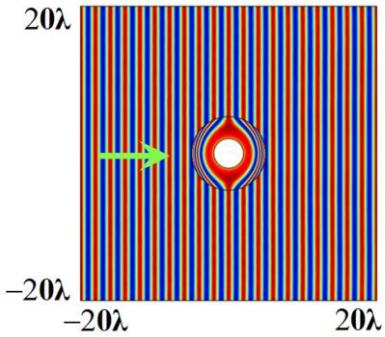

Figure 6: Cylindrical cloak using 3rd order TO technique

Another simulation was made for a cylindrical cloak using fifth order TO is shown below.

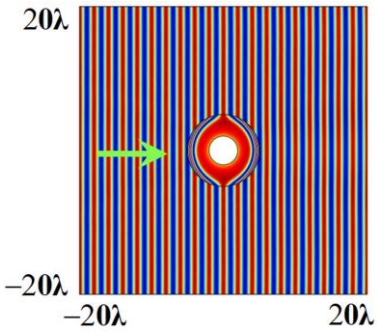

Figure 7: Cylindrical cloak using 5th order TO technique

A simulation was made using MATLAB to show the different material property tensors values needed to

complete the spatial transformation based on 3rd order and 5th order TO.

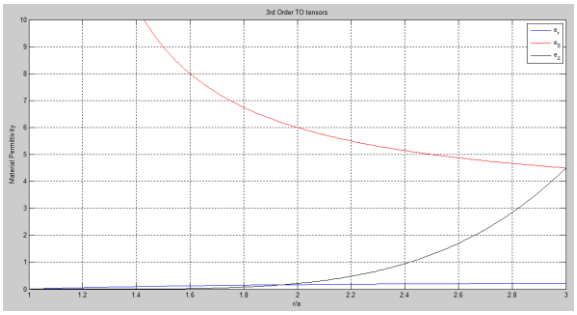

Figure 7: The required material properties based on 3rd order TO.

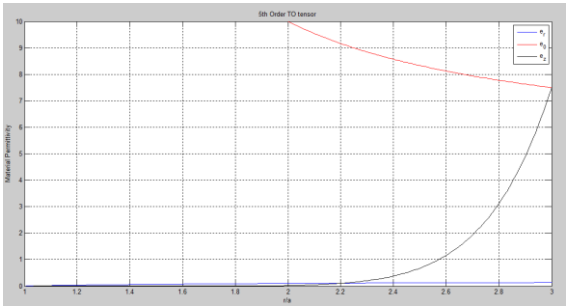

Figure 8: The required material properties based on 5th order TO.

[3] Conclusion

Combining the amazing properties of MetaMaterials with the Transformation Optics technique is proven to be the best method to achieve invisibility cloaks. Using High order TO is more efficient than Linear TO. Figure 9 shows the permittivity tensor for linear, 3rd order and 5th order TO.

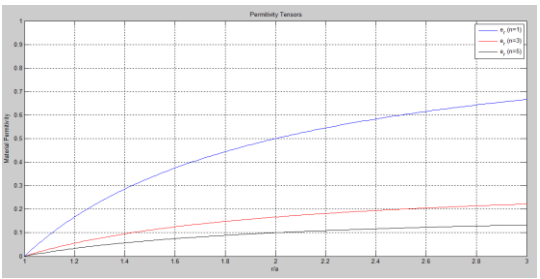

Figure 9: Material Permittivity values as a function of r for Linear, 3rd Order and 5th Order TO.

[4] References

[1] Wenshan Cai, Vladimir Shalaev (2010). *Optical Metamaterials Fundamentals and Applications.*

[2] Tretyakov, P. A. (march 2009). Electromagnetic Cloaking with Metamaterials. *Materialstoday*, 22-29.

[3] Jensen Li, Xiang Zhang (2008). *Quasiconformal Mapping in Transformation Optics.* California.

[4] Leonhardt, U. (June 2006). Optical Conformal Mapping. *Science*, 1777 - 1780.

[5] Nicolet, A., Zolla, F. and Guenneau, S. (2004). Modelling of twisted optical waveguides with edge elements. *The European Physics Journal of Applied Physic*, 28, 153157.

[6] Berry, M. V., Bloembergen, N., Erez, N., & Greenberg, D. M. (2007). *Progress in optics* (Vol. 50). E. Wolf (Ed.). Elsevier.

[7] Pendry, J. B., Schurig, D., & Smith, D. R. (2006). Controlling electromagnetic fields. *Science, 312(5781)*, 1780-1782.

Superposing Lorentzian resonance functions towards engineering target responses

Christopher A. Dirdal and Johannes Skaar

Department of Electronics and Telecommunications,
Norwegian University of Science and Technology, NO-7491 Trondheim, Norway
*corresponding author, E-mail: christopher.dirdal@iet.ntnu.no

Abstract

We prove that all complex valued response functions obeying the Kramers-Kronig relations can be approximated as superpositions of Lorentzian resonance functions, to any precision. A practical consequence is that arbitrary target response functions can be engineered in terms of common resonant metamaterial responses. A basic dispersion engineering methodology outlining these possibilities is presented, along with relevant metamaterial systems.

1. Introduction

The prospect of engineering metamaterials with tailor-made dispersion properties, rather than being limited to the dispersions of conventional media, is becoming a reality. Such dispersion engineering finds interesting applications within dispersion compensation [1, 2] broadband absorption [3], broadband ultra-low refractive index media [4], couplers [5], antenna design [6, 7], and filters [8], to mention but a few. The rapid developments made in metamaterial design and manufacturing towards this goal, allow us to speculate on what classes of dispersion behavior will be ultimately realizable as further progress is made. Important restrictions in this respect are for instance compliance with the Kramers-Kronig relations, which characterize the class of causal functions, and considerations such as whether the medium in question is to be passive or active. Since both of these conditions can be seen as somewhat lenient (the space of passive/active and causal functions is large), it seems natural to expect a significant degree of freedom for prospective metamaterial dispersions.

Contrary to this intuition, however, most treatments of dispersion phenomena commonly model dielectric media as superpositions of a single causal response function, the Lorentzian resonance, owing to its generality in describing a wide range of resonance phenomena and its simplicity [9–11]. It is natural to ask whether or not typical textbook discussions on dispersion therefore leave a significant number of possibilities out of view, and how large the possible gap in the function space between causal functions and Lorentzian superpositions is. With these considerations at hand, it comes as somewhat of a surprise that superpositions of Lorentzian functions can be shown to approximate any causal function obeying the Kramers-Kronig relations to any precision, as we have recently demonstrated [12]. In other words, there exists no gap in the function space between complex valued functions fulfilling the Kramers-Kronig relations and the superpositions of Lorentzian resonance functions commonly used in textbook treatments. The typical textbook approach to dispersion is therefore shown to encompass all responses fulfilling the Kramers Kronig relations.

In the context of this paper, the above results also demonstrate interesting practical consequences to the prospects of engineering desired dispersions. Since a number of metamaterial systems capable of realizing Lorentzian superpositions exist in literature [12–14], it seems possible to realize a given target response function, for which no physical system is known, by a metamaterial realization of its corresponding Lorentzian resonance superposition.

This paper will derive expressions for the relevant superpositions of Lorentzian resonance function, as well as outline a basic design methodology for the realization of arbitrary target response functions. With relation to our former discussions on Lorentzian resonance superpositions [12], this paper complements earlier results by providing a simpler proof, while expanding on inherent possibilities for realizing arbitrary target dispersions in metamaterials.

2. Identifying the superposition of Lorentzian resonance functions

A Lorentzian resonance function may be written in the form

$$L(\omega) = \frac{\omega_0}{\omega_0^2 - \omega^2 - i\omega\Gamma}, \tag{1}$$

where ω is the frequency and ω_0 and Γ are the resonance frequency and bandwidth, respectively. Fig. 1 displays its characteristic plot. For an arbitrary susceptibility function $\chi(\omega)$ that is analytic in the upper complex frequency plane, we shall now demonstrate that

$$\chi(\omega) = \frac{2}{\pi} \lim_{\Gamma \to 0} \int_0^\infty \mathrm{Im}\chi(\omega_0) \frac{\omega_0}{\omega_0^2 - \omega^2 - i\omega\Gamma} \mathrm{d}\omega_0, \tag{2}$$

which constitutes the main result of this paper. Eq. (2) shows that the susceptibility $\chi(\omega)$ can be expressed as a superposition of Lorentzian resonance functions weighted by $\mathrm{Im}\chi(\omega)$ under the limit $\Gamma \to 0$. This can be understood intuitively by noting that the imaginary part of (1) approaches

a δ-function as a distribution under the limit $\Gamma \to 0$, and that $\mathrm{Re}\chi(\omega)$ and $\mathrm{Im}\chi(\omega)$ are Hilbert transforms of each other, as discussed at length in [12]. However, this result is in fact simply a consequence of the analytic properties of $\chi(\omega)$ in the upper complex half plane. To show this, we first separate (1) into partial fractions

$$L(\omega) = \frac{1}{2(\omega_0 - \omega_p)} + \frac{1}{2(\omega_0 + \omega_p)}, \tag{3}$$

where $\omega_p = \sqrt{\omega^2 + i\omega\Gamma}$. The pole positions of (3) are displayed in Fig. 2 along with a semicircle contour curve C in the upper half-plane for ω_0. Note that despite being analytic in the upper complex ω-plane, (3) is not required to be analytic in the upper complex ω_0-plane, as observed in Fig. 2. Multiplying with the susceptibility function $\chi(\omega_0)$ and using Cauchy's Integral Formula and Cauchy's Integral Theorem over the contour C on each of the terms in (3), respectively, give

$$\frac{1}{2}\int_{-\infty}^{\infty} \frac{\chi(\omega_0)}{\omega_0 - \omega_p} \mathrm{d}\omega_0 = i\pi\chi(\omega_p) \tag{4}$$

$$\frac{1}{2}\int_{-\infty}^{\infty} \frac{\chi(\omega_0)}{\omega_0 + \omega_p} \mathrm{d}\omega_0 = 0, \tag{5}$$

when having assumed that the radius of the contour semicircle tends to infinity. Adding (4) and (5) together then gives

$$\int_{-\infty}^{\infty} \frac{\omega_0\chi(\omega_0)}{\omega_0^2 - \omega^2 - i\omega\Gamma} \mathrm{d}\omega_0 = i\pi\chi(\omega_p). \tag{6}$$

The reality of the time domain fields requires that $\chi(-\omega_0) = \chi^*(\omega_0)$ along the real ω_0 axis. This symmetry property allows us to re-express the integral and obtain

$$\chi(\omega_p) = \frac{2}{\pi}\int_0^{\infty} \mathrm{Im}\chi(\omega_0) \frac{\omega_0}{\omega_0^2 - \omega^2 - i\omega\Gamma} \mathrm{d}\omega_0. \tag{7}$$

Taking the limit $\lim_{\Gamma\to 0}\chi(\omega_p) = \chi(\omega)$ gives (2) and concludes this proof.

The superposition (2) corresponds to an infinite number of Lorentzian resonances with zero widths. We will

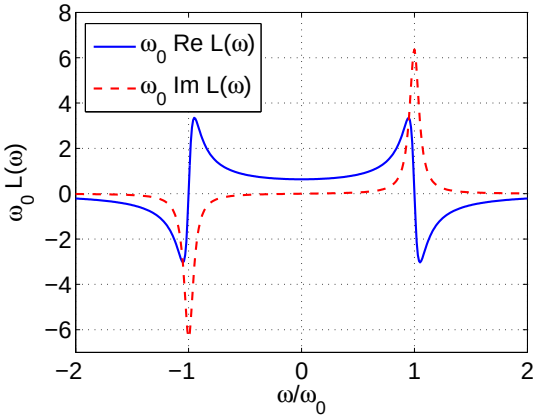

Figure 1: A Lorentzian resonance function.

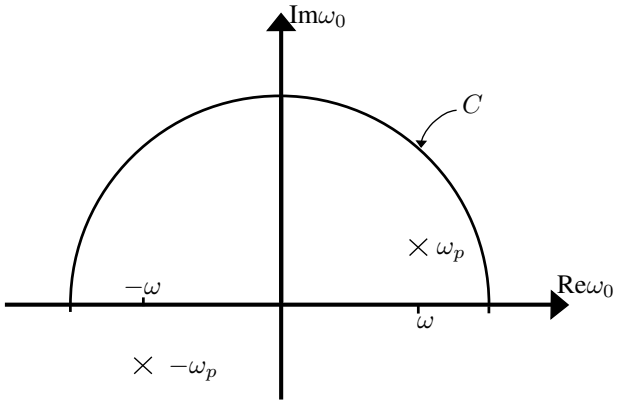

Figure 2: The complex plane of the resonance frequency ω_0. Note that the function (3) is not analytic in the upper complex half plane of ω_0, despite analyticity being ensured in the upper half plane for ω.

now show that $\chi(\omega)$ can be approximated by a finite sum of finite-width Lorentzian resonance functions to any degree of precision. As a first step, we therefore remove the limit $\Gamma \to 0$ from (2), thereby giving the right hand side of (7), which we rename $\chi_\Gamma(\omega)$. Since $\lim_{\Gamma\to 0}\chi_\Gamma(\omega) = \chi(\omega)$, it follows that $\chi_\Gamma(\omega)$ approximates $\chi(\omega)$ to any desired degree of precision. The next step is to approximate the integral in $\chi_\Gamma(\omega)$, as expressed in (7), by a finite sum of finite-width resonances giving

$$\chi_{\Gamma,\Delta}(\omega) = \frac{2}{\pi}\sum_{m=0}^{M-1} \mathrm{Im}\chi(\omega_m) \frac{\omega_m\Delta}{\omega_m^2 - \omega^2 - i\omega\Gamma}. \tag{8}$$

Here Δ is the spacing between the resonance frequencies, $\omega_m = \Delta/2 + m\Delta$, and M is a large integer. Intuitively a sufficient condition for $\chi_{\Gamma,\Delta}(\omega)$ to converge to $\chi(\omega)$ is to e.g. set $M = 1/\Delta$ and take the limit $\Delta \to 0$ before taking the limit $\Gamma \to 0$. This condition is however not practical as we desire to use a finite number of Lorentzian resonance functions. It can be shown that if we for instance set $\Delta = \Gamma^2/\sqrt{M}$ the error $|\chi_{\Gamma,\Delta}(\omega) - \chi(\omega)|$ converges in L^2 as $\Gamma \to 0$, and vanishes if we also let $M\Delta \to \infty$ [12]. This demonstrates that $\chi_{\Gamma,\Delta}(\omega)$, a finite sum of finite width Lorentzians, can approximate any $\chi(\omega)$ to any desired accuracy.

3. Engineering target dispersions by metamaterials

Owing to the generality of resonance phenomena in physical systems a number of material realizations exist for the response (1), and a number of metamaterial systems have demonstrated that it is possible to tailor its resonance strengths, widths and positions [13, 14]. This seems to suggest that it is possible to engineer desired responses $\chi(\omega)$ by use of superpositions of Lorentzian resonance functions

in the manner of (8). Here a basic design methodology shall be outlined.

3.1. Reducing the number of resonances

To facilitate the discussion, a simple target response $\chi(\omega)$ is chosen with the imaginary part

$$\mathrm{Im}\chi(\omega) = \begin{cases} \omega/\omega_c & \text{if } |\omega| < \omega_c \\ 0 & \text{elsewhere .} \end{cases} \quad (9)$$

Inserting this target function into (8) and choosing $\Gamma/\omega_c = 0.001$ and $\Delta/\omega_c = 0.0005$ yields the sum plotted in Fig. 3a. In order to accurately approximate the steep drop at $\omega/\omega_c = 1$, this sum contains 2000 narrow Lorentzian resonance functions. An interesting feature of this target $\chi(\omega)$ is that it leads to $\mathrm{Re}\chi(\omega) = -2$ in a narrow frequency region around ω_c. As a side remark we note that the Kramers-Kronig relations can be used to show that if the edge of $\mathrm{Im}\chi(\omega)$ is made infinitely steep at $\omega = \omega_c$ then one can achieve $\mathrm{Re}\chi(\omega_c) = -2$ with negligible loss for all frequencies [15]. Here we can at best hope to approximate this effect, since an infinitely steep drop would require using infinitely many Lorentzian resonance functions of zero width.

The high number of resonances in the sum (8) displayed in Fig. 3a may present a challenge towards metamaterial realization. Forty out of a total of 2000 are shown individually in Fig. 3b. However, making use of the observation that the bandwidth Γ and density of resonances do not have to be equal everywhere, it is possible to reduce the number of needed resonances dramatically. For $\mathrm{Im}\chi(\omega)$ defined by (9) we can for instance imagine placing many narrow resonances close to $\omega = \omega_c$, and few, though wider, resonances at lower frequencies. To help illustrate the process of placing resonances with varying widths in a systematic manner, it can be helpful to define two functions for the target characterized by (9):

1. **Placement function:** We set $\omega_m/\omega_c = 1-(m/N)^\nu$, where ω_m is the mth resonance out of a total of N resonances, and ν is a parameter one may vary. Setting $\nu = 1$ gives linear spacing between the resonances, while increasing ν concentrates them towards $\omega = \omega_c$. For our purpose we choose $\nu = 4$ and $N = 20$.

2. **Width function:** We simply choose $\Gamma/\omega_c = 1 - (\omega_m/\omega_c)^\gamma$, where γ is a parameter we shall vary. Setting $\gamma = 1$ makes the widths decrease linearly over the bandwidth, while we set $\gamma = 0.5$.

Figure 4 displays the resonance placements and widths for our chosen functions and parameters, leading to the superposition displayed in Fig. 5. This superposition is a Riemann sum similar to (8), but differs due to the fact that both Γ and Δ vary with respect to frequency. This superposition approximates the shape of Fig. 3a with only 20 Lorentzian resonance functions instead of the 2000 needed earlier, and

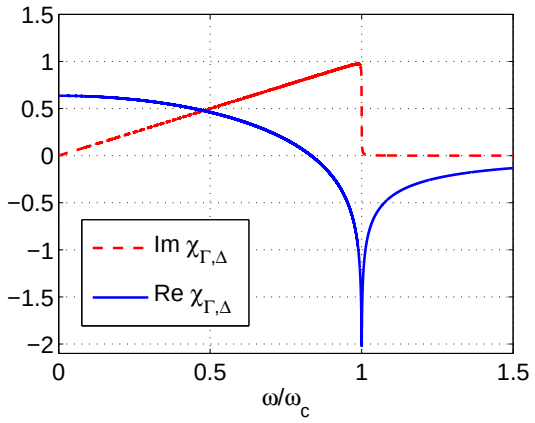

(a) Real and imaginary parts of the sum approximations by (8) for $\Gamma/\omega_c = 0.001$ and $\Delta/\omega_c = 0.0005$. There are 2000 Lorentzian resonance functions included in the sum. The red and blue curves correspond to $\mathrm{Im}\chi_{\Gamma,\Delta}$ and $\mathrm{Re}\chi_{\Gamma,\Delta}$, respectively.

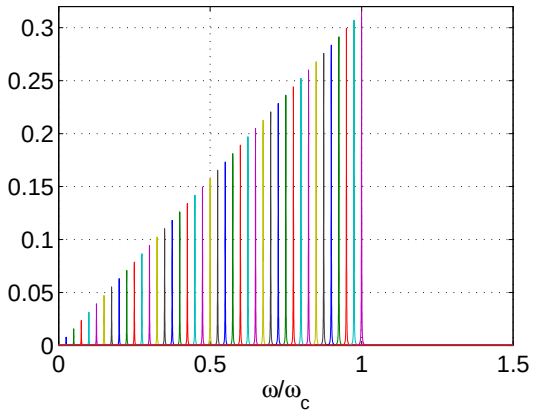

(b) The imaginary parts for one out of every fifty Lorentzians in the sum (8), when $\Gamma/\omega_c = 0.001$ and $\Delta/\omega_c = 0.0005$.

Figure 3

maintains $\mathrm{Re}\chi(\omega_c) \approx -2$ without any significant change in the amount of loss below ω_c.

Having found an approximation of the target function $\chi(\omega)$ by a superposition of Lorentzian resonance functions where the tradeoff between the needed accuracy and the maximum number of resonances has been satisfactory negotiated, the next step is to find a suitable metamaterial realization. Continuing with the target response characterized by (9), we shall consider two possible metamaterials in which the sum displayed in Fig. 5 can be realized.

3.2. Metamaterial realization 1: Network of loaded RLC transmission lines

Homogeneous dielectric or magnetic media can be given a network equivalent in the low frequency limit. A network of lumped circuit elements with unit cells much smaller than the operating wavelength results in effective parameters $\mu(\omega)$ and $\epsilon(\omega)$ for the magnetic permeability and the electric permittivity, respectively. These may be derived

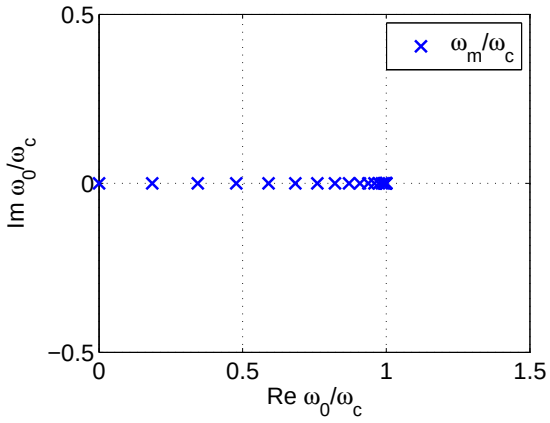

(a) Positioning of the resonance frequencies according to the placement function $\omega_m/\omega_c = 1 - (m/20)^4$ where ω_m is the mth resonance where $m = \{1, ..., 20\}$.

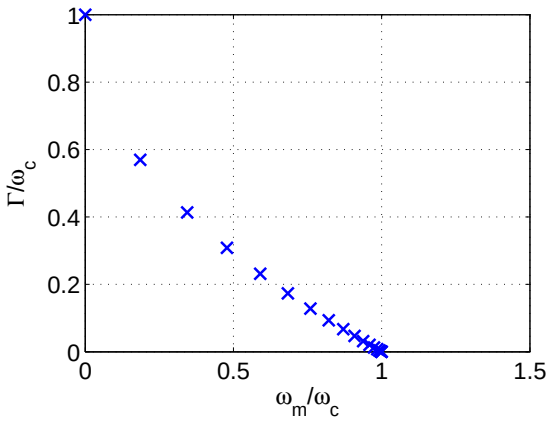

(b) Designation of the width $\Gamma(\omega_m)$ of each Lorentzian resonance function at each resonance frequency ω_m in (a), according to the width function $\Gamma/\omega_c = 1 - (\omega_m/\omega_c)^{0.5}$.

Figure 4

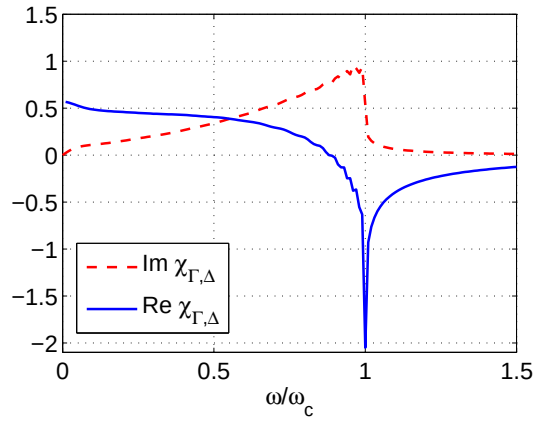

(a) Real and imaginary parts of a sum approximation of (2) where the resonances ω_m are placed according to Fig. 4a, and the widths Γ of each resonance are given by Fig. 4b. By varying the placements and widths of the resonances, a similar response to that displayed in Fig. 3a is achieved with only 20 resonances.

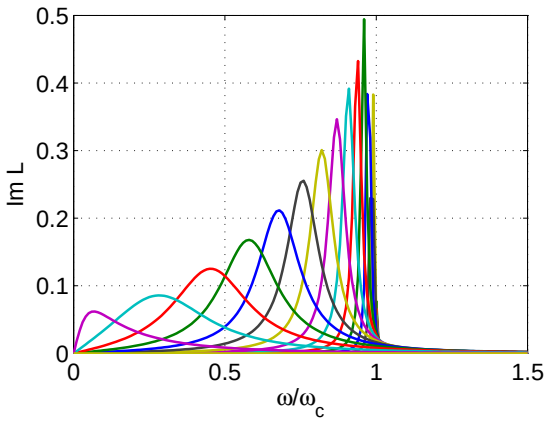

(b) Imaginary parts of the Lorentzian resonance functions constituting the sum displayed in (a). The widths Γ and resonance frequencies are varied according to the width- and placement functions displayed in Fig. 4.

Figure 5

through the use of the telegrapher's and Maxwell equations after having related the current and voltage in each unit cell to the magnetic and electric fields [16, 17]. In terms of the series impedance $Z(\omega)$ per unit length and the shunt admittance $Y(\omega)$ per unit length in a 1D unit cell displayed in Fig. 6a, one has

$$\mu(\omega) = -\frac{1}{i\omega\mu_0} Z(\omega) \tag{10}$$

$$\epsilon(\omega) = -\frac{1}{i\omega\epsilon_0} Y(\omega). \tag{11}$$

In order to realize Lorentzian resonance functions of the form $L(\omega)$ from (1), we must synthesize circuits that give the necessary impedance and/or admittance in (10) and (11) to achieve $\mu(\omega) - 1 = L(\omega)$ and/or $\epsilon(\omega) - 1 = L(\omega)$. This may for instance be achieved through straightforward application of Brune synthesis [18] leading to the circuits displayed in Fig. 6b. The impedance circuit leads to

$$\mu(\omega) = 1 + \frac{F}{\omega_0^2 - \omega^2 - i\omega\Gamma}, \tag{12}$$

where $F = 1/\mu_0 C$, $\Gamma = \mu_0 F/R$ and $\omega_0^2 = \mu_0 F/L$. Similarly, the admittance circuit gives the same form as (12) for $\epsilon(\omega)$ with $F = 1/\epsilon_0 L$, $\Gamma = \epsilon_0 FR$, and $\omega_0^2 = \epsilon_0 F/C$. The circuit elements with parameters L' and C' correspond to the inductance and capacitance per unit length of the transmission line, which we have set equal to μ_0 and ϵ_0, respectively. We observe that the resonator strength, width and resonance frequency of the resonances may be tailored by altering the values of the lumped elements in Fig. 6b for both $\mu(\omega)$ and $\epsilon(\omega)$. In order to realize the sum displayed in Fig. 5 for $\mu(\omega)$ and/or $\epsilon(\omega)$ we must construct a unit cell consisting of the circuit in (6b) repeated twenty times (apart from the elements corresponding to L' and C') for different values of R, L, C.

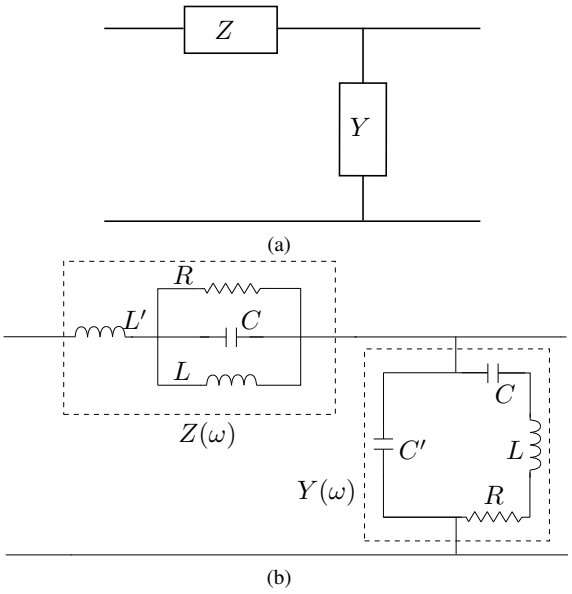

Figure 6

3.3. Metamaterial realization 2: Split ring cylinders of varying parameters

Split ring cylinder metamaterials are known to lead to resonances similar to that of the Lorentzian resonance function (1) [13]. We have recently shown elsewhere that a superposition of Lorentzian resonance functions with different resonance frequencies, widths and strengths can be realized in terms of split ring cylinders of differing radii r, capacitance C per m^2, resistance ρ per circumference-length ratio, and fractional volume F of the unit cell occupied by the interior of the cylinders [12]. The effective parameter in the case of N split ring cylinders per unit cell then becomes

$$\mu(\omega) - 1 = \sum_k^N \frac{\omega^2 F_k}{\frac{2}{\pi^2 \mu_0 C_k r_k^3} - \omega^2 - i\omega \frac{2\rho_k}{r_k \mu_0}}. \qquad (13)$$

where k represents the kth split ring cylinder in the unit cell. This expression becomes exact as the cylinder heights tend toward infinity. It is observed that the expression within the sum is similar to that of the Lorentzian resonance function (1), with the discrepancy in the numerator becoming negligible as the width of each resonance becomes small relative to the resonance frequency. The task of realizing the sum displayed in Fig. 5 therefore amounts to tailoring the geometry, material composition and density of a given split ring cylinder with parameters r_k, C_k, ρ_k, F_k so that its response approximates one of the resonances displayed in Fig. 5b.

4. Conclusion

It has been proven that causal susceptibility functions obeying the Kramers-Kronig relations can be approximated by superpositions of Lorentzian resonance functions, to any precision. Making use of the practical implications that follow from this result, a basic metamaterial design methodology for the realization of arbitrary target responses has been outlined. This consists in reducing the number of needed Lorentzian resonance functions by varying their widths and resonance frequencies, and then finding a suitable metamaterial system for their realization. Two metamaterial systems were identified: A network of RLC-loaded transmission lines, and split ring cylinder arrays.

References

[1] C.-Y. Cheng and R. Ziolkowski, "Tailoring double-negative metamaterial responses to achieve anomalous propagation effects along microstrip transmission lines," *IEEE Trans. Microw. Theory Tech.*, vol. 51, pp. 2306 – 2314, dec. 2003.

[2] N. Engheta and R. Ziolkowski, "A positive future for double-negative metamaterials," *IEEE Trans. Microw. Theory Tech.*, vol. 53, pp. 1535 – 1556, april 2005.

[3] Q. Feng, M. Pu, C. Hu, and X. Luo, "Engineering the dispersion of metamaterial surface for broadband infrared absorption," *Opt. Lett.*, vol. 37, no. 11, pp. 2133–2135, 2012.

[4] B. T. Schwartz and R. Piestun, "Total external reflection from metamaterials with ultralow refractive index," *J. Opt. Soc. Am. B*, vol. 20, pp. 2448–2453, Dec 2003.

[5] C. Caloz, A. Sanada, and T. Itoh, "A novel composite right-/left-handed coupled-line directional coupler with arbitrary coupling level and broad bandwidth," *IEEE Trans. Microw. Theory Tech.*, vol. 52, pp. 980 – 992, march 2004.

[6] W. Rotman, "Plasma simulation by artificial dielectrics and parallel-plate media," *IEEE Trans. Antennas Prop.*, vol. 10, pp. 82–95, january 1962.

[7] E. Lier, D. H. Werner, C. P. Scarborough, Q. Wu, and J. A. Bossard, "An octave-bandwidth negligible-loss radiofrequency metamaterial," *Nature Materials*, vol. 10, no. 3, pp. 216–222, 2011.

[8] M. Gil, J. Bonache, and F. Martín, "Metamaterial filters: A review," *Metamaterials*, vol. 2, no. 4, pp. 186 – 197, 2008.

[9] B. E. Saleh and M. C. Teich, *Fundamentals of photonics, 2nd ed.* John Wiley & Sons, Inc., 2007.

[10] J. Jackson, *Classical Electrodynamics*. Wiley, 1999.

[11] M. Dressel and G. Grüner, *Electrodynamics of Solids: Optical Properties of Electrons in Matter*. Cambridge University Press, 2002.

[12] C. A. Dirdal and J. Skaar, "Superpositions of lorentzians as the class of causal functions," *Phys. Rev. A*, vol. 88, p. 033834, Sep 2013.

[13] J. B. Pendry, A. J. Holden, D. J. Robbins, and W. J. Stewart, "Magnetism from conductors and enhanced nonlinear phenomena," *IEEE Trans. Microwave Theory and Tech.*, vol. 47, pp. 2075–2084, November 1999.

[14] J. A. Schuller, R. Zia, T. Taubner, and M. L. Brongersma, "Dielectric metamaterials based on electric and magnetic resonances of silicon carbide particles," *Phys. Rev. Lett.*, vol. 99, p. 107401, Sep 2007.

[15] C. A. Dirdal and J. Skaar, "Negative refraction in causal media by evaluating polar paths for rational functions," *J. Opt. Soc. Am. B*, vol. 30, pp. 370–376, Feb 2013.

[16] G. Eleftheriades, A. Iyer, and P. Kremer, "Planar negative refractive index media using periodically l-c loaded transmission lines," *Microwave Theory and Techniques, IEEE Transactions on*, vol. 50, pp. 2702–2712, Dec 2002.

[17] B. Nistad and J. Skaar, "Simulations and realizations of active right-handed metamaterials with negative refractive index," *Opt. Express*, vol. 15, pp. 10935–10946, 2007.

[18] O. Wing, *Classical Circuit Theory*. Springer US, 2009.

Distinction of Opto-Electronic Properties between Random and Ordered Nano-Holed Layers

Mikita Marus[1], Aliaksandr Hubarevich[1], Wang Hong[1], Eugeny Muha[2], Aliaksandr Smirnov[2], Sun Xiaowei[1*] and Fan Weijun[1*]

[1]School of Electrical and Electronic Engineering, Nanyang Technological University, Singapore
[2]Department of Micro- and Nano-Electronics, Belarusian State University of Informatics and Radioelectronics, Minsk, Belarus
*corresponding author, E-mail: EXWSun@ntu.edu.sg; EWJFan@ntu.edu.sg

Abstract

The distinction of opto-electrical properties in case of aluminum, gold and silver random and ordered nano-holed layers was demonstrated. It is found that transmittance drops due to the shortening of plasmon polaritons propagating length within the Anderson localization effect, while sheet resistance increases in regard of decrement of metal connections' volume. Eventually gold and silver possess the transmittance of more than 80% and the sheet resistance of 20 Ohm/sq regardless of holes' arrangement. Aluminum demonstrates comparable parameters only with ordered patterns.

1. Introduction

The future extinction of indium [1] which is main component of the indium-tin-oxide (ITO) leads the scientists to create alternative transparent conductive layers (TCLs) [2–8]. The novel TCLs must have transmittance and sheet resistance around 80% and 20 Ohm/sq, respectively [1], as well as large deposition area ranging from micrometers to tens of centimeters; moreover the formation method should be a cheap one.

The simplest TCLs are planar gold (Au) films of thickness less than 50 nm. The transmittance of 10 nm Au thick films is around 60% in visible wavelength spectrum and sheet resistance is 15 Ohm/sq [2]. The further patterning of films leads to optical properties' improvement, while the sheet resistance unfortunately grows. Therefore the type and dimensions of the patterning are crucial for optimizing the opto-electronic properties. This trade-off has currently been investigated in Refs. [8, 9]. However the primary research focus was concentrated on the uniform patterns while little attention has been paid to the random ones.

This paper presents the detailed theoretical study of random nano-holed metallic layers and their comparative analysis with uniform structures. Calculations show that opto-electronic parameters of metals with stronger plasmon resonance are less affected by disordering effect.

2. Methodology

The holed metallic layers of aluminum (Al), Au and silver (Ag) on glass substrates with size of 2x2 μm were used in simulations. Cylindrical shape holes were aligned parallel to *Z* axis. Holes' locations were distributed according to *p+dp*, where *p* is each hole initial position in the hexagonal arrangement and *dp* is its deviation along *XY* plane. Each holes radius was obtained by adding of deviated value to initial radius: *r+dr*. The normal and uniform distributions were used to get *dp* and *dr*. Furthermore, the normal one had a broader range of *dp* and *dr*.

The optical properties were simulated using the finite-difference time-domain method (FTDT) which is commercially available within Lumerical software [10]. The incident light distributed along *Z* axis. The periodic boundary conditions and perfectly matched layers were applied parallel and perpendicular to *Z* axis correspondingly.

The sheet resistance was calculated by using the percolation theory model [11]. According to this theory the following equation is used:

$$R_s = \frac{1}{h\sigma_0 \left(\phi_f - \phi_{crit}\right)^t}, \qquad (1)$$

where R_s, h, σ_0, ϕ_f, ϕ_{crit} and t are sheet resistance, layer thickness, unpatterned solid layer conductivity, patterned metal volume fraction, critical patterned metal volume fraction when conductivity is tending to zero and critical expo-

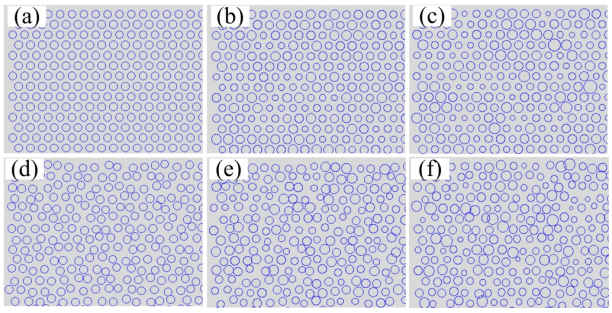

Figure 1: Nano-holed layers' simulation concept. Layer types: (a) constant interhole distance and holes' radius; (b, c) constant interhole distance and random holes' radius, obtained by uniform and normal distributions, accordingly; (d) random interhole distance and constant holes' radius; (e, f) random interhole distance and holes' radius, obtained by uniform and normal distributions, accordingly.

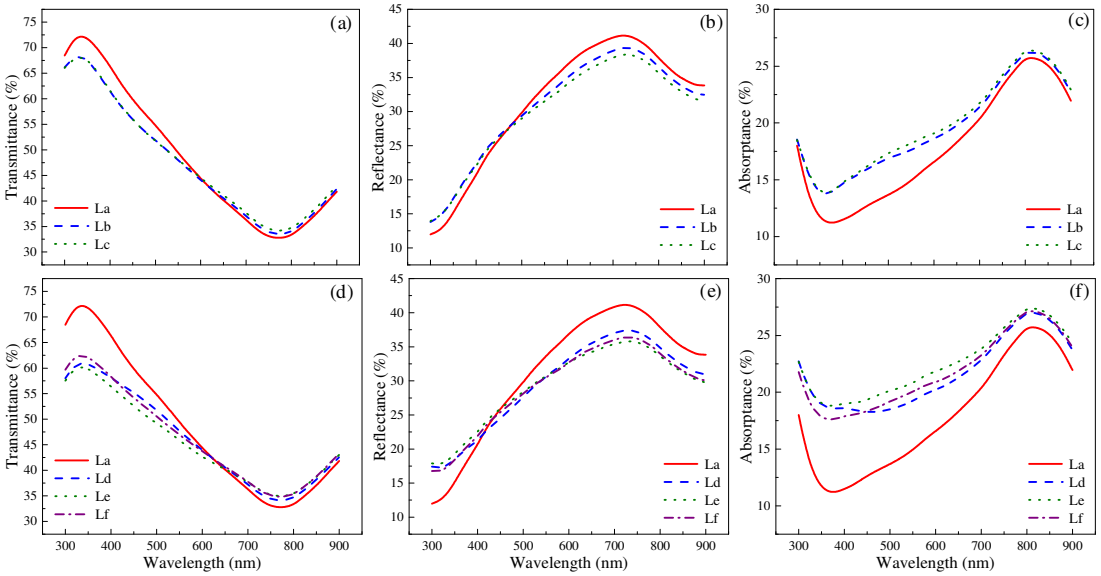

Figure 2: Al nano-holed layer optical properties. The curves' names are related to layer types L_a-L_f from Fig. 1.

nent, respectively. t value was chosen equal to 1.1 for 2D structure [11].

3. Results and discussion

The optical properties of metallic nano-patterns are characterized by incoming photons' communicate with free electrons in a metal lattice. There are two types of such communication. The first one is localized surface plasmons (LSPs); the patterns are optically isolated from each other. In this case an enhanced electric field appears around the patters, which, in turn, affects on the photon-electron relation. The second type is surface plasmon polaritons (SPPs); the patterns are optically close to each other, which permits electromagnetic waves propagate along the patterns. Therefore the nano-holed layers presented are to exhibit the first, the second or both relation types which are dependant mainly on the holes' geometry.

Table 1: Geometrical parameters of nano-holed layers.

layer type	holes' deviation dr [nm]	interhole distance deviation dp [nm]
L_a	0	0
L_b	[-8, 8]	0
L_c	(0, 6)	0
L_d	0	[-20, 20]
L_e	[-8, 8]	[-20, 20]
L_f	(0, 6)	(0, 10)

Holes' radius, interhole distance and thickness were fixed: 33, 100 and 10 nm correspondingly.
[-a, b] - uniform distribution in range form -a to b.
(a, b) - normal distribution with mean a and standard deviation b.

Fig. 1 presents the simulation concept, which was based on two approaches. The first one (Ap_1) evaluates layers' transmittance dependence on the holes' radius (see Fig. 1a-c); the second approach (Ap_2) estimates layers' transmittance dependence on both holes' radius and interhole distance (Fig. 1d-f).

Fig. 2a-c shows the optical properties of Al layer in case Ap_1, where parameters of the layer are shown in Table 1. The holes' transformation from ordered radius to disordered one causes the transmittance decrease. As we can see the transmittance drop is almost entirely determined by the absorbance. Further pattern disordering (Ap_2) provokes continued transmittance dropping; the influence of

Table 2: Nano-holed layers optical data.

material		Al		Au		Ag
range		vis	plasm	vis	plasm	vis*
L_a	T	49.26	55.87	77.64	79.23	79.07
	R	34.62	30.24	8.85	8.16	10.63
	A	16.12	13.89	13.51	11.66	10.3
L_d	T	47.41	52.39	73.71	75.09	73.98
	R	31.91	28.65	10.53	10.35	12.01
	A	20.68	18.96	15.76	14.56	14.01
L_e	T	46.15	52.39	73.66	75.19	73.70
	R	31.92	28.63	10.68	10.74	12.34
	A	21.93	18.98	15.66	14.07	13.96
L_e	T	48.1	55.87	75.61	77.37	74.84
	R	34.81	30.23	10.07	9.78	11.91
	A	17.09	13.90	14.32	12.85	13.25

T, R, A transmittance, reflectance, absorbance accordingly.
vis: 400-750 nm; plasm: 400-600nm for Al, 500-750nm for Au.
*vis = plasm in case of Ag.

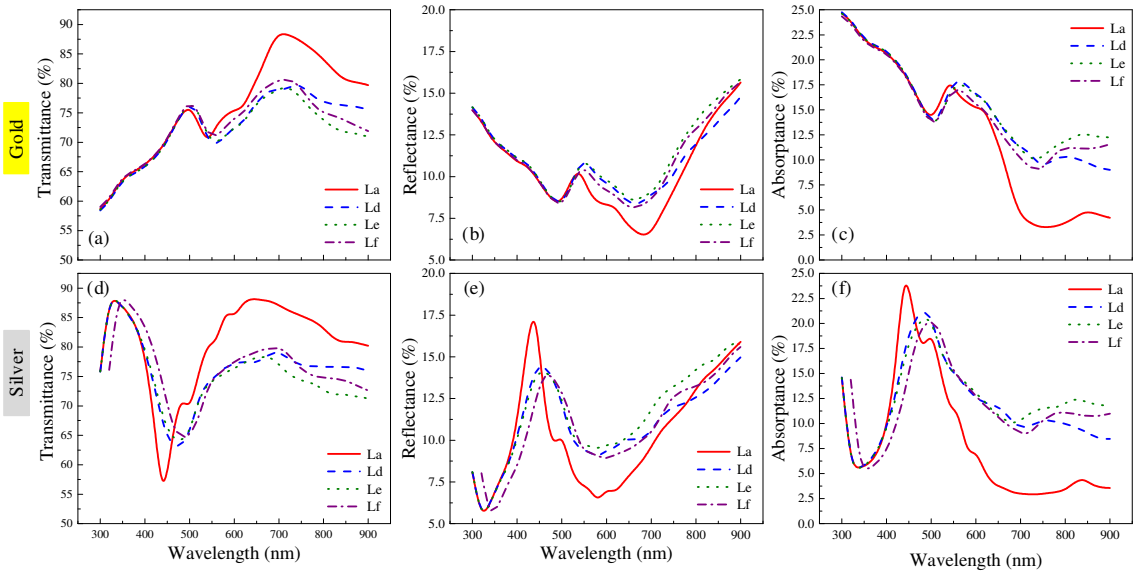

Figure 3: Au and Ag nano-holed layers' optical properties. The curves' names are related to layer types L_a-L_f from Fig. 1.

reflectance becomes noticeable. Surprisingly the effect of holes' radius deviation *dr* is negligible.

It is well known that Au and Ag possess strong plasmon resonance in visible optical range [12]. Therefore disordering influence on above mentioned metals is of interest to be investigated. Fig. 3 illustrates the optical properties of Au and Ag layer according to Ap_2. Ap_1 was omitted on account of the fact it changes the optical properties less significantly. To be mentioned firstly, the transmittance dropping for Au and Ag is larger in comparison with Al. Secondly, the transmittance drops in visible range only where plasmon resonance takes place: 550-750 nm for Au and 400-750 nm for Ag. Thirdly, the transmittance decrease is determined by reflectance and absorbance increments comparably. Lastly, it is observable that the both Au and Ag optical properties curves of the disordered cases generally shift to longer wavelengths. Corresponding optical value changes are presented in Table 2. In case of Al above mentioned effects are less observable due to the fact that its plasmon resonance range is located in ultraviolet range [12].

In 1958 P. W. Anderson suggested an explanation of electrons' localization inside semiconductor having large amount of impurities [13]. Later, Anderson localization was used to describe diffusion optical waves in random structures [14]. Photons are trapped in certain regions where constructive interference takes place. Indeed, it can be seen in Fig. 4 that random structure has definite areas of

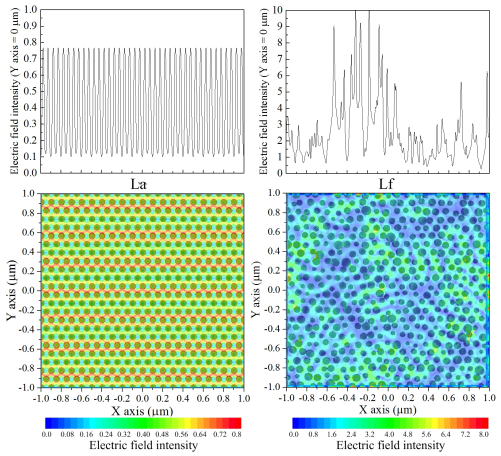

Figure 4: Electric field intensity distribution of random and ordered nano-holed Ag layers at 600 nm wavelength. XY plane is located at the center of layer thickness.

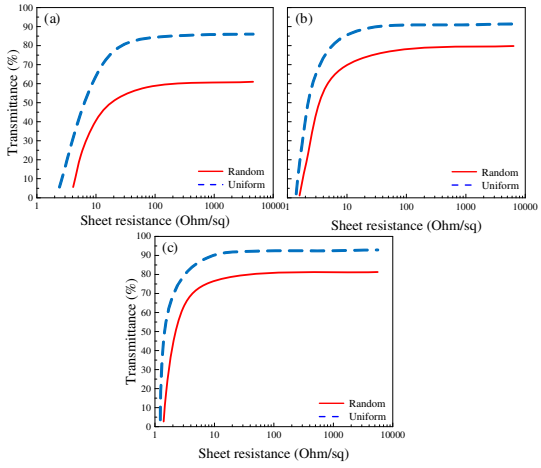

Figure 5: Average transmittance in range of 400-750 nm versus sheet resistance of random and ordered nano-holed Al (a), Au (b) and Ag (c) layers.

high electric field intensity, while uniform one has straight lines directed along electric field vector. This indicates reduction of SPPs propagation length; thus LSPs effect becomes dominative, which, in turn, is followed by increase of absorbance and reflectance.

According to percolation theory ϕ_{crit} is a key value affecting the sheet resistance in case of random and uniform (hexagonal in presented paper) structures' comparison; ϕ_{crit} is equal to 0.4 [15] and 0.1, accordingly. Fig. 5 illustrates the dependance of average transmittance in range of 400-750 nm on sheet resistance. In case with Al it is seen that only uniform patterns' design posses opto-electronic properties close to ITO while random patterns can attain only 55% transmittance at 20 Ohm/sq. Totally different situation is observable for Au and Ag. Uniform patterns of above mentioned materials have transmittance around 90% at 10 Ohm/sq; random ones possess around 75-80% at 20 Ohm/sq.

4. Conclusions

Opto-electronic properties' distinction between random and ordered nano-holed layers was studied. Disordering of holes' radius and interhole distance reduces their transmittance due to the shortening of SPPs propagation length. Sheet resistance, in its turn, drops on account of the increase of ϕ_{crit}. Simulations' results indicate that both random and ordered Au and Ag nano-holed layers possess opto-electronic parameters comparable to ITO which makes them potentially interesting as alternative TCLs. In case of Al these parameters can be obtained only with ordered patterning.

References

[1] Z. Chen, B. Cotterell, W. Wang, E. Guenther, and S. J. Chua, A mechanical assessment of flexible optoelectronic devices, *Thin Solid Films* 394: 201-205, 2001.

[2] R. A. Hatton, M. R. Willis, M. A. Chesters, D. Briggs, A robust ultrathin, transparent gold electrode tailored for hole injection into organic light-emitting diodes, *J. Mater. Chem.* 13: 722-726, 2003.

[3] B. OConnor, C. Haughn, K. H. An, K. P. Pipe, M. Shtein, Transparent and conductive electrodes based on unpatterned, thin metal films, *Appl. Phys. Lett.* 93: 223304, 2008.

[4] D. S. Ghosh, L. Martinez, S. Giurgola, P. Vergani, and V. Pruneri, Widely transparent electrodes based on ultrathin metals, *Opt. Lett.* 34: 325-327, 2009.

[5] J. Y. Lee, S. T. Connor, Y. Cui, P. Peumans, Solution-processed metal nanowire mesh transparent electrodes, *Nano Lett.* 8: 689-692, 2008.

[6] H. Wu, L. Hu, M. W. Rowell, D. Kong, J. J. Cha, J. R. McDonough, J. Zhu, Y. Yang, M. D. McGehee, Y. Cui, Electrospun metal nanofiber webs as high-performance transparent electrode, *Nano Lett.* 10: 4242-4248, 2010.

[7] M. G. Kang, T. Xu, H. J. Park, X. Luo, L. J. Guo, Efficiency enhancement of organic solar cells using transparent plasmonic ag nanowire electrodes, *Adv. Mater.* 22: 4378-4383, 2010.

[8] P. Kuang, J. M. Park, W. Leung, R. C. Mahadevapuram, K. S. Nalwa, T. G. Kim, S. Chaudhary, K. M. Ho, K. Constant, A new architecture for transparent electrodes: Relieving the trade-off between electrical conductivity and optical transmittance, *Adv. Mater.* 23: 2469-2473, 2011.

[9] Q. G. Du, K. Sathiyamoorthy, L. P. Zhang, H. V. Demir, C. H. Kam, X. W. Sun, A two-dimensional nanopatterned thin metallic transparent conductor with high transparency from the ultraviolet to the infrared, *Appl. Phys. Lett.* 101: 181112, 2012.

[10] https://www.lumerical.com.

[11] M. Weber and M. R. Kamal, Estimation of the volume resistivity of electrically conductive composites, *Polym. Compos.* 18: 711-725, 1997.

[12] M. Rycenga , C. M. Cobley , J. Zeng , W. Li , C. H. Moran , Q. Zhang , D. Qin, Y Xia, Controlling the Synthesis and Assembly of Silver Nanostructures for Plasmonic Applications, Chem. Rev. 111 (6): 3669-3712, 2011.

[13] P.W. Anderson, Absence of diffusion in certain random lattices, Phys. Rev. 109: 1492-1505, 1958.

[14] [14] A.R. McGurn, A.A. Maradudin, V. Celli, Localization effects in the scattering of light from a randomly rough grating. Phys. Rev. B 31: 4866-4871, 1985.

[15] Last, B. J., and D. J. Thouless, Percolation theory and electrical conductivity, Phys. Rev. Lett. 27: 1719-1721, (1971).

Plasmon coupling in three-dimensional magnetic SRR metamolecules

Wei-Lun Hsu[1,*], Wei-Yi Tsai[1], Pin Chieh Wu[2], Wei Ting Chen[2], Yao-Wei Huang[2], Chun Yen Liao[2], Ai Qun Liu[3], Greg Sun[4] and Din Ping Tsai[1,2,5]

[1]Department of Physics, National Taiwan University, Taipei, Taiwan
[2]Graduate Institute of Applied Physics, National Taiwan University, Taipei, Taiwan
[3]School of Electrical and Electronic Engineering, Nanyang Technological University, Singapore, Singapore
[4]Department of Physics, University of Massachusetts Boston, Boston, Massachusetts, U.S.A.
[5]Research Center for Applied Sciences, Academia Sinica, Taipei, Taiwan
*corresponding author, E-mail: ross6320@gmail.com

Abstract

In the past decade, a number of interesting designs have been proposed to generate artificial magnetism at optical frequencies using plasmonic metamaterials, but owing to the planar configurations of typically fabricated metamolecules that make up the metamaterials, the magnetic response is mainly driven by the electric field of incident electromagnetic wave. In this paper, we fabricated three-dimensional (3D) split ring resonators (SRRs) which behave as magnetic metamolecules sensitive to both the incident electric and magnetic fields upon excitation with the stronger induced magnetic energy in comparison to that of planar SRRs. Subsequently, we conduct experimentally and numerically to investigate the plasmon coupling between 3D SRRs by varying the distance in between. We found that magnetic plasmon coupling can be significantly enhanced by standing the SRR metamolecules and it indeed plays a role in 3D SRR dimers. This work offers an important method to enhance the interaction between incident fields and metamaterials as well as the plasmon coupling between metamaterials at optical frequencies. Since the smaller occupied area in the case of 3D SRRs, it also paves a way for localized surface plasmon (LSP) based sensing device applications with more pronounced spectral resonant signals.

1. Introduction

Metamaterials are far more easily constructed with planar sub-wavelength elements on substrates, even when they are stacked in multilayer structures, their magnetic dipoles are always perpendicular to the magnetic field of normal incident wave, resulting in a weak interaction. While the oblique incidence allows for the magnetic response to be observed to an certain degree [1], such an effect can be enhanced with the three-dimensional (3D) split-ring resonator (SRR) structure in which the metamolecules stand up vertically, because the LSPR are not only excited by the electric field, but also by the magnetic field directly under normal incidence [2-4]. In this work, using a recently developed accurate alignment technique, we have fabricated 3D SRRs which allowed us to study how incident electromagnetic fields interact with these 3D SRRs and to reveal the plasmon coupling between closely spaced SRR dimers. We first numerically investigate the plasmon excitation and the magnetic energy density between isolated planar and 3D SRR. The 3D configuration of the SRRs offers another clear advantage over the planar structure in that it gives us the freedom to increase the magnetic coupling strength of two SRRs by having them stand next to each other very closely (while in planar structure SRRs lay down next to each other and their magnetic dipoles are only weakly coupled). Therefore, with two SRRs of different dimensions, we have indeed further observed plasmon hybridization due to both electric and magnetic coupling between the LSPRs associated with each SRR that resulted in LSPR shifts and the amount of shifting depends on the coupling strength between them. From the energy calculation of dipole-dipole interaction, we show that the presence of the magnetic plasmon coupling is indeed essential and comparable to the electric plasmon coupling effect in the 3D SRR dimer structures.

2. Discussions

Figure 1(b) shows the schematic configuration with respect to incident wave for 2D (left) and 3D (right) SRR metamolecules. Such configurations make sure that 3D SRRs can be excited simultaneously with an electric field along its SRR opening (x-axis) and a magnetic field perpendicular to the SRR plane (y-axis). In order to purely compare the magnetic plasmon excitation and field enhancement between them, all the geometrical parameters are identical, as shown in Fig. 1(a). It has been proposed and demonstrated that the planar (2D) SRR structure can support the magnetic plasmon resonance under normal illumination by interacting with incident electric field and result in a strong magnetic field within the SRR opening between prongs (left figure in Fig. 1(d)). On the other hand, in comparison with the planar SRRs lying flat on the substrate, the 3D SRR structure has a clear advantage in that they couple directly with not only the electric field but also the magnetic field of a normal illumination. As shown in Fig.

1(c), the magnetic plasmon can be excited in both SRR cases leading to a sharp resonance dip in transmittance spectrum but in different wavelength. Due to the environment change, the resonance wavelength is blue shift when the SRR configuration transferred from the planar to the upright one which provides an advantage to the meta-devices operating in higher frequencies. In addition, thanks to the involvement on the incident magnetic field for plasmon excitation of 3D SRRs, a stronger magnetic plasmon excitation is approached which leading to the deeper resonance dip in transmittance spectrum and stronger magnetic energy density (Fig. 1(d)) between two prongs.

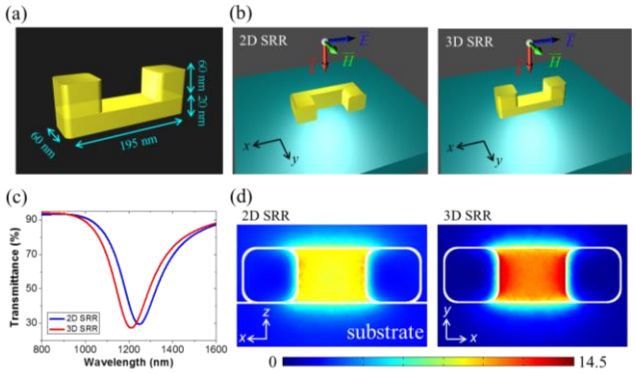

Figure 1: (a) Schematic diagrams for single SRR metamolecule and its dimensions. (b) The feature configurations with respect to the incident wave for 2D and 3D SRR metamolecule in identical dimensions as shown in (a). (c) Simulation transmittance spectra of 2D (blue curve) and 3D (red curve) SRR structure with 500 nm period in x and y directions. (d) The magnetic energy density at the interface between bottom rod structures and prongs for 2D (left) and 3D (right) SRRs.

Inspired by above results and discussions, we subsequently investigate the optical properties of a series of coupled 3D SRRs (dimers as SRR metamolecules) which may able to behave stronger magnetic plasmon interaction in between. Figure 2(a) shows the schematic of an array of 3D dimer (metamolecule) structures made of two 3D SRRs of different base rod lengths (L_1 = 170 nm and L_2 = 220 nm) that are placed in parallel along x-axis with their centers aligned on y-axis (the dimensions of this dimer sample is given in the caption of Fig. 2).

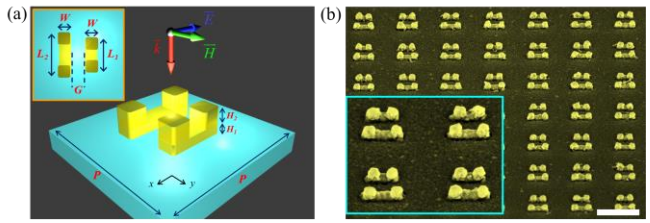

Figure 2: (a) Schematic diagrams of 3D SRR dimer unit cell with designed parameters: L_1 = 170 nm, L_2 = 220 nm, H_1 = 20 nm, H_2 = 60 nm, W = 60 nm and P = 500 nm. A parameter G is introduced for the gap separation between SRRs. (b) The 45° oblique and room in (inset) views for SEM micrographs (G = 50 nm) from fabricated samples. Scale bar: 500 nm.

Figure 2(b) shows the SEM images (oblique views) of the gold SRR dimer sample with 50-nm gap separation fabricated on a glass (BK7) substrate. The inset in Fig. 2(b) is an enlarged perspective view of four 3D SRR dimers with their two prongs sitting precisely on the two ends of the base rod.

Figure 3(a) represents the simulation transmittance spectra at four different gap separations between SRRs where two transmittance dips are well resolved and are associated with the SP resonances of the two SRRs of different sizes and their coupling. We have also observed the same behavior in the coupled 3D SRRs by systematically varying the separation G within a SRR dimer. Figure 3(b) shows the resonance wavelength (energy) separation $\Delta\lambda = \lambda_{a-b} - \lambda_{a+b}$ of the "anti-bonding" and "bonding" for the four samples with SRR spacing from 40 to 90 nm under normal illumination. For large SRR spacing (G > 90 nm), $\Delta\lambda$ remains largely unchanged, suggesting that these two SRRs are uncoupled with each supporting a plasmon mode (λ_a and λ_b), thus $\lambda_{a-b} - \lambda_{a+b} \approx \lambda_a - \lambda_b$. As the spacing reduces, the two SRRs become coupled as reflected by the trend of increasing $\Delta\lambda$ with the decreasing G. To reveal the contribution of electric and magnetic resonance on resonance wavelength separation, we individually calculate and purely compare the energy of electric and magnetic dipole-dipole interaction with varying gap sizes G. The energy of dipole-dipole interaction for both electric and magnetic can be descripted as:

$$E_{dipole} = \frac{\bar{d}_1 \cdot \bar{d}_2}{r^3} - \frac{3(\bar{d}_1 \cdot \bar{r})(\bar{d}_2 \cdot \bar{r})}{r^5}, \quad (1)$$

where (n = 1, 2) represent the electric dipoles ($\mathbf{P}_n = \frac{1}{i\omega}\int \mathbf{j}_n d^3r$) or magnetic dipoles ($\mathbf{M}_n = \frac{1}{2c}\int (\mathbf{r}_n \times \mathbf{j}_n) d^3r$). The j means the induced volume current density of each SRR metamolecule while plasmon excited. According to the above equations, the magnitude of normalized energy separation of dipole-dipole interaction can be further defined as the following:

$$Normalized\ \Delta E = \left| \frac{(E_{bonding} - E_{anti-bonding})_G}{(E_{bonding} - E_{anti-bonding})_{G=90nm}} \right|, \quad (2)$$

The larger normalized energy separation represents the stronger coupling at particular gap size. As shown in Fig. 3(c), we found that the normalized energy separation of both electric and magnetic dipole-dipole interaction are directly correlated with the coupling strength, that is, both the electric and magnetic coupling between 3D SRRs are substantially enhanced with smaller gap size, and the enhancement of magnetic dipolar interaction is as large as the electric one. More specifically, the normalized energy separation between electric and magnetic resonance is quite identical at each gap size indicating the magnetic dipoles

coupling can be dramatically enhanced. Although several other results show the magnetic dipole-dipole interaction between planar SRRs can be enhanced, it still exist an opening problem that can be only occurrence with particular orientations between SRRs. Some previous studies also claim that the coupling strength between two metamolecules can be further improved by stacked metamaterials or connecting two SRRs in which both the inductive and conductive coupling can be involved into the interaction process. Comparing with the other researches, our study provides a much effective way to directly enhance the inductive coupling between metamolecules because the distance between the centers of 3D SRRs can be significantly decreased. Furthermore, our approach is much suitable for SP based devices due to the SRR dimers is surrounded in free space without any dielectric material in vicinity. It is benefitting for LSP based refractive index sensor because most of the induced electromagnetic fields is able to expose in surrounding.

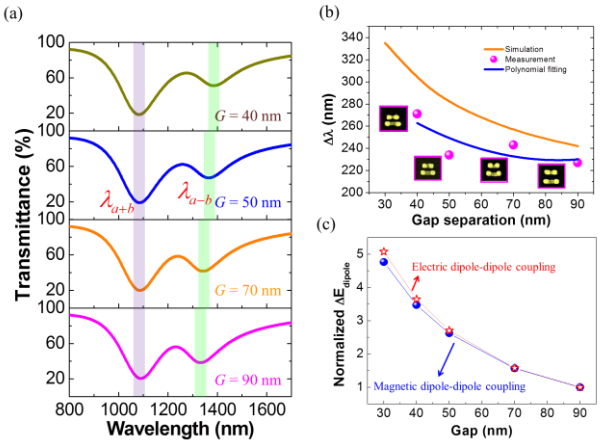

Figure 3: (a) Simulation transmittance spectra for 3D SRR dimer with various gaps. (b)The resonance wavelength gap of 3D SRR dimer at normal illumination with different separations between SRRs. Orange line and magenta dots are corresponding to the simulation and measurement results, respectively. Blue line: a second-order polynomial fitting for experimental results. Insets represent the corresponding SEM image with gap sizes G = 40, 50, 70 and 90 nm between SRRs (left to right). (c) Normalized energy separation of the electric (red) and magnetic (blue) dipole-dipole interaction

3. Conclusions

Comparison with traditional planar SRR structures, the 3D SRR metamolecules provides more pathways to interact with incident magnetic field under normal illumination which results in a stronger field enhancement in near field region. In addition, the shorter resonance wavelength and smaller floor space for 3D SRRs are benefiting for metamaterial based devices and applications due to the density of unit cell can be significantly increased. A series of 3D plasmonic dimers which composed of two SRRs in different feature dimensions have been fabricated by e-beam lithography with accurate alignment technique for studying the improvement in magnetic coupling strength between SRRs. Due to the inductive coupling between 3D SRRs in near-field regime, the resonance wavelength separation strongly depends on the distance in between. We indeed showed that the magnetic coupling strength between SRRs can be dramatically improved by standing the SRRs in order to significantly decrease the distance between SRRs. These results show that the electric and magnetic plasmon hybridization counteracts with each other and electric-induced plasmon plays a dominant role for two up 3D SRR dimers. This work provides a pathway for enhancing the plasmon excitation of metamaterials and plasmon coupling in between. It also paves a promising way for integrated opto-electronic devices due to the decreased connecting area and increased density of unit cell of metamolecules.

Acknowledgements

The authors acknowledge financial support from National Science Council, Taiwan under grant numbers 102-2745-M-002-005-ASP, 102-2911-I-002-505, 101-2911-I-002-107 and 101-2811-P-002-004, respectively. They are also grateful to National Center for Theoretical Sciences, Taipei Office, Molecular Imaging Center of National Taiwan University, National Center for High-Performance Computing, Taiwan, and Research Center for Applied Sciences, Academia Sinica, Taiwan for their support.

References

[1] X. Lu, J. Shi, R. Liu, C. Guan, Highly-dispersive electromagnetic induced transparency in planar symmetric metamaterials. *Opt. Express*, 20: 17581-17590, 2012.

[2] P. C. Wu, W. T. Chen, K. –Y. Yang, C. T. Hsiao, C. J. Chen, N. I. Zheludev, D. P. Tsai, Magnetic plasmon induced transparency in three-dimensional metamolecules. *Nanophotonics*, 1: 131-138, 2012.

[3] K. Fan, A. C. Strikwerda, X. Zhang, R. D. Averitt, Three-dimensional broadband tunable terahertz metamaterials. *Phys. Rev. B*, 87: 161104, 2013.

[4] W. T. Chen, C. J. Chen, P. C. Wu, S. Sun, L. Zhou, G.-Y. Guo, C. T. Hsiao, K.-Y. Yang, N. I. Zheludev, and D. P. Tsai, Optical magnetic response in three-dimensional metamaterial of upright plasmonic meta-molecules. *Opt. Express*, 19: 12837-12842, 2010.

Plasmonics and nanophotonics

Doped Metal-$LiNbO_3$-Metal Plasmonic Waveguides

Montasir Qasymeh*
Department of Electrical and Computer Engineering, Abu Dhabi University, Abu Dhabi, UAE
*corresponding author, E-mail: montasir.qasymeh@adu.ac.ae

Abstract

We investigate theoretically doped Metal-$LiNbO_3$-Metal nano-structure. We show that symmetric and anti-symmetric Surface Plasmon Polariton (SPP) modes can be coupled in such a structure by the mean of photorefractive effect. We found that the power transfer in the coupled modes is unidirectional from a strong symmetric mode to a week anti-symmetric mode. Either as an amplification or a mode-conversion process, the presented coupling process promises novel future applications. These include implementing known photorefractive applications in the plasmonic fields.

1. Introduction

Plasmonic technology has been proposed as a potential solution to the challenge of bringing together the two worlds of photonics and electronics [1]. In principle, plasmonic devices comprised of several metal-dielectric layers. The propagating light is coupled to the free electrons in the metal, which act like plasma at the optical frequency. It then follows that the propagating light modes are strongly confined. For instant, light can be confined to 100 times smaller than its wavelength. Such tight confinement is potential to open a new world of scalability and integration.

To date, several recent advances in plasmonic technology have been reported. These include plasmonic amplification and lasing, electrically controlled plasmonic devices, focusing and enhancing terahertz radiation using plasmonic waveguides, solitonic plasmonic waveguides, and all-optical nanoplasmonic logic gates [2-4], to mention a few examples. However, relatively little attention has so far been paid to plasmonic waveguides doped with impurities, and, to the best of our knowledge, the issue of doped Metal-$LiNbO_3$-Metal plasmonic waveguide has not yet been explored.

The photorefractive effect has been known since the early sixties; it was observed in many doped electro-optic crystals, including $LiNbO_3$, $BaTiO_3$, SBN, KTN, KNSBN, BSO, BGO, GaAs, InP, CdTe [5]. The photorefractive effect is an automatically phase-matched nonlinear phenomenon, whereby interfering light modes can generate a spatial space charge electric field in a host material. This spatial space charge electric field in turn couples the interfering light modes in a phase-matched fashion. Many applications have been proposed utilizing the photorefractive effect, such as dynamic holography, generation of optical phase conjugation, photorefractive resonators, nonreciprocal transmission window and laser beam clean up, and information storage, processing and communication [5-7].

In this work, we describe theoretically and evaluate numerically the evolution of co-propagating surface plasmon polariton modes (SPP) in a doped Metal-$LiNbO_3$-Metal plasmonic waveguide. Specifically, we consider a gold-$LiNbO_3$-gold nano-structure. We show that symmetric and anti-symmetric interfering SPP modes can be coupled by the mean of photorefractive effect. The power transfer between the considered interfering modes is calculated to quantify the modes interaction.

This paper is organized as follows. In section 2, a theoretical model is presented. In section 3, numerical simulations considering practical parameters, including losses, are presented and discussed. Section 4 provides concluding remarks.

2. Theory

Consider a MIM plasmonic waveguide consisting of two metallic layers sandwiching a lithium niobate ($LiNbO_3$) of thickness a. The $LiNbO_3$ is doped with donor and accepter impurities, and the waveguide is independent of the $y-$axis, as shown in Fig. 1. Given proper thickness of the $LiNbO_3$, two TM plasmonic modes are propagating. The two modes are of symmetric and anti-symmetric transvers field distribution, each of x and y electric field components.

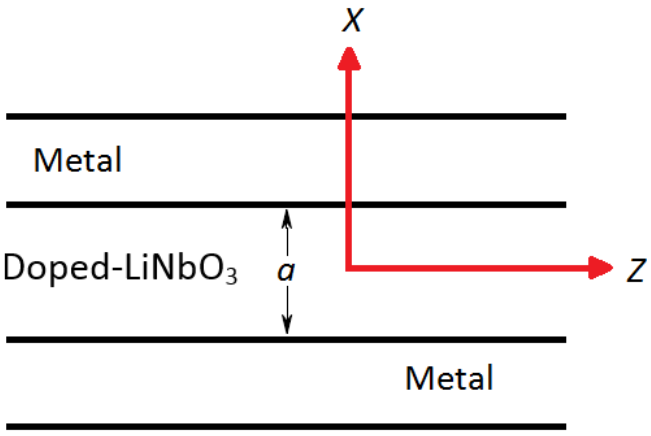

Figure 1: The Metal-$LiNbO_3$-Metal nano-structure. The $LiNbO_3$ is with thickness a and doped with impurities.

The interaction of the interfering SPP modes with the $LiNbO_3$ impurities is governed by the standard band transport model [5], which can be expressed mathematically in terms of the three coupled nonlinear differential equations. The first equation is the electron continuity equation, the second is the current density equation, and the third is Poisson's equation. It is known, however, that such a set of nonlinear coupled equations does not have closed-form analytical solutions. Nonetheless, in the steady state, a perturbation approach can be employed in the small depth intensity modulation limit i.e. $|A_1|^2+|A_2|^2 >> |A_1A_2^*|$, where A_1 and A_2 are the complex amplitudes of the anti-symmetric and symmetric propagating SPP fields, respectively.

The effective permittivity can be approximated by finding the space charge electric field and the $LiNbO_3$'s nonlinear polarization components.

The evolution of the interfering SPP modes can be evaluated by solving the governing nonlinear wave equation. It then follows that the slowly varying envelope of the SPP modes are given by [8]:

$$\frac{\partial A_1}{\partial z}+\frac{(i\omega)^2 C_1}{8ic^2\beta_1}\left(r_{13}\varepsilon_x^2\frac{\beta_2}{\beta_1}-r_{33}\varepsilon_z^2\frac{k_{d2}}{k_{d1}}\right)|A_2|^2 A_1=0\,, \qquad (1)$$

$$\frac{\partial A_2}{\partial z}+\frac{(i\omega)^2 C_1^*}{8ic^2\beta_2}\left(r_{33}\varepsilon_z^2\frac{k_{d1}}{k_{d2}}-r_{13}\varepsilon_x^2\frac{\beta_1}{\beta_2}\right)|A_1|^2 A_2=0\,, \qquad (2)$$

where $\beta_{1,2}$ and $k_{d1,2}$ are the propagation constant and the transverse decay factor of the anti-symmetric and symmetric SPP modes, respectively, r_{13} and r_{33} are the electro-optic coefficients of the $LiNbO_3$, $\varepsilon_{x,z}$ are the permittivity of the $LiNbO_3$, c is the speed of light in free space, and the constant C_1 (attributed to the photorefractive effect) is given by:

$$C_1=\frac{-ei\Delta\beta\left(C_{N_1}-C_{N_{D1}}\right)}{\varepsilon_0\varepsilon_x\left(k_{d1}+k_{d1}\right)^2-\varepsilon_0\varepsilon_z\left(\beta_1-\beta_2\right)^2}\left(\frac{\beta_1\beta_2}{\left(\omega\varepsilon_0\varepsilon_x\right)^2}-\frac{k_{d1}k_{d2}}{\left(\omega\varepsilon_0\varepsilon_z\right)^2}\right), \qquad (3)$$

where

$$C_{N_1}=\frac{a_1 b_2}{a_3 b_2-a_2 b_1}, C_{N_{D1}}=\frac{a_1 b_1}{a_2 b_1-a_3 b_2},$$

$$a_1=s\left(N_D-N_{D0}^i\right),\ a_2=N_0\gamma_R+s\bar{I}_0,\ a_3=N_{D0}^i\gamma_R,$$

$$b_1=-b_2+k_B T\mu\left[\left(k_{d1}+k_{d1}\right)^2-\left(\beta_1-\beta_2\right)^2\right],$$

$$b_2=\frac{e^2N_0\mu\left[\left(k_{d1}+k_{d1}\right)^2-\left(\beta_1-\beta_2\right)^2\right]}{\varepsilon_0\varepsilon_x\left(k_{d1}+k_{d1}\right)^2+\varepsilon_0\varepsilon_x\left(\beta_1-\beta_2\right)^2},$$

Here e is the electron charge, μ is the electron mobility, k_B is the Boltzmann constant, T is the temperature, N_D is donor density, N_0 and N_{D0}^i are the average of free electron and ionized donor densities, respectively, $\bar{I}_0$ is the average SPP total power, γ_R is the recombination constant, and s is the photoionization cross-section .

3. Results and Discussion

To illustrate the potential of the PR effect in plasmonic waveguides, we consider typical realistic values. In this work, we consider the telecom wavelength $\lambda=1550\,nm$. The $LiNbO_3$ permittivity is $\varepsilon_z=5.06$ and $\varepsilon_x=5.52$ at this wavelength. Also, we choose the gold (i.e. Au) as the cladding metal, that has a permittivity of $\varepsilon_m=-125.22+10i$ at $\lambda=1550\,nm$.

First, we numerically solve the coupled SVEA equations, i.e. (1) and (2), and calculate the gain of one of the two modes, while the latter is considered as a pump. Our numerical investigation shows that the power transfer is unidirectional and can be realized only from the symmetric mode (acting like a pump) to the anti-symmetric mode (acting like a signal). We explain this result by noting that the space charge electric field, which couples the two modes, has an anti-symmetric transverse distribution.

In the following numerical results, calculations will be carried out considering three different $LiNbO_3$ thicknesses: $a=150\,nm$, $a=160\,nm$, and $a=175\,nm$. By solving the dispersion relation graphically at $\lambda=1550\,nm$, we find that for $a=150\,nm$, we have $\beta_1/k_0=2.3495+0.0541i$, $\beta_2/k_0=2.6962+0.0277i$; for $a=160\,nm$ we have $\beta_1/k_0=2.34955+0.0249i$, $\beta_2/k_0=2.6767+0.0136i$; and for $a=175\,nm$ we have $\beta_1/k_0=2.3496+0.0226i$, and $\beta_2/k_0=2.6514+0.0127i$. In the following analysis, we first ignore the modal losses and characterize the photorefractive effect. Optimum doping concentration and input pump power values will be studied and identified. Then, losses will be taken into account, and the photorefractive effect will be characterized against the losses.

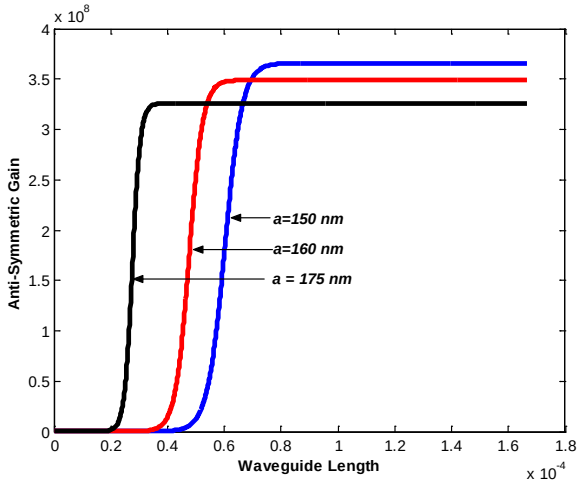

Figure 2: The anti-symmetric power gain versus waveguide length, for three different $LiNbO_3$ thicknesses.

In Figure 2, we present the anti-symmetric power gain versus the waveguide length, ignoring the modal losses. Here $N_D = 12\times10^{20} m^{-3}$, $|A_1(0)|^2 = 3.316\times10^2 V/m^2$, and $|A_2(0)|^2 = 3.316\times10^8 V/m^2$. The average power density $\bar{I}_0$ is 3.7643×10^{10}, 3.7254×10^{10}, and $3.6780\times10^{10} W/m^2$ for $a = 150$, 160, and $175\,nm$, respectively. As can be seen, the gain is larger for the smaller LiNbO3 thickness a; however, longer interaction length is needed.

In Figure 3, the anti-symmetric power gain versus the doping concentration is calculated for waveguide length $L = 0.5\,mm$, considering same input power densities as in Figure 2. Three different $LibNO_3$ thicknesses are considered as well. It can be seen from Fig. 3 that the gain is maximized over a band of the doping concentration values, while the band is wider for smaller thicknesses.

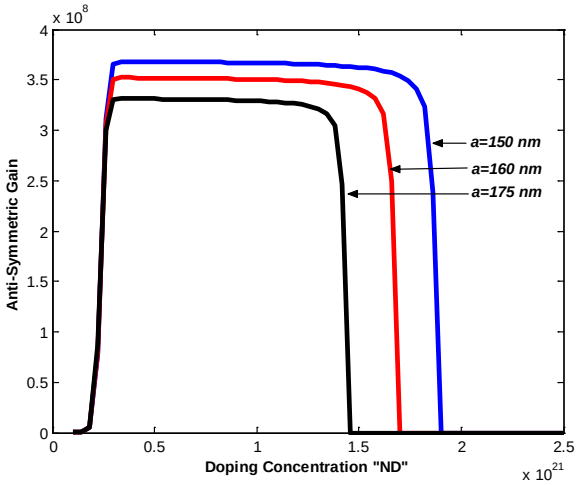

Figure 3: The anti-symmetric gain versus the doping concentration N_D, for there different $LiNbO_3$ thicknesses. Here, the wave guide length is $L = 5\times10^{-4} m$.

In Figure 4, the anti-symmetric power gain is presented versus the input ratio $\frac{A_1(0)}{A_2(0)}$, for a constant $A_2(0)$. The presented result here is for $a = 175\,nm$. No differences were noted for different thicknesses. As is expected in any photorefractive medium, the gain increased with decreasing input signal power ($|A_1(0)|^2$) for a fixed pump power ($|A_2(0)|^2$). This is quite promising for designing an optical oscillator, which starts operating from a tiny amount of noise.

In Figure 5, the anti-symmetric power gain versus the input pump field amplitude $A_2(0)$ is calculated for the waveguide length $L = 0.5\,mm$, $N_D = 1.3963\times10^{21} m^{-3}$ and $A_1(0)/A_2(0) = 10^{-3}$. Three different $LibNO_3$ thicknesses are considered as well. It can be seen from Fig. 5 that the gain is also maximized over a specific band of the input field amplitude values, $A_2(0)$, while the band is wider for smaller thicknesses.

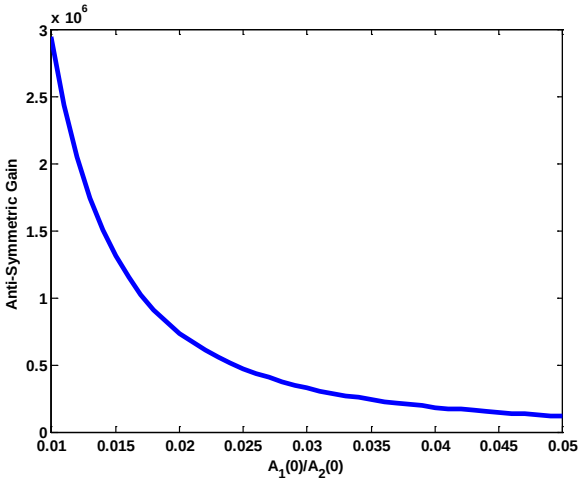

Figure 4: The anti-symmetric power gain versus the input ratio $A_1(0)/A_2(0)$, for constant $|A_2(0)|^2 = 3.316\times10^8 V^2/m^2$. Here $L = 5\times10^{-4} m$, $N_D = 1.3963\times10^{21} m^{-3}$ and $a = 175\,nm$.

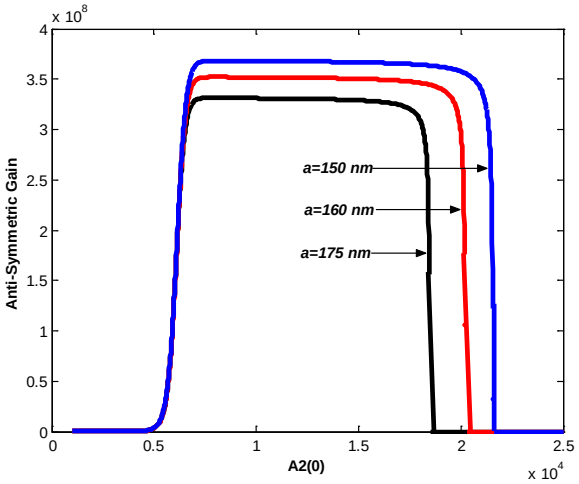

Figure 5: The anti-symmetric power gain versus the input pump field amplitude $A_2(0)$. Here $L = 5\times10^{-4} m$, $N_D = 1.3963\times10^{21} m^{-3}$, $A_1(0)/A_2(0) = 10^{-3}$.

The modal losses can be taken into account by incorporating the effective decay factor α_{eff} in the SVEA equations, (1) and (2). The effective decay factor α_{eff} is given by:

$$\alpha_{eff_m} = 2\,\mathrm{Im}\{\beta_m\} \qquad (4)$$

where $m \in \{1,2\}$. In the remaining simulation, the modal losses will be taken into account. As expected, losses limit the interaction dynamics by dissipating the pump and the signal powers. To minimize the impact of losses, we will

choose the doping concentration and input power values that maximize the anti-symmetric gain, inferred from the simulations in Figures 3 and 5.

In figure 6, the anti-symmetric power gain versus the waveguide length is presented, taking the modal losses into account. As a first iteration towards optimizing the response, let us consider the doping concentration and input pump amplitude values that maximize the gain in the ideal lossless case, taken from the simulation in Figures 3 and 5. Here, three different thicknesses are considered. As can be seen from Figure 6, no net gain can be achieved for $a = 150\,nm$. This is because losses dominate the photorefractive gain at this thickness. However, net gain can be experienced up to a certain waveguide lengths for $a = 160\,nm$, and $a = 175\,nm$. For instance, the maximum gain for $a = 150\,nm$ and $a = 175\,nm$ are achieved at $L = 6.7\,\mu m$ and $L = 13.38\,\mu m$ waveguides lengths, respectively.

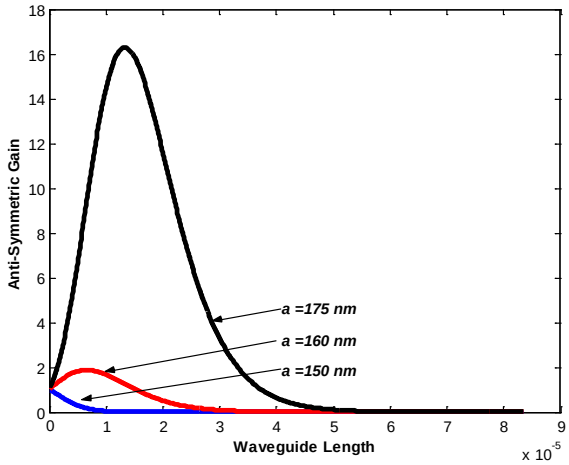

Figure 6: The anti-symmetric power gain versus waveguide length, for three different $LiNbO_3$ thicknesses, taking the modal losses into account.

In Figure 7, the anti-symmetric power gain versus the doping concentration is re-calculated, taking into consideration the modal losses. Here, the waveguide lengths are $L = 6.7\,\mu m$ and $L = 13.38\,\mu m$ for $a = 160\,nm$ and $a = 175\,nm$, respectively. The waveguide lengths are with optimum values taken from the simulation in Figure 6. As can be seen, the gain reaches its maximum at $N_D = 1.379\times10^{21}\,m^{-3}$ and $N_D = 1.629\times10^{21}\,m^{-3}$ for $a = 160\,nm$ and $a = 175\,nm$, respectively.

In Figure 8, the anti-symmetric power gain versus the pump input amplitude is also re-calculated, while losses are considered. Here, the waveguide lengths and the doping concentrations, are $L = 6.7\,\mu m$ and $L = 13.38\,\mu m$, and $N_D = 1.379\times10^{21}\,m^{-3}$ and $N_D = 1.629\times10^{21}\,m^{-3}$, for $a = 160\,nm$ and $a = 175\,nm$, respectively. These doping concentration are with optimum values taken from the simulation in Figure 7. As can be seen in Figure 8, the gain reaches its maximum at $A_2(0) = 1.82\times10^4\,V/m$ and $A_2(0) = 1.8199\times10^4\,V/m$ for $a = 160\,nm$ and $a = 175\,nm$, respectively.

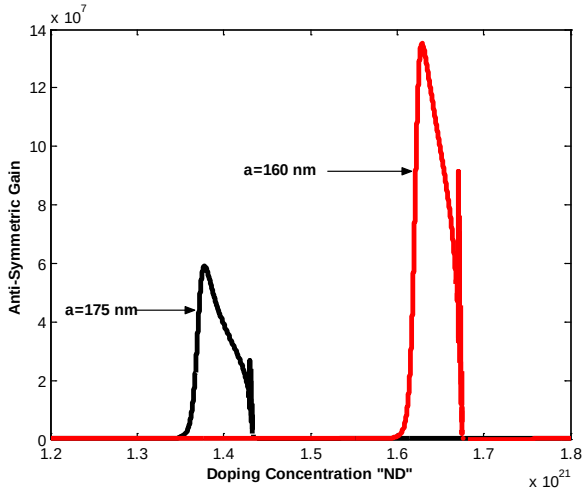

Figure 7: The anti-symmetric power gain versus the doping concentration N_D, taking the modal losses into account. Here, the wave guide lengths are $L = 6.7\,\mu m$ and $L = 13.4\,\mu m$ for $a = 160\,nm$ and $a = 175\,nm$, respectively.

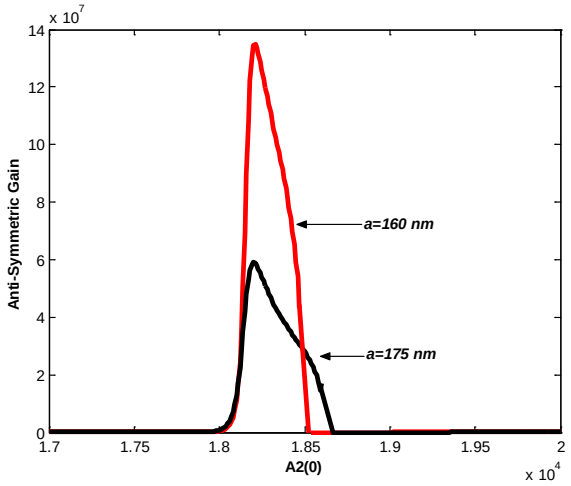

Figure 8: The anti-symmetric power gain versus the pump power amplitude, taking the modal losses into account.

In Figure 9, the anti-symmetric power gain versus the waveguide length is re-evaluated. Here, as a second iteration towards optimizing the response, we consider the doping concentration and the input pump amplitude values taken from the simulation of Figures 8 and 9. Namely, $N_D = 1.379\times10^{21}\,m^{-3}$ and $N_D = 1.629\times10^{21}\,m^{-3}$, and $A_2(0) = 1.82\times10^4\,V/m$ and $A_2(0) = 1.8199\times10^4\,V/m$ for $a = 160\,nm$ and $a = 175\,nm$, respectively. As can be seen, a significant net gain can be achieved despite losses for proper doping concentrations and pump amplitudes values. We note here that further iterations can be conducted towards more optimized parameters. However, the goal of this work is more to model and highlight the potential of the photorefractive effect in plasmonic waveguides.

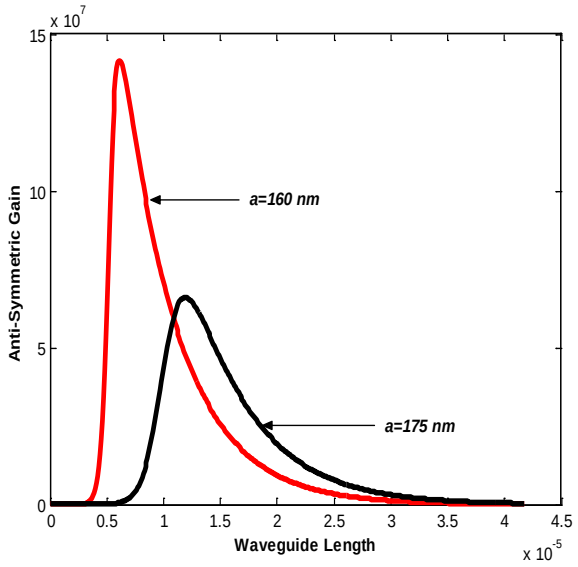

Figure 9: The anti-symmetric power gain versus waveguide length, taking the modal losses into account.

Figure 10 depicts the results of Figure 9 in dB units. As can be seen, given the assumed parameters, the maximum achieved gain can be $8\,dB$ and $7.77\,dB$, at $L=6.5\mu m$ and $L=12.1\mu m$, for $a=160\,nm$ and $a=175\,nm$, respectively. It can also be seen that the photorefractive effect dominates losses up to $L=97.8\mu m$ and $L=111.6\,\mu m$, at which zero dB gain is achieved, for $a=160\,nm$ and $a=175\,nm$, respectively.

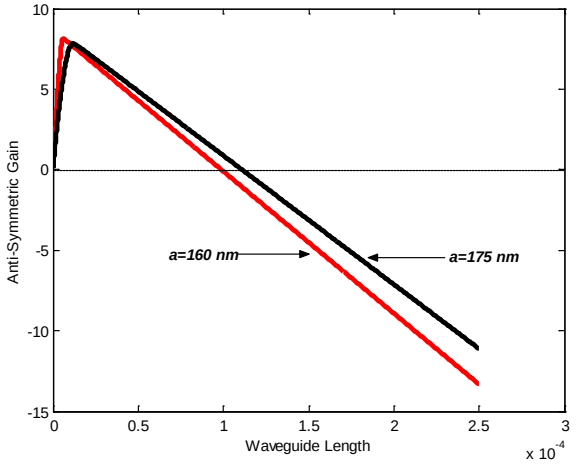

Figure 6: The anti-symmetric power gain in dB versus waveguide length, taking the modal losses into account.

4. Conclusions

In this paper, we investigated the evolution of two interfering symmetric and anti-symmetric SPP modes in a doped metal-LibNO_3-metal nano-structure. The interaction of the SPP modes with impurities was modeled by the band transport model. The evolution of the propagating fields was evaluated by solving the governing nonlinear wave-equation. Numerical simulations were carried out by considering gold as the gladding material. It was found that a unidirectional power transfer can be realized from symmetric to anti-symmetric SPP modes. The anti-symmetric gain was thus characterized and found to be maximized over a certain bands of the doping concentration and input power. The modal losses were also taken into account. The presented effect can be conducted either as a modal conversion process or all-optical amplification process. This work opens new opportunities for implementing known photorefractive applications in the nano-plasmonic devices.

References

[1] Ekmel Ozbay, Plasmonics: Merging photonics and electronics at nanoscale dimensions, *Science* 311:189-193, 2006.

[2] Pierre Berini and Israel De Leon, Surface plasmon-polariton amplifiers and lasers, *Nature Photon.* 6: 6-24, 2011.

[3] Wenshan Cai, Alok P. Vasudev, Mark L. Brongersma, Electrically controlled nonlinear generation of light with plasmonics, *Science* 333:1720-172, 2011.

[4] M. C. Schaafsma, H. Starmans, A. Berrier, and J. Gómez Rivas, Enhanced terahertz extinction of single plasmonic antennas with conically tapered waveguides, *New J. Phys.*15:015006, 2013.

[5] Pochi Yeh, Introduction to Photorefractive Nonlinear Optics, Wiley, New York, USA, 1993.

[6] Claire Gu, Yuan Xu, Yisi Liu, J. J. Pan, Fengqing Zhou, Henry He, Applications of photorefractive materials in information storage, processing and communication, *Optical Materials*, 23:219-227, 2003.

[7] A. E. Chiou, Photorefractive phase-conjugate optics for image processing, traping, and manipulation of microscopic objects, *Proceedings of the IEEE*, 87:2047-2085, 1999.

[8] Montasir Qasymeh, Photorefractive effect in plasmonic waveguides, *IEEE Journal of Quantum Electron*. Accepted.

A CMOS-Compatible Platform Based on Metal-Dielectric-Si Hybrid Plasmonic Waveguide for Integrated Plasmonic Circuits

Shiyang Zhu*, G. Q. Lo, and D. L. Kwong

Institute of Microelectronics, A*STAR (Agency for Science, Technology and Research), 117685, Singapore
*corresponding author, E-mail: zhusy@ime.a-star.edu.sg

Abstract

Owing to the capability of tight confinement of optical mode far beyond the diffraction limit, plasmonics provides a potential solution for miniaturization of the photonic devices in electronic and photonic integrated circuits to be comparable with the electronic counterparts. Among various plasmonic waveguides developed to date, a metal-dielectric-Si hybrid plasmonic waveguide (HPW) is an attractive one owing to its superior properties over other kinds of plasmonic waveguides. Various ultracompact passive and active photonic devices based on this HPW have been demonstrated using standard CMOS technology on SOI wafers, such as straight waveguides, 90° bend, s-bends, power splitters, Bragg reflector, ring resonators, and modulators, which are required to realize plasmonic integrated circuitry. This paper describes the current status, challenges, and future directions of these CMOS-compatible HPW-based photonic devices for integrated plasmonic circuits.

1. Introduction

In recent years, silicon photonics has attracted attention as an emerging technology for optical telecommunications and for optical interconnects in microelectronics [1]. Silicon electronic and photonic integrated circuits (EPICs) have been well developed. However, they are challenged by the size mismatch between the nanoscale electronic components and the microscale photonic components because the footprint of photonic components is limited by the diffraction effect. A potential solution to scale down the photonic components to be compatible with the electronic counterparts for future dense EPICs lies in plasmonics, which deals with surface plasmon polaritons (SPPs) propagating at metal-dielectric interfaces [2,3].

An essential building block of every plasmonic device to be integrated in EPICs is a plasmonic waveguide. A major problem in design of plasmonic waveguides is the inherent tradeoff between the propagation distance and the optical mode confinement. For seamless integration in the existing Si EPICs, the plasmonic waveguides should be CMOS-compatible. Moreover, the plasmonic waveguide should be flexible enough to allow active functions such as modulation and detection to be implemented. Many kinds of plasmonic waveguides have been developed, such as metallic strips and nanowires, structures of coupled nanowires [4,5], plasmonic slot waveguides [6,7], metallic grooves [8], metal-dielectric-metal structures [9], and dielectric-loaded plasmonic waveguides [10]. Among them, the recently proposed metal-dielectric-Si hybrid plasmonic waveguide (HPW) [11-13], especially that with the structure as shown in Fig. 1(a) [14], is an attractive candidate because (1) the optical field can be tightly confined in the thin dielectric layer as shown in Fig. 1(b), (2) it provides a longer propagation distance as compared to a metal-dielectric-metal plasmonic waveguide with the same light confinement factor, (3) its metal-oxide-semiconductor configuration allows active functions to be implemented, especially with a functional dielectric such as ITO, VO_2, or AlN etc, and (4) it is fully CMOS compatible when Cu or Al is used as the metal.

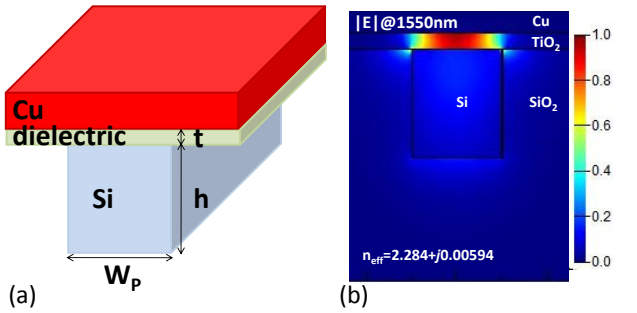

Figure 1: (a) Schematic diagram of Cu-dielectric-Si HPW for seamless integration in Si EPICs, and (b) Electric field ($|E|$) profile in the HPW. The optical field is tightly confined in the thin dielectric layer between the Cu cover and the Si core.

In this paper, various ultracompact photonic devices are developed based on the Cu-dielectric-Si HPW using standard CMOS technology on silicon-on-insulator (SOI) wafers. Because the plasmonic waveguide has much larger propagation loss than the conventional Si waveguide, the low-loss Si channel waveguide is used for long-distance light transmission and the high-loss plasmonic waveguide is used for realization of ultracompact functional devices, including passive devices such as power splitters, ring resonators, and MZI etc, and active devices such as detector and modulators, as shown schematically in Fig. 2. A coupler with high coupling efficiency is developed to link the plasmonic waveguide and the photonic waveguide.

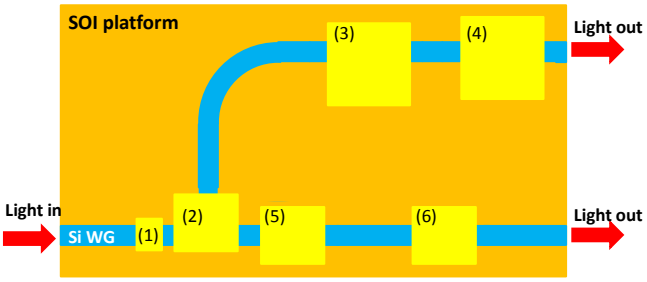

Figure 2: Schematic view of various ultracompact HPW-based photonic devices inserted in the conventional Si waveguide, including (1) plasmonic rotator, (2) plasmonic power splitter, (3) plasmonic ring- resonator, (4) plasmonic MZI, (5) plasmonic modulator, (6) plasmonic detector, and many others.

2. Fabrication and measurement

The devices are fabricated on 0.22-μm top-Si and 2-μm buried SiO_2 using the process flow shown in Fig. 3.

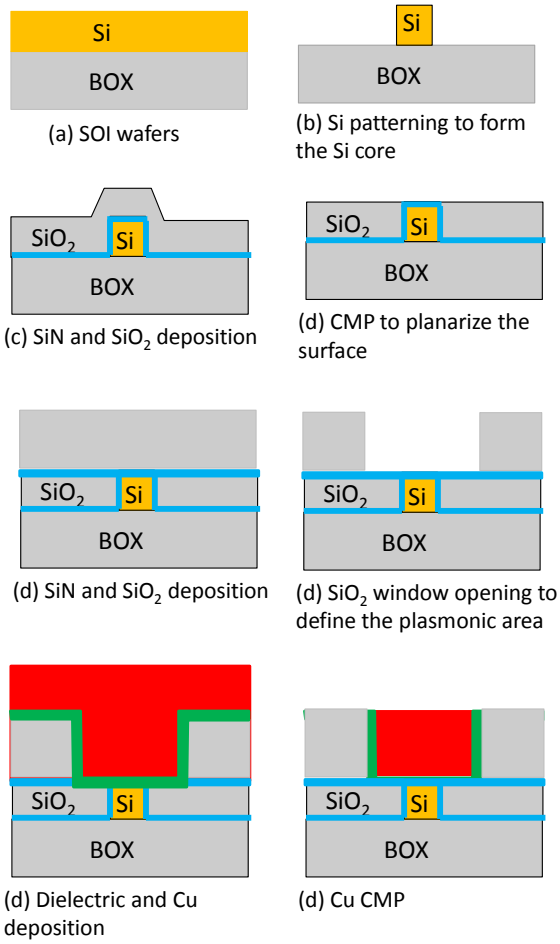

Figure 3: Process flow of the Cu-dielectric-Si HPW-based passive devices. More steps are necessary for active devices.

After Si patterning, as shown in Fig. 4(a), Si_3N_4 and SiO_2 were deposited sequentially, followed by SiO_2 chemical-mechanical polishing (CMP) to planarize the surface (using Si_3N_4 as the CMP stopping layer). Then, Si_3N_4 and SiO_2 were sequentially deposited again, followed by SiO_2 window opening to expose the plasmonic area (using Si_3N_4 as the etching stopping layer), as shown in Fig. 4(b). After wet etching the remaining Si_3N_4 in the windows, a thin dielectric layer was deposited. In this work, SiO_2, Si_3N_4, and TiO_2 are used as the dielectric. Then, a thick Cu layer was deposited, followed by Cu-CMP to remove Cu outside the windows. For active devices, more steps are necessary such as for doping and contact formation. The fabricated devices have cross section as shown in Fig. 4(c) and the top view as Fig. 4(d). One sees that the Cu covered plasmonic devices are inserted in conventional Si waveguides.

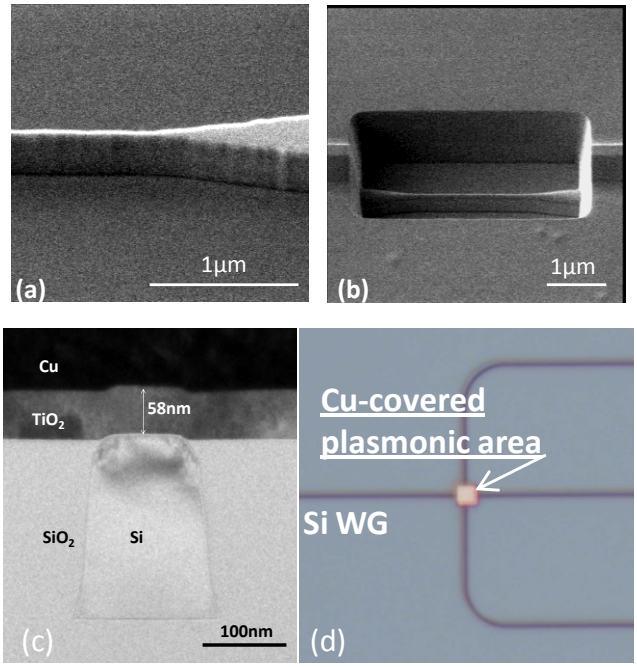

Figure 4: (a) SEM image of the Si core, (b) SEM image after SiO_2 window opening, (c) XTEM image of the fabricated Cu-dielectric-Si HPW, and (4) microscopy view of one of the plasmonic device.

After dicing, the chips were measured using a fiber-chip-fiber method as conventional Si photonic chips. Light from a broadband (1520-1620 nm) laser source was quasi-TM polarized by a polarizer and then coupled into the input Si waveguide through a polarization-maintaining fiber. The transmitted light from the output Si waveguide was monitored by an optical spectrum analyzer.

3. Results and discussion

3.1. Straight HPWs

The properties of HPW are generally characterized through the propagation loss, the effective index, and the confinement factor defined as the ratio of optical intensity inside the dielectric layer over the area of $W_P \times t$ [7]. Fig. 5(a) depicts the measured transmission spectra through straight HPWs with different length LP, as shown schematically in the inset of Fig. 5(b). One sees that the propagation loss is

almost wavelength independent in the range of 1520–1620 nm. Fig. 5(b) plots the measured output power as a function of L_P, after subtracting that of the reference Si waveguide. One sees that it exhibits good linearity. From linear fitting, the propagation loss is extracted to be ~0.122 dB/μm and the coupling loss between the HPW and the conventional Si waveguide is ~0.65 dB/facet.

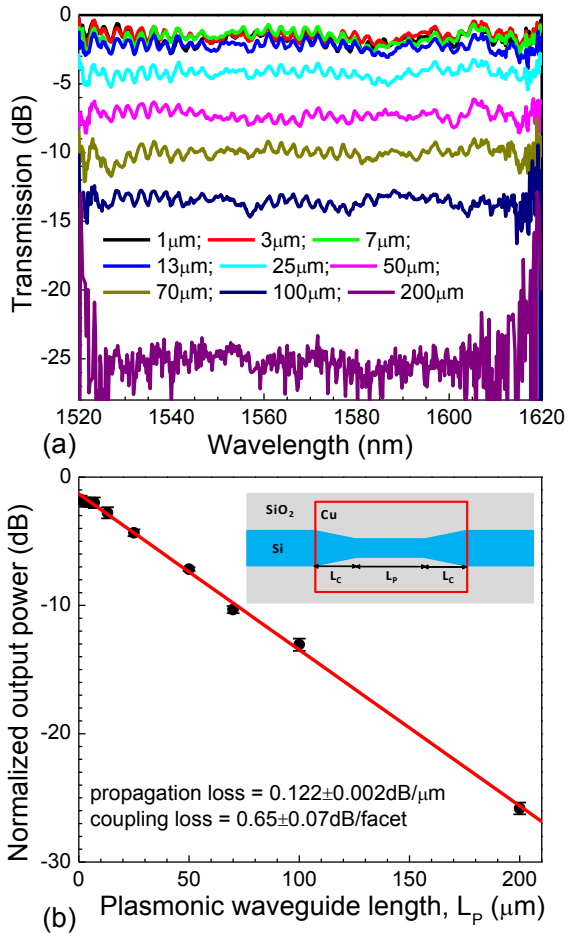

Figure 5: (a) The transmission spectra of one set of Cu/200-nm SiO_2/340-nm Si HPWs with L_P ranging from 1 to 200 μm, normalized by the transmission spectrum of the reference Si waveguide without the plasmonic area, and (b) Output power through the straight HPWs (shown schematically in the upper inset) versus the length (L_P), normalized by that of the reference Si waveguide without the plasmonic area, from which the propagation loss and the coupling loss between the HPW and the conventional Si waveguides can be extracted.

Fig. 6 plots experimental and theoretical propagation loss and confinement factor as a function of W_P for straight HPWs with the dielectric of 32-nm TiO_2, 58-nm TiO_2, or 35-nm SiO_2, and 220-nm-thick Si core. One sees that the tightest confinement is reached at W_P of 150–200 nm, regardless the n and t of the dielectric. Above this value the mode size increases with W_P increases while below this value the lateral confinement becomes poorer. On the other hand, the propagation loss changes little with W_P. Moreover, one sees that the larger n or the thicker t of the dielectric results in larger propagation loss and tighter confinement, reflecting the inherent tradeoff between the mode confinement and the propagation distance.

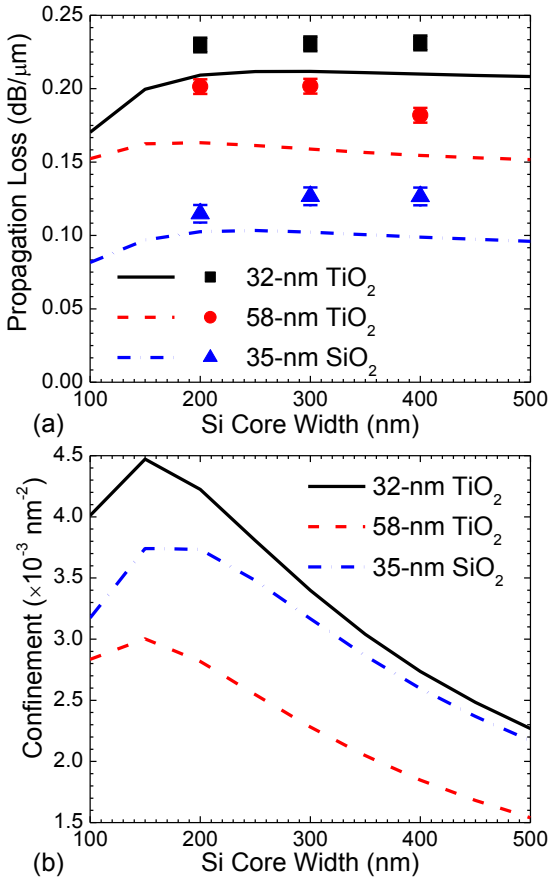

Figure 6: (a) Calculated and experimental propagation loss and (b) Calculated confinement factor as a function of W_P for straight HPWs (h = 220 nm) with 32-nm TiO_2, 58-nm TiO_2, and 35-nm SiO_2.

3.2. Tapered couplers

Tapered couplers as shown in Fig. 7 are studied, which link the conventional Si channel waveguide and the plasmonic waveguide. Figs. 8(a) and (b) plots the coupling losses as a function of geometric parameters L_m and L_C, respectively. One sees that a very high coupling efficiency can be reached with the optimal parameters. This is important as all plasmonic devices are inserted in the conventional Si waveguides.

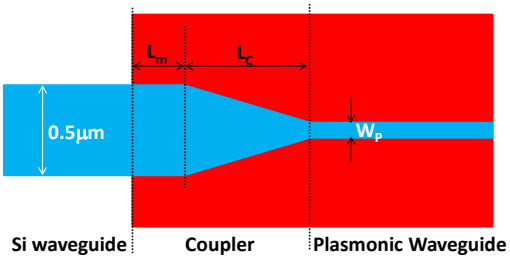

Figure 7: Top view of the tapered coupler links the Si waveguide and the HPW, which has same cross section as the HPW.

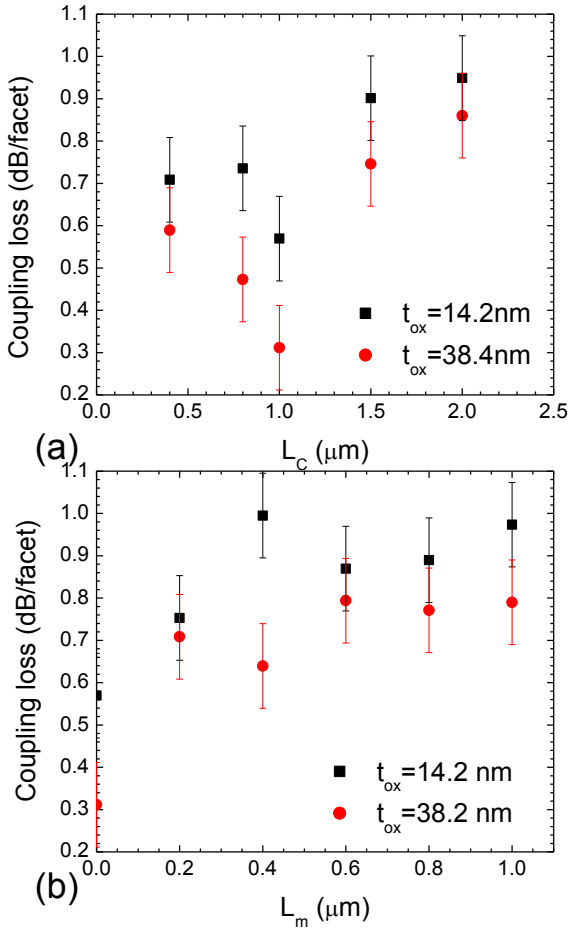

Figure 8: Measured coupling loss between the Si waveguide and the HPW as a function of (a) L_C and (b) L_m. High coupling efficiency is obtained with the optimal geometry.

3.3. Sharp 90° bends

The bending loss is studied using 90°-circular bends as shown in Fig. 9(a). Fig. 10(b) shows electric field profile along the middle of the 32-nm TiO_2 layer of a 0.5-μm-R bend, obtained using finite-difference time-domain (FDTD) simulation, showing that the HPW supports sharper bending than the conventional Si channel waveguide, thus enabling a more compact resonators.

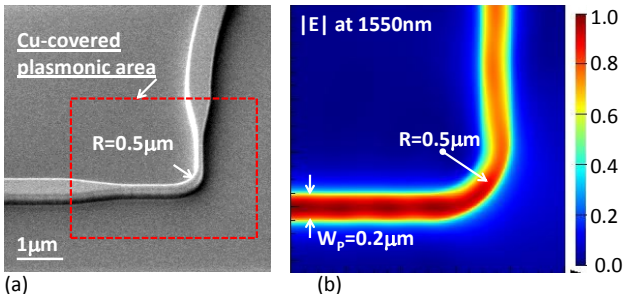

Figure 10: (a) SEM image of the Si core of a 90°-circular bend with 0.5-μm radius, the red rectangle is defined as the plasmonic area where a 32-nm TiO_2 layer and a thick Cu layer will be deposited, (b) Electric field profile along the middle of the 32-nm TiO_2 layer in a 0.5-μm-R bend.

90°-circular bends with radii of 0, 0.5, 1.0, and 2.0 μm are fabricated and measured using a broadband (1520-1620 nm) laser source. Fig. 11(a) shows the measured spectra for bends with 200-nm W_P, normalized by that of the corresponding straight HPW with the same length. One sees that the pure bending loss depends on wavelength weakly in the wavelength range of 1520–1620 nm. The experimental and theoretical bending losses are depicted in Fig. 11(b) as a function of R for bends with W_P of 200 or 400 nm, as well as that of a 500-nm-wide Si channel waveguide for comparison. As expected, the bending loss decreases with R increasing, approaching to a negligibly small value when R is sufficiently larger. The HPWs provide a smaller bending loss than the Si channel waveguide with the same R, making the HPW supports a smaller ring resonator than the conventional Si channel waveguide. The 200-nm-W_P HPW exhibits a smaller bending loss than the corresponding 400-nm-W_P HPW due to its tighter confinement.

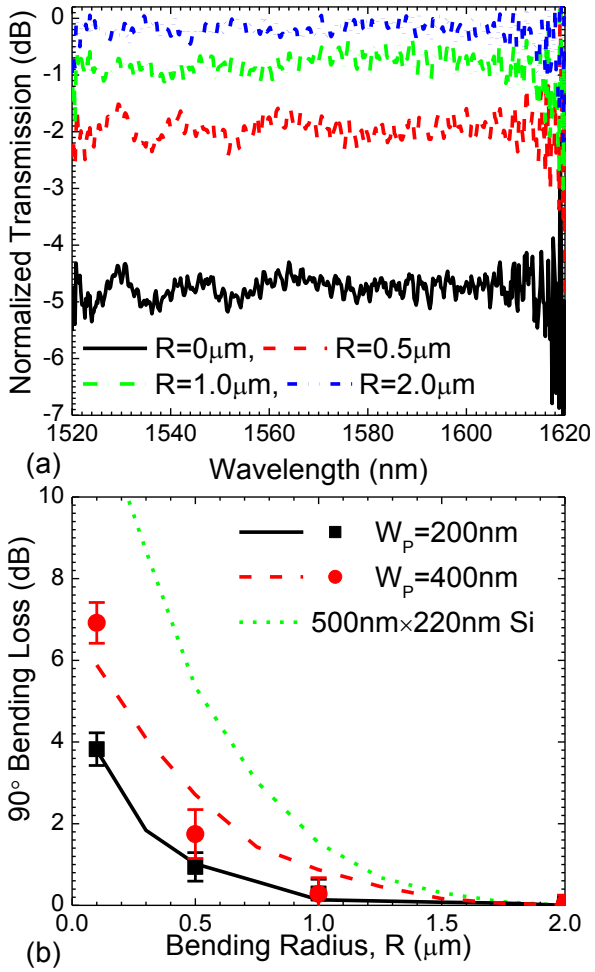

Figure 11: (a) Transmission spectra measured on 200-nm-W_P HPW 90°-circular bends with R of 0, 0.5, 1.0, and 2.0 μm, normalized by that measured on the corresponding straight HPWs with the same length, and (b) Experimental (represented by the symbols) and theoretical (represented by the curves) of pure bending losses versus R.

3.4. Bragg reflectors

Fig. 12 shows the schematic diagram of HPW-based plasmonic Bragg reflector (PBR) fabricated in this work [15]. The PBR is formed by periodically interrupting the Si core of the straight HPW along the propagation direction *x* to form *N* identical Si pillars with length of d_1 and interval (between two Si pillars) of d_2. The Si cores of HPW and the Si pillars have the same width and height. The grooves between Si pillars are filled by SiO_2, as shown in Fig. 12(b). It actually contains two periodically concatenated waveguide subsections along the *x*-direction: one is Cu-dielectric-Si and the other is Cu-dielectric-SiO_2.

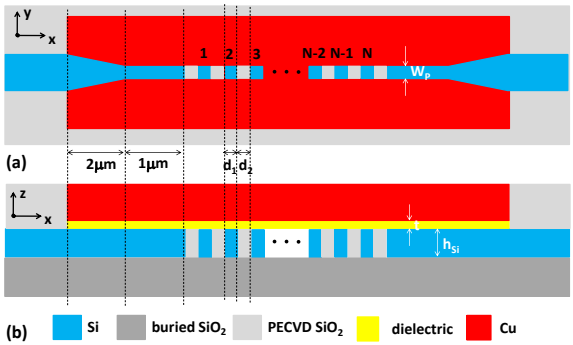

Figure 12: Schematic diagram of the Cu-dielectric-Si HPW based PBR inserted in the Si channel waveguide (a) top view and (b) cross sectional view.

Fig. 13 plots spectra measured on a set of PBRs with d = 230 nm and different periods N = 10, 15, and 20, respectively, normalized by that measured on the corresponding 2-μm-long straight HPW. Since the spectral range of our broad-band laser source (~100 nm) is smaller than the width of stop-band estimated from numerical simulation (~174 nm), only the right side of the stop-band is observed. One sees that the fabricated PBR with 20 periods (total length of ~10 μm) already exhibits favorable performance such as low transmission of ~-30 dB within the stop-band, insertion loss of ~-10 dB outside the stop-band, steep band edges of ~0.92 dB/nm, and small ripples in the transmission spectra beyond the band edges.

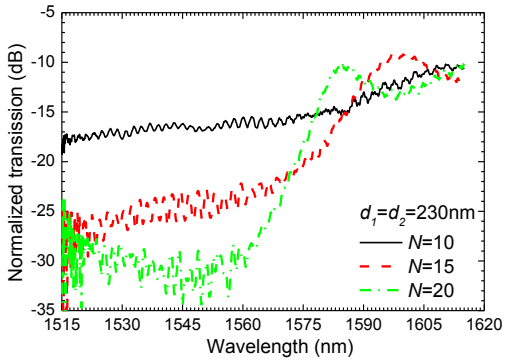

Figure 13: Transmission spectra measured on PBRs with d = 230 nm and different periods of 10, 15, or 20, normalized by that measured on the corresponding 2-μm-long straight HPW.

3.5. Ring resonators

HPW ring resonators with radii of 1.0, 1.5, and 2.0 μm are fabricated and measured. Since it is technically different to fabricate a small gap using the conventional UV lithography, the gap in the layout is set to 0.2 μm in this work. Fig. 14 shows the measured transmission spectra, normalized by that measured on the corresponding straight HPW without the ring. They exhibit a relatively large Q value as compared with those based on MIM plasmonic waveguides.

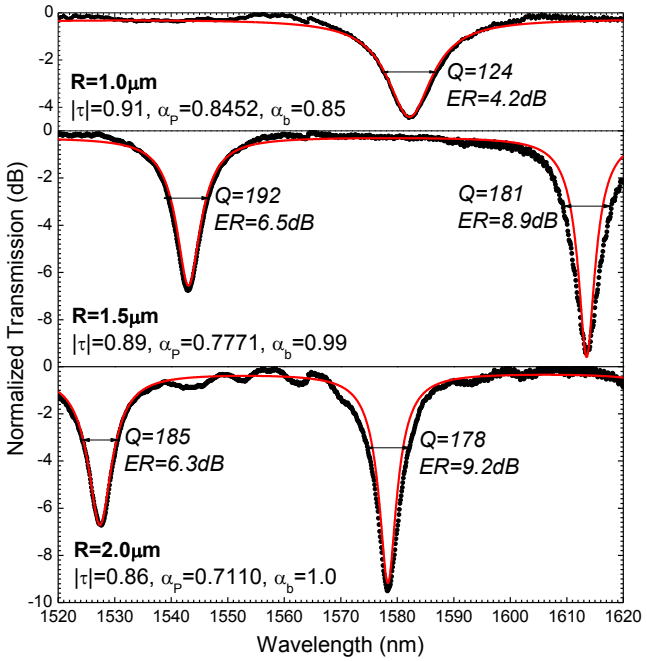

Figure 14: Transmission spectra measured on HPW ring resonators with radii of 1.0, 1.5, and 2.0 μm, normalized by that of corresponding straight HPW without the ring. The red lines are the fitting curves.

In general, the normalized transmission, T(λ), can be expressed as :

$$T(\lambda) = \frac{\alpha^2 + t^2 - 2\alpha t \cos\theta}{1 + \alpha^2 t^2 - 2\alpha t \cos\theta} \qquad (1)$$

where $\theta = (2\pi / \lambda) n_{eff} 2\pi R$ is the phase change around the ring, $\alpha = 10^{2\pi R \alpha_P / 10} \sigma_b$ is the field attenuation factor per roundtrip around the ring (α_P being the propagation loss in dB/μm and σ being a parameter accounting for the pure bending loss), $t = |t| \exp(i\phi)$ is the field transmission through the coupling region in the bus waveguide, and λ is the free-space wavelength. Assuming n_{eff} keeps the same for four WRRs and α_P is the same as that deducted from the straight HPWs, the spectra are fitted by Eq. 1 using n_{eff}, σ_b, |t|, and ϕ as the fitting parameters. The fitting curves are also plotted in Fig. 14 with the corresponding fitting parameters indicated.

3.6. Thermo-optic switchers

By add a TiN heater just above the Cu layer, the resonant wavelengths of ring resonators can be tuned with high efficiency and relatively fast speed. Such a plasmonic TO switch is fabricated, as shown in Fig. 15(a).

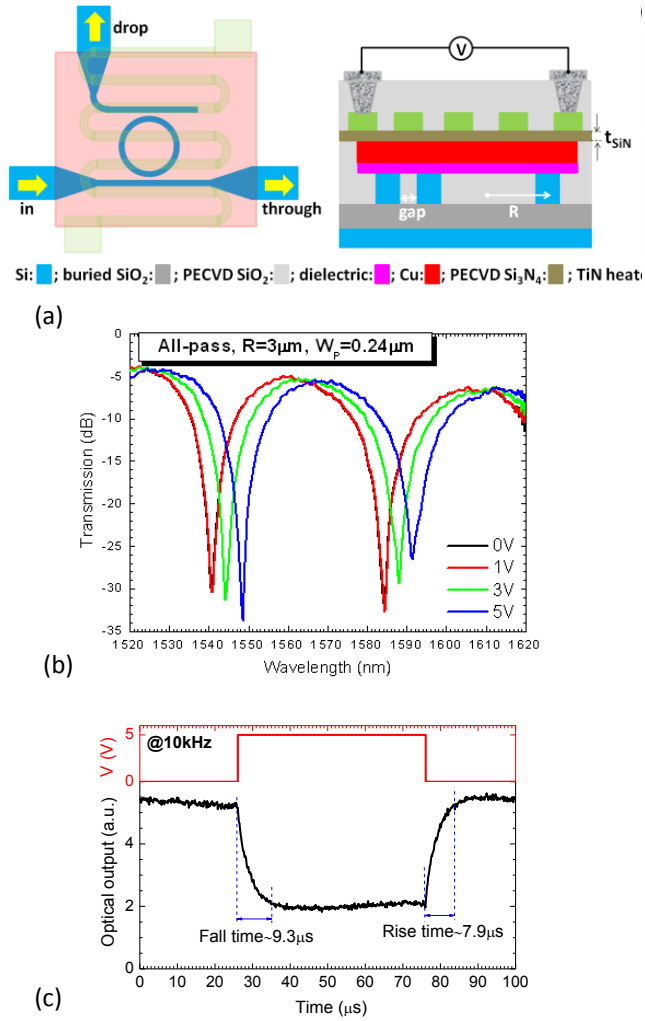

Figure 15: (a) Schematic of the Cu-dielectric-Si hybrid plasmonic waveguide ring resonator based TO device studied in this work. The TiN heater is placed above the Cu cap over a thin PECVD SiN layer of t_{SiN}. (b) Transmission spectra measured on an all-pass resonator with 3-μm R and 0.24-μm W_P under different voltages, normally by that measured on a reference Si waveguide without the plasmonic area, (c) Temporal response measured on the through port of the add-drop resonator at 1547 nm under 10-kHz 5-V square-wave voltage.

Fig. 15(b) shows the measured transmission spectrum of a 3-μm-R plasmonic ring resonator at the bias of 0 to 5V. One sees that the spectrum is red-shift with voltage increasing due to the thermal effect. The tuning efficiency is measured to be ~1.13 nm/mW for the 2.5-μm-R resonator and to be ~1.08 nm/mW for the 3.0-μm-R resonator, much larger than the conventional Si ring based TO devices (~67 pm/mW). The tuning speed of the plasmonic resonators is characterized by applying a 10 kHz/0-5V square-wave voltage on the TiN heater. Fig. 7(c) shows the temporal response measured on the through port of the 2.5-μm-R add-drop resonator at 1547-nm wavelength. The rise time is ~7.9 μs and the fall time is ~9.3 μs, which is much faster than the conventional Si ring based TO devices (~400 μs).

3.7. Electro-optic modulators

An electro-optical (EO) modulator [16], which converts an electronic signal to an optical signal, is designed based on the Cu-dielectric-Si HPWs, as shown in Fig. 16.

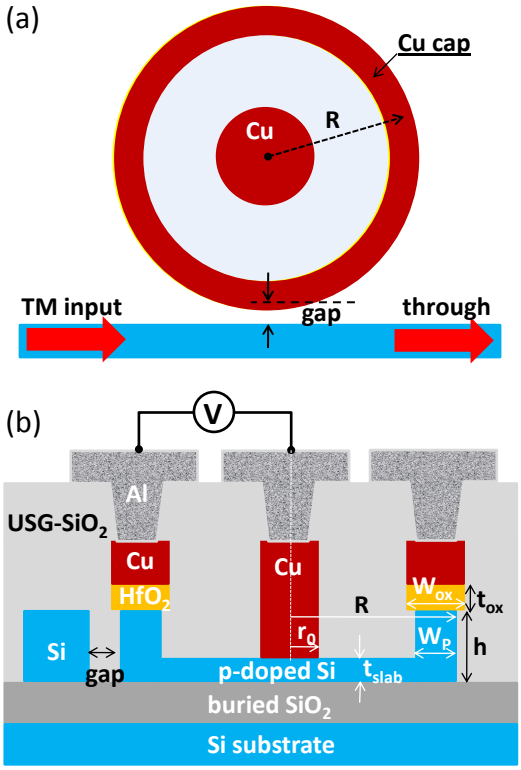

Figure 16: (a) Top view, and (b) cross-section side view of the proposed Si microdonut modulator based on Cu-insulator-Si hybrid plasmonic waveguide illustrating the ring-shaped high-κ dielectric gate, the Cu cap, and the Cu cylinder above the center-donut to contact the p-Si. A voltage is applied between the ring-shaped Cu cap and the center Cu cylinder contacted with Si.

Fig.17 plots the spectral transmittance of the modulator's output waveguide in the critical coupling condition in the depletion and accumulation states, respectively. The resonator has a loaded-Q value of ~400, close to that the experimental value. Δn_{eff} is calcualted to be ~0.0076, which leads to a $\Delta\lambda$ of ~4.3 nm. One sees that a large extinction ratio (ER) of >6 dB is already obtained at a relatively large wavelength range. Obviously, a larger ER can be obtained simply by increasing the accumulation charge density, but it is priced by a large driving voltage as well as a large driving energy. For the proposed device with t_{ox} = 5 nm and N_A = 1×10^{19} cm^{-3}, the voltage for depletion is calculated to be: V_{dep} = -1.45 V + V_{fb}, and the voltage for accumulation with N_{accu} of 2×10^{20} cm^{-3} is: V_{accu} = 1.45 V + V_{fb}. Therefore, the

required voltage swing is ~2.9 V. The oxide capacitance is calculated to be ~61fF. Thus, the switching energy E_s of the MOS modulator is calculated to be ~100 fJ based on the following equation:

$$E_s = \frac{1}{2} C_{dep} V_{dep}^{\ 2} + \frac{1}{2} C_{accu} V_{accu}^{\ 2} \qquad (2)$$

Because in practice the bit's energy usually occupies 50% of the time slot, we could assume that the modulator's switching energy per bit is approximately one-half of E_s, namely, ~50 fJ/bit, which is much smaller than the current Si modulators. The speed of the modulator is limited by the free-carrier transport time between the Si contact and the accumulation region as well as the RC delay time. The distance between the Si contact and the accumulation region is less than 1 μm for our modulator, thus the transport time is predicted to ~10 ps by assuming free carrier velocity of ~10^7 cm/s, corresponding to a speed of ~100 GHz. If the loaded resistance of our device is assumed to be ~50 Ω, the speed limited by the RC delay time is predicted to be ~50 GHz. Therefore, the proposed modulator is inherently very fast and its modulation speeds are probably of the order of >50 GHz.

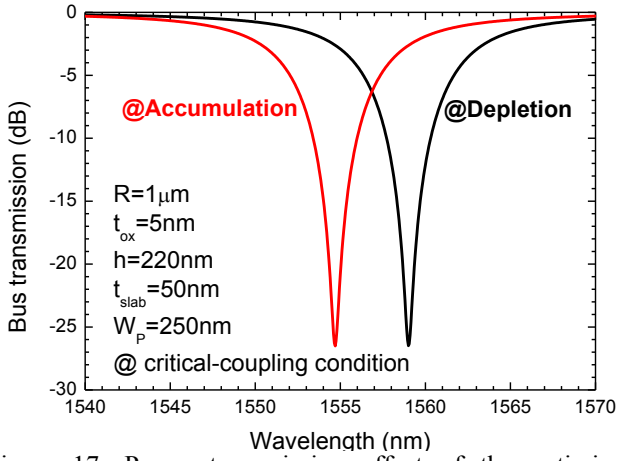

Figure 17: Power transmission effect of the optimized plasmonic donut modulator (in the critical coupling condition) in the depletion and accumulation states.

4. Conclusions

In this work, we describe various optical devices based on the recently develop Cu-insulator-Si hybrid plasmonic waveguides, including straight waveguides, tapered couplers to link the conventional Si waveguides and the HPW devices, sharp 90° bends, Bragg reflectors, ring resonators, thermo-optical switchers, and donut-based electro-optic modulators. The other devices such as s-bends, power splitters, racetrack resonators, and TE/TM splitters [17-19] are also demonstrated (not included in this paper). All these devices offer ultracompact size as compared with those based on the conventional Si waveguides owing to the tight mode confinement in the plasmonic waveguide structure. Combined with the fully compatibility, these HPW-based devices establish a platform for the integrated plasmonic circuits.

Acknowledgements

This work was supported by Singapore A*STAR-MINDEF Joint Grant 122-331-0074.

References

[1] D. J. Lockwood and L. Pavesi, *Silicon Photonics II: Components and Integration*, Springer-Verlag Berlin Hemisphere, 2011.

[2] D. K. Gramotnev and S. I. Bozhevolnyi, "Plasmonics beyond the diffraction limit," *Nat. Photon.* 4(2): pp. 83-91, 2010.

[3] V. J. Sorger, R. F. Oulton, R. M. Ma, and X. Zhang, "Toward integrated plasmonic circuits," *MRS Bulletin* 37: pp. 728-738, 2012.

[4] S. A. Maier, M. L. Brongersma, and H. A. Atwater, "Electromagnetic energy transport along arrays of closely spaced metal rods as an analogue to plasmonic devices**,"** *Appl. Phys. Lett 78*: pp. 16-18, 2001.

[5] H. S. Chu, W. B. Ewe, W. S. Koh, and E. P. Li, "Remarkable influence of the number of nanowires on plasmonic behaviors of the coupled metallic nanowire chain," Appl. Phys. Lett. 92: art. 103103, 2008.

[6] S. Y. Zhu, T. Y. Liow, G. Q. Lo, and D. L. Kwong, "Fully complementary metal-oxide-semiconductor compatible nanoplasmonic slot waveguides for silicon electronic photonic integrated circuits," *Appl. Phys. Lett. 98*: art. 021107, 2011.

[7] S. Y. Zhu, T. Y. Liow, G. Q. Lo, and D. L. Kwong, "Silicon-based horizontal nanoplasmonic waveguide for on-chip integration," *Opt. Express 19(9)*: pp. 8888-8902, 2011.

[8] S. I. Bozhevolnyi, V. S. Volkov, et al., "Channel plasmon subwavelength waveguide components including interferometers and ring resonators," *Nature 440*: pp. 508-511, 2006.

[9] J. A. Dionne, L. A. Sweatloak, and H. A. Atwater, "Plasmon slot waveguides: towards chip-scale propagation with subwavelength-scale localization," *Phys. Rev. B 73*: art. 035407, 2006.

[10] A. Kumar, J. Gosciniak, et al, "Dielectric-loaded plasmonic waveguide components: going practical," *Laser & Photonics Reviews 7(6)*: pp. 938-951, 2013.

[11] R. F. Oulton, V. J. Sorger, D. A. Genov, D. F. P. Pile, and X. Zhang, "A hybrid plasmonic waveguide for subwavelength confinement and long-range propagation," *Nat. Photon.* 2(8): 496-500, 2008.

[12] H. S. Chu, E. P. Li, P. Bai, and R. Hegde, "Optical performance of single-mode hybrid dielectric-loaded plasmonic waveguide-based components," *Appl. Phys. Lett.* 96**:** 221103, 2010.

[13] J. Ctyroky, P. Kwiecien, and I. Pichter, "Analysis of hybrid dielectric-plasmonic slot waveguide structures with 3D Fourier Modal Methods," *J. Europ. Opt. Rap. Public*., 8: 13024, 2013.

[14] S. Y. Zhu, G. Q. Lo, and D. L. Kwong, "Experimental demonstration of vertical Cu-SiO_2-Si hybrid plasmonic waveguide components on an SOI platform," *IEEE Photon. Techn. Lett.,* 24(14): pp. 1224-1226, 2012.

[15] S. Y. Zhu, H. S. Chu, G. Q. Lo, and D. L. Kwong, "CMOS-compatible plasmonic Bragg reflectors based on Cu-dielectric-Si structures," *IEEE Photon. Techn. Lett.,* 25(21): pp. 2115-2118, 2013.

[16] S. Y. Zhu, G. Q. Lo, and D. L. Kwong, "Theoretical investigation of ultracompact and athermal Si electro-optic modulator based on Cu-TiO2-Si hybrid plasmonic donut resonators," *Opt. Express* 21(10): pp. 12699-12712, 2013.

[17] S. Y. Zhu, G. Q. Lo, and D. L. Kwong, "Performance of ultracompact copper-capped silicon hybrid plasmonic waveguide-ring resonators at telecom wavelengths," *Opt. Express* 20(14): pp. 15232-15246, 2012.

[18] J. Chen, S. Y. Zhu, and G. Q. Lo, "CMOS compatible polarization splitter using hybrid plasmonic waveguide," *Opt. Express* 20(23): pp. 25345-25355, 2012.

[19] S. Y. Zhu, G. Q. Lo, and D. L. Kwong, "Submicro-radius plasmonic racetrack resonators in metal-dielectric-Si hybrid plamsonic waveguide," *IEEE Photon. Techn. Lett.,* to be published, DOI (identifier): 10.1109/LPT.2014.2308311.

Tuning the dispersion relation of a plasmonic waveguide via graphene contact

Yu Zhou, Cheng Wang, Di-Hu Xu, Ren-Hao Fan, Kun Zhang, Ru-Wen Peng*, Qing Hu, and Mu Wang

National Laboratory of Solid State Microstructures and Department of Physics,
Nanjing University, Nanjing 210093, China
*corresponding author, E-mail: rwpeng@nju.edu.cn

Abstract

In this work, we have investigated experimentally and theoretically the dispersion relation of a plasmonic slab waveguide, where the thin gold film with nano-aperature arrays is sandwiched by graphene and silica layer on silicon chip. It is shown that the plasmonic slab waveguides are compatible with silicon technology. We have found that when the light waves irradiate the nanostructured waveguides with or without graphene, surface plasmon polaritons are always excited at the metal-dielectric interface due to the interaction between the surface charge oscillation and the electromagnetic field of the light. But in the slab waveguide with graphene, the resonant dips definitely shift in the reflection spectra, which indicates that the contact of graphene can tune the dispersion relation of the waveguide in the visible regime. Experimental measurements on optical reflections are in good agreement with calculated plasmonic band structures. Further calculations show that the dispersion relation of plasmonic slab waveguide can be tuned by electron doping and nonlinear effect of graphene. The investigations provide a way to actively control the dispersion relation of plasmonic waveguides on silicon chips and benefit to the development graphene-related active optical devices.

1. Introduction

Surface plasmon polariton (SPP) is the surface wave that forms at the metal-dielectric interface [1]. It can propagate along the interface for a rather long distance and can confine light into deep subwavelength volumes beyond the diffraction limit [1,2]. Nowadays the SPP waveguide made by noble metal slab is regarded as a fundamental component in the plasmonic circuits [3,4]. Several approaches have been introduced to excite the SPPs via overcoming the momentum mismatch between the light in free space and the surface wave, including prism coupling [5,6], defect scattering [7], and periodic patterning [8]. The periodic patterning uses reciprocal vector to satisfy the momentum match and has been successfully used to launch SPPs at specific wavelength or frequency [9,10]. The excited wavelength is very sensitive to the surface condition, reminding us that one can alter the dispersion relation of the plasmonic waveguides by modifying its surface. Recently, there has been an increasing interest in graphene application in plasmonics [11,12]. Graphene-noble metal contact can serve as a good foundation for enhanced light-matter interaction [13-15], molecule sensing [16-19] and low loss plasmonic applications [20,21] due to the interaction between graphene electron and the surface plasmon. The properties of graphene can be tuned by doping or the nonlinear effect [22-25], providing a new way for tunable graphene-related device. In this work, we design a plasmonic slab waveguide that is compatible with silicon technology, and tune the dispersion relation of the waveguide via graphene contact. Shifts of the resonances in the reflection spectra are obvious and experimental measurements are in good agreement with calculated plasmonic band structures.

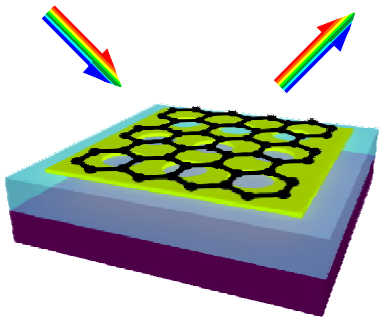

Figure 1: Design of the slab plasmonic waveguide. Materials from bottom to top are respectively silicon chip, 300nm SiO_2 layer, 40nm gold film and graphene.

2. Experiment results and theoretical model

2.1. Sample fabrication and measurement

Since silicon is very lossy in the visible range, an isolating layer is necessary to design a plasmonic waveguide compatible with silicon technology. Figure 1 is a schematic view of our design. In experiment, 300nm SiO_2 layer is formed on top of the Si substrate by thermal oxidation, which is thick enough to isolate the Si substrate from the metal waveguide above. The plasmonic waveguide is made of 40nm Au film fabricated by magnetron sputtering. To effectively excite the SPPs, periodic holes are milled in the metal film using focus ion beam (FIB). The radius of the hole is designed 100nm to ensure strong interaction with light in the visible range, and three samples with period 300nm, 350nm and 400nm are fabricated. Graphene layer was firstly grown by chemical vapor deposition (CVD)

method on copper and then transferred onto the waveguide by PMMA method [26]. Figure 2(a) and Figure 2(b) show the SEM image of samples with and without graphene, respectively. Inset in Fig. 2(b) indicates the region where the graphene is cracked. Fig. 2(c) is the Raman spectra of three samples after the deposition of graphene where the broad baseline is the photoluminescence of Au. Two sharp peaks on the baseline are G and 2D modes of graphene and the dominant 2D peaks indicating that the graphene is indeed monolayer [27,28]. The reflection spectra, in Fig. 2(d), are measured before and after the deposition of graphene using micro-spectrophotometer (Craic). We can see that after the deposition of graphene, resonant dips red shift.

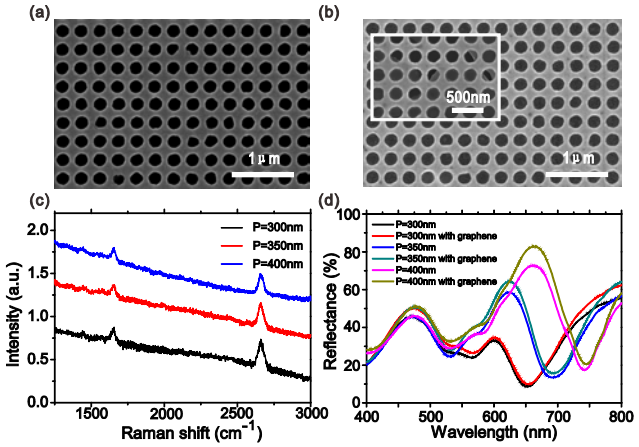

Figure 2: (a) SEM image of the sample with period 300nm before the deposition of graphene. (b) SEM image of the sample with period 300nm after the deposition of graphene. Inset: the region where the graphene cracks. (c) Raman spectra of three samples with period 300nm, 350nm and 400nm. (d) Reflection spectra of the three samples before and after the deposition of graphene.

2.2. Theoretical model

We use the commercial finite difference time domain (FDTD) software package (Lumerical FDTD Solutions) to calculate the band structure of the waveguide. In calculation, graphene layer is modeled as an ultra-thin metallic layer whose optical conductivity is exactly the optical conductivity of the pristine graphene ($\pi e^2/2h$) in visible range. We take the theoretical value of the graphene thickness 0.35nm in calculation. All the geometry parameters are set as the same as those in experiment. Figure 3 shows the band structure of the waveguide plotted in ω~k diagram, which is calculated from the reflection dip as a function of incident angle. The right/left side of the ω~k diagrams describes band structure before/after the deposition of graphene. Fig. 3(a)-(c) are band structures under TE incident. We can see that for all three samples two modes exist which behave differently as increasing the period. The mode which red shifts with the period is SPP mode and the other one is cavity mode. Fig. 3(d)-(f) are the band structures under TM incident. Except the cavity modes, there also exist SPP modes which can be more efficiently excited by TM rather than TE illumination. The dispersion relations of the SPP mode show clearly the plasmonic characters and red shift while increasing the period of the aperture arrays. At the centre of the band structure where $k_{//}$=0, the resonance dips stagger from each other. This is the case under normal incident corresponding to the reflection spectra in Fig. 2(d).

To further analyze the modes, we investigate the field distribution at the resonances. Figure 4 shows the field distributions from the cross-sectional and top views of the structure whose period is 400nm. Fig. 4(a) and Fig.4 (b) describe the field profile at 523nm from which we can conclude that it is cavity mode. The hole and the structures beneath form a cavity and the cavity mode can be excited under both TE and TM illuminations. Fig. 4(c) and Fig. 4(d) show the field profile at wavelength 731nm, corresponding to the second dip in Fig. 2(d). The propagation of the SPP along the metal layer indicating that such mode is SPP mode. Therefore, there are two kinds of modes in the structure, one is the cavity mode and the other is the SPP mode. We draw this conclusion based on the field profiles and the reflection spectra at the resonances.

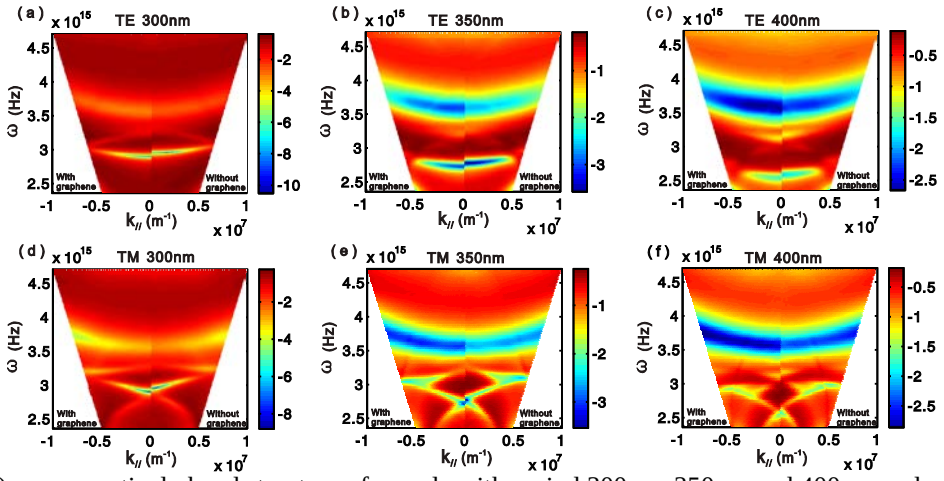

Figure 3: (a), (b), (c) are respectively band structure of sample with period 300nm, 350nm and 400nm under TE illuminations. (d), (e), (f) are respectively band structure of sample with period 300nm, 350nm and 400nm under TM illuminations.

For cavity mode, the field intensity is rather weak at the metal- dielectric interface and the resonance is in the silica layer, shown in Fig. 4(a); while there is no sign of wave propagation at the metal surface, as shown in Fig. 4(b). Another proof of the cavity mode is that it does not scale with the period, as described in Fig. 3(a)-(f). Unlike cavity mode, the SPP mode profile has maximum field intensity at the metal-dielectric interface (in Fig. 4(c)) and wave propagating along the metal film is rather obvious (in Fig. 4(d)). Furthermore, the resonance wavelength scaling with the period, described in Fig. 3(d)-(f), also indicates the existence of the SPP mode.

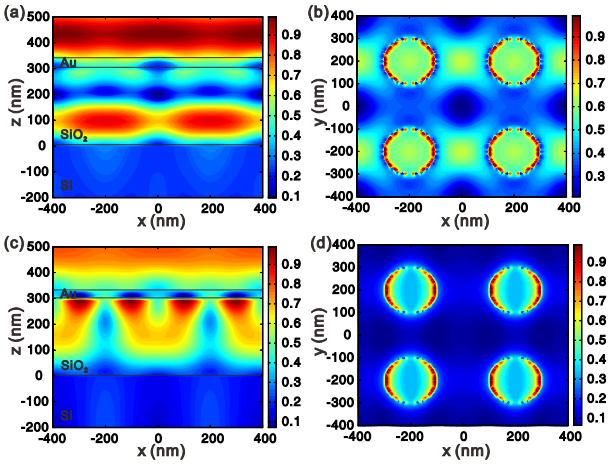

Figure 4: (a) Cross-sectional and (b) top views of the cavity mode at 523nm. (c) Cross-sectional and (d) top views of the SPP mode at 731nm.

Next, we compare the simulation results under normal incident with the measured ones, just as plotted in Figure 5. For all samples with different periods, the simulated results agree with the measured ones very well and two kinds of modes are all clearly identified in the reflection dips. In experiment, the reflection dips for the SPP mode is shallower and broader than the calculated ones. This can be attributed to the disorder effect in sample fabrications. Disorder of the hole period and radius will scatter and partially block the propagating SPPs, thus it will decrease the resonance depth and broaden the dip. We further plot the discrepancy between simulation and experiment for the cavity mode and the SPP mode (defined as Δ) as a function of the resonant wavelength in Fig. 5(g). Just as we can see, there exists only small disagreement between the theoretical and the experimental results.

3. Tuning the dispersion relation

One of great advantages of graphene over other materials is that its property can be easily tuned either by the electron doping or the nonlinear effect. Here we theoretically investigate that the dispersion relation of the waveguide can be tuned via graphene contact.

3.1. Electron doping effect

The interaction between light and graphene can be described by the optical conductivity which can be calculated by summing the interband and intraband conductivity. More explicitly [29,30],

$$\sigma_{\text{inter}}(\omega) = i\frac{e^2\omega}{\pi}\int_{\Delta}^{\infty} d\varepsilon \frac{1+\Delta^2/\omega^2}{(2\omega)^2-(\hbar\omega+i\Gamma)^2}\times\left[f(\varepsilon-E_F)-f(-\varepsilon-E_F)\right] \quad (1)$$

$$\sigma_{\text{intra}} = i\frac{e^2/\pi\hbar^2}{\omega+i/\tau}\int_{\Delta}^{\infty} d\varepsilon(1+\Delta^2/\varepsilon^2)\left[f(\varepsilon-E_F)+f(\varepsilon+E_F)\right] \quad (2)$$

where $f(\varepsilon-E_F)$ is the Fermi distribution function with Fermi energy E_F, Γ describes the broadening of the interband transitions, and τ is the momentum relaxation time due to intraband carrier scattering. The bandgap 2Δ, due to any interaction that breaks the symmetry between A and B atoms in the unit cell of graphene, is set to be zero in this paper. Switching on and off the interband transition by tuning the Fermi level provides the way to tune the optical conductivity thus the optical response of the graphene.

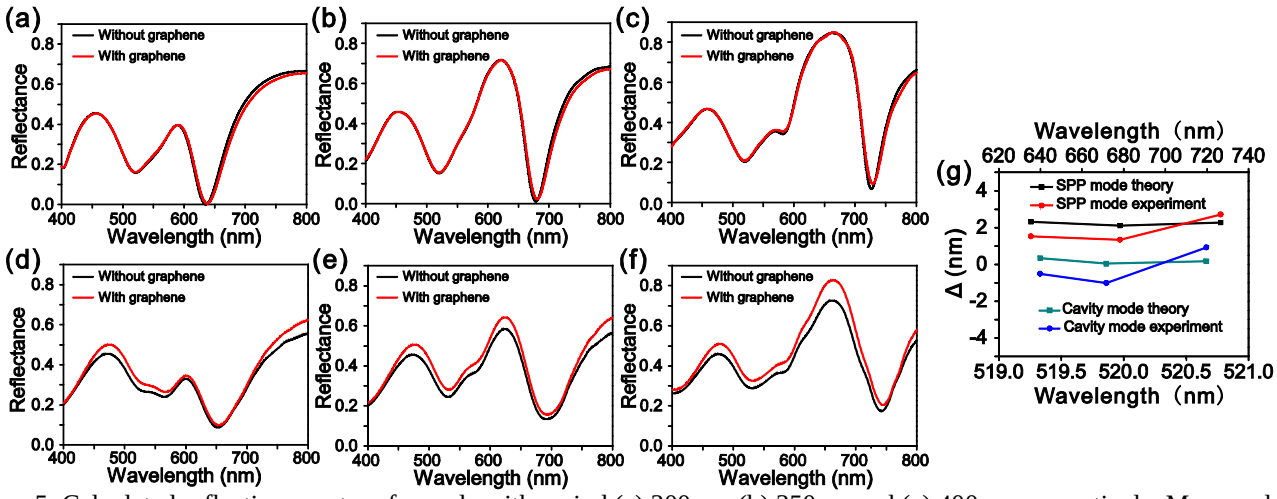

Figure 5: Calculated reflection spectra of sample with period (a) 300nm, (b) 350nm and (c) 400nm, respectively. Measured reflection spectra of sample with period (d) 300nm, (e) 350nm and (f) 400nm, respectively. (g) Resonances shift of the cavity mode and SPP mode as a function of resonant wavelength.

Figure 6 shows the reflection spectra for different doping levels of graphene and the inset plots the corresponding total optical conductivities. Just as we can see, the conductivity decreases drastically when switch off the interband transition, so the corresponding reflection dip shifts. Thus the dispersion relation of such waveguide can be tuned by doping the graphene, for example, via backgate voltage.

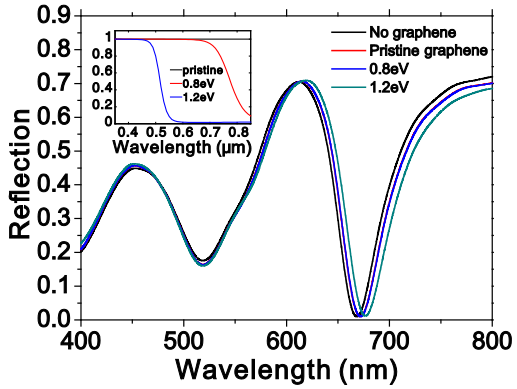

Figure 6: Reflection spectra for different doping levels of graphene. The Fermi level is set at 0eV, 0.8eV and 1.2eV. Inset: Real part of the graphene conductivity, in the unit of $\pi e^2/2h$.

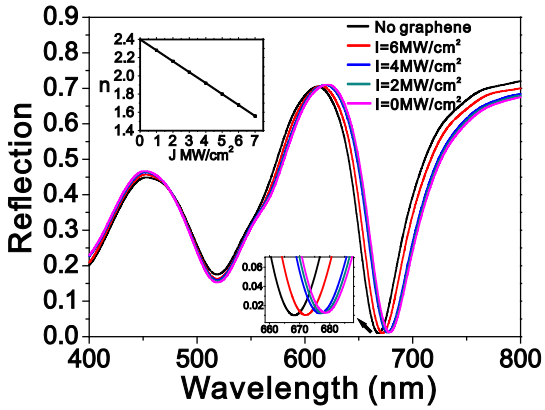

Figure 7: Reflection spectra under different pump intensities. Upper inset: The refractive index of graphene as function of pump intensity. Lower inset: enlarged figure near the SPP modes.

3.2. Nonlinear effect

It has been discovered that graphene has a giant nonlinear refractive index of $n_2 = -1.2\times10^{-7}cm^2/W$ [24] and ultrafast response of the order of 1ps due to fast carrier relaxation dynamics. Therefore, graphene is an excellent nonlinear optical material with an ultrafast response and high third-order optical nonlinearity. In this way, we can tune the dispersion relation of our waveguide by introducing intense optical pump. In simulation, we set the effective linear refractive index n_0 of graphene to be 2.4 as previously used by Yu Zhu *et.al* [25]. The effective refractive index n of graphene changes as a function of pump intensity I as $n=n_0+n_2I$, where n_0 and n_2 are effective linear and nonlinear refractive index of graphene, respectively. Upper inset of Fig. 7 shows the refractive index of graphene as a function of pump intensity, which decreases linearly as the pump intensity increases due to the negative nonlinear refractive index. Thus the resonance dips blue shift as the pump intensity increases, as shown in the lower inset of Fig. 7. Therefore the dispersion relation of the plasmonic waveguide can be tuned based on the nonlinear effect of graphene.

4. Conclusions

In this paper, a plasmonic waveguide compatible with silicon technology has been studied and the dispersion relation of the waveguide has been tuned via graphene contact. We have proposed a model of graphene in the visible range for FDTD calculation and the results coincide with the experiment. Two kinds of resonance, *i.e.* cavity mode and SPP mode, have been clearly identified and the effect of graphene has been discussed. Furthermore, by doping the graphene or using the nonlinear effect, we can theoretically tune the dispersion relation of the waveguide. Our work presents a useful effort in exploring hybrid Si/Graphene plasmonic waveguides and provides potential applications for tunable opto-devices.

Acknowledgements

This work was supported by the MOST of China (Grants No. 2012CB921502 and 2010CB630705) and the NSFC (Grants No. 11034005 and 91321312).

References

[1] W. L. Barnes, A. Dereux, T. W. Ebbesen, Surface plasmon subwavelength optics, *Nature* 424 824-830, 2003.

[2] D. K. Gramotnev, S. I. Bozhevolnyi, Plasmonics beyond the diffraction limit, *Nat. Photon.* 4:83-91, 2010.

[3] T. W. Ebbesen, C. Genet, S. I. Bozhevolnyi, Surface-plasmon circuitry, *Physics Today* 61:44-50, 2008.

[4] V. J. Sorger, R. F. Oulton, Ren-Min Ma, X. Zhang, Toward integrated plasmonic circuits, *MSR Bulletin* 37:728-738, 2012.

[5] E. Kretschmann, H. Raether, Radiative decay of nonradiative surface plasmons excited by light, *Z. Naturforsch.* A 23, 2135–2136, 1968.

[6] A. Otto, Exitation of nonradiative surface plasma waves in silver by the method of frustrated total reflection, *Z. Phys.* 216:398, 1968.

[7] B. Hecht, H. Bielefeldt, L. Novotny, Y. Inouye, D. W. Pohl, Local excitation, scattering, and interference of surface plasmons, *Phys. Rev. Lett.* 77: 1889-1892, 1996.

[8] R. H. Ritchie, E. T. Arakawa, J. J. Cowan, R. N. Hamm, *Phys. Rev. Lett.* 21: 1530-1533, 1968.

[9] Z. H. Tang, R. W. Peng, Z. Wang, X. Wu, Y. J. Bao, Q. J. Wang, Z. J. Zhang, W. H. Sun, and Mu Wang, Coupling of surface plasmons in nanostructured

metal/dielectric multilayers with subwavelength hole arrays, *Phys. Rev. B* 76: 195405, 2007.

[10] Feng Gao, De Li, Ru-Wen Peng, Qing Hu, Kuang Wei, Q. J. Wang, Y. Y. Zhu, and Mu Wang, Tunable interference of light behind subwavelength apertures, *Appl. Phys. Lett.* 95: 011104, 2009.

[11] A. N. Grigorenko, M. Polini, K. S. Novoselov, Graphene plasmonics, *Nat. Photon.* 6: 749-758, 2012.

[12] Q. L. Bao, K. P. Loh, Graphene photonics, plasmonics, and broadband optoelectronic devices, *ACS Nano* 6: 3677– 3694, 2012.

[13] F. H. L. Koppens, D. E. Chang, F. J. García de Abajo, Graphene plasmonics: a platform for strong light-matter interactions, *Nano Lett.* 11: 3370–3377, 2011.

[14] Q. Z. Hao, B. Wang, J. A. Bossard, B. Kiraly, Y. Zeng, I-Kao Chiang, L. J, Douglas, H. Werner, T. J. Huang, Surface-enhanced raman scattering study on graphene-coated metallic nanostructure substrates, *J. Phys. Chem. C* 116: 7249 – 7254, 2012.

[15] X. L. Zhu, L. Shi, M. S. Schmidt, A. Boisen, O. Hansen, J. Zi, Sanshui Xiao, N. Asger Mortensen, Enhanced light-matter interactions in graphene-covered gold nanovoid arrays, *Nano Lett.* 13: 4690− 4696, 2013.

[16] O. Salihoglu, S. Balci, C. Kocabas, Plasmon-polaritons on graphene-metal surface and their use in biosensors, *Appl. Phys. Lett.* 100: 213110, 2012.

[17] Y. Liu , X. Dong and P. Chen, Biological and chemical sensors based on graphene materials, *Chem. Soc. Rev.* 41: 2283-2307, 2012.

[18] V. G. Kravets, F. Schedin, R. Jalil, L. Britnell, R. V. Gorbachev, D. Ansell, B. Thackray, K. S. Novoselov, A. K. Geim, A. V. Kabashin, A. N. Grigorenko, Singular phase nano-optics in plasmonic metamaterials for label-free single-molecule detection, *Nat. Matter.* 12: 304-309, 2013.

[19] N. Reckinger, A. Vlad, Sorin Melinte, Jean-François, Colomer, M. Sarrazin, Graphene-coated holey metal films: Tunable molecular sensing by surface plasmon resonance, *Appl. Phys. Lett.* 102: 211108, 2013.

[20] L. Rast, T. J. Sullivan, V. K. Tewary, Stratified graphene/noble metal systems for low-loss plasmonics applications, *Phys. Rev. B* 87: 045428, 2013.

[21] A. Varykhalov, M. R. Scholz,Timur, K. Kim, O. Rader, Effect of noble-metal contacts on doping and band gap of graphene, *Phys. Rev. B* 82: 121101, 2010.

[22] R. Wu,Y. Zhang, S. Yan, F. Bian,W. Wang, X. Bai, X. Lu, J. Zhao, E. Wang, Purely coherent nonlinear optical response in solution dispersions of graphene sheets, *Nano Lett.* 11: 5159−5164, 2011.

[23] A. E. Nikolaenko, N. Papasimakis, E. Atmatzakis, Zhiqiang Luo, Z. X. Shen, F. D. Angelis, S. A. Boden, E. D. Fabrizio, N. I. Zheludev, Nonlinear graphene metamaterial, *Appl. Phys. Lett.* 100: 181109, 2012.

[24] H. Zhang, S. Virally, Q. Bao, L. K. Ping, S. Massar, N. Godbout, P. Kockaert, Z-scan measurement of the nonlinear refractive index of graphene, *Opt. Lett.* 37: 1856-1858, 2012.

[25] Y. Zhu, X. Hu, H. Yang, Q. Gong, On-chip plasmon-induced transparency based on plasmonic coupled nanocavities, *Sci, Rep.* 4: 3752, 2014.

[26] X. Li,Y. Zhu, W. Cai, M. Borysiak, B. Han, D. Chen, R. D. Piner, L. Colombo, R. S. Ruoff, Transfer of large-area graphene films for high-performance transparent conductive electrodes, *Nano. Lett.* 9: 4359-4363, 2009.

[27] A. C. Ferrari, J. C. Meyer, V. Scardaci, C. Casiraghi, M. Lazzeri, F. Mauri, S. Piscanec, D. Jiang, K. S. Novoselov, S. Roth, A. K. Geim, Raman spectrum of graphene and graphene layers, *Phys. Rev. Lett.* 97: 187401, 2006.

[28] A. C. Ferrari, D. M. Basko, Raman spectroscopy as a versatile tool for studying the properties of graphene, *Nat. Matter*. 8: 235-246, 2013.

[29] K. F. Mak, M. Y. Sfeir, Yang Wu, C. H. Lui, J.A. Misewich, Tony F. Heinz, Measurement of the Optical Conductivity of Graphene, *Phys. Rev. Lett.* 101: 196405, 2008.

[30] J. M. Dawlaty, S. Shivaraman, J. Strait, P. George, M. Chandrashekhar, F. Rana, M. G. Spencer, D. Veksler, Y. Chen, Measurement of the optical absorption spectra of epitaxial graphene from terahertz to visible, *Appl. Phys. Lett.* 93: 131905, 2008.

Retroreflection of light from nanoporous InP: Correlation with high absorption

S.Ya. Prislopski[1], I. M. Tiginyanu[2,3], L. Ghimpu[2], E. Monaico[3], L. Sirbu[2], and S.V. Gaponenko[1*]

[1]B. I. Stepanov Institute of Physics, National Academy of Sciences of Belarus, Minsk 220072, Belarus
[2]Institute of Electronic Engineering and Nanotechnologies "D.Ghitu", Academy of Sciences of Moldova, Chisinau MD-2028, Moldova
[3]National Centre for Materials Study and Testing, Technical University of Moldova, Chisinau MD-2004, Moldova
[*] corresponding author. Tel: (375 17) 284 04 48, e-mail: s.gaponenko@ifanbel.bas-net.by

Abstract

Pronounced retroreflection behavior is reported for a fishnet nanoporous strongly absorbing semiconductor material. Retroreflection appears along with diffusive specular reflection for all angles of incidence for light wavelength corresponding to interband optical transitions, where absorption coefficient is of the order of 10^5 cm^{-1} (green and red light). Retroreflection is apparent by the naked eye with day light illumination and exhibits no selectivity with respect to wavelength and polarization of incident light featuring minor depolarization of retroreflected light. Retroreflection vanishes for wavelength corresponding to optical transparency range where photon energy is lower than the InP bandgap (1.064 μm). The phenomenon can be classified neither as coherent backscattering nor as Anderson localization of light. The primary model includes light scattering from strongly absorptive and refractive super-wavelength clusters existing within the porous fishnet structure. We found that retroreflection vanishes for wavelength where absorption becomes negligible.

1. Introduction

Scattering of the light in complex nanostructured media is the subject of extensive research. Non-trivial phenomena in this field include coherent backscattering [1,2], Anderson localization of light [3,4,5,6], the photonic glass concept [7], propagation of waves in quasiperiodic [8] and fractal [9] structures, anisotropic scattering in aligned nanoporous dielectrics [10], and Letokhov's (random) lasers [11]. But all of the above phenomena necessarily imply nonabsorptive material forming desirable nanostructured media since multiple scattering and interference of scattered light waves are of principal importance. Recently we have observed yet another unusual feature in nanoporous semiconductor material, InP, namely pronounced retroreflection for light whose wavelength corresponds to interband optical transitions in bulk InP material [12]. In this experiment, green laser light was used (531 nm, 2.33 eV) to be compared with the bandgap energy E_g = 1.344 eV or bandgap wavelength 922 nm [13].

In this paper, we continue investigation of the retroreflection and scattering properties of fishnet nanoporous semiconductor InP not only in the spectral range of interband optical transitions where multiple scattering is inhibited by strong absorption, but also in the infrared spectral region where this material is transparent.

2. Sample preparation

Nanoporous InP samples were fabricated from (100)- and (111)-oriented n-type InP:Si wafers with variable free carrier concentration from 1.9×10^{16} cm^{-3} to 2×10^{19} cm^{-3}. The etching was carried out in an electrochemical double cell (Fig. 1) using a configuration of four platinum electrodes: reference electrode in the electrolyte (REE), reference electrode on the sample (RES), counter electrode (CE), and working electrode (WE), all of them connected to a Keithley 236 source measure unit. A 5% aqueous solution of HCl at different galvanostatic conditions was used as the electrolyte. Its temperature was kept constant at T = 23°C by means of a Julabo F25 thermostat on one side of the double cell (where pores were expected to grow).

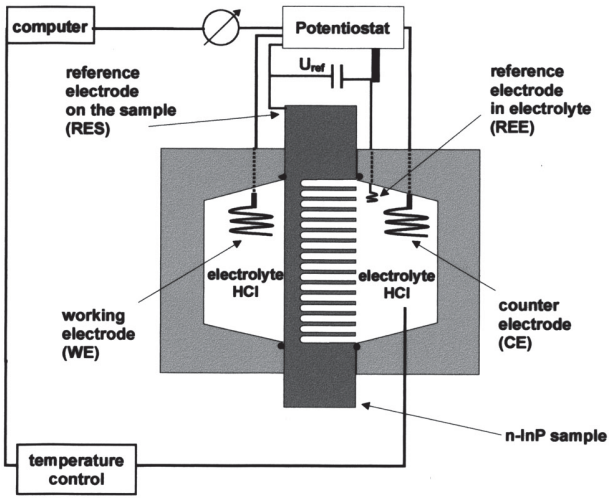

Figure 1: Electrochemical etching set-up.

The electrolyte was continuously pumped through both cells with peristaltic pumps. The area of the sample exposed to the electrolyte was 0.12 cm^2. The experiments were performed in the dark, and the holes necessary for the dissolution of the material were created by the breakdown of the depletion layer.

The morphology of the etched samples was examined using a VEGA TESCAN TS 5130MM scanning electron microscope (SEM) equipped with an Oxford Instruments INCA energy dispersive x-ray (EDX) system.

Scattering/reflectance indicatrices were measured in an experiment sketched in Fig. 2. The samples were illuminated by a beam from a cw Nd:LSB microchip solid state laser (LEMT, Belarus) with λ = 531 nm, from diode laser (BelOMA, Belarus) with λ = 654 nm and from Nd:YAG solid state laser (Solar LS, Belarus) with λ = 1064 nm. The beam was directed at incident angle α, and the spot size from the beam at the sample was approximately 2 mm. The scattered light was collected at varying angle β and guided to a spectrograph (Solar TII) followed by a detector (LN/CCD-1152-E 16-bit CCD array, Princeton Instruments).

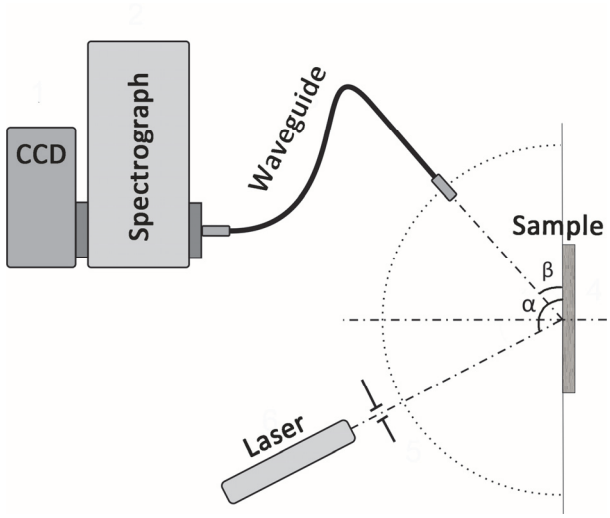

Figure 2. Experimental set-up

At a wavelength of 531 nm a real n and imaginary κ parts of the complex refraction index of InP are n = 3.8 and κ = 0.5 [13]. The latter corresponds to the absorption coefficient 1.3×10^5 cm^{-1}. At 654 nm wavelength n = 3.4, κ = 0.3 that corresponds to the absorption coefficient 0.6×10^5 cm^{-1} [13]. At 1064 nm wavelength the refractive index is 3.3 whereas the absorption coefficient can be treated as negligible [13].

3. Results and discussion

Pronounced retroreflection behavior was found for most of samples of nanoporous InP for laser wavelengths where absorption coefficient is very high because of interband optical transitions. Figs. 3–6 show the SEM micrographs for the four of the fabricated samples along with the scattering indicatrices. Remarkable is the systematic manifestation of retroreflection in scattering diagrams of every sample for the wavelengths of high (interband) optical absorption (531 and 654 nm). At the same time, retroreflective feature vanishes for 1064 nm wavelength where absorption is negligible. The diffuse reflection for 1064 nm shows angular dependence close to that typically observed in low-absorptive nanoporous materials (see, e.g. Ref. [12]). Notably, in a few cases (Figs. 3 and 4) mirror-like reflection develops. The latter is believed to arise from the length scale properties, namely, for longer wavelengths not only absorption becomes lower but also scattering cross-section goes down since a portion of scattering units becomes smaller than the wavelength**.**

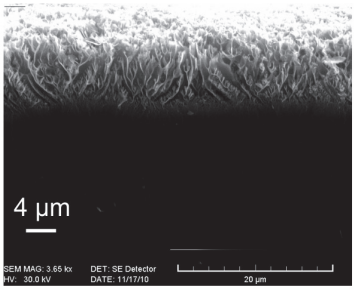

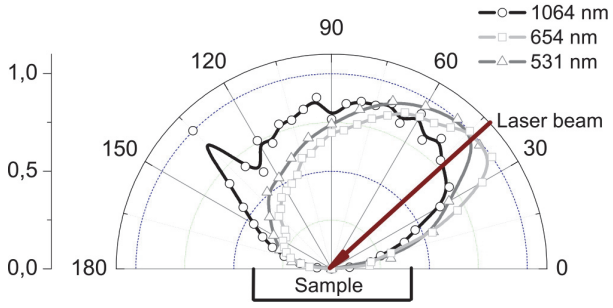

Figure 3: SEM image and scattering diagrams for the InP nanoporous sample #1 for the three laser wavelengths. The line with arrow represents the incident laser beam direction. Sample position is shown for clarity.

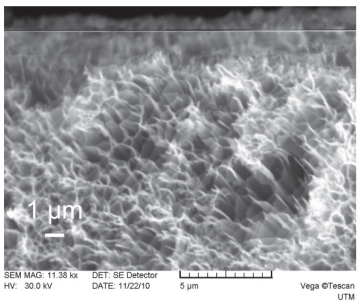

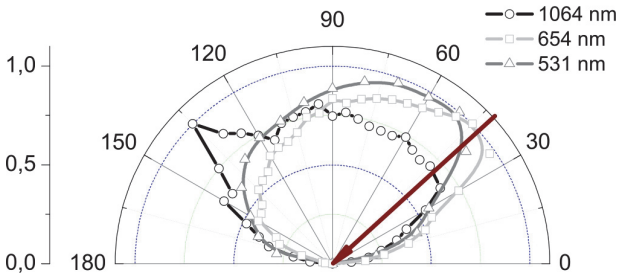

Figure 4. The same as in Fig. 3 for sample #2.

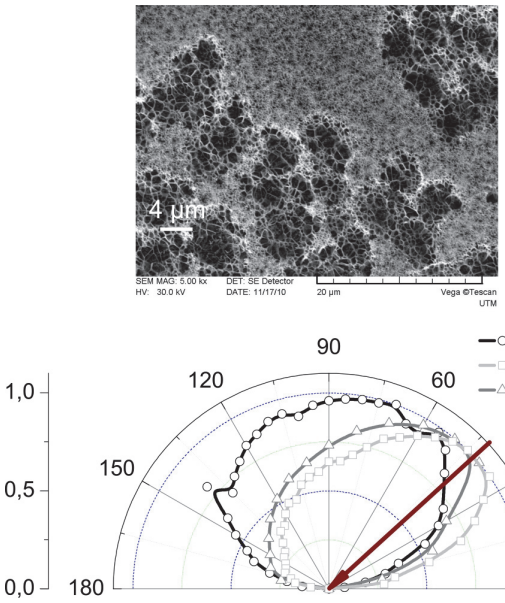

Figure 5. The same as in Fig. 3 for sample #3.

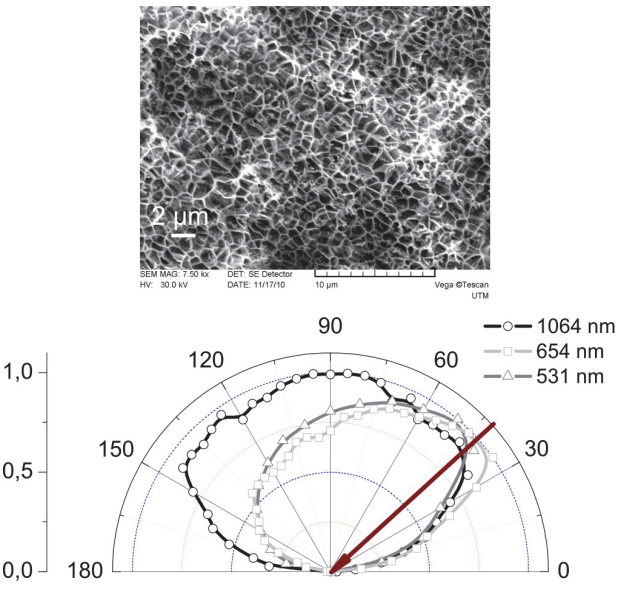

Figure 6. The same as in Fig. 3 for sample #4.

Therefore we believe that the previously reported anomalous retroreflection is inherent in a strongly absorbing nanoporous semiconductor material and vanishes for low-absorptive species. Retroreflection appears along with diffusive specular reflection for all angles of incidence. Retroreflection is apparent by the naked eye with day light illumination and exhibits no selectivity with respect to wavelength and polarization of incident light featuring minor depolarization of retroreflected light.

The observed retroreflection phenomenon can be classified neither as coherent backscattering nor as Anderson localization of light because high absorption excludes multiple scattering phenomena. The primary model [12] includes light scattering from strongly absorptive and refractive super-wavelength clusters existing within the porous fishnet structure**.** The typical diffusive reflection inherent in low-absorptive porous structures becomes inhibited owing to low mean free path resulting from high dissipative losses.

We consider that for further progress in understanding of the observed retroreflection phenomenon the time-resolved studies will be helpful as has been reported for many cases of complex light propagation in dense inhomogeneous medium. Time resolved studies will be the subject of the further research.

4. Conclusion

The retroreflection phenomenon for certain nanoporous semiconductor structures is reported and examined. The retroreflection is believed to arise from scattering of light under condition of the mean free path being defined mainly by dissipative losses. For spectral range corresponding to intense interband optical absorption the effect is pronounced in day light illumination. The effect was found to vanish for laser wavelength where optical absorption of InP can be neglected.

Acknowledgements

The work has been supported by the Belarus-Moldova Belarusian Republican Foundation for Fundamental Research (BRFFI) project and the Supreme Council for Research and Technological Development of the Academy of Sciences of Moldova. Helpful discussions with D. Wiersma are acknowledged.

References

[1] M. P. van Albada and A. Lagendijk, “Observation of weak localization of light in random media”. *Phys. Rev. Lett.,* vol. 55, no 8, pp. 2692—2694, June 1985.

[2] P. E. Wolf and G. Maret, “Weak localization and coherent backscattering of photons in disordered media”. *Phys. Rev. Lett.,* vol. 55, no 8, pp.2696—2698, June 1985.

[3] C. M. Aegerter, M. Storzer, S. Fiebig, W. Buhrer, and G. Maret, “Observation of Anderson localization of light in three dimensions”. *J. Opt. Soc. Am.,* vol. A 24, no 10, pp. A23—A27. October 2007.

[4] D. S. Wiersma, P. Bartolini, A. Lagendijk, and R. Righini, “Localization of light in a disordered medium”. *Nature,* vol. 390, no 7, pp. 671—675, July 1997.

[5] M. Segev, Y. Silberberg, D.N. Christodoulides. “Anderson localization of light.” *Nature Photonics,* vol. 7, no 5, pp. 197—204, March 2013.

[6] D. S. Wiersma. “Disordered photonics.” *Nature Photonics,* vol. 7, no 5, pp. 188—196, March 2013.

[7] P. D. Garcia, R. Sapienza, A. Blanco, and C. Lopez, “Photonic Glass: A Novel Random Material for Light”. *Adv. Mater.,* vol. 19, no 11, pp. 2597—2602, November 2007.

[8] E. Macia, “The role of aperiodic order in science and technology”, *Rep. Prog. Phys.,* vol. 69, no 2, pp. 397—455, February 2006.

[9] S. V. Zhukovsky, A. V. Lavrinenko, S. V. Gaponenko, "Spectral scalability as a result of geometrical self-similarity of fractal multilayers." *Europhys. Lett.* vol. 66, no 6, pp. 455—460. June 2004.
[10] A. Lutich, S. Gaponenko, N. Gaponenko, I. Molchan, V. Sokol, and V. Parkhutik, "Anisotropic light scattering in porous materials: A photon density of states effect." *Nano Letters*, vol. 4, no 9, pp.1755–1759, September 2004.
[11] D. S. Wiersma, "The smallest random laser". *Nature*, vol. 406, no 1, pp. 132–133, January 2000.
[12] S.Ya. Prislopski, E.K. Naumenko, I.M. Tiginyanu, L. Ghimpu, E. Monaico, L. Sirbu, and S.V. Gaponenko. "Anomalous retroreflection from strongly absorbing nanoporous semiconductors." *Optics Lett.,* vol. 36, no16, pp. 3227–3229, August 2011.
[13] O. Madelung, *Semiconductors: Data Handbook,* 3rd ed. Springer, 2004.

SERS scaling rules

Yoshiaki Nishijima[1,*], Yoshikazu Hashimoto[1], Lorenzo Rosa[2,3], Jacob B. Khurgin[4], Saulius Juodkazis[2,3]

[1]Department of Electrical and Computer Engineering, Graduate School of Engineering, Yokohama National University, 79-5 Tokiwadai, Hodogaya-ku, Yokohama 240-8501, Japan
[2]Centre for Micro-Photonics, Faculty of Science, Engineering and Technology, Swinburne University of Technology, Hawthorn, VIC 3122, Australia
[3]Melbourne Centre for Nanofabrication, the Australian National Fabrication Facility - ANFF, Wellington Rd. 151, Clayton, Vic 3168, Australia
[4]Department of Electrical and Computer Engineering, Johns Hopkins University, Baltimore, MD 21218, USA
*corresponding author, E-mail: nishijima@ynu.ac.jp

Abstract

We demonstrate a quantitative match between SERS intensity and the optical extinction experimentally and numerically. An analytical model is well matching SERS data not only from a simple square lattice array of nanostructures, but also for a rectangular lattice. It is shown how SERS selectivity of different Raman modes is controlled by the optical extinction at the excitation and scattering wavelengths. Both square and rectangular lattices have similar behavior, however, the rectangular pattern has a much higher selectivity of the SERS modes.

1. Introduction

Surface enhanced Raman Scattering (SERS) is a promising technique for detection of a small number of molecules on the surface of noble metals. Recently, with advances in nanotechnology and nanoengineering combining the top-down and bottom-up methods, a better control over surface properties and reproducibility are achieved and peculiarities of SERS mechanisms are better understood [1,2]. It is usually assumed that SERS intensity scales with the optical extinction. SERS has complex spectral properties due to multi modal scattering depending of a local atomic configuration on the surface. It is difficult to identify, even qualitatively, the Raman modes especially in multi-analyte systems. Recently, the scaling of SERS intensity was revealed in complex randomized periodic arrays of nanoparticles [3,4] and square lattice periodic patterns [2] with the radiative and nonradiative loss mechanisms playing an important part.

Here, we demonstrate the relationship between SERS intensity and optical extinction spectrum, also, a selectivity enhancement is revealed in the case of rectangular lattices of nano-disk particles. The revealed scaling can be used to maximize SERS in practical applications.

2. Samples, measurements, modeling

Samples were fabricated via standard procedures of electron beam lithography (EBL) and lift-off [2–5]. Two types of periodic patterns were prepared: (i) a square lattice and (ii) rectangular lattice arrays of nano-disks of Au on glass. Schematics is shown in Fig. 1. For the square lattice structure, the diameter, d, of the disks varied from 140 to 300 nm in steps of 10 nm, and the lattice period was correspondingly increasing by 10 nm for the each step varying from Λ = 450 to 610 nm. The thickness of the Au disks was 40 nm. In such design, the distance between neighboring disks was constant in all the patterns. For the rectangular lattice, which has the two different larger and smaller periods Λ_{L} and Λ_{S}, respectively, the period Λ_{S} was fixed to 300 nm while the larger Λ_{L} was varied from 500 to 680 nm in 20 nm steps. The disk diameter was fixed to 180 nm, thickness of disks was 50 nm.

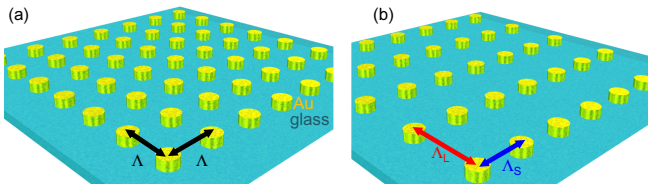

Figure 1: Schematic illustration of a square (a) and rectangular lattice (b) nano-disc array structures.

As SERS probe, the laser dye IR-26 (Exciton. Inc.) was used. Samples with gold nano-disks were immersed into a dye solution in dichloromethane 10^{-4} M for 10 hours. The extinction spectra were measured by microscopic spectroscopy techniques with an inverse microscope IX-71 (Olympus), with a 40$^{\times}$objective lens of numerical aperture $NA = 0.75$. SERS was measured with a dedicated Raman microscope inVIA (Renishaw plc.) at the excitation wavelength λ = 785 nm of a semiconductor laser with 20$^{\times}$ objective lens. Focusing was into a linear spot of 100×5 μm^2 cross-section on the sample surface. A single exposure for 10 s was required for every Raman spectra collection.

Numerical modeling of extinction spectra were carried out by 3D finite difference time domain (FDTD) simula-

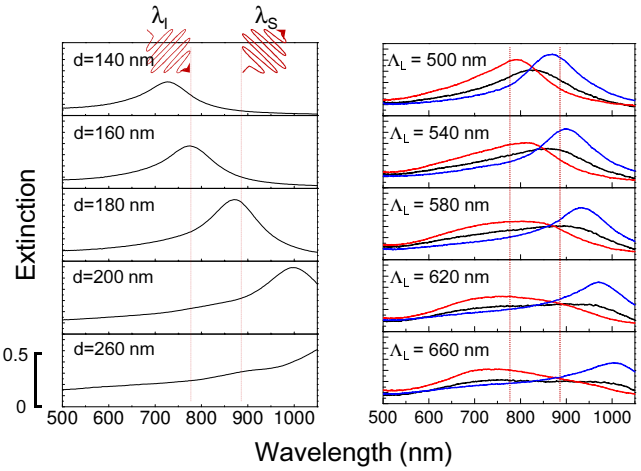

Figure 2: Typical extinction spectra of square lattice(left) and rectangular lattice (right) structures. The wavelength of excitation and Raman scattering are $\lambda_{l,S}$, respectively (λ_S corresponds to 1558 cm^{-1} mode). Polarizations along shorter, longer, and non-polarized light are shown for the rectangular lattice (see, conventions in Fig. 1). For rectangular pattern: $d = 180$ nm, $\Lambda_S = 300$ nm.

tions using Lumerical package.

3. Results and discussion

Figure 2 shows typical extinction spectra of a square and rectangular lattice arrays of nano-disks with marked 785 nm excitation and 894 nm (1558 cm^{-1}) SERS wavelengths. SERS spectrum is shown in Fig. 3. In case of square lattice, the plasmon resonance spectral shape behave as a single Lorentzian dipole resonance with inter-band transition absorption only at shorter than 500 nm. When diameter of disk was increased around 200 nm, a quadrupole resonance mode has appears around 800 nm as the shoulder of a Lorentzian dipole mode. These modes are not dependent on the linear polarization of the extinction light. However, in the case of rectangular arrays, a strong linear polarization dependence has been appeared. Linear polarization along the longer period - the Λ_L mode - appeared on the shorter wavelength wing and the Λ_S mode at the longer wavelengths. Detailed explanation of this polarization dependence was presented elsewhere [6] and in caused by an coupling of the modes. Due to this polarization dependency, the rectangular lattice patterns gives a rather flat extinction spectral profile as compared with a square lattice arrays.

Figure 3 shows a typical SERS spectrum of the IR-26 dye adsorbed on the Au nanodisks. We focused on the 1558 cm^{-1} Raman mode as the probe peak and the 685 cm^{-1} mode was used as a reference for evaluating the SERS selectivity (this reference peak is close to the laser excitation wavelength).

Figure 4 shows the normalized SERS intensity by the surface area. SERS intensity has not a simple linear scaling with extinction as revealed in this presentation where SERS intensity is plotted against the product of excitation at the excitation Ext_l and Raman scattering Ext_s wavelengths. For the qualitative expression of SERS intensity as the function of the extinctions the following scaling applies [2]:

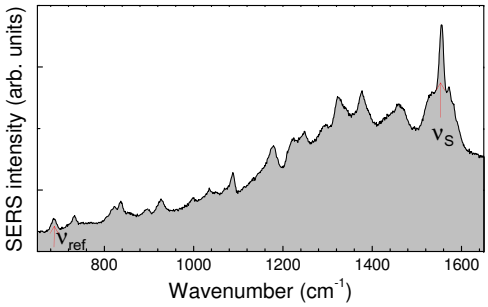

Figure 3: The typical SERS spectra obtained with experiments and DFT calculations. The Raman mode frequency is ν_S and the reference mode ν_{ref} is chosen close to laser excitation for selectivity calculations, see text for details.

$$\frac{SERS}{Ext_l \times Ext_s} \sim \frac{f_{dye}(d)}{\gamma(\nu_l, d)\gamma(\nu_s, d)}, \qquad (1)$$

where $\gamma = \gamma_{rad} + \gamma_{nr}$ represents the decay rate including the radiative and non-radiative components, f_{dye} is the integration over the volume with dye molecules. As is shown in Fig. 4, SERS intensity is maximal for the $d = 180$ nm disc diameters. For larger particles, size radiative decay rate γ_{rad} and the consequently γ is increasing. In the case of rectangular lattice and disk diameter $d = 180$ nm, a maximum of SERS intensity is achieved for the square lattice. However, additional enhancement of SERS is achievable by controlling the extinction at the excitation and Raman scattering wavelength in rectangular lattice as discussed next.

Figure 4 shows that the SERS scaling rule (eqn. 4) also fits experimental SERS data for rectangular lattice. Also, apparently SERS intensity can be further controlled via parameters of rectangular lattice. This is consistent with previously reported SERS increase in randomized periodic structures even though the extinction of plasmon resonance was reducing with disorder [3]. Disorder caused a strong EM field enhancement between clusters of several nanostructures and was the most strong then sizes of the nanoparticles was different (even the volume was the same). A nano-gap formation between two (or more) nanoparticles generate strong field enhancement and SERS despite smaller extinction. The same phenomenon is present but not discussed in relationship of SERS intensity and extinctions [7–9].

We can introduce SERS mode selectivity using SERS scaling [6]. The extinction at laser irradiation and Raman scattering wavelengths plays an important role for the overall SERS intensity (eqn. 1). SERS selectivity defined as the ratio of the two SERS peaks, here, we use the 685 cm^{-1} and 1558 cm^{-1} (marked in Fig. 3) vs the extinction ratio

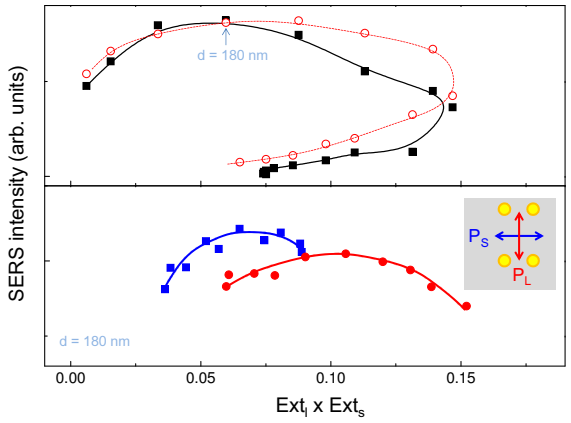

Figure 4: The SERS scaling trends upper is square lattice, experimental results (solid line) and analytical results by eqn. 1 (dashed line), bottom is rectangular lattice with Λ_L and Λ_S polarizations. The diameter (top) and period Λ_L (bottom) are increasing from left-to-right.

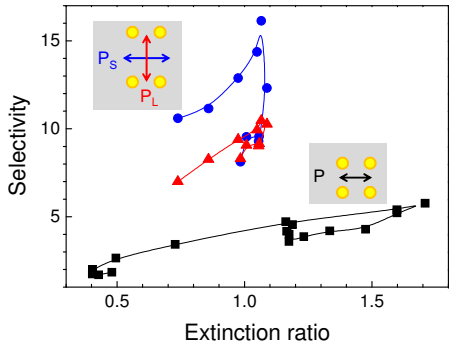

Figure 5: The selectivity of SERS for square lattices (black line), and rectangular lattices; corresponding polarizations P_L and P_S are shown in the insets.

at the corresponding wavelengths (frequencies) as shown in Fig. 5. The ratio of SERS intensities at the two modes reflects at two wavelengths makes the extinction at the excitation wavelengths canceled out. Figure 5 shows that selectivity is larger for the rectangular lattice as compared to square one.

There is an important difference between the square and rectangular lattices in selectivity. Namely, the maximum SERS selectivity of the rectangular lattice is obtained around the peak of SERS intensity, however in the case of square lattice, the maximum selectivity is for the largest values of $\mathrm{Ext_l} \times \mathrm{Ext_s}$. This is because, for the rectangular lattice, it is possible to fit both the irradiation and scattering wavelengths to the corresponding extinction spectral maximum. However, it is impossible for the square lattice, mainly, because narrower spectral profiles of extinction (a sharper resonance). The maximum selectivity for the 200 nm diameter disks in square lattice is achieved for a shoulder of plasmon peak and lower intensity (see Figs. 2, 2).

Next we test whether the experimentally observed

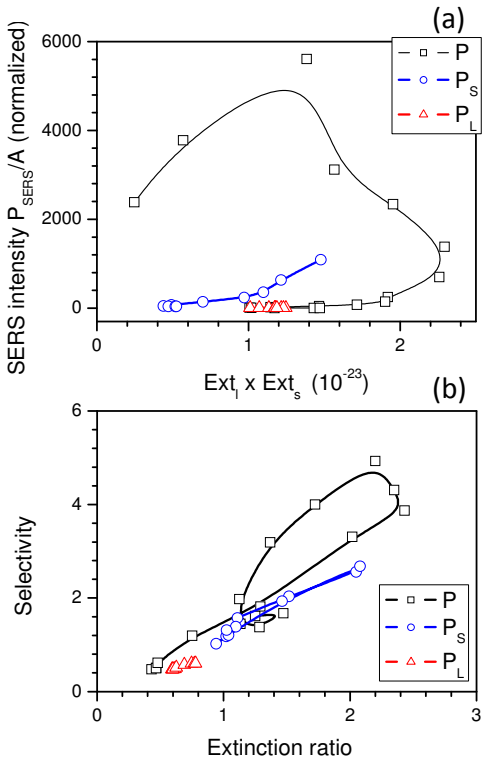

Figure 6: 3D-FDTD simulations of SERS scaling with extinction (a) and selectivity (b). To compare the results normalization to the Au particles surface area A was carried out.

(Fig. 4) and analytically predicted (eqn. 1) SERS intensity scaling with extinction for the square and rectangular lattices is corroborated by numerical FDTD simulations. This is an important quest since FDTD are known not to reproduce experimental results for the interfaces and surfaces due to inherent algorithm issue where the E- and H-fields are defined not at the same point [10]. For SERS, which is an interface phenomenon a correspondence between numerics and experiments has to be verified since an ideal shape nanoparticles are used for simulations.

Figure 6(a) shows 3D-FDTD simulation results. The square lattice simulations qualitatively well follows the experimental observation (Fig. 4). Selectivity of SERS modes is shown in Fig. 6(b) and differs from experimental data (Fig. 5). The main differences can be caused by unknown Raman scattering cross sections and their chemical and physical (EM) enhancements. FDTD simulations calculate an integrated light intensity outside and inside the particle. They corresponds to light field experienced by analyte molecules (outside the particle) and losses (inside particle) and are related to the radiative and non-radiative losses in SERS; they are accounted for analytically in eqn. 1.

4. Conclusion

We have demonstrated experimentally and numerically the relationship between SERS intensity and extinction for

square and rectangular arrays of nano-disks. A simple model of SERS and extinction scaling is capable to account qualitatively for the experimental results and fit the experimental data. SERS intensity increase via maximizing extinction at the excitation and Raman scattering wavelengths can be achieved using rectangular pattern. How the demonstrated SERS scaling with extinction could be used to increase sensitivity of SERS detection based on randomly nanotextured surfaces [11–13] needs further investigation.

Acknowledgement

YN gratefully thanks Prof. Toshihiko Baba, from Yokohama National University for fruitful discussions and granting access to fabrication and characterization facilities. This work was financially supported by Amada Foundation, The Hattori Hokokai Fundation, and JSPS Grants-in-Aid for Scientific Research. SJ is grateful for support via Australian Research Council DP130101205 project.

References

[1] S. Jayawardhana, L. Rosa, S. Juodkazis, and P. R. Stoddart, "Additional enhancement of electric field in surface-enhanced Raman scattering due to Fresnel mechanism," *Sci. Rep.*, vol. 3, p. 2335, 2013.

[2] Y. Nishijima, Y. Hashimoto, L. Rosa, J. B. Khurgin, and S. Juodkazis, "Scaling rules of SERS intensity," *Adv. Opt. Mat.*, vol. 2, p. DOI: 10.1002/adom.201300493, 2014 (online published).

[3] Y. Nishijima, J. B. Khurgin, L. Rosa, H. Fujiwara, and S. Juodkazis, "Randomization of gold nano-brick arrays: a tool for SERS enhancement," *Opt. Express*, vol. 21, no. 11, pp. 13 502–13 514, 2013.

[4] Y. Nishijima, L. Rosa, and S. Juodkazis, "Long-range interaction of localized surface plasmons in periodic and random patterns of Au nanoparticles," *Applied Physics A*, pp. 10.1007/s00 339–013–8057–9, 2013 (online published).

[5] Y. Nishijima and S. Akiyama, "Unusual optical properties of Au/Ag alloy nanostructures," *Opt. Maat. Express*, vol. 2, pp. 1226–1235, 2012.

[6] Y. Nishijima, J. B. Khurgin, L. Rosa, H. Fujiwara, and S. Juodkazis, "Tunable Raman selectivity via randomization of a rectangular pattern of nano-disks," *Photonics*, 2014 (submitted).

[7] D. K. Lim, K. S. Jeon, H. M. Kim, J. M. Nam, and Y. D. Suh, "Nanogap-engineerable Raman-active nanodumbbells for single-molecule detection," *Nat. Mat.*, vol. 9, pp. 60–67, 2010.

[8] T. Siegfried, Y. Ekinci, H. H. Solak, O. J. F. Martin, and H. Sigg, "Fabrication of sub-10 nm gap arrays over large areas for plasmonic sensors," *Appl. Phys. Lett.*, vol. 99, p. 263302, 2011.

[9] M. L. Pedano, S. Li, G. C. Schatz, and C. Mirkin, "Periodic electric field enhancement along gold rods with nanogaps," *Angew. Chem.*, vol. 122, pp. 82–86, 2010.

[10] G. Seniutinas, L. Rosa, G. Gervinskas, E. Brasselet, and S. Juodkazis, "3D nano-structures for laser nanomanipulation," *Beilstein J. Nanotechn.*, vol. 4, no. 1, pp. 534–541, 2013.

[11] G. Gervinskas, G. Seniutinas, J. S. Hartley, S. Kandasamy, P. R. Stoddart, N. F. Fahim, and S. Juodkazis, "Surface-enhanced Raman scattering sensing on black silicon," *Annalen der Physik*, vol. 525, no. 12, pp. 907–914, 2013.

[12] A. Chou, B. Radi, E. Jaatinen, S. Juodkazis, and P. Fredericks, "Trace vapour detection at room temperature using Raman spectroscopy," *Analyst*, p. doi:10.1039/C3AN01522J, 2014 (online published).

[13] R. Buividas, P. R. Stoddart, and S. Juodkazis, "Laser fabricated ripple substrates for surface-enahnced Raman scattering," *Annalen der Physik*, vol. 524, no. 11, pp. L5 – L10, 2012.

Engineering gold alloys for plasmonics

Yoshiaki Nishijima[1,*], Yoshikazu Hashimoto[1], Gediminas Seniutinas[2,3], Lorenzo Rosa[2,3], and Saulius Juodkazis[2,3]

[1]Department of Electrical and Computer Engineering, Graduate School of Engineering, Yokohama National University, 79-5 Tokiwadai, Hodogaya-ku, Yokohama 240-8501, Japan
[2]Centre for Micro-Photonics, Faculty of Engineering and Industrial Sciences, Swinburne University of Technology, Hawthorn, VIC 3122, Australia
[3]The Australian National Fabrication Facility -ANFF, Victoria node, Faculty of Engineering and Industrial Sciences, Swinburne University of Technology, Hawthorn, VIC, 3122, Australia
*corresponding author, E-mail: nishijima@ynu.ac.jp

Abstract

We demonstrate formation of metal alloys in Au-Ag, Au-Cu and Au-Pd systems and the experimental determination of their optical properties using optical transmission and reflection spectroscopy. The optical constants defines the plasmon resonance wavelength and EM field local intensity. However the optical constants behavior cannot be precisely modeled based on the data of pure metals due to unknown morphology and composition of the alloy. It has to be determined experimentally.

We demonstrate the surface enhanced Raman scattering (SERS) using alloy metals. Depending on the metal to which molecules are adsorbed, we observe enhancement of different Raman modes. It is mainly due to the chemical enhancement effect between metal and molecules.

1. Introduction

Alloying of different materials is an important tool that can be enriched the use of metals, ceramics and plastics in various applications and is a promising route to be wide explored in materials for plasmonics. Because plasmonic materials are limited to the metals family Au, Ag, Cu, Pd, Pt, Al, or highly doped semiconductors (i.e. Si, indium tin oxide (ITO), CuS) [1–3] alloy formation is very promising for engineering of required optical and chemical response. Recently we have developed an alloy for plasmonics from co-evaporation Au and Ag [4]. We showed the importance of the experimental determination of the optical constants of alloyed metals, because the permittivity has a certainly different value to the average of that of pure metals. Extending knowledge of alloying to the other optically and chemically active materials such as Au-Cu and Au-Pd systems is interesting for plasmon applications.

In this study, we directly measure optical properties of Au-Ag, Au-Cu, Au-Pd system for the plasmon applications. Also, we demonstrate that alloy is SERS active for the Au-Ag system, which is one of the most promising applications of the plasmonics. Typically, the SERS enhancement of Raman bands is due to the electromagnetic (EM) contribution and due to a chemical enhancement (CE), which is due to the resonance-like behavior of chemical bond formation. Recently EM mechanism is well understood on well-defined structures prepared by top-down nanotechnology approach. Usually, the EM factor is assumed scaling with optical extinction. We recently demonstrated an unusual SERS enhancement scaling with extinction which has competing contributions due to radiative and non-radiative losses which are nano-particle size and shape dependent [5]. However in case of CE, detailed mechanism is still under discussion. The SERS active molecule can adsorbed (or absorbed) on the metal surface through the coordination bond formation.

This bond formation can be though the origin of the chemical effect. The reports concerning the chemical effect are limited due to limitation of different materials. Alloy metals can solve this limitation and determine differences in EM and CE enhancements in SERS.

2. Experimental

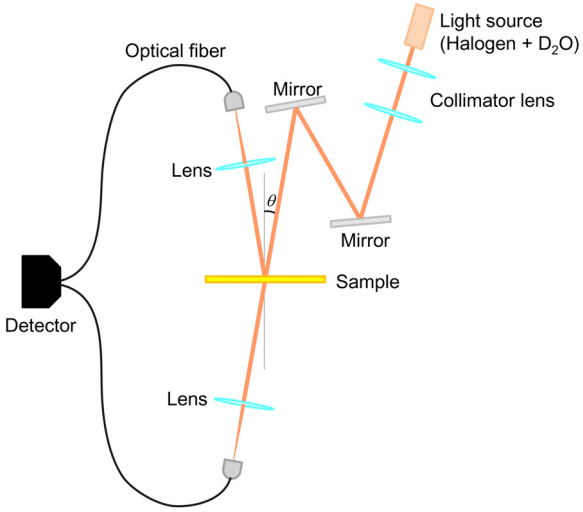

Figure 1: Schematic illustration for optical setup of refractive index determinations.

Optical constants of alloy materials were determined by the transmission and reflection spectroscopic measurements. Schematic illustration of the used optical set up is shown in Fig. 1. The light source from the optical-fiber-coupled hydrogen with D_2 IR-filter lamp (Hamamatsu Photonics Co. Ltd.) irradiated samples after beam collimation and steering setup comprised of lens and mirrors. Samples were tilted $\theta = 5°$ from normal incidence. The transmission and reflection was collected through the convex lens to the optical fiber and delivered onto spectrometer (Hamamatsu Photonics Co. Ltd.). The transmission configuration without sample was used for the reference measurement of transmission. In measurements, the same optical fiber was used for the transmission and reflection. Obtained transmission and reflection spectra were analyzed by an ellipsometry software (FE data analysis, Otsuka electronics Co. Ltd.).

Metal films were deposited on the glass substrate by thermal evaporation (Au, Cu, Ag) and magnetron radio frequency (RF) sputtering for Au and Pd. A 2-nm-thick adhesion layer of Cr or Ti was used. Samples of Au nanostructures on cover glass were fabricated by electron beam lithography (EBL) and standard lift-off procedures [4–8].

For SERS measurements, a 2,2'-bipyridine was used as analyte. Raman measurements were carried out with a Raman-dedicated inVIA (Renishaw) microscope. Samples were immersed into a methanol 10^{-4} M solution of the bipyridine and incubated for 10 hours [5–8]. Pyridine type molecules can be attached to the surface of metal via coordination bond formation. Comparing to the light metals such as aluminum, zinc, magnesium etc, the noble metals Au or Ag has weak bond strength/affinity to pyridine. Since pyridine groups have high activity in SERS, it is a good test material for the systematic study of the chemical enhancement effects.

3. Results and Discussions

3.1. Optical constants of Au-Ag and Au-Cu alloys

Recently, alloy nanoparticles of Au, Ag, and Cu are discussed as a new type of plasmonic metals for application to engineer color of materials. However, the importance of experimental determination of optical constants is not discussed [9–11] in spite of morphology differences depending on chemical, thermal of sputtering methods of alloying.

Typical transmission and refection spectra of Au films of different thickness are shown in Fig. 2. It reveals the plasmonic feature around 500 nm wavelength. For determination of optical constants precisely, it is required to measure 2 or 3 different thickness films from 20 to 50 nm range. The optical behavior of the metal, which is rich in free charge carriers (free electrons) is well described by the Drude model. However, the behavior of the bound electrons is following the Lorenz model. Therefore, for the determination of optical constants from UV to near-IR wavelength region, we used the Drude-Lorenz model, which is a linear combination of the Drude and Lorenz terms shown in eqn.

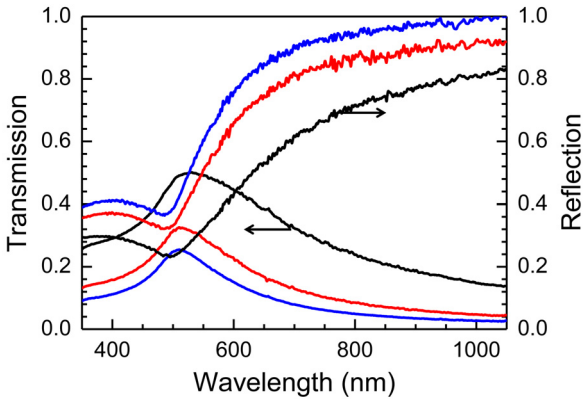

Figure 2: Optical transmission spectra of different three thickness (designed as 20, 30 40 nm) of Au films deposited on the glass substrate.

(1):

$$\varepsilon(\omega) = \varepsilon_1 + i\varepsilon_2 = n^2 - k^2 + 2ink$$
$$= \varepsilon_\infty - \frac{\omega_p^2}{\omega^2 + i\omega\Gamma_D} + \sum_j \frac{A_j \hbar\omega_{0,j}}{(\hbar\omega_{0,j})^2 - (\hbar\omega)^2 - i\Gamma_{L,j}\hbar\omega} \quad (1)$$

where, ε_∞ is the ε_1 value at high (infinite) angular frequency of light ω_∞, ω_p is the bulk plasma frequency defined as $(N_f e^2/\varepsilon_0 m_e V)^{1/2}$ with N_f being the number of free electrons in the volume V, e is the electron charge, ε_0 is dielectric constant of vacuum, m_e is the effective mass of electron. $\Gamma(= 1/\tau)$ is the damping constant with τ being the relaxation constant, (Γ_D is the damping constant of free electrons and Γ_L is that of the bound electrons as determined from the FWHM of the Lorentzian function of ε_2). The A_j is oscillator strength given as $A = e^2 N_b/(\varepsilon_0 m_e V)$, where N_b is the number of bound electrons and ω_0 is the resonance angular frequency.

In this study, we used $j = 15$ for the oscillation modes which reproduce well the transmission and reflection spectra. The n, k values were determined with fitting of experimental data with the model by the least-square method using three different thickness transmission and reflection spectra with the fitting parameters of the metal films thickness and optical constants $\varepsilon_\infty, \omega_p, \Gamma_D, A_j, \Gamma_{L,j}, \omega_0$. The fitting parameter F is used as $F = 1 - \sum |\Delta Y|^2/N$, where N is the number of spectral data points and ΔY represents the difference between experimental spectra and simulated spectra. All data are repeatedly and iteratively analyzed till F become over 0.8. For example, the gold film data shown in Fig. 2 converged to $F = 0.951$ for the thickness of films of 26.5, 40.2, 52.8 nm. The obtained n, k values are well matched to the chrestomatic reference of P. B. Johnson and R. B. Christy [12–14].

The Lorenz term, which is the sum of the Lorentzian oscillations in eqn. (1), is affected by the vibrational modes

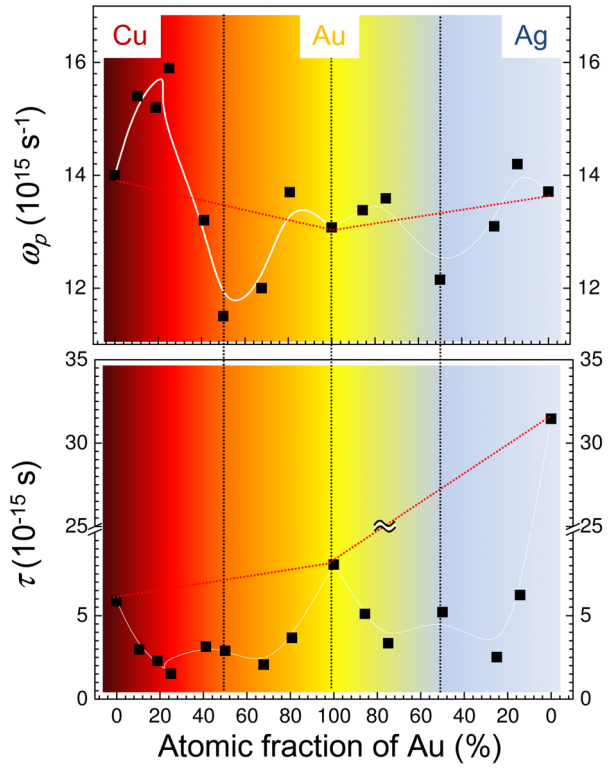

Figure 3: Experimentally determined ω_p and τ for Au-Cu and Au-Ag system.

of the bond electrons and the Drude term is due the free electrons motion. For the plasmon resonance, the Drude term is the most determining the optical properties of the surface plasmon polariton (SPP) and the localized surface plasmon resonance. It is defining the EM field enhancement as we reported previously [4].

Figure 3 shows the determined parameters of plasma frequency ω_p and relaxation time $\tau = 1/\Gamma$ from the Drude term. In both cases of ω_p and τ, the Au atomic fraction has a similar trend in the alloys. At the atomic fraction around 50% there was observed an unusual trend, i.e., a reduction of ω_p, which corresponds to the free electron density of the metal. It has a minimum at the 50% of atomic fraction. In Au, Ag and Cu, the 11th group elements originally have a similar density of free carrier. This can be seen in the pure metals ω_p: 13.1 (Au), 13.7 (Ag), 14.0 (Cu) in units of $\times 10^{-15}$ s^{-1}; all are similar to each other and the electron configuration of the outermost shell is similar.

The Au-Cu and Au-Ag system are well mixed with each other for alloy formation in any proportion and face centered cubic (fcc) lattice crystal is formed as confirmed by X-ray diffraction measurements [4]. However, the atomic radius (or a bond length) is slightly different to each other and electron negativity is also dependent on the metal. These small differences are a probable cause of a balance breaking between the free and bound electrons. The ω_p strongly affects the plasmon resonance wavelength of metal nanoparticles. Hence, the Au-Cu system is expected to have an interesting wavelength dependent spectral properties. On the other hand, the relaxation time which is corresponding to the EM field intensity of metal nanoparticles also shows a concentration dependence in the alloy (Fig. 3). In our series of alloying experiments, we observe compositions where the τ is larger than that of pure metal (even the Cu). Very specifically, at 50% of the atomic fraction, τ has a relatively larger value if compared with other composites. This composition is expected to have large EM field enhancement in the alloy system.

3.2. Optical properties of Au-Pd alloy

An attractive point to study alloy metals is to add an possibility to engineer dielectric function for plasmonic applications. Palladium has a plasmon resonance in UV and also an ability to absorb record larger volume fractions of hydrogen. Recently Pd and its alloy nanoparticles become prominent in hydrogen storage applications [16,17] including future solar hydrogen [18] where hydrogen is produced on the most efficient Pt electrode via the ionic cascading mechanism [19].

Our focus is on a possible use of Au-Pd alloy for the hydrogen gas sensor by exploring plasmonic resonances. The refractive index, n, and losses determined by imaginary part of the index k and their spectral properties have to be determined first. The Au-Pd system is known to form a fcc lattice crystal at the 50% intermixing at room conditions.

Figure 4 represents the real (n) and imaginary (k) parts of the refractive index in Au, Pd and Au-Pd systems. Comparing to the Au, both n, k values are larger than that of Au. From this result, it is clear that Pd has smaller ε_1 and larger of ε_2 in absolute terms. Also, the ω_p and τ are evaluated as 17 $\times 10^{15}$ s^{-1} and 1.1 $\times 10^{-15}$ s, respectively.

Therefore Pd has high propagation losses (roughly proportional to ε_2), and weak EM enhancement (relate to τ).

The interesting point of the Au-Pd alloy system is that these undesirable properties for the plasmonic applications are slightly improved by alloy formation. The ε_1 becomes larger and ε_2 is smaller as in pure Pd; the ω_p and τ are 21 $\times 10^{15}$ s^{-1} and 1.2 $\times 10^{-15}$ s, respectively. These slight improvements have not been seen in the Au-Ag or Au-Cu system (see. Fig. 3). The other compositions of Au-Pd alloy are now under preparation for determination of n, k.

3.3. SERS on the Au-Ag alloy

One of the most attractive application of alloy metals is expected in SERS applications where EM enhancement contributions are well understood [20]. The chemical mechanism can be invoked to increase further SERS sensitivity. The CE is thought as a bond formation between metal and analyte molecules with strong changes in electronic band structure which favors and/or enhances particular Raman vibrational modes.

As a model system of metal-molecule interaction, we use 2,2'-bipyridyl for SERS probe. Figure 5 shows the SERS spectra of 2,2'-bipyridyl adsorbed on the metal surface of a 200-nm-diameter disks of 40 nm height made out

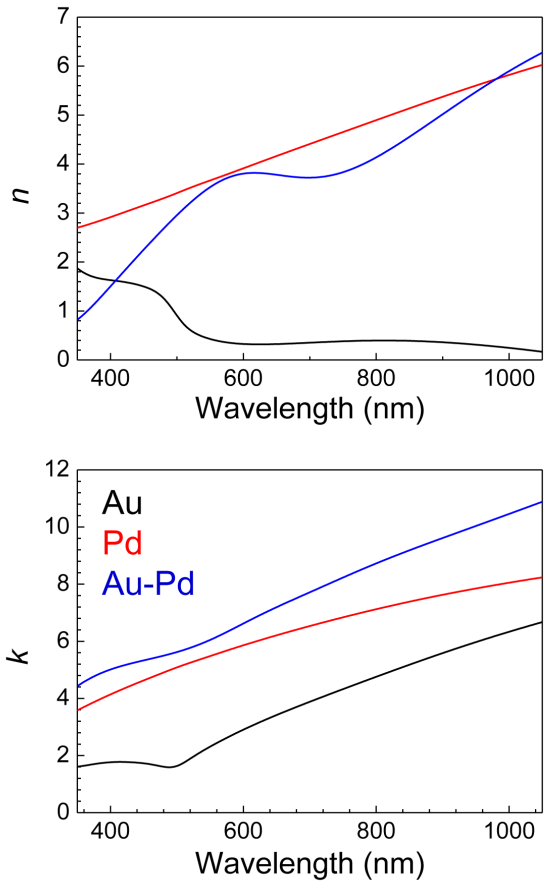

Figure 4: Optical constants of Au, Pd and Au-Pd alloy (50% of Au fraction).

of Au, Ag, and Au/Ag, respectively. Obviously, the vibrational modes in SERS spectra appear at different wavenumbers indicating differences in the analyte-surface interaction, presumably due to a chemical nature. Interestingly, some SERS bands observed on Au-Ag alloy are not present on pure Au and Ag. Namely, new peaks appeared around the 820, 1100, 1300, 1450 cm^{-1}.

For a complete characterization of these peaks, a quantum chemical calculations using the density functional theory (DFT) are required and should provide further insights into chemical bond formation between surface metal atoms and molecules at the atomic/molecular level. However even at present, it is apparent that these alloys could give rise a particular SERS sensitivity for complex molecular systems and could become a useful tool for the qualitative (and probably a quantitative) analysis of molecular detection.

4. Conclusion

In this study, we demonstrated that optical properties of alloying Ag, Cu, Pd with Au is possible by simple co-evaporation/sputtering. The Au-Ag and Au-Cu systems show a similar tendency to a change in Au atomic fraction for the ω_p and τ parameters. The balance between bound and free electrons affected by the crystal structures and electron negativity of the alloy.

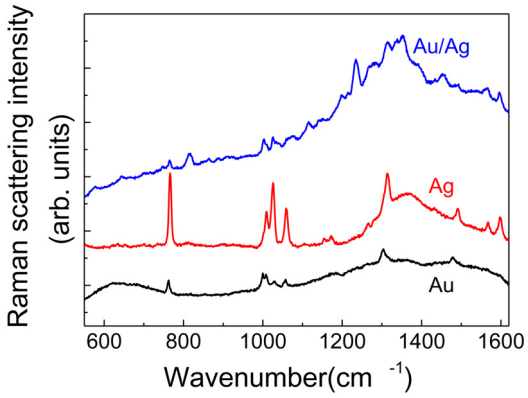

Figure 5: SERS spectra of Au, Ag and Au-Ag alloy system.

We found that 50% of atomic fraction have an unusual behavior to other composition of alloy system with a slightly worst EM enhancement, and SPP propagation length as compared with pure metals. However in the case of Au-Pd system, a 50% alloy slightly improves the optical properties from pure Pd from the point of plasmonics applications where local field enhancement and smaller losses (longer SPP propagation lengths) are required.

Also, we demonstrate SERS spectra on the Au-Ag alloy nano-disks. Some of spectral bands in SERS signal obtained from the alloy nanoparticles are different from the pure Au and Ag. This, most probably, is caused by the chemical effect in the SERS enhancement mechanism providing new method to facilitate molecular recognition and finger printing which is highly required for complex molecules and solutions. Alloys of noble metals can be used on large-surface-area photo-electrodes and sensors such as black Si [21, 22].

Acknowledgement

YN gratefully thanks Prof. Toshihiko Baba, from Yokohama National University for fruitful discussions and granting access to fabrication and characterization facilities. This work was financially supported by Amada Foundation, The Hattori Hokokai Fundation, and JSPS Grants-in-Aid for Scientific Research. SJ is grateful for support via Australian Research Council DP130101205 project.

References

[1] T. Wei, Y. Liu, W. Dong, Y. Zhang, C. Huang, Y. Sun, X. Chen, and N. Dai, Surface-Dependent Localized Surface Plasmon Resonances in CuS Nanodisks, *ACS Appl. Mater. Interfaces,* **5**, 10473-10477 (2013).

[2] M. M. Kjeldsen, J. L. Hansen, T. G. Pedersen, P. Gaiduk, and A. N. Larsen Tuning the plasmon resonance of metallic tin nanocrystals in Si-based materials, *Apply. Phys. A,* **100**, 31-37 (2010).

[3] S. Franzen, C. Rhodes, M. Cerruti, R. W. Gerber, M. Losego, J. P. Maria, and D. E. Aspnes, Plasmonic phenomena in indium tin oxide and ITO-Au hybrid films, *Opt.Lett.,* **34**, 2867-2869 (2009).

[4] Y. Nishijima and S. Akiyama, Unusual optical properties of Au/Ag alloy nanostructures, *Opt. Mater. Express,* **2**, 1226-1235 (2012).

[5] Y. Nishijima, Y. Hashimoto, L. Rosa, Jacob B. Khurgin, and S. Juodkazis, Scaling rules of SERS intensity, *Adv. Opt. Mater.,* DOI: 10.1002/adom.201300493 (2014).

[6] Y. Nishijima, L. Rosa, and S. Juodkazis, Surface plasmon resonances in periodic and random patterns of gold nano-disks for broadband light harvesting, *Opt. Express,* **20**, 11466-11477 (2012).

[7] Y. Nishijima, J. B. Khurgin, L. Rosa, H. Fujiwara, and S. Juodkazis, Randomization of gold nano-brick arrays: a tool for SERS enhancement, *Opt. Express,* **21**, 13502-13514 (2013).

[8] Y. Nishijima, L. Rosa, and S. Juodkazis, Long-range interaction of localized surface plasmons in periodic and random patterns of Au nanoparticles, *Appl. Phys. A,* DOI: 10.1007/s00339-013-8057-9 (2013).

[9] K.S. Lee, and M. A. El-Sayed, Gold and silver nanoparticles in sensing and imaging and sensitivity of plasmon response to size, shape, and metal composition, *J. Phys. Chem. B,* **110**, 19220-19225 (2006).

[10] N. E. Motl, E. E. Annan, I. T. Sines, L. Jensen, and R. E. Schaak, Au and Cu alloy nanoparticles with tunable compositions and plasmonic properties: experimental determination of composition and correlation with theory, *J. Phys. Chem. C,* **114**, 19263-19269 (2010).

[11] F. Hubenthal, N. Borg, and F. Träger, Optical properties and ultrafast electron dynamics in gold and silver alloy and core and shell nanoparticle, *Appl. Phys. B: Lasers and Optics,* **93**, 39-45 (2008).

[12] P. B. Johnson, and R. W. Christy, Optical constants of copper and nickel as a function of temperature, *Phys. Rev. B,* **11**, 1315-1323 (1975).

[13] P. B. Johnson, and R. W. Christy, Optical constants of the noble metals, *Phys. Rev. B,* **6**, 4370-4379 (1972).

[14] P. B. Johnson, and R. W. Christy, Optical constants of transition metals: Ti, V, Cr, Mn, Fe, Co, Ni, and Pd, *Phys. Rev. B,* **9**, 5056-5070 (1974).

[15] ASM, *ASM Handbook: Volume 3: Alloy phase diagrams,*; ASM International, (1992).

[16] H. Kobayashi, M. Yamauchi, R. Ikeda and H. Kitagawa, Atomic-level Pd-Au alloying and controllable hydrogen-absorption properties in size-controlled nanoparticles synthesized by hydrogen reduction, *Chem. Comm.,* 4806-4808 (2009).

[17] H. Kobayashi, M. Yamauchi, H. Kitagawa, Y. Kubota, K. Kato, and M. Takata, Atomic-Level PdPt Alloying and Largely Enhanced Hydrogen-Storage Capacity in Bimetallic Nanoparticles Reconstructed from Core/Shell Structure by a Process of Hydrogen Absorption/Desorption, *J. Am. Chem. Soc.,* **132**, 5576-5577 (2010).

[18] K. Juodkazis, J. Juodkazyte, P. Kalinauskas, E. Jelmakas, and S. Juodkazis, Photoelectrolysis of water: Solar hydrogen - achievements and perspectives, *Opt. Express:energy express,* **18**, A147 - A160 (2010).

[19] K. Juodkazis, J. Juodkazyte, B. Sebeka, S. Juodkazis, Reversible hydrogen evolution and oxidation on Pt electrode mediated by molecular ion, *Appl. Surf. Sci.*, **290**, 13-17 (2014).

[20] S. Jayawardhana, L. Rosa, S. Juodkazis, P. R. Stoddart, Additional Enhancement of Electric Field in Surface-Enhanced Raman Scattering due to Fresnel Mechanism, *Sci. Reports*, **3**, 2335 (doi:10.1038/srep02335) (2013).

[21] G. Gervinskas, G. Seniutinas, J. S. Hartley, S. Kandasamy, P. R. Stoddart, N. F. Fahim, S. Juodkazis, Surface-enhanced Raman scattering sensing on black silicon, *Ann. der Phys.*, **525**, 907-914 (2013).

[22] A. Žukauskas, M. Malinauskas, A. Kadys, G. Gervinskas, G. Seniutinas, S. Kandasamy, S. Juodkazis, Black silicon: substrate for laser 3D micro/nano-polymerization, *Opt. Express*, **12**, 6901-6909 (2013).

Propagation Characteristics Of Plasmonic Wavguides

Padmaja Bhanu Bandaru[1], R.K.Shevgoankar[2] A.N.Chandorkar[3],

[1] Fiber Optics Lab, Department of Electrical Engineering, Indian Institute of Technology Bombay, India
[2]Director, Indian Institute of Technology, Delhi, India
[3]Department of Electrical Engineering, Indian Institute of Technology Bombay, India
*Padmaja Bhanu Bandaru, E-mail: padmaja@ee.iitb.ac.in

Abstract

Propagation characteristics of plasmonic metal-insulator-metal wave guide (MIM) and dielectric-metal-dielectric (DMD) wave guide have been investigated. Waveguide dispersion of both the structures was studied. It was observed that asymmetric and symmetric modes get coupled in the both the structures. With increase in thickness of the core beyond 120nm surface waves get decoupled and tend towards photonic modes in MIM waveguide

1. Introduction

Plasmonics deals with generation and propagation of surface plasmon polaritons (SPP) in different types of structures. SPP's get coupled at the metal dielectric interface by light in the infrared and visible regions of the spectrum[1][2]. These are charge density oscillations with both longitudinal and transverse electromagnetic components. The field can be described by

$$E = \pm E_0 \exp[+i(k_x x \pm k_z z - \omega t) \quad (1)$$

Where k_x and k_z are the transverse and longitudinal wave vectors which are related as

$$\varepsilon_i \left(\frac{\omega}{c}\right)^2 = k_x^2 + K_z^2 \quad (2)$$

Where i=m for metal and d for dielectric. The wave vector k_x is continuous at the interface and can be written as

$$k_x = \frac{\omega}{c} \left[\frac{\varepsilon_m \varepsilon_d}{\varepsilon_m + \varepsilon_d}\right]^{1/2} \quad (3)$$

For obtaining real value of k_x, it requires that $\varepsilon_d = -\varepsilon_m$' where ε_d and ε_m' are the permittivity of dielectric and real part of the permittivity of metal. At optical frequencies the real part of the permittivity of metal is negative which satisfies the condition for generation of SPP's.

Plasmonic wave guides with having symmetric structures have been investigated. Two structures have been studied-MIM and DMD. The dielectric is glass with refractive index n_d = 1.46 and metal is silver with permittivity $\varepsilon(\omega)$. SPP's get coupled when excited by light to form either symmetric or antisymmetric modes. Symmetric mode can be characterized by electric field maxima in the core and decaying exponentially at the interface and anti symmetric mode has field maxima at the interface. Both modes exhibit dispersion with thickness of the core in MIM and DMD structures. Plasmonic waveguides have been reported in the literature. The conditions for existence of SPP and overall performance have been reported [1][2].Modes that can be coupled to finite film structures for different boundary and width variations have also been reported[3][4].Dispersion characteristics of MIM and DMD structures have been analyzed[5][6][7].In this work, dispersion of MIM and DMD waveguides due to thickness variation of guiding layer, changes in refractive index of dielectric material are being reported. In the metal stripe structure reported by authors [8], it was found that width of the stripe is a parameter based on which modes get excited. For realizing various plasmonic structures like gratings, couplers it is necessary to establish a relation which clearly defines variation of effective refractive index and attenuation with thickness. The dispersion relation [1] analytically was studied and plotted for required dimensions of the waveguide and verified with simulation results. The analytical relation of MIM and DMD waveguides have been studied to gain a better insight for realizing such plasmonic structures. The paper is organized as follows: In section II the basic structure is described and analyzed. In section III simulation results about the various characteristics are presented. Discussions and conclusions are presented in section IV and section V.

2. Analysis of DMD and MIM Waveguides

MIM and DMD waveguide structures used for analysis and simulation are shown in fig 2.1

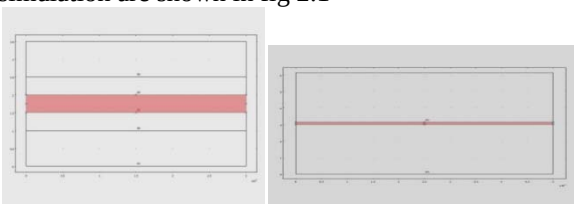

Figure 2.1: Basic structure of MIM and DMD wave guide with metal film as silver and dielectric as glass

In DMD waveguide core is metal with glass as dielectric cladding. The metal is modeled by drude model with metal permittivity as

$$\varepsilon(\omega) = \varepsilon_0 \left[1 - \frac{\omega_p^2}{\omega^2} + i\frac{\omega_p^2}{\omega^3 \tau}\right] \quad (4)$$

Where ω_p is the plasma frequency and τ is the extinction ratio [9]. At optical frequencies the equation becomes

$$\varepsilon_m(\omega) = \varepsilon_\infty - \frac{\omega_p^2}{\omega^2 + i\tau\omega} \quad (5)$$

with ω_p = 9.1ev, τ = 0.018ev and ε_∞ = 3.7 for silver[10]. The symmetric glass/silver/glass structure shows interesting properties and dispersion due to thickness. When the thickness of metal film is less than 20nm, the symmetry of the structure causes the field on both surfaces to interact giving raise to symmetric field distribution at the plane z=0 and anti symmetric field with different polarizations of light coupling these modes. The dispersion due to these fields is a function of both in plane wave vector k_x as well as thickness of the metal film. When the thickness of the metal film is made more than 55 nm, the surface modes at the interfaces do not interact and the dispersion curve tends to that of single metal-dielectric interface. Dispersion relation for the structure can be given as [1]

$$\varepsilon_m k_{zd} + \varepsilon_d k_{zm} tanh\left(\frac{-i}{2} k_{zm} d\right) = 0 \quad (6)$$

$$\varepsilon_m k_{zd} + \varepsilon_d k_{zm} coth\left(\frac{-i}{2} k_{zm} d\right) = 0 \quad (7)$$

The plot shown in fig 2.2 uses relation in equation 6 and displays field variations in anti symmetric mode for the DMD waveguide. The thickness is varied from 10nm and excitation wavelength from 550nm.

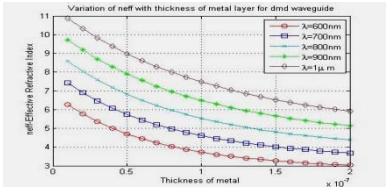

Figure 2.2: Variation of effective refractive index in DMD waveguide. Dielectric thickness = 50nm, metal thickness = 5nm~200nm, λ = 600nm ~1μm.

From the plot in fig.2.2 it was observed that dispersion curves shift right when excitation wavelength is increased due to increase in the value of in plane wave vector. It can also be observed that modes get decoupled and a sharp reduction in the value of effective refractive index. Attenuation in the metal film is also observed which limits the propagation length [5].

The MIM structure is shown in fig. 2.1 is also a symmetric structure with silver/glass/silver interface. As in the case of DMD structure the dispersion relation depends on the in plane wave vector as well as thickness of the insulator layer. As the skin depth of silver is approximately 26nm for optical frequency range, the metal cladding is chosen to have thickness of 50nm. The cladding is further bounded by air. The dispersion relation can be given as following [1][5]

$$k_{zd} + k_{zm} tanh\left(\frac{-i}{2} k_{zm} d\right) = 0 \quad (8)$$

$$k_{zd} + k_{zm} coth\left(\frac{-i}{2} k_{zm} d\right) = 0 \quad (9)$$

The plot in the fig 2.3 shows the anti symmetric mode as per the dispersion relation in 8. The value of effective refractive index for a given excitation wavelength is higher than DMD structure as the field maxima is at the surface. As the coupling is through the dielectric it is expected that propagation lengths of these structures will be long range in nature. The variation in effective refractive is gradual and the modes get slowly decoupled and tend to that of single metal-air interface structure.

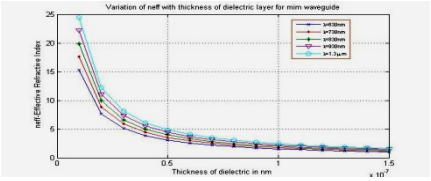

Figure 2.3: Dispersion characteristics of MIM structure

3. Propagation Characteristics of MIM and DMD Waveguides

3.1. MIM Wave guide

Propagation characteristics based on simulation results are presented in this section. The wave guide structure is shown in fig 2.1 with glass core of refractive index n_d=1.46, silver cladding which is further bounded by air. Using FEM analysis with in plane TM/TE excitation wave equation is solved hybrid modes for this structure. It was observed that TM excitation couples Anti symmetric Modes and TE excitation symmetric modes. These modes evolve independently and do not cutoff for any changes in thickness of core. However with increase in thickness, modes in the core tend to photonic and the energy distribution in the surface modes becomes minimal. The anti symmetric mode exhibits minimal attenuation and is a long range mode. The effective refractive index of the mode is also high indicating considerable modal confinement [5]. TE polarized excitation couples symmetric mode with high modal confinement for thinner core values. However this mode exhibits significant attenuation for thicker core dimensions and is a short range mode. From the simulation results dispersion characteristics are plotted for both the modes in fig 3.1.

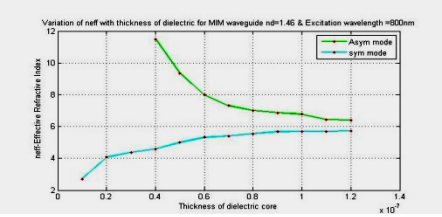

Figure 3.1: Dispersion characteristics of MIM waveguide from simulation results. Glass core with n_d=1.46, λ_o=800nm

It was observed for core thickness less than 40nm asymmetric mode cannot be excited. When thickness is increased beyond 40nm, long range SPP mode gets coupled with minimal attenuation and high effective refractive index. These modes evolve independently at each interface

and decouple into separate SPP modes with minimal energy distribution in the core. For thickness beyond 120nm, photonic modes evolve in the core and energy distribution of the surface modes rapidly decreases which results in decrease in effective refractive index of these modes. The excitation wavelength effects the in plane vector and hence the reduction in energy of these modes can be observed for smaller core thicknesses. The Symmetric mode gets excited for thickness even below 10nm. However these dimensions result in poor energy confinement and low effective refractive index. When core thickness is increased decoupling effects the energy distribution in the core and increases the surface energy distribution. Due to decoupling effect with increase in core dimensions both modes tend to similar value of refractive index and to that of single metal-dielectric interface. The effect on propagation characteristics due to core refractive index variations was also observed. It was seen that changes in the range of 10^{-3} effect the energy distribution significantly in both the modes. With changes in core refractive index in plane vector gets affected hereby causing these changes. It was also observed that when the metal cladding thickness is at least twice skin depth, it does not affect the characteristics.

3.2. DMD Wave guide

The waveguide structure shown in fig 2.1 is used for simulation. Changes in propagation characteristics due to metal film as core were noted. Similar to MIM wave guide symmetric and anti symmetric modes get excited with TM/TE polarized in plane waves. However the modes at the two interfaces are closely coupled and exhibit cutoff when thickness of metal film goes beyond 30nm. Energy distribution in the waveguide changes very rapidly for changes in core dimensions as compared to MIM structures. Propagation lengths are in tens of micrometers due to attenuation in the metal film. Dispersion characteristics are plotted as shown in fig. 3.2.

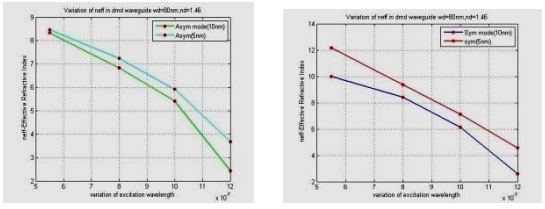

Figure 3.2: Dispersion characteristics of DMD waveguide a) symmetric mode b) anti symmetric mode

The cutoff of the waveguide depends on both the thickness of the metal layer as well as excitation wavelength. For metal thickness in the range of 10nm, cutoff depends on excitation wavelength. At excitation wavelength of 1.23µm, metal permittivity has significantly high value and the waveguide cutoff for both the modes. For thickness of metal core beyond 30nm, attenuation in the metal highly limits the energy in the surface waves and the propagation length gets reduced. It was noted that imaginary part of the k_x vector which signifies attenuation is a function of square of thickness of metal core as well as the permittivity of metal [1]. The simulation results agree to this as with increase in metal thickness, attenuation significantly increases limiting the propagation.

4. Discussion

Propagation characteristics of MIM and DMD plasmonic waveguides were analyzed. The dimensions of the structures are very much below excitation wavelength. It was observed that results due to analysis and simulation closely resemble each other. Modes coupled in the MIM structure have higher surface energy distribution and are coupled independently at each metal-dielectric interface. They have propagation lengths in hundreds of micrometers. Modes in DMD waveguide are always coupled to each other and due to significant loss in the metal film cut off for any given dimension.

5. Conclusions

From the simulation and analytical results which are in close resemblance, It can be observed that MIM waveguide is more suitable for wave guiding applications. Due to the dispersion characteristics which are dependent on the in plane wave vector and thickness several applications like filters, gratings and couplers can be realized. Variations due to core refractive index can be used for sensing applications.

References

[1] Heinz Raether , *Surface Plasmons on smooth and rough surfaces and on gratings*

[2] M. Dragoman, D. Dragoman, Plasmonic applications to nanoscale tetrahertz and optical devices, *Progress in Quantum Electronics, vol., 3*2:1−41, 2008.

[3] P. Berini, Plasmon-polariton waves guided by thin lossy metal films of finite width:Bound modes of symmetric structures, *Physical Review B, vol. 63, 10481-10490, 2000.*

[4] P.Berini, Plasmon-polariton waves guided by thin lossy metal films of finite width:Bound modes of asymmetric structures, *Physical Review B, vol. 63, 125417-1-125417-15, 2001.*

[5] J.A.Dionne, L.A.Sweatlock, H.A.Atwater , Plasmon Slot wave-guides: towards chip scale propagation with sub-wavelength scale localization, *Physical Review B, vol. 73, 2006*

[6] Rashid Zia, Mark D. Selker, Mark L. Brongersma, Leaky and Bound modes of suface Plasmon waveguides, *Physical Review B, vol. 71, 165431-39, 2005*

[7] A. Sellai, M. Elzain, Characteristics of dielectric-metal dielectric Plasmonic Wave Guide , *Physica E, vol. 41, 106-109, 2008*

[8]B.PadmajaBhanu,R.K.Shevgoankar,A.N.Chandorkar,Propagation Characteristics of metal stripe waveguides, *SPIE proceedings,Vol.8173,2011*

[9] Jean-Michel Lourtioz, *Photonic Crystals*

[10] E. Palik, *Handbook of Optical Constants*

Impact of process factors on the performance of hole-array metallic filters

Romain Girard-Desprolet[1,2], Sandrine Lhostis[2], Charlotte Beylier[2], Vincent Farys[2], Guy Vitrant[3], and Salim Boutami[1,*]

[1]CEA, LETI, MINATEC Campus, 17 Rue des Martyrs, Grenoble 38054, France
[2]STMicroelectronics ,850 rue Jean Monnet 38920 Crolles, France
[3]Grenoble INP, IMEP LAHC, Minatec, CNRS, UMR 5130, F-38016 Grenoble, France
*corresponding author: salim.boutami@cea.fr

Abstract

In this work, we evaluate through Rigorous Coupled Wave Analysis (RCWA) simulations the effect of various process-related inaccuracies on plasmonic filters performance, especially regarding cross-shaped-hole arrays. Focusing exclusively on CMOS-compatible materials, we demonstrate the potential of these structures for reliable integration and fabrication at wafer level. A high monitoring of the deposition parameters is required to control the transmission level and the resonant wavelength of the filters. Optical proximity calculations show that double patterning is a way to limit corner rounding and to avoid losing the resonant mode of the crosses. The impacts on plasmon resonances of the metal oxidation, or a sloped profile after metal etching, are evaluated. These results allow for a good anticipation regarding process issues to realize efficient plasmonic filters.

1. Introduction

Plasmonic structures have been widely investigated since Ebbesen clearly established the link between extraordinary optical transmission and surface plasmons [1]. Surface plasmons are collective oscillations of the electrons gas that can occur at the metal/dielectric interface when light impinges a metallic surface in proper conditions. Illuminating a periodically-structured metallic layer is a common way of exciting surface plasmons [2,3]. In the case of periodic hole-arrays in a metallic layer, the plasmon resonates inside the structure for a specific wavelength related to characteristic dimensions of the lattice. Hole-arrays are thus well-adapted for optical filters [4,5]. Moreover, some particular hole shapes have shown interesting optical properties. Cross-shaped-hole arrays indeed present the ability of being nearly insensitive to light incidence and polarization with proper design rules [6]. This property potentially allows for the realization of optical filters with very low color variations when light incidence and polarization state are changed.

Beside their appealing optical properties, such plasmonic devices also present a financial interest. Their simple structure – a single patterned metallic layer even for multi-colors filtering – implies a few number of fabrication steps, unlike Fabry-Perot filters which are made of several layers with varying thicknesses [7]. They also do not require any external infrared filter thanks to their infrared rejection capability, unlike color resists. All these features make plasmonic filters particularly attractive for industrial fabs. However, the integration of plasmonic structures in industrial products requires reliable fabrication guaranteeing drastic specifications dispersions. In the visible range though, the holes dimensions are small and fabricating such structures while keeping an accurate shape definition may be challenging, especially working at wafer level, on 300mm silicon wafers. In practice, the final processed shapes may substantially deviate from the targeted ones due to process limitations at each critical step of the fabrication route.

In this paper, we aim to evaluate the potential performance of cross-shaped-hole array filters fabricated with CMOS materials, especially with aluminum. The main weaknesses of each critical step are identified and we estimate how they impact the spectral response. Through RCWA computations, we first present the influence of film thickness and optical index standard deviations on a reference filter at 550nm. Then, we consider lithography inaccuracies using optical proximity calculations. The effect of rounded crosses on the filter performances is studied. A strategy is presented to obtain the best performances after the lithography step. Sloped etching profiles of metal holes are investigated, and then we simulate also the presence of a native oxide on the metal surface. This paper enables to anticipate the design rules required to get efficient plasmonic filters.

2. Filters modeling

In this work, cross-shaped-hole array filters are considered for their angular stability properties as mentioned earlier. They are defined with the following geometrical parameters: period P, metal thickness h_m, arm length a, arm width b and a radius of curvature in the corners R, as shown in Fig. 1. Except in the part regarding rounded crosses, R is set to 0 so that we deal with regular sharp crosses. The period is chosen

the same in the *x*- and *y*-axis. The metal used is aluminum and the dielectric material used for the superstrate, the substrate, and inside holes is SiO_2 due to its wide use in CMOS foundries. The superstrate and the substrate are both considered as semi-infinite.

The refractive indices of aluminum are extracted from Palik references. The refractive index of silica is considered constant at n=1.46 without imaginary part (no losses). The RCWA used for the calculations is an in-house code, and the simulations presented in this paper are using 8 harmonics ensuring adequate convergence.

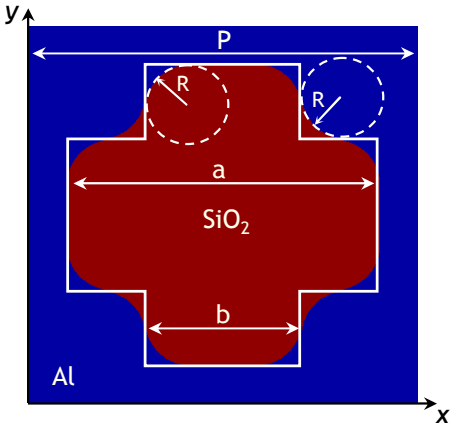

Figure 1: Scheme of cross-shaped designs modeled.

3. Main results

3.1. Process deposition standard deviations

An Al/SiO_2 plasmonic filter can be fabricated according to this simplified process route: i) SiO_2 deposition, ii) aluminum deposition, iii) aluminum etching and iv) SiO_2 filling. Deposition steps induce two kinds of process variations: deviations from targeted thicknesses and fluctuation of materials refractive indices, in particular for the SiO_2 surrounding the metallic layer. These two effects are taken into account in our study. We consider typical process dispersions that can be obtained in 300mm CMOS foundries: the standard deviation on the metal thickness σ_{hm} is chosen at 3% and the standard deviation on the refractive index of silica σ_{RI} is taken at 1.6%. In Fig. 2, the plasmonic filters are simulated with maximum dispersions of $\pm 3\sigma$ as generally considered in statistical process controls for the metallic thickness alone (blue curves), for the silica refractive index alone (green curves) and for the combination of the two dispersions (orange curves). The results show that these process variations have a moderate impact on plasmonic filter. The main effects are a transmission level modification and a shift of the resonance wavelength. Indeed, we show that a high control on the standard deviation on materials thickness and optical parameters would be profitable to avoid fluctuations of the transmission efficiency and the resonance wavelength.

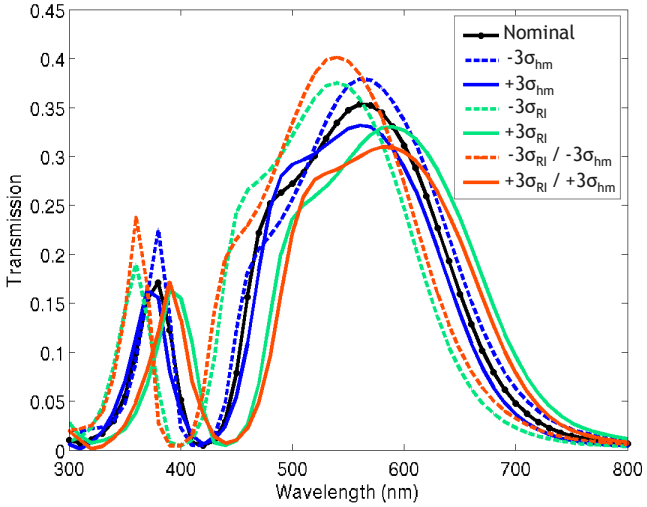

Figure 2: Spectral response variations of a plasmonic filter induced by process dispersions at $\pm 3\sigma$ for metal thickness with σ_{hm}=3% (blue), silica refractive index with σ_{RI}=1.6% (green) and both combined (orange). Filter dimensions are: P=250nm, a=200nm, b=100nm, h_m=300nm.

3.2. Lithography inaccuracies

The following step after metal deposition is lithography pattern to print the hole shape to be etched in the metal layer. For a filtering application in the visible range, the dimensions of the holes are approximately between 50nm and 250nm. For such small dimensions with current lithography techniques as 248 nm deep-UV, the internal and external right angles of the crosses are expected to be rounded after photoresist reveal, and subsequently on the final etched patterns.

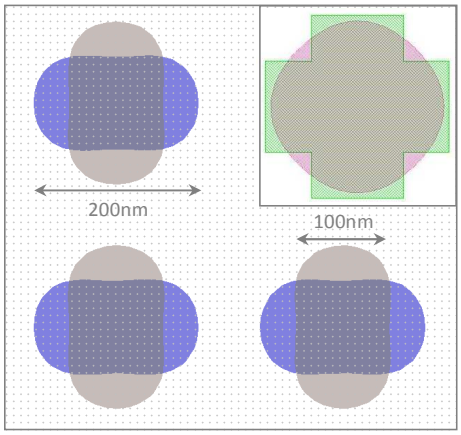

Figure 3: Optical proximity effects calculations for an array of crosses obtained with a double patterning with 248nm UV lithography. The inset presents the same cross (target shape in green) obtained with single patterning (in red). Filter dimensions are: P=250nm, a=200nm, b=100nm, h_m=300nm.

We have used optical proximity calculations tools to predict the actual shape of cross-holes after lithography. A few options are investigated to decrease the deviation from the targeted design based on different technological

strategies. The strategy of double patterning, where the two arms of the crosses are insolated sequentially, has shown to be the best solution. For instance, the shape obtained for a cross hole with a double patterning in 28nm CMOS technology is given in Fig. 3. This is consistent with the work presented by Landis *et al.* [8] where crosses are insolated in two steps to get proper shapes for nanoimprint.

These results help us to anticipate the main defaults of the actual shape that can be obtained after UV exposure and etching. The effect of rounded corners on cross holes plasmon resonances had not been investigated yet to our knowledge. We perform here a dedicated study with crosses rounded with different radii *R*, in both internal and external angles (Fig. 1). The spectral responses are examined to conclude on the impact on the filters properties.

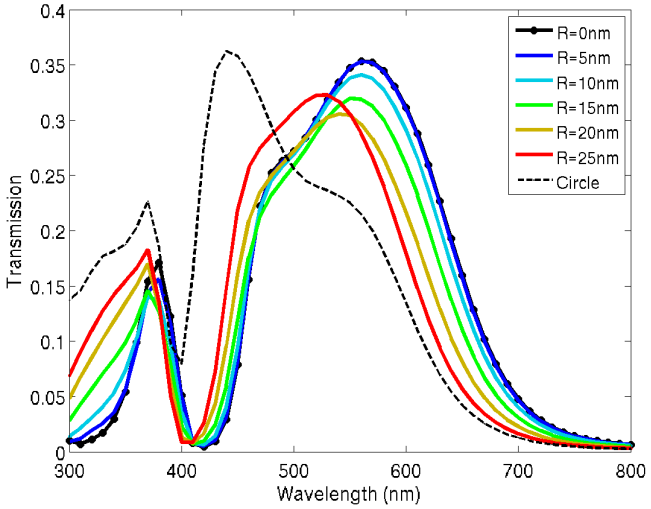

Figure 4: Evolution of the spectral responses of the filter with increasing corners rounding (increasing radii). Filter dimensions are: P=250nm, a=200nm, b=100nm, h_m=300nm. The spectra are compared to a circular-hole array with diameter a.

The results presented in Fig. 4 reveal that curving the crosses corners alters the optical properties of the filter, especially with a decrease of the transmission efficiency but also a blue-shift of the plasmon resonance. A circular-hole array with diameter a is also simulated to observe how it may fit to rounded crosses. While its spectral response seems to support the blue-shift noticed for highly rounded crosses, it may be tricky to conclude clearly since aperture areas of crosses are not the same when curvature radius increases, which may also affect spectra.

In order to dissociate the aperture area variation effect from the roundness effect, simulations are made with adaptive crosses dimensions to compensate the loss of aperture induced by rounded corners, so that the aperture area is the same whatever the R value (keeping ratio b/a=0.5). The results are very similar to previous ones, with slightly less transmittance losses (Fig. 5). This means that the loss of transmission efficiency is not attributable to the decrease of aperture area. When comparing the evolution of this filter with a circular-hole array of equivalent aperture area (diameter 195.5nm), it can however be confirmed that the blue-shift and the decrease of transmittance are due to the progressive loss of crosses' specific resonance properties, coming close to those of circular holes when R increases.

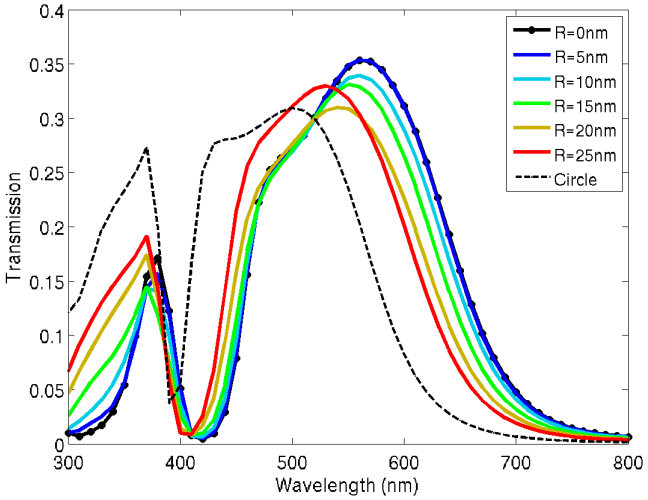

Figure 5: Evolution of the spectral responses of the filter with increasing corners rounding, keeping constant the cross aperture area. Filter dimensions are: P=250nm, a=(200nm, 200.07nm, 200.29nm, 200.64nm, 201.14nm and 201.78nm), b=0.5*a, h_m=300nm. The spectra are compared with a circular-hole array with equivalent aperture area (diameter 195.5nm).

3.3. Etching profile

Once the lithography step is performed, the metal has to be etched to create periodic patterns. A sloped profile of the hole may be expected when aluminum is etched, which can be detrimental to the optical properties of the device given the small dimensions and thicknesses of the filters. We have simulated filters with different slopes for a 300nm-thick Al layer to evaluate the effect of such holes profiles. The slopes are modelled with RCWA, using a decomposition of the metallic layer into N elementary layers of equal thickness h_m/N to create steps reproducing the sloped profile. The slope is defined with the angle θ relatively to the vertical direction (θ=0° corresponding to a perfect etching), as shown in Fig. 6.

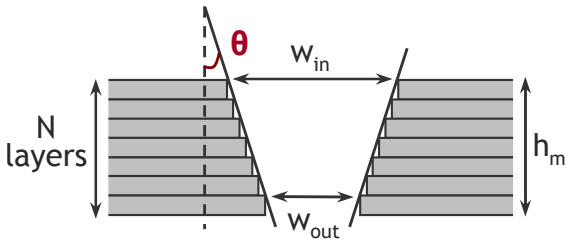

Figure 6: Modeling of sloped etching profiles with N steps in an aluminum filter. The angle θ defines the slope relatively to straight edges.

Before processing metallic filters, it has to be chosen whether the targeted hole dimensions have to be respected at the entrance or at the exit of the filter. For instance,

plasmons resonances may not be the same if we decide to have $w_{in}=a$ (top) or $w_{out}=a$ (bottom) in the case of cross-shaped-hole arrays. We propose to study both situations to understand the impact of slopes on plasmons. All the results are obtained with 25 elementary layers, which gave similar results to finer modeling. Different slopes from 0° to 7.5° are simulated for the reference filter.

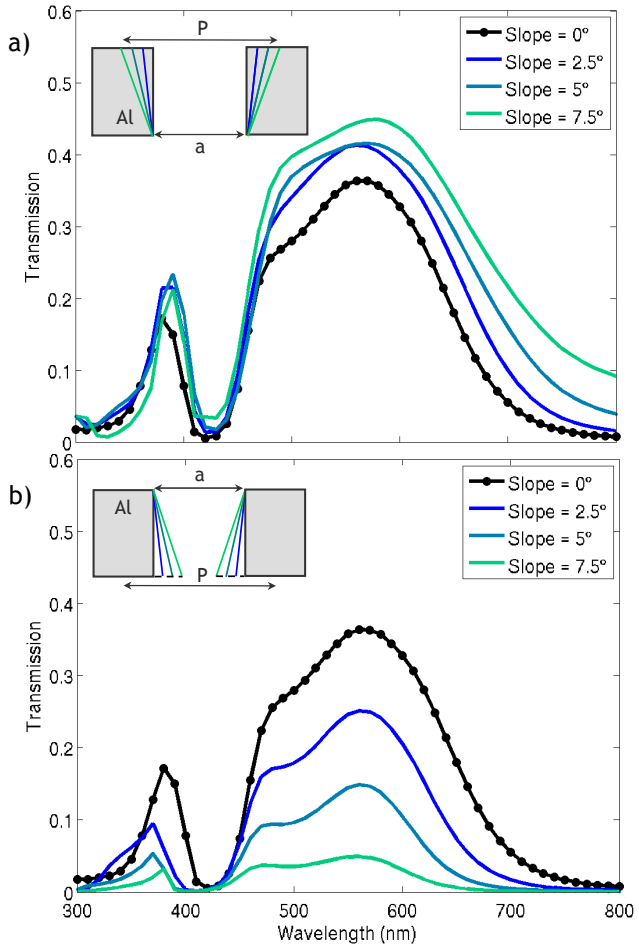

Figure 7: a) Evolution of the spectral response simulated with etching slopes of 0°, 2.5°, 5° and 7.5° in the case where a is fixed at the bottom of the filter. b) Same graph in the case where a is fixed at the top of the filter. Filters dimensions: P=250nm, a=200nm, b=100nm, h_m=300nm.

It can be observed in Fig. 7a that the transmission efficiency increases and the spectra broaden with increasing slopes, when the exit section is fixed. This highlights a kind of "funnel" effect where the widening of the hole induces a higher collection of light in the holes, leading to a strong confinement of the electromagnetic field at the exit of the filter. These results are in good agreement with the work of Shen and Maes on tapered metallic gratings [9], although they use higher w_{in}/w_{out} ratios in their study. Note that for a 7.5° slope, the arm length of the crosses on the top of the filter exceeds the period value by a few nanometers. In practice, fixing the exit section can be realized with proper anticipation on masks design and with a good knowledge of the etching chemistry. On the other hand, Fig. 7b shows that, in the case where the entrance section is fixed, sloped profiles lead to a dramatic loss of transmission efficiency. This can be simply explained by the fact that increasing the slope progressively obstructs the holes in this case.

In order to evaluate which of these two effects is prevalent on the filter response, we study a third situation where both the entrance and the exit sections vary with the slope (Fig. 8), and the nominal width is set at the middle of the metallic layer. As it can be seen, the two effects partially compensate, but the trend is nevertheless rather a decrease of the transmission efficiency with slope increase. This proves that the impact of the exit section is predominant over the input section. It is therefore more interesting to adjust the lithography masks so that the targeted dimensions are satisfied at the bottom of the filter. Note that the effect of sloped profiles would be significantly limited for thinner filters, but thin filters would have a worse rejection than thick ones.

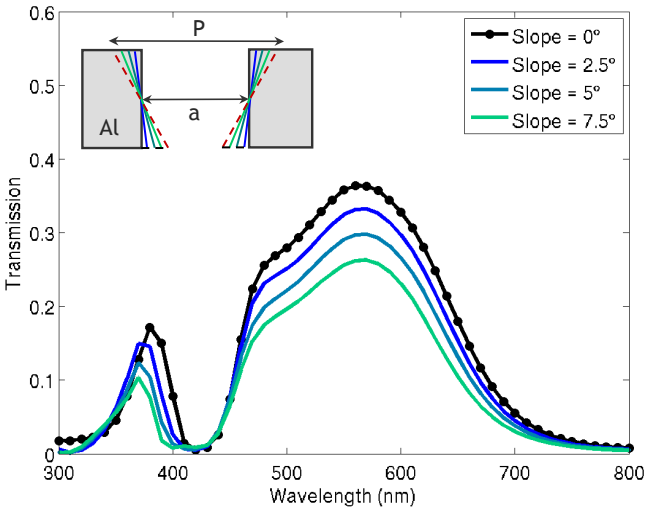

Figure 8: Evolution of the spectral response simulated with slopes of 0°, 2.5°, 5° and 7.5° in the case where a is fixed at the middle of the metallic layer. Filters dimensions are: P=250nm, a=200nm, b=100nm, h_m=300nm.

3.4. Metal oxidation

The last effect we consider is the potential oxidation of the metallic layer. Several studies regarding plasmonic filters use aluminum as metallic layer [4,5,10,11], but don't take into account a possible oxidation of the metal layer. There is either a formation of a native oxide layer Al_2O_3 at Al surface when the metal layer is in contact with air, as for example during chamber changing between two process steps or a formation of an aluminum oxide when it is in contact with another oxide such as SiO_2. In both cases, a few-nanometers-thick interfacial layer is formed with a stoichiometry close to Al_2O_3. The thickness of alumina generally grows up to a maximum of 10nm under room temperature [12]. In this work different values of alumina thickness are simulated to observe the evolution of the spectral response with the native oxide thickness.

For modeling simplification, we consider that the oxidation thickness is the same on all sides of aluminum that

means on bottom and top of Al layer and on hole sides as well. Al_2O_3 refractive indices are taken from in-house measurements (n=1.666+0.0032i at λ=633nm). The simulation results presented in Fig. 9 show that the oxidation of aluminum leads to an increase of the transmission efficiency, a widening of the spectrum and also a red-shift of the resonance, the latter being due to the higher refractive index of alumina compared to SiO_2. However, as for the holes corners rounding, there remains a bias in these results: the transmittance increase and the peak broadening may be partly due to the fact that the oxidation process removes metallic atomic layers at the metal/dielectric interface, as shown in the filter cross section scheme on Fig. 9a. This makes the obtained filter different from the targeted design, with larger aperture area and thinner metal, potentially leading to higher transmission.

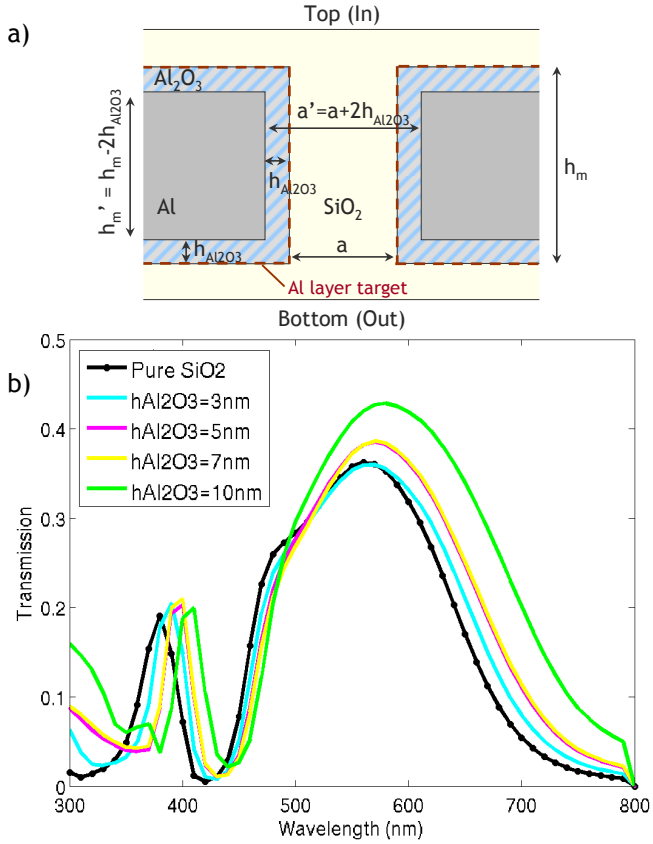

Figure 9: a) Case of oxidation leading to a reduction of aluminum dimensions. b) Corresponding spectral response evolution of a SiO_2-Al filter with different Al_2O_3 thicknesses around the aluminum layer. Filter dimensions are: P=250nm, a=200nm, b=100nm, h_m=300nm.

In order to understand the actual effect of alumina, it is necessary to dissociate from its effect the geometrical changes induced by the oxidation process. This can be easily done in practice by tailoring thickness deposition specification and the masks design so that the targeted aluminum shape is obtained after oxidation, as shown in Fig. 10a. In these conditions, it can be observed on Fig. 10b that the alumina layer itself does not have a significant impact on the filter spectrum. Increasing the oxide thickness nearly does not change the transmission of the filter. A slight red-shift is observed, since plasmons are interface phenomena, related to the refractive index of the dielectric directly in contact with the metal, and the alumina has a higher refractive index than silica.

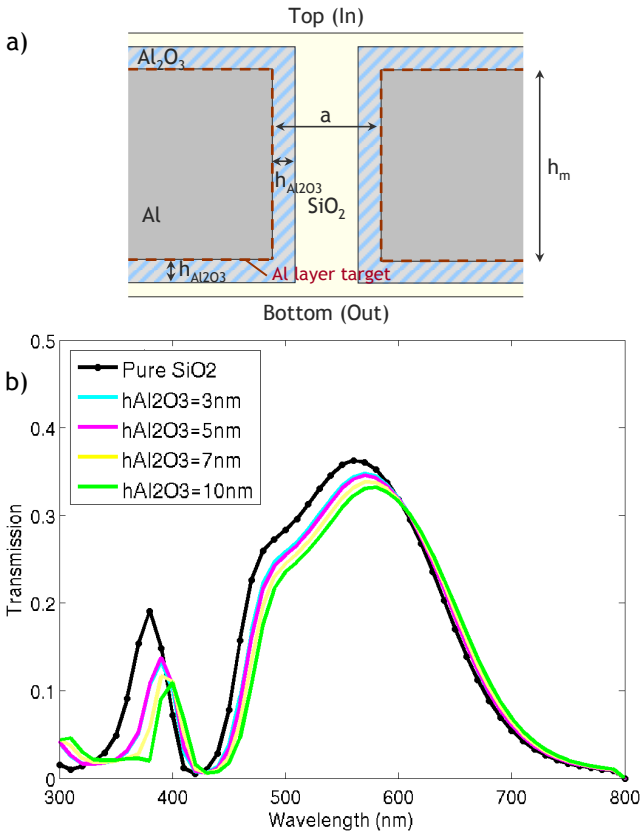

Figure 10: a) Case of oxidation with no modifications of aluminum dimensions (anticipation of metal dimensions through deposition and mask design). b) Corresponding spectral response evolution of a SiO_2-Al filter with different Al_2O_3 thicknesses around the aluminum layer. Filter dimensions are: P=250nm, a=200nm, b=100nm, h_m=300nm.

4. Conclusions

We have presented a review on the impact that can induce the process deviations specific to the different steps of the fabrication routes for cross holes aluminum visible filters. These results clearly show that the principle of plasmonics allows for an anticipation of these process variations on the design so that the final filter has a spectral response close to the targeted spectrum. Beside the benefit of an accurate monitoring on the process standard deviation on the metal thickness and the refractive indexes, we have demonstrated with this anticipatory methodology that a proper tailoring of the mask design and an adapted etching recipe can limit the impact of process inaccuracies on plasmon resonances. The effect of the metal oxidation is thus significantly reduced and the effect of sloped etching profiles can be limited with a tough control on the patterns dimensions at the bottom of the filters. Although this study was focused on Al-SiO_2 structures filtering light around 550nm, this methodology could be used for any kind of plasmonic filters, using

different holes shape, dielectric materials, metals, or having different operation bandwidths.

References

[1] T.W. Ebbesen, H.J. Lezec, H.F. Ghaemi, T. Thio, P.A. Wolff, Extraordinary optical transmission through sub-wavelength hole arrays, *Nature* 391(6668): 667−669, 1998.

[2] T.W. Ebbesen, C. Genet, Light in tiny holes, *Nature* 445: 39-46, 2007.

[3] K. Kumar, H. Duan, R.S. Hegde, S.C.W. Koh, J.N. Wei, J.K.W. Yang, Printing colour at the optical diffraction limit, *Nat. Nanotechnol.* 7: 557-561, 2012.

[4] S. Yokogawa, S.P. Burgos, H.A. Atwater, Plasmonic color filters for CMOS image sensor applications, *Nano Lett.* 12(8): 4349-4354, 2012.

[5] D. Inoue, A. Miura, T. Nomura, H. Fujikawa, K. Sato, Polarization independent visible color filter comprising an aluminum film with surface-plasmon enhanced transmission through a subwavelength array of holes, *Appl. Phys. Lett.* 98: 093113, 2011.

[6] R. Girard-Desprolet, S. Boutami, S. Lhostis, G. Vitrant, Angular and polarization properties of cross-holes nanostructured metallic filters, *Optics Express* 21(24): 29412−29424, 2013.

[7] L. Frey, P. Parrein, J. Raby, C. Pellé, D. Hérault, M. Marty, J. Michailos, Color filters including infrared cut-off integrated on CMOS image sensor, *Optics Express* 19(14): 13073-13080, 2011.

[8] S. Landis, P. Brianceau, V. Reboud, N. Chaix, Y. Desieres, M. Argoud, Metallic colour filtering arrays manufactured by NanoImprint lithography, *Microelectron. Eng.* 111: 193−198, 2013.

[9] H. Shen, B. Maes, Enhanced optical transmission through tapered metallic gratings, *Appl. Phys. Lett.* 100(241104): 1-4, 2012.

[10] Q. Chen, D. Chitnis, K. Walls, T.D. Drysdale, S. Collins, D. R.S. Cumming, CMOS photodetectors integrated with plasmonic color filters, *IEEE Photon. Technol. Lett.* 24(3): 197-199, 2012.

[11] D. Lerose, E.K. Hei, B.C. Ching, M. Sterger, L.C. Yaw, F.M. Schulze, F. Schmidt, A. Schmidt, K. Bach, CMOS-integrated geometrically tunable optical filter, *Appl. Opt.* 52(8), 1655–1662, 2013.

[12] L. P. H. Jeurgens, W. G. Sloof, F. D. Tichelaar, E. J. Mittemeijer, Growth kinetics and mechanisms of aluminum-oxide films formed by thermal oxidation of aluminum, *J. Appl. Phys.* 92(3): 1649-1656, 2002.

Plasmon-enhanced photovoltaics, photocatalysis, and solar fuels

$CuInS_2$ solar cell absorber plasmonically modified by gold nanoparticles

Taavi Repan [1], Leonid Dolgov[1]*, Atanas Katerski[2], Ilona Oja Acik[2], Erki Kärber[2], Arvo Mere[2], Valdek Mikli[2], Malle Krunks[2], Ilmo Sildos[1]

[1]Institute of Physics, University of Tartu, Riia 142, 51014 Tartu, Estonia
[2]Department of Materials Science, Tallinn University of Technology, Ehitajate tee 5, 19086 Tallinn, Estonia
*corresponding author, E-mail: dolgov@fi.tartu.ee

Abstract

Thin $CuInS_2$ light absorbing layer prospective for the solar cell applications is modified by gold nanoparticles. Theoretical and experimental possibilities of placement nanoparticles over or under the $CuInS_2$ coating were tested. It was revealed that placement of nanoparticles under the $CuInS_2$ layer is better in terms of spray pyrolysis technique. It results in more effective plasmon enhanced light absorption in the $CuInS_2$ layer at the visible/near infrared 650-700 nm spectral range.

1. Introduction

Development of solar cells made of thin films with possibility of their deposition on the flexible substrates is promising trend nowadays. In spite of comparative simplicity in production and low costs, efficiency of thin film solar cells inferiors to the crystalline analogues. One of the promising ways to increase efficiency of thin film solar cells at certain spectral ranges is doping them by noble metal nanoparticles. Resonance between the oscillations of surface electron plasma in metal nanoparticles and incident light results in strong concentration of light energy and electric field near the metal dopant [1]. It causes growth of light absorption and light scattering near metal nanoparticles in certain resonance spectral range.

When the metal nanoparticle is placed on the interface between two media, more part of light is scattered two the medium with higher refractive index. Thus metal nanoparticles placed on the top of solar cell active layer can provide more light scattering inside the material and increase light harvesting by such a way [2].

Another possibility can be realized for the nanoparticles incorporated directly inside the solar cell absorber layer. Since the cross section of plasmonic light absorption of the metal nanoparticle is larger than its geometrical cross-section, plasmon resonance in metal could support stronger light absorption in the semiconducting host in certain spectral range.

Realization of mentioned principles of plasmonic light harvesting requires adjustment of existing techniques for solar cell coatings with addition of noble metal nanoparticles. On the point of view of chemical doping, deposition of material by spray pyrolysis looks suitable for such modification. Indeed the ability to add gold or silver salt to the precursor was used for preparation of sprayed coatings for tinted glasses [3], layers for semiconductor sensors [4] and photovoltaic films [5]. Formation of Au or Ag via thermal decomposition of Au and Ag precursor salt such as $HAuCl_4 \cdot 3H_2O$ and $AgNO_3$, respectively, is discussed in [6].

Here we used $CuInS_2$ precursor for the solar cell absorber layer. Water solution of gold tetrachloride trihydrate salt was a precursor for the gold nanoparticles.

To check different locations of gold nanoparticles relatively to the absorber layer, we did not mixed gold and semiconductor precursors. The precursors were sprayed one after another to get gold over or under $CuInS_2$ coating. Optical, plasmonic and structural properties of prepared coatings were investigated to define optimal location of the gold nanoparticles providing plasmonically enhanced light absorption in the visible/near infrared spectral range.

2. Materials and methods

Two types of coatings on the glass slabs were prepared depending on the sequence of gold and $CuInS_2$ precursors spraying. Samples of the first type were obtained by spraying of gold solution over the $CuInS_2$. Samples of second type contain gold nanoparticles under the $CuInS_2$. Particular chemical features of preparation are described in more detail in our previous paper [7].

Here the procedure is described briefly. Gold nanoparticles were formed after the spraying of 2 mM aqueous solution of $HAuCl_4 \cdot 3H_2O$ on the 340°C hot substrates. Gold nanoparticles of different size were obtained depending on the amount of sprayed liquid (2.5, 5.0, 10, 15 ml). Aqueous solution containing $CuCl_2$, $InCl_3$ and $SC(NH_2)_2$ at molar ratio of 1:1:3 was sprayed on the 310°C pre-heated substrates to obtain resulting $CuInS_2$ films with thickness ~150 nm.

Mathematical modeling of light absorption was realized by Mie calculations modified for the application to the light absorbing medium [8]. For more complicated configurations finite element method software package

COMSOL Multiphysics 4.3a was used. To allow easier analysis only single particle was considered in the calculations. In reality closely packed particles can cause an additional red-shift of plasmon resonance [9, 10].

3. Results and discussion

3.1. Structure of samples

3.1.1 Gold over the $CuInS_2$

Gold nanoparticles on the surface of $CuInS_2$ layer form granular surface with average size of gold nanoparticles 20-60 nm (Fig. 1). Agglomerated particles with the size up to 200 nm are formed at increased amount of sprayed gold precursor. Gold nanoparticles on the $CuInS_2$ surface consist of the cubic gold nanocrystalites with the size 20-30 nm according to the analysis of X-ray data [7]. Precise measurements revealed that the $CuInS_2$ dissolves partly, when too big amount of gold precursor $HAuCl_4 \cdot 3H_2O$ is sprayed over it [7].

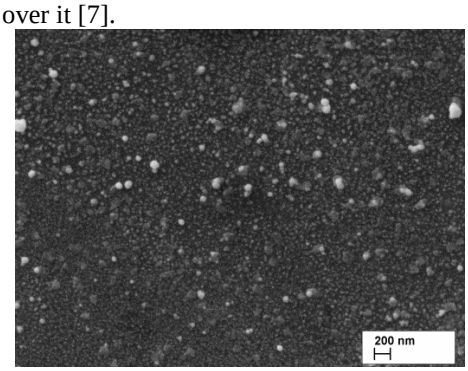

Fig. 1. Scanning electron misroscopy image of gold nanoparticles obtained after spraying of 10 ml of gold precursor over the $CuInS_2$ layer.

3.1.2 Gold under the $CuInS_2$

Undesirable destructive action of chlorine from the gold precursor is eliminated in case of deposition of $CuInS_2$ layer over the ready gold nanoparticles. X-Ray analysis testifies that the resulted coating consists of more pure $CuInS_2$ doped by 20-50 nm gold nanoparticles consisting of 15-20 nm cubic gold crystallites [7].

3.2. Optical properties of samples

3.2.1. Gold over the $CuInS_2$

Formation of gold nanoparticles over the $CuInS_2$ absorber layer was initially aimed to increase the amount of the energy scattered inside the sample from the incident light. In practice such approach works only for the sufficiently big nanoparticles formed from the enough big amount of the gold precursor. Smaller particles absorb more energy themselves than scatter into the $CuInS_2$ layer.

Light absorbance of the samples was obtained from their total transmittance. Plasmonic maximum on the experimental spectra is not very pronounced and situates in the range of 520-550 nm (Fig. 2, curves 2 and 3). Its spectral position and width correspond to the plasmonic light extinction calculated for the comparatively big gold nanoparticles ~ 150 nm (Fig. 3, curve 2), which are visible on the SEM image (Fig. 1).

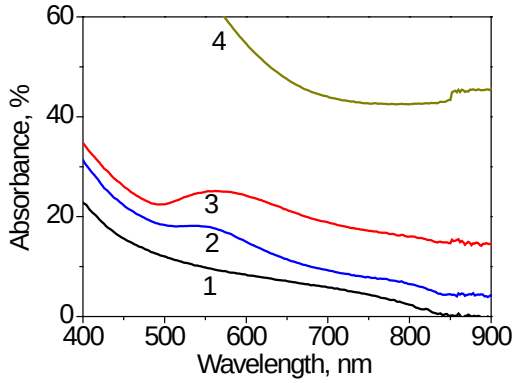

Fig. 2. Optical absorbance spectra of $CuInS_2$ films covered by gold nanoparticles. Amount of used gold precursor is: 1) 0 ml (referent CIS); 2) 2.5 ml; 3) 10 ml; 4)15 ml.

Experimentally measured resonant band with low intensity and significant width of spectral band (Fig. 2, curves 2, 3) can be a result of overlapping of many individual resonances from differently shaped and sized gold nanoparticles quite densely distributed on the surface. As a consequence, rising of light absorbance was detected in the range of all measured wavelengths at big content of gold precursor (Fig. 2, curves 3 and 4).

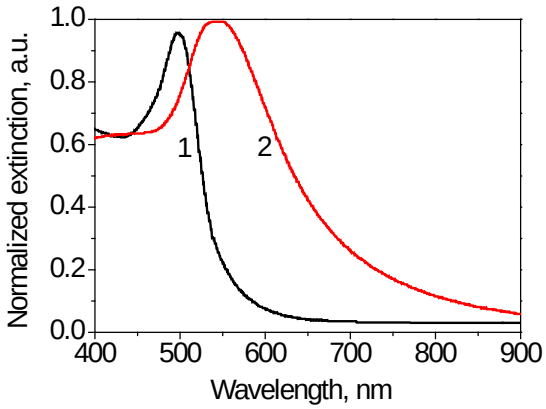

Fig. 3. Calculated normalized extinction cross sections for the gold nanoparticles with sizes: 1) 25 nm, 2) 150 nm.

Thus more dense arrangement of big nanoparticles with low degree of monodispersity can be the reason of stronger background light absorption in case of deposition of bigger amount of gold precursor solution (~15 ml) over the $CuInS_2$ layer (Fig. 2, curve 4).

3.2.2. Gold under the $CuInS_2$

Gold nanoparticles deposited under the $CuInS_2$ layer demonstrated more pronounced plasmonic behaviour. Gold nanoparticles become surrounded by $CuInS_2$ having higher refractive index, plasmon resonance in the experimental spectra of light absorption becomes more pronounced and shifted from 550 nm to 650 nm (see Fig. 4).

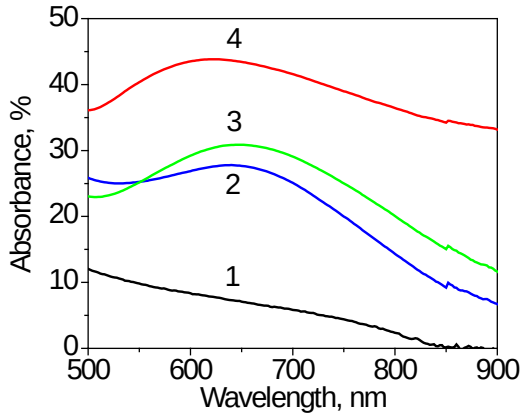

Fig. 4. Optical absorbance spectra of $CuInS_2$ films with embedded gold nanoparticles. Amount of used gold precursor is: 1) 0 ml (referent CIS); 2) 2.5 ml; 3) 5 ml; 4) 15 ml.

It results in plasmonic increase in light absorption by the $CuInS_2$ layer at 600-700 nm up to 2 times (Fig. 4, compare 1 with 2 and 3). Position of the calculated plasmonic light absorption band for the gold nanoparticle immersed into the $CuInS_2$ layer corresponds to the experimental data only at the assumption about the ~25 % porosity of $CuInS_2$ layer. Data calculated at such assumption are corresponding to the experimentally observed red shift of plasmonic resonance band to the 650 nm (Fig. 5). The assumption about porosity of $CuInS_2$ layer looks reasonable, while there is a need in its additional experimental verification. We suppose that plasmonically enhanced electric field near the metal nanoparticle stimulates more effective light absorption in contacting $CuInS_2$ material. Finite element method simulations testified that plasmonic enhancement in $CuInS_2$ light absorption is much higher than unwanted light absorption inside the metal.

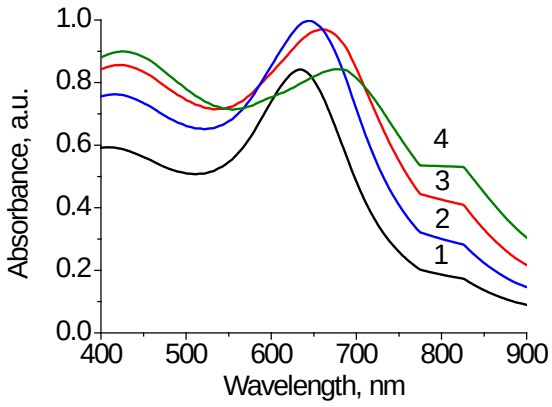

Fig. 5. Calculated optical absorption of gold nanoparticles in the $CuInS_2$ film. Sizes of nanoparticles are: 1) 20 nm; 2) 30 nm; 3) 40 nm; 4) 50 nm. Refractive index of $CuInS_2$ having ~25 % of pores was used for the calculations.

Thus measured near field enhancement of light absorption in the $CuInS_2$ layer in the vicinity of gold nanoparticle could help in more effective light harvesting in the visible/near infrared spectral range 650-700 nm.

The benefit of gold inside $CuInS_2$ film is in the absence of destruction of $CuInS_2$ film by gold precursor.

4. Conclusions

Plasmonically enhanced up to 2 times light absorption in the $CuInS_2$ layer caused by underlying gold nanoparticles was obtained in the spectral range of 650-700 nm. Spraying technique applied for the deposition of gold nanoparticles under the $CuInS_2$ layer turned out more suitable than placement of gold on the top causing undesirable chemical destruction of $CuInS_2$ layer. It was found that 2.5-5 ml of 2 mM gold precursor is an optimal amount resulting in the formation of gold nanoparticles with the size of 20-50 nm giving well defined plasmonic addition to the $CuInS_2$ light absorption. Development of presented technique for the preparation of plasmonic thin film solar cells by spray pyrolysis method is planned.

Acknowledgements

This work was financially supported by the projects: TK114 “Mesosystems: Theory and Applications” (3.2.0101.11-0029), AR12118 “Efficient plasmonic absorbers for solar cells” (3.2.1101.12-0023) and IUT 19-4.

References

[1] A. Polman, H. Atwater, Photonic design principles for ultrahigh-efficiency photovoltaics, Nat. Mater., 11: 174-177, 2012.

[2] H. Atwater, A. Polman, Plasmonics for improved photovoltaic devices, Nat. Mater., 9: 205-213, 2010.

[3] M. Garza et. al., Deposition of gold nanoparticles on glass substrate by ultrasonic spray pyrolysis, Mat. Sci. and Eng. B, 174(1-3): 9-12, 2010.

[4] N. Ramgir et. al., CO sensor derived from mesostructured Au-doped SnO2 thin film, Appl. Surf. Sci. 252(12): 4298–4305, 2006.

[5] N. Tarwal et. al., Spray deposited localized surface plasmonic Au–ZnO nanocomposites for solar cell application, Electrochim. Acta 72: 32– 39, 2012.

[6] K. Otto et. al., Thermal decomposition study of $HAuCl_4 \cdot 3H_2O$ and $AgNO_3$ as precursors for plasmonic metal nanoparticles, submitted to Journal of Thermal Analysis and Calorimetry.

[7] A. Katerski et. al., Modification of light absorption in thin $CuInS_2$ films by sprayed Au nanoparticles, submitted to Microelectron. Eng.

[8] Q. Fu, W. Sun, Mie theory for light scattering by a spherical particle in an absorbing medium, Appl. Optics 40(9): 1354–1361, 2001.

[9] W. Rechberger et al., Optical properties of two interacting gold nanoparticles, Opt. Commun. 220(1–3): 137-141, 2003.

[10] K.-H. Su et al., Interparticle Coupling Effects on Plasmon Resonances of Nanogold Particles, Nano Lett. 3 (8): 1087-1090, 2003.

Nanobiophotonics

Volatile Organic Compounds (VOCs) Detection with Surface Enhanced Raman Scattering (SERS) based on Plasmonic Bimetallic Nanogap Substrate

Chi Lok Wong,[‡ 1] U.S. Dinish,[‡ 1] Kavitha Devi Buddharaju [2] and Malini Olivo* [1, 3]

[1] Bio-optical Imaging Group, Singapore Bioimaging Consortium, Agency for Science, Technology and Research, Helios #01-02, 11 Biopolis Way, Singapore.
[2] Institute of Microelectronics, Agency for Science, Technology and Research, Science Park 2, Singapore.
[3] School of Physics, National University of Ireland, Galway, Co. Galway, Ireland.
‡ Joint first author
*corresponding author, E-mail: malini_olivo@sbic.a-star.edu.sg

Abstract

In this paper, we demonstrate volatile organic compounds (VOCs) detection with surface enhanced Raman scattering (SERS) based on the bimetallic nanogap plasmonic structure fabricated by deep UV photolithography. Measurements on ethanol (5.4%) and acetone (25.4%) vapor have been performed with the SERS VOCs sensing platform and highly reproducible results have been shown. Such system can find promising applications in health care, homeland security, chemical sensing and environmental monitoring.

1. Introduction

Volatile Organic Compounds (VOCs) detection has wide applications and commercial values in different areas, including chemical sensing [1,2], homeland security [3], environmental monitoring [4] and health care [5-7]. In health care, exhaled breath analysis is a powerful tool for the diagnosis of medical diseases [4-6]. It is a non-invasive detection method and it is readily acceptable by patient. Sample collection is easy and even can be obtained from the unconscious patients. VOCs (e.g. acetone, ethane, isoprene ethane, and pentane), inorganic gases (e.g. CO_2, H_2O_2) and non-volatile substances (e.g. isoprostanes, cytokines and nitrogen) are the common composition of human exhaled breath [8, 9]. VOCs and aerosolized particles are produced from the internal surface of lung [10], peripheral human cells and tissues, blood [11] and bacteria or microorganisms [12]. Carbon dioxide (CO_2), hydrogen peroxide (H_2O_2), acetone vapour and ethanol vapour are common breath disease biomarkers [5, 6]. Exhaled acetone and ethanol concentration has been found correlated to plasma glucose level [13] and exhaled acetone is also accepted as the breath biomarker for diabetes [6].

Gas chromatography (GC) system is the most widely using method for VOCs detection and analysis [4-7]. However, the physical dimension of GC is not suitable for on-site detection and the cost of the system is high. Ion-mobility spectrometry (IMS) is another common using method for chemical vapor detection [14]. Nevertheless, it is a destructive measurement technique and cannot be applied for the analysis of VOCs mixtures [14]. Raman spectroscopy provides the vibrational fringerprints of molecular structures [15, 16] for VOCs mixture identification in Raman spectrum. Due to the limited Raman scattering cross section value, the sensitivity of Raman signal is relatively low [15, 16].

Surface plasmon was discovered by Wood at 1902 [17]. He observed a photon-excited electrical resonance phenomenon at small metallic particles. Over the past decades, intensive research works have been on surface plasmon enhanced detection, such as surface plasmon resonance (SPR) [18-32], localized surface plasmon resonance (LSPR) [33, 34], surface plasmon field-enhanced fluorescence spectroscopy (SPFS) [35, 36] and surface plasmon-enhanced Raman scattering (SERS) [15, 16, 39-41]. In SERS, the electric field enhancement occurring at the surface plasmon hot spot of metallic plasmonic nano-structure provides an enhanced Raman signal in a factor of 10^{14} [15, 16, 38]. SERS has been demonstrated for single molecule detection [37], which is considered as the ultimate limit of detection. SERS also provides specific 'fingerprint' chemical information for different VOCs molecules [15]. In this paper, we propose SERS VOCs detection with the bimetallic nanogap plasmonic structure. Detections of acetone and ethanol vapor have been performed. With further development, the SERS VOCs sensor platform can find promising applications in point-of-care VOCs measurement, including on-site breath analysis for diabetes patients [5, 6].

2. Methodology

2.1 Fabrication of bimetallic nanogap plasmonic nanostructure

Deep UV photolithography (DUV) was used to pattern nanostructures on 8inch diameter single crystal p-type Si wafer. In the lithography process, positive photo-resist in 4100Å thick was applied. It followed with a baking step (at 130ºC for 90s) and the puddle development process. A single binary mask with circular patterns was used to generate different sizes of nano-gap structures by varying the exposure dosage form 66, 70, 74 to 78mJ/cm^2. Deep reactive ion etching system was used in silicon etching with SF_6 and C_4F_8 chemistry and the etching depth was about

150nm.The spacing of the nanostructure was controlled by dry oxidation at 900ºC for 2-6h. Then, Ag (30nm) and Au (15nm) plasmonic active layers were deposited subsequently deposited on the nanostructure by e-beam evaporation. A SEM image of the bimetallic nanogap plasmonic nanostructure is shown in Fig. 1.

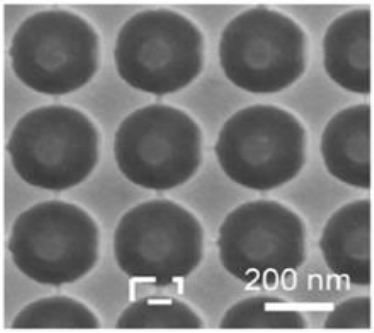

Figure 1: SEM image of the bimetallic nanogap plasmonic nanostructure

2.2 Experimental set-up

A sensor chip with the bimetallic nanogap plasmonic nanostructure was placed in a gas detection chamber for SERS detection. VOCs of acetone or ethanol vapor were generated as described in Fig. 2. During detection, excitation light from He-Ne laser (633nm) was incident on the Ag-Au coated nanostructure through an objective lens (50x, 0.75N.A.) and the surface enhanced Raman spectrum was recorded by a Raman spectrometer (Renishaw InVia). Different gas molecules possess characteristic fingerprint Raman peaks will help in the high sensitivity detection.

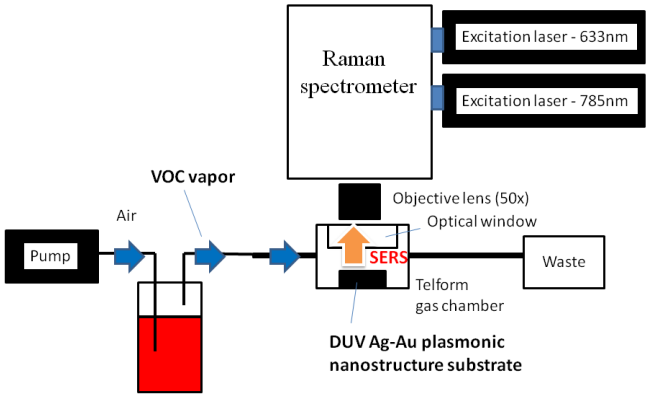

Figure 2: Schematic diagram of the experimental set-up

3. Results and discussion

Acetone vapor was detected with the SERS VOCs sensing platform. A reference spectrum was recorded before the vapor injection. As shown in Fig. 3a, no significant peak was found in the spectrum. After that, acetone vapor at 25.4% was generated and the surface enhanced Raman scattering signal excited at the bimetallic nanogap plasmonic nanostructure was shown in Fig. 3b. A significant peak at 790 cm^{-1} spectral range was observed, which was found correlated to the signature Raman peak of acetone molecule [40].

Cycling detection to acetone vapor has also been demonstrated and the results are shown in Fig. 3a-3d. As shown in Fig. 3c, the 790 cm^{-1} peak was not found in the Raman spectrum after the flashing process with air. However, the 790 cm^{-1} peak was shown in the Raman spectrum (Fig. 3d) when the same concentration of acetone vapor was injected to the surface of the sensing chip again. The cycling detection results reveal the high reproducibility of the SERS technique for VOCs detection.

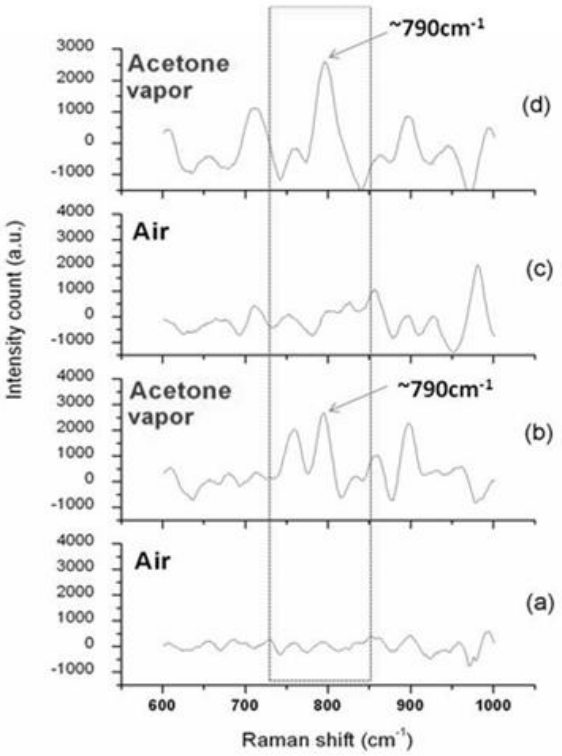

Figure 3: SERS spectra for acetone vapor detection a) Reference spectrum (air) b) Acetone vapor (25.4%) c) Reference spectrum (air) d) Acetone vapor (25.4%).

The sensor platform has further been applied for ethanol vapor detection. Fig. 4a shows the reference spectrum before the injection of ethanol vapor. After that, ethanol vapor at 5.4% was generated and injected to the surface of the bimetallic nanogap plasmonic nanostructure. The result was shown in Fig. 4b. As shown in the Raman spectrum, a peak at 880cm^{-1} spectral range was found, which is correlated with the signature Raman peak of ethanol molecule [40]. The surface of the sensor chip was then flashed with air for the removal of ethanol molecules. As shown in Fig. 4c, the 880cm^{-1} peak was not found in the Raman spectrum after the flashing process.

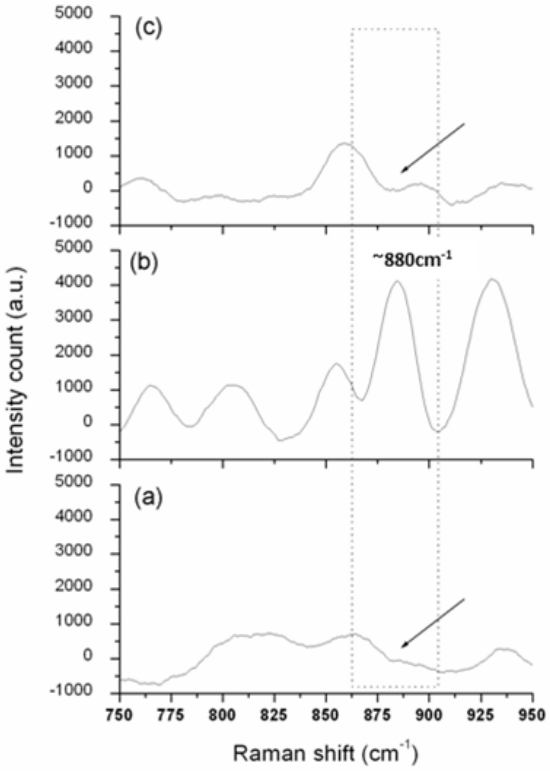

Figure 4: SERS spectra for ethanol vapor detection a) Reference spectrum (air) b) Acetone vapor (5.4%) c) Reference spectrum (air)

3. Conclusions

In this paper, we have successfully demonstrated VOCs detection based on the surface enhanced Raman scattering signal excited at the bimetallic nanogap plasmonic structure. Measurement results on ethanol (5.4%) and acetone (25.4%) vapor are highly reproducible and no chemical sensing layer is required. Such system can find promising applications in health care, homeland security, chemical sensing and environmental monitoring.

Acknowledgements

This work was supported by Singapore Bioimaging Consortium (SBIC).

Reference

[1] W. Zhang, Automotive fuels from biomass via gasification, *Fuel Process. Technol.* 91(8): 866–876, 2010.

[2] D. W. Lachenmeier, R. Godelmann, M. Steiner, B. Ansay, J. Weigel, and G. Krieg, Rapid and mobile determination of alcoholic strength in wine, beer and spirits using a flow-through infrared sensor, *Chem. Cent. J.* 4(1):1-10, 2010.

[3] U. A. Laskay, E. J. Kaleta, and V. H. Wysocki, Methods of Mass Spectrometry in Homeland Security Applications, *Mass Spectrometry Handbook* 7: 419, 2012.

[4] H. C. Menezes, L. C. A. Amorim, and L. C. Zenilda, Sampling and Analytical Methods for Determining VOC in Air by Biomonitoring Human Exposure, *Critical Reviews in Environmental Science and Technology* 43.1: 1-39, 2013.

[5] K. H. Kim, S. A. Jahan, E. Kabir, A review of breath analysis for diagnosis of human health, *TrAC Trends in Analytical Chemistry* 33:1–8, 2012.

[6] M. Zhou, Y. Liu, and Y. Duan, Breath Biomarkers in Diagnosis of Pulmonary Diseases. *Clinica Chimica Acta*, 413 (21-22): 1770-1780, 2012.

[7] T. D. C. Minh, D. R. Blake, P. R. Galassetti, The clinical potential of exhaled breath analysis for diabetes mellitus, *Diabetes Research and Clinical Practice*, 97 (2): 195-205, 2012.

[8] E. Babusikova, M. Jesenak, P. Durdik, D. Dobrota, P. Banovcin, Exhaled carbon monoxide as a new marker of respiratory diseases in children, *Journal of Physiology and Pharmacology* 59.6: 9-17, 2008.

[9] J. D. Pleil, Role of exhaled breath biomarkers in environmental health science, *Journal of Toxicology and Environmental Health* 11.8 (B): 613-629, 2008.

[10] W. Filipiak, A. Sponring, A. Filipiak, C. Ager, J. Schubert, W. Miekisch, A. Amann, J. Troppmair, TD–GC–MS analysis of volatile metabolites of human lung cancer and normal cells in vitro, *Cancer Epidemiol Biomarkers Prev* 19: 182–195, 2010.

[11] H. Xu, D. Song, Y. Cui, S. Hu, Q. W. Yu, Y. Q. Feng, Analysis of hexanal and heptanal in human blood by simultaneous derivatization and dispersive liquid–liquid microextraction then LC–APCI-MS–MS, *Chromatographia* 70: 775–781, 2009.

[12] M. Phillips, V. Basa-Dalay, G. Bothamley, R. N. Cataneo, P. K. Lam, M. P. R. Natividad, Breath biomarkers of active pulmonary tuberculosis, *Tuberculosis* 90: 145–151, 2010.

[13] P. R. Galassetti, B. Novak, D. Nemet, C. R. Gottron, D. M. Cooper, S. Meinardi, R. Newcomb, F. Zaldivar and D. R. Blake, Breath Ethanol and Acetone as Indicators of Serum Glucose Levels: An Initial Report, *Diabetes technology & therapeutics* 7(1): 115-123, 2005.

[14] S. Zimmermann, S. Barth, W. K. M. Baether, J. Ringer, Miniaturized Low-Cost Ion Mobility Spectrometer for Fast Detection of Chemical Warfare Agents, *Anal. Chem.* 80: 6671-6676, 2008.

[15] S. L. Kleinman, R. R. Frontiera, A. I. Henry, J. A. Dieringer, R. P. V. Duyne, Creating, characterizing, and controlling chemistry with SERS hot spots, *Phys. Chem. Chem. Phys.* 15: 21-36, 2013.

[16] B. Sharma, R. R. Frontiera, A. I. Henry, E. Ringe, R. P. V. Duyne, SERS: Materials, applications, and the future, *Materials today* 15 16-25, 2012.

[17] R.W. Wood, A suspected case of the electrical resonance of minute metal particles for light-waves. A new type of absorption. *Proc. Phys. Soc. Lond.* 18:1478, 1902.

[18] C. L. Wong and Malini Olivo, Surface Plasmon Resonance Imaging Sensors: A Review, *Plasmonics*: 1-16, 2014. doi 10.1007/s11468-013-9662-3.

[19] C.L. Wong, G. C. K. Chen, X. Li, B. K. Ng, P. Shum, P. Chen, Z. Lin, C. Lin, M. Olivo, Colorimetric surface plasmon resonance imaging (SPRI) biosensor array based on polarization orientation, *Biosensors and Bioelectrons* 47 545–552, 2013.

[20] C. L. Wong, G. C. K. Chen, X. Li, B. K. Ng, S. Agarwal, Z. Lin, P. Chen, H. P. Ho, Multiplex spectral surface plasmon resonance imaging (SPRI) sensor based on the polarization control scheme, *Optics Express* 19: 18965-18978, 2011.

[21] C. L. Wong, G. C. K. Chen, B. K. Ng, S. Agarwal, N. Fanani, Z. Lin, S. Vasudevan, P. Chen, Photothermal imaging of nanoparticles beyond the diffraction limit, *Optical Engineering* 50: 073201, 2011.

[22] C. L. Wong, H.P. Ho, Y.K. Suen, S.K. Kong, Q.L. Chen, W. Yuan, S.Y. Wu**,** Real-time protein biosensor arrays based on surface plasmon resonance differential phase imaging, *Biosensors and Bioelectronics* 24(4): 606-612, 2008.

[23] C. L. Wong, H. P. Ho, K. S. Chan, P. L. Wong, S. Y. Wu, C. Lin**,** Optical characterization of elastohydrodynamic lubricated (EHL) contacts using surface plasmon resonance (SPR) effect, *Tribology International* 41(5): 356-366, 2008.

[24] C. L. Wong, H. P. Ho, T. T. Yu, Y. K. Suen, W. Y. Chow, S.Y. Wu, W. C. Law, W. Yuan, W. J. Li, S.K. Kong, C. Lin, Two-dimensional biosensor arrays based on surface plasmon resonance phase imaging, *Applied Optics* 46: 2325-2332, 2007.

[25] H. P. Ho, C. L. Wong, S.Y. Wu, W.C. Law, Chinlon Lin and S.K. Kong, Optical sensing devices with SPR sensors based on differential phase interrogation and measuring method using the same, U.S. Patent (2007) Patent no - US2007/0008546 A1.

[26] C. L. Wong, Imaging surface plasmon resonance (SPR) photonic sensors. Doctoral dissertation, City University of Hong Kong, 2007.

[27] H. P. Ho, C.L. Wong, K.S. Chan, S.Y. Wu, C. Lin, Application of 2-D spectral surface plasmon resonance to the imaging of pressure distribution in elastohydrodynamic (EHD) lubricant films, *Applied Optics* 45: 5819-5826, 2006.

[28] C. L. Wong, H.P. Ho, K.S. Chan, S.Y. Wu, C. Lin, Application of surface plasmon resonance sensing to studying elastohydrodynamic lubricant films, *Applied Optics* 44: 4830-4837, 2005.

[29] C. L. Wong, H.P. Ho, K.S. Chan, S.Y. Wu, C. Lin**,** Application of spectral surface plasmon resonance to gas pressure sensing, *Optical Engineering* 44: 124403, 2005.

[30] W. Yuan, H. P. Ho, C. L. Wong, S.Y. Wu, Y. K. Suen, S. K. Kong, C. Lin, Sensitivity enhancement of phase sensitive surface plasmon resonance biosensor using multi-pass interferometry, *IEEE Sensors Journal* 7(1): 70-73, 2007.

[31] W. Yuan, H. P. Ho, C. L. Wong, S.Y. Wu, Y. K. Suen, S. K. Kong, C. Lin, Sensitivity enhancement based on application of multi-pass interferometry in phase-sensitive surface plasmon resonance biosensor, *Optics Communications* 275: 491-496, 2007.

[32] W. W. Lam, L. H. Chu, C. L. Wong, Y. T. Zhang, A surface plasmon resonance system for the measurement of glucose in aqueous solution, *Sensors and Actuators B: Chemical* 105, 138-143, 2005.

[33] K. M. Mayer and J. H. Hafner. Localized surface plasmon resonance sensors. *Chemical reviews* 111(6): 3828-3857, 2011.

[34] M. Estévez, M. A. Otte, B. Sepúlveda, L. M. Lechuga, Trends and challenges of refractometric nanoplasmonic biosensors: a review, *Analytica Chimica Acta* 806:55–73, 2014.

[35] M. Bauch, K. Toma, M. Toma, Q. Zhang and J. Dostalek, Plasmon-Enhanced Fluorescence Biosensors: a Review, *Plasmonics* :1-19, 2013.

[36] K. Toma, M. Vala, P. Adam, J. Homola, W. Knoll, J. Dostálek, Compact surface plasmon-enhanced fluorescence biochip, *Opt Express* 21:10121–10132, 2013.

[37] K. Kneipp, Y. Wang, H. Kneipp, L. T. Perelman, I. Itzkan, R. R. Dasari, and M. S. Feld, Single Molecule Detection Using Surface-Enhanced Raman Scattering (SERS), *Physical Review Letters* 78 (9): 1667, 1997.

[38] K. W. Kho, C. Y. Fu, U. S. Dinish, M. Olivo, Clinical SERS: are we there yet? *Journal of biophotonics* 4(10), 667-684, 2011.

[39] J. Bukowska, P. Piotrowski, *Optical Spectroscopy and Computational Methods in Biology and Medicine*, Springer, Netherlands, pp. 29-59., 2014.

[40] Sacher Lasertechnik^{Group}
http://www.sacherlaser.com/applications/overview/raman_spectroscopy/ethanol.html

Near-field optics and nano-optics

Far-field flat lens based on multilayered metal- dielectric structure

Vladimir Belyi[1], Mohammed Binhussain[2], Nikolai Khilo[1], Nikolai Kazak[1]

[1]Insitute of Physics of NAS Belarus, Minsk, Belarus
[2] The National Center for Building System, KACST, Riyadh, Saudi Arabia
corresponding author, E-mail: v.belyi@dragon.bas-net.by

Abstract

The detailed investigation has been made of the lens effect in plane multilayered metal-dielectric structures (Ag-TiO_2). The optical scheme of the lens has been studied with the radiation focusing in free space. The transfer function is calculated, where the phase profile determines definitely the possibility of focusing. The condition for far-field image formation is found using a flat lens. This condition is used for a numerical simulation of several lens designs with a various number of metal layers. It is found that considered flat lenses have close to limiting angular aperture and therefore the subwavelength resolution. It is established that at increase of a number of metal layers the object and image distances grow.

1. Introduction

One of the most important achievements in optics of metamaterials is to establish the possibility of light focusing by plane-parallel multi-layered metal-dielectric structures [1-3]. Lens effect in such structures is interesting for the optical microscopy, fluorescence imaging, lithography and so on. For a successful application of flat lens further it is necessary to explain not only the physical fundamentals of their functioning, but also to calculate and analyze their characteristics. Flat lenses in this respect differ advantageously from other nanostrucutres such as structures with nanocylinders, because lenses allow accurate calculations. In the study of flat lenses there is no necessity to use approximation of effective permeability or to introduce anisotropy. At the same time the comparison of the results of exact calculation with approximate ones allows one to understand deeper the physical meaning of approximations and to determine the limits of their applicability. Of course, this is important for further use of the approximate methods at calculations of more complex nanostructures.

2. Optical scheme of flat lens

The optical scheme illustrated in Fig.1 will be investigated. Here a layered metal-dielectric (MD) system is illuminated by a divergent light beam from the source located at the distance z_1 from the layered structure. The layered structure consists of several layers of metal and dielectric (in the studied case of Ag and TiO_2). Homogeneous media on both sides of lens in the general case are different (Fig.1b).

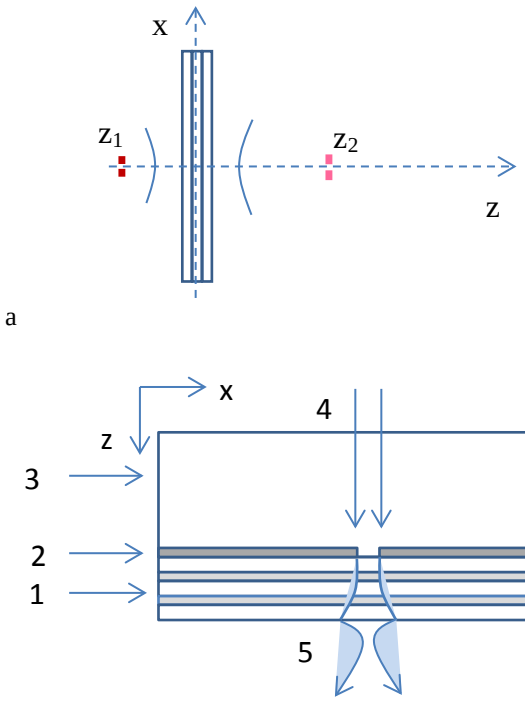

Figure 1. The principal scheme of far-field flat lens (a). The scheme of the lens calculated in the paper (b). Here: 1 – layered metal-dielectric system; 2 – non-transparent coating with one or several apertures; 3 – substrate; 4 – incident light beam; 5 – beam at the lens output.

Under certain conditions, which will be specified hereinafter, MD- system acts as a lens that means that at some distance z_2 source image is formed. The optical scheme of the lens, as it is presented in Fig.1b, makes focusing into free space. That is why the incident field propagates from the side of substrate. To investigated the focusing it is enough to use the scheme with one incident beam, but at calculation of spatial resolution also the scheme can be used with two close apertures, i.e. with illumination of lens by two parallel beams.

Far-field imaging by the lens is realized in a pure form if the source does not create an evanescent field or if distance z_1 is rather large and the evanescent field (at the lens input) disappears. In this case in the image plane the field will not be an evanescent one. The same regime of imaging takes place also when distance z_1 is short, but distance z_2 is large. Fig.1a illustrates also equiphase surfaces within the region of the source and the image. The presence of concave surface (in the image plane) within

the region of the image there is a necessary condition of functioning of lens in the regime of far-field imaging.
Finally, it should be pointed out that unlike conventional optical lenses the most important parameter of flat lenses is their energy efficiency. This is due to the presence of light-absorbing metal layers, number of which can be more than one.

3. Theory

To obtain the quantitative characteristics of flat lens the accurate method based on calculation the transfer matrix (TM) for TH- polarized field will be used. Applied to the vector field, the TM for x- component of electric field and y- component of magnetic field will be calculated. It will allow us to calculate the z- component of Pointing vector and at last the power efficiency of flat lens.
The relation between x- components of input (in) and output (out) electric fields for the flat lens it is possible to represent as

$$E_{\text{out},x}(n_x) = n_{out,z}(n_x)E_{\text{in},x}(n_x)\big/M_{1,1}^{-1}(n_x)\,. \qquad (1)$$

Here the particular case is studied of two-dimensional space of wave numbers (k_x, k_z) and hence the normalized transverse wave number $n_x = k_x/k_0$ is introduced, where $k_0 = 2\pi/\lambda$ and $k_z = k_0\sqrt{\varepsilon - n_x^2}$. $M_{1,1}$ is the component of TM of multilayer.
As it follows from the optical scheme the lens, their TM is a product of three multipliers $M = M_{\text{free1}}M_{ml}M_{\text{free2}}$, where indices (*free*) and (*ml*) relate to free space and multilayer.
The ability of formation of an image by the optical scheme under study is mainly determined by phase function in the relation following from Eq. (1)

$$E_{\text{out},x}(n_x) = t(n_x)\exp(i\varphi(n_x))E_{\text{in},x}(n_x)\,, \qquad (2)$$

If function $\varphi(n_x)$ depends weakly on the transverse wave number and function $t(n_x)$ is rather smooth in comparison with the source field, then the scheme in Fig.1 is considered to be as a flat lens. Let function $\varphi(n_x)$ be in a form of sum

$$\varphi(n_x) = \varphi_{free}(n_x) + \varphi_{ml}(n_x) \qquad (3)$$

where

$$\varphi_{free}(n_x, z_1, z_2) = k_0\sqrt{\varepsilon_{in} - n_x^2}\,z_1 + k_0\sqrt{\varepsilon_{out} - n_x^2}\,z_2 \quad (4)$$

and $\varphi_{ml}(n_x)$ is the phase function of multilayer.
In the Eq (4) the phase function of free space is positive. But it does not follow from it that for compensation of phase incursion phase function of multilayer should be negative. It is only important that function $\varphi_{ml}(n_x)$ increases while n_x becomes larger.
Then the condition of realization of the flat lens has the form

$$\varphi(n_x) \approx \text{const} \qquad (5)$$

The deviation of function $\varphi(n_x)$ from the constant value will be considered as a source of aberrations.

4. Calculation and analysis of specific systems

The simplest experimentally realized system is the layer of metal on the dielectric substrate. Let's study the system SiO_2(substrate)-Ag(20nm)-TiO_2(20nm).

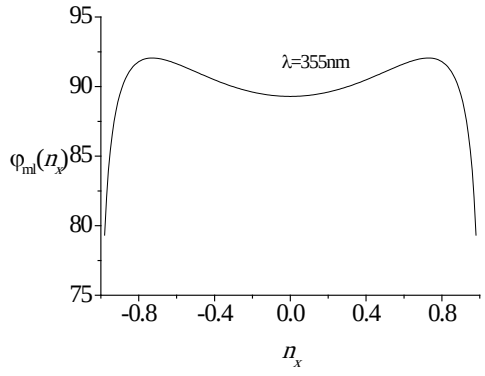

a

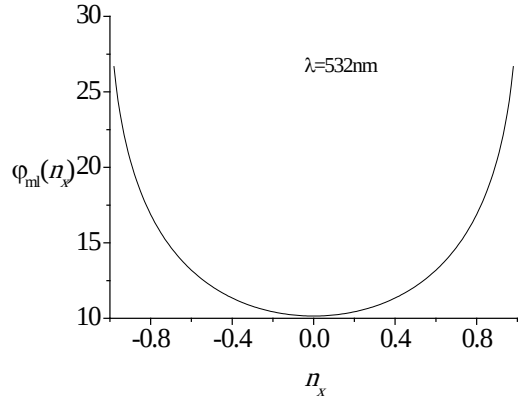

b

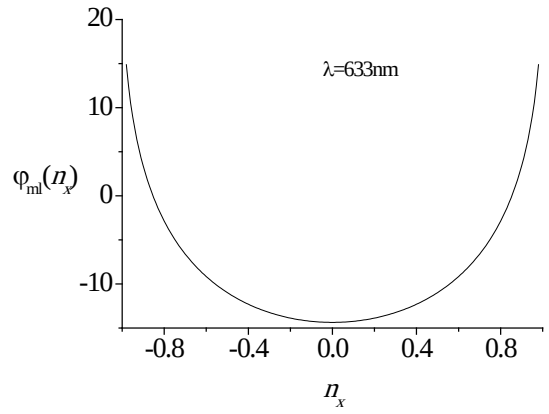

c

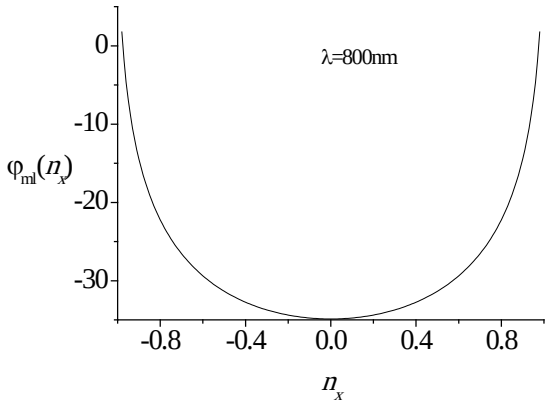

d

Figure 2. Phase functions of multilayer at wavelength λ = 355 nm(a); 532 nm(b); 633 nm(c); 800 nm(d). Here and in all figure the phase is measured in degrees.

As is seen from Fig.2, the phase function of this multilayer is concave almost in all considered cases. Hence the average phase shift decreases with the increase of the wavelength and becomes negative in near IR-region. But in this region the lens is the least energy-efficient.

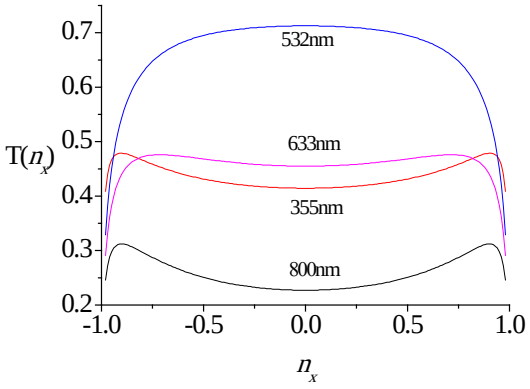

Figure 3. Angular dependence of the transmission coefficient for various wavelengths.

The above-mentioned least energy-efficiency is seen from Fig. 3, which illustrates that the transmission of the lens depends non-monotonically on the wavelength and is rather large for the wavelengths under study, except for λ = 800 nm.

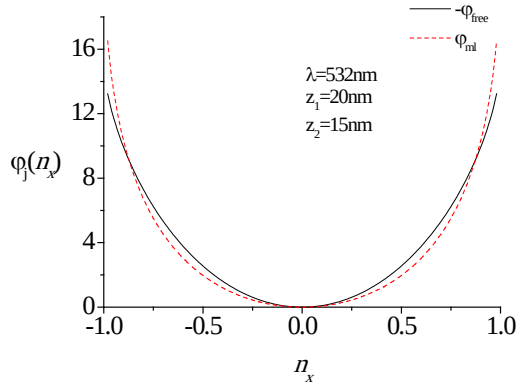

a

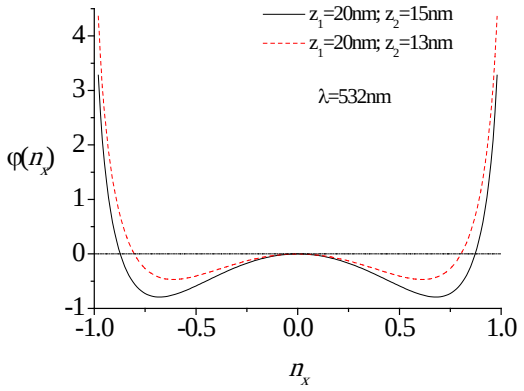

b

Fig. 4 Phase functions $-\varphi_{free}(n_x, 20, 15)$ (solid) and $\varphi_{ml}(n_x)$ (dash) (a) and total phase function $\varphi(n_x)$ (b).

Fig. 4 illustrates the degree of fulfillment of the approximation (5) for the studied scheme. The function $\varphi_{free}(n_x, z_1, z_2)$ can vary due to the change of distances z_1 and z_2, selecting them in such a way that difference of curves in Fig. 4a was minimal. Here the minimal values of both functions have been chosen equal to zero by subtracting the phase incursions at $n_x = 0$. Fig. 4b shows the phase function $\varphi(n_x)$ (Eq. 3). As is seen in Fig. 4, the difference of phase incursion is located within ± 1 degrees except for the extreme regions corresponding to close to grazing incidence. It means the considered lens has close to limiting angular aperture and hence the subwavelength resolution.

It should be also noted that for a given z_1 and slightly different values z_2 the phase distortion produced by the lens has a different character. According to Fig. 4b at change of z_2 from 15 nm up to 13 nm the distortions in the area of low spatial frequencies (SF) decrease and in the area of high SF increase. For full estimation of the quality of focusing in such cases it is necessary to take into account dependence of the lens transmission coefficient on the SF. In the case under the study, as follows from Fig. 3, lens transmission for λ = 532 nm in the area of high SF is sharply decreasing. That is why the phase distortion in this

area can be neglected in first approximation. Fig. 3 shows also that the degree of the fall of transmission function at high SF can depend essentially on the wavelength. So for description of the flat lens it is reasonable to introduce also the parameter of angular aperture $n_{x,\max}$. For example, for the case considered above $n_{x,\max} = 0.975$ in accordance with criterion of fall of transmission function in two times.

At the given parameter $n_{x,\max}$ the value has been investigated of the average phase error, which has been calculated using the formula

$$Err(\lambda, z_1, z_2) = \int_0^{n_{x,\max}} \left|\varphi(\lambda, n_x, z_1, z_2)\right| \mathrm{d}\, n_x \qquad (6)$$

At the given value of z_1 the minimum has been found for this integral depending on z_2. It is detected that the minimal value of integral (6) exists and depends on the magnitude z_1. Hence within the range z_1 from 14 nm up to 22 nm the distances z_1 and z_2 satisfy approximately the simple lens formula $z_1^{-1} + z_2^{-1} = f^{-1}$ with the value f ≈ 7.8nm.

The obtained result, however, has some limitations of the physical character. It is meant that within the range of values z_1 and z_2, pointed above, the far field will not exist in a pure form, because its overlap is possible with the evanescent field.

That is why the task is acute to search the possibilities of increasing the focal distance of such a type of lenses. Apparently, the only solution here is to move to the systems with larger number of layers. Consider for example, the structure Ag-TiO_2-Ag-TiO_2-Ag-TiO_2 on SiO_2 substrate. The individual layer thicknesses are 33, 28, 30, 28, 33 and 10 nm, respectively. Such a structure has been used in paper [5] as unite cell of more complex flat lens. Here layer TiO_2(10nm) is additionally introduced for modeling the protective coating of metal. Unlike [5] here the focusing not in substrate but in air is studied.

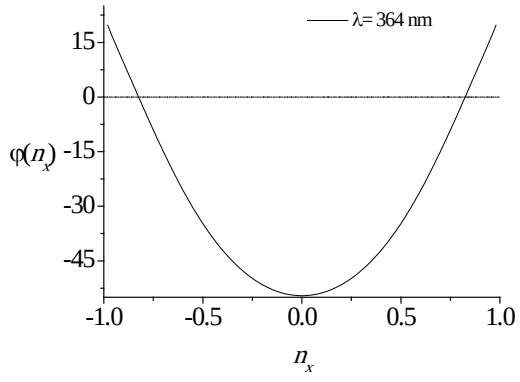

Figure 5. Phase function of the MD- system containing three layers of metal.

Phase characteristic of lens is shown in Fig.5. As is seen, the phase shift of light when passing through the lens is negative, except for small edge areas. But these areas are not essential that follows from Fig. 6 where the angular dependence of transmission of this lens is shown. As was expected, its energy efficiency reduces essentially. Parameter $n_{x,\max}$ here is approximately equal to 0.75.

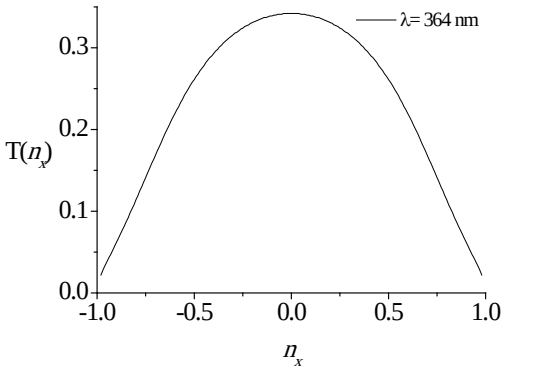

a

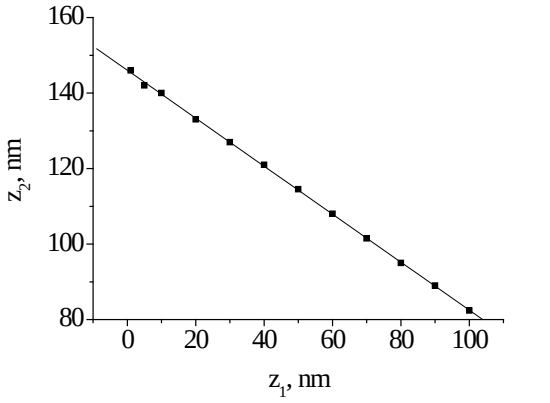

b

Figure 6. Transmission function of flat lens (a). Dependence $z_2(z_1)$ providing the minimum of phase distortion. Wavelength λ = 364 nm.

Further the calculation has been made of lengths z_1 and z_2, at which the phase distortion of lens is minimal. Fig. 6b illustrates dependence $z_2(z_1)$ and its approximation by straight line. The equation of straight line has the form

$$z_2 = tg(\theta)(z_0 - z_1) \qquad (7)$$

Here θ is the acute angle of the line with axis z_1. In the case under study θ is equal to 32.4 degrees, and z_0 = 230nm. The link of these parameters with the characteristics of multilayer is not still clear.

It should be also noted that the obtained before thin-lens-equation is not fulfilled here.

The plots in Fig. 6b shows that object distance z_1 and image distance z_2, as it is supposed, are essentially larger that for MD- lens with single metallic layer.

5. Conclusions

In the paper the description is made of flat lenses consisting of layered MD- structures. The description is based on the application of transfer matrix, which is

calculated numerically. Using the established components of transfer matrix further the transfer function is calculated of the layered structure and its phase characteristics. Also transmission function of lens is established determining its energy efficiency. At the next stage the phase distortion is calculated of flat lens in comparison with ideally imaging lens. From the condition of minimum of phase distortions the function is determined of link between object (z_1) and image (z_2) distances. The particular cases have been studied of layered structures with Ag and TiO_2 as the constituent materials on substrate of SiO_2, which differs by the number of metal and dielectric layers. It is shown that for the lens with a single Ag-layer values z_1 and z_2 are small and located in the region of 10÷20 nm. For lens with three layers of Ag the distances increase up to values of order of 100 nm. This trend is preserved further. Thus, the doubling of the second structures described above, the optimal values of z_1 and z_2 can be equal to 150 nm and 223nm, respectively. However, the transmittance of this lens is small and is at the level of several percents. Moreover, with the increase of the number of layers the phase characteristic of lens is deformed, i.e. phase distortions increase. The decrease of distortions is possible at reduction of the angular divergence of the input field that leads to a reduction in spatial resolution.

In a whole, as the calculations and analysis showed, flat lenses on the basis of layered MD structures are characterized by rather smooth transfer functions, parameters of which can be predictably changed due to the choice of geometric parameters of the layered structure.

Acknowledgements

The authors would like to thank King Abdul-Aziz City for Science and Technology (KACST) for Research Grant No. 814-33.

References

[1] J. B. Pendry. Negative refraction makes a perfect lens, *Phys. Rev. Lett.* 85: 3966–3969, 2000.

[2] S. Durant, Z. Liu, J. M. Steele, and X. Zhang, Theory of the transmission properties of an optical far-field superlens for imaging beyond the diffraction limit, *J. Opt. Soc. Am. B* 23: 2383-2392, 2006.

[3] D. Lu, Z. Liu. Hyperlenses and metalenses for far-field super-resolution imaging, *Nature Communications* 3:1205, 1-9, 2012.

[4] Yeh, P. *Optical Waves in Layered Media*, pp.118–143, Wiley, 1988.

[5] T. Xu, A. Agrawal, M. Abashin, K. J. Chau, H. J. Lezec. All-angle negative refraction and active flat lensing of ultraviolet light, *Nature* 497: 470–474, 2013.

Transformational electromagnetics

Asymmetric Cloaking Theory Based on Effective Electromagnetic Field for Photon

Masato Taki[1] **and Tomohiro Amemiya**[2]

[1]RIKEN Nishina Center for Accelerator-Based Science, Saitama, Japan
[2]Quantum Nanoelectronics Research Center, Tokyo Institute of Technology, Tokyo, Japan
*corresponding author, E-mail: taki@riken.jp, amemiya.t.ab@m.titech.ac.jp

Abstract

In this article, we provide an asymmetric generalization of the invisibility cloak. Our asymmetric invisibility cloak enjoys unidirectional transparency, and therefore a person inside this cloak can not be seen from the outside but can see the outside. Existing method for designing invisibility cloaks are based on the transformation optics [1, 2], and light travels along the geodesics for a given Riemannian metric. Therefore we can not apply this method to asymmetric situation. To overcome this problem, we propose employing tight-binding model to describes the metamaterial which enable us to introduce directionality into invisibility cloaking.

1. Introduction

An invisibility cloak realizes a shielded region that light coming from all quarters circumvents without going through nor reflecting on. Outer onlookers cannot see any object inside this shielded region as if there is nothing in the region. This mans a person will be invisible from the outside once he/she hides in the shielded region. Such devices are designed by using transformation optics. However, a serious, practical problem occurs: the hiding person inside will NEVER see outside since light cannot enters the shielded region. This greatly reduces the practical usefulness of invisibility cloaks.

To overcome this defect, we propose to generalize invisibility cloaking to directional one, that is asymmetric cloaking, to develop a device with unidirectional transparency. For this purpose, we formulate a theory for designing asymmetric cloaking. A person inside the shielded region of our asymmetric cloaking can see out, but other people outside cannot see the person inside. The transformation optics is not useful for this generalization. Our formulation is based on ‘ the theory of effective magnetic field for photons ’ proposed by Stanford University in 2012 [3]. In this paper, extending the Stanford ’ s theory to the concept of ‘ effective electro-magnetic field for photons ’ , we present new method for designing asymmetric cloaking devices in the real world. In the following, we first give a brief review on some background materials. We then explain the concept of effective electro-magnetic field for photons (Sect. 3), and propose the method of asymmetric cloaking based on this concept (Sect. 4), show the trajectory of light simulated for a simple example of asymmetric cloaks.

2. Symmetric Invisibility Cloak: A Review

As is well known, there are two familiar ways to bend optical path: the gravity force and medium configuration. The general relativity, the relativistic theory of gravity, tells us that the gravity force act as a curvature of the space-time, and an object travels along the minimal path in the curved space time. Light consists of coherent ensemble of massless particles, namely photons, and gravity affects on its trajectory. The optical path in a curved space is determined by the following geodesic equation

$$\frac{d^2x^i(s)}{ds^2} + \Gamma^i{}_{jk}\frac{dx^j(s)}{ds}\frac{dx^k(s)}{ds} = 0. \tag{1}$$

Is it possible to realize the same trajectory of light by a certain medium configuration? The answer to this question is yes. The key to the answer is the Maxwell equations which determines the light, that is electro-magnetic field, propagation. The Maxwell equations in a vacuum curved space time take the following covariant form

$$\partial_i(\sqrt{g}g^{ij}E_j) = \frac{\sqrt{g}\rho}{\epsilon_0}, \quad \partial_i(\sqrt{g}g^{ij}B_j) = 0, \tag{2}$$

$$\epsilon^{ijk}\partial_j E_k = \pm\frac{\partial\sqrt{g}g^{ij}B_j}{\partial t}, \tag{3}$$

$$\epsilon^{ijk}\partial_j B_k = \pm\frac{1}{c^2}\frac{\partial\sqrt{g}g^{ij}E_j}{\partial t} + \mu_0\sqrt{g}j^i. \tag{4}$$

On the one hand, the Maxwell equations in a medium are given by

$$\partial_i D^i = \rho, \quad \partial_i B^i = 0, \tag{5}$$

$$\epsilon^{ijk}\partial_j E_k = \frac{\partial B^i}{\partial t}, \quad \epsilon^{ijk}\partial_j H_k = \frac{\partial D^i}{\partial t} + j^i \tag{6}$$

The point is that these two sets of equations are very similar, and by setting the electric permittivities and magnetic permeabilities equal to the metric tensor of the curved space as

$$\epsilon^{ij} = \mu^{ij} = \pm\sqrt{g}g^{ij}, \tag{7}$$

these two take the same form. This means we can realize the optical path in a virtual and curved space time in the

real world by designing a medium with the above electric permittivities and magnetic permeabilities [1, 2].

The problem of this construction is that we need to set the electric permittivities and magnetic permeabilities equal to each other and they cannot have a directionality since the metric tensor of the Riemannian curved space does not depend on direction around a point. To overcome this shortcoming, we employ an another way to bend the optical path: ' the effective electro-magnetic force for photons '. At first sight, this concept sounds very strange because photons does not have the electro-magnetic charges and therefore electro-magnetic fields cannot act on themselves. Actually, this ' effective electro-magnetic force ' is not the genuine one but a virtual effect on the real photons as the virtual gravity force in the transformation medium. In the next section, we demonstrate how such a force is possible to realize.

3. Effective Electric and Magnetic Fields for Photons

3.1. Effective magnetic field for photons

As the starting point of our study, we introduce the notion of 'effective magnetic field for photons' proposed by Stanford University team [3, 4]. The point of this excellent theory is that a lattice configuration of photonic resonators, a sort of metamaterial, can generate a virtual field action on photons that is similar to a magnetic field for moving charged massive particles. Consider a lattice (see Fig. 1(a)) consisting of alternately arrayed two kinds of photonic resonators A and B with resonance frequencies ω_A and ω_B. Let us assume that each resonator has dynamic coupling with its nearest neighbors, and that the coupling strength is modulated harmonically. We can model this system by employing the second quantization scheme, and this model is the tight-binding model with the following Hamiltonian for a photon

$$H = \sum_i \hbar\omega_A a_i^\dagger a_i + \sum_j \hbar\omega_B b_j^\dagger b_j + V \sum_{<i,j>} \cos(\Omega t + \phi_{ij})\left(a_i^\dagger b_j + b_j^\dagger a_i\right), \tag{8}$$

where subscripts i and j label the position of resonators A and B on the lattice system. V is the coupling strength to the nearest neighbors, $\Omega/\hbar$ is the frequency of the coupling modulation, ϕ_{ij} is the relative modulation phase between two adjacent resonators at position i and j. The operators $a_i^\dagger$ and a_i are creation and annihilation operators for resonator A, and $b_j^\dagger$ and b_j are creation and annihilation operators for resonator B. The vacuum state $|0\rangle$ is therefore annihilated by a_i and b_j. This Hamiltonian consists of the free field part, that is composed of two types of harmonic oscillators with the frequencies ω_A and ω_B

$$H_0 = \sum_i \hbar\omega_A a_i^\dagger a_i + \sum_j \hbar\omega_B b_j^\dagger b_j, \tag{9}$$

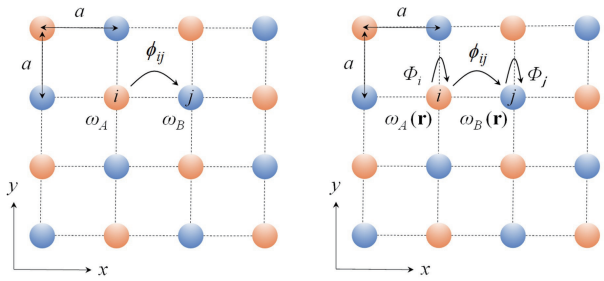

Figure 1: Lattice model for effective electromagnetic field for photon. (a) Magnetic field model. (b) Electromagnetic field model.

and the interaction part whose coupling is controlled by V. Let us move the picture of this quantum system from this Schrödinger picture to the interaction picture. The interaction picture is a hybrid of the Schrödinger picture and the Heisenberg picture, and the time evolution of an operator is given by the free Hamiltonian H_0 and a state evolves by the action of the interaction Hamiltonian. The creation and annihilation operators in the interaction picture are therefore

$$c_i(t) \equiv e^{\frac{itH_0}{\hbar}} a_i e^{-\frac{itH_0}{\hbar}} = e^{-\frac{it\omega_A}{\hbar}} a_i, \tag{10}$$

$$c_j(t) \equiv e^{\frac{itH_0}{\hbar}} b_j e^{-\frac{itH_0}{\hbar}} = e^{-\frac{it\omega_B}{\hbar}} b_j, \tag{11}$$

The Hamiltonian

$$H_I = e^{\frac{itH_0}{\hbar}} (H - H_0) e^{-\frac{itH_0}{\hbar}} = V \sum_{<i,j>} \cos(\Omega t + \phi_{ij})\left(c_i^\dagger(t) c_j(t) + c_j^\dagger(t) c_i(t)\right). \tag{12}$$

Let us assume $\hbar\Omega = \omega_A - \omega_B$ for simplicity. Using the rotational wave approximation then simplifies this Hamiltonian

$$H_I \simeq H_{\text{eff}} = \frac{V}{2} \sum_{<i,j>} \left(e^{-i\phi_{ij}} c_i^\dagger c_j + e^{i\phi_{ij}} c_j^\dagger c_i\right), \tag{13}$$

where this approximation drops the time-depending vibration terms $e^{\pm 2i\Omega t}$. This Hamiltonian consists of the time-independent creation/annihilation operators

$$c_i \equiv c_i(t=0),\ c_j \equiv c_j(t=0), \tag{14}$$

and the coefficients are also time-independent.

The point is that equation 13 has the same form as that of the tight-biding Hamiltonian for an electron in a magnetic field as we will show this fact in the next subsection. This means that the photonic resonator lattice produces a background field acting on the real photons. This field is not a genuine magnetic field but is called an 'effective magnetic field (EfM).' The configuration of EfM can be designed as desired by adjusting the spatial distribution of modulation phase difference ϕ_{ij}. A photon in the EfM background experiences a 'Lorentz-like' force as if it had the electromagnetic charge and felt the magnetic field. We can show this

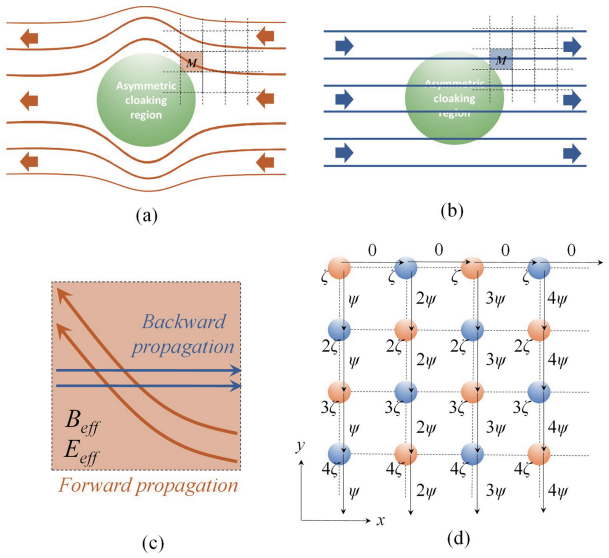

Figure 2: Concept of asymmetric cloaking. (a) Ray trajectory for forward direction. (b) Ray trajectory for backward direction. (c) Photon propagation in local area M. (d) Detail phase information in local area M.

phenomena explicitly by computing the motion of a wave packet of this system with computer simulation. The center of mass coordinate of a wave packet then travels along a circular trajectory.

3.2. Introducing effective electric field for photons

The concept of the EfM is the important key to achieve asymmetric invisibility cloaking. The EfM can break time-reversal symmetry in optics and give a certain extent of asymmetricity to the light propagation. But the EfM is not enough for our purpose since asymmetric cloaking requires a higher asymmetricity in light propagation. For example, as shown later in Sect. 4, forward-propagating light has to avoid and circumvent the cloaking region, whereas backward-propagating light has to go straight and enter the cloaking region. Such a nonreciprocity cannot be achieved only with the EfM.

To resolve this problem, we propose introducing an another background field acting on photons that is an analog of electric field for charged particles. Let us call this field an ‘effective electric field (EfE).’ Employing the EfE in addition to the EfM, we will be able to realize a light ray with high asymmetry. The EfE can be generated as follows, using the photonic resonator lattice.

Let us start with the resonator lattice shown in the previous section. We then make a change such that the resonance frequency of the resonators is not constant but depends on its position labelled by i or j (see Fig. 1(b)). We consider the resonance frequency $\omega_A(i) = \Omega_A + V_A\Phi_i$ for resonator A and $\omega_B(j) = \Omega_B + V_B\Phi_j$ for resonator B. V_A and V_B are frequency parameters, and Φ_i and Φ_j are dimensionless parameters associated with the resonators located at i and j. By adjusting these parameters, the spatial distribution of the resonance frequency can be set as desired. The tight-binding model Hamiltonian for a photon in this system is given by

$$H = \sum_i \left(\hbar\omega_A + V_A\Phi_i\right)a_i^\dagger a_i + \sum_j \left(\hbar\omega_B + V_B\Phi_j\right)b_j^\dagger b_j + V\sum_{<i,j>}\cos(\Omega t + \phi_{ij})\left(a_i^\dagger b_j + b_j^\dagger a_i\right) \quad (15)$$

We set $\hbar\Omega = \omega_A - \omega_B$ as in Eq. 13. Using the interaction picture and rotational wave approximation simplify the Hamiltonian into

$$H_{\text{eff}} = \frac{V}{2}\sum_{<i,j>}\left(e^{-i\phi_{ij}}c_i^\dagger c_j + e^{i\phi_{ij}}c_j^\dagger c_i\right) + \sum_i V_A\Phi_i c_i^\dagger c_i + \sum_j V_B\Phi_j c_j^\dagger c_j, \quad (16)$$

and the time-evolution of this system then obeys the Tomonaga-Schwinger equation for the Hamiltonian. The point here is that Equation 16 has the same form as that of the tight-binding Hamiltonian for a charged particle in an electro-magnetic background field [5]. The first term of the right-hand side corresponds to the motion of a photon introduced by the EfM introduced by the Peierls substitution [6]. The second and third terms lead to the motion induced by the EfE. The magnitude and direction of the EfE are controlled by the parameters V_A, V_B, Φ_i and Φ_j. A photon under the EfE experiences a ‘Coulomb-like’ force as if it is a charged massive particle. In this way, we can generate the EfE in addition to the EfM, employing the photonic resonator lattice.

4. Asymmetric Invisibility Cloaking using Effective Electric and Magnetic Fields

Dealing with a simple example, we illustrate our method for designing the asymmetric invisibility cloaks by making use of the EfE and the EfM. The procedure for designing is as follows.

Step 1: Designing the directed optical path for asymmetric cloaking

The first step is to decide what kind of asymmetric cloaking we need and draw the directed optical path diagram for the wanted cloaking. For example, let us consider a asymmetric cloaking device such that its wearer, when looking toward spectators, can see them but cannot be seen from them. In more detail, consider a specific cloaking device such that

(i) the device has a spherical cloaked region with forward-backward directionality, and its wearer directs the forward direction toward the spectators,

(ii) the wearer can see the spectators clearly, whereas the spectators can see only the background behind the wearer and cannot see the wearer itself.

For such unidirectional transparency, the device has to direct incident light to take a different path depending on the direction of incident light ray. Figures 2(a) and 2(b) illustrate the desired optical path on a plane passing through

the optical axis of the system. In this figures, the forward direction of the device is left-to-right, and spectators are on the right side of the device. The directional propagation of light we need is:
(a) forward-propagating light (left arrows in Fig. 2(a)) circumvents the cloaked region and return undisturbed to its original trajectory so that a wearer in the cloaked region will be invisible to the spectators on the right,
(b) backward-propagating light (right arrows in Fig. 2(b)) proceeds undisturbed so that the wearer in the cloaked region can see the spectators on the right.

Step 2: Directing light to follow the designed optical path

Next thing to do is to divide the space surrounding the cloaked region into small local regions and consider the propagation of light inside each local region. Let us take a local region denoted by M in Figs. 2(a) and 2(b) for example. In this region, as illustrated in Fig. 2 (c), forward-propagation photons (red arrows) need to deviate downward from usual path, whereas backward-propagating photons (blue arrows) need to travel straight without deflection. If propagating quanta were electrons, such propagation could be realized by introducing a magnetic field in the z direction and an electric field in the y direction, with appropriate magnitudes. For photons, the same propagation can be realized by a z-directed EfM and a y-directed EfE instead of a real magnetic and an electric field. For this purpose, we consider a photonic resonator lattice in region M and tune the parameters of the lattice system appropriately so that photons will travel along the directed optical path shown in Fig. 2(c). The whole cloaking device is built by putting a photonic resonator lattice configuration on every local region and adjusting the parameters of each region so that the local optical paths will be connected into the whole optical path illustrated in Figs. 2(a) and 2(b).

In order to create an z-directed EfM and an y-directed EfE in a resonator lattice, we tune the parameters ϕ_{ij} and Φ_j of the lattice as follows (see Fig. 2(d)). The parameter ϕ_{ij} is proportional to the column index and increases by ψ when a index increases one. Vertically adjoining lattice points on the same column share a same value of ϕ_{ij}, and ϕ_{ij} is equal to 0 for horizontally adjoining ones . The parameter Φ_j is proportional to the row index and increases by ζ when a index increases one, and equal between the resonators on the same row.

The lattice spacing a is sets sufficiently smaller than the dimension of local region in order to deal with the system in a continuum approximation. For simplicity, we assume a few relations between the parameters such as $V_A = V_B$. Under this condition, the magnitude B_{eff} of the z-directed EfM is given by

$$B_{\text{eff}} = \tfrac{1}{a^2} \oint \vec{A}(\vec{X}) \cdot d\vec{X}, \tag{17}$$

$$\tfrac{2\pi}{\phi_0} \int_{\vec{X}_i}^{\vec{X}_j} \vec{A}(\vec{X}) \cdot d\vec{X} = \phi_{ij}, \tag{18}$$

where $\phi_0 = hc/e$ is the quantum unit of magnetic flux. The magnitude E_{eff} of the y-directed EfE field is given by

$$E_{\text{eff}} \left(\tfrac{\vec{X}_k + \vec{X}_\ell}{2} \right) = -\tfrac{\varphi(\vec{X}_k) - \varphi(\vec{X}_\ell)}{a}, \tag{19}$$

$$\varphi(\vec{X}_k) = \tfrac{\hbar^2 V_A}{mea^2 V} \Phi_k, \tag{20}$$

where k and ℓ are adjoining two lattice points. The scalar potential for EfE is given by φ.

Under these EfM and EfE, a photon travels as if it was a charged massive particle with mass m in a magnetic and an electric field whose magnitudes are given by Beff and Eeff. Surrounding the cloaked region with many resonator lattices yields an appropriate spatial distribution of EfE and EfM around the cloaked region, thereby controlling the propagation of photons to realize asymmetric cloaking.

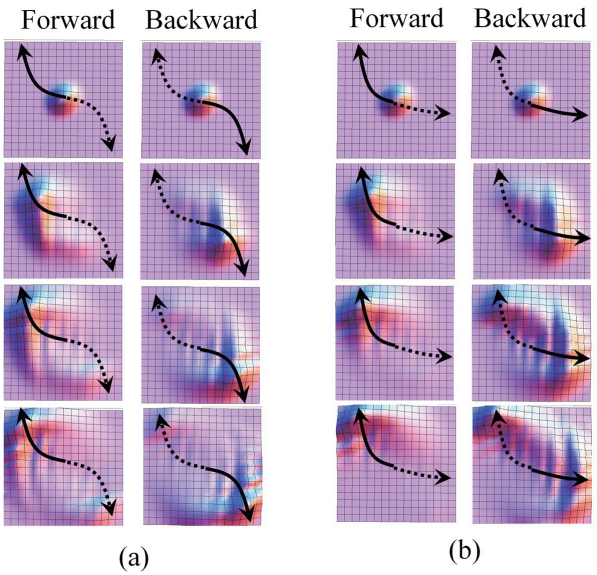

Figure 3: (a) Ray trajectory under effective magnetic field for photon. (b) Ray trajectory under effective electromagnetic field for photon.

Step 3: Simulating the unidirectional movement of photons to determine lattice parameters

Our final task is to determine appropriate parameter values for each resonator lattice to achieve a desirable optical path in the lattice. This can be performed with the aid of computer simulation. This lattice system has several parameters including ψ and ζ, and in this study we found their optimal values simply with exhaustive search technique, though there might be a more efficient method of searching.

To see the forward and the backward optical path in a given local region, we put a photon wave packet in the center of the local region and simulated its time-evolution. In our simulation, we consider the Tomonaga-Schwinger equation for the Hamiltonian Eq. 15 with an initial Gaussian wave packet state of a photon. Figure 3 shows an example of the time evolution of the photon wave packet for forward and backward traveling, simulated under the specific choice of the parameters $\psi = 0.3, \zeta = 0.3, V = 3$, and

$V_A = V_B = 2$ or 0. Figure 3(b) shows the time-evolution under a EfM and a EfE ($V = 3$ and $V_A = V_B = 2$) and Fig. 3(a) under only an EfM ($V = 3$ and $V_A = V_B = 0$). In these figures, the shape of the wave function on the lattice system is visualized with colored amplitude imaging. The center of mass position of the wave packet moves as the wave propagates, and its movement describes the light ray associated with the photon (a solid arrow describes the trajectory of the photon). An incident photon experiences a ' Lorentz-like ' and a ' Coulomb-like ' force and shows asymmetric movement depending on its propagation direction.

5. Conclusions

In summary, we demonstrated the new procedure for designing actual invisibility cloaks with asymmetry utilizing the photonic resonator lattice and confirmed their operation with the aid of computer simulation. A point in our analysis is the tight-binding model description of the photonic resonator lattice system, and this scheme enables us to construct systematically a ' Lorentz-like ' and a ' Coulomb-like ' force acting on photons. The EfM then breaks the time-reversal symmetry of the system, and then it leads to the desirable hight asymmetry of the cloaking device.

References

[1] J. B. Pendry et al., *Science* 312, 1780 (2006).

[2] U. Leonhardt, *Science* 312, 1777 (2006).

[3] K. Fang et al., *Nature Photon*. 6, 782 (2012).

[4] K. Fang et al., *Phys. Rev.* A 88, 043847 (2013).

[5] M. Graf et al., *Phys. Rev*. B 51, 4940 (1995).

[6] R. Peierls, *Z. Phys*. 80, 763 (1933).

Photonic crystals

Study on Modulating Properties of Magnetic Defect in Photonic Crystal in Terahertz Region

Hui Zhang[1]*, Xian-feng Xu[1], Sheng-jiang Chang[2], Cuiping Jia[1], Zhi-yong Jiao[1]
[1]College of Science, China University of Petroleum (East China), Qingdao, China
[2]Institute of Modern Optics, Nankai University,Tianjin, China
*corresponding author, E-mail: zhanghuizxh@126.com

Abstract

The resonance mode properties of the ferrite defect in photonic crystal in terahertz region are studied by using the finite difference time domain method. The results indicate that the resonance modes of the point defect exist with certain structures and change in large frequency domains(1.14THz-0.91THz and 0.99THz-0.9THz) when the permeability of ferrite material changes with external magnetic field . Furthermore, the transmission spectra and modulating properties of the ferrite defect coupled with photonic crystal waveguide are simulated. Controlled by the external magnetic field, the central frequency of the defect mode spectra with narrow bandwidth (about 0.017THz) change from 0.917THz to 0.993THz. These results provide a useful guide and a theoretical basis for the developments of terahertz modulation and tunable filtering.

1. Introduction

In recent years, terahertz (THz) technology and its applications have made great progress in many fields such as THz sensing, imaging, spectroscopy, and communication [1-6]. For the construction of compact application systems, THz functional devices such as THz modulators, filters, and phase retarders are indispensable. Among these devices, artificial structural materials including metamaterials and photonic crystals (PCs) have proved to be effective way to transmit and control THz waves[7-14]. Especially, in PC the changing of dielectric constant of materials and structure of the PC make the devices tunable. For example, Ghattan et al. [15] demonstrated the high density polyethylene (HDPE) PC with air holes filled with liquid crystal (LC) can be used as a switch with the extinction ratio of 13.3dB at 91GHz. Ying Li[16] have shown an omnidirectional reflector and a tunable filter by using the dielectric constant temperature sensitive semiconductor material InSb as a one dimensional photonic crystal defect. L. Fekete et al [17]proposed a narrowband modulation by using femtosecond laser pumped GaAs as defect of one dimensional photonic crystal. Overall, the devices are tunable mainly dependent on the dielectric constant changed by temperature, external electric or magnetic field and laser pumping. However, the modulating depths are limited by the tunable bandwidth of the materials. For example the laser pumping semiconductor with refractive index tunable within 0.02. Recently several reports on the electro- magnetic parameters of ferrite materials have shown that some kinds of ferrites have small absorption loss, which indicate that the ferrite is a kind of promising materials for the THz wave[18,19]. Moreover, some devices using ferrite materials have been designed and fabricated for the THz wave[20,21].

In this paper, according to the magnetic control mechanism of ferrite material LuBiIG in the THz regime, we proposed a tunable narrowband filter by using the ferrite material as point defects in PC. The bandgaps as well as the transmission and local properties of the ferrite point defect are investigated. The operating frequency of this narrow band filter can be broadly tuned by changing the external magnetic field . Moreover, we find a great transmission enhancement through this device for THz modulation and tunable filtering.

2. Material properties

The analyzed structure is shown in Fig. 1. The uniform in *z*-direction circular high-resistance silicon rods are oriented along the z axis. The space between the rods is filled with air. They form a square lattice in the plane *xy*. Then, a point defect of ferrite rod is produced by replacing a silicon rods. The magnetized LuBiLG ferrite rods is a tensor of the second rank $\overleftrightarrow{\mu}$ and the permittivity is a scalar ε_0 of 4.85[22]. A uniform dc magnetic field H_0 is applied to the crystal along z axis. Fully magnetized under the external static magnetic, the ferrites have a tensor relative permeability in the following form [24]:

$$\overleftrightarrow{\mu} = \begin{bmatrix} \mu & j\kappa & 0 \\ -j\kappa & \mu & 0 \\ 0 & 0 & \mu_0 \end{bmatrix} \quad (1)$$

The tensor element μ and κ are given by

$$\mu = \mu_0\left(1+\frac{\omega_{ex}\omega_m}{\omega_{ex}^2-\omega^2}\right) \quad (2)$$

$$\kappa = \mu_0\frac{\omega\,\omega_m}{\omega_{ex}^2-\omega^2} \quad (3)$$

where $\omega_{ex}=\gamma B_{ex}, \omega_m=\gamma\mu_0 M_s$, γ is the gyromagnitic ratio of 1.758×10^{11} rad/Ts, μ_0 is the permeability in the vacuum, ω is the circular frequency of the incident THz wave, B_{ex} is the external mag-netic flux density, and M_s = 1560 G is the saturation magnetization of ferrite materials. Yang et al. [19,23] measured the absorption

coefficient of LuBiIG single crystal with less than 0.3 cm−1 in the range of 0.2–1 THz by THz-TDS. The electro-magnetic parameters of LuBiLG used in the calculation come from these references. Because the magnetic field of the transverse magnetic (TM) wave does not interact with the magnetic dipoles of the ferrite, the permeability is μ_0. On the contrary, the magnetic field direction of the transverse electric (TE) wave is perpendicular to the external magnetic field which causes the movement of the magnetic dipole. Generally, the permeability for TE wave in the structure cannot be simply modeled by an effective isotropic medium with the permeability of a scalar value. However, For ellipsoids in a uniform external magnetic filed H_0, the magnetization in the saturated regime is uniform. Infinitely long cylinders are a particular case of ellipsoids, therefore the magnetization of them is also uniform. Thus, in this case the parameters of $\overleftrightarrow{\mu}$ are constant inside the ferrite elements. The permeability for TE wave can be calculated by Eq. (2). So the refractive index $n = \sqrt{\varepsilon\mu}$ will change in the range of 2.4–3.2[24].

3. Defect modes analysis

The analyzed structure is shown in Fig. 1. The uniform in z-direction circular high-resistance silicon rods are oriented along the *z* axis. The space between the rods is filled with air. They form a square lattice in the plane *xy*. The lattice constant *a* is 100μm. And the fill factor *r/a*=0.2,where *r* is the radius of the silicon rod. Then, a point defect of ferrite rod is produced by replacing a silicon rods. (the gray rod in Fig.1) The high-resistance silicon has a scalar permeability μ_0 of 1 and a scalar permittivity ε_0 of 11.7[25]. A uniform magnetic field H_0 is applied to the crystal along z axis. The permeability of the ferrite rods for TE wave is changed by the external field. So the refractive index for LuBiLG will change in the range of 2.4–3.2[24].

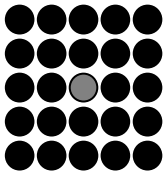

Fig. 1 2-dimension square lattice of circular cross-section silicon rods with one ferrite rods as defect.

The defect mode of the ferrite is the key for controlling the transmitting of THz wave. The defect mode can change with the refractive index and the radius of the ferrite rod. we analyze the bandgap and point defect mode change with the radius of ferrite rod. In the TE mode, the magnetic field of the mode is perpendicular to the external magnetic field, and thus it induces a precession of magnetic dipoles around the external field at the mode frequency. Therefore, we simulated the TE mode properties.

We study the influence of radius of the ferrite defect rods on the TE mode bandgaps. Fig. 2 shows the bandgap of photonic crystal with the radius of ferrite defect (expressed as Raduis1) when the refractive index of ferrite is 2.4 without external magnetic field applied. Fig. 3 shows the bandgap of photonic crystal with the radius of ferrite defect when the refractive index of ferrite is 3.2 with large external magnetic field applied. In fig. 2, the normalized frequency ($\omega a/2\pi c$) range of 0.28-0.42 (corresponding to 0.84-1.26THz) is the PC bandgap and the curves in the gap is the cavity defect mode. Obviously, there is no defect mode when the radius of ferrite rod is in the range of 28-33μm. And the defect mode frequency becomes lower from0.36-0.28(0.84-1.08THz) when the radius vary from 10μm to 28μm. The defect mode frequency decrease from 0.42-0.34(corresponding to 1.02-1.26THz) when the radius vary from 28-50μm. In figure 3, the radius range without defect mode existing is from 17μm to 26μm. Therefore, the radius of the ferrite rod should be within 10-17μm and 33-50μm, which make sure that the defect modes exist and vary with external magnetic field.

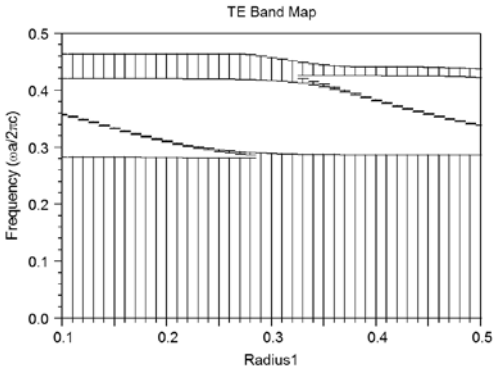

Fig. 2 The defect modes vary with the radius of ferrite defect when there is no external magnetic field applied.

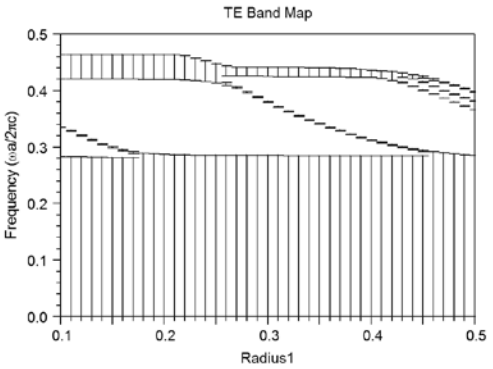

Fig. 3 The defect modes vary with the radius of ferrite defect when there is large external magnetic field applied.

Fig. 4 and fig. 5 shows the defect modes vary with the refractive index difference between the ferrite rod and air background when the defect radius is 15μm and 40μm, respectively. Obviously, in fig.4 the normalized frequency of the defect mode changes from 0.335 (1.02THz) to 0.30 (0.9THz) with the refractive index of ferrite controlled by the external magnetic field. And in fig.5,with the dielectric constant increasing, the frequency of the defect mode

gradually declines from 0.38(1.14THz) to 0.31(0.93THz). Overall, the defect modes have large tunable range with the external magnetic field at both cases.

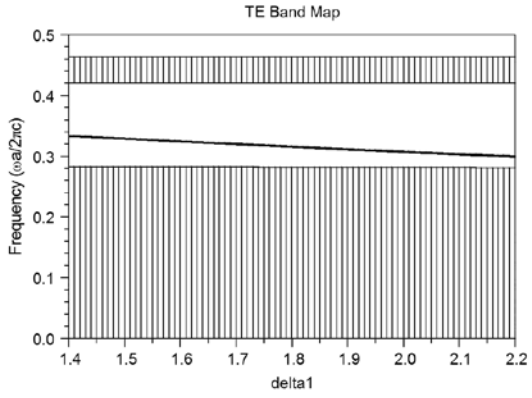

Fig.4 The bandgaps vary with the refractive index of the ferrite defect with radius 15μm

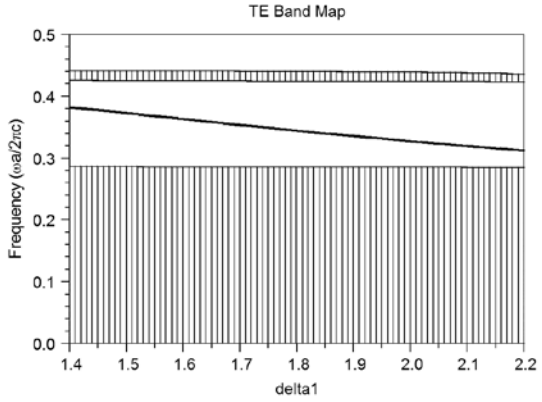

Fig.5 The bandgaps vary with the refractive index of the ferrite defect with radius 40μm

The bandgap characteristics of the ferrite defect PC determine propagation characteristics of a THz wave. Therefore, calculations of the propagation characteristics of the PC would be interesting in a way to show the modulating functions of the ferrite material. Therefore, we simulated the THz transmission spectra in the silicon photonic crystal waveguide including a ferrite defect. The structure is described in fig.6. A wideband THz wave is guided in the PC waveguide. Two waveguide monitors are settled in the output of the waveguide and the ferrite defect, respectively. A tunable external magnetic field is applied along the axial direction of the ferrite rod.

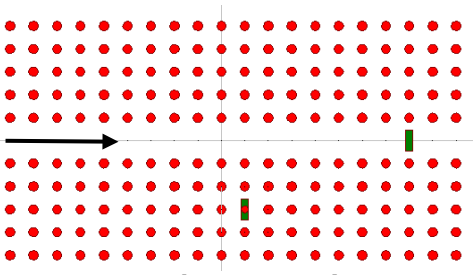

Fig.6 the transmission photonic crystal stucture

The transmission spectra and the defect mode in the defect are shown in fig.7. The dotted line is the transmission spectra in the output of the waveguide. Large bandwidth THz wave ranging from 2.3-3.3 (corresponding to 0.909THz-1.304THz) are transmitted in the waveguide. The dashed line is the spectra for the case of B = 0T, in which the refractive index of ferrite rod is corresponding to 2.4. The THz wave with normalized wavelength(λ/a) at about 3.01(corresponding to 0.997THz) is coupled into the ferrite defect, which well coincides with the description of the defect mode frequency shown in fig. 5. The spectra of the defect mode has a relative high peak and a narrow bandwidth in the range of 3.05-2.98 (0.984THz - 0.1001THz), which means a high cavity quality factor. The solid line is the spectra for the case of larger magnetic field, in which the refractive index of ferrite rods is 3.0. Obviously, the defect spectra peak moves to the lower frequency with central normalized wavelength at 3.27(corresponding to 0.917THz). The electromagnetic field distributions in the defect for an incident TE polarized THz wave at 0.917 THz are calculated and illustrated in fig. 8. Obviously, the energy of the THz wave can be located in the defect. Overall, the defect mode spectra are in good agreement with the analysis on the bandgaps.

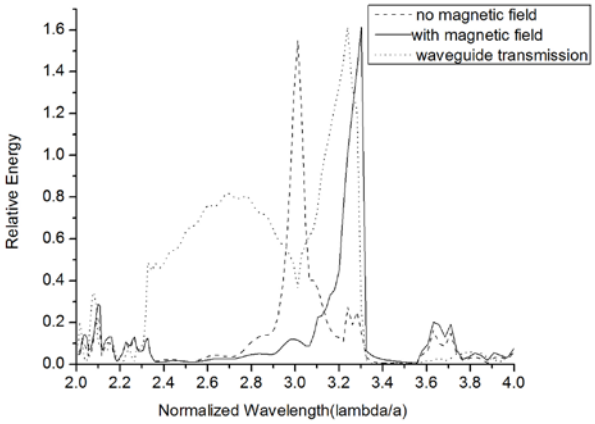

Fig.7 the transmission spectra

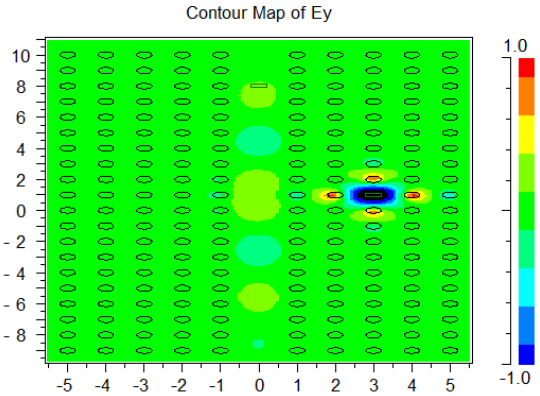

Fig.8 the electromagnetic field distributions in the defect

4. Conclusions

In conclusion, the transmission resonance modes modulating properties of a photonic crystal ferrite defect have been investigated in the terahertz regime. The numerical simulations show that the defect modes exist when the radius of the ferrite rods are in the range of 10 -17μm and 33-50μm. According to the mode analysis, the resonance frequency of the ferrite defect changes in a large domain (1.14THz-0.93THz and 1.02THz-0.9THz) with the external magnetic field. Finally, we show the transmission and modulating properties of the ferrite defect coupled with photonic crystal waveguide. These results provide a useful guide and a theoretical basis for the developments of THz modulation and tunable filtering.

Acknowledgements

This work is supported by the Fundamental Research Funds for the Central University (Grant no. 14CX02020A, 12CX04088A).

References

[1] J Liu, J Dai, S L Chin, X.-C. Zhang, "Broadband terahertz wave remote sensing using coherent manipulation of fluorescence from asymmetrically ionized gases," *Nature Photonics* vol. 4, pp. 627 – 631, 2010.

[2] T Hu, A. K Emil, C. S Andrew, et al, "Microwave and Terahertz wave sensing with metamaterials," *Opt. Express*, vol.19, no. 22, pp. 21620-21626, 2011.

[3] K B Cooper, R J Dengler, G A Chattopadhyay, "High resolution imaging Radar at 580 GHz," *IEEE Microwave and Wireless Components Letters*, vol. 18, no. 1, pp. 64-66, 2008.

[4] T Nagatsuma, S Horiguchi, Y Minamikata, et al, "Terahertz wireless communications based on photonics technologies," OPTICS EXPRESS , vol. 21, no. 20, pp. 23736-23747, 2013.

[5] J Liu and X C Zhang, "Enhancement of laser-induced fluorescence by intense terahertz pulses in gases," *IEEE J. Sel. Topics Quantum Electron.*, vol. 17, no. 1, pp. 229-236, 2011.

[6] Q. Chen and X.-C. Zhang Semiconductor Dynamic Aperture for Near-Field Terahertz Wave Imaging *IEEE J. Sel. Topics Quantum Electron.*, vol. 7, no. 4, 608-614, 2001

[7] D Shrekenhamerd, S Rout, A C Strikwerda, et al, "High speed terahertz modulation from metamaterials with embedded high electron mobility transistors," Opt. Express, vol. 19, no.10, pp. 9969-9975, 2011.

[8] T Kleine-Ostmann, M Koch, and P Dawson, "Modulation of THz radiation by semiconductor nanostructures," Microwave Opt. Technol. Lett., vol. 35, no.5, pp. 343-345, 2002.

[9] A L Bingham, D R Grischkowsky, "Terahertz 2-D photonic crystal waveguides," IEEE Microwave and Wireless Comp. Lett., vol.18, no.7, pp. 428-430, 2009.

[10] N Krumbholz, K Gerlach, M K Rutz, "Omnidirectional terahertz mirrors: A key element for future terahertz communication systems," Appl. Phys. Lett., vol. 88, no. 20, pp. 202905-202907, 2006.

[11] W L Zhang, A K Azad, and J Han, J Xu, J Chen, and X C Zhang, "Direct observation of a Transition of a surface plasmon resonance from a photonic crystal effect," Phys. Rev. Lett. ,vol. 98, no. 18, pp. 183901-183904, 2007.

[12] Y S Kim, S Y Lin, H Y Wu, et al, "A tunable terahertz filter and its switching properties in terahertz region based on a defect mode of a metallic photonic crystal," J. Appl. Phys., vol. 109, no. 12, pp. 123111-123114, 2011.

[13] J S Li, S Zouhdi, "Ultrafast and low-power terahertz wave modulator based on organic photonic crystal," Optics communications, vol. 285, no. 6, pp. 953-956, 2012.

[14] H Nemec, P Kuzel, L Duvillaret, et al., "Highly tunable photonic crystal filter for the terahertz range," Opt. Lett., vol. 30, no. 5, pp. 549-551, 2005.

[15] Z Ghattan, T Hasek, R Wilk, et al., "Sub-terahertz on–off switch based on a two-dimensional photonic crystal infiltrated by liquid crystals," Opt. Comm., vol. 281, no. 18, pp. 4623-4625, 2008.

[16] X Li, Y J Xiang, S C Wen, et al., "Tunable terahertz-mirror and multi-channel terahertz-filter based on one-dimensional photonic crystals containing semiconductors," J. Appl. Phys., vol. 110, no. 7, pp. 073111-073116, 2011.

[17] L Fekete, F Kadlec, P Kuzel, and H Nemec, "Ultrafast opto-terahertz photonic crystal modulator," Opt. Lett., vol. 32, no. 6, pp. 680–682, 2007.

[18] Q H Yang, H W Zhang, L Y Li, Q Y Wen, J Zha, "An artificially garnet crystal materials using in terahertz waveguide," Chinese Physics Letters, vol. 25, pp. 3957-3960, 2008.

[19] Q Y Wen, H W Zhang, H Q Yang, S Li, D G Xu, J Q Yao, "Fe-Doped Polycrystalline CeO2 as Terahertz Optical Material," Chinese Phys. Lett. vol. 26, no. 4, pp. 047803, 2009.

[20] Fei Fan, Sheng-JiangChang, ChaoNiu, YuHou, Xiang-HuiWang, Magnetically tunable silicon-ferrite photonic crystals for terahertz circulator, Optics Communications, vol. 285, pp. 3763–3769, 2012.

[21] Y J Yang, Y J Huang, G J Wen, J P Zhong, H B Sun, and O Gordon, "Tunable broadband metamaterial absorber consisting of ferrite slabs and a copper wire," Chin. Phys. B. vol. 21, no. 3, pp. 038501-038505, 2012.

[22] B D Cullty, C D Graham, "Introduction to magnetic materials," 2nd ed., Wiley & Sons, New Jersey, pp. 435–436, 2009.

[23] Q H Yang, H.W. Zhang, LY Li, Q Y Wen, Y L Liu, I M Syvorotka, I I Syvorotka, "Magneto-optical and Microwave Properties of LuBiIG Thin Films Prepared by Liquid Phase Epitaxy Method from Lead-Free Flux," Chinese Physics Letters, vol. 26, pp. 047401-047404, 2009.

[24] F Fan, Z Guo, J Bai, X Wang, S Chang, "Magnetically tunable magneto-photonic crystals for multifunctional

terahertz polarization controller," Acta Physica Sinica,vol. 60, no. 8, pp. 084219-084226, 2011.
[25] J Joannopouls, S Johnson, J Winn, R Meade, "Photonic Crystals Molding the Flow of Light," 2nd ed., Princeton University Press, New Jersey, pp. 83–86, 2008.

Two Dimension Photonic Crystal Y-Branch Beam Splitter with Variation of Splitting Ratio Based on Hybrid Defect Controlled

Teanchai Chantakit[1], Keerayoot Srinuanjan[1], Preecha P. Yupapin[1]

[1]Department of Physics, Faculty of Science, King Mongkut's Institute of Technology Ladkrabang, Thailand
*corresponding author, E-mail: tchantakit@gmail.com

Abstract

This article represents a new Y-branch hybrid design of 2D Photonic Crystal (PhC) with defect control. The structure is made of hexagonal arrays of InP nano-rods surrounded by air. This system is comprised of a modified add/change to a polymethymethacrylate (PMMA) rod, which can be applied to the beam splitter selection device. The optical properties and radial of PMMA defect rods has been transfigured. By selecting an appropriate temperature, a change of refractive index and expanded radius are occurred. The obtained results have shown that the selected optical amplitude in a hybrid semiconductor-polymer Y-branch can be separated to 50-50, 60-40 and 67-33 percent at wavelength 1.557 μm. Both of the Photonic Band Gap (PBG) and transmission spectra are calculated by using 2D Finite Different Time Domain (FDTD) method via OptiFDTD software. Such a device can be useful for photonic crystal switching devices in the integrated optical circuit.

Keywords: photonic crystal, beam splitter, finite different time domain, defect control, integrated optics

1. Introduction

The artificial periodic structure, photonic crystal (PhC), has the advantages property of small scale and low loss optical power waveguide due to unique photonic band gap (PBG). As the ability in controlling the light propagating direction, the different functional of PhC has become the next key component evolution on the photonic integrated circuit development [1, 3, 4, 9]. Particularly, the beam splitter has been widely investigated in many categories of photonic crystal [1-4], [8] and there is required for the many powerful optical research and applications, such as beam interferometers and the multimode interference devices including the optical communication artifacts in small scale optics. However, the conventional optical power splitter based on 2D PhC has a specific power separated ratio for a single structure.

In this research, the divided optical power with a defect controlling modification was designed by the 2D photonic crystal. The initiative design is made from nano rod array on a hexagonal lattice conformation which surrounded by air. The fabric 2D PhC waveguide in a shape of Y-junction path separate the incident wavelength into each arm equally. Consequently, to select the other splitting ratio, a hybrid system design of semiconductor-polymer dielectric rods had been implemented. The PMMA defect rods r_1 are added to inside waveguide and in band structure, indium phosphide (InP) rods r_2, are changed to PMMA rod (see in Fig. 1). The optical properties and dimension of PMMA is transfigured by heating the defect rods in single arm. Two defect rods are controlling the wavelength intensity pass through one port more than the other which applied to the beam splitter variation device.

The simulation results of the optical propagation in 2D photonic crystal hybrid system were analysed by the finite different time domain method via OptiFDTD software.

2. Numerical simulation method

The finite different time domain (FDTD) and plane wave expansion (PWE) method provided the analysis of PhC investigation. The various numerical approaches have been established as a powerful appliance for the electromagnetics (EM) wave of optical properties simulations [13]. As the rigorous of time-dependent Maxwell's equations solution, the derived curl 2D transverse electric (TE) wave equations for linear isotropic material polarized along the travelling direction in free region can be written in the following form [2, 13],

$$\frac{\partial E_y}{\partial t} = \frac{1}{\varepsilon}\left(\frac{\partial H_x}{\partial z} - \frac{\partial H_z}{\partial x}\right) \tag{1}$$

$$\frac{\partial H_x}{\partial t} = \frac{1}{\mu_0}\frac{\partial E_y}{\partial z} \tag{2}$$

$$\frac{\partial H_z}{\partial t} = -\frac{1}{\mu_0}\frac{\partial E_y}{\partial x} \tag{3}$$

where $\varepsilon = \varepsilon_0\varepsilon_R$ is the dielectric permittivity and μ_0 is the magnetic permeability in the vacuum. The E and H field are related on two polarized modes in 2D case which the E- and H-polarizations. The 2D wave propagation in real space and linear isotropic structure are following FDTD time stepping. These equations can be discretized in free region and time variant called Yee-cell technique. The spatial dimensions of the equations 1-3 is broken up into discrete two dimension mesh with step of time differential in the x-z coordinate system of the E-polarization [2],

$$H_x^{n+1/2}(i,k+1/2)=H_x^{n-1/2}(i,k+1/2)+\frac{\Delta t}{\mu_0 \Delta z}\left[E_y^n(i,k+1)-E_y^n(i,k)\right] \quad (4)$$

$$H_z^{n+1/2}(i+1/2,k)=H_x^{n-1/2}(i+1/2,k)-\frac{\Delta t}{\mu_0 \Delta x}\left[E_y^n(i+1,k)-E_y^n(i,k)\right] \quad (5)$$

$$E_y^n(i,k)=E_y^{n-1}(i,k)+\frac{\Delta t}{\varepsilon \Delta z}\left[H_x^{n-1/2}(i,k+1/2)-H_x^{n-1/2}(i,k-1/2)\right] - \frac{\Delta t}{\varepsilon \Delta x}\left[H_z^{n-1/2}(i+1/2,k)-H_z^{n-1/2}(i-1/2,k)\right] \quad (6)$$

where n is the index which labels the discrete time step, The indices i and k accounted the number of space steps in the x-z plane respectively. Δx and Δz are the interval between points on a grid along the x and z directions. Δt is the time step increased.

The numerical derivative of time step is proportional to the number of discretization points. The time stepping on the following condition of FDTD is defined,

$$\Delta t \le \frac{1}{c\sqrt{\Delta x^{-2}+\Delta z^{-2}}} \quad (7)$$

where c is the speed of light.

3. Hybrid structure design

In the presented design of optical power splitting variation with a defect rods controlled based on 2D PhC, the photonic crystal waveguide (PCW) comprise of the band structure and linear defect rods embedded in the double branches have formed into the semiconductor-polymer waveguide. These produce guided modes in PhC corresponding to orientated intensity between output ports. The system has considered both of band structure analysis and the defect rods.

3.1. 2D PhC beam splitter selected using defect rods

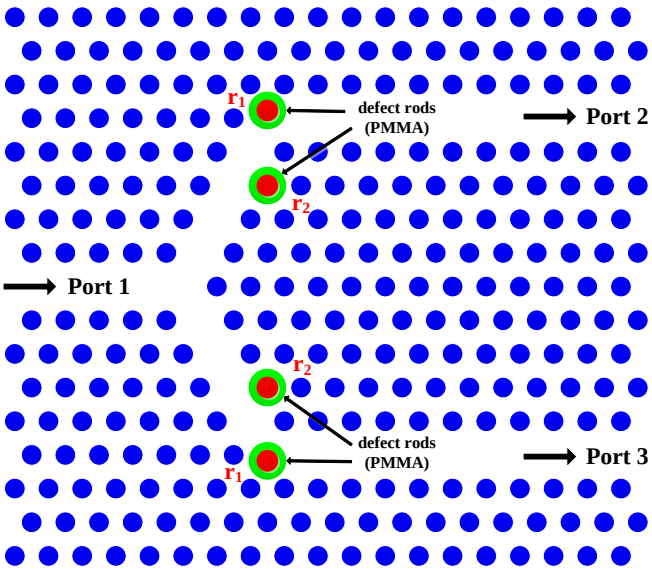

Fig. 1 Scheme of the hybrid Y-junction design with PMMA defect rods controlled in 2D PhC.

For a selected Y-splitter, a 2D photonic crystal of dielectric rods in air array on the hexagonal lattice of InP with index refractive, n = 3.1 had been designed. In most applications, the radius-constant lattice ratio r/a has always been chosen less than 0.5 [5]. The transverse electric propagation in the waveguide is determined by r/a = 0.2986 compatible with desired range of wavelength 1.557 μm. To control the power intensity pass through each arm, defect rods were placed in optical path of Y-splitter, positioning on r_1 and r_2 (Fig.1).

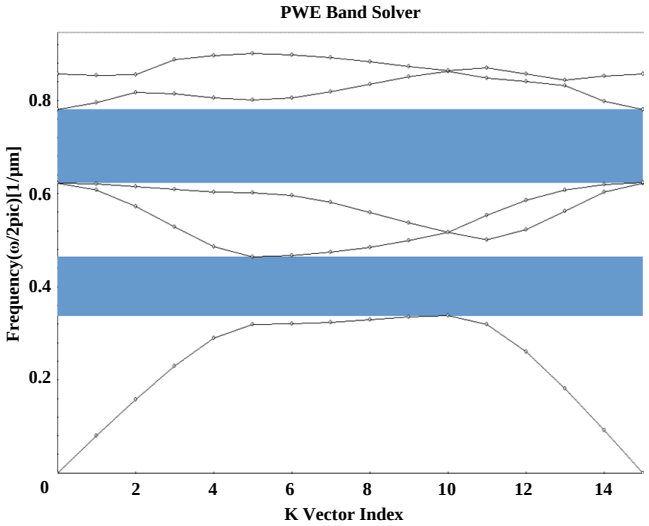

Fig. 2 PhC diagram of hexagonal lattice PBG in TE mode.

Moreover, the proposed hybrid structure has designed a 2D PhC with InP rods in air. The electric field component is oriented perpendicular to the travelling direction which the structure covering wavelength range has been found. The photonic band gap for the transverse magnetic modes (TM polarization) in 2D PhC lattice pattern was calculated by the plan wave expansion (PWE) method.

Based on PWE method, the PBG of 2D lattice structure is provided by the radius-constant lattice ratio r/a = 0.2986 with linear defect rods, PMMA, have shown in Fig. 2. The processed TM polarization PBG provides two normalized frequencies 0.33836-0.46410 and 0.62291-0.78022. The resolving PBG results donated the forbidden wavelength range $1.594\mu m \le \lambda \le 2.187\mu m$ and $0.948\mu m \le \lambda \le 1.188\mu m$ which the incident wavelength 1.557 μm guided through the region.

3.2. Description of the defect rod controlled

The polymethymethacrylate (PMMA) was used as a defect rod which the optical properties and dimension of PMMA can be changed by controlling the temperature of PMMA rods (r_1, r_2) in each arms. By heating the defect rods, the refractive index and radius of PMMA rods have selected to an appropriate temperature as shown in Fig. 3 and 4. With the suitable condition, the three values of the reasonable temperature results to the changed and expanded PMMA rods in a single port have been chosen for multiple splitter ratios transfiguration.

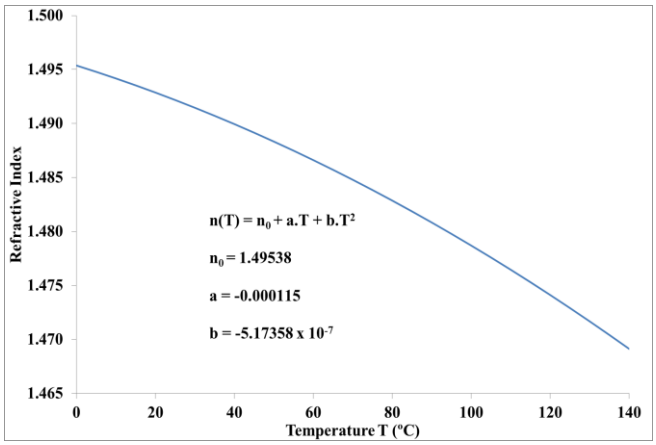

Fig. 3 Refractive index changes of PMMA with the variant temperature [10].

For heating the defect rods, the procedure imagined to beam the high intensity narrow laser pulse into the PMMA rods in a single path. The prescribe defect rods temperature was supposed to changes suddenly. In this hybrid system, the ground temperature was set place at 0 ^{0}C and 140 ^{0}C for the interested maximum point. By the thermal expansion of a PMMA, the remodelled dimension of rods related on the refractive index have been formed into the perfect condition of defect at coincided temperature.

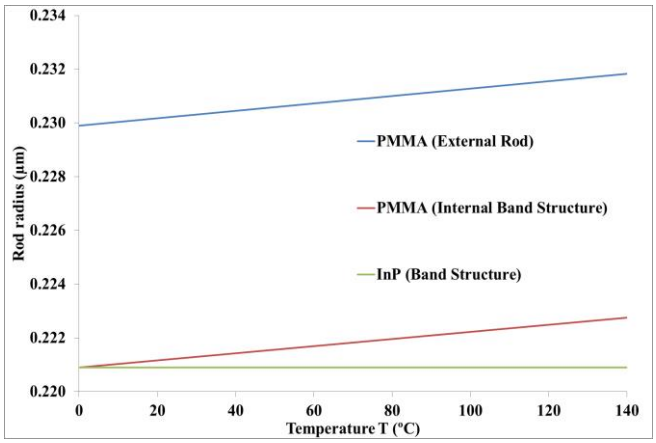

Fig. 4 Radial variation of the PMMA and InP rods based on thermal expansion.

Reasonably, the PMMA has high thermal expansion coeffient and optical properties can be variant easily which the temperature changed [10]. Although the heated rods are set place in the optical path, a high temperature has less effect to the neighbor lattice, InP, with both enlarge and refractive index of band structure and added rods (see in Fig. 4). Consequenly, the fervoured defect rods in the one single port have been controlled, the power intensity pass through 2D PhC optical waveguide in this path is more than non-heated defect in other output port which is set back to gruond temperature. The performance idea is based on the principle of a symmetry appearance signal of incident and double splitted arms with identical gaussian mode.

4. Simulation results and discussion

The power splitter propagation based on 2D PhC has been observed in x-z plane. The 2D FDTD method providing the simulated TE transmission wave of the variation optical separated with defect controlled in Y-junction modification. With the hybrid fabric system, the two specific appropriate temperature have been chosen for tunable the splitting ratio between the branches and one condition is set place at the ground temperature for the equivalent output signal. The 2D FDTD simulation allowed the light observation in an optical path with defect rods. In the FDTD analytical results at the wavelength 1.557 µm, PMMA rods (r_1 and r_2) in the upper branch or port 2 with r/a = 0.2986 were heated for monitor the travelling wave in a proposed design.

At first, the considered structure was determined to the ground temperature at 0 ^{0}C in the hybrid system. The beam transmission efficiency was divided into 50% for each arm. According to the added PMMA rods inside the optical path, they probably blocked some power transmission but, most of them can pass through the rods into both output ports. The resolving electric field amplitude simulation in the y-direction providing a poynting vector pattern and beam propagation of equivalent output signal that have shown in Fig. 5a and 6a.

Reaching the other splitting ratios can be formed by control the temperature of defect rods. The heated PMMA rods in the upper branch while the rods in port 3 is constant characteristic at 0 ^{0}C authorized the separate power input channelled more than the downward optical path. When the temperature of PMMA rods in port 2 reached to the 100 ^{0}C, the refractive index and the dimension of PMMA has been transfigurated following the relation as Fig. 3 and 4. In this system with the temperature controlled at the 100 ^{0}C, the mentioned results donate light intensity approximately 60 % at port 2 incured the poynting vector and TE propagating by 60-40 of power splitting ratio as shown in Fig. 5b and 6b.

Finally, the last separated ratio in the initiative design, the heated PMMA defect rods in the port 2 as though the previous procedure, it have been achieved to the 140 ^{0}C of temperature. The metamorphosis of operative PMMA rods is providing the changed qualification of optical properties caused the incident wavelength distinguished approximately 67 % into the port 2. Then, it has given the variation of the splitter ratio to the 67-33 allowed the poynting vector and the H-polarized travelling wave as shown in Fig. 5c and 6c.

As the results, in the first 2D FDTD simulation pattern, the light intensity that passed through the exhibit 2D PhC waveguide which whole system temperature established at the 0 ^{0}C. Given in Fig. 7a, the calculated spectra plot are overlapped precisely of port 2 and 3. The splitting ratio for 50-50 was surpassed by 83.60% or 0.78 dB of loss for TE transmission in the consistency of symmetrical Y-branch at wavelength 1.557 µm. Later, with heating PMMA rods in the upper arm that reached to 100 ^{0}C, the modification of the optical properties and effected by thermal expansion offering optical power separated to port 2 more than port 3. Consequenly, the Fig.7b have displayed the optical loss signal in a waveguide valued approximately 12.93% or 0.60 dB for the splitting ratio of 60-40 at wavelength 1.557 µm.

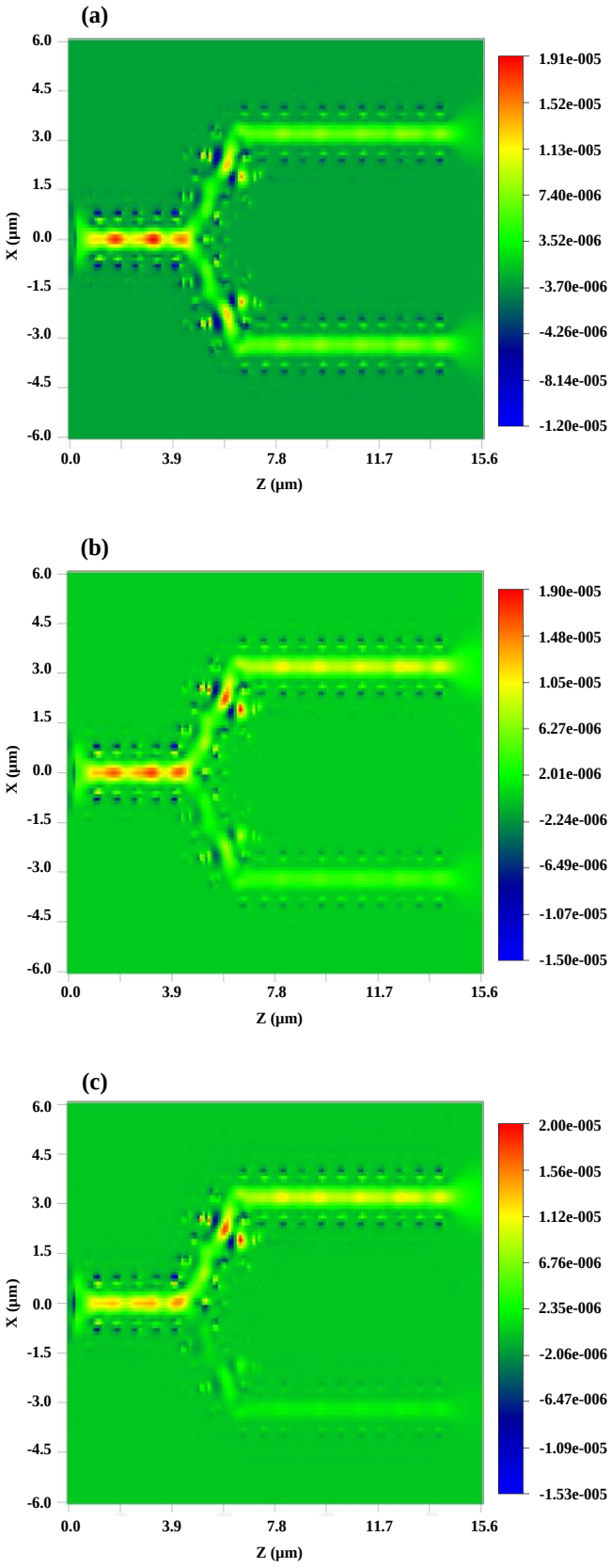

Fig. 5 The poynting vector pattern splitting of the y-branch at wavelength 1.557µm separated to the (a) 50% and 50%. (b) 60% and 40%. (c) 67% and 33%.

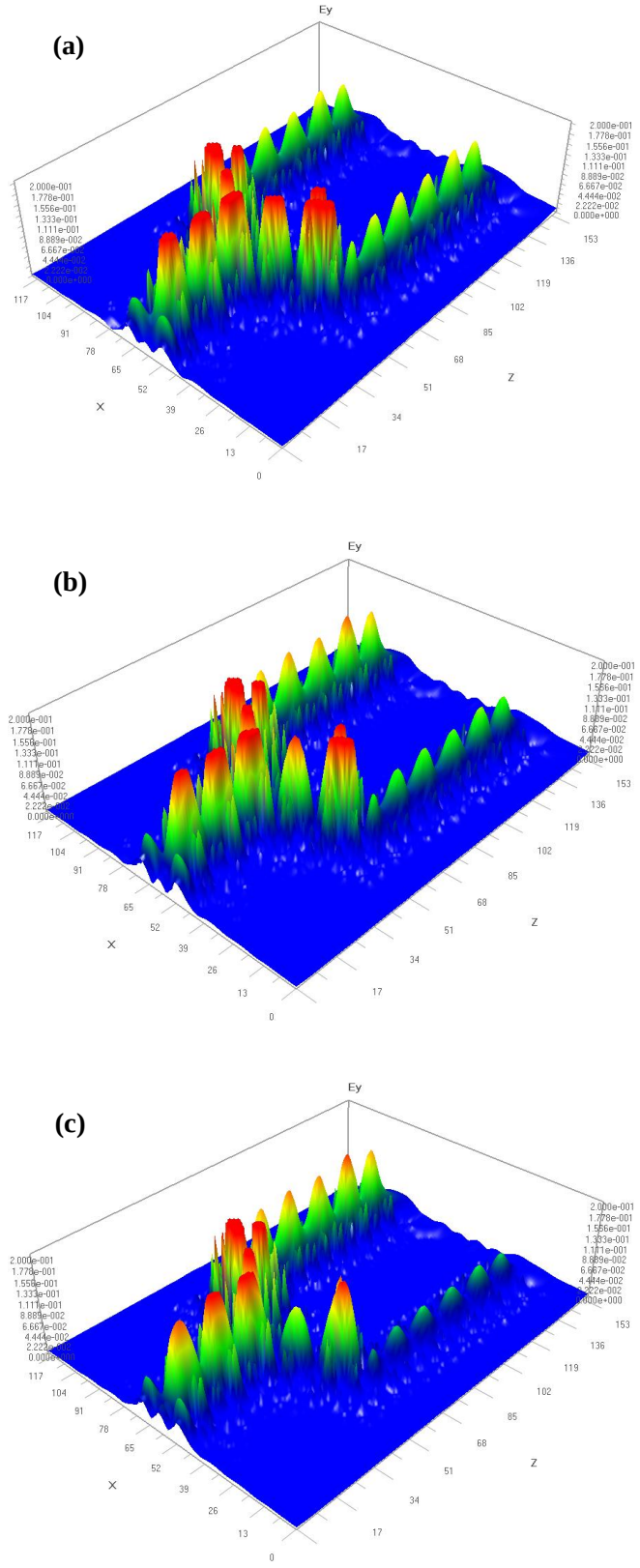

Fig. 6 TE wave propagation simulation by increasing the temperature of PMMA rods (r_1 and r_2) in port 2. (a) T=0 ^{0}C, beam splitting to 50% and 50%. (b) T =100 ^{0}C, beam splitting to 60% and 40%. (c) T=140 ^{0}C, beam splitting to 67% and 33%.

Eventually, by increasing temperature of PMMA rods into 140 ^{0}C, an influence of the defect rods transfiguration in port 2 result to improved the PhC beam splitter, in order to separate the transmission to port 2 by approximately 67 %. As shown in the Fig. 7c, the plots obtained splitting ratio 67-33 at wavelength 1.557 μm. The power has lossed by the structure and the transformed of PMMA properties has given by 10.67 % or 0.49 dB.

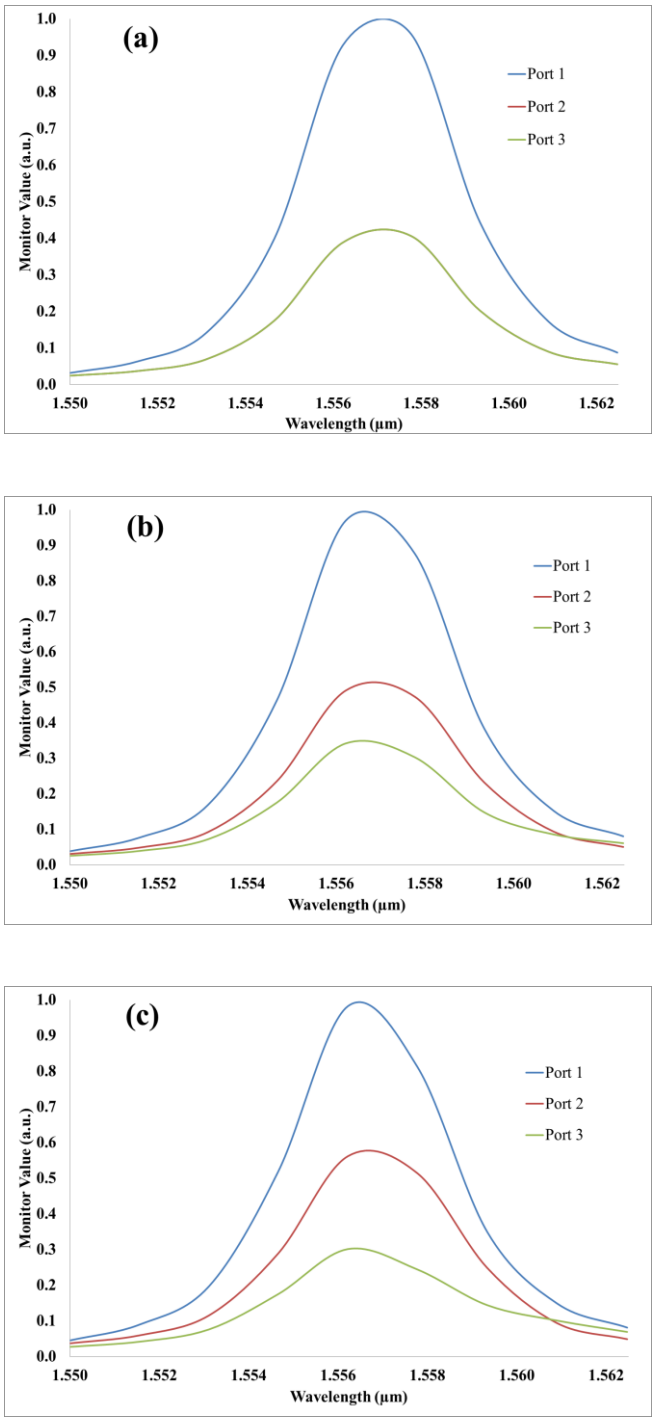

Fig. 7 Simulation results of the TE transmission efficiency at λ = 1.557 μm with the r/a = 0.2986. For the splitting ratio: (a) 50-50, (b) 60-40 and (c) 67-33.

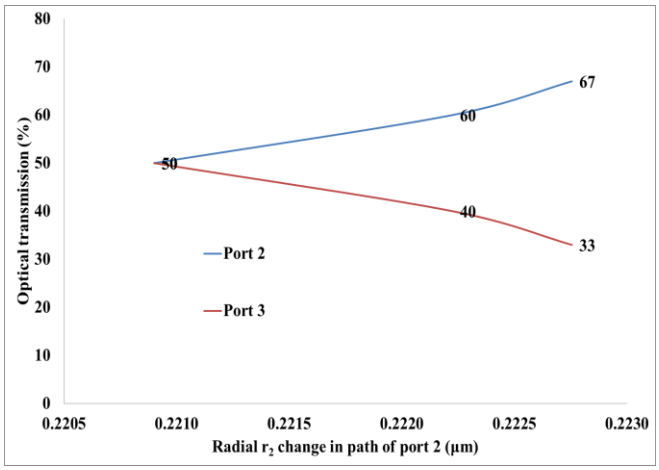

Fig. 8 Different optical transfer by changing the PMMA defect rod dimension inside band structure of InP (r_2) in port 2 furrow formed to tunable line of power splitter.

According to the three simulation results, the analysis of a proposed hybrid system with defect rods controlled in the perfect condition can be concluded in the tunable line of the separated optical power relation between port 2 and 3. Moreover, as the 2D FDTD simulation has observed in a single branch, the added defect rod r_1 assumed to obstruct the beam propagating in path. Simultaneously, the changed rod r_2 is controlling the light intensity pass through to the considered arm related to diminish optical power in the other branch as shown in Fig. 8 wherein the primitive defect rods remain at the initial state.

5. Conclusions

The artifact tunable power splitting ratio based on 2D Y-junction PhC has been analysed and simulated. The TE transmission wave separation is formed by the different guiding mechanisms of heated defect rods in a single optical path. With the PMMA aspect in a single branch of hybrid system is varied by a perfect condition, is caused the beam propagation pass through the operative arm more than the other which is due to the numerous of distinguished power proportion. According to the results, this artificial structure initiative can be applied to the Y-branch symmetrical design of adjustable beam splitter devices in photonics integrated circuit and the other complicated objectives. It offers the advantage of the optimized small scale optical invention that can be provided in widely applications such as the interferometers for photonic crystal holographic imaging and optical switching devices in the near future.

Acknowledgements

This work was supported fund by Science Achievement Scholarship of Thailand (SAST). And we would like to thank the Advance Research Center for Photonics and the Physics Department, Faculty of Science, King Mongkut's Institute of Technology Ladkrabang for providing Optiwave Inc. software and research facilities.

References

[1] T. Liu, A.R. Zakharian, M. Fallahi, J.V. Moloney, M. Mansuripur, Design of a Compact Photonic-Crystal-Based Polarizing Beam Splitter, *IEEE Photonics Tech. Letters*, vol. 17, no. 7, 1435-1437, July 2005.

[2] L. Dekkiche, R. Naoum, Improved transmission for photonic crystal Y-junctions, *Electrical Engineering*, vol.89, no.1, 71-77, 2006.

[3] Y. Tsuji, Y. Morita, K. Hirayama, Photonic Crystal Waveguide Based on 2-D Photonic Crystal With Absolute Photonic Band Gap, *IEEE Photonics Tech. Letters*, vol. 18, no. 22, 2410-2412, Nov. 2006.

[4] H. Ren, C. Jiang, W. Hu, M. Gao, J. Wang, Photonic crystal power-splitter based on mode splitting of directional coupling waveguides, *Optical and Quantum Electronics*, vol. 38, no. 8, 645-654, June 2006.

[5] O. Lyutakov, V. Švorčík, J. Siegel, N. Kasálková, I. Huttel, P. Slepička, Refractive index of polymethylmethacrylate oriented by fluid temperature under electrical field, *Journal of Materials Science: Materials in Electronics*, vol. 19, no. 11, 1064-1068, Nov. 2007.

[6] R.K. Sinha, S. Rawal, Modelling and design of 2D photonic crystal based Y type dual band wavelength demultiplexer, *Optical and Quantum Electronics*, vol. 41, no. 9, 603-613, July 2008.

[7] S.K. Morrison, Y.S. Kivshar, Observation of enhanced beaming from photonic crystal waveguides, *Applied Physics B*, vol. 94, no. 1, 149-153, Jan. 2009.

[8] S. Li, H.-W. Zhang, Q.-Y. Wen, Y.-Q. Song, W.-W. Ling, Y.-X. Li, Improved amplitude-frequency characteristics for T-splitter photonic crystal waveguides in terahertz, *Applied Physics B*, vol. 95, no. 4, 745-749, June 2009.

[9] H. Kaatuzian, M. Danaie, S. Foghani, Design of a High Efficiency Wide-Band 60 Degree Y-Branch for TE Polarization, *14th OptoElectronics and Communications Conference*, Hong Kong, China, July 2009.

[10] M.S. Kovacevic, A. Djordjevich, Variation of modal dispersion and bandwidth with temperature in PMMA based step-index polymer optical fibers, *Journal of Optoelectronics and Advanced Materials*, vol. 12, no. 2, 288-293, Feb. 2010.

[11] R. Goel, A.S. Vengurlekar, A.V. Gopal, Photonic crystal based polarization beamsplitter, *International Conference on Nanoscience, Technology and Societal Implications*, Bhubaneswar, India, Dec. 2011.

[12] R. Kun, R. XiaoBin, Y-shaped beam splitter by graded structure design in a photonic crystal, *Chinese Science Bulletin*, vol. 57, no. 11, 1241-1245, April 2012.

[13] A. Tavousi, Z. Rashki, M.A. Mansouri-Birjandi, M. Saffari, Performance Evaluation of Optical Wavelength Filters Based on Photonic Crystal Ring Resonators, *Majlesi Journal of Electrical Engineering*, vol. 6, no. 2, 1-9, June 2012.

Non-reciprocal transmission of terahertz waves through a photonic crystal cavity with graphene

Yu Zhou, Ye-Qing Dong, Kun Zhang, Ru-Wen Peng*, Qing Hu, and Mu Wang

National Laboratory of Solid State Microstructures and Department of Physics,
Nanjing University, Nanjing 210093, China
*corresponding author, E-mail: rwpeng@nju.edu.cn

Abstract

In this work, we theoretically investigate non-reciprocal propagation of terahertz (THz) waves through a photonic crystal cavity integrated with graphene under external magnetic field. The magnetic field applied perpendicular to the graphene plane introduces asymmetric conductivity tensor into the system, thus the Jones matrix for THz waves propagation in one direction is not the transpose of that in reversal direction. As a consequence, non-reciprocal propagation is achieved in THz regime, which has been verified by non-reciprocal photonic band structures, transmission spectra, and also electrical-field distributions. Further by tuning the magnetic field or the Fermi level of graphene, non-reciprocal transmission can be drastically tuned. This non-reciprocity at the level of material response enables us to design the photonic structure which can let specific mode pass but its time-reversal counterpart stop. The investigations may provide a unique approach to guide THz waves and achieve potential applications on one-way devices (*e.g.* isolators) in THz regime.

1. Introduction

The study on reciprocity in wave propagation has a long history. In 1959, de Hoop formulated his reciprocity theorem under the condition that all the materials in electromagnetic scattering problems are characterized by symmetry tensor and are independent on the electric and magnetic fields [1,2]. It is shown that asymmetry in the material response function, *i.e.* permittivity, permeability, or conductivity may lead to failure of this reciprocity [2-12]. A circularly polarized wave propagating through such asymmetric medium may have different transmission spectra and band structures from its time reversal counterpart. For example in magneto-optic media, magnetic field perpendicular to the plane introduces asymmetric off-diagonal terms into the permittivity tensor. In such media, Jones matrix for one direction is not the transpose of the one for the reverse direction [2] and thus the circularly polarized waves have different transmission depending on its direction. In recent years, there has been an increasing interest in non-reciprocal device [13-18]. Non-reciprocal devices such as isolators have many applications and have been intensely investigated. Most of the works are concerned about traditional magneto-optic [14,16] or nonlinear [17,18] materials, and mainly focus on microwave and infrared regions. However, there still lack nonreciprocal devices for THz waves, especially electric tunable ones.

Since the development of mechanical exfoliation method [19], graphene has been increasingly used in photonics and plasmonics [20,21]. Similar to magneto-optic materials, graphene possesses asymmetric conductivity tensor under the magnetic field [22,23]. Therefore, circularly polarized waves may have different transmission depending on its incident direction, *i.e.* non-reciprocal transmission. What's more, graphene has two advantages over other materials. Firstly, its properties can be easily tuned either by the external magnetic field or the Fermi level. Secondly, it has electromagnetic response in a rather broad frequency range, especially in THz region. In this paper, we have designed a photonic cavity in the THz region with two graphene sheets located in its center. A magnetic field is applied perpendicular to the plane to provide necessary condition for reciprocity breaking. And then the non-reciprocal effect is verified by the photonic band structure, the transmission spectra and the electrical-field distributions. Furthermore, by tuning the magnetic field or the Fermi level of graphene, the non-reciprocal transmission can be drastically tuned, which may provide an approach to design active non-reciprocal devices in THz region.

2. Theoretical model

We begin with designing a cavity consisting of three periods of photonic crystal unit cell mirroring itself, as shown in Figure 1. All the slabs are designed to be quanta wave plates at 336μm. The center of the cavity is made by two quanta wave slabs with the same refractive index ε_2=3.8, and the graphene sheet is placed at the center of each slab. Under magnetic field, graphene possesses Hall conductivity. The 2D conductivity becomes an asymmetric tensor which only depends on the direction of the external magnetic field, leading to reciprocity failure. Such a non-reciprocal effect can be directly demonstrated as the transmission spectra would be different for different illuminating directions (forward or backward).

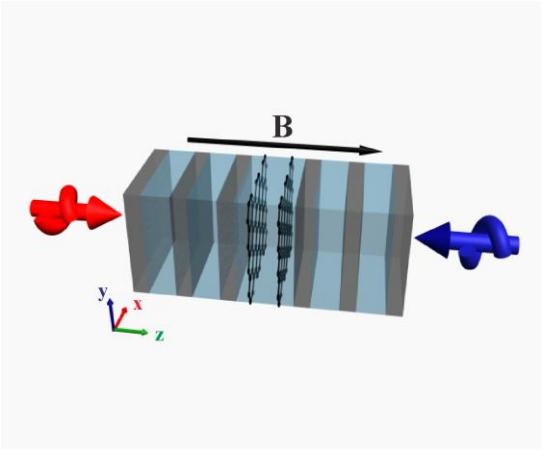

Figure 1: (Colour on-line) Schematic illustration of the photonic crystal cavity. All the slabs are designed to be quanta wave plates at 336μm. Grey and blue slabs are dielectric slabs with permittivity ε_1=11.7 and ε_2=3.8 , respectively. Two graphene layers are located in the center. Black arrow denotes the external magnetic field along +Z direction. Two spiral arrows in red and blue indicate the right circularly polarized THz waves for forward and backward propagating, respectively.

To calculate the transmission intensity in such a system, the S-matrix approach [4,6] is extended into a vector form for the consideration of hall conductivity, which will mix x and y polarizations. In this paper, spatial dispersion is neglected because we focus on low THz frequency region [23]. The graphene is treated as an infinitesimal thin conductive layer which has 2D conductivity tensor:

$$\sigma = \begin{pmatrix} \sigma_{xx} & \sigma_{xy} \\ \sigma_{yx} & \sigma_{yy} \end{pmatrix} = \begin{pmatrix} \sigma_l & \sigma_h \\ -\sigma_h & \sigma_l \end{pmatrix} \tag{1}$$

where σ_l and σ_h are longitudinal and hall conductivity of the graphene, respectively. Two diagonal terms are identical while two off-diagonal terms have opposite signs. It is apparent that the 2D conductivity is asymmetric and independent on the propagation direction of the incident waves. In the calculation, the temperature is set to be 300K. All the conductivity values are calculated using formula in Ref. 22. Scattering effects in graphene are taken into account by setting the imaginary part of energy to 6.8meV. Slight changes of these parameters will not affect the results.

We choose two tangential components of electric field E_x and E_y as independent variables. Then the normal component E_z can be easily derived by $E_z=(-k_x/k_y)E_x+(-k_x/k_y)E_y$, where k_x, k_y and k_z are x, y, z components of the wave vector k. The tangential magnetic field can also be derived using:

$$\begin{pmatrix} Z_0 H_x \\ Z_0 H_y \end{pmatrix} = T_{he} \begin{pmatrix} E_x \\ E_y \end{pmatrix} = \begin{pmatrix} -\frac{k_x k_y}{k_z k_0} & -\frac{k_y k_y}{k_z k_0} - \frac{k_z}{k_0} \\ \frac{k_z}{k_0} + \frac{k_x k_x}{k_z k_0} & \frac{k_x k_y}{k_z k_0} \end{pmatrix} \begin{pmatrix} E_x \\ E_y \end{pmatrix} \tag{2}$$

where matrix T_{he} denoted above transforms the electric field into the corresponding magnetic field. Here the magnetic field is multiplied by the vacuum impedance, so it has the same unit as the electric field. The S matrix for the graphene can be derived by imposing the boundary conditions: firstly, the tangential components of the electric field are continuous across the graphene; secondly, the discontinuity of the magnetic field at two sides of the graphene equals the surface current.

$$\begin{cases} \vec{E}_F^{(I)} + \vec{E}_B^{(I)} = \vec{E}_F^{(II)} + \vec{E}_B^{(II)} \\ \vec{H}_F^{(II)} + \vec{H}_B^{(I)} - \vec{H}_F^{(II)} - \vec{H}_B^{(II)} = \frac{1}{2} T \overleftrightarrow{\sigma} (\vec{E}_B^{(I)} + \vec{E}_F^{(I)} + \vec{E}_B^{(II)} + \vec{E}_F^{(II)}) \end{cases} \tag{3}$$

where $\vec{E}_F^{(i)} / \vec{H}_F^{(i)}$ and $\vec{E}_B^{(i)} / \vec{H}_B^{(i)}$ are electric/magnetic waves propagating forward and backward in region i (i=I or II, respectively indicate regions at two sides of graphene). Z_0 is the vacuum impedance. Matrix T is defined as

$$T = \begin{pmatrix} 0 & -1 \\ 1 & 0 \end{pmatrix} \tag{4}$$

Solving Equation 3, we can derive the S matrix of the graphene. Then the S matrix for the whole system can be constructed by iteration process.

3. Jones matrices and non-reciprocity effect

Non-reciprocity requires that the Jones matrix for the forward waves is not the transpose of the one for backward waves. Since the 2D conductivity tensor of graphene under magnetic field has rotation symmetry, it is impossible to tell whether the transmission is reciprocal only by the absolute values of t_{xy} and t_{yx}, which are two off-diagonal elements of the Jones matrix. One should look into the phases. The phases of the transmission coefficients under specific magnetic field B and Fermi level μ are plotted in Figure 2. Fig. 2(a), (b) are for B=6Tesla, μ=0.25eV and Fig. 2(c), (d) are for B=8Tesla, μ=0.15eV. We can see from Fig. 2(a) and Fig. 2(b) that the phase of t_{xy} for the forward waves (red circle in Fig. 2(a)) is not the same as the phase for t_{yx} for backward waves (blue stars in Fig. 2(b)). Similar conclusion can be found in Fig.2(c) and Fig. 2(d). Such non-reciprocity originates from the asymmetry of the 2D conductivity tensor of graphene, which only depends on the direction of the magnetic field. Further investigation reveals that the difference of the phases for the off-diagonal terms in one direction is equal to π for all frequencies. This indicates that the Jones matrix of the structure under magnetic field has a form for both directions:

$$J = \begin{pmatrix} t & t' \\ -t' & t \end{pmatrix} \tag{5}$$

where t and t' are diagonal and off-diagonal terms of the conductivity tensor, respectively. Furthermore, it can be seen from Fig.2 that the Jones matrix are different under different external magnetic fields and Fermi levels. So the non-reciprocal transmission coefficient of our structure is tunable by changing either the external magnetic field or the Fermi level of graphene.

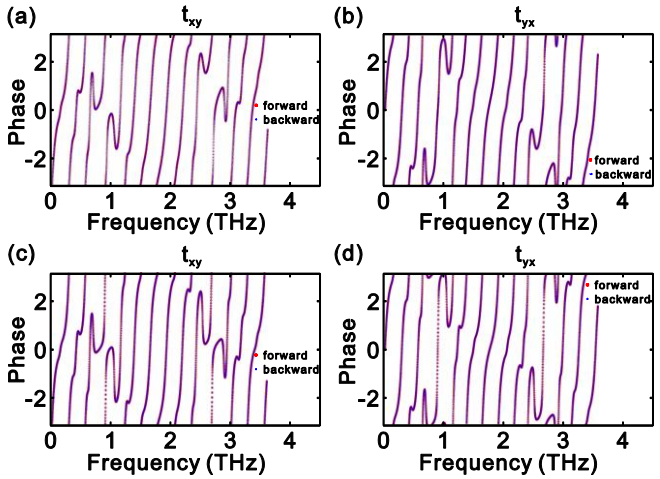

Figure 2: (Colour on-line) Phases of the transmission coefficient t_{xy} and t_{yx} under (a) (b) B=6 Tesla, μ=0.25eV (c) (d) B=8Tesla, μ=0.15eV. Red circles and blue stars mark the phases of forward and backward propagating waves, respectively.

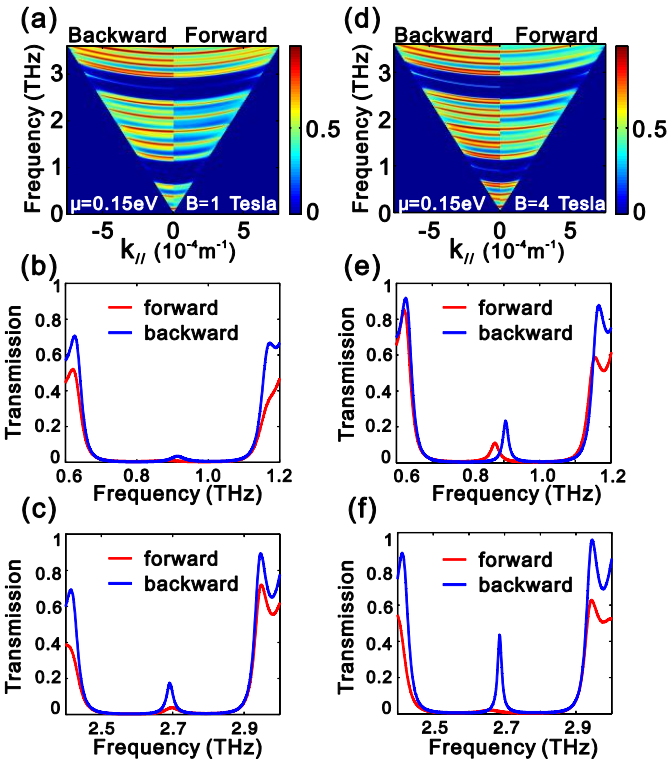

Figure 3: (Colour on-line) Band structure (a), first cavity mode (b) and second cavity mode (c) for the case of B=1T, μ=0.15eV. Band structure (d), first cavity mode (e) and second cavity mode (f) for the case of B=4T, μ=0.15eV.

4. Tunable non-reciprocal band structures and transmission spectra

In this section, we focus on the band structures and transmission spectra under the illumination of right circularly polarized THz waves. The band structures are calculated by the transmission under different incident angles. In the band gap, only the cavity mode can transmit, and first cavity mode and second cavity mode appear in the first and second band gap, respectively. Calculation results are shown in Figure 3 and Figure 4 and the corresponding magnetic field intensity and Fermi level are denoted therein. We can see from these figures that both band structures and transmission spectra are different for forward and backward propagating waves. In this design, backward propagating waves have higher transmission than forward propagating waves. Mode splitting and suppression may occur under specific magnetic field intensity and Fermi level. For example, in Fig. 4(f), the second cavity mode for forward propagating wave is completely suppressed and no peak appears in the band gap while for backward propagating wave the transmission peak is relatively high.

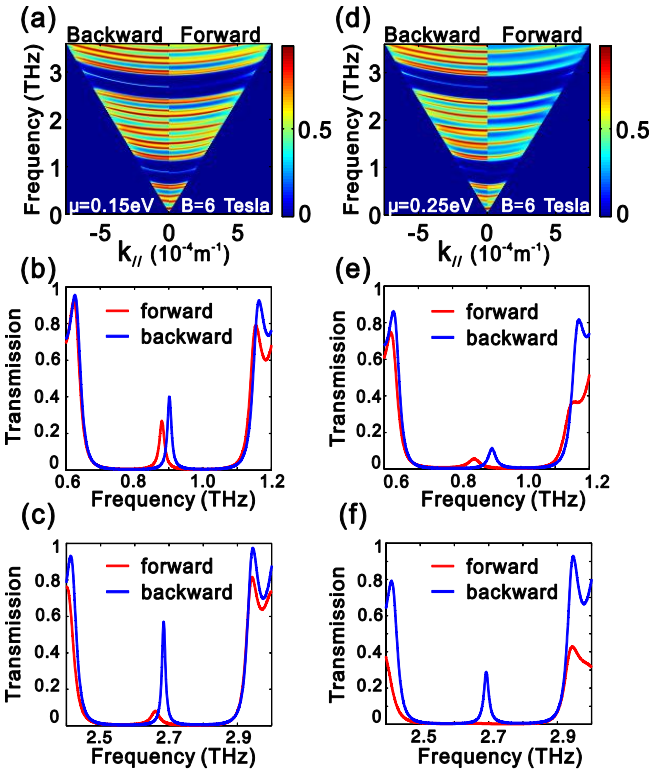

Figure 4: (Colour on-line)Band structure (a), first cavity mode (b) and second cavity mode (c) for the case of B=6T, μ=0.15eV. Band structure (d), first cavity mode (e) and second cavity mode (f) for the case of B=6T, μ=0.25eV.

As mentioned above, asymmetric band structures and transmission spectra originate from the off-diagonal terms of graphene conductivity, *i.e.* if $\sigma_{xy}=0$, non-reciprocity would vanish. To further quantificationally measure the asymmetry, we define the contrast factor as $f=(T_b-T_f)/(T_b+T_f)$, which equals zero if the spectra are symmetric and equals to 1 if transmission of one direction is completely blocked. Contrast factors plotted as a function of magnetic field or Fermi level are shown in Figure 5. All the points are taken at the transmission peaks of backward waves. Fig. 5(a) plots the contrast factor as a function of the Fermi level while keeping the magnetic field fixed at 6T. As for μ=0, *i.e.*, pristine graphene without doping, there exists no significant non-reciprocity effect. For graphene with doping, there exists an optimized Fermi level where

the contrast factor reaches its maximum. Fig. 5(b) shows the contrast factor as a function of magnetic field intensity while the Fermi level μ=0.15. The lowest magnetic field is set to be 1 Tesla. One can see from the curves that for a fixed Fermi level, there also exists an optimized magnetic field intensity that will maximize the contrast factor. Thus tunable non-reciprocal band structure and transmission spectra can be achieved by tuning either the external magnetic field or the Fermi lever of graphene. What's more, we mention here that the external magnetic field can be replaced by intrinsic time-reversal (TR) symmetry breaking of the graphene layer. In bi-layer graphene, quantum anomalous Hall state are naturally TR breaking providing asymmetric conductivity tensor without external magnetic field, thus providing non-reciprocal transmission of THz waves in the same design. The nonreciprocity in THz propagation presented here provides us a method to develop some one-way devices, such as the THz isolators and modulators.

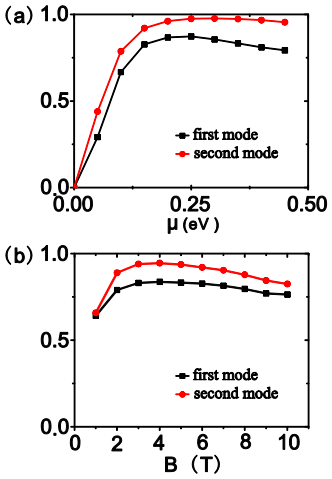

Figure 5: (Colour on-line) (a) Contrast factor plotted as a function of Fermi level while B=6T. (b) Contrast factor plotted as a function of magnetic field intensity while μ=0.15eV.

5. Non-reciprocal field distributions

Since the S matrix involves iteration process, it will be much more convenient for one to take the transfer matrix (T matrix) in field distribution calculations. Once the fields at one of the ports (input or output ports) are known, the fields in the cavity structure can be derived by simple T matrix multiplication. Fig. 6 and Fig. 7 show field distributions under the same magnetic field intensities B and Fermi levels μ as in Fig. 3 and Fig. 4, respectively, and all the field distributions correspond to the transmission peaks of backward propagating waves. At these frequencies, backward waves have higher field distributions than the forward waves, which is in accordance with the transmission spectra in Fig. 3 and Fig. 4 where backward waves dominate. Without graphene, the cavity mode is strictly symmetric and has perfect transmission [24,25]. In the presence of graphene, loss is unavoidable which will lower the transmission peak of the cavity mode and even break the symmetry of field distribution. Under magnetic field and finite electron doping, non-reciprocal field distribution occurs. This non-reciprocal field distribution has the same origin as the transmission spectra and the band structures, which is the asymmetry of the graphene conductivity tensor.

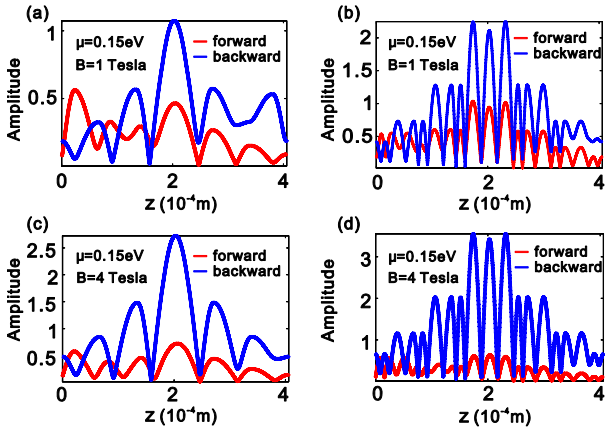

Figure 6: (Colour on-line) Field amplitude distribution for (a) the first cavity mode and (b) the second cavity mode at the peak of backward propagating waves (blue lines) in Fig. 3(a). Field amplitude distribution for (c) the first cavity mode and (d) the second cavity mode at the peak of backward propagating waves(blue lines) in Fig. 3(d).

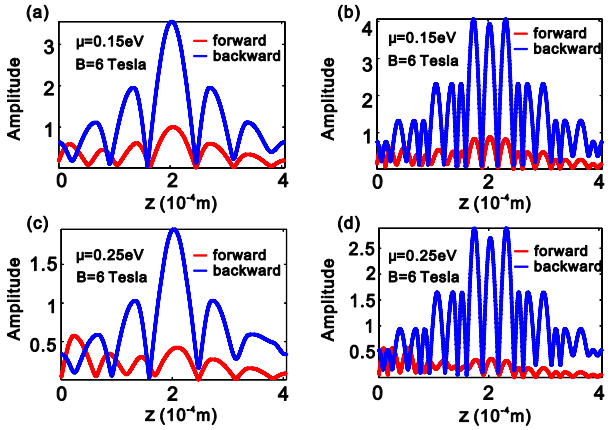

Figure 7: (Colour on-line) Field amplitude distribution for (a) the first cavity mode and (b) the second cavity mode at the peak of backward propagating waves (blue lines) in Fig. 4(a). Field amplitude distribution for (c) the first cavity mode and (d) the second cavity mode at the peak of backward propagating waves(blue lines) in Fig. 4(d).

6. Conclusions

In this paper, we theoretically investigate tunable non-reciprocal transmission and band structure of terahertz waves through a photonic cavity integrated with graphene. Under magnetic field, 2D conductivity of graphene is asymmetric which leads to the failure of reciprocity. As a result, right circularly polarized waves propagating in two directions have different transmission spectra and field amplitude distributions. Such non-reciprocity at the level of material response enables us to design the photonic

structure which can let specific mode pass but its time-reversal counterpart stop. By tuning the external magnetic field intensity or Fermi level of the graphene, one can tune the band structures, transmission spectra and field intensity distributions of the structure. Our investigations may provide a unique approach to guide THz waves and achieve potential applications on one-way devices (*e.g.* isolators) in THz regime.

Acknowledgements

This work was supported by the MOST of China (Grants No. 2012CB921502 and 2010CB630705) and the NSFC (Grants No. 11034005 and 11321063).

References

[1] A. T. De hoop, A reciprocity theorem for the electromagnetic field scattered by an obstacle, *Appl. Sci. Res.* B 8: 135-140, 1959.

[2] R. J. Potton, Reciprocity in optics, *Rep. Prog. Phys.* 67: 717–754, 2004.

[3] L. J. Aplet and J. W. Carson, A Faraday effect optical isolator, *Appl.Opt.* 3:544-545, 1964.

[4] A. Figotin and I. Vitebsky, Nonreciprocal magnetic photonic crystals, *Phys. Rev. E* 63: 066609, 2001.

[5] P. A. Belov, S. A. Tretyakov, A. J. Viitanen, Nonreciprocal microwave band-gap structures, *Phys. Rev. E* 66: 016608, 2002.

[6] A. Figotin, I. Vitebskiy, Electromagnetic unidirectionality in magnetic photonic crystals, *Phys. Rev. B* 67: 165210, 2003.

[7] Z. Yu, Z. Wang, S. Fan, One-way total reflection with one-dimensional magneto-optical photonic crystals, *Appl. Phys. Lett.* 90: 121133, 2007.

[8] H. Takeda, S. John, Compact optical one-way waveguide isolators for photonic-band-gap microchips, *Phys. Rev. A* 78: 023804, 2008.

[9] Z. Yu, G. Veronis, Z. Wang, S. Fan, One-way electromagnetic waveguide formed at the interface between a plasmonic metal under a static magnetic field and a photonic crystal, *Phys. Rev. Lett.* 100: 023902, 2008.

[10] A. Christofi, N. Stefanou, Nonreciprocal optical response of helical periodic structures of plasma spheres in a static magnetic field, *Phys. Rev. B* 87: 115125, 2013.

[11] A. R. Davoyan, N. Engheta, Non-reciprocal rotating power flow within plasmonic nanostructures, *Phys. Rev. Lett.* 111: 047401, 2013.

[12] H. Y. Dong, J. Wang, T. J. Cui, One-way Tamm plasmon polaritons at the interface between magnetophotonic crystals and conducting metal oxides, *Phys. Rev. B* 87: 045406, 2013.

[13] Z. Yu, S. Fan, Complete optical isolation created by indirect interband photonic transitions, *Nat. Photon.* 3: 91-94, 2009.

[14] L. Bi, J. Hu, P. Jiang, D. Kim, G. F. Dionne, L. C. Kimerling, C. A. Ross, On-chip optical isolation in monolithically integrated non-reciprocal optical resonators, *Nat. Photon.* 5: 758-762, 2011.

[15] H. Lira, Z. Yu, S. Fan, M. Lipson, Electrically driven nonreciprocity induced by interband photonic transition on a silicon chip, *Phys. Rev. Lett.* 109: 033901, 2012.

[16] M. Shalaby, M. Peccianti, Y. Ozturk, R. Morandotti, A magnetic non-reciprocal isolator for broadband terahertz operation, *Nat. Commun.* 4: 1558, 2013.

[17] M. D. Tocci, M. J. Bloemer, M. Scalora, J. P. Dowling, C. M. Bowden, Thin-film nonlinear optical diode, *Appl. Phys. Lett.* 66: 2324, 1995.

[18] V. V. Konotop, V. Kuzmiak, Nonreciprocal frequency doubler of electromagnetic waves based on a photonic crystal, *Phys. Rev. B* 66: 235208, 2002.

[19] K. S. Novoselov, A. K. Geim, S. V. Morozov, D. Jiang, Y. Zhang, S. V. Dubonos, I. V. Grigorieva and A. A. Firsov, Electric field effect in atomically thin carbon films, *Science* 306: 666, 2004.

[20] A. N. Grigorenko, M. Polini, K. S. Novoselov, Graphene plasmonics, *Nat. Photon.* 6: 749-758, 2012.

[21] Q. Bao, K. P. Loh, Graphene Photonics, Plasmonics, and Broadband Optoelectronic Devices, *ACS, Nano.* 6: 3677– 3694, 2012.

[22] A. Ferreira, J. Viana-Gomes, Y. V. Bludov, V. Pereira, N. M. R. Peres, A. H. Castro Neto, Faraday effect in graphene enclosed in an optical cavity and the equation of motion method for the study of magneto-optical transport in solids, *Phys. Rev. B* 84: 235410, 2011.

[23] A. Fallahi, J. Perruisseau-Carrier, Design of tunable biperiodic graphene metasurfaces, *Phys. Rev. B* 86: 195408, 2012.

[24] R. W. Peng, X. Q. Huang, F. Qiu, Mu Wang, A. Hu, S. S. Jiang, and M. Mazzer , Symmetry-induced Perfect Transmissions of Light Waves in Quasiperiodic Dielectric Multilayers, *Appl. Phys. Lett.* 80: 3063, 2002.

[25] Z. Wang, R. W. Peng, F. Qiu, X. Q. Huang, Mu Wang, A. Hu, S. S. Jiang, D. Feng, Selectable-frequency and tunable-Q perfect transmissions of electromagnetic waves in dielectric heterostructures, *Appl. Phys. Lett*. 84: 3969, 2004.

Optical Properties of Metamaterial Based Devices Modulated by a Liquid Crystal

Filiz Karaomerlioglu[1,2,*], Amirullah M. Mamedov[2,3], Ekmel Ozbay[2]

[1]Department of Electrical and Electronics Engineering, Mersin University, Mersin, Turkey
[2]Nanotechnology Research Center (NANOTAM), Bilkent University, Ankara, Turkey
[3]International Scientific Center, Baku State University, Baku, Azerbaijan
*corresponding author, E-mail: filizkrm@mersin.edu.tr

Abstract

Due to the fact that it is possible to manipulate light with photonic crystals, photonic crystals hold a great potential for designing new optical devices. There has been an increase in research on tuning the optical properties of photonic crystals to design devices. We presented a numerical study of optical properties of metamaterial based devices by liquid crystal infiltration. The plane wave expansion method and finite-difference time-domain method for both **TE** and **TM** modes revealed optical properties in photonic crystal structures in an air background for a square lattice. E7 type has been used as a nematic liquid crystal and $SrTiO_3$ as a ferroelectric material. We showed the possibility of the metamaterials for a two dimensional photonic crystal cavity on a ferroelectric base infiltrated with a nematic liquid crystal.

Keywords: Ferroelectric, Metamaterial, Photonic Crystal, Liquid Crystal, $SrTiO_3$

1. Introduction

Progress in solid-state physics, optics of 3D artificial structures, and nanotechnologies based on a variety of the physical and chemical processes has strongly stimulated and motivated the investigation into the properties of photonic crystals (PCs) and has resulted in the growth of applications of photonic band gap (PBG) materials, i.e. artificially structured materials where the optical parameters are periodically modulated in space with a period of a unit PC cell on the order of the optical wavelength. Previous studies about PBG structures, PBG materials, and PCs have been important investigations [1, 2]. The basic feature of PCs is the presence of permitted and forbidden frequency bands for light. It is possible to manipulate the light with PCs. Due to this property, PCs hold great potential for designing new optical devices. There has been an increase in research on tuning the optical properties of PBG to design devices. Some tunable PBG research has been conducted in one-dimensional (1D) and two dimensional (2D) and 3D [3-6] PCs.

Recently, new investigations have reached a point of view of LCs because of the tunable light wave propagation. LCs' refractive indices can be changed by rotating the directors of LCs [7]. Liu investigated the tunable light wave propagation in two-dimensional hole-type photonic crystals infiltrated with nematic liquid crystal and the tunable absolute band gap in two-dimensional anisotropic photonic crystal structures modulated by a nematic liquid crystal [8, 9]. Liu and Chen proposed the tunable field-sensitive polarizer using hybrid conventional waveguides and PC structures with nematic liquid crystals, the tunable PC waveguide coupler with nematic liquid crystals, the tunable PC waveguide Mach–Zehnder interferometer based on nematic liquid crystals, the tunable full band gap in a three-dimensional PC structure modulated by a nematic liquid crystal, the tunable channel drop filter in a two-dimensional photonic crystal modulated by a nematic liquid crystal and the tunable band gap in a photonic crystal modulated by a nematic liquid crystal [10-15]. Liu et al. created the tunable bandgap in three-dimensional anisotropic photonic crystal structures modulated by a nematic liquid crystal and an efficient tunable negative refraction photonic crystal achieved by an elliptic rod lattice with a nematic liquid crystal [16, 17].

Negative refraction has investigated recently. In contrast to double negative metamaterials (left-handed materials), single negative materials and indefinite materials, photonic crystals (PCs) made of synthetic periodic dielectric materials can exhibit negative refraction behaviors that are solely determined by the characteristics of their band structures and equi-frequency contours [18-21].

In the present paper, we theoretically demonstrated and developed the optical properties in the 2D PC structure of ferroelectric rods modulated by nematic LCs. The investigation was achieved by controlling the intensity of the optical properties that had different materials added to a certain structure.

2. Method of Calculation

The fundamentals of the plane wave expansion (PWE) method and finite-difference time-domain (FDTD) method are based on a direct numerical solution of the time-dependent Maxwell's equations as illustrated [22].

On the other hand, Bloch's theorem [23] is used to expand the $H(\vec{r})$ field in terms of plane waves since the light waves are transmitted in periodic structures, as

$$H(\vec{r}) = \sum_{\vec{G}} h(\vec{G}) \hat{e}_{\vec{G}} e^{i(\vec{k}+\vec{G})\cdot\vec{r}} \quad (1)$$

Where $\vec{k}$ is a wave vector in the Brillouin zone of the lattice and $\hat{e}_{\vec{G}}$ is the direction that is perpendicular to the wave vector $(\vec{k}+\vec{G})$ owing to the transverse character of the magnetic field $H(\vec{r})$, $\nabla \cdot H(\vec{r}) = 0$.

3. Results of the Calculation

The PBG is manipulated by the rotating directors of LCs under the impact of an applied electric field. Using the PWE and the FDTD methods, the PC structure, composed of a PC in ferroelectric rods infiltrated with nematic LCs in an air background, is designed for the square lattice. PCs structures that are designed as round rods and square rods with a square lattice shape are computed. $SrTiO_3$ was used as ferroelectric material and E7 type as nematic LCs.

This paper is aimed at describing and comparing 2D PC structures which differ by the characteristics of their band gap, transmission, equi-frequency and group velocity dependences.

3.1. Band gap and transmission

We considered the results obtained from the calculation of the band structure of the spectrum for the sample of the 2D PC of the $SrTiO_3$ rods type, which consists of the elements in the form of dielectric cylinder forming a square lattice filled without and with LC. The calculations are performed for the PCs with the permittivity of the cylinders 5.772 and the period of the structure $a = 1\mu m$. E7 type LCs has two different principle refractive indices as the ordinary-refractive index $n_0 = 1.52131$ and the extraordinary refractive index $n_e = 1.73657$. The filling factor is 30%.

Schematic views of the proposed 2D PC of $SrTiO_3$ round and square rods with nematic LC-infilled in an air background $(\varepsilon_a = 1)$ in a square lattice are shown in Figure 1 (a). The photonic band structure for **TE** and **TM** mode is calculated along direction that includes the high symmetry points Γ, X and M for the Brillouin zone in a square lattice. It is assumed that $r_1 = 0.3a$ and $r_3 = 0.1a$ denote the outer radius and inner radius of $SrTiO_3$ round rods, and $r_2 = 0.2a$ round rods air-infilled.

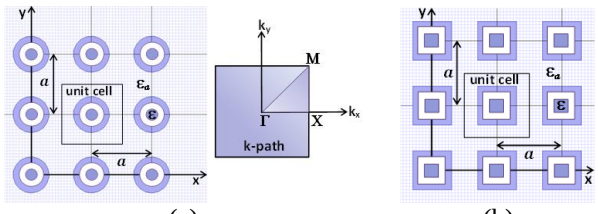

(a) (b)

Figure 1: 2D PC structure for square lattice (a) $SrTiO_3$ round rods (b) $SrTiO_3$ square rods in an air background.

There is no band gap for 2D PC of $SrTiO_3$ round and square rods with air-infilled and rods with nematic LC-infilled in **TE** mode.

Figure 2 shows the seed band structure of the PC (inset, from figure 1 (a)) with the permittivity of the dielectric cylinders and the permittivity of free space 1. For the filling factor 30%, this PC has the maximum width of the first complete band gap. In this case, the PC band gap along the direction between high symmetry points $\Gamma - X$ direction of the Brillouin zone lies in the frequency range from $1.049(2\pi c/a)$ to $1.092(2\pi c/a)$. For $SrTiO_3$ round rods with air-infilled, relative widths are 4.07% of **TM** mode.

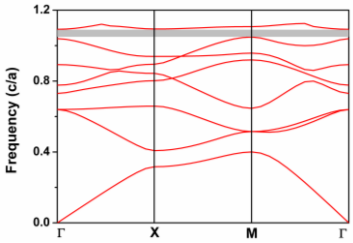

Figure 2: The photonic band structure of **TM** mode in square lattice for $SrTiO_3$ round rods with air-infilled.

The dispersion of the PC structure in combination with the dispersion of the LC leads to the appearance of additional band gaps in the continuous spectrum of the seed PC and additional narrow transmission bands in the band gap of the PC, (which are imperceptible on the scale of Figure 2). These effects are illustrated in Figure 3. It can be seen from Figure 3 that the presented fragment of the band structure of the spectrum exhibits an additional band gap with the width $\Delta\omega = \omega - \omega_0$. This width exceeds the width of the LC resonance lines by an order of magnitude when the frequencies of the LC $1.024(2\pi c/a)$ and $1.063(2\pi c/a)$ are in the continuous spectrum near the high frequency edge of the third band gap.

A different situation arises when the LC frequencies $0.365(2\pi c/a)$, $0.623(2\pi c/a)$ and $1.024(2\pi c/a)$ are in the band gap of the PC (Figure 3). In this case, a narrow transmission band with the width exceeding the width of the LC lines by an order of magnitude appears in the band gap.

The widths of the additional transmission band and the band gap can be controlled by varying the type of nematic LC.

When $SrTiO_3$ round rods are infiltrated with nematic LC, three band gap in **TM** mode for the extraordinary refractive index is shown in Figure 3 (a). The band gap has relative widths of 8.68%, 2.98% and 3.72%, and center normalized frequencies of $0.382(2\pi c/a)$, $0.633(2\pi c/a)$ and $1.044(2\pi c/a)$. As the results obtained for ordinary-refractive index and extraordinary refractive index of nematic LC are different, it is an indication of anisotropy. Using the anisotropic features of LCs different results for **TE** and **TM** mode were obtained. This means that either the structure is rotated into a certain direction or it is infiltrated with – LCs –, that have different directors (orientations of

the LCs molecules along order's direction) into the structure in order to be able to change the features of these structures. It is well known that an anisotropic nanostructuring photonic band structure array is capable of changing the polarization state of transmitted or reflected light. Therefore, we also calculated the optical response of the photonic band structure for different directors of the LCs and the light polarization transmitted through a photonic band array. The numerical results of the variation of full transmission by changing the director of LC for the PC structure are presented. The transmission spectrum as a function of the frequency is computed for extraordinary refractive index of nematic LC in a square lattice. The transmission of $SrTiO_3$ round rods with nematic LC-infiltrated is zero at frequencies between $0.296(2\pi c/a)$ and $0.394(2\pi c/a)$,between $0.614(2\pi c/a)$ and $0.679(2\pi c/a)$, between $0.863(2\pi c/a)$ and $0.891(2\pi c/a)$, between $1.021(2\pi c/a)$ and $1.054(2\pi c/a)$, between $1.089(2\pi c/a)$ and $1.194(2\pi c/a)$, (Figure 3 (b)).

Let us turn to the analysis of the results obtained from the calculation of the band structure of the spectrum for the sample of a PC infiltrated by LC of the $SrTiO_3$ round rods type, which consists of elements in the form of infinite hollow cylinders that are filled with an LC and form square lattice in a dielectric matrix. Figure 2 shows the seed band structure for the $SrTiO_3$ round rods type PCs sample with the parameters the permittivity of the air 1, and the filling factor 30%.

For the filling factor 30% this PC has the maximum width of the complete band gap. In this case, the photonic band gap along the direction between high symmetry points $\Gamma - X$ direction of the Brillouin Zone lies in the frequency range around $1.07(2\pi c/a)$.

A comparison of Figure 2 and Figure 3 shows that the spectra of seed PC of both types have a similar structure. This is obviously explained by the fact that these crystals have close factors of filling with dielectric materials.

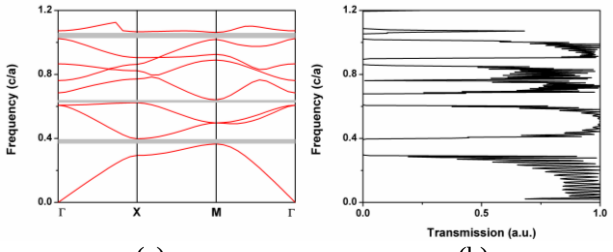

(a) (b)

Figure 3: (a) The photonic band structure in **TM** mode (b); Transmission spectrum of $SrTiO_3$ round rods with nematic LC-infilled with extraordinary refractive index in air background in square lattice.

Structure and material are very important to determine the optical properties of a PC structure as aforementioned. Therefore, we changed the PC structure in order to obtain optimum results. The materials' refractive index values have the same values as in the above calculations.

We consider that 2D PC of $SrTiO_3$ square rods in an air background in a square lattice with lattice constant $a = 1\mu m$. Parameters $l_1 = 0.6a$ and $l_3 = 0.2a$ denote the outer and inner length of $SrTiO_3$ and $l_2 = 0.4a$ length of the air and the sides of the square rods are parallel to the primitive reciprocal lattice vectors in Figure 1 (b). The photonic band structure is calculated along with the high symmetry point for the Brillouin zone in a square lattice (Figure 4). According to Figure 4 there is also no band gap in **TM** mode. When $SrTiO_3$ square rods are compared with $SrTiO_3$ round rods in a square lattice, it is seen that there is a reduction in the band gap number of the square structure.

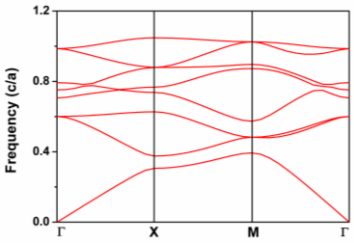

Figure 4: The photonic band structure in **TM** mode of $SrTiO_3$ square rods with air-infilled in air background in square lattice.

The photonic band structure of $SrTiO_3$ square rods modulated by nematic LC is studied again for extraordinary refractive index of LC. There is only one band gap in **TM** mode as shown in Figure 5 (a). Their relative widths are 2.63%, and the center normalized frequencies are $0.361(2\pi c/a)$.

The transmission spectrum of $SrTiO_3$ square rods with nematic LC-infiltrated is zero at frequencies between $0.293(2\pi c/a)$ and $0.383(2\pi c/a)$, between $0.599(2\pi c/a)$ and $0.664(2\pi c/a)$, between $0.762(2\pi c/a)$ and $0.776(2\pi c/a)$, between $0.870(2\pi c/a)$ and $0.891(2\pi c/a)$, between $1.075(2\pi c/a)$ and $1.187(2\pi c/a)$ in Figure 5 (b). When the PC structure is turned into $SrTiO_3$ square rods, it can be clearly seen that PBG has become narrow and that there was a decrease in the band gap.

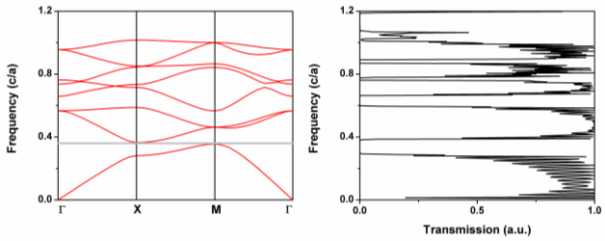

(a) (b)

Figure 5: (a) The photonic band structure in **TM** mode (b); Transmission spectrum of $SrTiO_3$ square rods with nematic LC-infilled with extraordinary refractive index in air background in square lattice.

3.2. Equi-frequency surface

Because, the momentum conservation law is satisfied at the reflection and refraction of waves, it is convenient to analyze the reflection and refraction of a certain wave in the space of wave numbers $\sum_{\vec{k}} = \{0; k_x, k_y, k_z\}$ by introducing the equi-frequency surface of the wave. This surface is directly described by the dispersion relation of the anisotropic medium at the fixed frequency ω. Then, the group velocity $\vec{V}_g$ of the wave in an anisotropic medium can be found as the frequency gradient in the space of wave vectors [24]. It is known that for an electromagnetic wave propagating in an anisotropic medium with a fixed frequency ω, the equi-frequency surface represents a sphere. In this case, the wave vector $\vec{k}$ and group velocity vector $\vec{V}_g$, which determines the ray direction, are always parallel. However, equi-frequency surface is not spherical for anisotropic media and the vectors $\vec{V}_g$ and $\vec{k}$ are not parallel. By analogy with 3D case, the propagation, reflection, and refraction of the wave in 2D structure can be describe in terms of the equi-frequency dependence which can be considered as the section of the dispersion surface $\omega(k_y, k_z)$ in the space of variables $\{\omega, k_y, k_z\}$ by the plane corresponding to constant frequency. It is well known that the analysis of equi-frequency dependences is most efficient in the studies of 2D geometries, especially in solving problems when only orientations of the $\vec{V}_g$ and $\vec{k}$ vector of incident, reflected, and refracted waves are of interest, and are not the amplitudes of the reflected and refracted rays. The equi-frequency dependence has a simple physical meaning for the analysis of 2D geometries: since this dependence describe all the possible waves with the given frequency ω and various wave vectors, the directions of the reflected and the refracted rays can be determined by simply finding the points in equi-frequency dependences of media that satisfy the momentum conservation law at a known orientation of the boundary and a given angle of incidence of the wave.

Now, we present some numerical examples for our PC structures. In all these examples, we exploit symmetry to calculate the equi-frequency surfaces over the irreducible Brillouin Zone of the entire Brillouin Zone. First, we consider the equi-frequency surface of a square lattice of air hole in a dielectric medium for the $\vec{H}$ –polarization. In Figure 6 we reproduce PC with $SrTiO_3$ round rods in an air background $(\varepsilon_a = 1)$ in the square lattice parameters the lattice constant $a = 1\ \mu$m, radius $r_1 = 0.3a$ and $r_3 = 0.1a$ and refractive index of $SrTiO_3$ $n = 2.40252$, radius $r_2 = 0.2a$ and refractive index of the air $n = 1$. Here, the map was discretized using six field points per edge of the unit cell for the first band in Figure 6 (a). The map was discretized using four field points per edge of the unit cell for the second band in Figure 6 (b). The curves shown correspond to equi-frequency surfaces of the lowest order band up to frequencies just below the band gap starting at around $1.048(2\pi c/a)$.

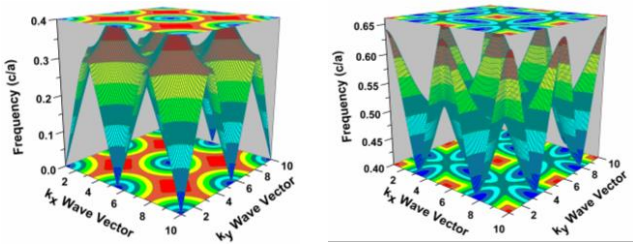

(a) (b)

Figure 6: The equi-frequency contours of PC with $SrTiO_3$ round rods in an air background for the square lattice (a) first band (b) second band.

In Figure 7, we reproduce for PC with $SrTiO_3$ round rods of nematic LC-infill in an air background for the square lattice parameters the same for $SrTiO_3$ round rods and extraordinary refractive index of E7 type LCs $n_e = 1.73657$ for radius $r_2 = 0.2a$. The map was discretized using five field points per edge of the unit cell for the first band in Figure 7 (a). For the second band, the map was discretized using four field points per edge of the unit cell in Figure 7 (b). The curves shown correspond to equi-frequency surfaces of the lowest order band up to frequencies just below the band gap starting at around $0.365(2\pi c/a)$. Because of the three band gap, the band gap from band 3 to band 4 are between $0.623(2\pi c/a)$ and $0.642(2\pi c/a)$, and the band gap from band 7 to band 8 are between $1.024(2\pi c/a)$ and $1.063(2\pi c/a)$.

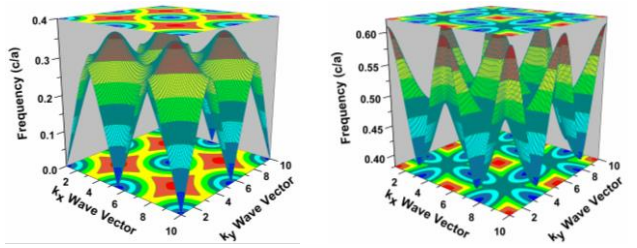

(a) (b)

Figure 7: The equi-frequency contours of PC with $SrTiO_3$ round rods of nematic LC-infill in an air background for the square lattice (a) first band (b) second band.

In Figure 8, we reproduce for PC with $SrTiO_3$ square rods in an air background for the square lattice parameters $l_1 = 0.6a$ and $l_3 = 0.2a$ the outer and inner length of $SrTiO_3$ and $l_2 = 0.4a$ length of the air. For the first band, the map was discretized using five field points per edge of the unit cell (Figure 8 (a)). The map was discretized using four field points per edge of the unit cell for the second band in Figure 8 (b). The curves shown correspond to equi-frequency surfaces of the non-band gap.

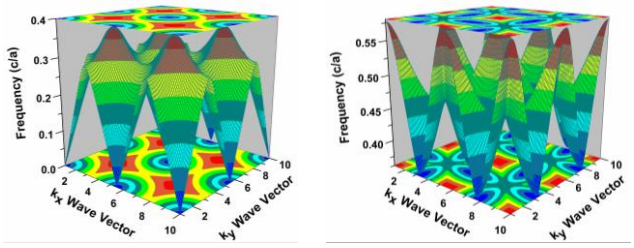

(a) (b)

Figure 8: The equi-frequency contours of PC with $SrTiO_3$ square rods in an air background for the square lattice (a) first band (b) second band.

In Figure 9 we reproduce for PC with $SrTiO_3$ square rods of nematic LC-infill in an air background for the square lattice parameters the same for $SrTiO_3$ square rods and $l_2 = 0.4a$ length of the LCs. The map was discretized using six field points per edge of the unit cell for the first band in Figure 6 (a). For the second band, the map was discretized using four field points per edge of the unit cell (Figure 6 (b)). The curves shown correspond to the equi-frequency surfaces of the lowest order band up to frequencies just below the band gap starting at around $0.356(2\pi c/a)$.

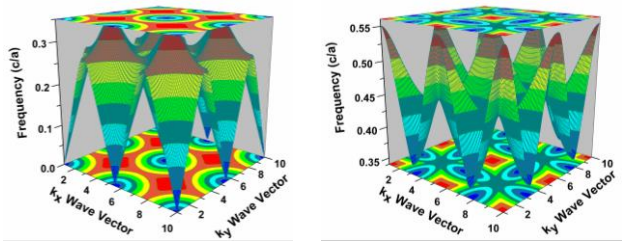

(a) (b)

Figure 9: The equi-frequency contours of PC with $SrTiO_3$ square rods of nematic LC-infill in an air background for the square lattice (a) first band, (b) second band.

3.3. Group velocity

We believe a pulse of light propagating along the PC let the pulse be finite in dimension along the direction of propagation. Theoretically, such a pulse can be represented as a wave packet formed as a superposition of the modes, but with a different propagation constant [25]. From [25], it follow that the envelope of the wave packet propagates with the velocity $V_g^z = \omega_n(\beta)$, where β is propagation constant. The direct calculation of the derivative of the dispersion relation calculated numerically is not always convenient and can give error. As shown in [26], the group velocity of the wave packet V_g^z, is equal to the velocity of energy transfer by the mode $n\beta$. Thus, by using the results of [26] the group velocity can be always calculated more accuracy, irrespective of the number of points in the dispersion curve.
Figures 10 and 11 show the results of calculations of the group velocity of the wave packet formed of the differently polarized localized modes in PC with $SrTiO_3$ round rods, PC with $SrTiO_3$ round rods of nematic LC-infill, PC with $SrTiO_3$ square rods, and PC with $SrTiO_3$ square rods of nematic LC-infill in an air background in the square lattice, respectively.

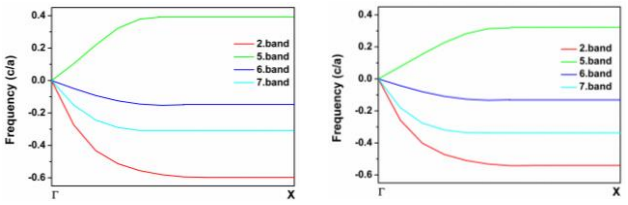

(a) (b)

Figure 10: The group velocity in **TM** mode of (a) PC with $SrTiO_3$ round rods (b) PC with $SrTiO_3$ round rods of nematic LC-infill in an air background for the square lattice.

From Figures 10 and 11, it is evident that the components of the group velocity versus the high symmetry direction (Γ–X) vary over wide limits. The dependences $V_g^z(\beta)$, which describe the wave packets of localized modes of any polarization and any order, exhibit (generally) a maximum at certain propagation constants. This means that the dispersion of group velocity can be positive, negative, or zero [27].

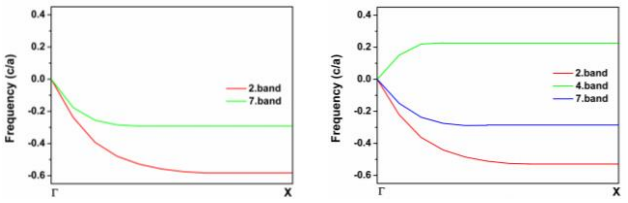

(a) (b)

Figure 11: The group velocity in **TM** mode of (a) PC with $SrTiO_3$ square rods (b) PC with $SrTiO_3$ square rods of nematic LC-infill in an air background for the square lattice.

Therefore, as can be seen in Figure 12 the group velocity of **TE** polarized wave packets is almost always higher than that of the **TM**-polarized packets.

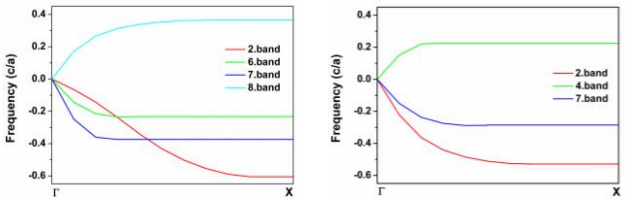

(a) (b)

Figure 12: The group velocity of PC with $SrTiO_3$ square rods of nematic LC-infill in an air background for the square lattice in (a) **TE** mode, (b) **TM** mode.

4. Conclusions

We analyzed the optical properties in a 2D PC structure of ferroelectric round and square rods filled without and with nematic LCs in a square lattice. The photonic band structure for **TE** and **TM** mode is calculated along with the high symmetry point for the Brillouin zone.
It has been shown that the dispersion of 2D seed photonic structure in combination with the dispersion of nematic LC

leads to qualitative changes in the band structure of the spectrum of the intrinsic electromagnetic excitations of the LC infiltrated PC.

In practical applications, such LC infiltrated photonic crystals are promising materials for use in the design of narrow band filters and a new type of optoelectronic devices.

Acknowledgements

One of the authors (Filiz Karaomerlioglu) would like to thank The Scientific and Technological Research Council of Turkey (TUBITAK) Postdoctoral Fellowship.

References

[1] E. Yablonovitch, Photonic band-gap structures, *J. Opt. Soc. Am. B* 10: 283-295, 1993.

[2] J. D. Joannopoulos, S. G. Johnson, J. N. Winn and R. D. Meade, *Photonic Crystals: Molding the Flow of Light*, Princeton University Press, Princeton, NJ, 2008.

[3] C. Sibilia, T. M. Benson, M. Marciniak, T. Szoplik, *Photonic Crystals: Physics and Technology*, Springer, Italia, 2008.

[4] K. Sakoda, *Optical Properties of Photonic Crystals*, Springer, Germany, 2005.

[5] M. C. Gupta, J. Ballato, *The Handbook of Photonics*, CRC Press, USA, 2007.

[6] J. M. Brosi, *Slow-Light Photonic Crystal Devices for High-Speed Optical Signal Processing*, University of Karlsruhe, Germany, 2009.

[7] I. C. Khoo, S. T. Wu, *Optics and nonlinear optics of liquid crystals: Electro-optical properties of liquid crystals*, World Scientific; Singapore, pp.100-258, 1993.

[8] C. Y. Liu, Tunable lightwave propagation in two-dimensional hole-type photonic crystals infiltrated with nematic liquid crystal, *Physica E* 44: 313-316, 2011.

[9] C. Y. Liu, Creation of tunable absolute band gaps in a two-dimensional anisotropic photonic crystal modulated by a nematic liquid crystal, *Phy. Lett. A* 372: 5198-5202, 2008.

[10] C. Y. Liu, L. W. Chen: Tunable field-sensitive polarizer using hybrid conventional waveguides and photonic crystal structures with nematic liquid crystals, *Optics Commun.* 256: 114-122, 2005.

[11] C. Y. Liu, L. W. Chen: Tunable photonic-crystal waveguide Mach-Zehnder interferometer achieved by nematic liquid-crystal phase modulation, *Opt. Express* 12: 2616-2624, 2004.

[12] C. Y. Liu, L. W. Chen: Tunable photonic crystal waveguide coupler with nematic liquid crystals, *IEEE Photonics Tech. Lett.* 16: 1849-1851, 2004.

[13] C. Y. Liu, L. W. Chen: Tunable full band gap in a three-dimensional photonic crystal modulated by a nematic liquid crystal, *Physica E* 35: 173-177, 2006.

[14] C. Y. Liu, L. W. Chen: Tunable channel drop filter in a two-dimensional photonic crystal modulated by a nematic liquid crystal, *J. Nanomaterials* 2006: 1-6, 2006.

[15] C. Y. Liu, L. W. Chen: Tunable band gap in a photonic crystal modulated by a nematic liquid crystal, *Phys. Rev. B* 72: 045133-045138, 2005.

[16] C. Y. Liu, Y. T. Peng, J. Z. Wang, L. W. Chen: Creation of tunable band gaps in a three-dimensional anisotropic photonic crystal modulated by a nematic liquid crystal, *Physica B* 388: 124-129, 2007.

[17] C. Y. Liu, N. W. Zhang, H. W. Wang, L. W. Chen: Efficient tunable negative refraction photonic crystal achieved by an elliptic rod lattice with a nematic liquid crystal, *Physica B* 404: 4060-4070, 2009.

[18] G. Sun, A. G. Kirk, Analyses of negative refraction in the partial bandgap of photonic crystals, *Optics Express* 16 (6): 4330-4336, 2008.

[19] L. Shi, H. Yin, X. Zhu, X. Liu, J. Zi, Direct observation of iso-frequency contour of surface modes in defective photonic crystals in real space, *App. Phy. Lett.* 97: 251111, 1-3 , 2010.

[20] Y. Y. Wang, L. W. Chen, Tunable negative refraction photonic crystals achieved by liquid crystals, *Opt. Express* 14: 10580-10587, 2006.

[21] G. V. Eleftheriades, K. G. Balmain, *Negative-Refraction Metamaterials: Fundamental Principles and Applications*, John Wiley & Sons, Canada, 2005.

[22] A. Taflove, *Advances in computational electrodynamics: The Finite-Difference Time-Domain Method: A survey of The Finite-Difference Time-Domain literature*, MA: Artech House, London, pp.1-30, 1998.

[23] C. Kittel, *Introduction to Solid State Physics*, John Wiley & Sons, New York, 2005.

[24] E. H. Lock, The properties of isofrequency dependences and the laws of geometrical optics, *Physics-Uspekhi* 51(4): 375-393, 2008.

[25] A. S. Spitsyn and G. F. Glinskii, Properties of Waveguide Modes in a Photon Crystal Based on Slotted Silicon with a Defect, *Semiconductors* 42(10): 1237-1243, 2008.

[26] A. Yariv, P. Yeh, *Photonics: Optical Electronics in Modern Communications*, Oxford University Press, USA, 2007.

[27] A. V. Kildishev, V. M. Shalaev, Transformation optics and metamaterials, *Physics-Uspekhi* 54(1): 53-63, 2011.

Numerical study on the structural color of blue birds by a disordered porous photonic crystal model

Tsuyoshi Ueta[1*], Garuda Fujii[2], Gen Morimoto[3], Kiyoshi Miyamoto[4], and Akinori Kosaku[4]

[1]Physics Laboratory, The Jikei University School of Medicine, Tokyo, Japan
[2]Faculty of Engineering, Shinshu University, Nagano, Japan
[3]Department of Life Sciences, Rikkyo University, Tokyo, Japan
[4]Insitiute for Medical Science, Dokkyo University School of Medicine, Tochigi, Japan
*corresponding author, E-mail: tsuyoshi_ueta@jikei.ac.jp

Abstract

It has been observationally confirmed that the color of birds, such as kingfisher and red-flanked bushrobin, is a structural color owing to interference of the light within a sponge structure inside a barb. In this study, we consider the air rod photonic crystal to which disorder is introduced into the translation vectors and the radius as a model of the structural color of red-flanked bushrobin, and the optical property of the model is numerically analyzed and is compared with that of the structural color.

1. Introduction

The essential structure producing the structural color has been vigorously investigated for various creature like a morpho butterfly, a kingfisher, etc.[1, 2, 3, 4, 5, 6, 7, 8] It has been shown that the three-dimensional cuticular structures in the butterfly wing of some papilionids and lycaenids can be modelled by gyroid structures with various filling fractions and lattice parameters by analytically modelling published scanning and transmission electron microscopy images.[9] It expresses three-dimensional optical photonic crystals.

Concerning avian cases, study on the peacock whose interference structure is rather simple has already been progressed.[10, 11, 12] It has been observationally found that the sponge structure within the ramus of a feather produces the blue color of the kingfisher etc. The gyroid structures are similar to the sponge structures, whereas the former are periodic and the latter are disordered. The complexity of the structure however prevents progress of theoretical study.

On the other hand, it was numerically shown that the structure "photonic amorphous diamond (PAD)" possesses a sizable three dimensional photonic band gap (PBG) and that it can confine light at a defect as strongly as conventional photonic crystals can, where PAD is based on a "continuous-random-network (CRN)" of diamondlike tetrahedral-bonding configuration. The photonic density of states and the spectral intensities for the PAD were calculated by a finite difference time domain (FDTD) spectral method.[13, 14]

Figure 1: A photo of red-flanked bushrobin, Tarsiger cyanurus.

Although this model might explain the avian structural color, the constructing way of the model is unnatural compared with that of biomaterial. By experience of the numerical analysis of the optical property of photonic crystals and random lasers,[15, 16, 17] furthermore, we consider that the numerical analysis of such a complicated structure assuming a structural color requires a numerical method beyond the FDTD method in accuracy.

In this paper, we propose a sponge structure model as a model of a barb of the red-flanked bushrobin, Tarsiger cyanurus, whose sponge layer is rather thin and whose bubbles within the sponge structure are long in the direction of the barb.

Although the goal of our project is to analyze the optical property of the whole system of the model numerically by means of the finite element method[16, 17], here, results of analysis of a more simplified model with the vector KKR method[15] are reported as progress.

2. Numerical Model

We pay attention to the cross-sectional structure of the barb of the red-flanked bushrobin since the bubble in a barb is long in the direction of a barb.[13, 18] The berb is mod-

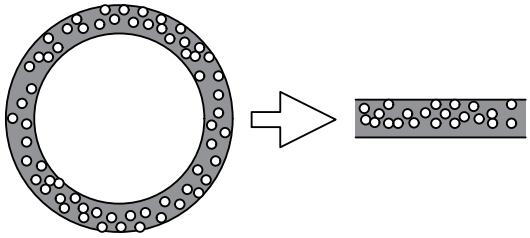

Figure 2: A model of a barb of the red-flanked bushrobin.

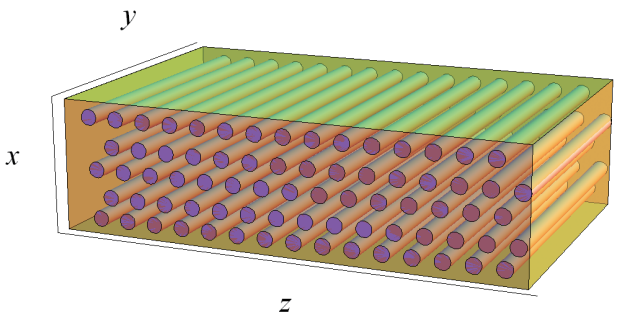

Figure 3: A model of the disordered porous photonic crystal.

eled by a infinitely wide dielectrics plate with randomly arranged cylindrical holes (air rods) (Fig.2). Here, the curvature on the surface of a barb is disregarded. We consider a plane layer in which air rods are infinitely arranged at parallel and a porous photonic crystal (PPC) made by piling up five of the layer so that the rods configure the triangular lattice (Fig.3). In this case, the disorder is introduced into the PPC by assuming the translation vector and the radius of the rods with randomness of 30% of the layers, respectively.

3. Numerical Method

In order to compute the exact scattering matrix (S matrix) for a monolayer, we employ the vector KKR method in which the tensor Green function is expanded in terms of the vector cylindrical waves.[15]

By using the layer-doubling method with the S matrix for a monolayer, we may obtain the S matrix for an entire system of stacked layers. From the S matrix for the entire system, the transmission and reflection spectra are calculated directly.[19]

For a system of arrayed cylinders, the necessary quantities and formulations are all given in Ref. [15].

The S matrices are, now, defined including the phase factors which result from the translation between layers. The key point to calculate the S matrix for the present system of disordered structure is to compute the monolayer S matrix with the random radius a and the random translation vector $\mathbf{t}$ defined by

$$a = \bar{a} + \sqrt{3}\sigma_a\,(2\ \mathrm{rnd}_1 - 1)\,, \tag{1}$$

$$\mathbf{t} = \frac{d}{2}\left(1, \sqrt{3}\right) + \sqrt{\frac{3}{2}}\sigma_d(2\ \mathrm{rnd}_2 - 1, 2\ \mathrm{rnd}_3 - 1) \tag{2}$$

where $\bar{a}$ and d are the average radius of a air rod and the lattice constant of the triangular lattice, and σ_a and σ_d are the standard deviation of the radius and that of the lattice constant, respectively. rnd_1, rnd_2 and rnd_3 are independent uniform random numbers in the range from 0 to 1.

The S matrix of n layers is obtained by combining the S matrix of $n-1$ layers and that of monolayer. It was confirmed that the latter transmits the incident light without reflection and refraction. The composite S matrix for the total system is then obtained by applying $n-1$ times the layer-doubling method.

Here each S matrix is expressed as

$$\mathbf{S} = \begin{pmatrix} \mathbf{T} & \mathbf{R}' \\ \mathbf{R} & \mathbf{T}' \end{pmatrix} \tag{3}$$

and the rule for the layer doubling is given by

$$\mathbf{S}_1 \otimes \mathbf{S}_2 = \begin{pmatrix} \mathbf{T}_1 & \mathbf{R}'_1 \\ \mathbf{R}_1 & \mathbf{T}'_1 \end{pmatrix} \otimes \begin{pmatrix} \mathbf{T}_2 & \mathbf{R}'_2 \\ \mathbf{R}_2 & \mathbf{T}'_2 \end{pmatrix} \tag{4}$$

$$= \begin{pmatrix} \mathbf{T}_2\left(\mathbf{I} - \mathbf{R}'_1\mathbf{R}_2\right)^{-1}\mathbf{T}_1 & \mathbf{R}'_2 + \mathbf{T}_2\mathbf{R}'_1\left(\mathbf{I} - \mathbf{R}_2\mathbf{R}'_1\right)^{-1}\mathbf{T}'_2 \\ \mathbf{R}_1 + \mathbf{T}'_1\mathbf{R}_2\left(\mathbf{I} - \mathbf{R}'_1\mathbf{R}_2\right)^{-1}\mathbf{T}_1 & \mathbf{T}'_1\left(\mathbf{I} - \mathbf{R}_2\mathbf{R}'_1\right)^{-1}\mathbf{T}'_2 \end{pmatrix} \tag{5}$$

where I being the unit matrix. The matrices **I**, **T**, **R**, **T'** and **R'** are $3N \times 3N$ block matrices, where N is the number of one-dimensional reciprocal-lattice vectors parallel to the z axis that are equal to the number of scattering channels, open or closed, which were taken into account for the numerical evaluation of the S matrices. The factor 3 in the dimension comes from the number of the components of the electric field, (E_x, E_y, E_z).

The S matrix of the whole system computed in this way enables us to compute the transmission and reflection coefficients for the incident fields with any polarization and any incident angle. We, now, assume a 5 layers system and a plane wave at normal incidence.

4. Numerical Results

According to the material of a avian barb, the relative dielectrics of the base material, that is, the background is set to $\varepsilon = 2.16$. The absorption by a substance is not taken into consideration.

By our measurement, we obtained numerical data as follows: the average radius of air rods $\bar{a} = 52.5$nm and the average interval between air rods $d = 242$nm, the standard deviation of the radius $\sigma_a = 7.5$nm and the standard deviation of the lattice constant $\sigma_d = 37$nm. The scaled radius of the air rod is set to $a/d = 0.216942$.

The reflection spectrum for the perpendicular incidence of a plane wave to the regular PPC (namely, $\sigma_a = 0$ and $sigma_d = 0$) is shown in Fig. 4. Even the system of only five layers has high-reflection domains in both of

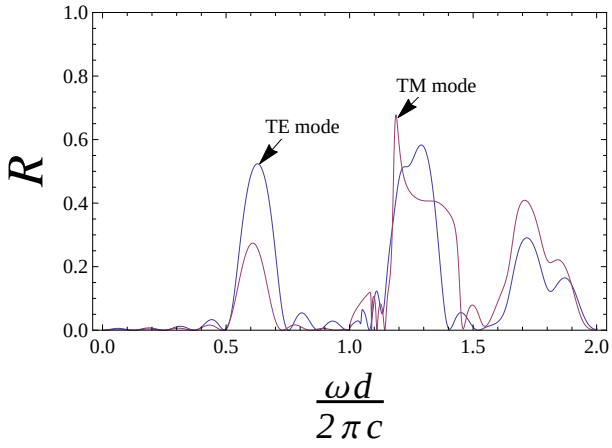

Figure 4: The reflection spectrum for the perpendicular incidence of a plane wave to the regular porous photonic crystal.

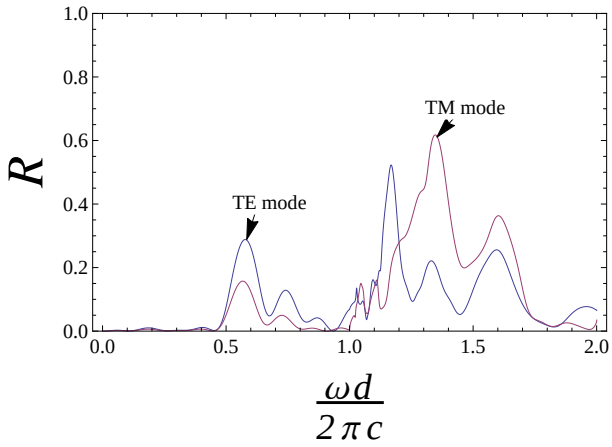

Figure 5: The reflection spectrum for the perpendicular incidence of a plane wave to a certain configuration of the disordered porous photonic crystal with $\sigma_a/a = 0.143$ and $\sigma_d/d = 0.153$.

TE and TM modes at $0.5 < \omega d/(2\pi c) < 0.73$, $1.15 < \omega d/(2\pi c) < 1.4$ and $1.65 < \omega d/(2\pi c) < 1.9$, and they show formation of photonic band gaps.

Figure 5 shows the reflection spectrum of a certain configuration of the disordered system the disordered porous photonic crystal with $\sigma_a/a = 0.143$ and $\sigma_d/d = 0.153$. The disorder broadens the peaks more in higher frequency where spectrum is sensitive to fine structure and forms subpeaks. The reflection spectrum of the TM mode is more sensitive to disorder than that of the TE mode.

We find that the blue structural color of the red-flanked bushrobin originates in the reflection by the first photonic band gap.

In Fig. 6, the averaged reflection probability (%) about 10 configurations is plotted versus the wavelength λ nm. The wavelength range where the reflection probability is

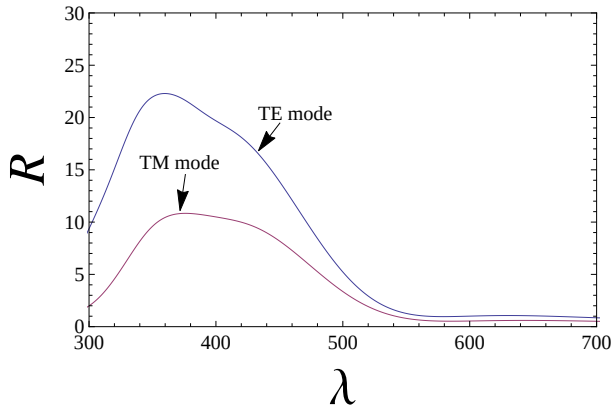

Figure 6: the wavelength λnm dependence of the reflection probability (%) averaged about 10 configurations.

significant agrees well with that of Fig. 1 of Ref. [10], and the structure with a tail to the long wavelength side is also well alike each other. The peak position of the reflection spectrum , however, differs from that of Fig. 1 of Ref. [10]. It would be attributed to the extreme simplification of our model.

5. Conclusions and Discussions

We proposed the disordered air rod photonic crystal as a model of the structural color of the feather of blue birds, and computed the reflection properties. It was found that the reflection spectra are broadened more at higher frequency due to disorder of the lattice of the photonic crystal. The blue structural color is attributed to the reflection by the first photonic band gap of the disordered porous photonic crystal.

Edagawa *et al* found that a full three-dimensional (3D) PBG in a photonic amorphous structure in spite of complete lack of periodicity.[13, 14] Edagawa emphasized that the key of this phenomenon would be that the unit structure has four bonds. In the 3D case of our model, that is, a dielectric substance with randomly arranged air spheres, when the air spheres grow up and overlap each other, the dielectric substance forms continuous network of Plateau boundaries like a dry foam.[20] Then, a usual junction consists of four Plateau boundaries. Namely, this case of our model is essentially same as CRN, and our model is more general and simple to describe.

As already mentioned, our goal is to analyze the whole system by means of FEM which is generally considered to be a numerical method of high accuracy. We have already started to analyze the scattering by the whole structure shown in Fig. 7 by using FEM. We have found that an incident plane wave with a wavelength of 470nm which is a reflection peak position of Fig. 1 of Ref [10] is strongly reflected on the surface of and within the sponge structure of doughnut shape. These detailed results will appear soon elsewhere.

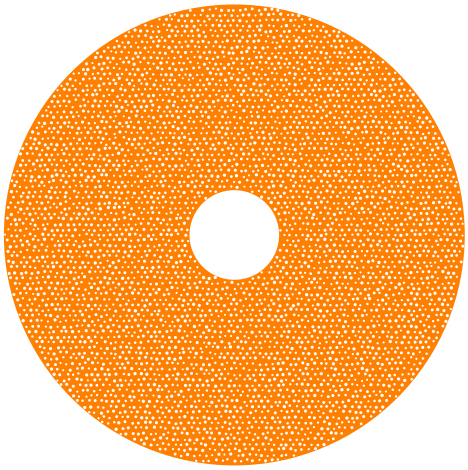

Figure 7: A model of a feather barb for FEM analysis.

Acknowledgement

This work was supported by JSPS Grant-in-Aid for Scientific Research (C), Grant No. 23540436.

References

[1] D. S. Wiersma, Disordered photonics, *Nature Photonics*, 12: 188–196, 2013.

[2] Helen Ghiradella, Light and color on the wing: structural colors in butterflies and moths, *Applied Optics*, 30: 3492–3500, 1991.

[3] K. Michielsen and D. G. Stavenga, Gyroid cuticular structures in butterfly wing scales: biological photonic crystals, *J. R. Soc. Interface*, 5: 85–94, 2008.

[4] A. L. Ingram and A. R. Parker, A review of the diversity and evolution of photonic structures in butterflies, incorporating the work of John Huxley (The Natural History Museum, London from 1961 to 1990), *Phil. Trans. R. Soc. B*, 363: 2465–2480, 2008.

[5] Géza I. Márk, Zofia Vértesy, Krisztián Kertész, Zsolt Bálint and László P. Biró, Order-disorder effects in structure and color relation of photonic-crystal-type nanostructures in butterfly wing scales, *Phys. Rev. E*, 80: 051903, 2009.

[6] Dong Zhu and Shuichi Kinoshita, Investigation of structural colors in Morpho butterflies using the nonstandard-finite-difference time-domain method: Effects of alternately stacked shelves and ridge density, *Phys. Rev. E*, 80: 051924, 2009.

[7] Ying-Ying Diao and Xiang-Yang Liu, Mysterious coloring: structural origin of color mixing for two breeds of Papilio butterflies, *Optics Express*, 19: 9232–9241, 2011.

[8] P. Vukusic and J.R. Sambles, Photonic structures in Biology, *Nature*, 424: 852–855, 2003.

[9] K Michielsen and D.G Stavenga, Gyroid cuticular structures in butterfly wing scales: biological photonic crystals, *J. R. Soc. Interface*, 5: 85–94, 2008.

[10] Gen Morimoto, Noriyuki Yamaguchi and Keisuke Ueda, Plumage color as a status signal in male-male interaction in the red-flanked bushrobin, Tarsiger cyanurus, *J. Ethol.*, 24: 261–266, 2005.

[11] Richard O. Prum, Rodolfo H. Torres, Scott Williamson and Jan Dyck, Coherent light scattering by blue feather barbs, *Nature*, 396: 28–29, 1998.

[12] Vinodkumar Saranathan, Jason D. Forster, Heeso Noh, Seng-Fatt Liew, Simon G. J. Mochrie, Hui Cao, Eric R. Dufresne and Richard O. Prum, Structure and optical function of amorphous photonic nanostructures from avian feather barbs: a comparative small angle X-ray scattering (SAXS) analysis of 230 bird species, *J. R. Soc. Interface*, doi:10.1098/rsif.2012.0191, 2012

[13] Keiichi Edagawa, Satoshi Kanoko and Masaya Notomi, Photonic AmorphousDiamond Structure with a 3D Photonic Band Gap, *Phys. Rev. Lett.*, 100: 013901, 2008.

[14] Shigeki Imagawa, Keiichi Edagawa, Keisuke Morita, Toshiki Niino, Yutaka Kagawa and Masaya Notomi, Photonic band-gap formation, light diffusion, and localization in photonic amorphous diamond structures, *Phys. Rev. B*, 82: 115116, 2010.

[15] Kazuo Ohtaka, Tsuyoshi Ueta and Katsuki Amemiya, *Phys. Rev. B*, 57: 2550–2568, 1998.

[16] G. Fujii, T. Matsumoto, T. Takahashi and T. Ueta, Finite Element Analysis of Laser Modes within Photonic Random Media, *J. Phys. B: At. Mol. Opt. Phys.*, 45: 085404, 2012.

[17] G. Fujii, T. Matsumoto, T. Takahashi and T. Ueta, Study on transition from photonic-crystal laser to random laser, *Optics Express*, 20, 7300–7315, 2012.

[18] B. Q. Dong, X. H. Liu, T. R. Zhan, L. P. Jiang, H. W. Yin, F. Liu and J. Zi, Structural coloration and photonic pseudogap in natural random close-packing photonic structures *Optics Express*, 18: 14430–14438, 2010.

[19] Tsuyoshi Ueta, Kazuo Ohtaka, Noriko Kawai and Kazuaki Sakoda, *J. Appl. Phys.*, 84: 6299-6304, 1998.

[20] Denis Weaire and Stefan Hutzler, *The Physics of Foams*, (Oxford University Press, 1999).

FSS, HIS and Extraordinary transmission

Analysis of Periodic Strong Chiral - Metamaterial Structures as Frequency Selective Surfaces and Polarization Rotators Using Transfer Matrix Method

M. J. Mughal[1], S. K. Marwat[2,*], N. Amin[2], M. Omar[2]
[1]Department of Electrical Engineering, COMSATS Institute of Information Technology, Islamabad, Pakistan
[2]Faculty of Electrical Engineering, Ghulam Ishaq Khan Institute, Topi(23640), Pakistan
*Corresponding author: safiullah.khan@hotmail.com

***Abstract*—In this paper, an electromagnetic wave of millimeter wavelength is incident on multilayered metamaterial structure. Transfer matrix method is used to find the fields on either side of the structure. Field equations are the function of frequency, chirality, angle and length. Numerical results for both normal and oblique incident angles are presented in the paper. All the cases satisfy the power conservation law. The structures behave as bandpass and/or band-reject filters. These structures can be used in filter, radomes and polarization rotators.**

I. Introduction

Multilayered structures are used to construct radomes and frequency selective surfaces [1], [2]. Radome is used to protect antenna from unwanted signal interferences. It blocks all irrelevant signals and only allows relevant signals that an antenna transmits and receives, with minimum attenuation [3]. The radiation pattern of the actual antenna differs from that of the mounted antenna radiation pattern (which is highly undesirable). This happen because strong radiations present near an antenna interfere with its radiation pattern and effect the antenna performance. The difference of radiation pattern is the effect due to interference caused by the induced current. Therefore, an antenna is shielded and protected to avoid distortion. Furthermore, generation of polarization rotators with good and broad sideband suppressions are useful in data transmission applications [4].

The structures presented in this paper are composed of multilayered metamaterials (MTMs). MTMs are man made artificial materials that donot exist in nature. These materials can be engineered to achieve desired electromagnetic properties. Chiral (CH) material have the property of non-superposable to their mirror image. Lakhtakia introduced the nihility term for material whose $\epsilon = \mu = 0$ for certain range of frequency and chirality is non-zero [5]. Strong chiral (SC) materials have chirality to refractive index ratio greater than 1 ($\kappa_r \geq 1$) [6]. Also, materials whose permeability and permittivity both are negative are called double negative (DNG) materials. Multilayered structures composed of such materials results in high bandwidth and suppressed sidebands thereby giving freedom to operate in the larger bands and achieve desired results.

II. Formulation

Figure 1 depicts the five layered structure layout and essential parameters associated with it. Incident and transmitted

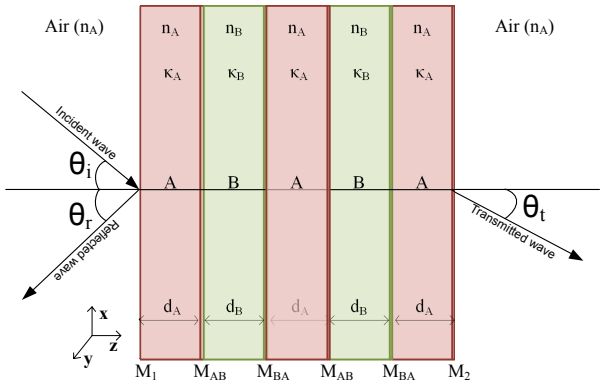

Fig. 1: Five layered metanaterial structure

medium is air. Slab A is of strong chiral material and slab B is strong chiral, dielectric and double negative material. Transfer matrix method is used to relate fields on either side of the structure [7]. The incident, reflected and transmitted fields in air can be written as in [8],

$$\mathbf{E}_i = [E_{i\|}(\hat{x}\cos_{\theta_i} + \hat{z}\sin_{\theta_i}) + E_{i\perp}\hat{y}]e^{-jk_\circ(\hat{z}\cos_{\theta_i} - \hat{x}\sin_{\theta_i})} \tag{1}$$

$$\mathbf{E}_r = [E_{r\|}(\hat{x}\cos_{\theta_r} - \hat{z}\sin_{\theta_r}) + + E_{r\perp}\hat{y}]e^{jk_\circ(\hat{r}\cos_{\theta_r} + \hat{x}\sin_{\theta_r})} \tag{2}$$

$$\mathbf{E}_t = [E_{i\|}(\hat{x}\cos_{\theta_t} + \hat{z}\sin_{\theta_t}) + E_{t\perp}\hat{y}]e^{-jk_\circ(\hat{z}\cos_{\theta_t} - \hat{x}\sin_{\theta_t})} \tag{3}$$

$$\mathbf{H}_i = \frac{1}{\eta}[E_{i\|}\hat{y} - E_{i\perp}(\hat{x}\cos\theta_i + \hat{z}\sin\theta_i)]e^{-jk_\circ(\hat{z}\cos_{\theta_i} - \hat{x}\sin_{\theta_i})} \tag{4}$$

$$\mathbf{H}_r = \frac{1}{\eta}[E_{r\perp}(\hat{x}\cos\theta_r - \hat{z}\sin\theta_r - E_{r\|}\hat{y})]e^{jk_\circ(\hat{r}\cos_{\theta_r} + \hat{x}\sin_{\theta_r})} \tag{5}$$

$$\mathbf{H}_t = \frac{1}{\eta}[E_{t\|}\hat{y} - E_{t\perp}(\hat{x}\cos\theta_t + \hat{z}\sin\theta_t)]e^{-jk_\circ(\hat{z}\cos_{\theta_t} - \hat{x}\sin_{\theta_t})} \tag{6}$$

where k_0 and η are wave number and wave impedance for substrate (i.e. air) respectively. It is assumed that both the component parallel and perpendicular exist for the incident, reflected and transmitted wave. Parallel and perpendicular components are represented by $\|$ and $\perp$, respectively. The structure is composed of metamaterial slabs. Electromagnetic

fields within the structure are written as in [9].

$$\mathbf{E}^{+} = \mathbf{E}_L^{+} e^{-jk_L(z\cos\theta_L - x\sin\theta_L)} + \mathbf{E}_R^{+} e^{-jk_R(z\cos\theta_R - x\sin\theta_R)} \tag{7}$$

$$\mathbf{E}^{-} = \mathbf{E}_L^{-} e^{jk_L(z\cos\theta_L + x\sin\theta_L)} + \mathbf{E}_R^{-} e^{jk_R(z\cos\theta_R + x\sin\theta_R)} \tag{8}$$

$$\mathbf{H}^{+} = \mathbf{H}_L^{+} e^{-jk_L(z\cos\theta_L - x\sin\theta_L)} + \mathbf{H}_R^{+} e^{-jk_R(z\cos\theta_R - x\sin\theta_R)} \tag{9}$$

$$\mathbf{H}^{-} = \mathbf{H}_L^{-} e^{jk_L(z\cos\theta_L + x\sin\theta_L)} + \mathbf{H}_R^{-} e^{jk_R(z\cos\theta_R + x\sin\theta_R)} \tag{10}$$

where,

$$\mathbf{E}_L^{+} = E_L^{+}(\hat{x}\cos\theta_L + \hat{z}\sin\theta_L + j\hat{y}) \tag{11}$$

$$\mathbf{E}_R^{+} = E_R^{+}(\hat{x}\cos\theta_R + \hat{z}\sin\theta_R - j\hat{y}) \tag{12}$$

$$\mathbf{E}_L^{-} = E_L^{-}(-\hat{x}\cos\theta_L + \hat{z}\sin\theta_L + j\hat{y}) \tag{13}$$

$$\mathbf{E}_R^{-} = E_R^{-}(-\hat{x}\cos\theta_R + \hat{z}\sin\theta_R - j\hat{y}) \tag{14}$$

$$\mathbf{H}_L^{+} = \frac{-j}{\eta} E_L^{+}(\hat{x}\cos\theta_L + \hat{z}\sin\theta_L + j\hat{y}) \tag{15}$$

$$\mathbf{H}_R^{+} = \frac{j}{\eta} E_R^{+}(\hat{x}\cos\theta_R + \hat{z}\sin\theta_R - j\hat{y}) \tag{16}$$

$$\mathbf{H}_L^{-} = \frac{-j}{\eta} E_L^{-}(-\hat{x}\cos\theta_L + \hat{z}\sin\theta_L + j\hat{y}) \tag{17}$$

$$\mathbf{H}_R^{-} = \frac{j}{\eta} E_R^{-}(-\hat{x}\cos\theta_R + \hat{z}\sin\theta_R - j\hat{y}) \tag{18}$$

In the above field equations, k_L and k_R are the wave number for left circularly polarized (LCP) and right circularly polarized (RCP) waves, respectively. Wave number is defined as $k_g = \omega(\sqrt{\epsilon\mu} \mp \kappa\sqrt{\epsilon_0\mu_0})$ $(g = L, R)$. Applying boundary conditions on the field equations of air and structure at every interface, transition matrix is obtained.

$$\begin{bmatrix} E_{i\parallel} \\ E_{i\perp} \\ E_{r\parallel} \\ E_{r\perp} \end{bmatrix} = T \begin{bmatrix} E_{t\parallel} \\ E_{t\perp} \end{bmatrix} \tag{19}$$

where T is the transition matrix of order 4×2. It relates the total field on one side of the five layered structure to the fields on the other side.

$$T = [\mathrm{M}_1][\mathrm{P}_A][\mathrm{T}_1]^m[\mathrm{M}_2] \tag{20}$$

$$T_1 = [\mathrm{M}_{AB}][\mathrm{P}_B][\mathrm{M}_{BA}][\mathrm{P}_A] \tag{21}$$

The field equations are true for any odd number of slabs $(2m+1$, where m is a positive integer). Propagation matrices for slab A and slab B are $[\mathrm{P}_A]$ and $[\mathrm{P}_B]$, respectively. Furthermore, matching matrices $[\mathrm{M}_1]$, $[\mathrm{M}_{AB}]$ & $[\mathrm{M}_{BA}]$ are of order 4×4 whilst $[\mathrm{M}_2]$ in (20) is a matching matrix of order 2×4.

III. Results and Discussion

1) SC-SC Structure: In the first investigation, slabs at even places and slabs at odd places both are filled with strong chiral medium having $\kappa_r = 1.66$. Optical width of each slab is $\lambda_\circ/4$, where $\lambda_\circ$ is the operational wavelength at 1 THz. Figure 2 shows the reflected power at oblique incidence. It is seen that perpendicular component of reflection never increase more than 25%. Whereas, parallel component is approximately zero at 14° and 21°. Figure 3, which shows the transmit power as a function of incident angle tells that maximum transmission of 95% occurs at 11° for parallel component. Perpendicular component of the transmit power is 80% at 18°. Reflected power as a function of frequency at normal incidence is shown in Figure 4. It shows that the rejection bands are not sharp and strong. Also, zero reflection occurs at (≈0.43, 1.0, ≈1.58, and 2.0) THz. Maximum transmission occurs at 1.0 THz as can be seen in Figure 5. Occurrence of perpendicular transmission component for normal incidence means that the structure finds its application in polarization rotating devices.

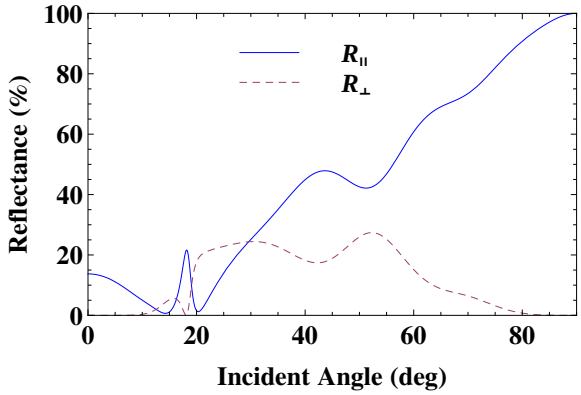

Fig. 2: Power reflected from five layered SC-SC structure when $n_A = 0.76, n_B = 0.46, \kappa_A = \kappa_B = 0.8, \mid n_A \mid d_A = \mid n_B \mid d_B = \lambda_\circ/4$, and $f = 1.5$ THz

2) SC-dielectric Structure: As a second examination, slabs at odd places are replaced with dielectric medium having dielectric constant of 4.8. The structure behaves as a band-reject filter as seen in Figure 6. In Figure 7, there is no transmission for incident angle greater than 40°. Furthermore, Figure 8 shows that the structure acts as a band-reject filter for wide range of frequencies (0.5 - 1.5) THz. Reflection coefficient is unity for (0.7 - 1.3) THz. Figure 9 points to the polarization conversion behavior of the structure. As it can be seen that perpendicular component of the transmission exist whereas normal wave with parallel polarization was incident.

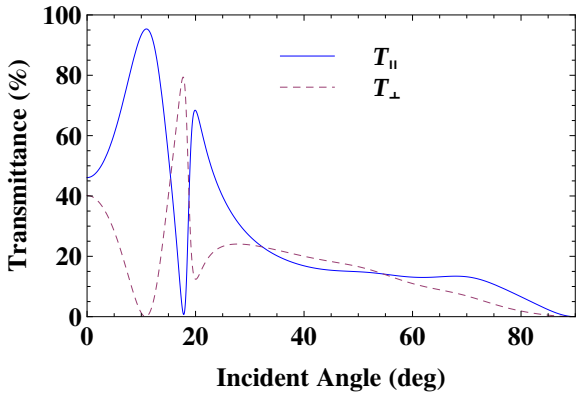

Fig. 3: Power transmitted through five layered SC-SC structure when $n_A = 0.76, n_B = 0.46, \kappa_A = \kappa_B = 0.8, \mid n_A \mid d_A = \mid n_B \mid d_B = \lambda_\circ/4$, and $f = 1.5$ THz

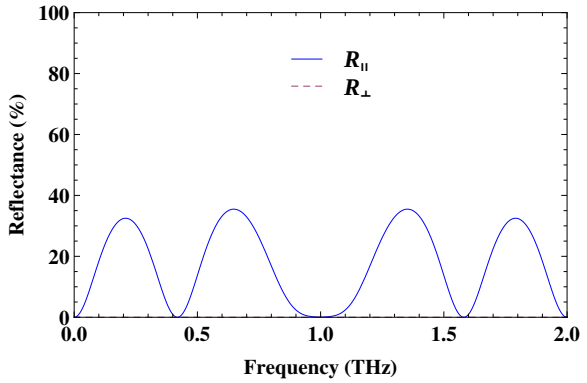

Fig. 4: Power reflected from five layered SC-SC structure when $n_A = 0.76, n_B = 0.46, \kappa_A = \kappa_B = 0.8, \mid n_A \mid d_A = \mid n_B \mid d_B = \lambda_\circ/4$, and $\theta_i = 0^\circ$

The propagation through the structure resulted in polarization conversion. Narrow bands of transmission occur with centre frequency at (0.2, 0.42, 1.58, 1.82, and 2.0) THz. At even harmonics parallel component of transmission is always unity. Therefore, this structure acts as wide band-reject filter with high efficiency and narrow bandpass filter.

3) SC-DNG Structure: In order to examine the performance of strong chiral - double negative interface in the presence of a plane wave, a five layered structure is composed. Slab A and slab B are filled with strong chiral material and double negative material, respectively. The optical width of both slabs remains to be quarter wavelength. Figure 10 reveals the fact that this surface has a unity (100%) reflection power over a wider range of frequencies. The important aspect of this structure is that it does not have sidebands or ripples. A filter that completely rejects EM plane wave (high power band-reject filter) over a range of frequencies can be designed by exploiting this feature. Figure 11 shows that the power transmitted at even harmonics is maximum and at these frequencies very low power perpendicular component also exists. It means these structure can be used to design narrow bandpass filters, which are very precise and works in narrow band of frequencies. Reflectance and transmittance as a function of incident angle

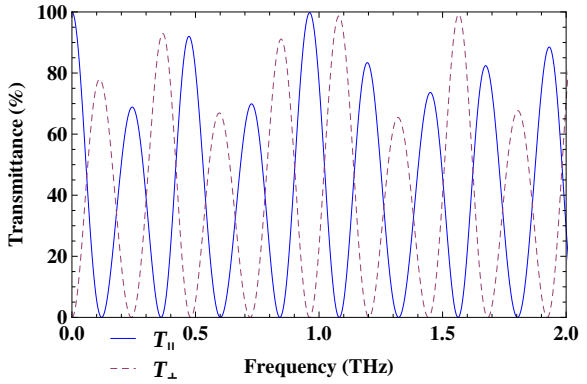

Fig. 5: Power transmitted through five layered SC-SC structure when $n_A = 0.76, n_B = 0.46, \kappa_A = \kappa_B = 0.8, \mid n_A \mid d_A = \mid n_B \mid d_B = \lambda_\circ/4$, and $\theta_i = 0^\circ$

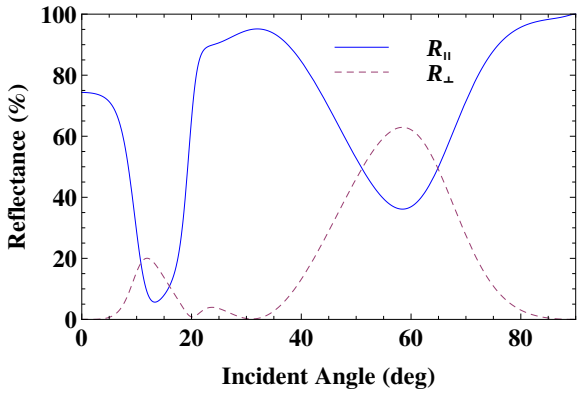

Fig. 6: Power reflected from five layered SC-dielectric structure when $n_A = 0.46, n_B = 2.2, \kappa_A = 0.8, \kappa_B = 0, \mid n_A \mid d_A = \mid n_B \mid d_B = \lambda_\circ/4$, and $f = 1.5$ THz

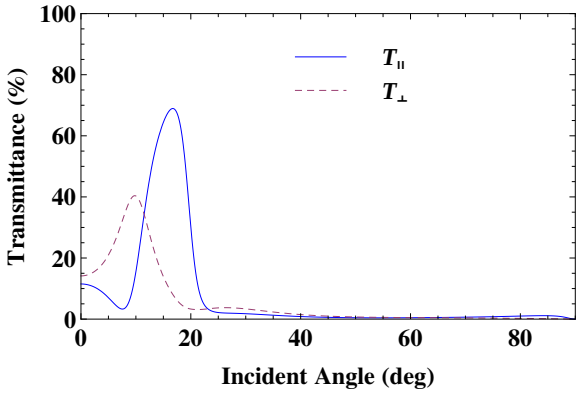

Fig. 7: Power transmitted through five layered SC-dielectric structure when $n_A = 0.46, n_B = 2.2, \kappa_A = 0.8, \kappa_B = 0, \mid n_A \mid d_A = \mid n_B \mid d_B = \lambda_\circ/4$, and $f = 1.5$ THz

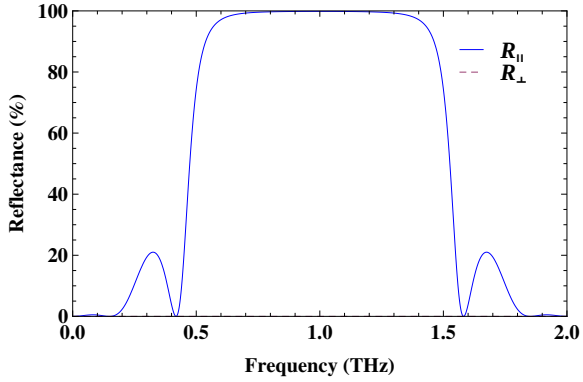

Fig. 8: Power reflected from five layered SC-dielectric structure when $n_A = 0.46, n_B = 2.2, \kappa_A = 0.8, \kappa_B = 0, \mid n_A \mid d_A = \mid n_B \mid d_B = \lambda_\circ/4$, and $\theta_i = 0^\circ$

are shown in Figure 12 and Figure 13, respectively. It is observed that the structure reflects all the power except at 22° narrow transmission band with $\approx$75% power exist. This structure works as an excellent band-reject filter with suppress sideband (no ripples) at oblique and normal incidences. It is

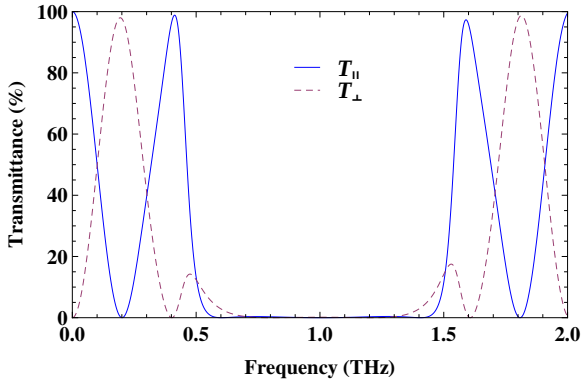

Fig. 9: Power transmitted through five layered SC-dielectric structure when $n_A = 0.46, n_B = 2.2, \kappa_A = 0.8, \kappa_B = 0, \mid n_A \mid d_A = \mid n_B \mid d_B = \lambda_\circ/4$, and $\theta_i = 0^\circ$

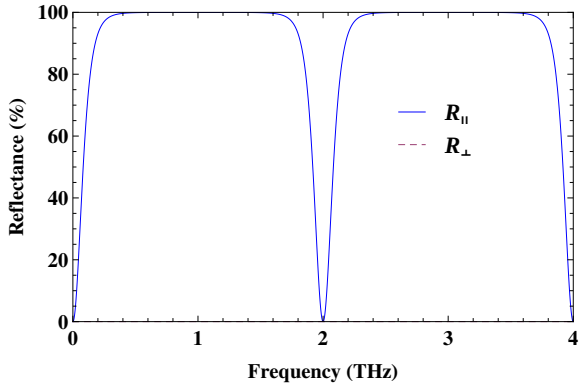

Fig. 10: Power reflected from five layered SC-DNG structure when $n_A = 0.46, n_B = -4.6, \kappa_A = 0.8, \kappa_B = 0, \mid n_A \mid d_A = \mid n_B \mid d_B = \lambda_\circ/4$, and $\theta_i = 0^\circ$

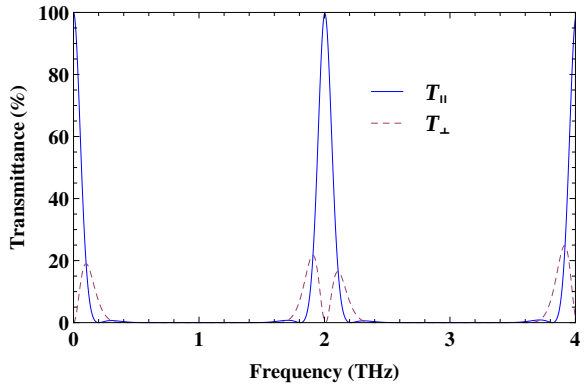

Fig. 11: Power transmitted through five layered SC-DNG structure when $n_A = 0.46, n_B = -4.6, \kappa_A = 0.8, \kappa_B = 0, \mid n_A \mid d_A = \mid n_B \mid d_B = \lambda_\circ/4$ and $\theta_i = 0^\circ$

seen that sc-dng structure exhibits resonance behaviour at even harmonics.

Therefore, these structures can be used to achieve desired behaviour by varying optical width of slabs, number of slabs, chirality and refractive indices. This study also helps in understanding the behaviour at a specific angle of incidence.

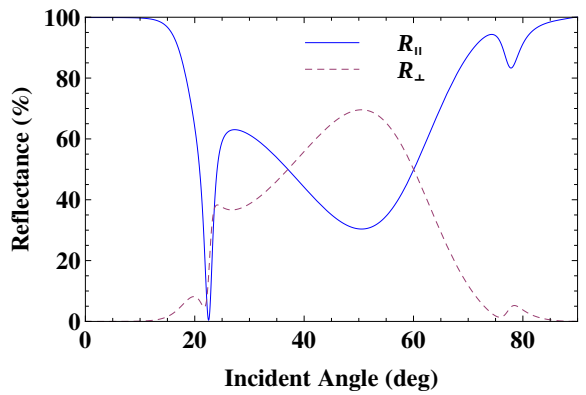

Fig. 12: Power Reflected from five layered SC-DNG structure when $n_A = 0.46, n_B = -4.6, \kappa_A = 0.8, \kappa_B = 0, \mid n_A \mid d_A = \mid n_B \mid d_B = \lambda_\circ/4$, and $f = 1.5$ THz

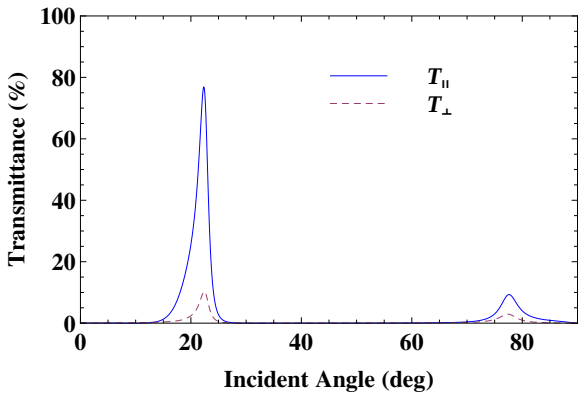

Fig. 13: Power transmitted through five layered SC-DNG structure when $n_A = 0.46, n_B = -4.6, \kappa_A = 0.8, \kappa_B = 0, \mid n_A \mid d_A = \mid n_B \mid d_B = \lambda_\circ/4$, and $f = 1.5$ THz

IV. Conclusions

In this paper, the study of multilayered structures reveals that they can used as bandpass and band-reject filters with excellent sideband suppression. Reflection and transmission coefficients are analytically computed for normal and oblique incidence. Incident angle and frequency response of the stratified structure composed of three different materials: SC-SC, SC-dielectric and SC-DNG are presented. Characteristics and features of these structures for millimeter wave are observed from numerical results. All the results fulfill the law of conservation of power. The proposed structures can be used in filters and frequency selective surfaces such as reflection coatings, anti-reflection coatings, cloaks, polarization conversion devices.

References

[1] C. H. Liu, N. Behdad, "High-power microwave filters and frequency selective surfaces exploiting electromagnetic wave tunneling through - negative layers", *Journal Of Applied Physics*, Vol. 113, (2013).

[2] H. Oraizi and M. Afsahi,"Design of metamaterial multilayer structures as frequency selective surfaces, *Progress In Electromagnetics Research C*, Vol. 6, 115-126, 2009.

[3] Vesselin N. Peshlov, Plamen I. Dankov, Boyan Hadjistamov,"Models Of Multilayer Antenna Radomes With Anisotropic Materials," *European Conference on Antennas and Propagation (EuCAP)*, 2006

[4] Cumali Sabah and Hartmut G. Roskos," Terahertz Polarization Rotator consists of Chiral Metamaterial and Dielectric Slabs, *Infrared, Millimeter and Terahertz Waves (IRMMW-THz)*, 2011

[5] A. Lakhtakia, "An electromagnetic trinity from negative permittivity and negative permeability," *Internattional Journal Millimeter and Infrared Waves*, Vol. 22, 1731-1734, 2001.

[6] M. J. Mughal, M. M. Ali, A. A Rahim,"Analytical solution for electromagnetic resonance in strong chiral filled spherical cavity," *IEEE Symposium Wireless Technology and Applications (ISWTA)*, 224–228, 2012.

[7] N. A. Shah, F. Ahmad, A. A. Syed, Q. A. Naqvi, "Effects on reflected and transmitted powers of planar stratified structures involving chiral nihility meta-materials," *Journal of Applied Electromagnetics and Mechanics*, JAE1724, 2013.

[8] Bassiri, S., C. H. Papas, N. Engheta, "Electromagnetic wave propagation through a dielectric-chiral interface and through a chiral slab," *Journal of Optical Society of America*, Vol. 5, 1450-1459, 1988.

[9] M. Mahmood Ali, *Analysis of Electromagnetic Fields and Waves in Microwave Devices Containing Strong Chiral Metamaterial*, MS Thesis, GIK Institute, Pakistan 2011.

Analytical and numerical modelling

A Bloch mode expansion approach for analyzing quasi-normal modes in open nanophotonic structures

Jakob Rosenkrantz de Lasson*, Philip Trøst Kristensen, Jesper Mørk and Niels Gregersen

DTU Fotonik, Department of Photonics Engineering,
Technical University of Denmark, Ørsteds Plads, Building 343, DK-2800 Kongens Lyngby, Denmark
*corresponding author, E-mail: jakob@jakobrdl.dk

Abstract

We present a new method for determining quasi-normal modes in open nanophotonic structures using a modal expansion technique. The outgoing wave boundary condition of the quasi-normal modes is satisfied automatically without absorbing boundaries, representing a significant advantage compared to conventional techniques. The quasi-normal modes are determined by constructing a cavity roundtrip matrix and iterating the complex mode wavelength towards a unity eigenvalue. We demonstrate the method by determining quasi-normal modes of cavities in two-dimensional photonic crystals side-coupled to W1 waveguides.

1. Introduction

In micro- and nanostructured media, such as micropillars and photonic crystals (PhCs), characteristic feature sizes are on the order of the wavelength of light which makes analysis of light propagation in these systems intricate. Design of such structures therefore relies on an interplay between theory, computations and fabrication, and to avoid analysis and design based on trial-and-error transparent and efficient numerical methods are indispensable. In open structures, the natural modes are so-called quasi-normal modes which are solutions to the frequency domain wave equation satisfying an outgoing wave boundary condition (BC) [1]. Numerical modeling often includes artificial BCs to ensure finite-sized computation domains, needed to handle the computations in computers. Simple choices include Dirichlet and periodic BCs that give rise to normal modes which, however, suffer from parasitic reflections at the artificial boundaries. These unwanted effects can to some extent be suppressed by means of absorbing boundaries like perfectly matched layers (PMLs) [2], but their implementation remains problematic, in particular in geometries featuring infinite periodic structuring like PhCs. The outgoing wave BC is thus difficult to satisfy with conventional spatial discretization techniques like the finite-difference time-domain (FDTD) method and the finite element method (FEM) due to their need for absorbing BCs.

In this work, we present a new method for determining quasi-normal modes using a modal expansion method [3, Chap. 6], a scattering matrix approach [4] and Bloch modes of periodic structures [5, Chap. 3]. In Fig. 1, two quasi-normal modes in two-dimensional PhC cavities are displayed. Light propagates in the z-direction, and as detailed in the following sections the outgoing wave BC in this direction is satisfied automatically; this represents a significant advantage of the new method.

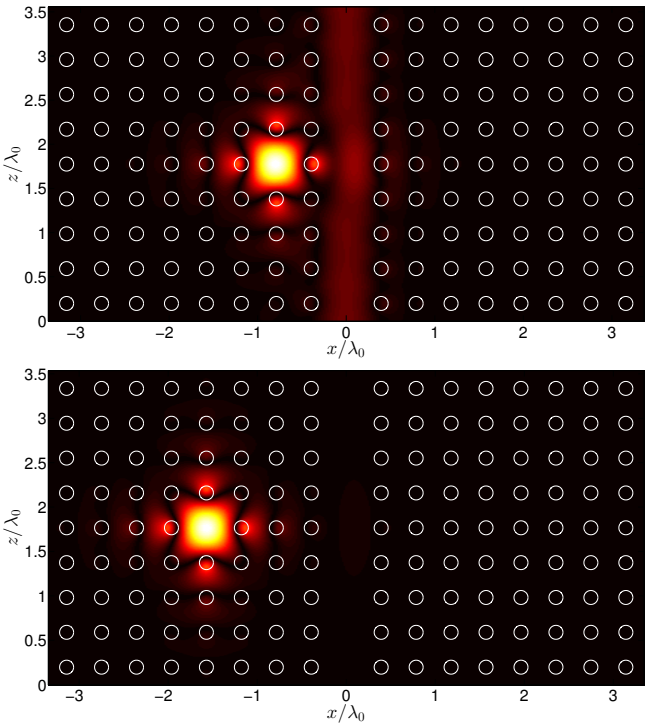

Figure 1: Quasi-normal mode field distribution ($|E_y|$ [a.u.]) in cavity side-coupled to W1 waveguide in two-dimensional rectangular lattice PhC. The complex mode wavelengths are $\lambda_0/a = 2.53 + 0.0087\mathrm{i}$ (top panel) and $\lambda_0/a = 2.55 + 0.000064\mathrm{i}$ (bottom panel), with $a = 0.4\,\mu\mathrm{m}$ being the PhC lattice constant and $\epsilon_{\mathrm{Rods}} = 8.9$ and $\epsilon_{\mathrm{Back}} = 1$.

2. Bloch mode expansions and quasi-normal modes

2.1. Bloch modes and scattering matrices

In the modal expansion technique used here [3, Chap. 6], the structure to be analyzed is sliced into periodic sections along a chosen propagation direction, taken here as the z-direction. The periodicity along z, with period a, implies

that the electromagnetic fields in each section w can be expanded on Bloch modes $\mathbf{e}_j^w(\mathbf{r}_\perp, z)$,

$$\mathbf{E}^w(\mathbf{r}) = \sum_j c_j^w \mathbf{e}_j^w(\mathbf{r}_\perp, z), \tag{1}$$

that are quasi-periodic functions of the z-coordinate [5, Chap. 3]

$$\mathbf{e}_j^w(\mathbf{r}_\perp, z + a^w) = \exp(\mathrm{i}k_j^w a^w)\mathbf{e}_j^w(\mathbf{r}_\perp, z), \tag{2}$$

where k_j^w is the wavenumber of the jth Bloch mode. This wavenumber is purely real for a propagating Bloch mode while inside a bandgap it has a finite imaginary part giving rise to exponentially decaying waves. For uniform sections, like translation invariant ridge waveguides, the Bloch modes become the well-known waveguide modes, but the description using the more general Bloch modes provides a powerful framework for analyzing, for example, PhCs. The Bloch mode form in Eq. (2) holds the analytic z-dependence of the electromagnetic fields, and this is what allows to satisfy the outgoing wave BC of the quasi-normal modes in the z-direction without using artificial BCs. In Eq. (1), c_j^w are expansion coefficients determined to satisfy the electromagnetic BCs across section interfaces. This is handled using a scattering matrix formalism [4], which in particular relates the incoming and outgoing Bloch mode amplitudes via the total scattering matrix $\mathbf{S}$

$$\mathbf{c}_{\mathrm{out}} = \mathbf{S}\mathbf{c}_{\mathrm{in}}. \tag{3}$$

2.2. Quasi-normal modes

It has been suggested that quasi-normal modes in nanophotonic structures can be calculated as non-zero solutions $\mathbf{c}_{\mathrm{out}}$ of Eq. (3) for a vanishing input $\mathbf{c}_{\mathrm{in}} = \mathbf{0}$ [6, 7]. This yields the following equation

$$\mathbf{S}^{-1}(\lambda_0)\mathbf{c}_{\mathrm{out}} = \mathbf{0}, \tag{4}$$

where we have written the wavelength dependence of the inverse scattering matrix explicitly. This equation, in general, only has non-trivial solutions at complex values of λ_0, the quasi-normal mode complex wavelength. The search for these complex wavelengths is in principle straightforward, but for advanced structures that require the inclusion of a large number of modes the associated scattering matrix is comparatively large, and the construction of the inverse scattering matrix in Eq. (4) may be complicated and unstable.

In this context, we suggest a new and simpler formulation for determining the quasi-normal modes. For a given structure, the relevant cavity section w_{c} is identified, and the cavity roundtrip matrix [8] $\mathbf{M}^{w_{\mathrm{c}}}$ is constructed

$$\mathbf{M}^{w_{\mathrm{c}}}(\lambda_0) \equiv \mathbf{R}^{\mathrm{bot}}\mathbf{P}_-^{w_{\mathrm{c}}}\mathbf{R}^{\mathrm{top}}\mathbf{P}_+^{w_{\mathrm{c}}}, \tag{5}$$

where $\mathbf{R}^{\mathrm{bot}}$ ($\mathbf{R}^{\mathrm{top}}$) is the scattering reflection matrix between the cavity section and the bottommost (topmost) section. $\mathbf{P}_+^{w_{\mathrm{c}}}$ and $\mathbf{P}_-^{w_{\mathrm{c}}}$ are diagonal matrices accounting for the propagation of the Bloch modes through the cavity section.

At real wavelengths, the eigenvalues of $\mathbf{M}^{w_{\mathrm{c}}}$ have absolute values below unity since the reflectivities of the mirrors surrounding the cavity section are smaller than unity; in every roundtrip, a fraction of the light leaks out of the cavity and into the mirrors. However, by analytically continuing the definition of $\mathbf{M}^{w_{\mathrm{c}}}$ into the complex wavelength plane it is possible to compensate the mirror losses by making the elements in the propagation matrices $\mathbf{P}_+^{w_{\mathrm{c}}}$ and $\mathbf{P}_-^{w_{\mathrm{c}}}$ larger than unity. We therefore iterate the complex wavelength λ_0 to find an eigenvalue of $\mathbf{M}^{w_{\mathrm{c}}}$ equal to unity; the associated eigenvector gives the quasi-normal mode distribution in the cavity section

$$\mathbf{M}^{w_{\mathrm{c}}}(\lambda_0)\mathbf{c}^{w_{\mathrm{c}}} = \mathbf{c}^{w_{\mathrm{c}}}. \tag{6}$$

The finite imaginary part of the quasi-normal mode wavelength gives rise to a finite Q-factor of the mode [9, Chap. 11]

$$Q = \frac{\mathrm{Re}(\lambda_0)}{2\mathrm{Im}(\lambda_0)}, \tag{7}$$

and also means that the quasi-normal modes diverge when propagating outwards; this renders the associated mode volume non-trivial to calculate [10, 11].

3. Example: W1 waveguide and side-coupled cavity in rectangular lattice photonic crystal

We consider two-dimensional structures that are uniform and infinitely extended in the y-direction. In this case, Maxwell's equations decouple into TE- and TM-polarizations in which the fields may be described completely by the scalars E_y and H_y, respectively. We focus on two-dimensional rectangular lattice PhCs with dielectric rods ($\epsilon_{\mathrm{Rods}} = 8.9$) suspended in free-space ($\epsilon_{\mathrm{Back}} = 1$). This structure is known to possess a TE-bandgap [5, Chap. 5], with the electric field having only its y-component E_y non-zero. By removing one row of holes a W1 waveguide is created, and for wavelengths inside the bandgap light may be guided through this waveguide. By furthermore removing one rod in the bulk of the PhC lattice and in the vicinity of the waveguide a cavity is formed, see Fig. 1; we here focus on determining the quasi-normal modes of this structure.

We first crudely locate the quasi-normal mode spectrally by calculating the transmission of the guided Bloch mode through the structure; a dip in the transmission spectrum indicates the excitation of the cavity mode. Subsequently, we use the spectral position of the transmission minimum as a starting point for the iteration using a Newton-Raphson algorithm towards a complex wavelength that gives an eigenvalue of unity for $\mathbf{M}^{w_{\mathrm{c}}}(\lambda_0)$. We do the above for two positions of the cavity; separated by one rod and by three rods from the waveguide. The quasi-normal mode distributions ($|E_y|$) are shown in the top and bottom panels of Fig. 1, respectively, and the associated quasi-normal mode wavelengths are $\lambda_0/a = 2.53 + 0.0087\mathrm{i}$ and $\lambda_0/a = 2.55 + 0.000064\mathrm{i}$, respectively, with $a = 0.4\,\mu\mathrm{m}$ being the PhC lattice constant. We note that both modes have roughly the same real part of

the mode wavelength, while the imaginary part decreases as the cavity is moved further away from the waveguide. Using Eq. (7), the Q-factors are found to be $Q = 145$ (top panel) and $Q = 19820$ (bottom panel), and for this structure we gain approximately an order of magnitude in Q when the cavity is moved a lattice constant away from the waveguide.

We have tested the method with other structures that exhibit lower Q-factors, and this in general challenges the numerical stability of the formalism since it corresponds to wavelengths with comparatively large imaginary parts. We have, however, been able to determine modes with Q as low as 25, and this demonstrates that the method can be useful for plasmonic structures, that usually feature low-Q modes, as well.

4. Conclusion

We have proposed a new method for determining quasi-normal modes in open nanophotonic structures using a Bloch mode expansion approach. The scheme relies on an iteration of the complex quasi-normal mode wavelength to determine a unity eigenvalue of the cavity section roundtrip matrix. The unity eigenvalue approach is analogous to the lasing condition in laser cavities and is thus more intuitive, more efficient and simpler than other methods that rely on inversion of the total scattering matrix. The use of modal expansion techniques to determine quasi-normal modes as compared to conventional techniques like FDTD and the FEM is advantageous since the outgoing wave BC of the quasi-normal modes can be satisfied automatically and without artificial absorbing boundaries. We have demonstrated the use of our method by determining quasi-normal modes in side-coupled cavities in two-dimensional rectangular lattice PhCs, and we have discussed the effect of the cavity position with respect to a nearby W1 waveguide on the quasi-normal mode Q-factor.

Acknowledgement

This work was funded by project SIQUTE (contract EXL02) of the European Metrology Research Programme (EMRP). The EMRP is jointly funded by the EMRP participating countries within EURAMET and the European Union. Support from the Villum Foundation via the VKR Centre of Excellence NATEC is gratefully acknowledged.

References

[1] P. T. Kristensen and S. Hughes, "Modes and mode volumes of leaky optical cavities and plasmonic nanoresonators," *ACS Photonics*, vol. 1, no. 1, pp. 2–10, 2014.

[2] J.-P. Berenger, "A perfectly matched layer for the absorption of electromagnetic waves," *J. Comput. Phys.*, vol. 114, no. 2, pp. 185–200, Oct 1994.

[3] A. V. Lavrinenko, J. Lægsgaard, N. Gregersen, F. Schmidt, and T. Søndergaard, *Numerical Methods in Photonics*. CRC Press, 2014.

[4] L. Li, "Formulation and comparison of two recursive matrix algorithms for modeling layered diffraction gratings," *J. Opt. Soc. Am. A*, vol. 13, no. 5, pp. 1024–1035, May 1996.

[5] J. Joannopoulos, S. Johnson, J. Winn, and R. Meade, *Photonic Crystals: Molding the Flow of Light*, 2nd ed. Princeton University Press, 2011.

[6] T. Weiss, N. A. Gippius, S. G. Tikhodeev, G. Granet, and H. Giessen, "Derivation of plasmonic resonances in the Fourier modal method with adaptive spatial resolution and matched coordinates," *J. Opt. Soc. Am. A*, vol. 28, no. 2, pp. 238–244, Feb 2011.

[7] D. A. Bykov and L. L. Doskolovich, "Numerical methods for calculating poles of the scattering matrix with applications in grating theory," *J. Lightwave Technol.*, vol. 31, no. 5, pp. 793–801, Mar 2013.

[8] N. Gregersen, S. Reitzenstein, C. Kistner, M. Strauss, C. Schneider, S. Höfling, L. Worschech, A. Forchel, T. Nielsen, J. Mørk, and J.-M. Gérard, "Numerical and experimental study of the Q factor of high-Q micropillar cavities," *IEEE J. Quant. Electron.*, vol. 46, no. 10, pp. 1470–1483, Oct 2010.

[9] L. Novotny and B. Hecht, *Principles of Nano-Optics*, 2nd ed. Cambridge University Press, 2012.

[10] P. T. Kristensen, C. V. Vlack, and S. Hughes, "Generalized effective mode volume for leaky optical cavities," *Opt. Lett.*, vol. 37, no. 10, pp. 1649–1651, May 2012.

[11] C. Sauvan, J. P. Hugonin, I. S. Maksymov, and P. Lalanne, "Theory of the spontaneous optical emission of nanosize photonic and plasmon resonators," *Phys. Rev. Lett.*, vol. 110, p. 237401, Jun 2013.

Equivalent Circuit Model of Jerusalem Cross FSS Using Vector Fitting

Payal Majumdar*, Zhiya Zhao, Chunlin Ji and Ruopeng Liu

State Key Laboratory of Meta-RF Electromagnetic Modulation Technology,
Kuang-Chi Institute of Advanced Technology, Shenzhen, Guangdong, P.R.China-518000.
* E-mail: payalmajumdar.udsc@gmail.com

Abstract

In this study, we present the analysis and modeling of Jerusalem cross frequency selective surfaces adopting an efficient vector fitting procedure which is a new approach for rational macro modeling that ensures high accuracy with arbitrary terminal conditions. The simulations of microstructure are performed with full wave simulation tool CST Microwave Studio on single-substrate for different physical parameters, oblique incidence and effect of TE / TM polarization as well. Then circuit models are extracted and developed using the vector fitting tool and implemented in a circuit simulator enabling both time and frequency analyses along with effect of polarization and angle of incidence. Then ADS SPICE generator is used for verifying circuit models developed using simulated results. The developed model is within 1% of average deviation against reference data.

1. Introduction

Frequency Selective Surfaces (FSS) have recently been widely used in a variety of electromagnetic applications, such as radomes (terrestrial and airborne), electromagnetic shielding, absorbers and antennas [1]. There has been a great deal of research on the analysis and design of the FSS element using analytical or numerical electromagnetic methods (FEM, FDTD or MoM). Despite their accuracy in analysis, these techniques require time - consuming simulations and do not allow designer to have a good insight into the physics behind the structures. Among the possible methods, the equivalent circuit model approach to the design of FSSs is very popular because of the ease with which it can be understood. The evaluation of transmission and reflection properties of FSSs become simple and accurate with the help of circuit approach. Moreover, the approximate analysis, based on the parallel between real structure and a lumped - RLC - network counterpart is also useful for acquiring physical insights into the working principles of FSS [2].

There is a growing demand for developing an accurate circuit model for FSS so that one can synthesize a desired frequency response (center frequency, bandwidth, insertion loss and tuning range) by an optimization method in a reasonably short time using a circuit simulator [3]. In this paper, an equivalent circuit model for the analysis of Jerusalem cross (JC) has been presented, as shown in Fig.1. For this purpose, vector fitting (VF) technique [4-6] is used for determination of their poles and residues from simulated S-parameters [7]. Then the SPICE - compatible equivalent circuit model [3] of frequency-domain responses approximated by rational functions are developed. The transmission and reflection properties of JC FSS are evaluated through a simple and accurate circuit approach. The developed model is within 1% of average deviation against reference data.

(a) (b)

Figure 1: (a) Layout of JC and (b) its equivalent circuit.

2. Equivalent Circuit Using Vector Fitting

An efficient broadband modeling of transmission lines must also take into account the frequency-dependent behaviour of dielectrics. These effects materialize as a frequency domain variation in the resistance, inductance and capacitance matrices used in the formulation of the model. In practice, the frequency dependent responses are obtained via calculation or measurements as discrete functions of frequency.

An attempt at formulating a general fitting methodology was introduced as VF method. Consider the rational function approximation [4]

$$f(s) = \sum_{n=1}^{N} \frac{c_n}{s - a_n} + d + sh \qquad (1)$$

The residues c_n and poles a_n are either real quantities or come in complex conjugate pairs, while d and h are real. The problem at hand is to estimate all coefficients in equation - (1) so that a least squares approximation of $f(s)$ is obtained over a given frequency interval.

Vector fitting solves the equation-(1) sequentially as a linear problem in two stages, both times with known poles [4-5]. The first stage was carried out with complex poles distributed over the frequency range of interest. In addition, an unknown frequency dependent scaling parameter was introduced which permitted the scaled function to be accurately fitted with the prescribed poles. From the fitted

function a new set of poles were obtained and then used in the second stage in the fitting of the unscaled function. This method ensures that the poles of the generated closed-form responses are stable or all poles have non-positive real parts.

In this section, circuit representation for complex pairs is presented for the generation of SPICE [3] compatible equivalent circuit of JC FSS from three-dimensional models. In the rational approximation of a transfer function *f(s)* , as shown in equation-(1), the *n*th residue and pole have been extracted by using a fitting procedure mentioned in [4]. It has been assumed that the constant term *d* and the *s*-proportional one can be synthesized with a resistance and a capacitance whose values are *1/d* and *h*. It is convenient to distinguish the case of real poles from that of complex pairs. The detailed methodology and expressions can be obtained from [3].

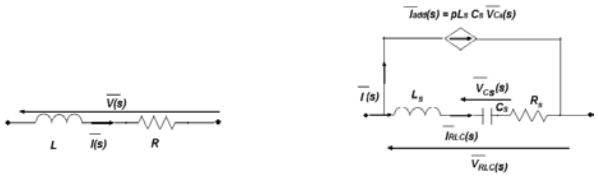

(a) (b)

Figure 2: (a) Equivalent RL circuit for real pole synthesis; and (b) Equivalent series RLC circuit for complex pole pair synthesis.

The following synthesis approach has been used in this research work to achieve the SPICE-compatible equivalent circuit of JC FSS microstructure:

Step 1) Scattering parameter extraction by means of a full - wave electromagnetic simulation of FSS microstructure. In this work CST Microwave Studio is used;
Step 2) ABCD parameters evaluation;
Step 3) Building of the Π equivalent circuit as shown in Fig.3;
Step 4) Residues and poles extraction of admittances $\overline{Y}_A$, $\overline{Y}_B$ and $\overline{Y}$;
Step 5) SPICE-compatible equivalent circuit synthesis [3].

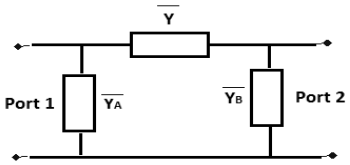

Figure 3: Equivalent Π circuit.

The VF technique has been adopted to extract poles and residues of admittances $\overline{Y}_A$, $\overline{Y}_B$ and $\overline{Y}$, which have been synthesized in the equivalent circuit, as shown in Fig.2, of FSS microstructure and simulated in a ADS SPICE [8] environment enabling both time and frequency analyses according to this approach. It is worth mentioning that the standard VF procedure while ensuring the stability which is enforced flipping the poles with Re(pole) > 0 in the left-half plane, does not provide residues satisfying necessarily, the conditions specified in [4]. This means that, although it is able to evaluate a good rational approximation of the given transfer function, it may not be passive. Passivity is here enforced, when needed, by means of the technique described in [6].

3. Parametric Study of JC FSS

To develop a better understanding of operation of FSS and to arrive at an accurate model, sensitivity analyses using a full-wave simulator are carried out. The full-wave approach is also necessary to establish the relationship between the physical parameters of the miniaturized unit cell and the lumped elements of the circuit model. So, JC FSS structure is studied and investigated on single-substrate for different physical parameters using CST Microwave Studio [9-10]. The effects of oblique incidence and TE / TM polarization are also studied. TM - incidence occurs when the E-field is polarized parallel to the plane of incidence, i.e. $\theta = 0^\circ$; and TE - incidence when the E-field is perpendicular to the plane of incidence, i.e. $\Phi = 0^\circ$.
The geometrical parameters of the designed JC FSS are w = 3.5 mm, g = 0.5 mm, d = 1 mm, p = 7 mm and L = 10 mm. All the FSS designs are simulated on *FR4* substrate with permittivity ε_r = 4.4, loss tangent *tan* δ = 0.025 and substrate thickness h = 1 mm.

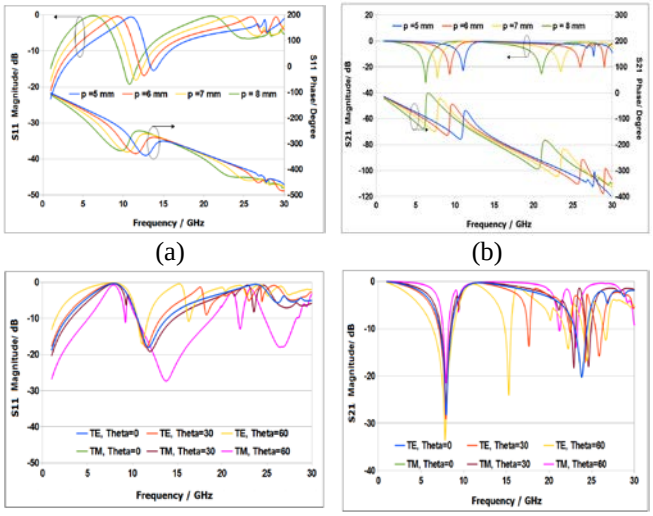

(a) (b)

(c) (d)

Figure 4: Plane-wave reflection and transmission response for JC FSS.

Fig. 4 shows the parametric study of JC FSS at normal and oblique incidence. For the sake of brevity, few results are shown here. Fig.4(a) and 4(b) show magnitude and phase of reflection and transmission characteristics respectively for different cross sizes. It can be observed that by increasing cross size there is shift in resonance towards lower frequency. By decreasing cell size there is shift in resonance peak towards lower frequency for transmission

characteristics. By increasing substrate thickness, there is shift in resonance towards lower frequency. Fig.4(c) and 4(d) show the effect of oblique incidence and TE/TM polarization on magnitude of reflection and transmission characteristics of JC FSS.

4. Model Verification and Simulation Results

In this section, the results of reflection and transmission characteristics of JC FSS obtained from the developed circuit model using VF tool, circuit model available from literature and CST simulations are compared against each other.

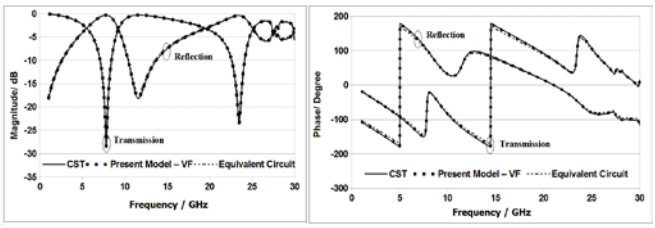

(a) (b)

Figure 5: JC FSS - (a) Magnitude and (b) Phase.

The reflection and transmission characteristics of JC FSS have been fitted by using 12 poles [4]. The fitting procedure has provided two real poles and five complex pairs, which can be synthesized in ADS SPICE generator using repeated units shown in Fig.2. Table 1 shows extracted poles and synthesized component values of JC FSS. Fig. 5 shows the plots of the magnitude and phase of reflection and transmission characteristics, those obtained by simulation, equivalent circuit from Fig.1(b) and equivalent circuit using VF technique.

Table 1: Extracted Poles and Synthesized component values of JC FSS.

Poles
-0.0166e+11
-1.1793e+11
(-0.1147+0.0693i)e+11
(-0.1147-0.0693i)e+11
(-0.1057+0.1763i)e+11
(-0.1057-0.1763i)e+11
(-0.0078+0.2188i)e+11
(-0.0078-0.2188i)e+11
(-0.0920+1.0949i)e+11
(-0.0920-1.0949i)e+11
(-0.1287-1.163i)e+11
(-0.1287-1.163i)e+11

Poles	R_s [Ω]	L_s[H]	C_s [F]	bL_sC_s [S]
r_1	5.00e-003	1.10e-011		
r_2	2.89e+004	1.74e-006		
c_1	2.51e-003	5.50e-012	1.28e-008	2.84e-002
c_2	2.51e-003	5.50e-012	3.19e-009	7.09e-003
c_3	2.51e-003	5.50e-012	1.42e-009	3.15e-003
c_4	2.51e-003	5.50e-012	7.98e-010	1.77e-003
c_5	2.51e-003	5.50e-012	5.11e-010	1.13e-003
c_6	2.51e-003	5.50e-012	3.55e-010	7.88e-004
c_7	2.51e-003	5.50e-012	2.61e-010	5.79e-004
c_8	2.51e-003	5.50e-012	1.99e-010	4.43e-004
c_9	2.51e-003	5.50e-012	1.58e-010	3.50e-004
c_{10}	2.51e-003	5.50e-012	1.28e-010	2.82e-004

The proposed synthesis allows a satisfactory approximation of all the considered FSS being the percentage errors on magnitude and phase of the order of 1%.While the equivalent circuits available in literature have the percentage errors on magnitude and phase of the order of 2%. All the equivalent circuits are designed and simulated using ADS SPICE generator. In future work, this work will be extended to multilayer substrates.

5. Conclusions

The present work reports detailed investigation and study of JC FSS with resonant unit cells. The simulations are performed with CST Microwave Studio on single-substrate for different physical parameters, oblique incidence and effect of TE / TM polarization as well. The VF tool is employed to extract equivalent circuits from S-parameters of JC FSS microstructure to use in circuit simulators to avoid time consuming 3D simulations. Then ADS SPICE generator is used for verifying circuit models developed using simulated results. All the models are within 1% of average deviation against reference data.

Acknowledgements

This research work has been supported by grants from State Key Laboratory of Meta-RF Electromagnetic Modulation Technology (No. 2011DQ782011), Guangdong Province Engineering Laboratory for Millimeter Wave Meta-RF (No.1111), Shenzhen Key Laboratory of Data Science and Modeling (No. CXB201109210103A), Shenzhen Science and Technology Plan (No. JC201105201150A) and Shenzhen Science and Technology Plan (No. ZD201111080127A).

References

[1] B.A. Munk, *Frequency-selective surfaces: Theory and Desig*n, Wiley, New York, 2000.

[2] F. Costa, A. Monorchio and G. Manara, Efficient Analysis of Frequency-Selective Surfaces by a Simple Equivalent-Circuit Model, *IEEE Antenna and Propagation Magazine* 54: 35-48, 2012.

[3] G. Antonini, SPICE Equivalent Circuits of Frequency-Domain Responses, *IEEE Trans. on Electromagnetic Compatibility* 45:502-512, 2003.

[4] B. Gustavsen and A. Semlyen, Rational approximation of frequency domain responses by Vector Fitting, *IEEE Trans. Power Delivery* 14: 1052-1061, 1999.

[5] B. Gustavsen and A. Semlyen, Fast passivity assessment for S-parameter rational models via a half-size test matrix, *IEEE Trans. Microwave Theory And Techniques* 56: 2701-2708, 2008.

[6] B. Gustavsen and H.M.J. De Silva, Inclusion of Rational Models in and Electromagnetic Transient Program- Y-Parameters, Z-Parameters, S-Parameters, Transfer Functions, *IEEE Trans. Power Delivery* 28: 1164-1174, 2013.

[7] CST Studio Suite v 2009, CST GmbH–Computer Simulation Technology, www.cst.com.

[8] Agilent Advanced Design System v 2011.

[9] C.K. Lee and R.J. Langley, Equivalent- Circuit Models for Frequency-Selective Surfaces at oblique angle of incidence, *IEE Proc* 132:395-399, 1985.

[10] R.J. Langley and A.J. Drinkwater, An Improved Empirical Model for the Jerusalem Cross, *IEE Proc., Part H : Microwaves, Opt. Antenna* 129:1-6, 1982.

Noname manuscript No.
(will be inserted by the editor)

Electromagnetic small-scale modeling of composite panels involving periodic arrays of circular fibers

C.Y. Li · D. Lesselier · Y. Zhong

Received: date / Accepted: date

Abstract Electromagnetic modeling of composite panels as planar multilayers involving a periodic set of circular cylindrical fibers in each constitutive layer is considered. As a first step, the case of a single layer is studied. Combining multipole method and plane-wave expansion leads to full-wave field representations in all space, yielding in particular reflection and transmission coefficients for TE/TM oblique plane-wave illuminations. Gaussian beams are accounted for via a Fourier transform and numerical quadrature scheme. Comparisons with data available for photonic crystals show the accuracy of the method, while results for fiber-reinforced composites illustrate its effectiveness.

Keywords Electromagnetic modeling · Multilayer structure · Periodic · Photonic crystals · Fiber-reinforced composites

1 Introduction

The time-harmonic electromagnetic response of multilayer periodic structures is investigated. The approach is intrinsically broad-band and holds for any isotropic constitutive material, though emphasis is put on fiber-reinforced composite structures as in aeronautic and automotive parts. The latter are modeled as stacks of planar layers, each being a regular periodic arrangement of long cylinders (fibers) with same circular sections embedded in a given material (matrix), all oriented into the same direction. Orientations possibly differ from one layer to the next. (This is a small-scale view, refer to [1] for a large-scale view wherein homogeneization of any given layer leads to them having uniaxial permittivities.)

In that case, each layer behaves like an infinite array, and is prone to Floquet-related solutions, which is to be weighted in vs. the limited extent of most real-world sources and sensors. Carbon-fiber-reinforced polymers (highly conductive fibers and strong electric contrasts) and glass-fiber-reinforced polymers (almost lossless fibers and weak electric contrasts) are of main interest, though the work is as already said valid for a wide range of frequency, materials and dimensions.

Here one studies a single-layer structure. Results sought are reflection and transmission coefficients for TE/TM plane-wave illuminations under oblique incidence and the total field distribution for Gaussian beams obliquely impinging onto the structure.

Reflection and transmission coefficients are calculated by combining a multipole method and plane-wave expansion, borrowing in good part from pioneering poro-acoustics and elasticity analyses [2] and photonic ones (in a limited-extent case) [3]. Scattering of Gaussian beams follows via a Fourier transform and numerical quadrature scheme. The incident beam is a superposition of elementary plane waves with different amplitudes and incident angles. The total scattered field is a superposition of the corresponding scattered fields. The method extends to out-of-plane incidences and provides

C.Y. Li
Département de Recherche en Electromagnétisme-Laboratoire des Signaux et Systèmes
UMR8506 (CNRS-SUPELEC-Univ Paris-Sud)
E-mail: changyou.li@lss.supelec.fr

D. Lesselier
Département de Recherche en Electromagnétisme-Laboratoire des Signaux et Systèmes
UMR8506 (CNRS-SUPELEC-Univ Paris-Sud)

Y. Zhong
A*STAR, Institution of High Performance Computing, 138632 Singapore.

the main elements to approach full-wave scattering by a multi-layered structure in a next step.

2 The electromagnetic scattering of plane wave

The structure is sketched in Fig. 1. Circular cylinders of radius c parallel to one another and oriented in the y direction are embedded in a planar slab infinite in both x and y directions with interfaces Γ_a ($z = a$) and Γ_b ($z = b$). They are arranged periodically in the x direction with period d. So the reference (unit) cell is at the center, with height $L = a - b$ and width d. The space itself is divided into four subspaces R_0^+ above the slab, R_0^- below it, R_1 in it and outside the cylinders and R_2, the cylinders. All materials are linear isotropic, possibly lossy (save R_0^+), with ϵ_j and μ_j, $j = 0, 1, 2$, as permittivities and permeabilities.

Here, a TM plane wave with plane of incidence $x-z$ is obliquely impinging with angle θ_i upon the slab. Its electric field is $\mathbf{E}_{inc} = \hat{y}E_{inc}e^{i(k_x^i x - k_z^i(z-a))}$, implying time-harmonic dependence $e^{-i\omega t}$. $\mathbf{k}^i$ is the wave vector of the incident wave, with amplitude k^i, letting $k_x^i = k^i \sin\theta_i$, $k_z^i = k^i \cos\theta_i$. The fields in the TE case of illumination follow from duality.

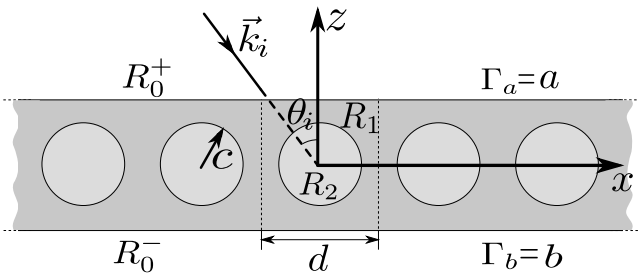

Fig. 1 Sketch of the structure.

The key feature is the transverse periodicity of the inclusions, since repeating the primary cell into both $+x$ and $-x$ directions enables to build up the structure. According to the Floquet theorem, $E_{jy}(x+d, z) = E_{jy}(x, z)e^{i\alpha_0 d}$, $E_{jy}(x, z)$ as the fields in different regions — fields in R_0^+ and R_0^- being denoted as $E_{0y}^+(x, z)$ and $E_{0y}^-(x, z)$. The latter can be plane-wave expanded as

$$E_{0y}^+(x,z) = \sum_{p\in\mathbb{Z}} (E_{inc}e^{-i\beta_{0p}(z-a)}\delta_{p0} + R_p e^{i\beta_{0p}(z-a)})e^{i\alpha_p x} \quad (1)$$

$$E_{0y}^-(x,z) = \sum_{p\in\mathbb{Z}} T_p e^{i(\alpha_p x - \beta_{0p}(z-b))}, \quad (2)$$

with R_p and T_p the reflection and transmission coefficients of the plane wave indexed by p, δ_{p0} the Kronecker symbol, $\alpha_p = \alpha_0 + 2p\pi/d$, and $\beta_{jp} = \sqrt{k_j^2 - \alpha_p^2}$, $j = 0, 1$. Because of the continuity of α_{jp} across Γ_a and Γ_b, α_p is used everywhere instead of α_{jp}.

For R_1, the field is consisted of the field diffracted by the boundary of the plate and the boundary of the central cylinder. Applying the Green's second identity around the boundary of one primary cell [4,5] with the periodic Green's function

$$G(\mathbf{r}) = \frac{1}{2id}\sum_{p=-\infty}^{+\infty}\frac{1}{\beta_p}e^{i(\alpha_p x + \beta_p|z|)}, \quad (3)$$

the field diffracted by the central cylinder is obtained. Combining the plane-wave expansion of the field inside R_1, we have the field representations

$$E_{1y}^{\pm}(x,z) = \sum_{p\in\mathbb{Z}}(f_p^- e^{-i\beta_{1p}z} + f_p^+ e^{i\beta_{1p}z})e^{i\alpha_p x} + \sum_{p\in\mathbb{Z}}\sum_{m\in\mathbb{Z}} B_m K_{pm}^{\pm} e^{i(\alpha_p x \pm \beta_{1p}z)} \quad (4)$$

with $K_{pm}^{\pm} = 2(-i)^m e^{\pm im\theta_p}/(d\beta_{1p})$, and $+$ and $-$ mean $z > c$ and $z < c$, respectively. Magnetic fields easily follow. Matching the boundary conditions on Γ_a ($z = a$) and Γ_b ($z = b$) yields

$$\begin{cases} T_p = \dfrac{1}{D_p}\Big[-4\chi_{0p}\chi_{1p}E_{inc}\delta_{p0} + \displaystyle\sum_{m\in\mathbb{Z}}\frac{8(-i)^m\chi_{1p}B_m}{d\beta_{1p}} \\ \qquad \times [i\chi_{0p}\sin(\beta_{1p}a - m\theta_p) - \chi_{1p}\cos(\beta_{1p}a - m\theta_p)]\Big] \\ R_p = -\dfrac{1}{D_p}[2i\sin(\beta_{1p}L)(\chi_{1p}^2 - \chi_{0p}^2)E_{inc}\delta_{p0} \\ \qquad + \displaystyle\sum_{m\in\mathbb{Z}}\frac{8(-i)^m\chi_{1p}B_m}{d\beta_{1p}}(\chi_{1p}\cos(\beta_{1p}b - m\theta_p) \\ \qquad + i\chi_{0p}\sin(\beta_{1p}b - m\theta_p))] \end{cases}$$

with $D_p = 2i\sin(\beta_{1p}L)(\chi_{0p}^2 + \chi_{1p}^2) - 4\chi_{0p}\chi_{1p}\cos(\beta_{1p}L)$, $\chi_{jp} = \beta_{jp}/\mu_j$, $j = 0, 1$. It is obvious that the reflection and transmission coefficients are related to the multipole expansion coefficients B_m which can be calculated by matching the boundary conditions around the cylinders [2]. The necessary field representation in region R_1 in polar coordinates is obtained from the above form (4) in Cartesian coordinates via $x = r\cos\theta$, $z = r\sin\theta$, $\alpha_{1p} = k_1\cos\theta_p$, $\beta_{1p} = k_1\sin\theta_p$ and identity $e^{ikr\cos\theta} = \sum_{m\in\mathbb{Z}} i^m J_m(kr)e^{im\theta}$. Its lengthy expression is omitted here [2–5].

3 Gaussian beam plane-wave expansion

As sketched in Fig. 2, a 2D Gaussian beam impinges on the structure with angle φ^i with respect to the z-axis in the $x-z$-plane, the center of the beam being located

at $(-d_x, d_z)$. In the local coordinate system (x', y', z'), it is expressed as

$$E_{y'}(x', z') = E_0 \frac{w_0}{w(z')} \exp\left(-\frac{x'^2}{w^2(z')} - i\frac{k_i x'^2}{2R(z')} - ik_i z' + i \arctan\frac{z'}{z'_0} \right); \quad (5)$$

z' is the beam propagating distance from the beam waist at $z' = 0$, w_0 is the spot size, $z'_0 = \pi w_0^2/\lambda$, $w(z')$ and $R(z')$ are defined as

$$w(z') = w_0 \left[1 + \left(\frac{z'}{z'_0} \right)^2 \right]^{\frac{1}{2}}, \quad R(z') = z' \left[1 + \left(\frac{z'_0}{z'} \right)^2 \right].$$

Applying a Fourier transform [6–8], one has

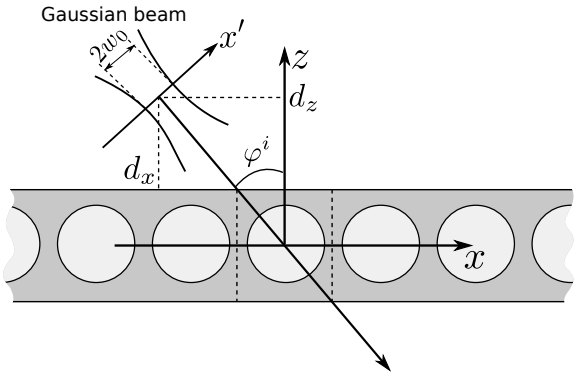

Fig. 2 A Gaussian beam incident on a slab with a periodic arrangement of circular fibers.

$$E_{y'}(x', z') = \sqrt{\pi} w_0 E_0 \int_{-\infty}^{+\infty} \exp\left(-\pi^2 f_{x'}^2 w_0^2\right) \times \exp\left[2\pi i \left(f_{z'} z' + f_{x'} x'\right)\right] df_{x'}. \quad (6)$$

Let $\mathbf{f} = f_{x'}\hat{x} + f_{z'}\hat{z}$ and the wave vector $\mathbf{k_i}$ as $2\pi\mathbf{f} = \mathbf{k_i} = k^i_{0x'}\hat{x} + k^i_{0z'}\hat{z} = k^i_0(\sin\vartheta\hat{x} + \cos\vartheta\hat{y})$, where $k_i = |\mathbf{k}|$, and ϑ is the angle between $\mathbf{k_i}$ and the z' axis. From (6),

$$E_{y'}(x', z') = \frac{k_i w_0 E_0}{2\sqrt{\pi}} \int_{-\pi/2}^{\pi/2} \exp\left(-\frac{k_i^2 w_0^2 \sin^2\vartheta}{4}\right) \times \exp\left[ik_i\left(\sin\vartheta x' + \cos\vartheta z'\right)\right] \cos\vartheta d\vartheta, \quad (7)$$

where integration limits account only for non-evanescent waves — no energy is taken away by evanescent ones [6]. By numerical quadrature, (7) is written as a discrete plane wave spectrum [7, 8]

$$E_{y'}(x', z') = \sum_{n=1}^{N} A'(\vartheta_n) \exp\left[ik_i\left(\sin\vartheta_n x' + \cos\vartheta_n z'\right)\right],$$

where

$$A'(\vartheta_n) = \frac{k_i w_0 E_0}{2\sqrt{\pi}} \exp\left(-\frac{k_i^2 w_0^2 \sin^2\vartheta_n}{4}\right) \cos\vartheta_n \Delta\vartheta.$$

$\Delta\vartheta = \pi/N$ and $\vartheta_n = -\pi/2 + n\Delta\vartheta$, $n = 0, 1, ..., N$. Going back to the global coordinate system (x, y, z) via

$$\begin{aligned} x' &= (x - d_x)\cos\varphi^i + (z - a - d_z)\sin\varphi^i \\ z' &= (x - d_x)\sin\varphi^i - (z - a - d_z)\cos\varphi^i \end{aligned} \quad (8)$$

yields the plane wave expansion of the Gaussian beam

$$E_y(x, z) = \sum_{n=1}^{N} A(\vartheta_n) \exp\left[ik_i(x\sin(\vartheta_n + \varphi^i) - (z - a)\cos(\vartheta_n + \varphi^i))\right], \quad (9)$$

where

$$A(\vartheta_n) = \frac{k_i w_0 E_0}{2\sqrt{\pi}} \exp\left(\frac{-k_i^2 w_0^2 \sin^2\vartheta_n}{4}\right) \times \exp\Big(- ik_i(d_x \sin(\vartheta_n + \varphi^i) - d_z\cos(\vartheta_n + \varphi^i))\Big) \cos\vartheta_n \Delta\vartheta$$

The scattered field associated to the nth incident plane wave $E_{y,n}(x, z) = A(\vartheta_n) e^{i\left(\alpha_n^0 x - \beta_n^0 (z-a)\right)}$, $\alpha_n^0 = k_i \sin(\vartheta_n + \varphi^i)$ and $\beta_n^0 = \sqrt{k_i^2 - {\alpha_n^0}^2}$, is obtained by the method in section 2.The total scattered field follows by summing up the scattered fields of all such waves [8].

4 Lattice sums

A class of Schlömilch series (lattice sums) arises in the investigation of wave scattering by periodic structures. In this 1-D periodic, 2-D scattering case, they are $S_m = \sum_{n=1}^{\infty} \mathrm{H}_m^{(1)}(k_1 nd)[e^{i\alpha_0 nd} + (-1)^m e^{-i\alpha_0 nd}]$, where $\mathrm{H}_m^{(1)}(x)$ is the first-kind Hankel function of m-th order, $\alpha_0 = k_0 \sin\theta_i$. This representation yields slowly convergent numerical results. Much literature exists for accelerating convergence [9–13].

Here, one uses [13]. The series is transformed into a new expression with elementary functions, fast yielding accurate lattice sums. For a 5 GHz TM wave normally incident upon a glass-fiber-reinforced slab, letting $L = d = 0.1$ mm, results with relative error below 10^{-6} are achieved in less than 0.03s on a PC with Intel i7 CPU and 8G memory. Computing the lattice sums directly, the convergence is much slower, see Fig. 3.

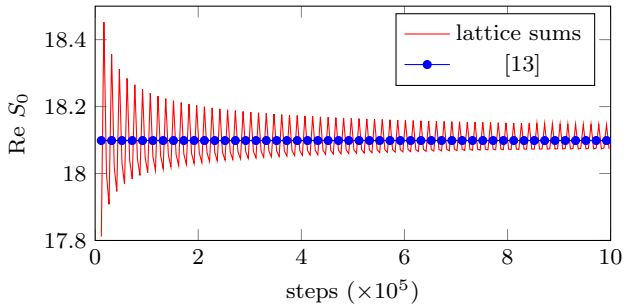

Fig. 3 Computed values of the real part of S_0 for 5 GHz, $\theta_i = 0$, $L = d = 0.1$ mm.

5 Numerical results

Infinite sums $\sum_{p\in\mathbb{Z}}$ and $\sum_{m\in\mathbb{Z}}$ are truncated as $\sum_{p=-P}^{P}$ and $\sum_{m=-M}^{M}$ with $P = \text{Int}\,(d/2\pi(3\Re(k_1) - \alpha_0))$, $M = \text{Int}\,\big(\Re(4.05\times(k_1c)^{1/3}) + k_1c\big)$. Defining the relative error $|\mathcal{R}^{n+1} - \mathcal{R}^n|$, $n = P$, M, the influence of M and P is shown in Fig. 4. Truncating as $M = 11$ and $P = 5$, a relative error less than 10^{-6} is obtained.

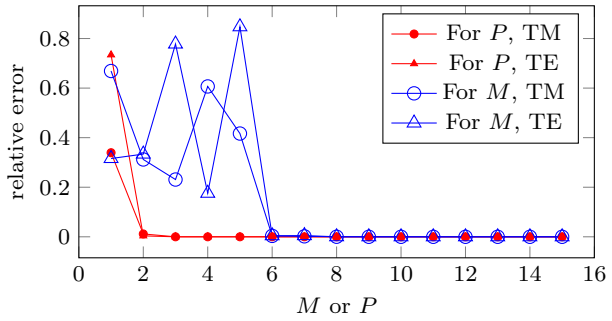

Fig. 4 Relative error versus M or P for glass fibers with epoxy matrix. $d = \lambda_i = 0.1$ mm, $L = 2d$, $c = 0.4d$.

The power reflection and transmission coefficients are defined as $\mathcal{R} = \sum_{p\in\mathbb{Z}} \Re(\beta_0)\|R_p\|^2/(k_0\|E^{\text{inc}}\|^2)$, $\mathcal{T} = \sum_{p\in\mathbb{Z}} \Re(\beta_0)\|T_p\|^2/(k_0\|E^{\text{inc}}\|^2)$. The power absorption coefficient then is $\mathcal{A} = 1 - \mathcal{R} - \mathcal{T}$.

To check the results the power reflection coefficients of an incident TE/TM wave are compared with those in [14], [15]. Figs. 5(a) and (b) show comparisons of results for a TM-illuminated array of lossless or perfect electric conductor (PEC) fibers (the matrix is air). In Fig. 5(c) one compares with TM and TE results computed by the COMSOL FEM code for carbon ($\epsilon_r = 12$, $\sigma = 3.3\times10^2$ S/m) fibers and epoxy ($\epsilon_r = 3.6$) matrix.

The proposed approach is now focused onto power reflection and transmission properties of carbon or glass-fiber-reinforced polymers. Epoxy resin is the most common matrix material, its relative permittivity being taken as 3.6 and its conductivity as zero (below 10^{-10} S/m in practice). For carbon fibers, relative permittivity ranges

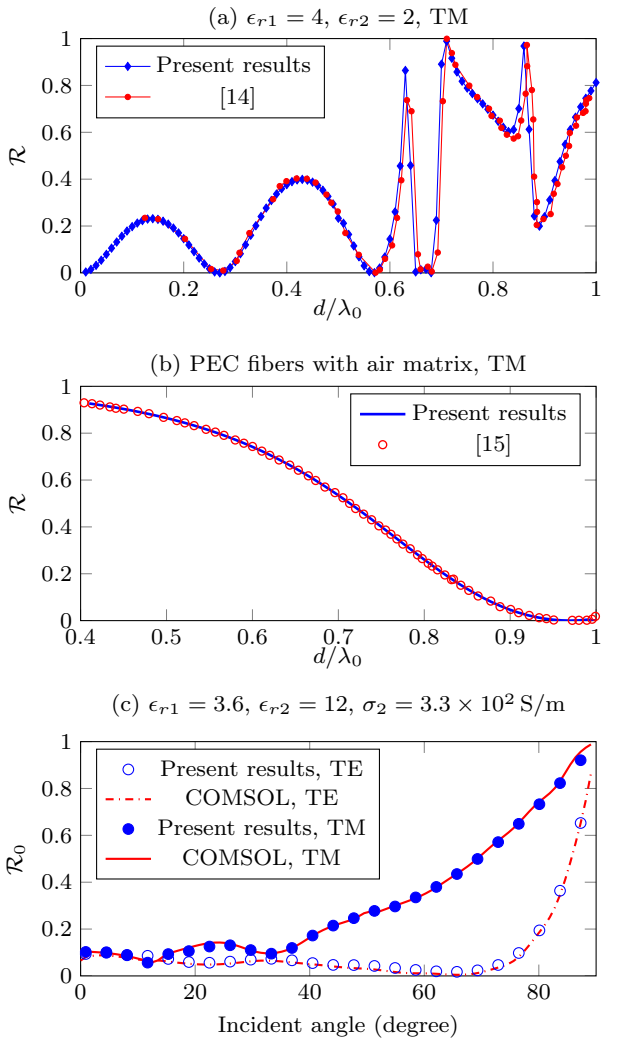

Fig. 5 Comparison of results. (a) TM case, $d = 0.2\,\mu$m, $L = 0.95d$, $c = 0.375d$, (b) PEC fibers, $d = 0.1$ mm, $L = d$, $r = 0.15d$, (c) TE and TM cases, $d = \lambda_i = 0.1$ mm, $L = 2d$ and $c = 0.4d$ for 0-th mode.

between $\approx$ 10 and 15, and conductivity is high in their axis direction, $\approx 2.5\times10^6$ S/m [17–19], yet in the cross-section, it is $\approx 3.3\times10^2$ S/m [20,21], as now considered. For glass fibers, relative permittivity ranges between $\approx$ 3.7 and 10.

Power coefficients for carbon-fiber-reinforced composites (epoxy matrix) in the TM case are shown in Fig. 6 for $0 < d/\lambda_0 < 1$. Weak power absorption is observed when d/λ_0 is close to zero. When λ_0 is close to d, there is strong absorption. In the usual test band of carbon-fiber-reinforced composites, 1 MHz to 1 GHz, the power reflection coefficient is around 0.3.

For glass-fiber-reinforced composites (epoxy matrix), most testing is carried out from 10 to 60 GHz. Power reflection coefficients are shown in Fig. 7. Comparing the results involving glass fibers ($\epsilon_2 = 6\epsilon_0$) with those for

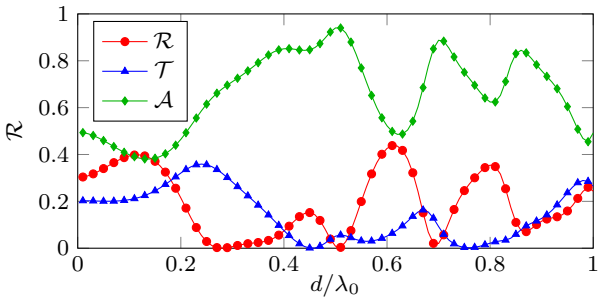

Fig. 6 Variation of $\mathcal{R}$ and $\mathcal{T}$ with d/λ_0 for carbon-fiber composites illuminated by a TM wave. $L = 0.1\,\text{mm}$, $c = 0.25d$, $d = L$, $\epsilon_1 = 3.6\epsilon_0$, $\epsilon_2 = 12\epsilon_0$, $\sigma_2 = 3.3 \times 10^2\,\text{S m}^{-1}$

a homogeneous plate ($\epsilon_2 = \epsilon_1 = 3.6\epsilon_0$), the periodic structure exhibits the same behavior in the frequency band chosen.

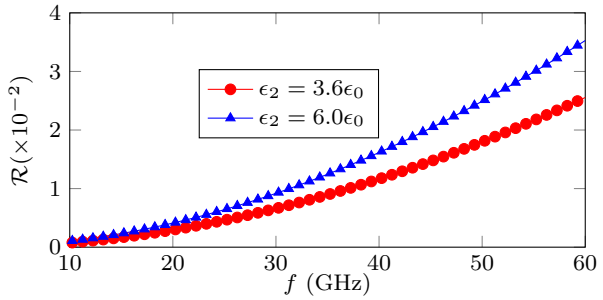

Fig. 7 Coefficients $\mathcal{R}$ and $\mathcal{T}$ for glass-fiber-reinforced epoxy composites from 10 GHz to 60 GHz, TM wave, $L = 0.1\,\text{mm}$, $c = 0.25d$, $d = L$, $\epsilon_1 = 3.6\epsilon_0$

To accurately model a Gaussian beam, N in (9) must be properly chosen. One defines a relative error

$$Error = \frac{1}{N_p} \sum_{1}^{N_p} \frac{|\tilde{E}_{y'} - E_{y'}|^2}{|E_{y'}|^2} \tag{10}$$

taking $\tilde{E}_{y'}$ as the approximate value of the plane wave expansion and $E_{y'}$ referring to the exact value from (5). N_p is the total number of field points computed. Fig. 8 shows the relative error for region $-4\lambda_0 < x' < 4\lambda_0$ and $-3\lambda_0 < z' < 3\lambda_0$, meshed into $N_p = 200 \times 200$, λ_0 as the wavelength of the beam. When $N > 60$, in all cases shown, the approximation works well, the largest error being below 10^{-4}.

Expanding the Gaussian beam into 80 plane waves enables to achieve a relative error less than 10^{-6}. The field intensity distributions for an epoxy matrix with carbon, glass and metal fibers are given in Figs. 9 (glass fibers), 10 (carbon fibers) and 11 (PEC fibers as a limit case). The incident wavelength is $\lambda_0 = 0.1\,\text{mm}$, letting $w_0 = 2\lambda$ and $d_x = d_z = 0$. For the composites, $d = 0.1\,\text{mm}$, $L = 2d$ and $c = 0.15d$.

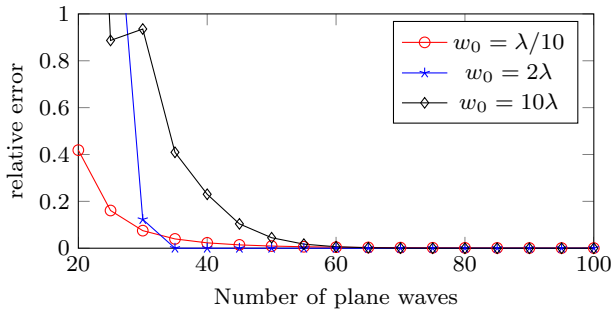

Fig. 8 Relative error versus number of plane waves $\lambda = 0.1mm$.

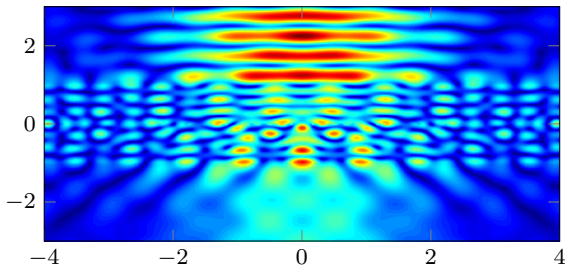

Fig. 9 Gaussian beam impinging on glass-fiber-reinforced slab (refer to text).

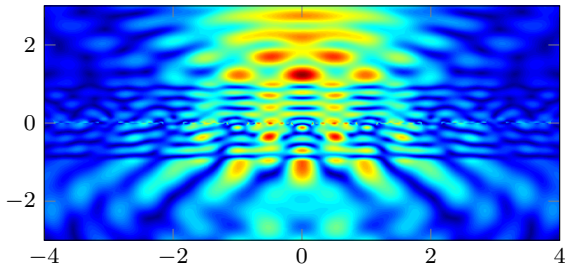

Fig. 10 Gaussian beam impinging on carbon-fiber-reinforced slab (refer to text).

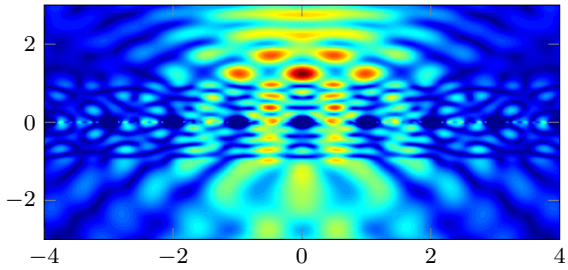

Fig. 11 The limit case of a Gaussian beam impinging on a PEC-fiber-reinforced slab (refer to text).

6 Conclusion

Scattering from a single-layer slab with TE/TM or 2D Gaussian beam illumination has been investigated in the above. A full-wave formulation has been proposed in both situations, once said that the beam-wave case proceeds from the plane-wave case provided that the

beam is properly decomposed into elementary plane waves, each scattered individually, and the resulting beam being recomposed afterwards. Among key points illustrated, the need to devise a fast and convergent way to calculate so-called lattice sums has been considered, as well as the fact that infinite expansions arising in the formulation need careful truncations to preserve the accuracy. The focus otherwise has been on reflection and transmission properties of carbon- or glass-fiber reinforced composite medium, here in the simple case of a single polymer-matrix panel, with also the limit case of fibers in air (meaning just a periodic array of cylinders in air), of the photonic-crystal type. Notice that in the case of fiber-reinforced polymer composites, the adequate frequency bands have been chosen in carrying out the numerical experiments, in harmony with those usually considered during non-destructive testing of such composites. One has also validated, in the air matrix case, at high accuracy the proposed results via a finite-element approach, while successfully retrieved the results of an earlier approach.

The work as summarized is about a 2-D scattering situation, but it has recently been extended to a 2.5D case, wherein the wave vector of the incident wave is no more orthogonal to the fibers axes, which means TE/TM mode conversion in particular. Stacking up the periodic slabs one above the other, the circular cylinders in different layers being oriented in different directions, will be the next step.

The periodicity of the structure might be lost by taking away or displacing cylinders. That disorganization could also be caused by changes of electromagnetic properties or of shapes of cylinders in the layers. To image such disorganized periodic structures, a good understanding of the electromagnetic behavior of both periodic and disorganized periodic structures is a prerequisite, considering that dyadic Green's functions as needed in most imaging procedures follow from plane-wave expansions of the fields due to elementary dipoles set inside or outside. It is believed that the present work and forthcoming contributions pave the way to such investigations.

References

1. Y. Zhong *et al.*, Electromagnetic response of anisotropic laminates to distributed sources, *IEEE Trans. Antennas Propagat.*, **62**, 247-256, 2014
2. J.-P. Groby *et al.*, Acoustic response of a rigid-frame porous medium plate with a periodic set of inclusions, *J. Acoust. Soc. Am.*, **126**, 685-693, 2009
3. J.-P. Groby and D. Lesselier, Localization and characterization of simple defects in finite-size photonic crystals, *J. Optical Soc. Am. A*, **25**, 146-152, 2008
4. S. Wilcox *et al.*, Modeling of defect modes in photonic crystals using the fictitious source superposition method, *Phys. Rev. E*, **71**, 056606-1-056606-11, 2005
5. L. C. Botten *et al.*, Formulation for electromagnetic scattering and propagation through grating stacks of metallic and dielectric cylinders for photonic crystal calculations. Part I. Method, *J. Opt. Soc. Am. A*, **17**, 2165-2176, 2000
6. J. W. Goodman, *Introduction to Fourier Optics*, McGraw-Hill, New York, 1968.
7. E. E. Kriezis *et al.*, Diffraction of a Gaussian beam from a periodic planar screen, *J. Opt. Soc. Am. A*, **11**, 630-636, 1994
8. J. Yang *et al.*, Two-dimensional scattering of a Gaussian beam by a periodic array of circular cylinders, *IEEE Trans. Geosci. Remote Sens.*, **43**, 280-285, 2005
9. V. Twersky, On scattering of waves by the infinite grating of circular cylinders, *IEEE Trans. Antennas Propagat.*, **10**, 737-765, 1962
10. K. Yasumoto *et al.*, Efficient calculation of lattice sums for free-space periodic Green's function, *IEEE Trans. Antennas Propagat.*, **47**, 1050-1055, 1999
11. A. Moroz, Exponentially convergent lattice sums, *Opt. Lett.*, **26**, 1119-1121, 2001
12. M. Kavaklioglu, On Schlömilch series representation for the transverse electric multiple scattering by an infinite grating of insulating dielectric circular cylinders at oblique incidence, *J. Phys. A: Math. Gen.*, **35**, 2229-2234, 2002
13. C. M. Linton, Schlömilch series that arise in diffraction theory and their efficient computation, *J. Phys. A: Math. Gen.*, **39**, 3325-3339, 2006
14. H. Roussel *et al.*, Electromagnetic scattering from dielectric and magnetic gratings of fibers - a T-matrix solution, *J. Electromagn. Waves Applicat.*, **10**, 109-127, 1996
15. T. Kushta *et al.*, Electromagnetic scattering from periodic array of two circular cylinders per unit cell, *PIER*, **29**, 69-85, 2000
16. J. A. Kong, *Electromagnetic Wave Theory*, EMW Publishing, Cambridge MA, 2008
17. M. Antunes *et al.*, Broad-band electrical conductivity of carbon nanofibre-reinforced polypropylene foams, *Carbon*, **49**, 708-717, 2011
18. M. Hotta *et al.*, Complex permittivity of graphite, carbon black and coal powders in the ranges of x-band frequencies (8.2 to 12.4 GHz) and between 1 and 10 GHz, *ISIJ International*, **51**, 1766-1772, 2011
19. A. Galehdar *et al.*, The conductivity of unidirectional and quasi isotropic carbon fiber composites, *2010 European Microwave Conference (EuMC)*, 882-885, 2010.
20. X. Luo *et al.*, Carbon-fiber/polymer-matrix composites as capacitors, *Compos. Sci. Technol.*, **61**, 885-888, 2001.
21. Y. J. Kim *et al.*, Electrical conductivity of chemically modified multiwalled carbon nanotube/epoxy composites, *Carbon*, **43**, 23-30, 2005.

Scattering Characteristics of Structures of Lossy Metamaterial – Semiconductor Cylinders

Juozas Bucinskas[1], Liudmila Nickelson[2,3], Romanas Martavicius[2],

[1] Faculty of Physics, Vilnius University, Sauletekio str. 9, Vilnius, Lithuania
[2] Faculty of Electronics, Vilnius Gediminas Technical University, Naugarduko str. 41, Lithuania
[3] Center for Physical Sciences and Technology, Gostauto 11, LT- 01108, Vilnius, Lithuania
*corresponding author, E-mail: lucynickelson@gmail.com

Abstract

Here we present for the first time the rigorous boundary problem solution of the Maxwell's equations for the determination of scattering characteristics of a structure. The structure consists of a finite set of infinite parallel circular cylinders that can be made of different lossy isotropic materials. We numerically analyzed two structures that differ only in the symmetrical arrangement of semiconductor cylinders in relation to a central metamaterial cylinder. The electrical radii of cylinders can be arbitrary. Both polarizations of the incident microwave are considered in this work. The Pointing vector of the plane microwave that reflected from and transmitted through the strictures analyzed here. We investigated dependency on the radius of an arc where are placed the semiconductor cylinders, the semiconductor specific resistivity, the operating frequency at two radii of the metamaterial cylinder. We discovered that the structure can have features of a bandgap photonic crystal dependent on the topology and the polarization of the incident microwave. We have found that the structure can operate as a microwave reflector at the certain radius of the arc on which are located thirteen n-Si cylinders. The Pointing vector is very sensitive to the value of semiconductor specific resistivity when the incident microwave is the parallel polarized.

1. Introduction

Large quantity of articles about investigations of metamaterial waveguides and metamaterial scattering structures shows the need for the development of microwave devices with unique characteristics [1−4]. The particular properties of structures with some metamaterial elements can be achieved by the sign variations (plus or minus) of the metamaterial permittivity and/or permeability, as well as by effects when the metamaterial has the very low (near-zero) refractive index at different frequencies of electromagnetic (EM) waves. The metamaterial elements are especially interesting to use in microwave devices that developed on the base of photonic crystals. At the last decade photonic crystals are a subject of the active research and they open novel technical possibilities [5, 6]. There are a large range of modern technical developments by using microwave synergetic of photonic crystals and metamaterial elements. The mentioned modern structures can be multifunctional and they can alternately allow the propagation of EM waves in certain directions, the confining waves within a limited volume, the full or partial reflection of waves from the structure at the desired frequency ranges [7-10]. One of great request among the structures is the one consisting of many parallel cylinders. On the base of the structures have been created many devices, such for example, controlled antenna reflectors, filters, polarizers, beam switching antennas, bandgap photonic crystals for transmission of EM waves, the impedance transformers [3-10].

The topologies of mentioned structures become more complex with the development of microwave technology. This fact entails the increasing of complexity of boundary conditions of electrodynamical problem. For this reason, the development of new methods is relevant. The scattering problem for last structures has been analyzed by various analytical or numerical techniques [10-13].

2D infinite metallic cylinders array in the square configuration is studied in [11]. An important assumption is that the cylinder radius $r << a$, when the parameter a is the cylinder array periodicity. Here the finite-element method for the simulation of scattering parameters is used. In [12] is given a solution of the Helmholtz equation by modified multiple-scattering method for an arbitrary arrangement of N identical 2D circular scatterers. The plane wave could incident normally or obliquely on circular scatterers.

The rigorous semi-analytic method based on the cylindrical Floquet mode expansion is given in [13]. There are calculation results of concentric and eccentric cylindrical EM band gap structures that are composed of the perfect conductor and dielectric cylinders. The structures are excited by a Hertzian dipole source. An incident wave is the plane one. Resonances and stopband regions of the transmission spectra are numerically studied there.

Early we have presented our solutions for the single multilayered isotropic cylinder and single anisotropic one. It was presented the scattered and absorbed powers of the incident microwave by the single two layered metamaterial-glass cylinder in [14]. The diffraction characteristics of a single conductor cylinder coated with twelve glass and semiconductor layers on the semiconductor specific resistivity was given in [15]. The single three-layered cylinder with a middle layer made of gyrotropic ferrite or metamaterial was analyzed in [16].

Here we present our new algorithm for determination of the scattering characteristics of the system containing a finite set of circular cylinders. The quantity of cylinders can be arbitrary. The limitation on the cylinders' quantity is imposed by the capabilities of a used computer.
The cylinders can have different radii and be placed in the arbitrary positions. The ones cannot intersect with each another. Any cylinder of the set can be made of various materials. The material can be a perfect conductor or some isotropic materials including the high absorption properties of the ones. The permittivity and/or the permeability of a material can have complex values with any signs of their components. The permittivity and/or permeability of materials can by very small (near zero) as well as very large. Our home-made computer code let us calculate the Pointing vector, scattered and absorbed power densities, scattering patterns as well as all EM wave components depending on the wave incident angles, polarizations, operating frequency of microwave of considered structures.

2. Scattering Problem Formulation and solution

Here we present the rigorous boundary problem solution of the Maxwell's equations for the determination of scattering characteristics of a multi-cylindrical structure. The structure consists of a set of infinite parallel cylinders that can be made of various lossy materials.
The problem is formulated like this. There are N parallel cylinders that are placed in an isotropic homogeneous medium with the permittivity ε_0 and the permeability μ_0. The radii of cylinders are R_s, s=1,…,N and the relative material parameters of every cylinder are ε_s, μ_s. The axis of the every cylinder is parallel to the z axis of the Cartesian coordinate system. The designation of any cylinder center is r_s, s=1,…, N at the plane z=0. There is a requirement:

$$|\vec{r}_s - \vec{r}_p| \geq R_s + R_p, \quad s, p = 1,...,N, \quad s \neq p, \qquad (1)$$

that all cylinders would not cross each other and no one of cylinder can be inside of other one. Cylinders can touch to each another only by their external surfaces. We denote the cylinder for which we write the boundary conditions on it interface with index "s" and the other cylinders which are participated in the boundary conditions with index "p".

In this work we present the structure which consists of fourteen cylinders. The central cylinder of metamaterial is placed in the origin of the coordinate system and the identical semiconductor n-Si cylinders are equidistantly placed on the arc. The radius of the arc is R (Fig.1). The vector $\vec{k}$ is the wave vector of the incident EM wave. The external EM field is composited by an incident EM wave and scattered EM waves of all cylinders of the set. The EM field inside and outside of cylinders convenient describe by using of the transverse electric (TE) mode and the transverse magnetic (TM) mode potentials [14]. The solution of the Maxwell's equations in the cylinder area,

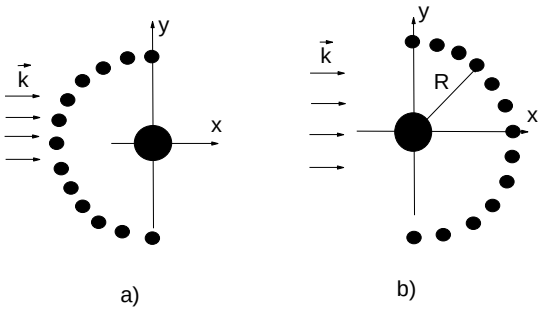

Figure 1: Lossy metamaterial−semiconductor structures when (a) - thirteen semiconductor cylinders are placed on the left side of the central metamaterial cylinder; (b) - the ones are placed on the right side of the central metamaterial cylinder.

after the Fourier transformation with respect to the coordinate z, can be written in the form:

$$E_z = -\frac{1}{\rho}\left\{\frac{\partial}{\partial\rho}\rho\frac{\partial W}{\partial\rho} + \frac{\partial}{\partial\phi}\frac{1}{\rho}\frac{\partial W}{\partial\phi}\right\}, \qquad (2.1)$$

$$E_\rho = \mathrm{i}h\frac{\partial W}{\partial\rho} - \frac{\mathrm{i}\omega\mu_0\mu}{\rho}\frac{\partial V}{\partial\phi}, \qquad (2.2)$$

$$E_\phi = \frac{\mathrm{i}h}{\rho}\frac{\partial W}{\partial\phi} + \mathrm{i}\omega\mu_0\mu\frac{\partial V}{\partial\rho}, \qquad (2.3)$$

$$H_z = -\frac{1}{\rho}\left\{\frac{\partial}{\partial\xi^2}\rho\frac{\partial V}{\partial\rho} + \frac{\partial}{\partial\phi}\frac{1}{\rho}\frac{\partial V}{\partial\phi}\right\}, \qquad (2.4)$$

$$H_\rho = \frac{\mathrm{i}\omega\varepsilon_0\varepsilon}{\rho}\frac{\partial W}{\partial\phi} + \mathrm{i}h\frac{\partial V}{\partial\rho}, \qquad (2.5)$$

$$H_\phi = -\mathrm{i}\omega\varepsilon_0\varepsilon\frac{\partial W}{\partial\rho} + \frac{\mathrm{i}h}{\rho}\frac{\partial V}{\partial\phi}. \qquad (2.6)$$

Here W and V are TM wave and TE wave potentials respectively that satisfied the Helmholtz equation, ε , μ - relative permittivity and permeability of area. The magnitude h is the Fourier parameter.
The equations with respect to potentials are

$$\frac{1}{\rho}\frac{\partial}{\partial\rho}\rho\frac{\partial W}{\partial\rho} + \frac{1}{\rho^2}\frac{\partial^2 W}{\partial\phi^2} + (k^2\varepsilon\mu - h^2)W = 0, \qquad (3.1)$$

$$\frac{1}{\rho}\frac{\partial}{\partial\rho}\rho\frac{\partial V}{\partial\rho} + \frac{1}{\rho^2}\frac{\partial^2 V}{\partial\phi^2} + (k^2\varepsilon\mu - h^2)V = 0 \qquad (3.2)$$

The solution of scattering problem is constructed by using Graf's additional theorem. The potential $W(\vec{R}_S)$ for the TM - waves and the potential $V(\vec{R}_S)$ for the TE – waves on the surface of cylinder s the potentials can be expressed as:

$$W(\vec{R}_s) = \sum_{n=-\infty}^{\infty} A_{s,n}^{\mathrm{sc}} H_n(\beta R_s)\exp(\mathrm{i}n\varphi) + \sum_{\substack{p=1 \\ p\neq s}}^{N} \sum_{n=-\infty}^{\infty} A_{p,n}^{\mathrm{sc}} \sum_{m=-\infty}^{\infty} \exp(\mathrm{i}m\varphi) J_m(\beta R_s) T(m-n \mid \beta r_{ps}) \quad (4)$$

$$V(\vec{R}_s) = \sum_{n=-\infty}^{\infty} B_{s,n}^{\mathrm{sc}} H_n(\beta R_s)\exp(\mathrm{i}n\varphi) + \sum_{\substack{p=1 \\ p\neq s}}^{N} \sum_{n=-\infty}^{\infty} B_{p,n}^{\mathrm{sc}} \sum_{m=-\infty}^{\infty} \exp(\mathrm{i}m\varphi) J_m(\beta R_s) T(m-n \mid \beta r_{ps}) \quad (5)$$

Here $\vec{R}_s$ is a radius vector of any point on the surface of cylinder s. We denoted $\vec{r}_{ps} = \vec{r}_p - \vec{r}_s$, $r_{ps} = |\vec{r}_{ps}|$, $R_s = |\vec{R}_s|$, $T(m \mid \beta r_{ps}) = H_m(\beta r_{ps})\exp(-\mathrm{i}m\varphi_{ps})$, φ_{ps} is the angle between vector $\vec{r}_{ps}$ and axis x, $0 \le \varphi_{ps} < 2\pi$, the magnitudes $A_{s,n}^{\mathrm{sc}}$, $B_{s,n}^{\mathrm{sc}}$, $s = 1,...,N$ are the unknown scattered wave magnitudes to be found from boundary conditions, $H_n(\beta R_s)$, $H_n(\beta r_{ps})$ are the Hankel functions of the second kind, $J_m(\beta R_s)$ is the Bessel function, the propagation constant $\beta = \sqrt{k^2 \varepsilon\mu - h^2}$ in external to cylinders area and the propagation constant $\beta_s = \sqrt{k^2 \varepsilon_s \mu_s - h^2}$ inside of cylinder s, $k=\omega/c$, c is the speed of light in vacuum, $\omega=2\pi f$ is an angular frequency, f is an operating frequency of an incident microwave.

We can find the scattered wave field by formulae (2.1)-(2.6), when the wave amplitudes $A_{s,n}^{\mathrm{sc}}$ and $B_{s,n}^{\mathrm{sc}}$ are known. The electric and magnetic fields of the incident plane wave have the form:

$$\vec{E}^{\mathrm{inc}} = \vec{E}_0 \exp(-\mathrm{i}\vec{k}\vec{r}\sqrt{\varepsilon\mu}), \quad \vec{H}^{\mathrm{inc}} = \vec{H}_0 \exp(-\mathrm{i}\vec{k}\vec{r}\sqrt{\varepsilon\mu}) \quad (6)$$

We use the standard boundary conditions, i.e. the equalization of the electric and magnetic field tangential components on the surface of the cylinder [14]. The set of boundary condition equations after integration through polar angle (angular coordinate) φ give us the system of algebraic linear equations with respect to the wave amplitudes inside $A_{s,n}^{\mathrm{v}}$, $B_{s,n}^{\mathrm{v}}$ and outside $A_{s,n}^{\mathrm{sc}}$, $B_{s,n}^{\mathrm{sc}}$ $s = 1,..., N$ of the cylinders:

$$\begin{aligned} &A_{s,m}^{\mathrm{sc}} \beta^2 H_m(\beta R_s) \\ &+ \sum_{\substack{p=1 \\ p\neq s}}^{N} \sum_{n=-M}^{M} A_{s,n}^{\mathrm{sc}} \beta^2 J_m(\beta R_s) T(m-n \mid \beta r_{ps}) \\ &- A_{s,m}^{\mathrm{v}} \beta_s^2 J_m(\beta_s R_s) = Q E_{0z} (-\mathrm{i})^m J_m(\beta R_s), \\ &\quad s = 1,..., N \end{aligned} \quad (7)$$

$$\begin{aligned} &B_{s,m}^{\mathrm{sc}} \beta^2 H_m(\beta R_s) \\ &+ \sum_{\substack{p=1 \\ p\neq s}}^{N} \sum_{n=-M}^{M} B_{s,n}^{\mathrm{sc}} \beta^2 J_m(\beta R_s) T(m-n \mid \beta r_{ps}) \\ &- B_{s,m}^{\mathrm{v}} \beta_s^2 J_m(\beta_s R_s) = Q H_{0z} (-\mathrm{i})^m J_m(\beta R_s), \\ &\quad s = 1,..., N \end{aligned} \quad (8)$$

$$\begin{aligned} &A_{s,m}^{\mathrm{sc}} \left(-\frac{hm}{R_s} H_m(\beta R_s) \right) \\ &+ \sum_{\substack{p=1 \\ p\neq s}}^{N} \sum_{n=-M}^{M} A_{s,n}^{\mathrm{sc}} \left(-\frac{hm}{R_s} J_m(\beta R_s) T(m-n \mid \beta r_{ps}) \right) \\ &+ B_{s,m}^{\mathrm{sc}} \left(\mathrm{i}kZ_0 \mu \beta H_m'(\beta R_s) \right) \\ &+ \sum_{\substack{p=1 \\ p\neq s}}^{N} \sum_{n=-M}^{M} B_{s,n}^{\mathrm{sc}} \left(\mathrm{i}kZ_0 \mu \beta J_m'(\beta R_s) T(m-n \mid \beta r_{ps}) \right) \\ &+ A_{s,m}^{\mathrm{v}} \left(\frac{hm}{R_s} J_m(\beta_s R_s) \right) - B_{s,m}^{\mathrm{v}} \left(\mathrm{i}kZ_0 \mu_s \beta_s H_m'(\beta R_s) \right) \\ &= -Q(-\mathrm{i})^m \left(-E_{0x} \frac{m}{\beta R_s} J_m(\beta R_s) + \mathrm{i}E_{0y} J_m'(\beta R_s) \right), \\ &\quad s = 1,..., N \end{aligned} \quad (9)$$

$$\begin{aligned} &A_{s,m}^{\mathrm{sc}} \left(-\frac{\mathrm{i}k\varepsilon}{Z_0} \beta H_m'(\beta R_s) \right) \\ &+ \sum_{\substack{p=1 \\ p\neq s}}^{N} \sum_{n=-M}^{M} A_{s,n}^{\mathrm{sc}} \left(-\frac{\mathrm{i}k\varepsilon}{Z_0} \beta J_m'(\beta R_s) T(m-n \mid \beta r_{ps}) \right) \\ &+ B_{s,m}^{\mathrm{sc}} \left(-\frac{hm}{R_s} H_m(\beta R_s) \right) \\ &+ \sum_{\substack{p=1 \\ p\neq s}}^{N} \sum_{n=-M}^{M} B_{s,n}^{\mathrm{sc}} \left(-\frac{hm}{R_s} J_m(\beta R_s) T(m-n \mid \beta r_{ps}) \right) \\ &+ A_{s,m}^{\mathrm{v}} \left(\frac{\mathrm{i}k\varepsilon}{Z_0} \beta_s J_m'(\beta_s R_s) \right) + B_{s,m}^{\mathrm{v}} \left(\frac{hm}{R_s} J_m(\beta R_s) \right) \\ &= -Q(-\mathrm{i})^m \left(-H_{0x} \frac{m}{\beta R_s} J_m(\beta R_s) + \mathrm{i}H_{0y} J_m'(\beta R_s) \right), \\ &\quad s = 1,..., N. \end{aligned} \quad (10)$$

Here $Q = \sqrt{2\pi}\delta(h + k_z\sqrt{\varepsilon\mu})\exp(-\mathrm{i}\vec{k}\vec{r}_s\sqrt{\varepsilon\mu})$, $\delta(h + k_z\sqrt{\varepsilon\mu})$ is the Dirac Delta function, M is an arbitrary value of summation parameter for which summation truncated. The used magnitudes of a magnetic field of an incident microwave and the intrinsic impedance are:

$$\vec{H}_0 = \frac{1}{k}\sqrt{\frac{\varepsilon_0\varepsilon}{\mu_0\mu}}\left[\vec{k}, \vec{E}_0\right], \quad Z_0 = \sqrt{\frac{\mu_0}{\varepsilon_0}} \quad (11)$$

We took the opportunity to eliminate the wave amplitudes inside of cylinders in our algorithm and the solution to this problem has been simplified. The solution is reduced to only finding the external amplitudes.

We can define the scattering and absorption characteristics dependent on geometry of structure, the distance between cylinders, radius and material of cylinders, frequency and polarization of incident EM wave. The calculations were fulfilled by our homemade computer code in FORTRAN language.

3. Numerical results and discussions

Here is numerically analyzed two structures depicted in Fig. 1. The Figs 1(a) and 1(b) differ only in the symmetrical arrangement of semiconductor cylinders in relation to the central metamaterial cylinder. In our calculations the radius of all thirteen *n*-Si cylinders is 1 mm. The metamaterial cylinder has radius R_1 equal to 2 mm (Figs 2−4, 7, 8) or 4 mm (Figs 5, 6). The radius of the arc R is taken in our calculations (Figs 2−4, 7, 8) to be equal to R=12 mm. The metamaterial UCSD30815 complex permittivity ε_1 and permeability μ_1 dependencies on the frequency were taken from [17]. The semiconductor *n*-Si material with the specific resistivity ρ is the dispersive lossy material. The *n*-Si permittivity is ε_S=11.8-i/($\omega\varepsilon_0\rho$) and the permeability is $\mu_s = 1$.

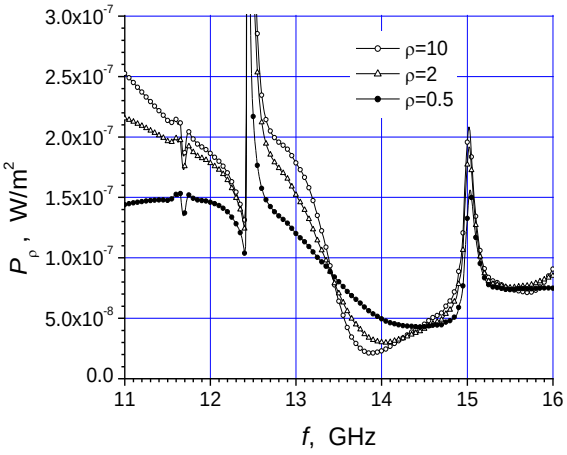

Figure 2: Pointing vector P_ρ dependency on the parallel polarized incident wave frequency for the structure Fig. 1(a) at $\varphi = \pi$ and R_1 = 2 mm.

We present here dependencies of the Pointing vector radial component P_ρ on the operating frequency f at the parallel (Fig. 2. 3, 5, 7) and perpendicular (Figs 4, 6, 8) polarizations of the incident microwave. The specific resistivity of *n*-Si cylinders are ρ=0.5, 2, 10 Ω·m.

In Figs 2−8 are given the component P_ρ dependencies at the distance of 100 meters from the origin of the system coordinate for both structures (Fig. 1). The component P_ρ is given in the point that lies in the direction of the negative axis x when the polar angle $\varphi=\pi$ (Figs 2−6). The component P_ρ is given in the point that lies on the positive axis x, i.e. in the direction of propagation of the incident microwave, when the polar angle $\varphi = 0$ (Figs 7, 8).

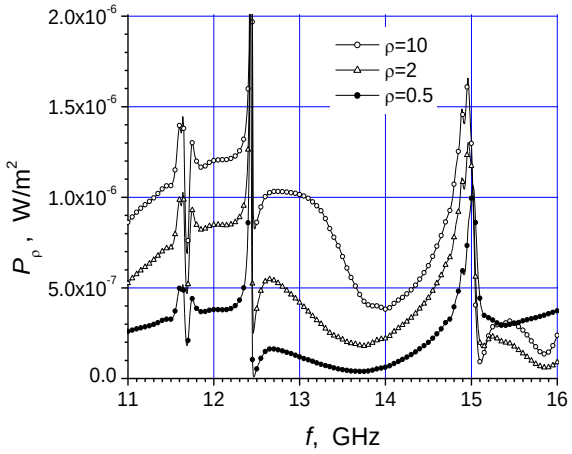

Figure 3: Pointing vector P_ρ dependency on the parallel polarized incident wave frequency for the structure Fig. 1(b) at $\varphi = \pi$ and R_1 = 2 mm.

In Fig. 2 and 3 are shown dependencies of the component P_ρ for an EM wave reflected from structures on the frequency of the incident parallel polarized microwave. We see that the Pointing vector values at the same point lying on the negative axis x is approximately one order larger for the structure Fig. 1(b) in the comparison with the structure Fig. 1(a). The behavior of curves' changing is also considerably different. Magnitudes P_ρ decrease for structure Fig. 1(a) and increase for structure Fig. 1(b) in the range between 11 and 12.4 GHz.

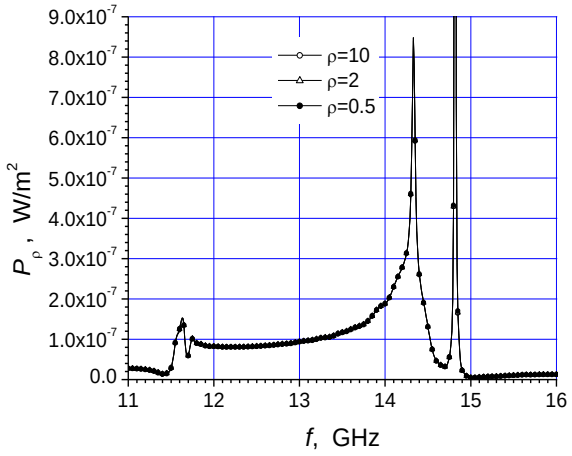

Figure 4: Pointing vector P_ρ dependency on the perpendicular polarized incident wave frequency for the structure Fig. 1(b) at $\varphi = \pi$ and R_1 = 2mm.

The resonant peaks are also different for both structures. The resonant ones are very narrow for structure Fig. 1(b) and they are relatively wide for structure Fig. 1(a) at f~12.5 GHz.

The values of P_ρ do not dependent on the specific resistivity ρ for the structure Fig. 1(a) at f~14.5-16 GHz (Fig. 2). There

is a significant dependency of P_ρ on the specific resistivity for structure Fig. 1(b) at the same frequencies (Fig. 3). It is possible to use the last dependency for the determination of a material specific resistivity at different frequencies.

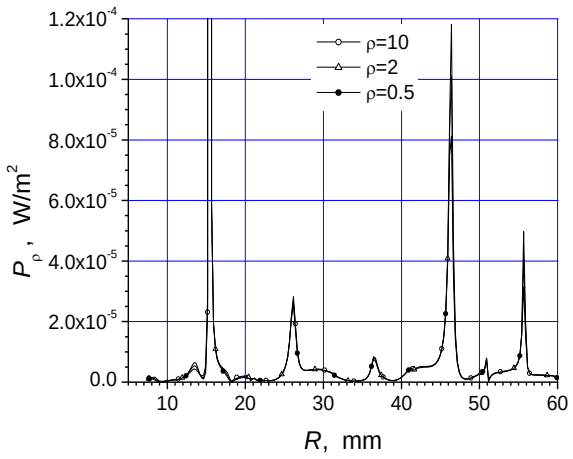

Figure 5: Pointing vector P_ρ dependency on the distance R for the structure Fig. 1(b) at the parallel polarized incident wave f = 15 GHz, $\varphi = \pi$ and R_1 = 4 mm.

In Fig. 4 is presented the analogical characteristics for the structure Fig. 1(b) when the incident microwave has the perpendicular polarization. The comparison of Figs 3 and 4 shows how strongly characteristics of the structure are changed with the changing of polarization. The resonant peaks of P_ρ are shifted on other frequencies. The second resonant peak shifted from ~12.5 to 14.3 GHz and the third peak shifted from ~15 to 14.8 GHz.

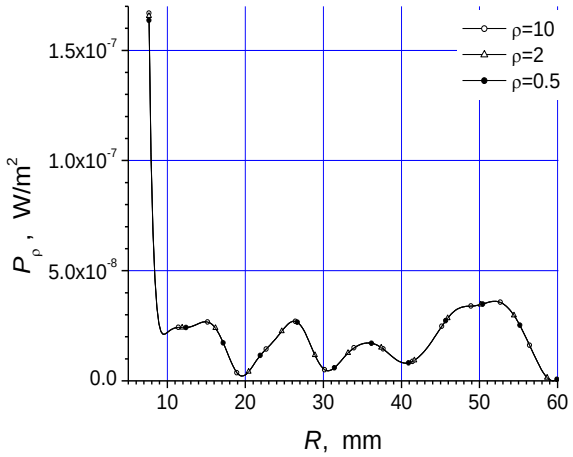

Figure 6: Pointing vector P_ρ dependency on the distance R for the structure Fig. 1(b) at the perpendicular polarized incident wave f = 15 GHz, $\varphi = \pi$ and R_1 = 4 mm.

Two resonant peaks of the Pointing vector are next to each other in the narrow frequency interval for the perpendicular polarized microwave. The largest reflection of the microwave from the structure is at the resonant peaks' frequencies. On these frequencies the structure can works as a reflector of a microwave signal. The dependency on the specific resistivity disappears for the perpendicular polarized microwave (Fig. 4).

In Figs 5 and 6 are shown the dependency of component P_ρ on the distance R between the central metamaterial cylinder and the n-Si cylinders for both polarizations. Here the metamaterial cylinder radius is equal to 4 mm, i.e. it is twice as larger than before (Figs 2-4). We see that the character of the Pointing vector distribution dependent on the distance R is completely different for both polarizations.

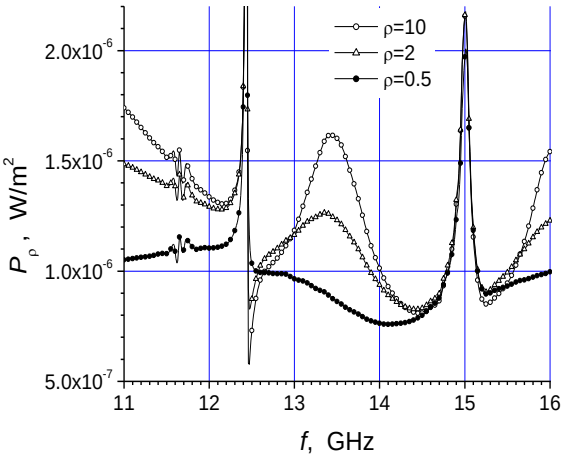

Figure7. Pointing vector P_ρ dependency on the parallel polarized incident wave frequency for the structure Fig.1b at $\varphi = 0$ and R_1 = 2mm.

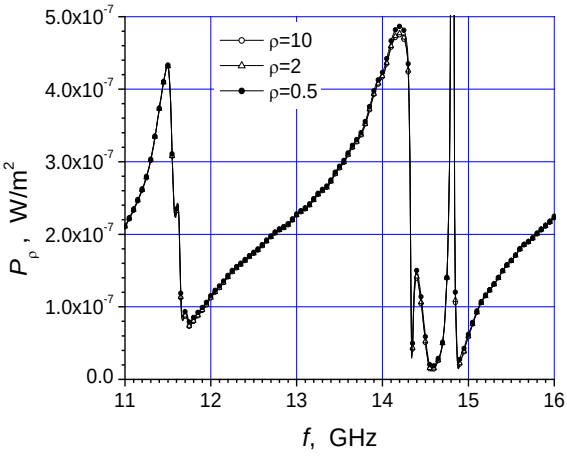

Figure 8: Pointing vector P_ρ dependency on the perpendicular polarized incident wave frequency for the structure Fig. 1a at $\varphi = 0$ and R_1 = 2mm.

The Pointing vector of the reflected parallel polarized microwave from the structure is about three orders larger in the comparison when the microwave has another polarization. The structure Fig. 1(b) is possible to use as a

microwave reflector when the component P_ρ has resonant peaks, for instance R~ 15 mm and 46 mm (Fig.5) at the certain frequency.

In Figs 7 and 8 presented the value P_ρ dependencies at the distance 100 m along the positive axis x (Fig. 1b) from the origin of the system coordinate in the direction of propagation of the microwave $\vec{k}$ for both polarizations. We see that characteristics are markedly different. Dependencies on the specific resistivity ρ of silicon material appeared stronger at the parallel polarization. The Pointing vector is usually the larger when the semiconductor cylinders have the largest specific resistivity. It is possible to explain by the smallest losses of EM energy by semiconductor cylinders of the structure. For this reason the largest portion of EM energy passes through structure (Fig. 7).

It is possible to control the quantity of microwave energy that can pass through the structure by the changing of the semiconductor specific resistivity of cylinders (Fig. 7).

4. Conclusions

The boundary problem of the plane EM wave' scattering by the structure of many lossy isotropic cylinders has been solved. Numerical results for two structures that consist the central metamaterial cylinder and thirteen silicon cylinders that are located equidistantly on the semicircle arc are presented here as an illustration of our solution. We discovered that the structure can have features of a bandgap photonic crystal dependent on it topology at the certain polarization of the incident microwave. We find that the structure can have properties of a microwave reflector at the certain sizes of the elements. The Pointing vector values are strongly dependent on the semiconductor specific resistivity of the cylinders when the incident microwave has the parallel polarization. This fact can be used to control the Pointing vector value by changing of the semiconductor specific resistivity.

References

[1] *Metamaterial*, Edited by Xun-Ya Jiang, InTech, 620 p., DOI: 10.5772/2319, 2012.

[2] W. X. Jiang and T. J. Cui, Radar illusion via metamaterials. *Physical Review E* 83: Issue2, 026601, 2011.

[3] C.-W. Qiu, S. Zouhdi, Y. L. Geng, Shifted Resonances in Coated Metamaterial Cylinders: Enhanced Backscattering and Near-Field Effects, *Physical Review E* 77: Issue 4, 046604, 2008.

[4] P.-H. Tichit, S. N. Burokur, C.-W. Qiu, A. de Lustrac, Experimental verification of isotropic radiation from a coherent dipole source via electric-field-driven LC resonator metamaterials, *Phys. Rev. Lett.* 111: issue13, 133901, 2013.

[5] J. D. Joannopoulos, S. G. Johnson, J. N. Winn, R. D. Meade, *Photonic crystals*. Princeton University Press. Princeton and Oxford, 285 p., 2008.

[6] S. Bittner, B. Dietz, M. Miski-Oglu, A. Richter, Extremal transmission through a microwave photonic crystal and the observation of edge states in a rectangular Dirac billiard, *Phys. Rev. B* 85: Issue 6, 064301, 2012.

[7] M. Hase, H Miyazaki, M. Egashira, N. Shinya, K. M. Kojima, S. Uchida, Isotropic photonic band gap and anisotropic structures in transmission spectra of two-dimensional fivefold and eightfold symmetric quasiperiodic photonic crystals, *Physical review B* 66, 214205, 2002.

[8] D. Hermann, M. Diem, S. F. Mingaleev, A. García-Martín, P. Wölfle, K. Busch, Photonic crystals with anomalous dispersion: Unconventional propagating modes in the photonic band gap. *Phys. Rev. B* 77, 035112, 2008.

[9] A. Tikhonov, J. Bohn, S. A. Asher, Photonic crystal multiple diffraction observed by angular-resolved reflection measurements, *Phys. Rev. B* 80: 235125, 2009.

[10] C.-H. Kuo, Z. Ye. Electromagnetic energy and flows in photonic crystals made of parallel dielectric cylinders, *Physical Review E* 70: 046617, 2004.

[11] R. Zhou, H. Zhang, H. Xin. Metallic wire array as low-effective index of refraction medium for directive antenna application. *IEEE Trans. Antennas Propagat.* 58: No1, 79-87, 2010.

[12] P. A. Martin, Multiple scattering by random configurations of circular cylinders: Reflection, transmission, and effective interface conditions, J. Acoust. Soc. Am. 129: No 4, 1685-1695, 2011.

[13] V. Jandieri, K. Yasumoto, Y. K. Cho. Rigorous analysis of electromagnetic scattering by cylindrical EBG structures. *PIER*: 121, 317-342, 2011.

[14] J. Bucinskas, L. Nickelson, V. Sugurovas, Microwave scattering and absorption by a multilayered lossy metamaterial−glass cylinder. *PIER* 105: 103−118, 2010.

[15] L. Nickelson, J. Bucinskas, Microwave diffraction dependencies of a conductor cylinder coated with twelve glass and semiconductor layers on the *n*-Si specific resistivity. *Electron. Elec. Eng.* 115: No 9, 47−50, 2011.

[16] J. Bucinskas, L. Nickelson, and R. Martavicius, Microwave scattering diagrams of three-layered SiC-metamaterial/gyrotropic ferrite-SiC cylinders. *Appl. Phys. A*., DOI 10.1007/s00339-013-8039-y, 2014.

[17] D. R. Smith, P. Rye, D. C. Vier, A. F. Starr, J. J. Mock, Design and measurement of anisotropic metamaterials that exhibit negative refraction. *IEICE Trans. Electron.* E87-C: No. 3, 359−370, 2004.

Level set-based topology optimization for whispering gallery mode resonator circuits incorporating surface effects

Garuda Fujii[1], Tsuyoshi Ueta[2], Mamoru Mizuno[3] and Masayuki Nakamura[1]

[1] *Department of Environmental Science and Technology, Shinshu University - 4-17-1 Wakasato, Nagano 380-8553, Japan*
[2] *Physics Laboratory, The Jikei University School of Medicine - 8-3-1 Kokuryo-cho, Chofu, Tokyo 182-8570, Japan*
[3] *Faculty of Systems Science and Technology, Akita Prefectural University - 84-4 Aza Ebinokuchi, Tsuchiya, Yurihonjo, Akita 015-0055, Japan*

PACS 42.60.Da – Resonators, cavities, amplifiers, arrays, and rings
PACS 42.15.Eq – Optical system design
PACS 47.55.dr – Interactions with surfaces

Abstract – A level set-based topology optimization method for whispering gallery mode resonator circuits is presented. The effect of total internal reflection at the surfaces of dielectric disks are simulated by modeling clearly defined dielectric boundaries in the process of optimizing the topology. The electric field intensity in an optimal resonator became more than 20 times larger than the initial intensity. Dielectric structures were expressed by level set functions defined as piecewise-constant values. The expression obtained provided precise optimal configurations without any grayscale, which is the intermediate density between the dielectric materials and air. The clear dielectric boundaries of the optimal configurations were defined as iso-surfaces of the level set functions and the zero-points of the level set functions were obtained based on linear interpolations of the functions.

Introduction. – Recent development on the fabrication of micro-nano structures has resulted in advanced optical devices such as lasers [1–5], waveguides [6], and cloaks [7, 8]. Whispering gallery mode (WGM) lasers [9–13] are one of the advanced devices used to realize low-threshold laser oscillations. Light waves propagated along the surfaces of disk resonators by repeated total internal reflection. The light trajectory became circular or polygonal when WGM occurred. Hence, it is necessary to model clearly defined dielectric surfaces in simulations of WGM oscillations to incorporate the effects of reflections.

Topology optimizations [14] are powerful numerical methods for designing high performance optical devices. These optimization methods have been applied to the designs of cloaks [15], super lenses [16], and metamaterials with a negative permeability [17, 18]. In the topology optimizations, some structural expressions have been proposed and topology optimizations based on homogenization [14, 19] and density methods [20] are widely used for designing materials in engineering. However, these methods provide optimal configurations that include grayscales, which are the intermediate densities between the materials and air [21]. The presence of the grayscales makes it difficult to fabricate designed structures and graded optimal configurations that need discrete filtering schemes [21]. Grayscales greatly affect the device properties and the use of filtering schemes degrade the devices performances considerably when grayscales are filtered out to provide discrete configurations. To overcome the grayscale problem, a topology optimization method based on a level set expression [22] is proposed. Level set functions are defined as piecewise-constant values and become zero at structural boundaries. The level set-based topology optimization can remove the grayscale from inside the optimal configurations. However, the grayscale still exists along the structural boundaries in the optimal configurations. To design optical devices that incorporate the effect of dielectric surfaces, topology optimizations that consider clearly defined dielectric boundaries are needed.

In this work, we present a topology optimization for WGM resonator circuits based on the level set expression. Clearly defined dielectric boundaries were obtained

by linear interpolations of the level set functions and the effect of the dielectric surfaces was incorporated into the optimization processes. The structures of the dielectric disk resonators were expressed as level set functions and grayscale-free optimal configurations were obtained. Optimally designed WGM resonator circuits could enhance the electric field intensity in resonators and improve the performance of devices.

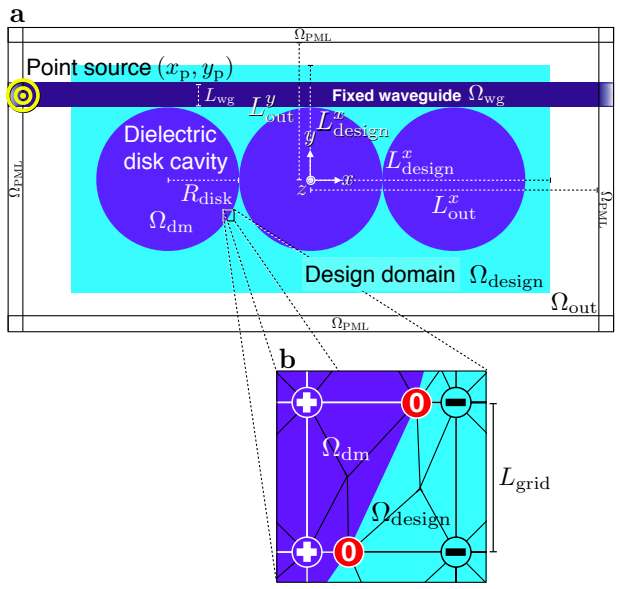

Fig. 1: (Color online) (a) Structure of a WGM resonator circuit. The domains sizes are $L^y_{\rm design} = 0.5 \times L^x_{\rm design}$, $L^x_{\rm out} = 1.2 \times L^x_{\rm design}$, $L^y_{\rm out} = 0.6 \times L^x_{\rm design}$, $L_{\rm wg} = 0.12 \times L^x_{\rm design}$, $L_{\rm grid} = L^x_{\rm design}/300$, and $R_{\rm disk} = 0.3 \times L^x_{\rm design}$. The position of posing source is $(x_{\rm p}, y_{\rm p}) = (-L^x_{\rm out}, R_{\rm disk} + L_{\rm wg}/2)$. (b) The dielectric boundaries were defined as the iso-surfaces of the level set functions. The zero-points of the level set functions were obtained by linear interpolation of the level set functions. Finite elements were created based on the clear dielectric boundaries obtained. The numbers of nodes and elements were approximately 550000 and 1060000, respectively.

Formulation and implementation. – Figure 1(a) shows a schematic illustration of the problem for the optimization of a WGM resonators circuit. A circuit with dielectric disk resonators $\Omega_{\rm dm}$ was designed. The resonators were designed and underwent a transformation in the design domain, $\Omega_{\rm design}$. A fixed waveguide, $\Omega_{\rm wg}$ guided the light waves emitted from a point source located at $(x_{\rm p}, y_{\rm p})$. The width of the waveguide was $L_{\rm wg}$. The intensity of the electric field was maximized in the $\Omega_{\rm dm}$. A perfectly matched layer absorbing boundary condition (PML-ABC) [23] and an optimized absorbing function [24] were used to simulate light scattering in the open regions.

Figure 1(b) shows the level set functions defined on grid points and at the dielectric boundary. The zero-points of the function were obtained by linearly interpolating the function, and the iso-surfaces of the level set functions were interpreted as the dielectric boundaries. Finite elements were created based on the dielectric boundaries obtained and the grids.

Governing equation. It was assumed that there was a TM mode and that the total electric field E_z could be expressed as the sum of the scattered and incident fields $E_{\rm s}$ and $E_{\rm i}$, respectively, as:

$$E_z = E_{\rm s} + E_{\rm i}.$$

The relationship between the scattered and incident fields can be expressed with a Helmholtz equation:

$$\nabla^2 E_{\rm s} + \frac{\omega^2}{c^2}\epsilon(\mathbf{x})E_{\rm s} = -\frac{\omega^2}{c^2}[\epsilon(\mathbf{x}) - \epsilon_{\rm air}]E_{\rm i},$$

where ω is the circular frequency of light, c is the speed of light in a vacuum and $\epsilon_{\rm air}$ is the relative permittivity of air.

Level set expression of the dielectric structures. The optimal arrangement of the position-dependent relative permittivity $\epsilon(\mathbf{x})$ was designed. The relative permittivity $\epsilon(\mathbf{x})$ is defined as:

$$\epsilon(\mathbf{x}) = \begin{cases} \epsilon_{\rm air} + \chi(\epsilon_{\rm dm} - \epsilon_{\rm air}) & \mathbf{x} \in \Omega_{\rm design} \\ \epsilon_{\rm air} & \mathbf{x} \in \Omega_{\rm out} \\ \epsilon_{\rm dm} & \mathbf{x} \in \Omega_{\rm wg} \end{cases},$$

where $\epsilon_{\rm dm}$ is the relative permittivity of the dielectric material and χ is a characteristic function defined in the $\Omega_{\rm design}$ as:

$$\chi(\phi(\mathbf{x})) = \begin{cases} 1 & \text{if} \quad \mathbf{x} \in \Omega_{\rm dm} \\ 0 & \text{if} \quad \mathbf{x} \in \Omega_{\rm design} \backslash \Omega_{\rm dm} \end{cases},$$

where $\phi(\mathbf{x})$ are the level set functions and are defined as the signed distances to the dielectric material boundaries such that:

$$\begin{cases} -1 \le \phi(\mathbf{x}) < 0 & \text{for} \quad \forall \mathbf{x} \in \Omega_{\rm design} \backslash \Omega_{\rm dm} \\ \phi(\mathbf{x}) = 0 & \text{for} \quad \forall \mathbf{x} \in \Gamma_{\rm dm} \\ 0 < \phi(\mathbf{x}) \le 1 & \text{for} \quad \forall \mathbf{x} \in \Omega_{\rm dm} \backslash \Gamma_{\rm dm} \end{cases}.$$

The values of the level set functions were determined with respect to the grid points, as shown in Fig. 1(b), and were linearly interpolated at each location, having a value of 0 at the dielectric boundaries.

Objective functional. To design WGM resonator circuits, the total electric field $E_{\rm z}$ in the resonators $\Omega_{\rm dm}$ must be maximized. Hence, the objective functional for maximizing the light intensity in the resonators is defined as:

$$\underset{\phi}{\text{maximize}} \qquad F = \frac{1}{F_0}\int_{\Omega_{\rm dm}} E_z E_z^* d\Omega, \tag{1}$$

where E_z^* is the complex conjugate of E_z, and F_0 is the integrated intensity of the total electric field for the initial configuration:

$$F_0 = \int_{\Omega_{\rm dm}} E_z E_z^* d\Omega \Big|_{\rm Initial}. \tag{2}$$

Topology optimizations need regularization to obtain optimal configurations because such optimizations are an ill-posed problem. Based on the formulation of the level set-based topology optimization method [22], the objective functional (1) was regularized by adding a fictitious interfacial energy term derived from the phase field model, as follows:

$$\underset{\phi}{\text{minimize}} \qquad F_{\mathrm{r}} = -F + \int_{\Omega_{\mathrm{design}}} \frac{1}{2}\tau|\nabla\phi|^2 d\Omega, \qquad (3)$$

where τ is a positive regularization parameter that represents the ratio of the objective functional to the fictitious interfacial energy term. The above regularization with the fictitious energy term also acted as a perimeter control, a type of geometrical constraint. The geometrical constraint became weaker and the optimal configurations became more complex. For details on this geometrical constraint, please refer to the theoretical papers previously published [15, 22].

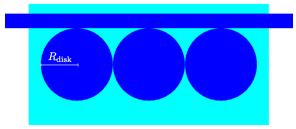

(a) Initial configuration, $L_{\mathrm{p}}/L^x_{\mathrm{design}} = 5.65 \times 10^0$, $R_{\mathrm{disk}} = 0.3 \times L^x_{\mathrm{design}}$.

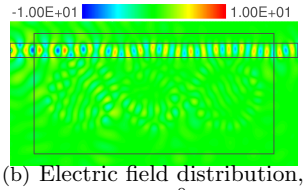

(b) Electric field distribution, $F = 1.00 \times 10^0$.

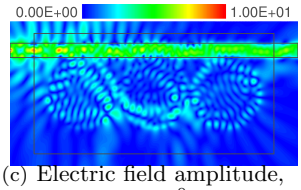

(c) Electric field amplitude, $F = 1.00 \times 10^0$.

Fig. 2: (Color online) An initial configuration, electric field distribution $E_z/|E_{\mathrm{i}}^{\mathbf{0}}|$ and electric field amplitude $|E_z|/|E_{\mathrm{i}}^{\mathbf{0}}|$ for the initial configuration. $E_{\mathrm{i}}^{\mathbf{0}}$ is the incident electric field at the center of the Ω_{design} The relative permittivity values were $\epsilon_{\mathrm{dm}} = 4.0$ and $\epsilon_{\mathrm{air}} = 1.0$. The normalized frequency was $\omega L^x_{\mathrm{design}}/2\pi c = 5.0$.

Results. – Figure 2 shows the initial configuration, a normalized electric field distribution, its amplitude and the corresponding objective functional value, F. The value of F became 1 because the objective functional value was normalized by itself in Eq. (1).

In Figs. 2(b) and 2(c), the light waves radiated from the light source and propagated in the waveguide and a small amount of light was observed in the resonators. WGMs were not observed in the dielectric disks.

Figure 3 shows the optimal configurations obtained for $\tau = 1\times10^{-6}$ and 1×10^{-7}, and the distributions of the total electric field and its amplitude for the optimal configuration. The Fs for the optimal configuration reached values roughly 20 times higher than the initial configuration. A

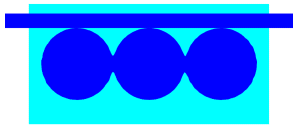

(a) Optimal configuration, $\tau = 1 \times 10^{-6}$, $L_{\mathrm{p}}/L^x_{\mathrm{design}} = 5.11 \times 10^0$.

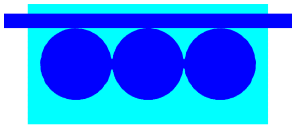

(b) Optimal configuration, $\tau = 1 \times 10^{-7}$, $L_{\mathrm{p}}/L^x_{\mathrm{design}} = 5.33 \times 10^0$.

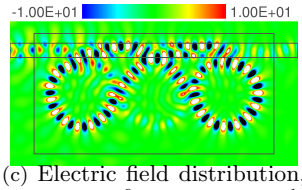

(c) Electric field distribution, $\tau = 1 \times 10^{-6}$, $F = 2.05 \times 10^1$.

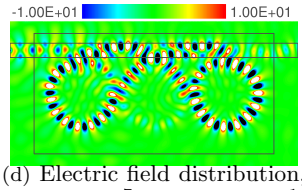

(d) Electric field distribution, $\tau = 1 \times 10^{-7}$, $F = 2.23 \times 10^1$.

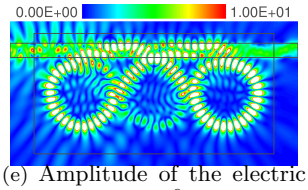

(e) Amplitude of the electric field, $\tau = 1\times10^{-6}$, $F = 2.05\times10^1$.

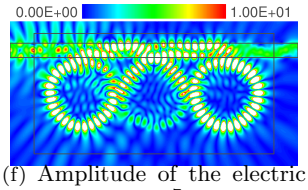

(f) Amplitude of the electric field, $\tau = 1\times10^{-7}$, $F = 2.23\times10^1$.

Fig. 3: (Color online) The optimal configurations, electric field distributions $E_z/|E_{\mathrm{i}}^{\mathbf{0}}|$ and electric field amplitudes $|E_z|/|E_{\mathrm{i}}^{\mathbf{0}}|$. The corresponding objective functional values (F) are shown in the sub-captions. The relative permittivity values were $\epsilon_{\mathrm{dm}} = 4.0$ and $\epsilon_{\mathrm{air}} = 1.0$.

large structural difference was not observed between the initial and the optimal configurations, as shown in Figs. 3(a) and 3(b). In Figs. 3(c) to 3(f), "circuits" of light trajectories along the disk surfaces and the waveguides were observed.

When the optimal configurations were compared with the initial configuration, a difference was observed be-

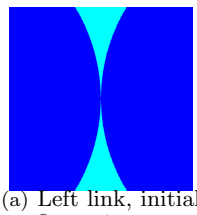

(a) Left link, initial configuration.

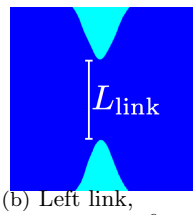

(b) Left link, $\tau = 1 \times 10^{-6}$.

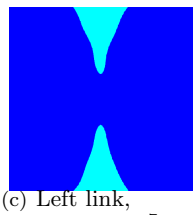

(c) Left link, $\tau = 1 \times 10^{-7}$.

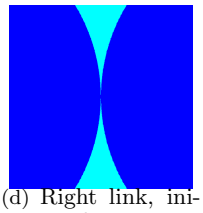

(d) Right link, initial configuration.

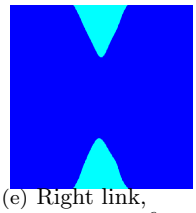

(e) Right link, $\tau = 1 \times 10^{-6}$.

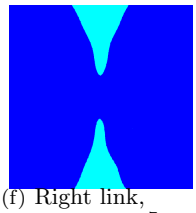

(f) Right link, $\tau = 1 \times 10^{-7}$.

Fig. 4: (Color online) Link structures between neighboring disks.

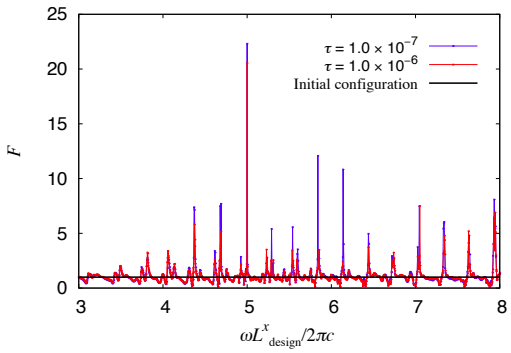

Fig. 5: (Color online) Normalized frequency $\omega L^x_{\rm design}/2\pi c$ versus the objective functional values (F) for $\epsilon_{\rm dm} = 4.0$.

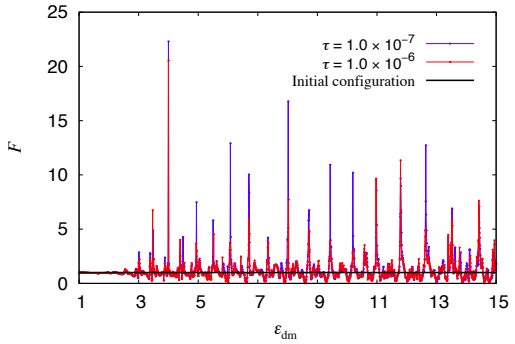

Fig. 6: (Color online) Relative permittivity of a dielectric material $\epsilon_{\rm dm}$ versus the objective functional values (F) for $\omega L^x_{\rm design}/2\pi c = 5.0$.

tween the initial and the optimal configurations, linking the structures between the neighboring dielectric disks. Figure 4 shows a close-up of the link structures. The link structures were regarded as the most important difference between the initial and optimal configurations. The perimeters of the configurations ($L_{\rm p}$) are shown in the sub captions in Figs 2(a), 3(a) and 3(b) to investigate the width of the link structures ($L_{\rm link}$). The difference in the perimeters between the initial and optimal configurations for $\tau = 1\times10^{-6}$ became $\Delta L_{\rm p}/L^x_{\rm design} = 5.65-5.11 = 0.54$. When the width of the link structures in the initial configuration was $L_{\rm p} = 0.00$ and the left and right link structures in each optimal configuration were regarded as the same, the difference in the perimeters $\Delta L_{\rm p}$ and $L_{\rm link}$ have the following relation:

$$\Delta L_{\rm p} \approx 4 L_{\rm link},$$

and the width of link structures became:

$$\begin{aligned} L_{\rm link}/L^x_{\rm design} &= 1.35\times10^{-1} \qquad \tau = 1\times10^{-6}, \\ L_{\rm link}/L^x_{\rm design} &= 8.01\times10^{-2} \qquad \tau = 1\times10^{-7}. \end{aligned} \tag{4}$$

The wavelength ($\lambda_{\rm dm}$) in the dielectric structures ($\Omega_{\rm dm}$) can be written as:

$$\begin{aligned} \lambda_{\rm dm}/L^x_{\rm design} &= 1/[(\omega L^x_{\rm design}/2\pi c)\sqrt{\epsilon_{\rm dm}}] \\ &= 1.0\times10^{-1}. \end{aligned}$$

The wavelength ($\lambda_{\rm dm}$) and the width of the optimal link structures ($L_{\rm link}$) were roughly equal to each other. The link structures need to reflect the light to confine the light waves in each dielectric disk as a resonator, and they need to transmit the light to the connected circuit. To satisfy both of the above contradictory functions, the widths of the link-structures need to be on the same scale as the wavelength.

Figures 5 and 6 show the frequency and relative permittivity responses of the objective functional value. Periodic steep peaks of the F are observed in Fig. 5 and there are repeated peaks in Fig. 6. When the data shown in Fig. 6 were plotted as the relation between F and $\sqrt{\epsilon_{\rm dm}}$, the repeated peaks emerged periodically. The periods in Fig. 5 were $\Delta(\omega L^x_{\rm design}/2\pi c) = 0.296$ and 0.300 for $\tau = 1\times10^{-6}$ and 1×10^{-7}, respectively. In Fig. 6, $\Delta\left(\sqrt{\epsilon_{\rm dm}}\right) = 0.121$ for both $\tau = 1\times10^{-6}$ and 1×10^{-7}.

The circuit length ($L_{\rm circuit}$) is considered to be the most important length for feedback in the circuit, becoming an integral multiple of the wavelength in a dielectric material as:

$$L_{\rm circuit} = N\lambda_{\rm dm},$$

where N is an integer. The above relation can be rewritten as:

$$\frac{\omega L^x_{\rm design}}{2\pi c}\sqrt{\epsilon_{\rm dm}} = N\frac{L^x_{\rm design}}{L_{\rm circuit}}.$$

When difference between integers $N+1$ and N is taken into consideration, the difference between the oscillating frequencies and the relative permittivity of the dielectric material can be derived as:

$$\begin{aligned} \Delta\left(\frac{\omega L^x_{\rm design}}{2\pi c}\right) &= \frac{L^x_{\rm design}}{L_{\rm circuit}\sqrt{\epsilon_{\rm dm}}}, \\ \Delta\left(\sqrt{\epsilon_{\rm dm}}\right) &= \frac{L^x_{\rm design}}{L_{\rm circuit}}\left(\frac{\omega L^x_{\rm design}}{2\pi c}\right)^{-1}, \end{aligned}$$

which leads to following relations:

$$\frac{L^x_{\rm circuit}}{L_{\rm design}} = \frac{1}{\Delta\left(\frac{\omega L^x_{\rm design}}{2\pi c}\right)\sqrt{\epsilon_{\rm dm}}} \tag{5}$$

$$\frac{L^x_{\rm circuit}}{L_{\rm design}} = \frac{1}{\frac{\omega L^x_{\rm design}}{2\pi c}\Delta\left(\sqrt{\epsilon_{\rm dm}}\right)} \tag{6}$$

The circuit length $L^x_{\rm circuit}$ could be obtained from the values of the periods and the circuit lengths shown in Tables 1 and 2.

The average $L_{\rm circuit}/L^x_{\rm design}$ in Tables 1 and 2 is:

$$\frac{L_{\rm circuit}}{L^x_{\rm design}} = 1.66. \tag{7}$$

Table 1: The values of the period and the circuit length obtained from Fig. 5 and Eq. (5).

τ	$\Delta\left(\frac{\omega L^x_{\rm design}}{2\pi c}\right)$	$\sqrt{\epsilon_{\rm dm}}$	$\frac{L_{\rm circuit}}{L^x_{\rm design}}$
1×10^{-6}	0.296	2.0	1.68
1×10^{-7}	0.300	2.0	1.66

Table 2: The values of the period and the circuit length obtained from Fig. 6 and Eq. (6).

τ	$\frac{\omega L^x_{\rm design}}{2\pi c}$	$\Delta\sqrt{\epsilon_{\rm dm}}$	$\frac{L_{\rm circuit}}{L^x_{\rm design}}$
1×10^{-6}	5.0	0.121	1.65
1×10^{-7}	5.0	0.121	1.65

The perimeter of the disks $L_{\rm disk}$ is:

$$\frac{L_{\rm disk}}{L^x_{\rm design}} = 2\pi\frac{R_{\rm disk}}{L^x_{\rm design}} \tag{8}$$

$$= 1.88. \tag{9}$$

$L_{\rm circuit}$ was nearly the same as $L_{\rm disk}$. Hence, the resonance in the disk was considered to be the most important feedback mechanism in the WGM resonator circuit.

Conclusions. – The topology optimization for a WGM resonator circuit based on a level set expression was presented. Clear dielectric boundaries were obtained by linear interpolations of level set functions and the effect of dielectric surfaces was taken into consideration in the topology optimization process. The link structures between neighboring disks were improved and the light trajectory circuits along the surfaces of the dielectric disks were observed in the optimal configurations. The widths of the link structures were on the scale of the wavelength of light and the widths provided an appropriate rate of reflection and transmission for resonance to occur in the disks, creating a light circuit.

* * *

This work was supported by the CASIO SCIENCE PROMOTION FOUNDATION.

REFERENCES

[1] Wiersma D. S., *Nature Phys.*, **4** (2008) 359.
[2] Wiersma D. S., *Nature Photon.*, **7** (2013) 188.
[3] Fujii G., Matsumoto T., Takahashi T. and Ueta T., *Opt. Express*, **20** (2012) 7300.
[4] Fujii G., Matsumoto T., Takahashi T. and Ueta T., *J. Phys. B: At. Mol. Phys.*, **45** (2012) 085404.
[5] Fujii G., Matsumoto T., Takahashi T. and Ueta T., *Appl. Phys. A*, **107** (2012) 35.
[6] Notomi M., Shinya A., Mitsugi S., Kuramochi E. and Ryu H.-Y., *Opt. Express*, **12** (2004) 1551.
[7] Leonhardt U., *Science*, **312** (2006) 1777.
[8] Pendry J. B., Schurig D. and Smith D. R., *Science*, **312** (2006) 1780.
[9] McCall S. L., Levi A. F. J., Slusher R. E., Pearton S. J. and Logan R. A., *Appl. Phys. Lett.*, **60** (1992) 289.
[10] Vahala K. J., *Nature*, **424** (2003) 839.
[11] Armani D. K., Kippenberg T. J., Spillane S. M. and Vahala K. J., *Nature*, **421** (2003) 925.
[12] Hossein-Zadeh M. and Vahala K. J., *Opt. Express*, **14** (2006) 10800.
[13] He L. and Ş. K. Özdemir L. Y., *Laser Photon. Rev.*, **7** (2013) 60.
[14] Bendsøe M. P. and Kikuchi N., *Comput. Methods Appl. Mech. Engrg.*, **71** (1988) 197.
[15] Fujii G., Watanabe H., Yamada T., Ueta T. and Mizuno M., *Appl. Phys. Lett.*, **102** (2013) 251106.
[16] Dobson D. C. and Simeonova L. B., *Appl. Math. Optim.*, **60** (2009) 133.
[17] Diaz A. R. and Sigmund O., *Struct. Multidisc. Optim.*, **41** (2010) 163.
[18] Otomori M., Yamada T., Izui K., Nishiwaki S. and Andkjær J., *Comput. Methods Appl. Mech. Engrg.*, **237–240** (2012) 192.
[19] Bendsøe M. P. and Sigmund O., *Topology Optimization: Theory, Methods and Applications* (Springer) 2003.
[20] Bendsøe M. P., *Struct. Optim.*, **1** (1989) 193.
[21] Sigmund O. and Petersson J., *Struct. Optimiz.*, **16** (1998) 68.
[22] Yamada T., Izui K., Nishiwaki S. and Takezawa A., *Comput. Methods Appl. Mech. Engrg.*, **199** (2010) 2876.
[23] Berenger J. P., *J. Comput. Phys.*, **114** (1994) 185.
[24] Bermúdez A., Hervella-Nieto L., Prieto A. and Rodríguez R., *J. Comput. Phys.*, **223** (2007) 469.

Characterization of Blade Bragg Grating Modeling With Different Incident Angle Profiles For Strain Sensor Applications

Niparat Cheamanunkul[1], Keerayoot Srinuanjan[1], Preecha P. Yupapin[1],

[1]Department of Physics, Faculty of Science, King Mongkut's Institute of Technology Ladkrabang, Thailand
*corresponding author, E-mail: ncheamanunkul@gmail.com

Abstract

This paper presents some preliminary results of sensing properties of single-mode silica blade Bragg gratings model which is coated by a poly(methyl methacrylate) (PMMA). The proposed mathematic model of Blade Bragg Gratings consists of alternated periodic slabs waveguide with inclined angle is analyzed by using the principle of multilayer transfer matrix for photonic crystal. By varying the incident angle, the slabs angle, the proposed model is simulated for all of the parameters, regarding to the sensor applications. The simulation results were shown and discussed. According to the simulation results, this model can be used for sensitive stain sensor applications.

Keywords: Blade Bragg Grating, incident angle poly(methyl methacrylate) (PMMA), photonic crystal transfer matrix

1. Introduction

A Blade Bragg Grating is a periodic perturbation of the refractive index along the length of waveguide which is formed by exposure of the core to an intense optical interference pattern [1]. When light is propagated by the periodically alternate regions of higher and lower refractive index, it is partially reflected at each interface between those regions. If the pitch of grating is properly designed, then all partial reflections add up in phase and can be grow up to nearly 100%, for a specific wavelength even though the individual reflections are tiny [2]. Blade Bragg Gratings have been received the increasing applications in an optical sensing. Their Bragg wavelength shift is proportional to the temperature strain or an inclined angle of the waveguide when it's experience to the gratings [3, 4].

In this paper, we offered the mathematical model of blade Bragg grating in PMMA by analyzing the optical field when propagation into the interface regions in which it has an inclined angle of the slab waveguide and we also used the multilayer transfer matrix modeling to describe the optical output field. The analytic mathematical model is achieved and demonstrated in the paper description. The number of slab layers and the inclined angle of them, i.e. the incident angle of the optical filed into the Blade Bragg Grating are varied. Then, the relation between the number of slab layers, the incident angle and the center peak wavelength have been presented and discussed. The simulation results have shown the center peak wavelength of the optical output field is shift when the slab angle is change. The proposed model could be used for the sensitive stain sensor applications [5, 6, 7].

2. Mathematical Model

The model of Blade Bragg Grating consists of several layers of difference refractive index slab waveguide. For the mathematical modeling, we analyzed each region, term by term, throughout the rang of the grating all over the system, and the schematic diagram is show in Fig. 1

At first, we applied the Gaussian pulse, an optical field (E_{in}) into the model. The operating wavelength (λ) range is set between 1.300 – 1.800μm, and the center wavelength λ_0 is 1.550 μm, which is described by

$$E_{in} = A_0 e^{\frac{1}{2}(\lambda-\lambda_0)^2/T_0^2} \quad (1)$$

Where A_0 is the amplitude and T_0 is the full wide at half maximum of the optical field. Then, optical field propagated into the waveguide and incident into the interface regions as show in Fig.2

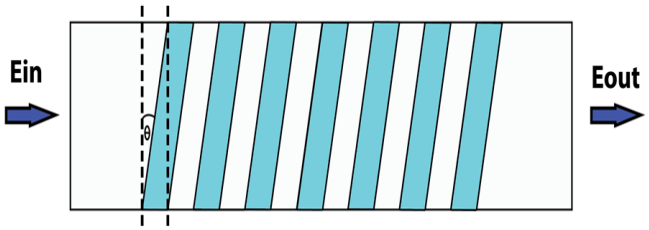

Fig.1. The schematic diagram of Blade Bragg Grating

At the interface regions, the optical filed incident into the boundary with an angle θ_0 that equivalent to the incline angle of the slab. Then, the light propagates through the next slab. The Snell's law is applied to the refraction, which gives a refraction angle θ_{t0} (or transmission angle), and then the light incident into the next slab with an incident angled θ_{i1} and so on. The concept of propagation rays throughout the grating can be explained as follows.

Layer 0; $n_L \sin\theta_0 = n_H \sin\theta_{t0}$

Layer 1; $n_H \sin\theta_{i1} = n_L \sin\theta_{t1}; \theta_{t0} = \theta_{i1}$

Layer 2; $n_L \sin\theta_{i2} = n_H \sin\theta_{t2}; \theta_{t1} = \theta_{i2}$

Layer 3; $n_H \sin\theta_{i3} = n_L \sin\theta_{t3}; \theta_{t2} = \theta_{i3}$

Layer 4; $n_L \sin\theta_{i4} = n_H \sin\theta_{t3}; \theta_{t1} = \theta_{i4}$ ……

Layer n; $n_H \sin\theta_{in} = n_L \sin\theta_{tn}; \theta_{t(n-1)} = \theta_{in}$ (2)

where n = 0, 1, 2, … , n

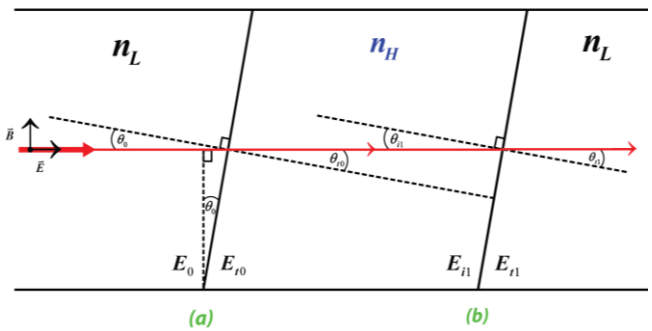

Fig.2 The schematic diagram of the propagation rays in Blade Bragg Grating

The boundary conditions for the electric field at the two interfaces became

$$E_a = E_0\cos\theta_0 + E_{r0}\cos\theta_0 = E_{t0}\cos\theta_{t0} + E_{i0}\cos\theta_{t0} \quad (3)$$

$$E_b = E_{i1}\cos\theta_{t0} + E_{r1}\cos\theta_{t0} = E_{t1}\cos\theta_{t1} \quad (4)$$

Where E_a is the input electric field, E_0 is the incident electric field, E_{r0} is the reflective electric field at the first boundary (between air and first layers), E_{t0} is the transmission electric field and E_{i0} is the incident electric field at the second boundary (between air and first layers), E_a is the output electric field, E_{i1} is the incident electric field, E_{r2} is the reflective electric field and E_{t1} is the leaves out electric field at the next boundary (between first and second layers) and so on.

Corresponding equations for the magnetic field are

$$B_a = B_0\cos\theta_0 - B_{r0}\cos\theta_0 = B_{t0}\cos\theta_{t0} - B_{i0}\cos\theta_{t0} \quad (5)$$

$$B_b = B_{i1}\cos\theta_{t0} - B_{r1}\cos\theta_{t0} = B_{t1}\cos\theta_{t1} \quad (6)$$

Where B_a is the input magnetic field, B_0 is the incident magnetic field, B_{r0} is the reflective magnetic field at the first boundary (between air and first layers), B_{t0} is the transmission magnetic field and B_{i0} is the incident magnetic field at the second boundary (between air and first layers), B_a is the output magnetic field, B_{i1} is the incident magnetic field, B_{r2} is the reflective magnetic field and B_{t1} is the leaves out magnetic field at the next boundary (between first and second layers) and so on.

From $B = n\sqrt{\varepsilon_0\mu_0 E}$ (7)

Where ε_0 and μ_0 is the permittivity and permeability in free space, n is the refractive index, and, from eq. (5) we have

$$B_a = (B_0 - B_{ro})\cos\theta_0 = (B_{t0} - B_{i1})\cos\theta_{t1} \quad (8)$$

$$B_a = (E_0 - E_{r0})n_L\sqrt{\varepsilon_0\mu_0}\cos\theta_0 = (E_{t0} - E_{i0})n_H\sqrt{\varepsilon_0\mu_0}\cos\theta_{t0} \quad (9)$$

$$B_a = \gamma_L(E_0 - E_{r0}) = \gamma_H(E_{t0} - E_{i1}) \quad (10)$$

Which $\gamma_L = n_L\sqrt{\varepsilon_0\mu_0}\cos\theta_{tL}$ and $\gamma_H = n_H\sqrt{\varepsilon_0\mu_0}\cos\theta_{tH}$

Where n_L and n_H are the low and high refractive index of a slab, θ_{tL} and θ_{tH} are the low and high transmission angle, respectively. From eq. (6)

$$B_b = (B_{i1} - B_{r1})\cos\theta_{t1} = B_{t1}\cos\theta_{t1} \quad (11)$$

$$B_b = (E_{i1} - E_{r1})n_H\sqrt{\varepsilon_0\mu_0}\cos\theta_{t0} = E_{t1}n_L\sqrt{\varepsilon_0\mu_0}\cos\theta_{t1} \quad (12)$$

$$B_b = \gamma_L(E_0 - E_{r0}) = \gamma_H E_{t0} \quad (13)$$

When light propagated from $E_{t0} \to E_{i1}$ the phase difference is δ transversal of the model for half the phase difference.

$$\Delta = 2nt\cos\theta \quad (14)$$

So,

$$\delta = k_0\Delta = \left(\frac{2\pi}{\lambda_0}\right)nt\cos\theta \quad (15)$$

Where δ is phase difference, k_0 is wave number, t is the thickness of slab layer, θ is the incline angle of the slab, and n is the slab refractive index.

So, Matrix form

$$E_a = (\cos\delta)(E_b) + \left(\frac{i\sin\delta}{\gamma}\right)(B_b) \quad (16)$$

$$B_a = (i\gamma\sin\delta)(E_b) + (\cos\delta)(B_b) \quad (17)$$

The optical field propagates into the blade Bragg grating: the optical field is analyzed by the multilayer transfer matrix, where E_{in} is the optical field enters to the blade Bragg grating. Then the optical field that propagated throughout the waveguide is in term of $M_T E_{in}$, Where M_T is the transfer matrix of multilayer slab, and E_{out} is the optical field leaves out the waveguide.

The relationship between input and output of the optical field at each boundary of the interface layer in blade Bragg grating can be written in the form of matrix equation. The transfer function of the blade Bragg grating consist of the high-low refractive index (n_H and n_L) of multilayer slab matrix representation, which is described by

$$M_T = M_H \cdot M_L \cdot M_H \cdot M_L \cdot \ldots \cdot M_H \quad (18)$$

Where M_T is transfer matrix; M_H and M_L are the transfer high (n_H) and low (n_L) refractive index matrix which is described by

$$M_H = \begin{bmatrix} \cos\left(\left(\frac{2\pi}{\lambda_0}\right)n_H t\cos\theta_2\right) & \frac{i\sin\left(\left(\frac{2\pi}{\lambda_0}\right)n_H t\cos\theta_2\right)}{n_H\sqrt{\varepsilon_0\mu_0}\cos\theta_2} \\ in_H\sqrt{\varepsilon_0\mu_0}\cos\theta_2\sin\left(\left(\frac{2\pi}{\lambda_0}\right)n_H t\cos\theta_2\right) & \cos\left(\left(\frac{2\pi}{\lambda_0}\right)n_H t\cos\theta_2\right) \end{bmatrix} \quad (19)$$

$$M_L = \begin{bmatrix} \cos\left(\left(\frac{2\pi}{\lambda_0}\right)n_L t\cos\theta_1\right) & \frac{i\sin\left(\left(\frac{2\pi}{\lambda_0}\right)n_L t\cos\theta_1\right)}{n_L\sqrt{\varepsilon_0\mu_0}\cos\theta_1} \\ in_L\sqrt{\varepsilon_0\mu_0}\cos\theta_1\sin\left(\left(\frac{2\pi}{\lambda_0}\right)n_L t\cos\theta_1\right) & \cos\left(\left(\frac{2\pi}{\lambda_0}\right)n_L t\cos\theta_1\right) \end{bmatrix} \quad (20)$$

Where θ_1 and θ_2 is the incident angle and transmission angle, respectively. The electric field of the optical input is defined by

$$E_{out} = M_T E_{in} \quad (21)$$

And the output intensity of the optical field is defined by

$$|E_{out}|^2 = |M_T E_{in}|^2 \quad (22)$$

Where E_{in} and E_{out} is the input optical field and output optical field, that enter and leave the model, respectively. For the mathematical model simulation, the values of all parameters are simulated as follows: the refractive index of waveguide n_L = 1.4778 (The material is PMMA)[8, 9] which the length of the Blade Bragg Grating L_B = 4.9001 μm. The Blade Bragg Grating consists of the periodic high-low refractive index, 13-19 multilayers. High refractive index (n_H) is 1.5277, and the low refractive index (n_L) is 1.4778; The incident angle is varied, from 10 - 30 degree; i.e., stain-sensor region. The wavelength of Blade Bragg Grating reflection is defined by the relationship, $\lambda_B = 2\Lambda n_{eff}$ where n_{eff} provides the effective index, and Λ is the period of the grating. The simulation results are plotted and shown in Fig. 3.

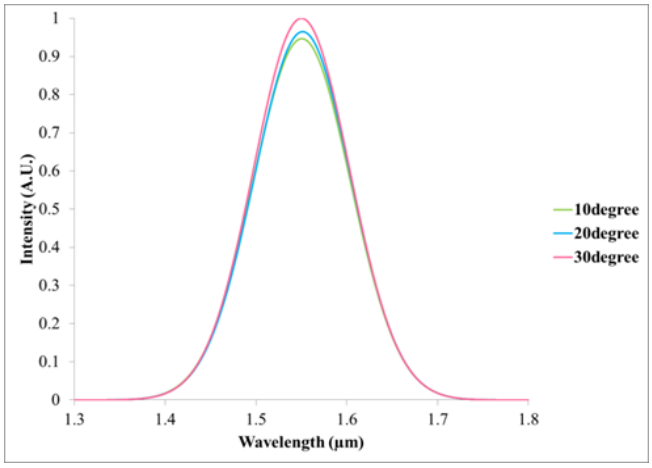

(a)

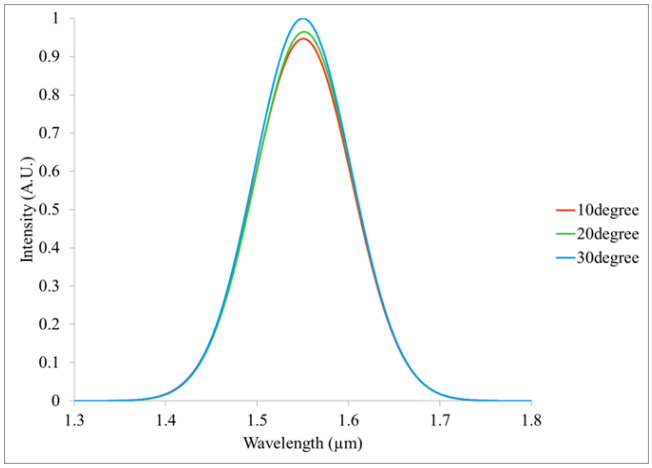

(b)

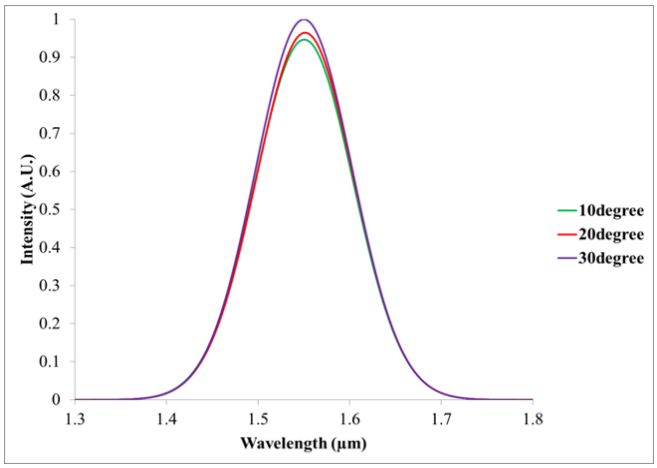

(c)

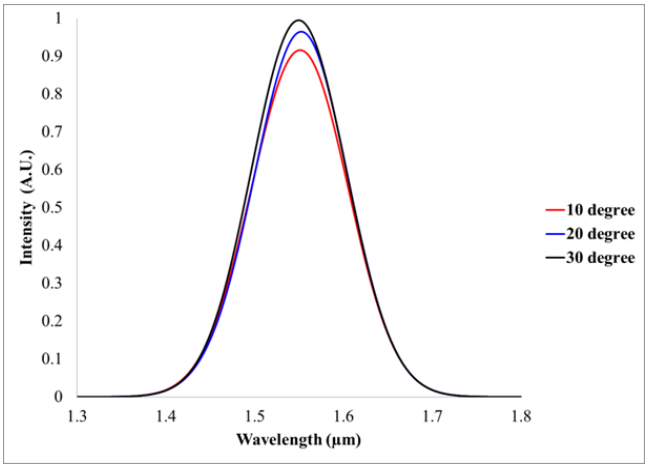

(d)

Fig.3 The relationship between intensity and wavelength of the optical output, which the inclined angle of the slab, i.e. an incident angle, is varied from 10-30 degree. And the slab layers are (a) 13 layers (b) 15 layers (c) 17 layers (d) 19 layers, respectably

3. Simulation and discussion

The simulation results of the mathematical model with periodic refractive index are obtained. Fig.3 shows the relationship between intensity and wavelength of an optical output where the grating layers is varied from 13-19 layers and the incline angle of the slab is also varied for 10-30 degree for each layer. From the results, it is shown that the center peak wavelength is shift when the angle is changed.

From the Fig. 4, the relationship between the inclined angles of the slab, i.e. an incident angle, and the center peak wavelength have shown. The simulation results show that it has linear relationship between the intensity and center peak wavelength, which is preferable for the sensing properties. The most linear mentioned relationship has been found in the 17 slab layers of Bragg Grating initiative design as show in the Fig. 5.

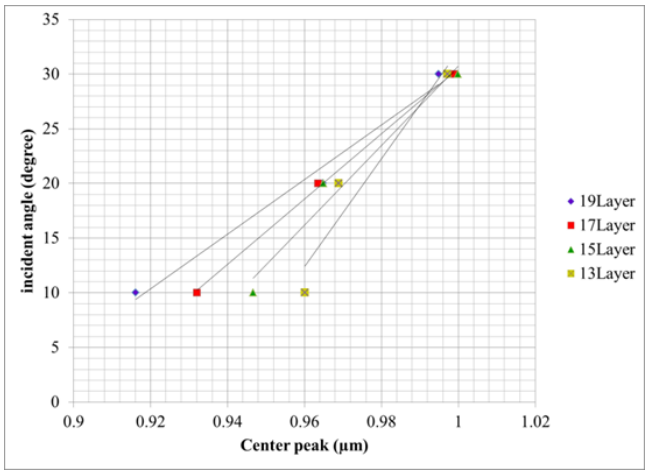

Fig.4. The relationship between the inclined angle of the slab, i.e. an incident angle, and the center peak wavelength.

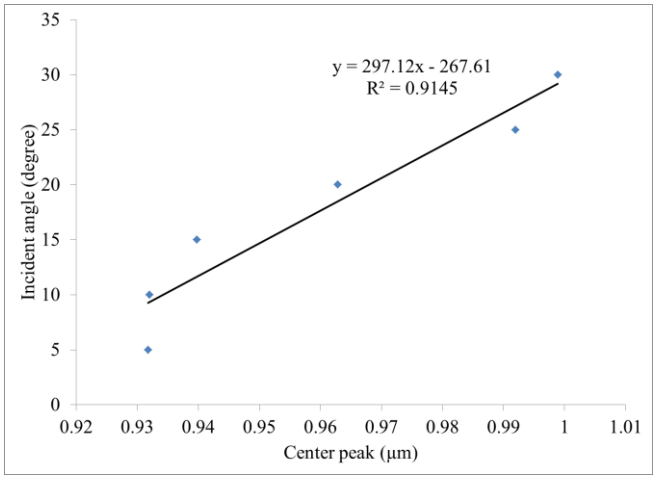

Fig.5 The relationship between the inclined angle of the slab, i.e. an incident angle, and the center peak wavelength, of the 17 slab layers.

4. Conclusions

In conclusion, the model of Blade Bragg Grating in PMMA waveguide and its application have proposed and analyzed. The mathematical model is then analyzed base on inclined angle at the interface considered region and the multilayer transfer matrix method. The simulation results have shown the relationship between the incident angle and the center peak wavelength for each parameter which varies with incident angle of the periodic layers, where the linear relationship is seen, the least square is R^2 = 0.9145, that it is preferable for good sensing applications. According to the property, our model can be applied for the stain sensor device in which the sample is deformed or bended in curve shape.

Acknowledgements

The authors are grateful to Faculty of Science, King Mongkut's Institute of Technology Ladkrabang for partially financial supporting.

References

[1] K.O. Hill, G. Meltz, Fiber Bragg Grating Technology Fundamentals and Overview, *Journal of Light wave Technology*, vol.15, pp. 1263-1276, 1997.

[2] S. Ugale, V. Mishra, Fiber Bragg Grating Modeling, Characterization and Optimization with different index profiles, *International Journal of Engineering Science and Technology*, vol.2(9), pp.4463-4468, 2010.

[3] K. Srinuanjan, W. Tipaphong, P.P. Yupapin, Photonic Waveguide Bragg Grating Ring Resonator for Bio-sensor Applications, *Science and Engineering* conference, pp.465-470, 2013.

[4] O.V. Butov, K.M. Golant, A.L. Tomashuk, M.J.N. van Stralen, A.H.E. Breuls, Refractive index dispersion of droped silica for fiber optics, *Optics Communications* ,vol.213, pp.301-308 , 2002.

[5] H.B. Liu, H.Y. Liu, G.D. Peng, P.L. Chu, Strain and temperature sensor using a combination of polymer and silica fibre Bragg gratings, *Optics Communications* , vol.219, pp.139-142, 2003.

[6] W. Du , X.M. Tao , H.Y. Tam , C.L. Choy , Fundamentals and applications of optical fiber Bragg grating sensors to textile structural composites , *Composite Structures* , vol.42, pp. 217-229, 1998.

[7] K. Tian, Y. Liu, Q. Wang, Temperature-independent fiber Bragg grating strain sensor using bimetal cantilever, *Optical Fiber Technology*, vol.11, pp.370-377, 2005.

[8] A.A. Bettiol , S.V. Rao , T.C. Sum , J.A. van Kan , F. Watt , Fabrication of optical waveguides using proton beam writing , *Journal of Crystal Growth*, vol.288, pp.209-212, 2006.

[9] M. Balakrishnan, E.J. Klein, M.B.J. Diemeer, A. Driessen , Fabrication of an electro-optic polymer microring resonator, *IEEE/LEOS Benelux chapter* Conference, pp.73-76, 2006.

Improved Analytical Model for Short-wire Metamaterials

Zahra Mostajabi, Jalil-Agha Rashed-Mohassel, Leila Yousefi*

Center of Excellence on Applied Electromagnetic Systems, School of ECE, College of Engineering, University of Tehran, Iran
*corresponding author: lyousefi@ut.ac.ir

Abstract

Short wire metamaterial is a kind of metamaterial, which has a very simple manufacturing process. In spite of regular metamaterials whose fabrication requires compressing and stacking of several printed circuit boards (PCBs), short-wire metamaterials can be fabricated using standard multi-layer PCB fabrication. These metamaterials have already been introduced and modeled; however, the reported analytical models have a big deviation from simulation and measurement results. Here; we propose an accurate analytical model for prediction of the resonant frequency of these metamaterials. The analytical model has been verified through comparison with previously reported measurement results.

1. Introduction

Metamaterials are in general artificial structures providing unusual electromagnetic properties not found in nature [1-12]. Metamaterials can be designed to provide high permittivity (ε) and/or high permeability (μ), or even negative values of ε and/or μ , creating an epsilon negative (ENG) or a mu negative (MNG) medium or even a double negative (DNG) medium. DNG metamaterials or so called left handed materials (LHMs) were first theoretically investigated by Veselago [1] and then experimentally demonstrated by the use of an array of split ring resonator (SRRs) and continuous wires[2,3].

Short wire or cut wire metamaterial structures are a branch of metamaterials [8, 9] which can provide MNG or even LHM. At Microwave frequencies this structure first introduced in 2006 by Zhou et al [11]. They consist of two short parallel plates, printed on both sides of a PCB (Fig. 1). The short wires are designed in such a way to play the role of a magnetic resonator to produce negative permeability. Adding metallic wires to this structure, yields negative permittivity simultaneously, thus a planner negative index metamaterial can be achieved [11]. Making negative index metamaterial with just short wire sets is investigated in [12], where a design schedule for bringing both electric and magnetic resonance close to each other is stated.

The most important advantage of this structure is its simple fabrication. In spite of most metamaterial structures, such as SRR where numerous PCB boards, each containing a unit cell, are stacked together to provide an effective medium [2-7], 3-dimemtional short wires can be fabricated easily by using standard multi-layer PCB fabrication. All short wires are made on two sides of one PCB board and in this way fabrication will be much easier, especially at higher frequencies [8, 9].

Some parametric studies of this structure such as the effect of number of layers, spaces between layers and the widths of short wires are also reported [13,14]. New methods to reduce the loss of this structure, especially at THz frequencies and in the optical regime have been also reported [15].

In this paper, a modified formula for the resonant frequency of cut-wire metamaterials is developed, and verified through comparison with measured results reported in [13]. The developed analytical model has much better accuracy than previously reported models [11, 12], and also incorporate the effect of all important geometrical properties of the metamaterial structure.

1. Proposed Analytical Model

To predict the resonant frequency of this structure, some simple equivalent circuit models are reported in [11,12], as the resonant frequency was approximated by $f_m = \frac{1}{2\pi\sqrt{LC}} = \frac{c_0}{\pi l\sqrt{\varepsilon_r}}$, where c_0 is the speed of light in vacuum and l is the length of short wires as shown in Fig. 1.

This formula states that the resonant frequency just depends on the length of short wires and the relative permittivity, but as shown in [13], both experimentally and numerically, the resonant frequency depends on the widths of short wires as well.

The resonant frequency of short wire sets can be easily calculated by accurately calculating the inductance and capacitance of their equivalent circuit model. Here we propose analytical formulas to accurately calculate capacitance, C and inductance, L. The advantage of this formula is its dependency on the structure parameters and simplicity while having good agreement with measured data.

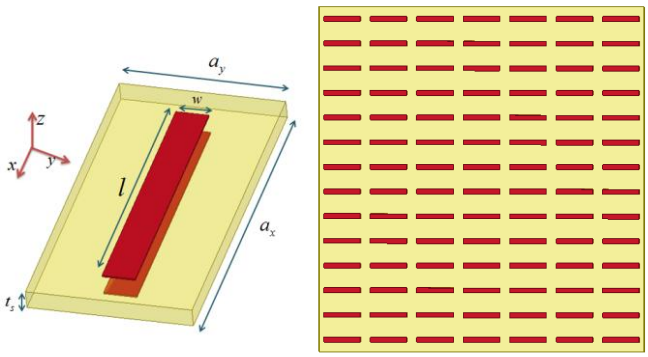

(a) (b)

Figure 1: (a) short wire unit cell, (b) periodic structure, all on one board (top view).

1.1. Inductance of the short wire sets

To develop an accurate formula for the effective inductance, here first we investigate the behavior of the metamaterial unit cell through numerical simulation using HFSS13. In this simulation, the dimensions of the unit cell are considered as follows: $a_x = 7mm$, $a_y = 3.5mm$, $l = 5.5mm$, $w = 1mm$, permittivity of the substrate as $\varepsilon_r = 4.8$, substrate thickness of $0.4mm$ and a copper thickness of $0.36\mu m$. These dimensions are chosen to be the same as the ones investigated in [13], in order to be able to compare the results of our resonant frequency with the measured data reported in [13].

In simulation, a unit cell with appropriate boundary conditions was used to imulate an infinite structure. Perfect electric boundary condition and perfect magnetic boundary conditions are used in the x, and y directions, respectively. Using two wave ports at the top and bottom of the cell, in conjunction of the mentioned boundary conditions provides a plane wave radiating orthogonally to the cell.

Figure 2 illustrates the results of this simulation. In this figure, the magnitude of the magnetic field along the width of the unit cell (in the y direction, for $x = 0$ and $z = 0$) is plotted. As shown in this figure, although the magnitude of $\vec{H}$ decreases as we go away from the middle of the short wire, the value is still considerable. It is well-known that at the resonant frequency, an enormous magnetic field is produced in the opposite direction of the incident $\vec{H}$ field. Therefore; the inductance of this structure can be calculated as a solenoid inductance, considering the periodic wires in the y direction. Using the solenoid formula, the inductance can be approximated as:

$$\vec{B} = \mu_0 \frac{NI}{Na_y} \hat{y} , \quad (1)$$

$$\varphi = \int \vec{B}.d\vec{s} = \vec{B}.\vec{s} = \mu_0 \frac{It_s l}{a_y} , \quad (2)$$

$$L_t = \frac{\psi}{I} = \frac{N\varphi}{I} = \mu_0 N \frac{t_s l}{a_y} , \quad (3)$$

Where L_t is the total inductance of a row of short wires in the y direction, the inductance of a cell (L) is calculated as:

$$L = \frac{L_t}{N} = \mu_0 \frac{t_s l}{a_y} , \quad (4)$$

The formula derived above also shows that as a_y increases, the inductance decreases, as we expect from physical properties of the unit cell. The formula reported in [11] for the inductance, is independent of a_y .

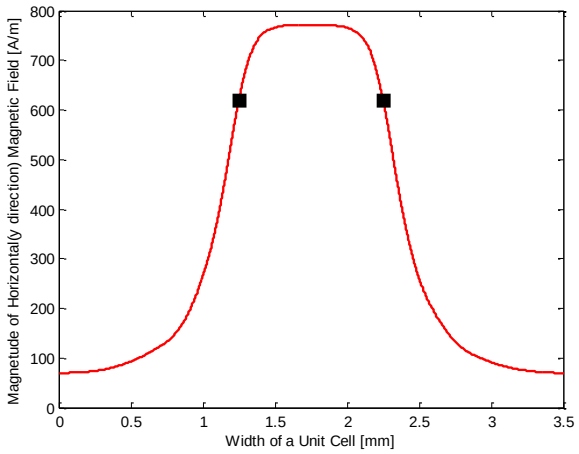

Figure 2: Numerical results for the magnetic field at $x = 0$, $z = 0$ versus the width of the cell.

1.2. Capacitance of short wire sets

The model used in [11] takes each short wire cell as two parallel plates in series with each other (each has a length of $l/2$),

$$C = \varepsilon_0 \varepsilon_r \frac{wl}{4t_s} , \quad (5)$$

Because the vertical electric field or $\vec{E}_z$ on short wires circulates (meaning that if at one end $\vec{E}_z$ is in the $\hat{z}$ direction, at the other end it is in the $-\hat{z}$ direction) as shown in [12], the short wires set of a cell can be taken as two series capacitors. To determine the accuracy of this formula, here we numerically calculate the vertical electric field. Figure 3 shows the magnitude of $\vec{E}_z$ on a line along a_x , exactly in the middle of the cell. ($y = 0$, $z = 0$)

Again, the simulation is done with HFSS13 and the geometrical parameters are the same as [13]. As can be seen, the magnitude of the induced electric field between short wires is enormous with the maximum value of the order of 10^5, and the minimum value exactly at the middle of a_x (Fig. 1). As can be observed in this figure, at the middle of the strips, very sharp derivative exists and the value of the field goes near zero. If we assume the values more than 10^4 as uniform and expect these parts as a parallel plate capacitance, and other places as earth, it is observed that just the distance between the square (which shows the beginning of the short wire strip) and dashed line (which has the values of 10^4) has lower values of field. In other words, $0.26mm$ of the $5.5mm$ short wires have a lower field. Also, fringing field exists, so if we want to take into account the effect of fringing fields, we should consider a longer effective length for the strip. The space between the short wires and beginning of the unit cell in the x direction is $0.75mm$, as shown on Fig. 3 with a square mark. For taking the effect of fringing field into account, a dashed line with a value of 10^4 is drawn. So the effective length of short wires can be estimated as $l_{eff} = 6mm$, just 0.09 of the strip length. Later we show that considering the effect of fringing field for this structure improves the accuracy of the predicted magnetic resonant frequency. In fact two simplifying assumptions offset each other. The middle part of the line has a very low electric field magnitude, therefore the length of each capacitance should be less than $l/2$. On the other hand, fringing field increases the effective length associated with the capacitance which is neglected in [11]. As the numerical simulation shows, considering fringing effect changes the length from $5.5mm$ to $6mm$ which seems to have a small effect.

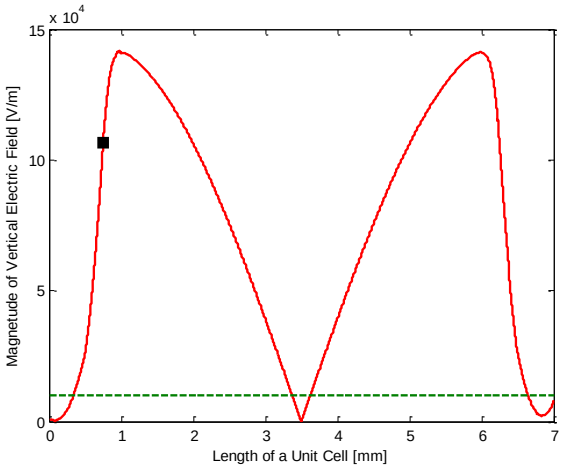

Figure 3: The magnitude of z-component of Electric field ($\vec{E}_z$) versus the length of the cell .

Therefore the magnetic resonance frequency, using C in [11] and L obtained here, can be written as:

$$f_m = \frac{1}{2\pi\sqrt{LC}} = \frac{c_0}{\pi l\sqrt{\varepsilon_r \frac{w}{a_y}}}, \qquad (6)$$

This formula shows the dependency of magnetic resonant frequency on both the width and the separation of cells in the y direction and shows that if $\frac{w}{a_y}$ is constant for a certain l, f_m is unchanged.

To verify the accuracy of our model, the resonant frequencies estimated by different methods are illustrated and compared in figure 5. In this figure, Squares are the experimental results reported in [13].
As shown in this figure, the formula suggested here has a good agreement with the measured data reported in [13], while the previously reported method has a big deviation from the measured data.

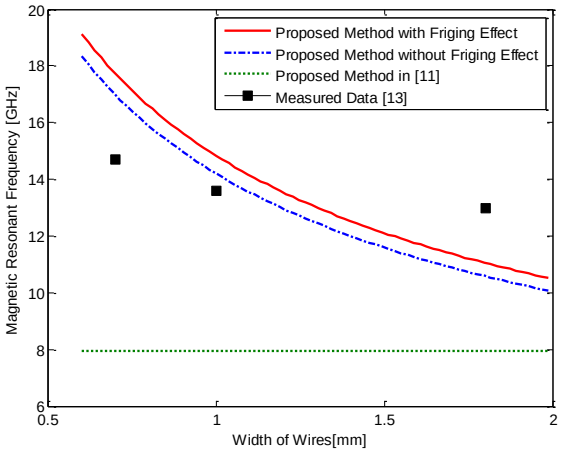

Figure 5: Composition of the magnetic resonant frequency predicted by different methods: Squares are the measured data from [13], dotted line is resonant frequency suggested in [11], solid line is the formula suggested here without fringing effect and blue dashed one is suggested formula with a fringing coefficient.

This figure shows that the formula suggested here is much more accurate than the formula in [11], which is determined with a dotted line. It should be noted that fringing coefficient is achieved by a numerical simulation for the case in which wires width is $1mm$, that's why it agrees very good with the measured data in that width (the difference between predicted and measured data in this width is only $0.6GHz$). Also as can be seen the accuracy of the formula decreases as the width of wires decreases. That's because we assumed to have uniform magnetic field along y direction. When the wires become very thin with respect to a_y, this assumption becomes weaker. On the other hand, as the width of wires increases, coupling

between adjacent cells increases. This time coupling decreases the accuracy of our formula.

As stated in figure 4 of [13], which compares simulation results with experimental ones, magnetic resonant frequency decreases as the width of short wires increases, which is clearly predicted by the formula developed here.

2. Conclusions

An analytical model was developed to calculate the magnetic resonance frequency of short-wire metamaterials. The model is more accurate than previously reported models, and encounters all the geometrical parameters of the metamaterial unit cell. The analytical results were compared to previously reported experimental data, and good agreement is observed.

References

[1] V . G. Veselago Veselago, "The electrodynamics of substances with simultaneously negative values of ε and μ," Sov. Phys. Uspekhi , vol. 10, no. 4, pp. 509 – 514, 1968.

[2] J. B. Pendry, A. J. Holden, D. J. Robbins, and W. J. Stewart, "Magnetism from conductors and enhanced nonlinear phenomena," *IEEE Trans. Micr. Theory. Tech.*, vol. 47, no. 11, pp. 2075–1084, Nov. 1999.

[3] D. R. Smith, W. J. Padilla, D. C. Vier, S. C. Nemat-Nasser, and S. Schultz, "Composite medium with simultaneously negative permeability and permittivity," *Phys. Rev. Lett.*, vol. 84, no. 18, pp. 4184–4187, May 2000.

[4] L. Yousefi, and O. M. Ramahi, "Artificial Magnetic Materials Using Fractal Hilbert Curves ", IEEE Transactions on Antennas and Propagation, vol. 58, no. 8, pp. 2614 - 2622, Auguest 2010.

[5] A. Kabiri, L. Yousefi, and O. M. Ramahi, "On the fundamental limitations of artificial magnetic materials", IEEE Transactions on Antennas and Propagation, vol. 58, no. 7, pp. 2345-2353, July 2010.

[6] M. M. Bait-Suwailam, L. Yousefi, B. Alavikia, and O. M. Ramahi, "Analytical Models for Predicting the Effective Permittivity of Complementary Metamaterial Structures", Microwave and Optical Technology Letters, Vol. 55, No. 7, July 2013.

[7] L. Yousefi, M. S. Boybay, and O. M. Ramahi, "Characterization of Metamaterials using a Strip Line Fixture", IEEE Transactions on Antennas and Propagation, vol. 59, no. 4, pp. 1245-1253, April 2011.

[8] A. N. Lagarkov, and A. K. Sarychev, "Electromagnetic properties of composites containing elongated conducting inclusions," *Physical Review B* 53, no. 10, 6318, 1996.

[9] *L. V.* Panina, A. N. *Grigorenko, D. P. Makhnovskiy*, "Optomagnetic composite medium with conducting nanoelements," *Phys.Rev.B 66, 155411*,2002.

[10] G. Dolling, C. Enkrich, M. Wegener, J. F. Zhou, C. M. Soukoulis, and S. Linden, "Cut-wire pairs and plate pairs as magnetic atoms for optical metamaterials," *Optics letters* 30, no. 23, pp. 3198-3200, 2005.

[11] J.Zhou, L. Zhang, G. Tuttle, T. Koschny, and C. M. Soukoulis, "Negative index materials using simple short wire pairs," *Physical Review B, 73*(4), 041101,2006.

[12] Z. Jiangfeng, E. N. Economon, T. Koschny, and C. M. Soukoulis, "Unifying approach to left-handed material design," *Optics letters* 31, no. 24, pp. 3620-3622, 2006.

[13] V. D. Lam, J. B. Kim, S. J. Lee, Y. P. Lee, and J. Y. Rhee, "Dependence of the magnetic-resonance frequency on the cut-wire width of cut-wire pair medium," *Optics Express* 15, no. 25 pp. 16651-16656, 2007.

[14] V. D. Lam , J. B. Kim, N. T. Tung, S. J. Lee, Y. P. Lee, and J. Y. Rhee, "Dependence of the distance between cut-wire-pair layers on resonance frequencies," *Optics express* 16, no. 8 pp. 5934-5941, 2008.

[15] J. Zhou, T. Koschny, and C. M. Soukoulis, "An efficient way to reduce losses of left-handed metamaterials," *arXiv preprint arXiv,0807.2302*, Jul 2008.

Electromagnetic Field and Dispersion Characteristic Analysis of Absorbing Onion-Like Carbon Tube Waveguides

Liudmila Nickelson[1,2], Arturas Bubnelis[1,2], Romanas Martavicius[1], Steponas Asmontas[2]

[1] Faculty of Electronics, Vilnius Gediminas Technical University, Naugarduko str. 41, Lithuania
[2] Center for Physical Sciences and Technology, Gostauto 11, LT- 01108, Vilnius, Lithuania
*corresponding author, E-mail: lucynickelson@gmail.com

Abstract

Here we present our calculation results of the electromagnetic (EM) field distributions and the dispersion characteristics of open cylindrical tube waveguides. The analyzed waveguides are made of the onion like carbon (OLC) material. The solution of the boundary problem was fulfilled by the partial area method [1]. We have determined the complex roots of the dispersion equation by using of the Muller method. It was discovered the very complicated dependencies of the phase and attenuation constants on the waveguide radii. Such dependencies arise because the OLC material is the highly dispersive and absorbing one. We have investigated the high-frequency cutoff frequency of the propagating hybrid modes HE_{11} and HE_{12} dependent on the tube waveguide external and internal radii. We found that it is possible to reach the one-mode regime of OLC tube waveguide.

1. Introduction

There are many experimental investigations of the modern OLC materials and the innovative appliances on their basis in the ultra-wide frequency range from tens of hertz till THz and extending into the infrared range. The intensive research of the material synthesis and industrial applications continues over the past two decades.

The OLC material is predicted to have properties different from other carbon nanostructures as graphite or nanotubes due to their highly symmetric structure. The material consists of spherical closed carbon shells which have concentric layered topology alike that of an onion. OLC materials can depict as shell fullerenes with certain important electro-physical behaviors as a very small weight, a higher specific surface area and adhesion properties, thermal stability [2–4]. The material can have the higher conductivity and capacitive performances, also possess the high EM shielding properties. OLC materials can be used as the radar absorbing material, as components of magnetic recording systems, magnetic fluid. The material also is using in the applications as fuel cells, optical limiting devices [3–6]. There are broad prospects for developing a variety of devices on the base of OLC materials [7-10].

Here we present the numerical investigations of a cylindrical tube (hollow) waveguides with different external and internal radii of tube made of the OLC material. Our homemade computer code lets us to investigate a full spectrum of the waveguide modes, i.e. the fundamental (main) and higher modes. We have been calculated the EM field components of the propagating hybrid waveguide modes. Here we presented the distributions of the electric and magnetic fields in two cross-sections of the waveguide. The complex permittivity $\varepsilon = \varepsilon' + \mathrm{i}\,\varepsilon''$ of the OLC material was taken from the experimental results [7].

2. Electric and magnetic field analysis

We present here the electric and magnetic field distributions and the dispersion characteristics of the hybrid modes of the tube waveguides. The considered waveguides are the open (without any metallic screens) waveguides. In our calculations the external waveguide radii R are equal to 2.5 mm and 5 mm. The internal waveguide radii r can take different values dependent on the external radius R. The OLC material permittivity is matched to the frequency range 26–38 GHz as in [7]. For this reason we have calculated the waveguide dispersion characteristics in this frequency range. We calculated the six components of EM field at the middle frequency of the given range, i.e. 32 GHz.

Here we present the EM field distributions only for the fundamental mode HE_{11} of OLC tube waveguide. Because the fundamental mode is only propagating at f = 32 GHz.

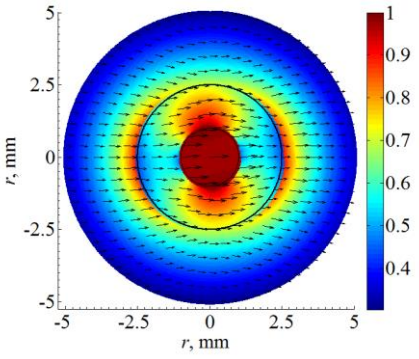

(a)

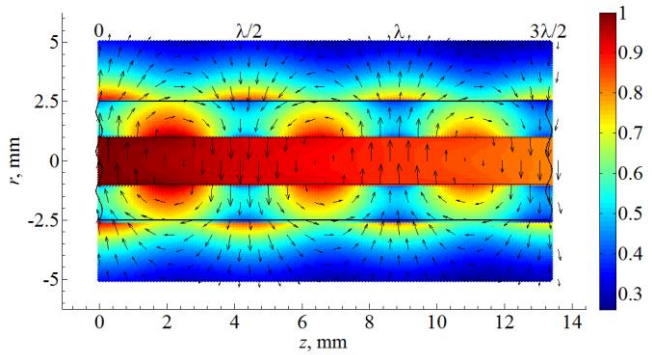

(b)

Figure 1. Distribution of electric vector fields and intensity of the fundamental mode in the transversal (a) and longitudinal (b) cross-sections of OLC tube waveguide at the frequency f = 32 GHz when R = 2.5 mm and r = 1 mm.

The electric field (Figs. 1 and 3) and the magnetic field (Figs. 2 and 4) distributions outside and inside of the OLC waveguide, including an air space (channel) in the waveguide center are shown in these figures.

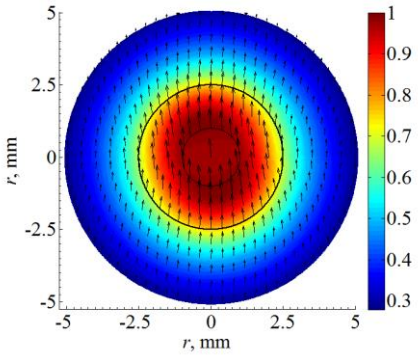

(a)

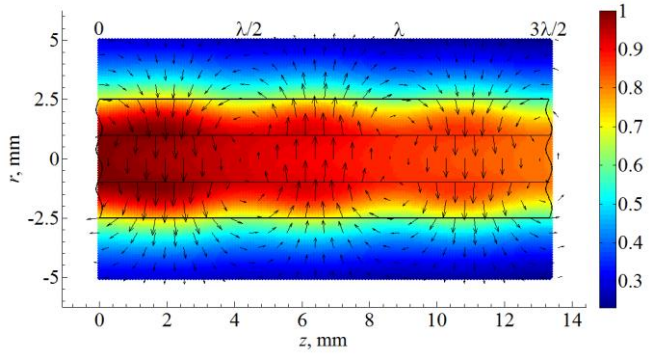

(b)

Figure 2. Distribution of magnetic vector fields and intensity of the fundamental mode in the transversal (a) and longitudinal (b) cross-sections of OLC tube waveguide at the frequency f = 32 GHz when R = 2.5 mm and r = 1 mm.

In Figs 1–4 the external radii of waveguides were R = 2.5 mm and 5 mm and the internal radius was chosen by the requirement that the ratio R / r would be equal to 2.5.

Since the electric and magnetic fields are vector quantities, we have represented here the EM fields by the vector arrows. The electric field strength (intensity) and magnetic one are represented by the field lines in Figs. 1–4. The EM field visualizations are given by the collection of arrows with a given magnitude and direction at every chosen point in the plane. We have defined the field vectors in 20000 points of the transversal (Figs. 1(a)–4(a)) and in 30000 points of the longitudinal (Figs. 1(b)–4(b)) waveguide cross-sections. For greater visibility here are also presented the electric and magnetic field densities by colors. The normalized intensity of the EM field is shown in the scale that is placed on the right side of the distributions. The red color is the maximum intensity and the blue one is the minimum intensity of the electric (Figs. 1, 3) or magnetic (Figs. 2, 4) fields.

In figures 1 and 2 are depicted the electric and magnetic field structures inside and outside of the tube waveguide when the external radius R is equal to 2.5 mm and the internal radius r is equal to 1 mm (Figs. 1 and 2). It is shown the similar field structures at the waveguide radii R = 5 mm and r = 1 mm in figures 3 and 4. The fundamental mode can only propagate at the operating frequency f = 32 GHz.

We can see the common properties all four pictures (Figs. 1–4) of the EM field distribution by analyzing the ones. The EM field outside of the waveguide rapidly fades out (the blue color outside of the waveguides and the small magnitude of vector arrows). The longitudinal distributions of the electric and magnetic fields point how fast the EM field energy is attenuated along of the waveguide. We can see the significant attenuation of EM wave energy in the direction of propagation of the wave. The Pointing vector is directed along the positive axis z.

The electrical lines are perpendicular to the magnetic lines in the every point of waveguide cross-section. As the distributions of EM fields are fulfilled at f = 32 GHz, then the wavelength of EM wave in free space is λ_0 = 9.375 mm at this frequency. The longitudinal distribution of EM field let us define that the wavelength of wave in the OLC tube waveguide λ_{OLC}. We see that λ_{OLC} changes dependent on the radii R and r. The wavelength λ_{OLC} is 8.876 mm at R = 2.5 mm and r = 1 mm (the thickness of tube wall is $t = R - r$ = 1.5 mm) and λ_{OLC} is 7.667 mm at R = 5 mm and r = 2 mm (t = 3 mm). It means that the EM field energy is more concentrated in the OLC material when the thickness of the tube wall is larger. The larger the thickness of tube wall, the shorter the wavelength in OLC waveguide (see, Figs. 1(a) and 3 (a)).

We can see that the EM field is concentrated inside the OLC waveguide in the area of the first interface air-OLC that is close to the center. The strongest EM field is into the air channel of the tube waveguide. The EM field on the second (outer) waveguide interface is weaker in the comparison with interface that was mentioned before. The analysis of the electric field distribution in the waveguide transversal cross-section (Figs. 1(a) and 3(a)) shows that there is only the one field variation on the angular and radial coordinates. The fundamental hybrid HE_{11} mode can propagate on the analyzed waveguides at f = 32 GHz.

The comparison of Fig. 1 and Fig. 3 shows that the distribution of the electric fields is different. The field is stronger concentrated in the central air channel in the waveguide with R = 2.5 mm. The electric field concentrates in the OLC wall area of the tube waveguide with R = 5 mm. The electric field location is weaker into central air channel in the last waveguide.

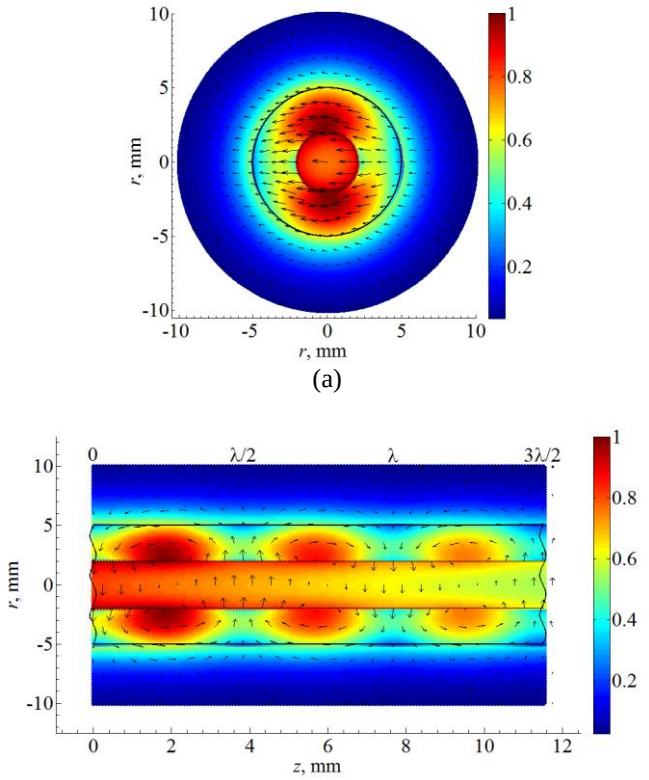

(a)

(b)

Figure 3. Distribution of electric vector fields and intensity of the fundamental mode in the transversal (a) and longitudinal (b) cross-sections of OLC tube waveguide at the frequency f = 32 GHz when R = 5 mm and r = 2 mm.

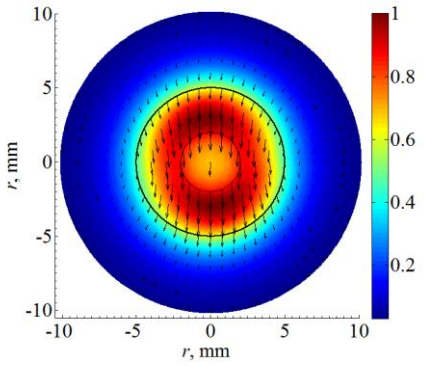

(a)

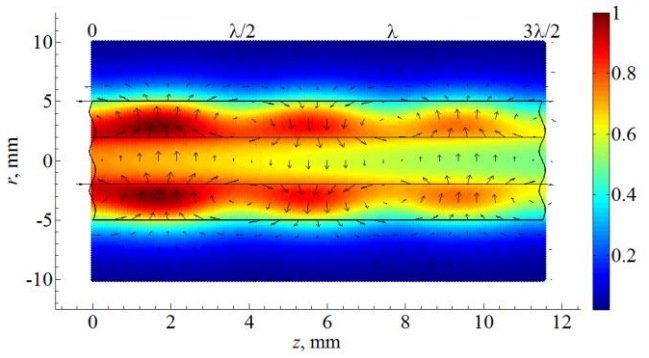

(b)

Figure 4. Distribution of magnetic vector fields and intensity of the fundamental mode in the transversal (a) and longitudinal (b) cross-sections of OLC tube waveguide at the frequency f = 32 GHz when R = 5 mm and r = 2 mm.

We can clearly see that the field outside the waveguide fades quickly in the waveguide with R = 5 mm (Figs. 1(a) and 3(a)). The comparison of the longitudinal field distributions (Figs. 1(b) and 3(b)) shows that attenuation of the propagating hybrid mode HE_{11} is larger when the thickness of the tube wall is bigger.

3. Phase and attenuation constant analysis

We have investigated the complex longitudinal propagation constant $h = h'-ih''$ of OLC tube waveguides with the external radii 2.5 mm (Fig. 5) and 5 mm (Fig. 6). The calculations were fulfilled in the frequency range 26–38 GHz according to [7]. In Figs. 5(a) and 6(a) are presented the phase constant $h' = 2\pi/\lambda_{OLC}$, where λ_{OLC} is the wavelength of the tube waveguide. In Figs. 5(b) and 6(b) are given the attenuation constant (the losses) h''.

We see that only the fundamental mode can propagate in the waveguide with R = 2.5 mm (Fig. 5). Our calculations were made at the internal radii r equal to 0.5, 1.0, 1.5 mm. We can observe the high-frequency cutoff $f_{cut\text{-}h}$ of the mode in the Fig. 4. The cutoff frequency of the mode $f_{cut\text{-}h}$ is equal to 35.73 GHz, 35.58 GHz, 34.96 GHz when the internal radii r are 0.5, 1.0, 1.5 mm, respectively.

We would like to draw your attention to the fact that we cannot observe the low-frequency cutoff $f_{cut\text{-}l}$ at the chosen frequency range and sizes R, r of the tube waveguide.

We see that the values of h', h'' and $f_{cut\text{-}h}$ have bigger values when the thickness of tube wall t=R-r is larger. The losses of the tube waveguide heavily decrease with reducing of wall thickness.

The value λ_{OLC} becomes larger and losses become smaller with growing of the operating frequency. It is possible to explain by the growing amount of the propagating EM wave energy in the area of the central air channel. We can watch the same effect when the radius of the air channel is increasing.

In Fig. 6 is presented dispersion characteristics of the waveguide with R = 5 mm. The internal radii of this waveguide are 1, 2 and 3 mm. Here we see curves h', h'' of the fundamental mode HE_{11} at three internal radii r

(presented at the top of Fig. 6(a)) and two curves of the first higher mode HE_{12} at the radii r = 1 mm and 2 mm. The high-frequency cutoff $f_{cut\text{-}h}$ of the fundamental mode is larger in the comparison with the cutoff $f_{cut\text{-}h}$ of the first higher mode. The fundamental mode cutoff $f_{cut\text{-}h}$ are equal to 37.04 GHz, 36.92 GHz and 36.57 GHz at the internal radii are equal to 1, 2 and 3 mm, respectively.

The first higher mode cutoff $f_{cut\text{-}h}$ are equal to 27.41 GHz and 26.59 GHz at the internal radii are equal to 1 mm and 2 mm. The high-frequency cutoff $f_{cut\text{-}h}$ of the fundamental mode is larger than the first higher mode one. Of course the fundamental mode has the low-frequency cutoff $f_{cut\text{-}l}$ lower than the higher modes. The low-frequency cutoff $f_{cut\text{-}l}$ of modes is at the lower frequency than 26 GHz and is outside of the considered frequency range.

The losses of the hybrid HE_{11} and HE_{12} modes are approximately commensurate. The EM field distributions of the first higher mode are more complicated.

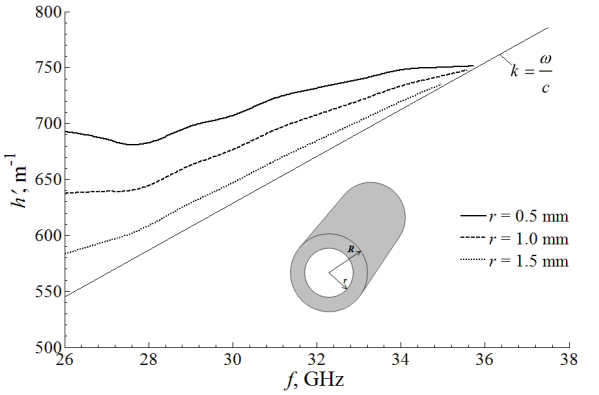

(a)

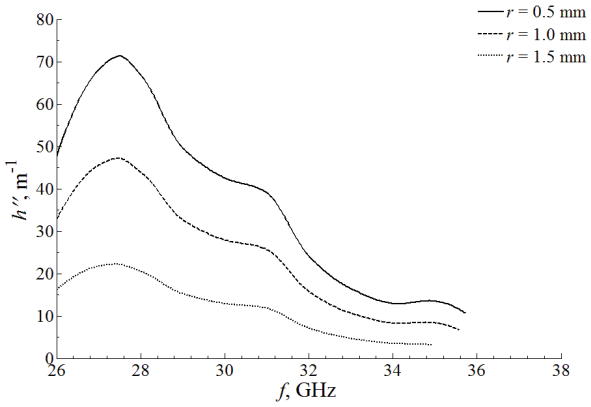

(b)

Figure 5. Dependences of the OLC tube waveguide propagation constant h' and attenuation constant h'' on the frequency at the external radius R = 2.5 mm and three internal radii r.

On the base of the phase constant dependency (Fig. 6 (a)) we can come to the conclusion that the large part of EM field energy of HE_{12} mode propagates in the air space comparing with the fundamental one. We have also examined the EM field distribution of the first mode. We can see more variations on the radial coordinate in first higher mode distributions. It is interesting to note that the EM field of HE_{12} mode concentrates on the outer interface of waveguide and the field is relatively weak into the air channel. The EM field of the HE_{12} mode outside the OLC waveguide fades slowly in the comparison with the fundamental HE_{11} mode.

There is a one-mode regime in the waveguide when the internal radius is equal to r = 3 mm, i.e. here propagates only the fundamental mode (Fig. 5(a) and Fig. 6(a)) in the considered frequency range. The phase constant of the tube waveguide with r = 3 mm is approximately ~750 m^{-1} and this value varies insignificantly in the considered frequencies (Fig. 6a).

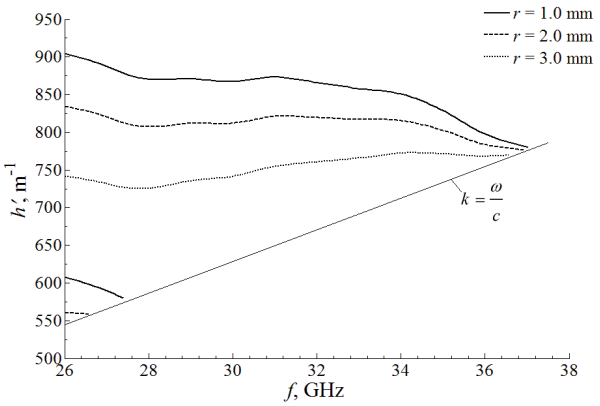

(a)

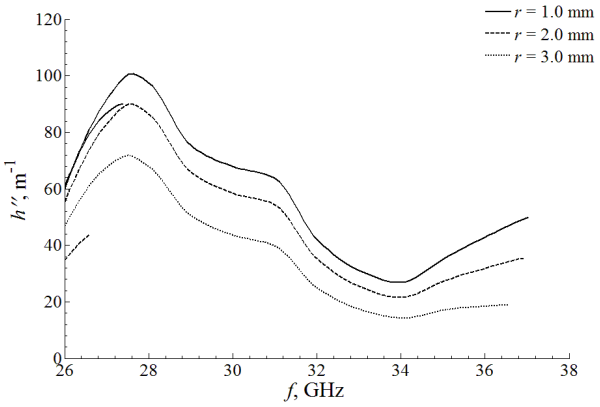

(b)

Figure 6. Dependences of the OLC tube waveguide propagation constant h' and attenuation constant h'' on the frequency at the external radius R = 5 mm and three internal radii r.

The behavior of the dispersion characteristics (Figs. 5(a), 6(a)) is unusual in the comparison with the open lossless dielectric waveguide. The fundamental mode attenuation constant has extreme at certain frequencies. Maximum values are observed at frequency 27.5 GHz and the minimum values at ~34 GHz.

The attenuation constant h'' extreme value as well as the whole behavior of the curve are very much depended and strong connected with the magnitude of the imaginary part value of the OLC material permittivity ε''.

The waveguide attenuation constant is high enough (Figs. 5(b), 6(b)). For this reason the tube waveguides can be used

for microwave absorber applications with the air channel inside of waveguide that can be useful in different technical solutions.

Table 1: Attenuation constant values of the tube waveguide at two frequencies.

R, mm	*r*, mm	Attenuation, dB/mm	
		27.5 GHz	34.0 GHz
2.5	0.5	0.619	0.112
	1.0	0.409	0.071
	1.5	0.192	0.030
5.0	1.0	0.873	0.232
	2.0	0.782	0.187
	3.0	0.624	0.124

In the table 1 are given the attenuation of the OLC waveguides with three internal radii r at $f = 27.5$ GHz and 34 GHz. The larger wall thickness t is the greater the losses of the OLC waveguides are. The attenuation is reduced with increasing of the frequency. The last dependency is possible to explain by the concentrating of EM wave energy into the central air channel.

The values of the propagation constant h' and the attenuation constant h'' (Figs. 5 and 6) are not normalized as it is usually done for many dielectric waveguides. The dispersion characteristic of OLC tube waveguide is more complicated.

The propagation constant is not directly proportional to the waveguide radius. It is happened due to the fact that the calculations are evaluated losses in the OLC material that can be large at some frequencies.

4. Conclusions

Here was analyzed the tube waveguides made of the highly dispersive and absorbing onion like carbon material. The boundary problem was solved electrodynamically rigorously. The homemade codes are used here for analyzing of the EM fields and the dispersion characteristics.

We have investigated two waveguides with the external radius 2.5 mm and 5 mm at the several radii of the central air channel.

The visualization of the electric and magnetic field distributions of the fundamental hybrid HE_{11} mode by two methods of images is clearly shown the locations of EM field energy in the waveguide transversal and longitudinal cross-sections.

We have investigated the high-frequency cutoff $f_{cut\text{-}h}$ dependencies of hybrid modes HE_{11} and HE_{12} on the waveguide radii. These dependencies can be used for a development of a microwave switch.

We have discovered that the maximum of losses of the fundamental mode are approximately at the same value of the operating frequency for all investigated waveguides. The waveguide propagation constant is not directly proportional to the waveguide radius because the onion like carbon material is the highly dispersive and absorbing one.

References

[1] L. Nickelson, Asmontas S., Gric T., Bucinskas J., Bubnelis A., *Electrodynamical Analysis of Open Lossy Metamaterial Waveguide and Scattering Structures*, pp. 27-58, METAMATERIAL, Ed. by X.-Y. Jiang, ISBN 978-953-51-0591-6, InTech, 620 p., 2012.

[2] G. Wu, M. Nelson, S. Ma, H. Meng, G. Cui, P. K. Shen, Synthesis of nitrogen-doped onion-like carbon and its use in carbon-based CoFe binary non-precious-metal catalysts for oxygen –reduction. *Carbon. ELSEVIER* 49: 3972-3982, 2011.

[3] S. N. Bokova-Sirosh, A. V. Pershina, V. L. Kuznetsov & et al. Roman spectra for characterization of onion-like carbon. *Nanoelectronics and Optoelectronics*, 8: 106–109, 2013.

[4] Y. Wang, T. Li, L. Zhao & et al. Research progress on nanostructured radar absorbing material. *Energy and Power Engineering*, 3: 580–584, 2011.

[5] J. Macutkevic, D. Seliuta, G. Valušis & et al. High dielectric permittivity of percolative based on onion-like carbon. *Applied Physics Letters* 95: 112901(1–3), 2009.

[6] R. Langlet, Ph. Lambin, A. Mayer & et al. Dipole polarizability of onion-like and electromagnetic properties of composites. *Nanotechnology* 19: No11, 115706(1–8), 2008.

[7] P. Kuzhir, S. Maksimenko, D. Bychanok & et al. Nano-scaled onion like carbon: prospective material for microwave coatings. *Metamaterials* 3: Issue 3–4: 148–156, 2009.

[8] D. S. Bychanok, S.I. Moseenkov, V. L. Kuznecov & et al. Onion-like carbon in microwaves: electromagnetic absorption bands and percolation effect. *J. Nanoelectronics and Optoelectronics* 4: 257–260, 2009.

[9] Y. Wang, F. Yan, S.W. Liu, A.Y. Sheng T. H. Song, X. W. Sun, H.Y. Yang, Onion-like carbon matrix supported Co_3O_4 nanocomposites: a highly reversible anode material for lithium ion batteries with excellent cycling stability, *J. of Material Chemistry A* 1: Issue 17, 5212–5216, 2013.

[10] P. Ganesh, P.R. C. Kent, V. Mochalin, Formation, characterization, and dynamics of onion-like carbon structures for electrical energy storage from nanodiamonds using reactive force fields, *J. Appl. Phys*. 110: 073506, 2011.

[11] P. Kuzhir, A. G. Paddubskaya, S. A. Maksimenko & et al. Carbon onion composites for EMC applications. *IEEE Trans. on Electromagnetic Compatibility*, 54: Issue 1, 6–16, 2012.

Investigation of surface roughness influence on hyperbolic metamaterial performance

Serge Kozik[1*], Mohammed A Binhussain[2], Andrei Smirnov[1], Nikolai Khilo[1], Vladimir Agabekov[3]

[1]B.I.Stepanov Institute of Physics, National Academy of Sciences of Belarus, Minsk, Belarus
[2]The National Center for Building System KACST, Riyadh, Saudi Arabia
[3]Institute of Chemistry of New Materials NASB, Minsk, Belarus
*corresponding author, E-mail: s.kozik@dragon.bas-net.by

Abstract

Light scattering on rough surface with nano-sized features needs simulation with rigorous electromagnetic solver. The performance of such grid method as FDTD is closely connected with mesh size of computational domain and curvilinear surface approximation. The main goal of this work was to introduce simple model of surface roughness which does not involve objects with complicated shapes and could help to reduce computational costs. We described and proved numerically that the influence of surface roughness at the interfaces in metal-dielectric composite materials could be described by proper selection of refractive index of dielectric layers. Our calculations show that this model works for roughness with RMS value about 1 nm and below. Some examples of roughness realization with narrow spatial spectrum and high LER value could not be described properly by simple dielectric index modification, thus forming the limits of this simple roughness model applicability.

1. Introduction

The necessary stage for every metamaterial engineering process is numerical simulation which predicts reflection, transmission spectra, effective refractive index and other measurable parameters depending on its structural design. Since plasmon resonances are highly sensitive to shape of structures and presence of closely situated objects it is very important to include imperfection of real structures in simulation model for better agreement with experimental performance of the samples [1]. Hyperbolic metamaterial behavior could be described by effective medium theory based on permittivity averaging. However, light scattering on rough surface with nano-sized features should be simulated with rigorous electromagnetic solver. We used finite-difference time-domain method (FDTD) with code written by the authors [2].

Modeling of surface roughness is closely connected with mesh size of computational domain and curvilinear surface approximation in FDTD. It is known that "staircace" approximation of complex shaped objects in rectangular grid is the most sufficient error source in FDTD calculation of dispersion materials. When dielectric materials are considered, there is effective technique of improving grid resolution by averaging of material parameters over a unit grid cell [3]. Some works show that smoothing is possible for plasmonic problems with flat interfaces [4], for 2D problems [5] and for the case of simple Drude model of permittivity dispersion [6]. Size of grid step should be small enough to satisfy fast spatial field decay near metallic surface when localized plasmon resonance occurs, especially at the sharp corners. This leads to grid steps of about 0.001 of wavelength and causes great demands in memory and time consumption. The main goal of this work is to introduce simple model of surface roughness in FDTD which does not involve objects with complicated shapes and helps to reduce computational costs.

2. Introducing of Surface Roughness in FDTD

Two-dimensional spatial Fourier spectrum is a versatile approach for rough surfaces description because it is capable of precise transfer of experimentally measured roughness of given materials to the simulation program. Let define components of Fourier spectrum as $C_{k,p}$:

$$C_{k,p} = \sum_{j=0}^{J-1}\sum_{m=0}^{M-1} x_{j,m} e^{2\pi i(jk/J+pm/M)}, \qquad (1)$$

where J, M are lengths of an array in two dimensions; $x_{j,m}$ is array of deviation of surface position from ideal contour. User definition of roughness spatial spectrum is also available, one can specify spectrum contour as superposition of Gauss-shape functions:

$$\left|C_{k,p}\right| = \frac{1}{2\pi\delta_k\delta_p}\exp\left(-\frac{(k-\omega_k)^2}{2\delta_k^2}-\frac{(p-\omega_p)^2}{2\delta_p^2}\right), \qquad (2)$$

where δ_k, δ_p are standard deviation, defining spectrum width for two dimensional face of a figure; ω_k, ω_p are main spatial modes. Phase of spectrum components is chosen as random number:

$$C_{k,p} = \left|C_{k,p}\right| \cdot \exp(2\pi i\varphi_k\varphi_p), \qquad (3)$$

where φ_k, φ_p are random values with uniform distribution in a range from 0 to 1. Maximum value of $C_{k,p}$ spectrum defines root mean square (RMS) of surface deviation, often

referred to as line edge roughness (LER), which could be obtained by experimental measurements as follows:

$$\sigma_j = \sqrt{\frac{\sum_m x_{j,m}^2}{M}}. \qquad (4)$$

Arbitrary shaped object in our program could be defined as a set of primitive figures: parallelepipeds, spheres, cylinders, hollow cylinders, spherical sectors, truncated pyramids. The surface of geometrical primitive is divided in several faces, each face can have its own roughness parameters, which consist of value of LER and components of two-dimensional complex spatial spectrum.

Several types of rough surfaces with different spatial spectrum are considered in simulation below. Examples of surface realization are showed in Fig. 1. Surface roughness is introduces at the top and bottom surface ((x,y) plane) of Ag layer, covered by TiO_2 layers from both sides. Here spatial spectrum is assumed to be symmetrical with $\sigma=\sigma_x=\sigma_y$, $\delta=\delta_x=\delta_y$, $\omega=\omega_x=\omega_y$. The boundary conditions of FDTD in x- and y-directions are periodic, and in z-direction perfectly absorbing boundary condition (convolutional perfectly matched layer, C-PML) is placed.

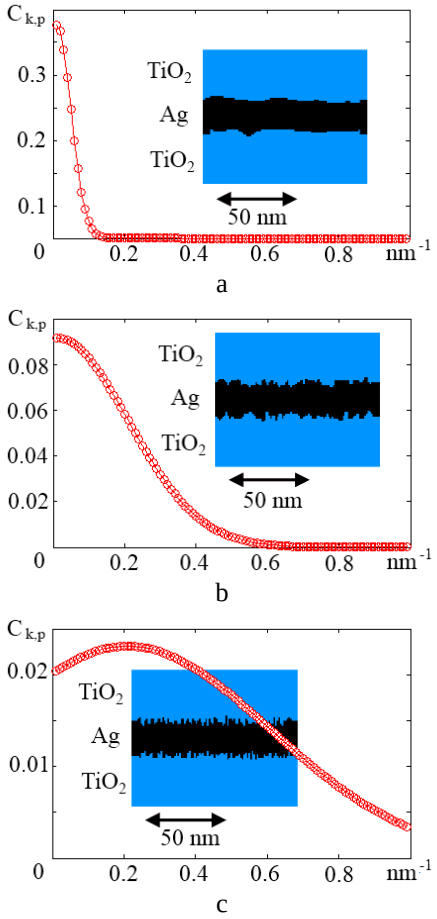

Figure 1: Examples surface profile realizations for different parameters of surface roughness of Ag layer, σ=1 nm, δ=0.04 nm^{-1}, ω=0.0 nm^{-1} (a); σ=1 nm, δ=0.2 nm^{-1}, ω=0.0 nm^{-1} (b); σ=1 nm, δ=0.4 nm^{-1}, ω=0.2 nm^{-1} (c)

3. Method of obtaining of effective parameters for roughness model

Frequently used model of surface roughness considers replacement of roughness by intermediate layers with thickness depending on value of LER and refractive index averaged over indices of neighboring layers. This model comes from ellipsometry [7]. We failed to employ this approach for our test structures, since it did not provide reflection and transmission coefficients coincided with FDTD simulated results for rough surfaces. Possibly, it is not suitable for layers with thickness of about 30 nm. As a result of our investigation we concluded that the proper model of surface roughness is to modify refractive index of dielectric layers in metal-dielectric stratified medium. Appropriate index values could be found by inverse problem solving. FDTD simulation of reflection and transmission coefficients of the structure with surface roughness gives results of direct problem solving. Modified values of dielectric layers refractive index pass to transfer matrix method which gives reflectance and transmittance that are compared to coefficients simulated with FDTD. Thus, values of refractive index of dielectric layers are found by minimizing target function:

$$f(a,b) = |r-a| + |t-b|, \qquad (5)$$

where a, b are reflection and transmission coefficients calculated by transfer matrix method for multi-layered structure; r, t are reflection and transmission coefficients calculated by FDTD for definite profile of the structure with rough surface. Conjugate gradient method for nonlinear equations was used for minimizing of function (5).

4. Test structures description

Parameters of test structures were chosen according to design of flat lens with hyperbolic dispersion, described in [8].

Surface roughness in test structures was set at silver layers while titanium dioxide layers were considered flat having modified refractive index. Test structures examined below were consisted of either 3 or 5 layers. Number of rough layers occurred to be important parameter that affects transmittance of multilayered structures.

Three-layered test structure consists of 20 nm Ag layer surrounded by 30 nm TiO_2 layers (Fig. 1) with air above and below. Length of the computational domain in both directions parallel to the surface is taken 100 nm. Periodic boundary conditions assume infinite duplication of the test structure along x and y axes parallel to the layer interfaces. Three different numerical simulations for obtaining real (n) and imaginary (k) part of titanium dioxide refractive index were performed in FDTD for each set of roughness parameters. The structure was illuminated by normal incident plane wave with the wavelength of 358 nm. Comparing results of amplitude of reflection (|r|) and transmission (|t|) coefficients one can estimate repeatability of parameters restoration for different realization of metal surface with the same roughness. Value of target function (f) was shown for understanding convergence of inverse

problem solving, magnitude of target function corresponds to difference between amplitude coefficients calculated by transfer matrix method and by FDTD (Table 1).

Table 1: Effective parameters evaluation for three-layered structure.

roughness parameters	|r|	|t|	n(TiO_2)	k(TiO_2)	f [10^{-4}]
ω=0 nm^{-1}	0.552	0.76	2.5746	0.0181	8.7
δ=0.04 nm^{-1}	0.552	0.7625	2.5734	0.017	7.8
σ=2 nm	0.5571	0.7631	2.5768	0.0149	7
ω=0 nm^{-1}	0.5184	0.7362	2.5632	0.0407	3
δ=0.04 nm^{-1}	0.5312	0.7342	2.5731	0.032	3.1
σ=4 nm	0.5112	0.7308	2.56	0.0457	8.7
ω=0 nm^{-1}	0.5648	0.7636	2.582	0.0124	4
δ=0.2 nm^{-1}	0.5642	0.7637	2.582	0.0128	8.7
σ=0.5 nm	0.5649	0.7631	2.58	0.0126	3.7
ω=0 nm^{-1}	0.5519	0.748	2.581	0.0242	0.36
δ=0.2 nm^{-1}	0.551	0.7471	2.5802	0.0243	1.3
σ=1 nm	0.5511	0.7482	2.5809	0.0249	1.16
ω=0.2 nm^{-1}	0.562	0.7611	2.581	0.0143	11
δ=0.4 nm^{-1}	0.562	0.7612	2.5803	0.0143	8.8
σ=0.5 nm	0.5618	0.7614	2.5805	0.0143	10
ω=0.2 nm^{-1}	0.5518	0.7494	2.58	0.0231	8
δ=0.4 nm^{-1}	0.5513	0.7489	2.579	0.0241	7
σ=1 nm	0.5518	0.7494	2.58	0.0231	8

Table 2: Effective parameters evaluation for five-layered structure.

roughness parameters	|r|	|t|	n(TiO_2)	k(TiO_2)	f [10^{-4}]
ω=0 nm^{-1}	0.56	0.383	2.0807	0.0883	3.3
δ=0.04 nm^{-1}	0.5595	0.3824	2.0808	0.0888	4.9
σ=0.5 nm					
ω=0 nm^{-1}	0.5522	0.3804	2.0641	0.0902	3.55
δ=0.04 nm^{-1}	0.5740	0.3678	2.1083	0.0106	5.2
σ=1 nm					
ω=0 nm^{-1}	0.5803	0.3289	2.1119	0.1546	0.2
δ=0.04 nm^{-1}	0.5368	0.3688	2.0269	0.0995	3.14
σ=2 nm					
ω=0 nm^{-1}	0.5963	0.3377	2.8708	0.14	8.6
δ=0.04 nm^{-1}	0.5988	0.3376	2.8746	0.1387	8.1
σ=0.5 nm					
ω=0 nm^{-1}	0.5897	0.3029	2.1289	0.1924	4.5
δ=0.2 nm^{-1}	0.5868	0.3049	2.1201	0.1886	2.8
σ=1 nm					
ω=0 nm^{-1}	0.5714	0.2511	1.9463	0.2476	1.6
δ=0.2 nm^{-1}	0.572	0.2498	1.663	0.13	1.4
σ=2 nm					
ω=0 nm^{-1}	0.5577	0.1588	no		
δ=0.2 nm^{-1}	0.5587	0.1591	result		
σ=4 nm					

Refractive index of titanium dioxide was considered 2.55 in FDTD calculations. According to Table 1, imaginary part of refractive index of dielectric layers rises proportionally to LER value for the surfaces with wide spatial spectrum. Reflection and transmission coefficients become dependent on random surface realization for the LER values more than 2 nm.

Five layer test structure consists of following sequence: 32 nm Ag layer, 30 nm TiO_2 layer, 30 nm Ag layer, 30 nm TiO_2 layer, 32 nm Ag layer [8].
Amplitude coefficients for ideal smooth layers from FDTD calculations are |r|=0.5592, |t|=0.5218. According to Table 2, scattering on rough surfaces of Ag significantly reduces transparency of the samples. Increase of number of layers from 3 to 5 produces worse convergence of effective parameters calculations. Different variants of surface distribution with narrow spatial spectrum and RMS>1 nm show divergence in reflection and transmission coefficients calculation, while samples with wide spatial spectrum have similar coefficients when the same RMS is considered. On the other hand rising of RMS for wide spectrum roughness realizations produces results that do not match transfer matrix method and the model of effective index for roughness description is invalid (see table 2 for ω=0 nm^{-1}, δ=0.2 nm^{-1}, σ=4 nm).

5. Simulation of flat lens with rough surfaces

In this section we examine suitability of roughness model for description of propagation of diffracted light in flat lens. Fig. 2 presents ideal planar structure consisted of 5 layers with TiO_2 refractive index of n=2.55. Linearly polarized light with wavelength of λ=358 nm passes through 50 nm wide slit in 60 nm thick Ag layer. The distribution of amplitude of electric field after the last Ag layer is shown in contour plot normalized to the maximum of amplitude of incident wave.

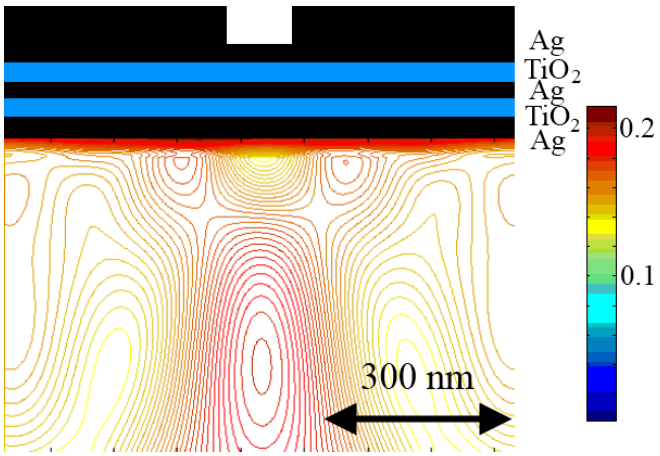

Figure 2: Diffraction of electric field after passing through hyperbolic metamaterial with flat surface.

According to effective medium theory, effective electric permittivity of composite material presented in Fig. 2, should be $\varepsilon_x=\varepsilon_y=1.8655+i0.2731$; $\varepsilon_z=-1.9629+i0.9177$; effective refractive index: $n_x=n_y=1.3695+i0.0997$; $n_z=0.3193+i1.4370$ (after parameters used in simulation: $\varepsilon(Ag)=-2.2745+i0.7214$, $\varepsilon(TiO_2)=6.5025$, filling factor of Ag $\eta=0.6104$). Negative part of electric permittivity for wave components, travelling parallel to metal-dielectric

interface, causes diffracted waves change direction at Ag-air interface. Thus small focusing effect is observed. In Fig. 3 surface roughness on Ag layers is placed. Roughness parameters for this case are ω=0 nm^{-1}, δ=0.2 nm^{-1}, σ=1 nm, which corresponds to modified refractive index of n(TiO_2)=2.1201+i0.1886 according to Table 2. This refractive index was substituted in calculation shown in Fig. 4.

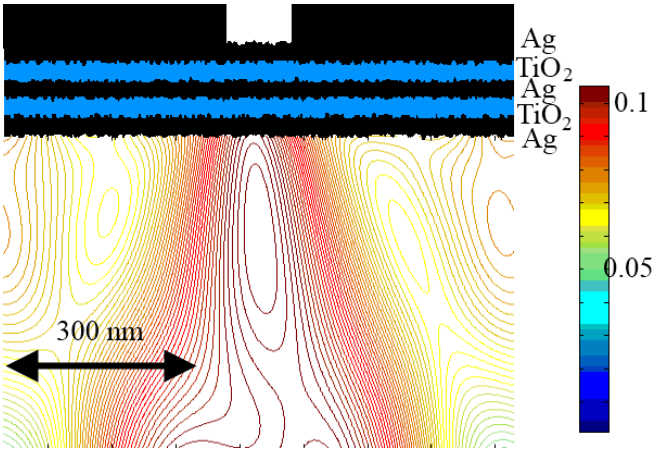

Figure 3: Distribution of module of electric field after passing through hyperbolic metamaterial with rough surface.

Effective electric permittivity of metal-dielectric slab in a case of refractive index of TiO_2 taken from Table 2 should be $\varepsilon_x=\varepsilon_y$=1.0695+i0.5847; ε_z=-1.9758+i1.0581; $n_x=n_y$= 1.0697+i0.2733; n_z=0.3643+1.4521. Small increase of imaginary part of refractive index is obtained. Presence of surface roughness gives similar diffracted field patterns and transmission coefficient as in the case of planar layers with modified refractive index. Asymmetry in Fig. 3 could explained by presence of random surface deviations, which have the size comparable to slit width.

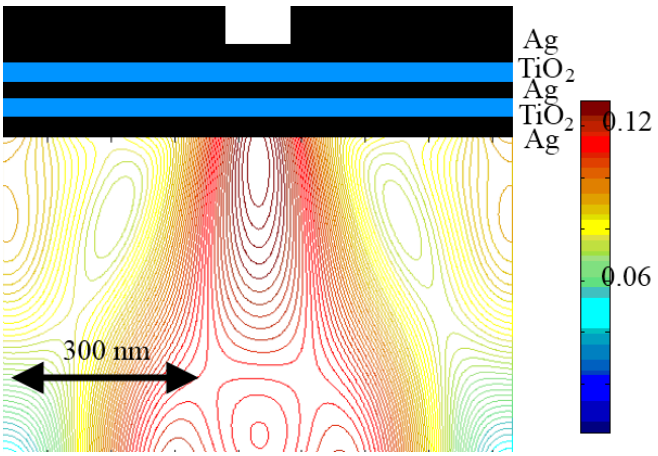

Figure 4: Distribution of module of electric field after passing through hyperbolic metamaterial with index of dielectric layers n(TiO_2)=2.1201+i0.1886.

6. Conclusions

We described and proved numerically that the influence of surface roughness at the interfaces in metal-dielectric composite materials could be described by proper selection of refractive index of dielectric layers. This approach is better than introducing additional intermediate layers or setting rigorous roughness profile in such grid method as FDTD, because it does not need fine grid resolution. It also allows employing simple and fast matrix transfer method for simulation of stratified structures with rough surfaces. However, understanding limits of application of this method of refractive index modification needs further study. Our calculation show, that some examples of roughness realization with narrow spatial spectrum and high LER value could not be described by results of transfer matrix method.

Acknowledgements

The authors would like to thank King Abdul-Aziz City for Science and Technology (KACST) for Research Grant No. 814-33.

References

[1] H.K. Yuan, U.K. Chettiar, W. Cai, A.V. Kildishev, A. Boltasseva, V.P. Drachev, V.M. Shalaev, A negative permeability material at red light, *Optics Express* 15: 1076–1083, 2007.

[2] S.E. Kozik, A.G. Smirnov, Full-scale simulation of angular-resolved focused-beam scatterometry applied to aperiodic isolated features: model validity analysis and numerical results, *Proc. SPIE* 8083: 80830A-1–80830A-13, 2011.

[3] A. Farjadpour, D. Roundy, A. Rodriguez, M. Ibanescu, P. Bermel, J. D. Joannopoulos, and S. G. Johnson, Improving accuracy by subpixel smoothing in the finite-difference time domain, *Opt. Letters* 31: 2972–2974, 2006

[4] A. Mohammadi, M. Agio, Dispersive contour-path finite-difference time-domain algorithm for modeling surface plasmon polaritons at flat interfaces, *Optics Express* 14: 11330–11338, 2006.

[5] Y. Zhao, P. Belov, Y. Hao, Accurate modelling of left-handed metamaterials using a finite-difference time-domain method with spatial averaging at the boundaries, *J. Opt. A: Pure Appl. Opt.* 9: S468, 2007.

[6] A. Deinega, I. Valuev, Subpixel smoothing for conductive and dispersive media in the finite-difference time-domain method, *Opt. Lett.*, 32: 3429–3431, 2007.

[7] H. Fujiwara, *Spectroscopic Ellipsometry: Principles and Applications*, Wiley, Chichester, 2007

[8] T. Xu, A. Agrawal, M. Abashin, K.J. Chau, H.J. Lezec, All-angle negative refraction and active flat lensing of ultraviolet light, *Nature* 497: 470–474, 2013

cations: micro and nanofabrication, active plasmonic components, cloa

NiZn ferrite/Fe Hybrid Epoxy-based Composites: Extending Magnetic Properties to High Frequency

Yunqi Wang*, Patrick S. Grant

Department of Materials, University of Oxford, Parks Road, OX1 3PH, UK
*corresponding author, E-mail: yunqi.wang@materials.ox.ac.uk

Abstract

Hybrid ferromagnetic composites composed of $Ni_{0.4}Zn_{0.6}Fe_2O_4$ ferrite powder and Fe particles in an epoxy matrix with various composition ratios were prepared by a simple mould casting route. Planetary ball milling was then introduced to pre-grind Fe and NiZn ferrite filler mixtures before casting, which resulted in fragmentation of the NiZn ferrites and modification of the Fe morphology from spherical particles to sub-micron flakes. Composites containing the ball milled fillers exhibited a remarkable improvement in electromagnetic properties over the as-supplied materials, especially in the suppression of dielectric and magnetic loss. By combining the characteristics of high resonant frequency of the Fe and low energy losses of the ferrite, an optimum mixture of ball milled 15 vol.% NiZn ferrite and 38 vol.% Fe in a hybrid epoxy-based composite gave an approximately one order of magnitude higher extended operating bandwidth over a ferrite-only containing composite, suppressing dielectric and magnetic loss tangents to approximately 10^{-2} up to 150 MHz without significant deterioration of permeability. This approach of manipulating multi-phase ferromagnetic material fractions and their structure provides for flexibility in the development of bespoke electromagnetic materials for applications in electrically small antenna and metamaterials.

1. Introduction

The development of materials for the manipulation of electromagnetic waves for applications across photonics, radar and microwave communications has led to the advent of metamaterials that exhibit unusual combinations of physical behaviour. Meanwhile, the ever-increasing demand for smaller, longer lasing and novel design portable electronic devices has accelerated the development of multifunctional materials with low energy losses and high permeability for miniaturizing electronic components such as antennas, magnetic inductors [1] and current convertors [2-4]. Nowadays, many electronic devices operate in the very high frequency (30-300 MHz) range, such as television broadcasting, land-based mobile telephone stations and air traffic control communications, and therefore materials with low energy losses and high permeability that are able to operate at these and higher frequencies are in high demand, both for conventional and possible metamaterial applications [5-7].

According to Snoek's law $\mu f_r \propto M_s$ (where μ is the real permeability, f_r is the ferromagnetic resonant frequency and M_s is the saturation magnetization), magnetic materials with high M_s are favored for high permeability at high frequencies. Therefore, metallic magnetic materials that are known to have high saturation magnetization have been extensively investigated as fillers embedded in an easy-to-process non-conducting polymer matrix - magnetic composites. The magnetic properties of metallic fillers has been improved by using planar, anisotropic morphologies, extending useful operation characteristics up to a few gigahertz, such as those based on carbonyl iron flakes [8,9], planar $Fe_{50}Ni_{50}$ powder [10], $Fe_{65}Co_{35}$ thin films [11], and $Fe_{74}Cr_2Mo_2Sn_2P_{10}Si_4B_4C_2$ flakes [12]. However, these composites have tended to have high dielectric losses ($\tan\delta_\varepsilon \geq 0.1$), which is generally considered undesirable for device applications.

Soft magnetic ferrites have low dielectric losses ($\tan\delta_\varepsilon \sim 10^{-2}$) but magnetic properties are degraded or even absent (i.e. materials with permeability close to 1) as the frequency approaches the range 100 MHz to 1 GHz [13], due to ferromagnetic resonant behaviour, which limits the device operating frequency. Metallic magnetic materials generally have higher resonant frequency than ferrites due to their larger saturation magnetization, but suffer from high energy losses because of induced eddy currents, creating difficulties in the design and engineering of practical devices using these materials [14]. Merging the characteristics of these two kinds of magnetic materials might produce an attractive balance of properties, depending on the frequencies at which magnetic response might be maintained while at comparatively low loss.

In this study, we report further development of a novel and simple mould casting method [15] to fabricate epoxy based NiZn ferrite/Fe hybrid composites. The electromagnetic properties of two series of hybrid composites composed of ball milled and un-milled $Ni_{0.4}Zn_{0.6}Fe_2O_4$ ferrite and Fe particles with various composition ratios have been studied. A co-axial airline technique was used to characterize the complex permittivity and permeability of the composites in

the frequency range 10 MHz to 4GHz. Ball milling reduced dielectric loss dramatically, compensating for the losses normally associated with introducing Fe. The electromagnetic properties of an optimized hybrid epoxy-based composite with ball milled 15 vol.% NiZn ferrite and 38 vol.% Fe fillers was significantly better than similar ferrite-only containing composites, suggesting promise for magnetic applications in the very high frequency range.

2. Experimental

Sintered $Ni_{0.4}Zn_{0.6}Fe_2O_4$ ferrite powder (F16 MagDev Ltd. UK) and Fe powder (<10 μm, Alfa Aesar Ltd. UK) were ball milled for 4 hours in a high-energy planetary mill (Pulverisette 6, Fritsch GmbH, Germany) at a rotational speed of 300 rpm with a ball-to-powder weight ratio of 10:1 in ethanol, and then dried. Table 1 shows the range of ferrite/Fe ratios investigated.

Magnetic composites were prepared using an epoxy matrix (Epon™ 812 substitute) with two different hardeners: 2 dodecenylsuccinic anhydride (DDSA) and methylnadic anhydride (NMA) (Sigma Aldrich Ltd. UK), by a simple casting route. By changing the ratio of the two hardeners, the hardness and brittleness of the final cured epoxy could be adjusted. After fully magnetic stirring of the epoxy mixture, the accelerator 2,4,6-tris(dimethylaminomethyl) phenol (DPM-30) was added, and then the filler powders (see Table 1) were added under stirring followed by 5 min ultrasonication in an ice bath. The composite slurry was then degassed under low vacuum and poured into a silicone mould to produce a toroidal shaped casting with an outer diameter of 7.0 mm, an inner diameter of 3.04 mm, and a thickness of 7.0 mm. These dimensions were chosen to fit tightly within a coaxial air-line jig for electromagnetic measurements. The composites were cured at 60 °C overnight.

Table 1: Compositions of epoxy based composites for both ball milled and as-supplied powder fillers

Sample	Composition	Fe/(Fe + NZ) Vol. ratio
53NZ	53 vol.% NiZn ferrite	0
48NZ5Fe	48 vol.% NiZn ferrite/5 vol.% Fe	0.094
42NZ11Fe	42 vol.% NiZn ferrite/11 vol.% Fe	0.207
38NZ15Fe	38 vol.% NiZn ferrite/15 vol.% Fe	0.283
26.5NZ26.5Fe	26.5 vol.% NiZn ferrite/26.5 vol.% Fe	0.5
15NZ38Fe	15 vol.% NiZn ferrite/38 vol.% Fe	0.717
11NZ42Fe	11 vol.% NiZn ferrite/42 vol.% Fe	0.793
5NZ48Fe	5 vol.% NiZn ferrite/48 vol.% Fe	0.906
53Fe	53 vol.% Fe	1

Scanning electron microscopy (SEM) images were taken using a JEOL JSM-840F field emission electron microscope after microtome (Ultracut E, Reichert, Inc.) cross-sectioning. The electromagnetic properties of the composites were measured using a coaxial air-line method in which the toroidal sample was inserted between the inner and outer conductors of the coaxial line that worked in a transverse electromagnetic (TEM) mode. The reflection and transmission amplitude coefficients were measured from 10 MHz to 4 GHz by a calibrated Vector Network Analyser (MS4644A, Anritsu). The complex permittivity and permeability of the material were then extracted from the reflection and transmission coefficients according to the Nicolson-Ross-Weir algorithm [16,17].

3. Results and discussion

Figs. 1a and b show SEM images of the as-supplied Fe powder and the NiZn ferrite powder respectively, with comparable particle dimensions of 1 to 10 μm. After ball milling, as shown in Fig. 1c, the spherical Fe particles were deformed into flakes with lateral dimensions of a few micrometers and sub-micrometer thickness. The NiZn ferrite particles were ground to sub-micrometer diameter and became distributed evenly on the surface of Fe flakes, as "satellites". Fig. 1d shows a typical fractured cross-section of a 15 vol.% NiZn ferrite and 38 vol.% Fe hybrid composite, indicating an adequate homogeneity of filler particle dispersion with no large agglomerates or excessive air bubbles.

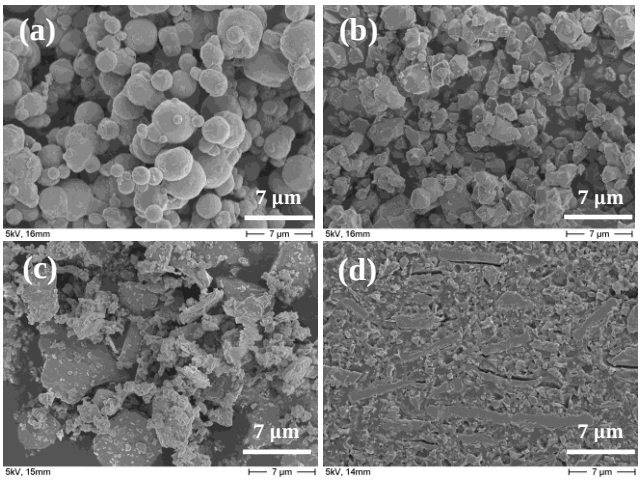

Figure 1: SEM images of (a) as-supplied Fe particles; (b) as-supplied NiZn ferrite; (c) 15 vol.% NiZn ferrite/38 vol.% Fe powder mixture after ball milling; and (d) a cross-section of a 15 vol.% NiZn ferrite/38 vol.% Fe hybrid composite.

The complex permittivity and permeability of as-received NiZn ferrite/Fe epoxy-based composites, and after ball milling, with different volume ratios are shown in Fig. 2 and Fig. 3 respectively. The real part (ε') and imaginary part (ε'') of relative permittivity for as-supplied and milled composites increased with Fe volume ratio, most notably at low frequencies for composites with a high Fe fraction (> 38 vol. % for as-supplied, > 42 vol.% for ball milled) due to the high electrical conductivity of Fe and the charge accumulation at the interfaces between the Fe and the matrix, which is known as interfacial polarization [18]. At the lower frequencies, the charges had sufficient time to accumulate at the interfaces and tended to orientate fully

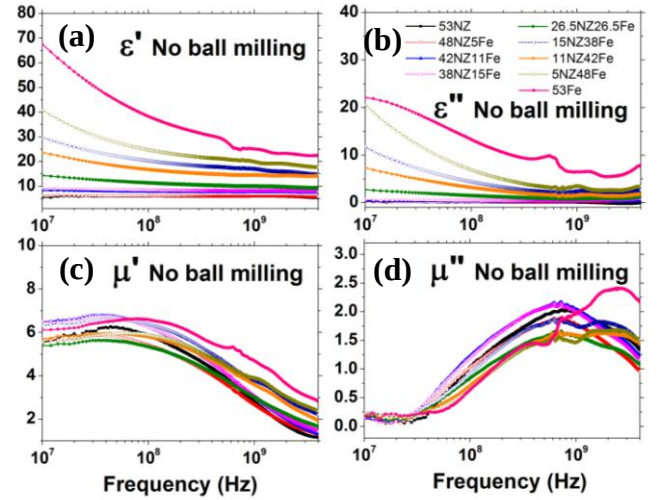

Figure 2: Complex permittivity and permeability spectra for composites with un-milled NiZn ferrite/Fe fillers in various volume ratios: (a) real and (b) imaginary part of complex permittivity; and (c) real and (d) imaginary part of complex permeability

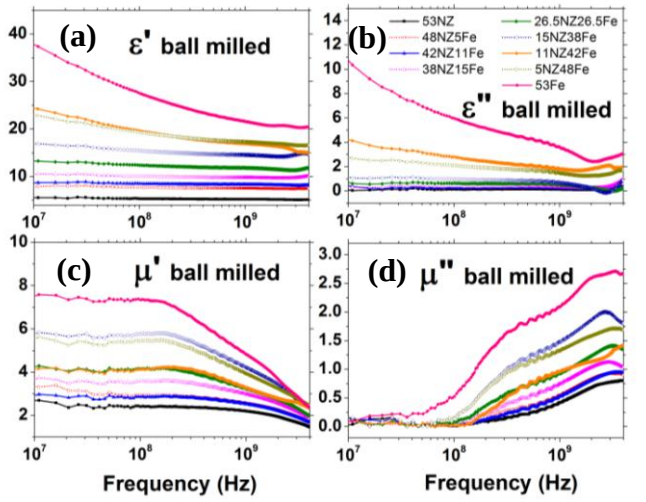

Figure 3: Complex permittivity and permeability spectra for composites with ball milled NiZn ferrite/Fe fillers in various volume ratios: (a) real and (b) imaginary part of complex permittivity, and (c) real and (d) imaginary part of complex permeability.

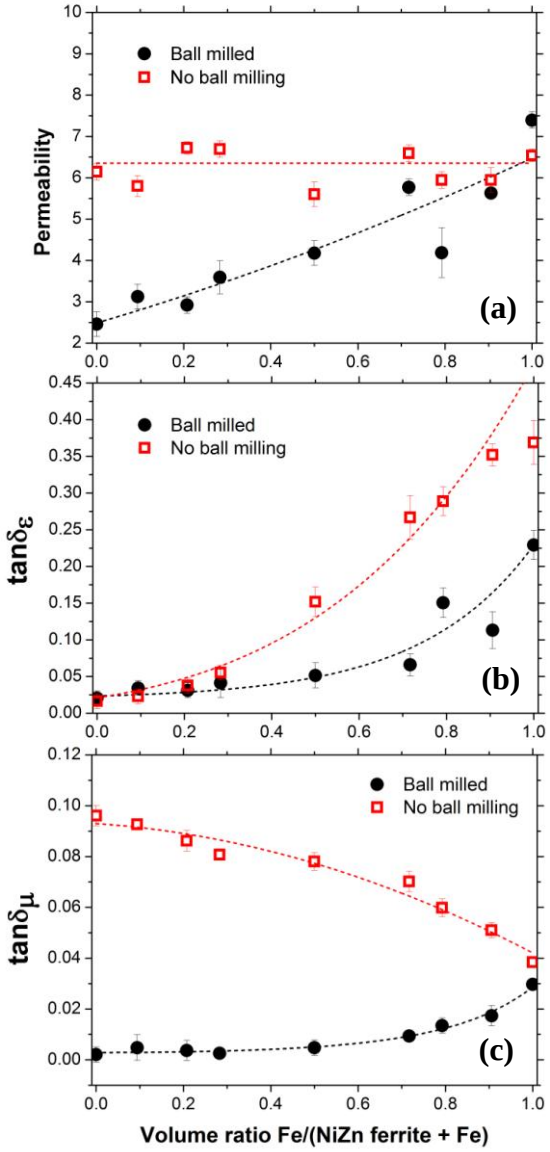

Figure 4: The (a) real part of complex permeability, (b) dielectric loss tangent, and (c) magnetic loss tangent of epoxy-based composites with ball milled and un-milled NiZn ferrite/Fe fillers in various volume ratios at 50 MHz.

along the applied field direction, enhancing charge movement and increasing energy dissipation. At low Fe fraction, the permittivities of both types of composites were almost constant at < 20 in the 10 MHz to 4 GHz frequency range. In general, the values of ε′ and ε″ for milled composites were lower and less dispersive than those of as-supplied composites at the same composition because for the ball milled filler composites, the smaller sub-micrometer ferrite particles that decorated the Fe flakes acted as physical "spacers" that improved the partial insulation of Fe by facilitating the ingress of the epoxy matrix between the Fe flakes, as suggested by the microstructural observations in Fig. 1d. On the other hand, without milling, the aggregated as-supplied Fe particles were generally not well-separated or isolated, and the similarly sized as-supplied NiZn ferrites did not form satellites on the Fe, thus there was no effective physical mechanism to inhibit Fe agglomeration. The composites based on as-supplied powder therefore showed a higher complex permittivity and were more "lossy".

In general, the real part of complex permeability μ' for both types of composites with various filler ratios responded similarly, with a flat response at low frequency before gradually decreasing as frequency increased. The imaginary

part of complex permeability μ'' remained relatively low at 0.01 to 0.3 below several tens of MHz, but increased to form a broad peak around the resonant frequency, where domain wall motion was no longer able to follow the applied alternating magnetic field and magnetic loss increased [19].

The real permeability of all the epoxy-based composites containing as-supplied NiZn ferrite/Fe fillers were comparable at ~ 6 at low frequency, but decreased more rapidly for composites with higher NiZn ferrite volume fractions because of the smaller saturation magnetization of the NiZn ferrite (see Fig. 2c). At a frequency of 4 GHz, the 53 vol.% Fe composite had the highest permeability of 3, whereas the real permeability of the 53 vol.% NiZn ferrite composite had reduced to 1.5.

For the composites with ball milled fillers, the real permeability decreased from ~ 7.5 to ~ 2.5 with increasing NiZn ferrite fraction, as shown in Fig. 3c, which was attributed to the lower permeability of the smaller NiZn ferrite particles: smaller ferrite particles have lower permeability because they contain more defects that pin domain walls [20]. The effective permeability may also have been lowered by a higher demagnetizing field in the composite evoked by the larger gaps between smaller particles when compared with larger particles at the same volume fraction [20]. The real permeability of the 53 vol. % Fe milled composite was ~ 7.5 before resonance occurred, compared with ~ 6 for the 53 vol.% Fe as-supplied composite, and was ascribed to the thin (< 1 μm) flake morphology after milling that has previously been suggested to reduce eddy current loss [21].

Fig. 4 shows the real permeability, dielectric loss tangent ($\tan\delta_\varepsilon = \varepsilon''/\varepsilon'$) and magnetic loss tangent ($\tan\delta_\mu = \mu''/\mu'$) of composites with milled and as-supplied fillers at various Fe/total filler volume ratios at 50 MHz. In all cases the total amount of filler was 53 vol.% of the epoxy-based composite, but the Fe/(Fe+NiZn ferrite) ratio changed systematically. The values of μ', $\tan\delta_\varepsilon$ and $\tan\delta_\mu$ for as-supplied powders were almost constant at ~ 6, increased from 0.016 to 0.370, and decreased from 0.096 to 0.038 respectively as the Fe/(Fe+NiZn ferrite) ratio increased from 0 to 1. After ball milling, μ', $\tan\delta_\varepsilon$ and $\tan\delta_\mu$ increased from 2.5 to 7.5, 0.02 to 0.22, and 0.002 to 0.03 respectively over the same range. Therefore, both dielectric and magnetic losses were reduced systematically when a ball milling pre-treatment was used.

For electronic device components and especially antennas, low dielectric and magnetic losses combined with high permeability are especially desirable, but become more mutually exclusive as frequency increases for monolithic materials. However in the case of the composites investigated here, an optimum balance between high permeability ($\mu' = 5.8$) and low energy losses ($\tan\delta_\varepsilon = 0.06$ and $\tan\delta_\mu = 0.009$) can be identified at a Fe/(Fe+NiZn ferrite) volume ratio of 0.717 (15 vol.% NiZn ferrite and 38 vol.% Fe) for the ball milled filler composites.

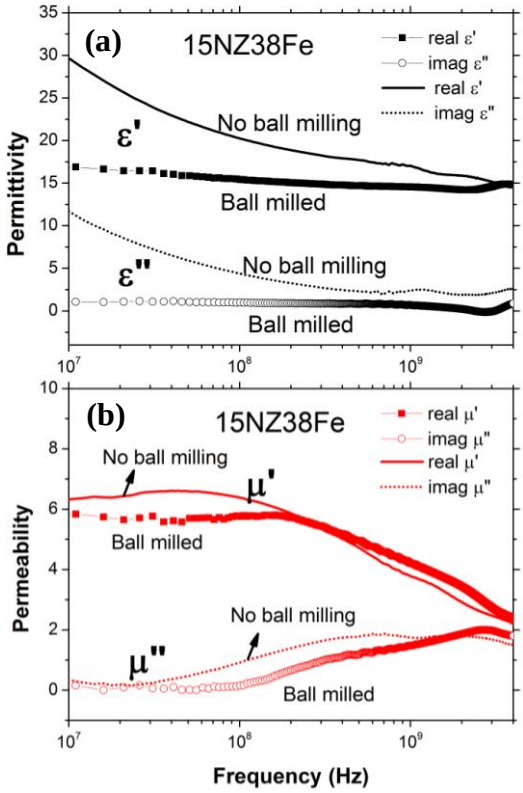

Figure 5: Frequency dispersions of (a) complex permittivity and (b) complex permeability for epoxy-based composites with ball milled and un-milled particle fillers of 15 vol.% NiZn ferrite/38 vol.% Fe.

A direct comparison of the complex permittivity and permeability spectra for epoxy-based composites with ball milled and as-supplied fillers of 15 vol.% NiZn ferrite/38 vol.% Fe are shown in Figs. 5a and b respectively, where the ε' and ε'' response decreased and flattened after the ball milling process, as previous described. The slightly more frequency-independent permeability of the composite with milled powders reduced from 6.6 to 5.8 as frequency increased, but dielectric and magnetic tangents were suppressed to $\leq 10^{-2}$ up to 150 MHz, providing a wider practical operating bandwidth than composite variants containing as-supplied powders at the same ratio, or for the ferrite-only containing composite.

To further assess the benefit of the hybrid 15 vol.% NiZn ferrite/38 vol.% Fe hybrid composite over a similar composite containing only as-supplied NiZn ferrite with same overall filler fraction, their magnetic properties are shown in Fig. 6. Both composites has a comparable real permeability of ~ 6 up to 30 MHz, but whereas permeability then reduced for the NiZn ferrite only composite, the hybrid composite maintained a higher permeability to ~ 300 MHz.

Although the real permeability of the ball milled 15 vol.% NiZn ferrite/38 vol.% Fe hybrid composite was slightly lower than un-milled 53 vol.% NiZn ferrite alone at lower

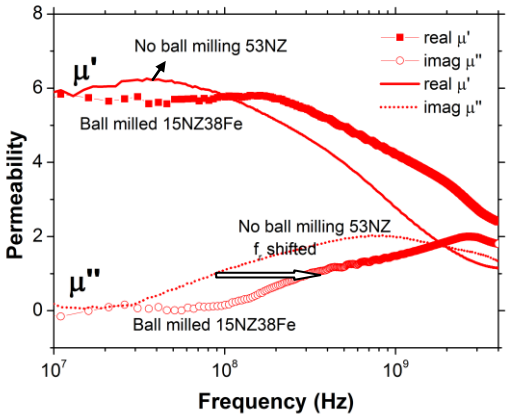

Figure 6: Frequency dispersions of complex permeability for epoxy-based composites with a un-milled 53 vol.% NiZn ferrite loading and a ball milled 15 vol.% NiZn ferrite/38 vol.% Fe loading. The hybrid composite showed permeability similar to the ferrite only composite, but with extended operating bandwidth.

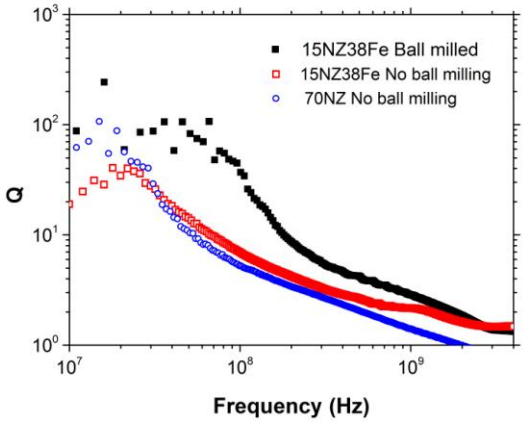

Figure 7: Quality factor Q versus frequency for epoxy-based composites with ball milled 15 vol.% NiZn ferrite/38 vol.% Fe, un-milled 15 vol.% NiZn ferrite/38 vol.% Fe, and un-milled 53 vol.% NiZn.

frequency, an important figure of merit is the magnetic quality factor $Q = \mu'/\mu''$, which is plotted as a function of frequency in Fig. 7. Q was significantly improved over the measured frequency range in the case of the hybrid composite, indicating a more practical balance of permeability and loss behaviour, especially at higher frequencies.

4. Conclusions

The electromagnetic properties of epoxy-based composites containing both ball milled and un-milled NiZn ferrite and Fe particulate fillers were investigated over the frequency range 10 MHz - 4 GHz. The changes in size and morphology of the particles that were introduced by the ball milling process suppressed dielectric and magnetic losses of the NiZn ferrite/Fe hybrid composites to higher frequencies. A hybrid composite with a filler loading of ball milled 15 vol.% NiZn ferrite/38 vol.% Fe showed an almost one order of magnitude improvement in operating frequency with low loss when compared with a similar but un-milled 53 vol.% NiZn ferrite composite, with only a slight reduction in permeability. The striking points of the hybrid composites were a relatively high permeability (~ 6) and low magnetic and dielectric losses (~ 10^{-2}) over the high frequency range of interest, which suggested they may be well-suited for applications in electrically small devices operating in the very high frequency range. The addition of Fe to NiZn ferrite can also be expected to lower the fabrication cost for a given filler content, and improved loss performance over solely ferrite containing composites. The ease of casting these epoxy based composites into a range of shapes and sizes further enhances the attractiveness of these materials. The concept of manipulating permeability and permittivity of easy-to-process composites by introducing multi-phase ferromagnetic materials with contrived morphologies and size ratios may also help to advance applications such as cloaking, energy transfer, sensors and security according to the theory of spatial transformations, which relies on the provision of bespoke dielectric and magnetic properties in practical materials.

Acknowledgements

The authors would like to thank the UK Engineering and Physical Sciences Research Council for funding through Programme Grant EP/I034548/1 “The Quest for Ultimate Electromagnetics using Spatial Transforms (QUEST)” and the UK Defence Science and Technology Laboratory for additional financial support. The authors would also like to thanks Dr. Ian Hopper at the University of Exeter for his help with electromagnetic measurements and access to equipment in the Electromagnetic and Acoustic Materials group.

References

[1] J. F. Godsell, S. Kulkarni, T. O’Donnell, Precessional dynamics of $Ni_{45}Fe_{55}$ thin films for ultrahigh frequency integrated magnetic. *J. Appl. Phys.* 107: 033907_1-8, 2010.

[2] M. Yamaguchi, Y. Miyazawa, K. Kaminishi, H. Kikuchi, S. Yabukami, K.I. Arai, T. Suzuki, Soft magnetic applications in the RF range, *J. Magn. Magn. Mate.* 268: 170-177, 2004.

[3] Y. Hayakawa, A. Makino, H. Fujimori, A. Inoue, High resistive nanocrystalline Fe-M-O (M=Hf, Zr, rare-earth metals) soft magnetic films for high-frequency applications, *J. Appl. Phys* 81: 3747-3752, 1997.

[4] M. E. McHenry, M.A. Willard, H. Iwanabe, R.A. Sutton, Z. Turgut, A. Hsiao, D.E. Laughlin, Nanocrystalline materials for high temperature soft

magnetic applications: A current prospectus, *Bull. Mater. Sci.* 22: 495-501, 1999.

[5] T. Kasagi, T. Tsutaoka, K. Hatakeyama, Particle size effect on the complex permeability for permalloy composite materials. *IEEE Trans. Magn*. 35: 3424 - 3426, 1999.

[6] Y. W. Zhao, T. Zhang, J. Q. Xiao, Explosion compacted FeCo particles coated with ferrites: A possible route to achieve artificial soft ferrites, *J. Appl. Phys.* 93: 8014-8016, 2003.

[7] Y. W. Zhao, C. Y. Ni, D. Kruczynski, X. Zhang, J. Q. Xiao, Exchange-coupled soft magnetic FeNi−SiO_2 nanocomposite, *J. Phys. Chem. B* 108: 3691-3693, 2004.

[8] R. B. Yang, W. F. Liang, Microwave properties of high-aspect-ratio carbonyl iron/epoxy absorbers, *J. Appl. Phys.* 109: 07A311_1-3, 2011.

[9] F. S. Wen, L. Qiao, H. B. Yi, D. Zhou, F. S. Li, Calculation of high frequency complex permeability if carbonyl iron flakes in a nomagnetic matrix, *Chin. Phys. Lett.* 25:751-754, 2008.

[10] J. Q. Wei, Z. Q. Zhang, R. Han, T. Wang, F. S. Li, Microwave reflection properties of planar anisotropy $Fe_{50}Ni_{50}$ powder/paraffin composites, *Chin. Phys. B.* 21:037601_1-6, 2012.

[11] Y. Wang, H. Geng, J. B. Wang, D. Nie, L. S. Wang, Y. Chen, D. L. Peng, Magnetic propertied of [$Fe_{65}Co_{35}$-O/SiO_2]n multilayer thin films for high-frequency application, *Appl. Phys. A* 111:569-574, 2013.

[12] K. H. Liu, T. C. Liu, J. L. Liu, L. Zhang, H. H. Zhang, D. R. Li, Z. C. Lu, S. X. Zhou, High frequency complex permeability of flak-shaped $Fe_{74}Cr_2Mo_2Sn_2P_{10}Si_4B_4C_2$ particle composite material, *Sci. China Ser. E* 53:1056-1059, 2010.

[13] L. Parke, I. R. Hooper, R. J. Hicken, C. E. J. Dancer, P. S. Grant, I. J. Youngs, J. R. Sambles, A. P. Hibbins, Heavily loaded ferrite-polymer composites to produce high refractive index materials at centimeter wavelengths, *APL Mater.* 1:042108_1-7, 2013.

[14] J. R. Brauer, Z. J. Cendes, B. C. Beihoff, K. P. Phillips, Laminated steel eddy-current loss versus frequency computed using finite elements, *IEEE Trans. Ind. Appl.* 36:1132-1137, 2000.

[15] Y. Wang, E. Edwards, I. Hooper, N. Clow, P. S. Grant, Low-cost scalable polymer based ferrite composites with matching permeability and permittivity for high-frequency applications, *J. Appl. Phys.* submitted.

[16] A. M. Nicolson, G. F. Ross, Messurement of the intrinsic properties of materials by time domain techniques, *IEEE Trans. Instrum. Meas.* 19:377-382, 1970.

[17] W. B. Weir, Automatic measurement of complex dielectric constant and permeability at microwave frequencies, *Proc. IEEE* 62: 33-36, 1974.

[18] R. W. Sillars, The Behaviour of Polar Molecules in Solid Paraffin Wax, *Proc. R. Soc. Lond. A*. 169: 66-83, 1938.

[19] H. Su, H. Zhang, X. Tang, and Y. Jing, Influence of microstructure on permeability dispersion and power loss of NiZn ferrite, *J. Appl. Phys.* 103: 093903_1-5, 2008.

[20] M. Anhalt, Systematic investigation of particle size dependence of magnetic properties in soft magnetic composites, *J. Magn. Magn. Mater.* 320: 366-369, 2008.

[21] D. M. Pozar, *Microwave Engineering*, 4th ed.,Wiley, New York, 2012.

A Study of Metamaterial Absorber Based on Circular Ring Structure With and Without Copper Lines

Osman Ayop[1], Mohamad Kamal A. Rahim[1], Noor Asniza Murad[1]

[1]Department of Communication Engineering, Faculty of Electrical Engineering, Universiti Teknologi Malaysia, Malaysia
*corresponding author, E-mail: osman@fke.utm.my

Abstract

This report presents a study of circular ring metamaterial absorber with the existing of copper lines. The structure is designed using lossy FR4 substrate with thin copper layers. The circular ring shape with copper lines is printed on the top surface of FR4 substrate while at the bottom surface is printed with full copper ground plane. Parametric study is done to investigate the effect of copper lines on the resonance frequency. From the simulation, the circular ring metamaterial absorber with vertical copper lines can resonates at lower frequency but this structure is polarization sensitive. This drawback can be improved by adding horizontal copper lines simultaneously with the vertical copper lines.

1. Introduction

Metamaterial, since many years has attracted great attention among researchers since a lots of interesting properties can be found when deal with this structures. Some of them are left-handed metamaterial [1] that can offer an unusual material properties which is double negative of permittivity and permeability at certain operating frequency, electromagnetic band gap metamaterial [2] which can suppress unwanted surface waves within a bandgap frequency region, frequency selective surface metamaterial [3] that can select specific electromagnetic waves like a filter effect and artificial magnetic conductor metamaterial [4] which can reinforce an image currents with the real currents for more efficient low profile antenna.

In 2008, N. I. Landy et al. [5] successfully demonstrated an experimental result of perfect metamaterial as an electromagnetic absorber. Since then, many papers on metamaterial absorber have been published from microwave region [6] up to optical region [7]. Several issues such as polarization sensitivity and wide operating angle [8] are discussed within the study of metamaterial absorbers.

2. Proposed Design, Simulation and Discussion

This report proposes three designs, which is initially started by circular ring structure. Circular ring structure is selected due to their nature of the shape that is highly symmetrical for all rotational angles. Then, some modification of the circular ring structure is made by introduce several inductive lines. The matamaterial absorber is designed based on 0.8 mm thick lossy FR4 substrate which has dielectric constant of 4.6 and tangent loss of 0.019. The 0.035 mm thick copper layer is located at the both side of the FR4 substrate with a conductivity of 5.8 x 10^7 S/m. The proposed design is shown in Figure 1. This structure is simulated using CST software.

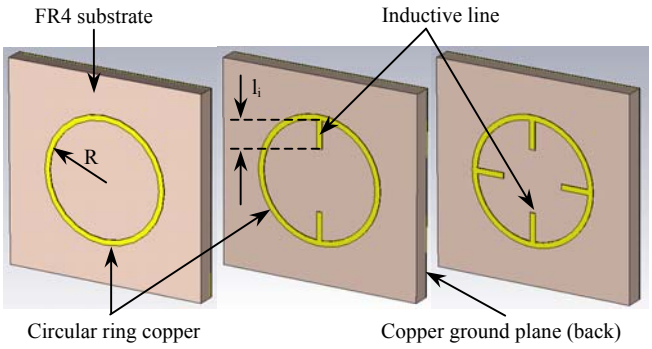

Figure 1: Proposed metamaterial absorber: (a) circular ring structure, (b) circular ring structure with vertical copper line and (c) circular ring structure with vertical and horizontal copper line.

2.1. Circular ring metamaterial absorber

Figure 1 shows a unit cell structure of circular ring metamaterial absorber. They consist of a thin circular ring structure on the top of FR4 substrate and copper ground plane at the bottom of the substrate. This structure is simulated for different radius size, R to obtain circular ring radius on the specific resonance frequencies. The width of

Table 1: The effect of average radius, R of the circular ring metamaterial absorber on resonance frequency

average radius, R [mm]	resonance frequency [GHz]	absorbance at resonance [%]
3.32	8	97.45
2.96	9	95.69
2.68	10	92.93
2.46	11	89.40
2.27	12	87.59

the circular ring is set to 0.24 mm for all cases. The results are presented in Table 1. From Table 1, the average radius, R of the ring is 3.32 mm, 2.96 mm, 2.68 mm, 2.46 mm, and 2.27 mm to achieve resonance frequencies at 8, 9, 10, 11, and 12 GHz respectively.

2.2. Circular ring metamaterial absorber with vertical copper lines

Figure 1 (b) shows a unit cell of circular ring metamaterial absorber with the additional of vertical copper line. The radius of the ring is set to 2.68 mm, which is originally resonating at 10 GHz. A parametric study is done for different length of copper line, l_i. The width of the copper line is set to 0.24 mm as same as the width of the circular ring structure. The simulation is done for E-plane polarization incident wave for normal incident angle. The result is presented in table 2.

Table 2: The effect of different length of copper line, l_i on resonance frequency of metamaterial absorber

length of copper line, l_i [mm]	resonance frequency [GHz]	absorbance at resonance [%]
0	10	92.93
0.715	9.5	96.49
1.240	9.0	99.33
1.790	8.5	99.49
2.265	8	94.16

From Table 2, as the length of copper line increased, the resonance frequency is decreased. The existing of copper line gives additional inductive effect hence reducing the operating frequency of the circular ring metamaterial absorber. When compactness is the main consideration, this kind of structure can be used to obtain lower operating frequency for smaller size of unit cell.

2.2.1. Polarization effect

Since the additional of the vertical copper line within the circular ring structure, the symmetrical properties of the structure do not fully observed. So, the polarization effect is studied for this kind of structure. The structure in Figure 1 (b) is simulated for difference polarization angles, which are 0^0, 22.5^0, 45^0, 67.5^0, and 90^0.

From Figure 2, as the polarization of the incident wave altered, the absorbance property and the operating frequency are also changed. Initially, the polarization angle of incident EM waves is 0^0. The operating frequency is 9 GHz with absorbance value of 99.33%. As the polarization angle altered to 22.5^0, the structure still resonates at 9 GHz with absorbance of 99.53%. However, small resonance is noticed at 10 GHz with absorbance of 37.74%. The polarization angle is then increased to 45^0. The second resonance occurs at 10 GHz with a magnitude of 87.91%, nearly equal to absorbance at 9 GHz, which is 80.10%. As the polarization angle increased to 67.5^0, the frequency of 10 GHz dominates the resonance mode with the absorbance

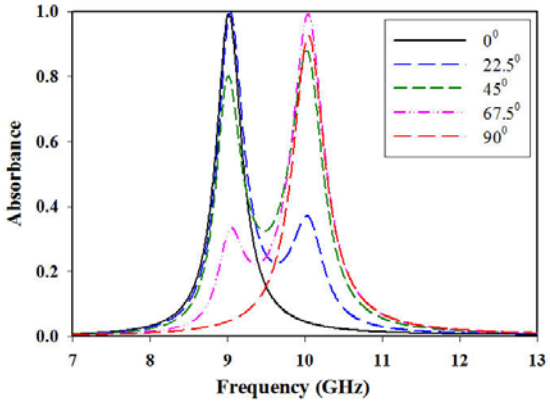

Figure 2: Polarization effect of circular ring metamaterial absorber with vertical copper lines

of 99.15% while the absorbance of 9 GHz became less effective, which is only 33.32%. The resonant mode totally converted to 10 GHz as the polarization angle become 90^0 with the absorbance of 92.51%.

The polarization dependence can be explained by observing the current distribution of the structure for different polarization angle. The E-field strength is recorded in Table 3. As can be seen, the E-field of 9 GHz is strong for polarization angle, θ of 0^0. This is due to the full effect of the copper lines that are placed vertically, parallel to the electrical component of incident electromagnetic waves. As the polarization angle increased, the E-field strength is decreased accept for θ of 45^0. At this polarization angle, dual resonant modes occur which is at 9 GHz due to the copper lines effect and 10 GHz due to the circular ring effect at the horizontal part. For E-field at 10 GHz, it shows the strength is increased as the θ increased. This is because the effect of copper line is decreased if θ increased and the structure can resonate at maximum when $\theta = 90^0$ for 10 GHz due to the absence of copper lines at the horizontal part of the circular ring absorber.

Table 3: The E-field strength for different polarization angle

Polarization angle [θ^0]	E-field at 9 GHz [x 10^5 V/m]	E-field at 10 GHz [x 10^5 V/m]
0	18.2	3.77
22.5	3.19	1.61
45	5.73	4.89
67.5	1.72	4.04
90	1.62	7.15

2.3. Circular ring metamaterial absorber with vertical and horizontal copper lines

As discussed earlier, the additional of copper lines within the copper ring shape will reduce the operating frequency of the metamaterial absorber, which is excellent if a compact size is the main consideration in the design. But, the polarization dependence makes this kind of structure impractical for certain application. To improve this problem, another copper lines are introduced horizontally

on the circular ring structure, as shown in Figure 1 (c). Based on Table 2, the length of copper lines is set to 1.24 mm to obtain resonant frequency of 9 GHz. The structure is then simulated for different polarization angles and the result is shows in Figure 3.

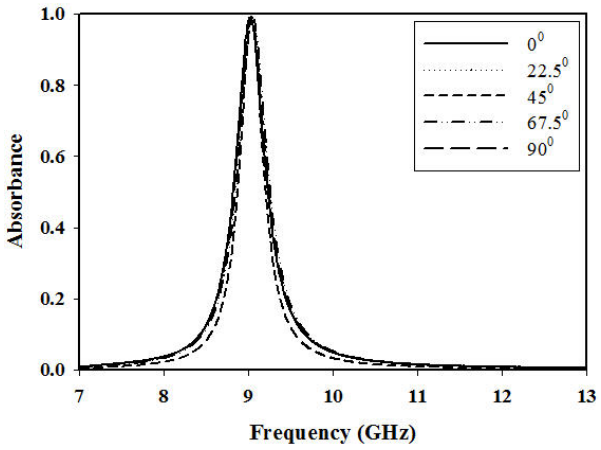

Figure 3: Polarization effect of circular ring metamaterial absorber with vertical and horizontal copper lines

From Figure 3, as the polarization of the incident wave altered from 0^0 to 22.5^0, 45^0, 67.5^0 and 90^0, the absorbance magnitudes and the resonance frequencies are almost unchanged. This indicates that this structure do not sensitive to any polarization angles. Figure 4 and Figure 5 shows the current distribution for different polarization angles. As can be seen in both figures, E-field and H-field can be maintain at high magnitudes for all polarization states due to the existing of both horizontal and vertical copper lines.

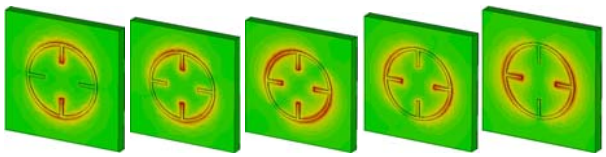

(a) 0^0 (b) 22.5^0 (c) 45^0 (d) 67.5^0 (e) 90^0

Figure 4: E-field Current distribution for different polarization angles

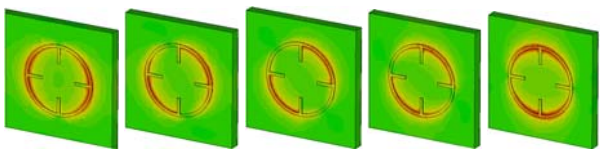

(a) 0^0 (b) 22.5^0 (c) 45^0 (d) 67.5^0 (e) 90^0

Figure 5: H-field Current distribution for different polarization angles

3. Conclusions

In conclusion, this report presents a comparison of three different shapes of metamaterial absorber. The existing of vertical copper lines will reduce the operating frequency for E-plane polarization incident waves but this structure is polarizations sensitive since the absorbance magnitude and resonance frequency are vary for each case. To overcome the polarization sensitivity, the horizontal copper lines are introduced together with the vertical copper lines in the circular ring structures.

Acknowledgements

Acknowledgements The authors thank the Ministry of Higher Education (MOHE) for supporting the research work, Research Management Centre (RMC), School of Postgraduate (SPS), Communication Engineering Department (COMM) Universiti Teknologi Malaysia (UTM) and all members of Advanced Microwave Lab P18 FKE-UTM for giving motivation, knowledge sharing and support of the research under grant no R.J130000.7923.4S007/04H38/4L811.

References

[1] H.A. Majid, M.K.A. Rahim, T. Masri, Microstrip antenna's gain enhancement using left-handed metamaterial structure, *Progress in Electromagnetics Research M*, Vol. 8, pp. 235−247, 2009.

[2] T. masri, M.K.A. Rahim, O.B. Ayop, F. Zubir, N.A. Samsuri, H.A. Majid, *Electromagnetic band gap structures incorporate with dula band microstrip antenna array*, Progress in Electromagnetics Research M, Vol. 11, pp. 111−122, 2010.

[3] J.A. Bossard, Xiotao Liang, Ling Li, Seokho Yun, D.H. Werner, B. Weiner, T.S. Mayer, P.F. Cristman, A. Diaz, *Tunable frequency selective surfaces and negative-zero-positive index metamaterials based on liquid crystal*, IEEE Transaction on Antenna and Propagation, Vol. 56, pp. 1308−1320, 2008.

[4] M. Abu, M.K. Abd Rahim, O.B. Ayop, Triple-band printed diploe antenna with single-band AMC-HIS, *Progress in Electromagnetics Research B*, Vol. 20, pp. 225−244, 2010.

[5] Landy, N. I., S. Sajuyigbe, J. J. Mock, D. R. Smith, and W. J. Padilla, Perfect metamaterial absorber, *Physical Review Letters*, Vol. 100, 207402, 2008.

[6] M. Li, H.-L. Yang, X.-W. Hou, Y. Tian, D.-Y. Hou, Perfect metamaterial absorber with dual bands, *Progress in Electromagnetics Research*, Vol. 108, pp. 37−49, 2010.

[7] K.B. Alici, A.B. Turhan, C.M. Soukoulis, E. Ozbay, Optically thin composite resonant absorber at the near-infrared band: a polarization independent and spectrally broadband configuration, *Optics Express*, Vol. 19, pp. 14260−14267, 2011.

[8] Xiopeng Shen, Tie Jun Cui, Junming Zhao, Hui Feng Ma, Wei Xiang Jiang, Hui Li, Polarization-independent wide-angle triple-band metamaterial absorber, *Optics Express*, Vol. 19, pp. 9401−9407, 2011.

Compact Wideband Antenna above a Wideband Non-Uniform Artificial Magnetic Conductor

Lana Damaj, Anne-Claire Lepage and Xavier Begaud

Institut Mines Telecom, Telecom ParisTech - LTCI CNRS UMR 5141, 46 rue Barrault, 75634 Paris Cedex 13, France.
*corresponding author, E-mail: Xavier.Begaud@telecom-paristech.fr

Abstract

Abstract— A compact wideband antenna place above a non-uniform Artificial Magnetic Conductor (AMC) is presented. The antenna is composed of a wideband Coplanar Waveguide (CPW) fed antenna, with wideband harmonic suppression characteristic using non-uniform defected ground structure (DGS). Besides, a non-uniform wideband Artificial Magnetic Conductor (AMC) is designed. The AMC unit cell is composed of a square patch into which a four arms spiral shape is etched. It exhibits a wider +/-90° bandwidth than the spiral unit cell and a smaller size than the square patch unit cell. The antenna is placed above the proposed AMC structure formed by 6x5 unit cells. The overall dimensions of the complete structure are $0.7x0.6\ \lambda_0^2$, where λ_0 is the free-space wavelength at the lowest frequency. It offers a low profile configuration with a total thickness of $\lambda_0/14.3$ and it is matched between 2.5 GHz and 5.4 GHz (73.5%). Furthermore, it has a stable main lobe radiation pattern in the E and H planes within the operating frequency band. Moreover, compared to the antenna without AMC, the broadside realized gain is significantly increased. A prototype has been realized and there is a good agreement between simulated and measured results. Furthermore, the proposed structure presents a size reduction of about 34 %, and better radiation characteristics in comparison with the conventional square AMC.

1. Introduction

Since the advent of the Artificial Magnetic Conductor (AMC), known also as High Impedance Surface (HIS), many researchers have used them to design novel electromagnetic devices or enhance the performance of the existing ones. AMC is a type of reflectors based on metamaterials and has been introduced by D. Sievenpiper in 1999 [1].

One of the main applications of these artificial structures is the design of low-profile or high-performance antennas (gain enhancement …). In this case, these artificial structures serve as the antenna ground plane. Actually, impenetrable ground planes are desirable in many communication systems to protect electronic devices, located beneath the antenna, from radiation and also to increase the gain of the antenna. The low profile design usually refers to an antenna structure whose overall height is less than one-tenth of the operating wavelength [2].

AMC surface is characterized by the reflection phase. It can be calculated by illuminating the surface with a plane wave at normal incidence and evaluating the phase difference between the reflected electric field and the incident electric field at the reflecting surface. The phase of the reflection coefficient of AMC, usually called reflection phase, varies from -180º to +180º with frequency. The AMC operating bandwidth is defined when the reflection phase varies from -90° to +90°, according to [3]. In this frequency band constructive interference occurs. Owing to this interesting characteristic, the AMC surface is used as a reflector to design low profile antenna. The most well known unit cell is the mushroom-like HIS composed of a square patch on a dielectric grounded slab and a via connecting the patch and the ground plane [1]. Subsequent studies have been done with different shapes of HIS unit cell. In [4], authors investigate the reflected phase response for several AMCs: mushroom-like, uniplanar compact EBG (Electromagnetic BandGap), Peano curve and Hilbert curve. They demonstrate that the mushroom-like unit cell exhibits a broader band than others.

However, these structures have a limited operating bandwidth. For wideband applications, several structures have been proposed. In [5], the AMC operating bandwidth, defined when the reflection phase varies from -90° to +90°, is 55.4% and it covers the entire Ku-band (from 12 GHz to 18 GHz). The AMC unit cell is composed of four squares patches with a cross in the center. Furthermore, this structure presents a relatively stable behavior with respect to the variation of the incident angle. The proposed structure in [6] is based on hexagonal unit cells without via. This structure exhibits a broad AMC operation bandwidth of more than 20% using a thin and low relative dielectric permittivity. Most of wideband structures are designed with a resonant frequency greater than 15 GHz. In [7], a parametric study for an AMC composed of metallic square patches has been performed. It has been shown that when the patch width increases, the resonant frequency and the +/-90° bandwidth decrease. Consequently, it is difficult to design wideband AMC at low frequencies.

2. Wideband AMC design principle

In order to develop AMC structures which exhibit wide bandwidth and stable resonant behavior with the change in incident angle, the non-uniform AMC structure has been introduced. The idea returns to the following equation [8] which provides the surface impedance of PEC parallel strips facing a TE plane wave:

$$\frac{X}{\eta_0} = F(p,w,\lambda) = \frac{p\cos\theta}{\lambda}\left[\ln\left(\frac{1}{\sin\left(\frac{\pi w}{2p}\right)}\right) + G(p,w,\lambda,\theta)\right] \quad (1)$$

Where jX is the surface impedance, η_0 and λ are free space wave impedance and wavelength respectively. G is a correction term for large angles of incidence. The width of the metal strip is w and the period is p. The incidence angle is θ. In [9], authors choose to increase p against the increase of θ, in order to keep X stable when w and λ are fixed. In other words, by gradually increasing p (increasing the gap between metal strips) from center elements to the side ones, more angular stability is achieved. In [9], a half wavelength dipole antenna is placed above a PEC ground plane, a uniform AMC and a non-uniform AMC, while all structures dimensions are kept fixed. The dipole is placed very close to the surface at $\lambda/12$. Comparison of different structures results shows that the non-uniform AMC exhibits a wider bandwidth than the uniform AMC, and a nearly identical gain. Similarly, using (1), it can be deduced that when p and λ are fixed, X can be kept stable by a proper decrease of w against the increase of θ. In [10], authors prove that the bandwidth is enhanced when the non-uniform AMC is used.
In this communication, from equation (1), in order to enhance the bandwidth of an AMC structure, we propose to vary the wavelength λ. When the period p and the width w are fixed, X can be kept stable by appropriate increase of the resonant frequency (decrease of λ) against the increase of θ, which means by gradually increasing f_0 from center elements to the side ones. The proposed AMC unit cell that accomplishes this characteristic is presented in the section 4. Then, the antenna, presented in section 3, above the proposed AMC is detailed in section 5. Finally, the conclusion of this work is given in section 6.

3. Antenna Design

The antenna consists of a CPW-fed bowtie antenna. The radiating element and the ground plane are printed on the top of a FR4 substrate with a thickness of h=0.8 mm, a relative permittivity of ε_r=3.7 and a loss tangent of tanδ=0.02. The upper part and lower part (ground plane) of the antenna have the same shape with almost the same dimensions. The width and the gap of the feed line are w=3 mm and g=0.25 mm respectively, in order to obtain an impedance of 50 Ω. This 50 Ω feed line is connected to the radiating element through a wideband tapered structure. This tapered transition transforms the antenna input impedance to 50 Ω. Then, a compact filter based on Defected Ground Structure (DGS) has been designed, in order to reject higher harmonics. The filter is composed of three non-uniform bowtie DGS unit cells. It is integrated in the ground plane (lower part) of the bowtie CPW-fed antenna as shown in Fig. 1. This co-designed antenna-filter operates in the frequency range between 2 GHz and 5.4 GHz (92%).

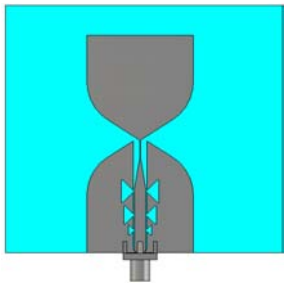

Figure 1: Geometry of the antenna with integrated filter

The harmonics are effectively rejected beyond 5.4 GHz. The antenna has an omnidirectional dipole-type radiation pattern. More details on this antenna can be found in a previous letter [11].

4. Choice of the AMC unit cell

Table 1 presents three AMC unit cells: the square patch as a reference, the spiral [12] and the proposed unit cell which is formed by a square patch where a spiral shape is etched.

Table 1: The studied AMC unit cells

AMC unit cells	f_0 (GHz)	Δf=+/-90° bandwidth (%)	Period p
Square patch 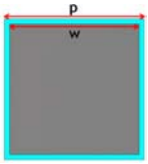	4.66	15	$0.2\lambda_0$
Spiral 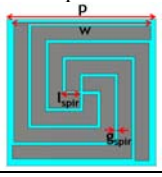	3.53	3.14	$0.165\lambda_0$
The proposed AMC 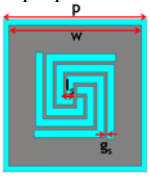	3.88	8	$0.18\lambda_0$

All unit cells presented in Table 1 have the same dimensions (p=14 mm and w=13 mm) and they are printed on the same substrate (FR4, ε_r=3.7, thickness=1.6 mm, tanδ=0.02). As it can be seen, the square patch AMC exhibits the widest +/-90° bandwidth but it has the biggest size compared to the free space wavelength at the resonant frequency (f_0). The spiral unit cell (l_{spir}=1.625 mm, g_{spir}=0.3 mm) has the smallest size and the narrower bandwidth. The proposed AMC unit cell (l_s=1 mm, g_s=0.3 mm) is a trade-off between both other unit cells. In fact, it exhibits a wider +/-90° bandwidth than the spiral unit cell and a smaller size than the square patch unit cell.

Moreover, when the size of the spiral slot, etched on the square patch, changes the resonant frequency varies also. Figure 2 shows the reflection phase coefficient of the proposed unit cell when the parameter l_s varies (all other parameters are fixed: p=14 mm, w=13 mm and g_s=0.3 mm). As can be seen, the resonant frequency f_0 shifts up when l_s decreases. Furthermore, f_0 also increases when g_s increases (Fig. 3). Therefore, using this unit cell we can vary f_0 when the period p and the width w are kept fixed.

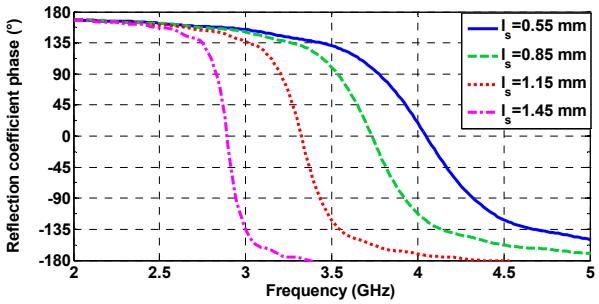

Figure 2: Reflection phase diagram when 'l_s' varies from 0.55 mm to 1.45 mm

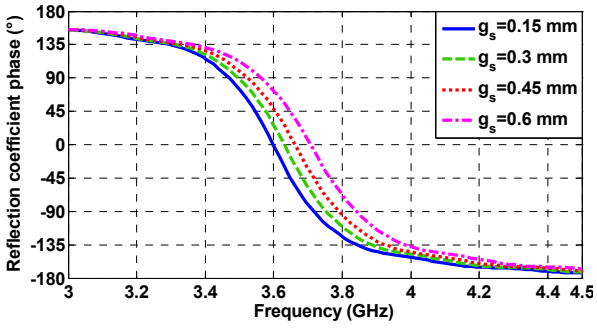

Figure 3: Reflection phase diagram when 'g_s' varies from 0.15 mm to 0.6 mm

5. Antenna performances above the proposed AMC

The previous antenna is placed above the proposed AMC structure formed by 6x5 unit cells (Fig. 4). The AMC surface is composed by six columns: the two columns at the center are designed to operate at the lower frequency of the operating bandwidth. Then the resonant frequency is increased gradually along the x axis and it does not change along y axis. A rectangular shape is engraved in the AMC structure below the CPW-fed filter in order to maintain performances of the matching transition and filter (Fig. 4b).

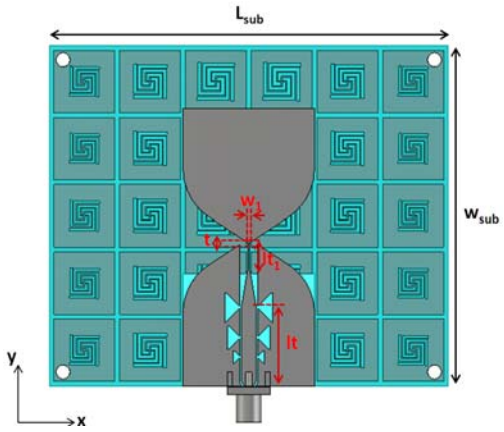

(a)

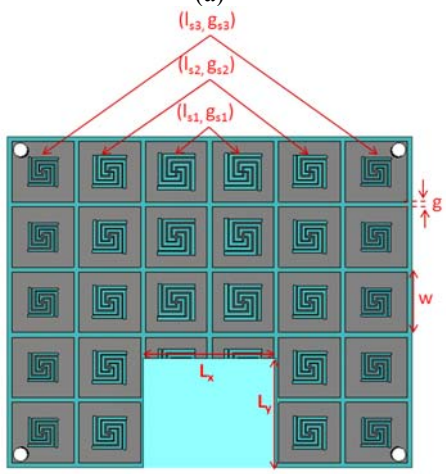

(b)

Figure 4: (a) Front view of the antenna above the AMC structure and (b) the bottom layer (the AMC structure)

An air layer is inserted between the antenna and the AMC structure to enhance the reflection coefficient and the broadside gain (Fig. 5a). Figure 5b presents the reflection coefficient of the whole structure (antenna-filter above the AMC structure) when the thickness of the air layer varies from 2 mm to 8 mm. A comparison indicates an improvement in the reflection coefficient when the thickness of the air layer h_{air} increases, thus we choose a thickness of 6 mm.

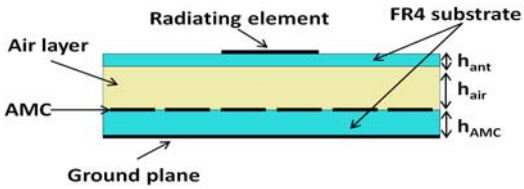

(a)

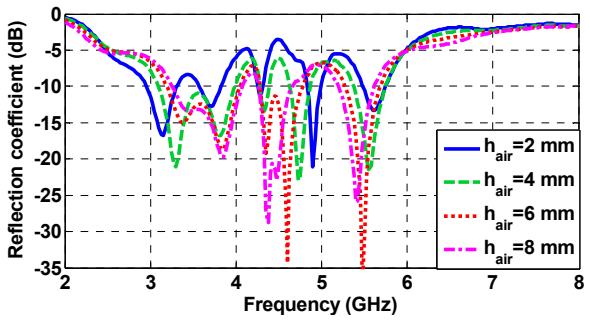

(b)

Figure 5: (a) Side view of the structure and (b) Reflection coefficient for different values of 'h_{air}'

The optimal dimensions of the proposed structure are listed in Table 2. The width and the gap of the feed line are w=3 mm and g=0.5 mm respectively, in order to obtain an input impedance of 50 Ω.

Table 2: Physical Parameters of the whole structure

Parameters	Values (mm)	Parameters	Values (mm)
L_{sub}	85	W_1	0.25
W_{sub}	71	t	3.4
Lt	11	L_x	28
lt_1	12	L_y	23.5
l_{s1}	1	g_{s1}	0.25
l_{s2}	0.9	g_{s2}	0.25
l_{s3}	0.8	g_{s3}	0.3
W	13	p	14
h_{air}	6	h_{AMC}	1.6
h_{ant}	0.8		

An experimental prototype of the antenna above the proposed AMC with optimal design was realized and tested in order to validate simulation results (Fig. 6). The simulations were performed using CST Microwave Studio® (transient solver). The simulated and measured magnitudes of the reflection coefficient ($|S_{11}|$) are shown in Fig. 7. There is a good agreement between simulated and measured $|S_{11}|$. The proposed structure (antenna above AMC) is matched between 2.5 GHz and 5.4 GHz (73.5%) when maintaining $|S_{11}|$ less than -10 dB over the operating bandwidth. The designed structure covers many standards such as : UWB (Lower Band in Europe, 3.1-4.8 GHz), IEEE 802.16 (WiMAX) (2.5 - 2.6 GHz, 3.4 - 3.6 GHz) and LTE (2.5 - 2.7 GHz). Figure 7 shows also that higher harmonics are reduced. The complete structure has a total size of 85 x 71 mm^2 = 0.7 x 0.6 λ_0^2 with a thickness of h_t=8.4 mm≈λ_0/14.3 (λ_0 being the free space wavelength at 2.5 GHz).

(a)

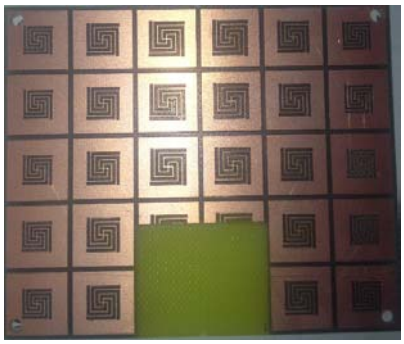

(b)

Figure 6: (a, top layer) Antenna prototype and (b, bottom layer) the proposed AMC

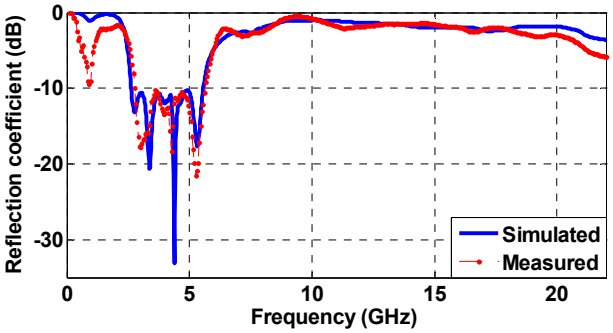

Figure 7: Simulated and Measured reflection coefficient of the whole structure

The simulated and the measured radiation pattern realized gains in E and H-planes are depicted in Fig. 8 and Fig. 9. There is a good agreement between simulated and measured results despite a slight difference in the HPBW angle. The cross-polar radiation pattern level is 10 dB less than the co-polar radiation pattern level in the H-plane. In E-plane, the simulated cross-polar level is lower than -20dB. The antenna above the AMC has a directional radiation pattern in both planes. There is a slight dissymmetry in the E-plane at 3.5 GHz due to the dissymmetry of the structure in this plane. Simulations show that the HPBW on the E-plane varies from 35° to 75° and on H-plane from 41° to 68°.The measured HPBW fluctuate from 40° to 80° on the E-plane and from 50° to 72° on the H plane.

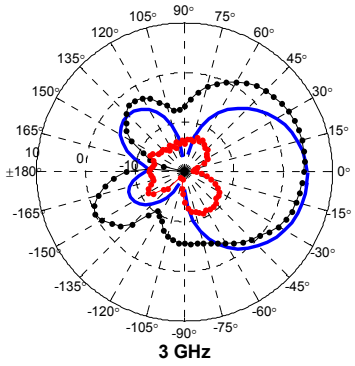

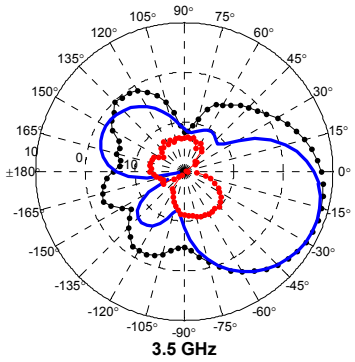

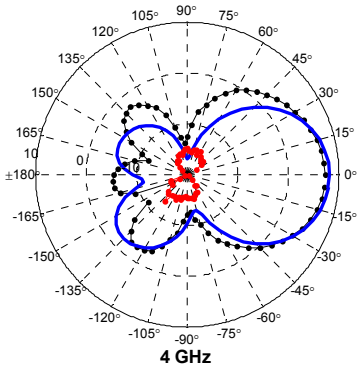

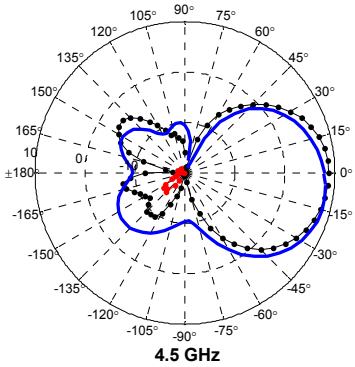

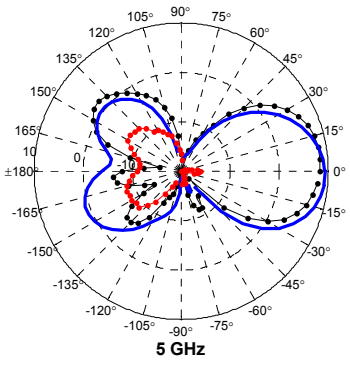

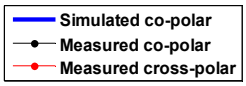

Figure 8: Simulated and measured realized gain (dB) radiation pattern in E-plane (yoz)

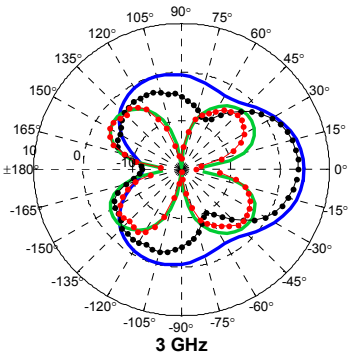

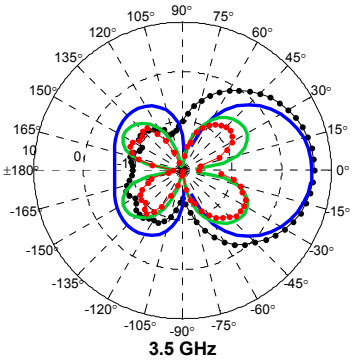

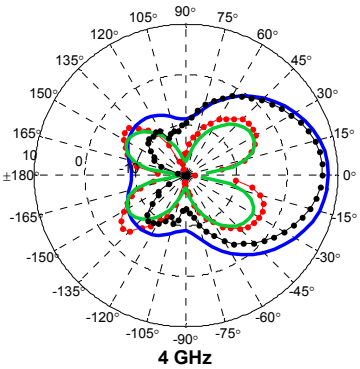

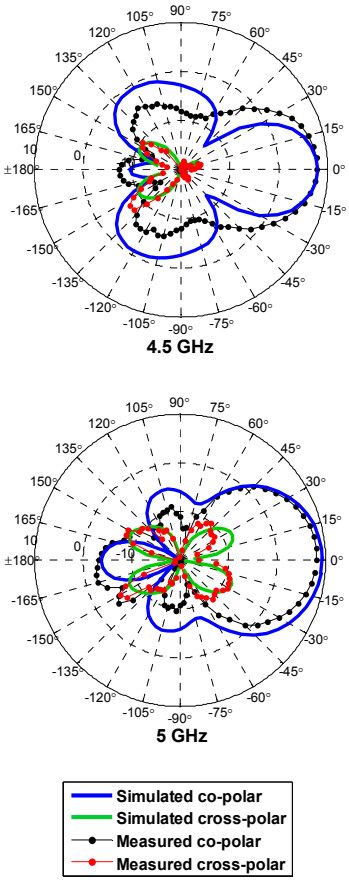

Figure 9: Simulated and measured realized gain (dB) radiation pattern in H-plane (xoz)

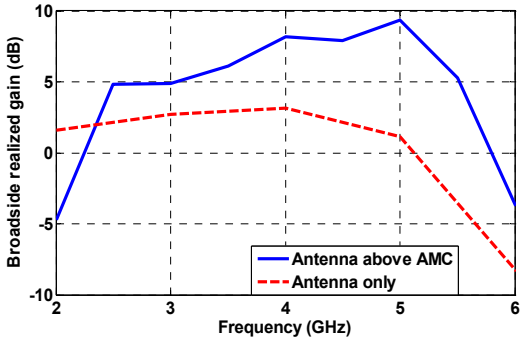

Figure 10: The broadside realized gain of the antenna-filter with and without AMC

The broadside realized gain of the whole structure varies from 5 dB to 9.5 dB within the operating bandwidth, which yields to an average gain improvement of about 5 dB (Fig. 10).

6. Conclusion

In this contribution, wideband bowtie CPW-fed antenna having wideband harmonic suppression above a non-uniform AMC structure has been presented. The realized structure operates in the frequency range between 2.5 GHz and 5.4 GHz (73.5%). The measured and simulated reflection coefficients are in good agreement. The antenna has a directional radiation pattern in E and H planes. The total size of the complete structure is $85\text{x}71\text{mm}^2=0.7\text{x}0.6\lambda_0^2$, where λ_0 is the free-space wavelength at 2.5 GHz. Moreover, the broadside realized gain of the antenna with AMC increases.

References

[1] D. Sievenpiper, *High-Impedance Electromagnetic Surfaces*, Ph.D. Dissertation, University of California, Los Angeles, 1999.

[2] F. Yang, Y. Rahmat-Samii, *Electromagnetic Band Gap Structures in Antenna Engineering*, Cambridge University Press, Chapter 6, 2009.

[3] D. Sievenpiper, L. Zhang, R. Broas, N. Alexopolous, E. Yablonovitch, High-impedance electromagnetic surfaces with a forbidden frequency band, *Microwave Theory and Techniques, IEEE Transactions on*, vol. 47, no. 11, pp. 2059-2074, November 1999.

[4] J.R. Sohn, K.Y. Kim, H.-S Tae, H.J. Lee, Comparative study on various artficial magnetic conductors for low-profile antenna, *Progress In Electromagnetics Research*, Vol. 61, 27-37, 2006.

[5] Y. Wenwen, H. Guang, H. Wei, Wideband artificial magnetic conductor structure for Ku-band antenna applications, *Microwave, Antenna, Propagation and EMC Technologies for Wireless Communications, 2009 3rd IEEE Intern. Symposium on,* pp. 954-957, 27-29 October 2009.

[6] M. de Cos, Y. Alvarez, F. Las-Heras, Novel Broadband Artificial Magnetic Conductor With Hexagonal Unit Cell, *Antennas and Wireless Propagation Letters, IEEE,* vol. 10, pp. 615-618, 2011.

[7] M. Grelier, *Miniaturisation des antennes large bande à l'aide de matériaux artificiels*, Ph.D. Dissertation, Telecom ParisTech, Paris, France, Chapter 4, 2011.

[8] N. Marcuvitz, *Waveguide Handbook* (IEE Electromagnetic Waves), New Ed ed.Institution of Engineering and Technology, chapter 5, 1986.

[9] M. Hosseini, A. Pirhadi, M. Hakkak, Design of a Non-uniform High Impedance Surface for a Low Profile Antenna, *Progress In Electromagnetics Research Symp, Cambridge, USA,* 2006.

[10] M. Hosseini, A. Pirhadi, R. Fallahi, M. Hakkak, Bandwidth Enhancement of a Low Profile Antenna by Applying non-Uniformity to its High Impedance Ground Plane, *Mathematical Methods in Electromagnetic Theory, 2006 International Conference,* pp. 202-204, 26-29 June 2006.

[11] L. Damaj, A.C. Lepage, X. Begaud, Compact wideband harmonic suppressed antenna using non-uniform cascaded defected ground structure, *Microwave and Optical Technology Letters*, vol.55, no.4, pp.829-835, 27 February 2013.

[12] L. Mouffok, L. Damaj, X. Begaud, A.C. Lepage, H. Diez, Mutual coupling reduction between dual polarized microstrip patch antennas using compact spiral Artificial Magnetic Conductor, *Antennas and Propagation (EUCAP), Proceedings of the 5th European Conference on,* pp. 909-912, 11-15 April 2011.

Keynote presentations

Light Harvesting with Metasurfaces: Applications to Sensors and Energy Generation

David T. Crouse[1], Eli Lansey[2], Isroel Mandel[3], Ian Hooper[4]

[1]Department of Electrical Engineering, The City College of New York, 160 Convent Avenue, N.Y. 10031, USA
[2]Riverside Research, 156 William St, N.Y. 10038, USA
[3]Department of Physics, The City College of New York, 160 Convent Avenue, N.Y. 10031, USA
[4]Electromagnetic and Acoustic Materials Group, Department of Physics and Astronomy,
University of Exeter, Stocker Road, Exeter EX4 4QL, UK
David Crouse, dcrouse@ccny.cuny.edu

Abstract

Metasurfaces have been receiving increasing interest due to the complex array of radiation controlling properties that are possible with single layer films. This talk and work will focus on metasurfaces that can provide light filtering according to wavelength, polarization, and other properties of an incident beam, and applied to a variety of sensors. Also, metasurfaces that exhibit light trapping and localization that can be used for energy generation will be described. One last group of metasurfaces will be discussed that display complex dispersion curves that exhibit fast and slow light properties that can be used to study complex electromagnetic phenomena.

1. Introduction

Composite engineered surfaces of various forms have been researched for years in many different technology fields (e.g., microwave, RF, optical) for applications that include electromagnetic (EM) radiation filtering to determine the polarization state and/or wavelength of an incident beam, or to perform beam steering, light harvesting, and light concentrating [1-19]. This field has received increased attention recently because of the development of surface structures, composed of optically resonant metal structures (i.e., antennas) that operate in the infrared and visible spectral regions [20]. Yet a clear line that delineates what is, and what is not, a metasurface does not exist. From an applications perspective, and from the perspective of device engineers, such a delineation is artificial and irrelevant - what matters is designing a surface that performs a particular desired function. To be considered a true metamaterial or metasurface, it is often thought necessary that the structural feature sizes of the "meta-atoms" need to be smaller than $\lambda/10$ where λ is the wavelength of light to which the metamaterial is designed to respond. Restricting oneself to such materials and surfaces is very limiting and does not include the wide array of important electromagnetic phenomena that occur within photonic crystals, plasmonic structures, and other structures (e.g., the optical antenna arrays that typically make up the new generation of metasurface structures). With these structures, the feature sizes of the structural elements, the meta-atoms, may be approximately $\lambda/4$ to $\lambda/2$ in size, yet with these structures, one can perform a wide range of light management functions, from complex polarization and wavelength filtering for advanced imaging systems, to light trapping and harvesting for renewable energy devices, light concentration to increase the sensitivity of detectors, and beam-steering and forming. And with these structures being able to have EM properties that go well beyond what naturally occurring materials can achieve, they legitimately fit within a broader definition of metamaterials. This paper will review some of the work that our group at the National Science Foundation Industry/University Cooperative Research Center for Metamaterials are doing on the development of metasurfaces.

In this paper, metasurfaces that perform photon sorting in the microwave spectral range will be reviewed and described, as well as engineered surfaces with which one can engineer the shape of surface plasmon dispersion curves.

2. Photon Sorting using Waveguide Cavity Modes within Patterned Metal Surfaces

One particularly attractive light-management tool is the ability of a surface to sort EM radiation according to wavelength and to channel photons with different energies to different regions of a surface. The resulting sorted photons can then be individually absorbed, collected or detected. Such a surface can be used for several important applications. One application is dual wavelength IR discrimination and detection within a single small device. A second application is for renewable energy applications where the incoming solar radiation is split according to wavelength and the different energy photons are channeled to different absorbers that collect the light and transfer the optical energy to electrical energy; this structure avoids the "thermalization losses" inherent in single-junction silicon solar cells.

With the devices developed in our works [21-22], we aimed to have the engineered surfaces perform three functions: photon sorting, light localization, and absorption. Additionally, the devices were designed to perform these functions on incident light of any polarization and over a wide range of angles of incidence. As stated in [22], there has been some prior research on multi-band frequency selective surfaces (FSSs) to increase the capabilities of multi-frequency microwave antennas, yet these structures add discrete

subreflectors that perform frequency specific reflection and these additional discrete structures add weight and size to the antenna. Additionally, photon sorting has been performed using bimetallic nanoantennas, and plasmonic gratings in the visible spectral regime. Yet these devices performed only one function, i.e., photon sorting, and often suffered from polarization dependence and angle of incidence dependence of the incident radiation, as opposed to the structures described in this paper.

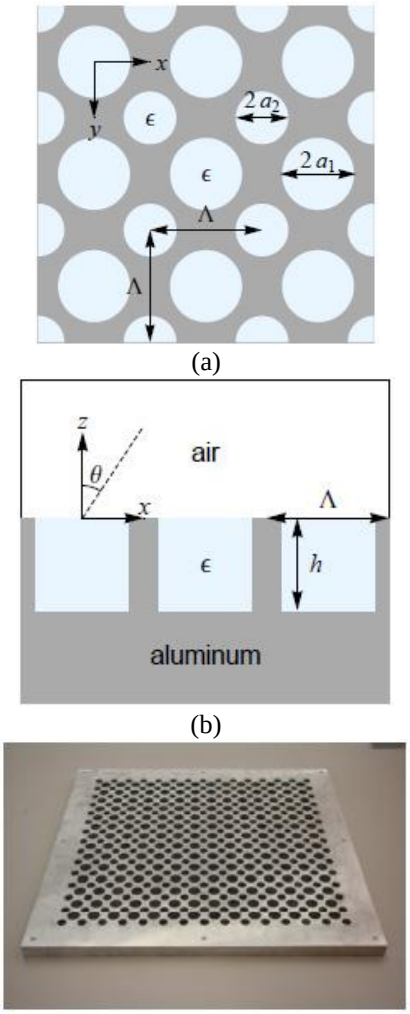

Figure 1: A schematic of periodic cylindrical cavities in a metal is shown from top down (a), in a cross section through one set of cavities (b), and the final fabricated device (c). The gray region represents the metal, the light blue regions are the dielectric-filled apertures, and the white is the superstrate (air) above the cavities. Here Λ= 26 mm, a_1 = 8.03 mm, a_2 = 5.74 mm, h = 7 mm, and θ is the angle of incidence [22].

In our work described in [22], a sub-wavelength sized aperture array (SAA) was designed to locally (i.e., near the surface) split microwave radiation according to frequency and to channel the light to differently sized apertures within each repeating unit cell and to individually absorb the photons within two non-overlapping spectral bands. The SAA was then fabricated and tested. Even though this particular structure was designed to operate in the microwave spectral region, the underlying principles can be applied to SAA that operate in other spectral regions [21]. To do this, one scales the geometric feature sizes of the structure and the wavelength of operation is correspondingly scaled (i.e., reducing all the dimensions of the physical features, say by one half reduces the wavelength of operation by one half). Of course, scaling the structure by a very large amount, say from the microwave to the visible spectral region, generally requires one to include the increased optical loss of the materials and also generally requires the use of different materials for the SAA.

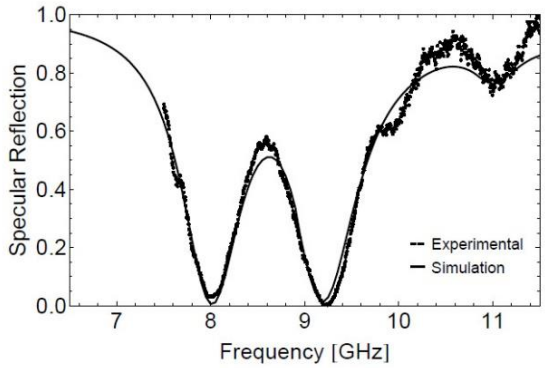

Figure 2: The simulated and experimental specular reflection from the metasurface for *s*-polarized radiation at θ=17˚ angle of incidence. The individual dips at 8.10 GHz and 9.25 GHz are due to the two different WCMs [22].

But in the microwave, metals such as copper and aluminum are low loss. The structure that was designed in [22] is a compound cavity array. The cavities were not deeply subwavelength in size, they were approximately $\lambda/2\sqrt{\epsilon}$ where ϵ is the complex dielectric permittivity of the material filling the cavities. Thus, this structure is not a pure metamaterial or metasurface that appears to be homogenous from the perspective of the incident radiation. The EM modes responsible for the SAA's properties are waveguide cavity modes (WCMs) that can be supported by the cavities. The photon sorting and light channeling themselves can be understood by considering the time-reversed situation, because Maxwell's equations are time-reversal invariant (with some important exceptions [22]). In the time-reversed situation, if one can excite the WCMs of different energies supported by differently sized cavities, then the WCMs will not be entirely confined to the cavity and will radiate out into free space, with the outwardly radiating energy diverging. This outwardly radiating diverging beam in the time-reversed frame of reference is an inwardly incident beam that converges to cavities in the forward-time frame of reference. This simple explanation describes how the light can experience the effects

of the cavities prior to encountering any physical object (i.e., the metal surface); more detailed explanations can be found in [22].

The photon sorting structure is a two-dimensional square array of subwavelength cylindrical cavities embedded in aluminum. Each unit cell contains two cavities of different radii and identical heights, arranged in a rhombic lattice, see Fig. 1. The individual cavities within the unit cell are designed to support an effective-cavity resonance or cavity mode (CM) with amplified EM fields, where the lowest order mode's frequency dependence is approximately given by [22]:

$$f \approx \frac{c}{2\pi\sqrt{Re[\varepsilon]}}\left[\left(\frac{\pi}{h_{eff}}\right)^2 + \left(\frac{1.841}{a}\right)^2\right]^{1/2} \qquad (1)$$

where a is the cavity radius and h_{eff} is the effective height of the cavity (consisting of the physical geometric height plus some additional length as determined by the WCM's energy and mode order). Because the structure is to absorb the photons channeled to the two different apertures within each unit cell, an absorbing material was placed in the cavities. This material was a silicone elastomer dielectric (Sylgard 184) doped with 8.36% graphite; this resulted in an complex permittivity of $\varepsilon = 4.33 + 0.22i$. This value of ε was carefully chosen to maximize concentration and achieve optimal coupling between the incident beam and the cavity mode [23]. The two cavities were designed such that isolate two non-overlapping absorption bands that occur at 8.10 GHz and 9.25 GHz. To achieve this, the dimensions of the structure was a_1 = 8.03 mm, a_2 = 5.74 mm and h = 7 mm.

The simulated results were obtained using HFSS. The experimental results were obtained using a vector network analyzer and broad band horn antennas for the emission and detection of the s and p-polarized radiation for angles of incidence between 5 and 35 degrees. Figure 2 shows the simulated and measured specular reflection showing an agreement between the two curves. Figure 3 shows the simulated absorption in each cavity, showing that there is a high level of photon sorting and separate absorption.

As was stated before, the use of WCMs to perform photon sorting and detection can be applied to different spectral regions. Of particular interest is photon sorting in the infrared and visible spectral ranges. In the IR, multi-band IR detectors can be designed; whereas in the visible and near-IR spectral regions, multi-junction solar cells can be developed. To demonstrate this concept in the IR, we described in [21] the design, fabrication and testing of a IR photon sorting meta-surface of a very similar design as the microwave structure shown in Fig. 1, but with the structural feature sizes scaled down considerably: Λ = 500 nm, a_1 = 80 nm, a_2 = 125 nm, h = 35 nm, and with the metal being gold (with the complex permittivity provided by Palik [24]) and amorphous silicon (a-Si) filling the cavities, as shown in Fig. 4b. In this structure, photon sorting and selective transmission through the two differently sized apertures were the objectives. The results of the photon sorting in this higher energy spectral range (relative to the microwave) are not as dramatic in terms of photon sorting efficiency and agreement between simulated and measured results due to several issues. One issue being the increased optical absorption within the metal. The second issue is the quality of the fabricated structure; better defined cavities, more consistently shaped cavities can be achieved for the larger size scale microwave structures than for the IR metasurfaces.

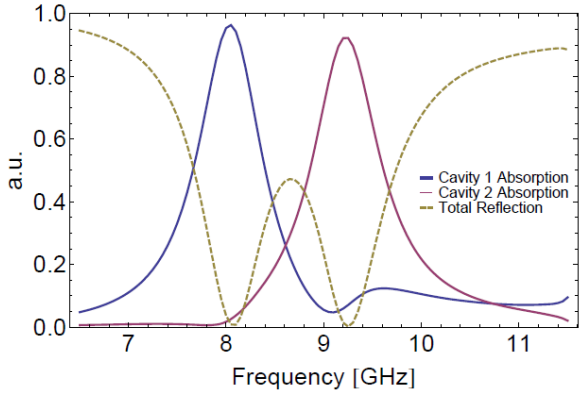

(a)

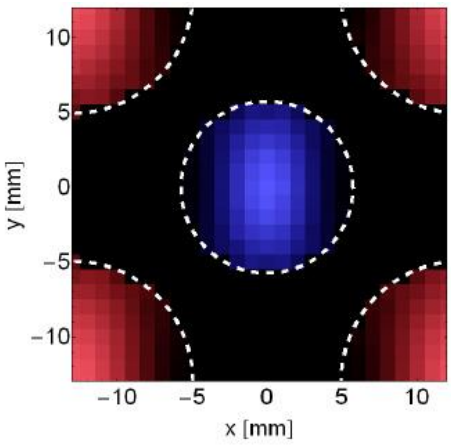

(b)

Figure 3: (a) The simulated total reflection and the absorption in the two different cavities. It is seen that the structure performs efficient photon sorting and absorption. (b) A false-color plot of the volume loss density at a height of 3.5 mm inside the cavities at 8.10 GHz (red) and 9.25 GHz (blue) overlaid on the same plot [22].

Yet the concept of photon sorting and individual absorption/detection via polarization independent WCMs (largely polarization independent, see [21] for more discussions) is still evident, and further optimization and fabrication process development could provide a compelling way to perform dual-wavelength IR detection in a small, lightweight single layer metasurface.

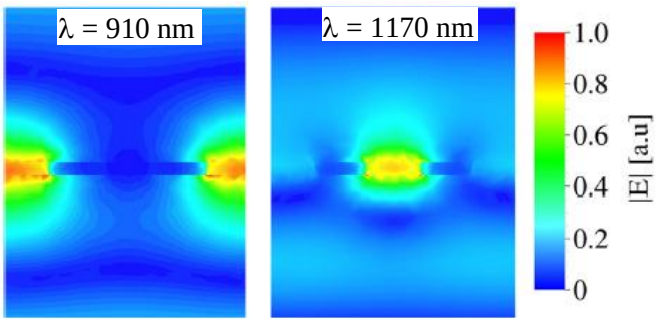

(a)

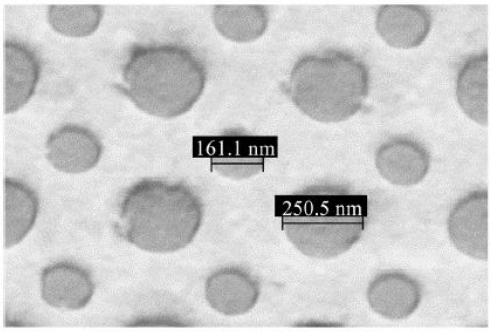

(b)

Figure 4: (a) The fabricated structure (dimensions given in the text). (b) The simulated electric field magnitude for a normal incident beam of λ = 910 nm and λ = 1170 nm. The simulated results show that efficient photon sorting should occur, yet due to the more challenging fabrication of these small structures, the structural variations produce widening and shifts of the absorption peaks [21].

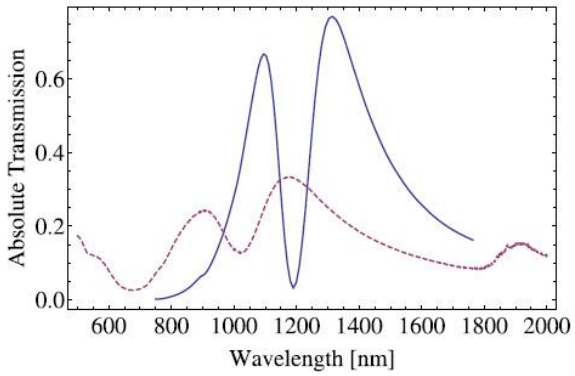

Figure 5: The simulated (solid blue) and measured (dashed red) absolute transmission. It is seen that the two observed (measured) peaks are shifted and broadened relative to the simulated peaks.

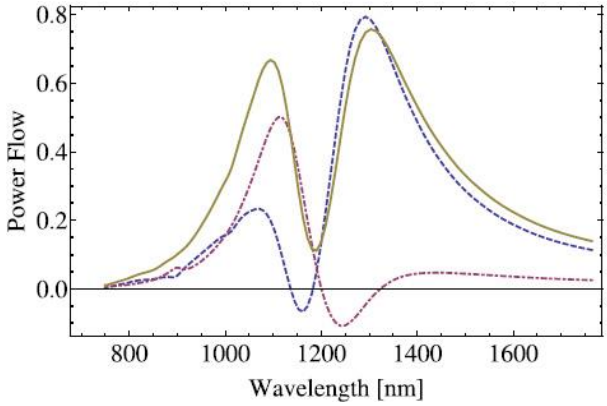

Figure 6: The simulated power flow through the structure. The smaller (red dot-dashed) cavity selects and transmits IR radiation of smaller wavelength (910 nm) while the larger (blue dashed) cavity selects and transmits IR radiation of larger wavelength (1170 nm) [21].

3. Dispersion Engineered Plasmonic Structures

The ability to custom design the dispersion curves of surface plasmons (SPs) would have great utility in the study of complex EM phenomena including the filtering and trapping of SP modes, and in studying slow and fast light phenomena. For such studies, one would like a material that supports SPs that has a dispersion curve that exhibits a zero group velocity or a negative group velocity. Dispersion curves for SPs are dependent on the shape of the metal surface and the overall structure of the metal/dielectric system. For example, for flat metal surfaces, the SP dispersion curve is given by:

$$k_{sp} = k_o \left(\frac{\varepsilon_m \varepsilon_d}{\varepsilon_m + \varepsilon_d}\right)^{1/2} \qquad (2)$$

where k_{sp} is the in-plane momentum of the SP, $k_o = \omega/c$ and ε_m and ε_d are the frequency dependent complex permittivities of the metal and bounding dielectric material respectively. Eq. 2 results in a monotonically increasing dispersion curve for frequencies below $\omega_p/\sqrt{2}$ and for a bounding dielectric of vacuum. Thus there are no SP momentum ranges where the SP displays a negative or zero group velocity that could be used to trap or concentrate the SPs. There are systems that display negative and/or zero SP group velocities, including SPs in thin metal films that has symmetric and asymmetric SP modes and SPs on elliptically shaped metallic particles [25-28], yet such systems do not provide the flexibility to "dial-in" the desired SP dispersion curve that one would want in order to study complex SP phenomena.

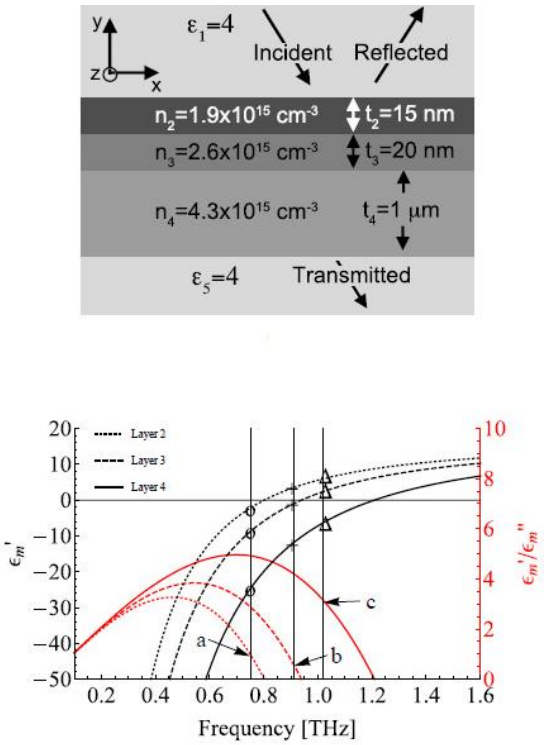

Figure 7: *Top:* The structure studied in this work and in [29]. *Bottom:* The real part of the permittivity of each layer, and the ratio of the real to the imaginary part.

In [29], we describe a method to engineer SP dispersion curves by using multiple, flat and unpatterned layers where each layer has a different free electron concentration *n*. Such control of *n* can be achieved using doped semiconductors and doped oxides [30] and can be used to tune the value of ε_m for each layer, as described by the Drude model:

$$\varepsilon_m = \varepsilon_\infty - \frac{\omega_p^2}{\omega(\omega+i\Gamma)} \qquad (3)$$

where ε_∞ is the high frequency permittivity, $\Gamma = e/m_{eff}\mu_e$ is the damping rate with *e* being the electron charge, m_{eff} and μ_{eff} the electron effective mass and mobility respectively, and with $\omega_p^2 = ne^2/\varepsilon_o m_{eff}$ being dependent on *n*. Thus each layer can have a different ε_m and when applying this to Eq. (2) leads to different steps in the dispersion curve given by the equation [29]:

$$\omega_{step,i} = \frac{\sqrt{\omega_{p,i}^2 - \Gamma^2(\varepsilon_\infty+\varepsilon_d)/4}}{\sqrt{\varepsilon_\infty+\varepsilon_d}} \qquad (4)$$

where the subscript *i* refers to the layer. This concepts relies on how the EM fields of the SP modes change (i.e., distribute themselves or confine themselves) as the in-plane momentum k_{sp} goes from a small value to larger values.

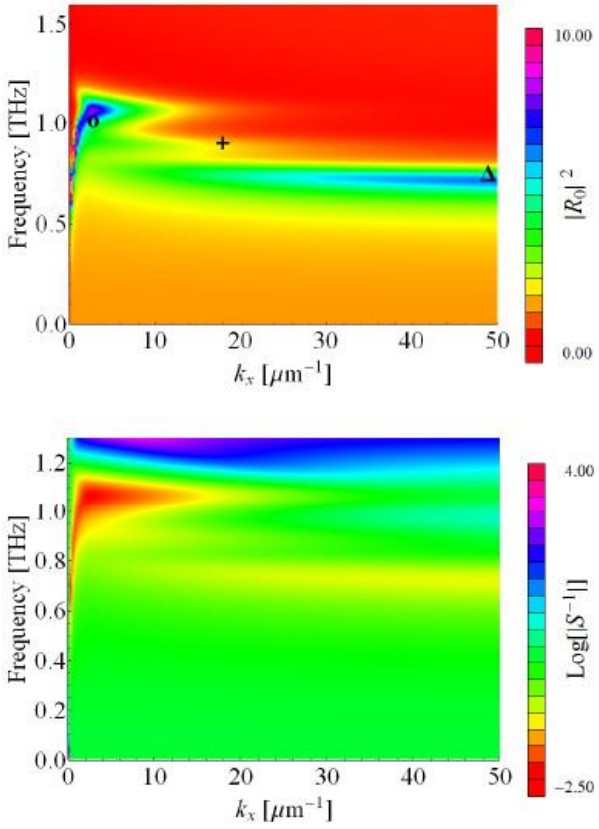

Figure 8: *Top:* The reflectance (i.e., $|R|^2$), assuming a unit amplitude plane wave. Of course, for such large k_x values, the plane wave is not within the light cone, but such excitation can be achieved with radiating dipoles placed near the surface. *Bottom:* The value of the logarithm of $|S^{-1}|$. Self-sustaining modes, such as SPs have poles in $|S^{-1}|$ [29].

Because of the relationship $k_\perp = i\kappa = \sqrt{\varepsilon_d k_o^2 - k_{sp}^2}$, where $k_\perp$ is the out-of-plane momentum and κ is the decay constant, at low k_{sp} values, the EM fields of the SP extend to a greater extent throughout all the layers of the structure. But as k_{sp} increases, so does κ and the fields are increasingly confined to evermore higher-lying layers (i.e., layers that are nearer the source exciting the SPs).

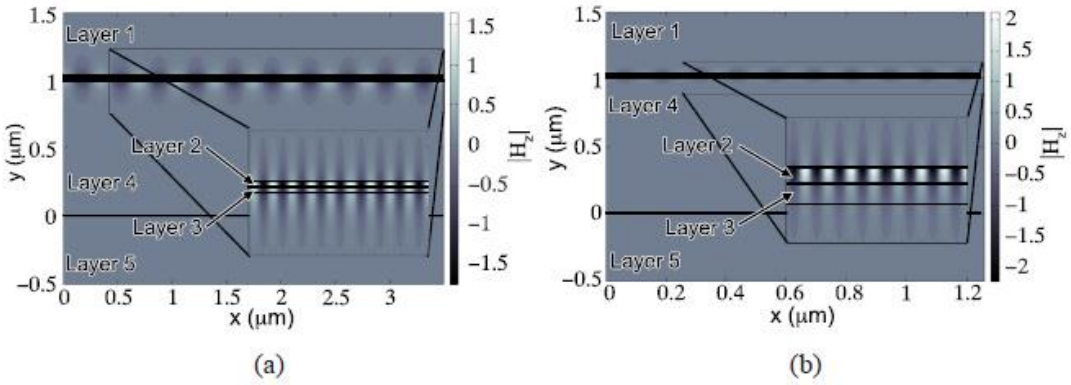

Figure 9: *Left:* The value of *Re(H_z)* for ν = 0.91 THz and $k_x = 18\ \mu m^{-1}$ (point "+" in the *Top* figure in Fig. 8). The EM fields of the SP are largely confined to Layers 1, 2 and 3. *Right:* The value of *Re(H_z)* for ν = 0.75 THz and $k_x = 50\ \mu m^{-1}$ (point "Δ" in the *Top* figure in Fig. 8). The EM fields of the SP are largely confined to Layers 1 and 2 [29].

Thus for low k_{sp}, the energy of the SPs will tend to assume the value of the thickest, bottom most layer, and as k_{sp} increases, changes in the SP energy will occur as the SP assumes the value appropriate for the layer within which its fields are increasingly confined. Figures 7 - 10 illustrate this concept for a simulated 3 layer system (with two additional semi-infinite layers being the superstrate and substrate of $\varepsilon = 4$). The structure has 3 layers of different doping, Layers 2, 3, and 4. Layer 2 has the following properties: $n_2 = 1.9 \times 10^{15} cm^{-3}$ and t_2 = 15 nm; Layer 3 $n_3 = 2.6 \times 10^{15} cm^{-3}$ and t_3 = 20 nm; Layer 4 $n_4 = 4.3 \times 10^{15} cm^{-3}$ and t_4 = 1 μm. All layers have $\mu_e = 1.5 \times 10^5\ cm^2/V\ s$, $m_{eff} = 0.015 m_o$, and $\varepsilon_\infty = 15.7$. Layers 1 and 5 are considered dielectrics with frequency independent permittivity values of $\varepsilon = 4$.

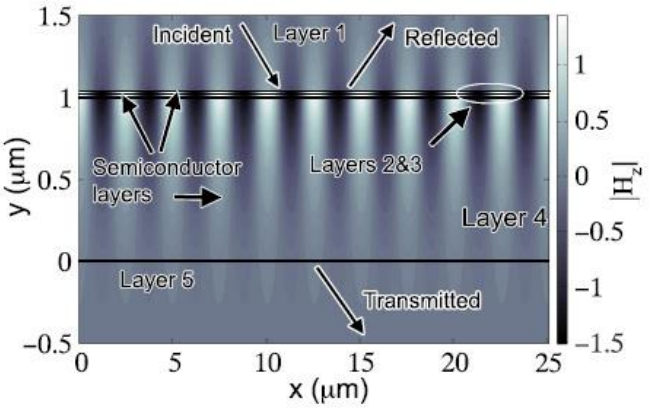

Figure 10: The value of *Re(H_z)* for ν = 1.02 THz and $k_x = 2.5\ \mu m^{-1}$ (point "o" in the *Top* figure in Fig. 8). It is seen that the EM fields of the SP for this mode extends throughout the entire structure, thus the thick Layer 4 will largely determine the energy of this SP mode [29].

With three separate layers, each having different values of *n* and thus different SP frequencies given by Eq. (4), one would expect 3 different steps in the dispersion curve with the steps at the frequencies given by Eq. (4). Using both a rigorous coupled wave algorithm (RCWA), and finite difference time domain (FDTD) methods (Lumerical), the dispersion curves do indeed show steps, or levels with the frequencies predicted by Eq. (4). And by studying the EM field distributions for SP modes at the three different "steps" of the dispersion curve, the distributions agree with what is expected, namely that the EM fields of the SPs for increasing k_{sp} are increasing confined to the top thinner layers of the structure which impart to the SP a different energy according to the layer's free electron concentration *n*.

4. Discussion and Conclusions

Two different concepts involved with sorting and absorbing electromagnetic modes were reviewed and described in this work. The first concept involved photon sorting and individual absorption by using compound aperture arrays in metal films. The two differently shaped cavities supported two waveguide cavity modes of different energy, and as incoming light approaches the film, the photons converge to the cavity that supports excitations that match their energy. Once the WCM is excited, the EM radiation is absorbed and can be used to generate a photocurrent, as would be done in dual-wavelength detectors, or to drive electron-hole pair generation, separation and collection, as would be done in a solar cell. The second concept involved the method to engineer the dispersion curves of surface plasmons to produce SP modes that have zero or negative group velocities. The structures required for this are simple and are only flat multi-layered semiconductors of varying free electron charge concentrations. With such a system, SP trapping and filtering can be studied that would include slow and fast light phenomena.

References

[1] S. John, "Strong localization of photons in certain disordered dielectric superlattices," Phys. Rev. Lett. **58**, 2486–2489 (1987).

[2] E. Yablonovitch, "Inhibited spontaneous emission in solid-state physics and electronics," Phys. Rev. Lett. **58**, 2059–2062 (1987).

[3] M. Lester and D. C. Skigin, "An optical nanoantenna made of plasmonic chain resonators," J. Opt. **13**, 035105 (2011).

[4] T. Li, S. M. Wang, J. X. Cao, H. Liu, and S. N. Zhu, "Cavity-involved plasmonic metamaterial for optical polarization conversion," Appl. Phys. Lett. **97**, 261113 (2010).

[5] R. A. Shelby, D. R. Smith, S. C. Nemat-Nasser, and S. Schultz, "Microwave transmission through a twodimensional, isotropic, left-handed metamaterial," Appl. Phys. Lett. **78**, 489–491 (2001).

[6] R. A. Shelby, D. R. Smith, and S. Schultz, "Experimental verification of a negative index of refraction," Science **292**, 77–79 (2001).

[7] `D. Schurig, J. J. Mock, B. J. Justice, S. A. Cummer, J. B. Pendry, A. F. Starr, and D. R. Smith, "Metamaterial electromagnetic cloak at microwave frequencies," Science **314**, 977–980 (2006).

[8] J. Valentine, J. Li, T. Zentgraf, G. Bartal, and X. Zhang, "An optical cloak made of dielectrics," Nat. Mater. **8**, 568–571 (2009).

[9] D. Crouse, "Numerical modeling and electromagnetic resonant modes in complex grating structures and optoelectronic device applications," IEEE Trans. Electron Devices **52**, 2365–2373 (2005).

[10] D. Crouse, A. P. Hibbins, and M. J. Lockyear, "Tuning the polarization state of enhanced transmission in gratings," Appl. Phys. Lett. **92**, 191105 (2008).

[11] D. Crouse, E. Jaquay, A. Maikal, and A. P. Hibbins, "Light circulation and weaving in periodically patterned structures," Phys. Rev. B **77**, 195437 (2008).

[12] D. Crouse and P. Keshavareddy, "Polarization independent enhanced optical transmission in one-dimensional gratings and device applications," Opt. Express **15**, 1415–1427 (2007).

[13] D. Crouse and P. Keshavareddy, "A method for designing electromagnetic resonance enhanced silicon-on-insulator metal-semiconductor-metal photodetectors," J. Opt. A: Pure Appl. Opt. **8**, 175–181 (2006).

[14] Mandel, I., Gollub, J. N., Bendoym, I., & Crouse, D. T. (2013). Theory and Design of a Novel Integrated Polarimetric Sensor Utilizing a Light Sorting Metamaterial Grating. *Sensors Journal, IEEE*, *13*(2), 618-625.

[15] Mandel, I., Lansey, E., Gollub, J. N., & Crouse, D. T. (2012, October). An effective cavity resonance model for enhanced optical transmission through a periodic array of subwavelength square apertures. In *SPIE NanoScience+ Engineering* (pp. 845735-845735). International Society for Optics and Photonics.

[16] Bendoym, I., Golovin, A. B., & Crouse, D. T. (2012). The light filtering and guiding properties of high finesse phase resonant compound gratings. *Optics Express*, *20*(20), 22830-22846.

[17] Lansey, E., Pishbin, N., Gollub, J. N., & Crouse, D. T. (2012). Analytical analysis of the resonance response of subwavelength nanoscale cylindrical apertures in metal at near-ultraviolet, optical, and near-infrared frequencies. *JOSA B*, *29*(3), 262-267.

[18] Enemuo, A., Nolan, M., Jung, Y. U., Golovin, A. B., & Crouse, D. T. (2013). Extraordinary light circulation and concentration of s-and p-polarized phase resonances. *Journal of Applied Physics*, *113*(1), 014907.

[19] Crouse, D. T., & Lo, Y. H. (2004). Nonsteady-state surface plasmons in periodically patterned structures. *Journal of applied physics*, *95*(8), 4163-4172.

[20] Yu, N., Genevet, P., Kats, M. A., Aieta, F., Tetienne, J. P., Capasso, F., & Gaburro, Z. (2011). Light propagation with phase discontinuities: generalized laws of reflection and refraction. *Science*, *334*(6054), 333-337.

[21] Mandel, I. M., Lansey, E., Gollub, J. N., Sarantos, C. H., Akhmechet, R., Golovin, A. B., & Crouse, D. T. (2013). Photon sorting in the near field using subwavelength cavity arrays in the near infrared. *Applied Physics Letters*,*103*(25), 251116.

[22] Lansey, E., Hooper, I. R., Gollub, J. N., Hibbins, A. P., & Crouse, D. T. (2012). Light localization, photon sorting, and enhanced absorption in subwavelength cavity arrays. *Optics express*, *20*(22), 24226-24236.

[23] S. Herminghaus, M. Klopfleisch, and H. J. Schmidt, "Attenuated total reflectance as a quantum interference phenomenon," Opt. Lett. **19**, 293–295 (1994).

[24] E. D. Palik, Handbook of Optical Constants of Solids (Academic Press, 1985)

[25] H. Raether, *Surface Plasmons on Smooth and Rough Surfaces and on Gratings*, Vol. 11 of *Springer Tracts in Modern Physics* (Springer-Verlag, 1988).

[26] R. Zia, M. D. Selker, P. B. Catrysse, and M. L. Brongersma, "Geometries and materials for subwavelength surface plasmon modes," J. Opt. Soc. Am. A **21**, 2442–2446 (2004).

[27] V. Chegel, Y. Demidenko, V. Lozovski, and A. Tsykhonya, "Influence of the shape of the particles covering the metal surface on the dispersion relations of surface plasmons," Surf. Sci. **602**, 1540–1546 (2008).

[28] P. Yeh, *Optical Waves in Layered Media*, Vol. 95 of *Wiley Series in Pure and Applied Optics* (Wiley, 1988).

[29] Mandel, I. M., Bendoym, I., Jung, Y. U., Golovin, A. B., & Crouse, D. T. (2013). Dispersion engineering of surface plasmons. *Optics Express*, *21*(26), 31883-31893.

[30] P. West, S. Ishii, G. Naik, N. Emani, V. Shalaev, and A. Boltasseva, "Searching for better plasmonic materials," Laser Photonics Rev. **4**, 795–808 (2010).

Metasurfaces at Terahertz, Infrared and Optical Frequencies

Programmable Terahertz Metamaterials through V-beam Electrothermal Devices

Antonios X. Lalas, Nikolaos V. Kantartzis, and Theodoros D. Tsiboukis

Department of Electrical and Computer Engineering, Aristotle University of Thessaloniki, Thessaloniki, Greece
*corresponding author, E-mail: tsibukis@auth.gr

Abstract

A reconfigurable THz complex medium, obtained from the embedment of a V-beam electrothermal actuator as a tuning mechanism in a split-ring resonator (SRR), is proposed in this paper. When the appropriate actuation voltage is applied on the electrothermal microelectromechanical systems (MEMS), a controllable metamaterial, presenting enhanced bandwidth tunability at two different resonances, is accomplished. Several polarization arrangements are investigated to enlighten the diverse attributes of the complex medium. The merits of the proposed device are thoroughly examined via a precise finite element method (FEM).

1. Introduction

Various aspects of modern RF technology are accompanied by artificially engineered complex media, such as metamaterials [1], exhibiting extraordinary electromagnetic performance not available in nature. This unique behavior is exploited in many contemporary applications, especially in the THz frequencies [2], [3]. Furthermore, metamaterials' involvement in wireless power transfer is deemed critical for establishing high-end applications, since it facilitates the development of highly efficient devices [4]-[6]. However, their inherent lack of wide spectral bandwidths introduces several constraints in the development of real-life applications. To overcome this limitation, several techniques have been proposed incorporating various reconfiguration mechanisms, such as magnetically or thermally controlled liquid crystals, and optically reconfigurable silicon apparatuses. Nevertheless, radio-frequency microelectromechanical systems (RF-MEMS) [7], [8] have been proven the most capable devices to attain advanced bandwidth controllability. Among them, thermal and electrostatic RF-MEMS, like cantilevers, curved membranes and comb drives, have been employed to establish the required performance tunability [9]-[12]. Additionally, a controllable metamaterial, that associates the double two-hot arm electrothermal actuator with a split-ring resonator (SRR), has been presented [13]. These setups yield a tunable mu-negative (MNG) behavior.

In this paper, V-beam MEMS electrothermal actuators [14] are introduced as a tuning mechanism of complex materials. In particular, this kind of actuator is exploited to develop a programmable SRR. The proposed device is capable of sustaining MNG and ENG resonances as well. The inherent anisotropic performance of the structure is adequately examined via diverse polarization topologies. The movement of the actuator's tip provides the required frequency shifting, resulting in bandwidth enhancement of the associated frequency regions. The new arrangement successfully exhibits this trait, as verified by extensive numerical simulations.

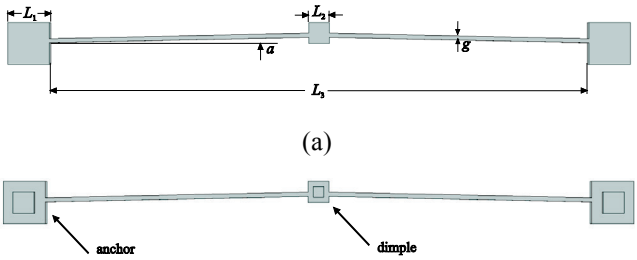

Figure 1: Geometry and design parameters of the V-beam electrothermal actuator (a) upper view and (b) bottom view.

2. The controllable THz complex medium

2.1. Characteristics of the V-beam MEMS actuators

The V-beam actuator is capable of generating enhanced levels of in-plane deflection, whereas its principal operation is based on the thermal expansion of the associated beams, when excited by a potential difference. The device consists of two long beams, which are held fixed by two anchors at a specific angle. An actuation voltage is applied between them, creating an electric circuit. In this manner, electric current travels along the beams, resulting in resistive heating and thermal expansion. Hence, an in-plane displacement of the associated tip occurs owing to the expansion of the beams. A voltage-driven actuator of this kind is depicted in Fig. 1.

The design parameters of the proposed structure are selected as: $L_1 = 2\ \mu$m, $L_2 = 1\ \mu$m, $L_3 = 26\ \mu$m, $a = 1.33^{o}$, and $g = 0.2\ \mu$m. The device comprises a 1.5 μm thick PolySilicon layer. Also, the height of dimples and anchors is set to 0.5 μm, while the height of the remaining actuator is 1 μm. Based on the above notions, a coupled electric, thermal and structural analysis, along with a parametric study for the actuation voltage, are conducted in order to identify the primary characteristics of the device. The FEM approach is employed, while the actuator is discretized into 374 prisma-

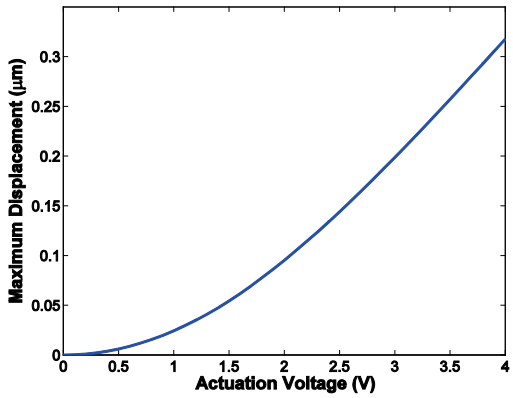

Figure 2: Maximum tip displacement for different values of the actuation voltage.

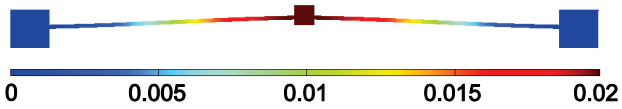

Figure 3: Total displacement distribution (in μm) at the actuation voltage of 3 V.

tic elements with 13590 degrees of freedom. In this framework, the maximum tip displacement is calculated for different values of the actuation voltage, as depicted in Fig. 2. Furthermore, its corresponding total displacement distribution, together with the deformed geometry of the structure, at an actuation voltage of 3 V, are presented in Fig. 3.

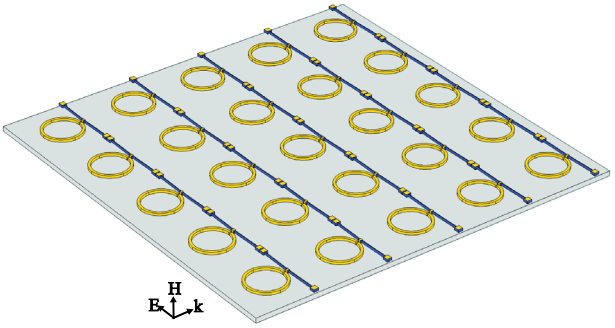

(a)

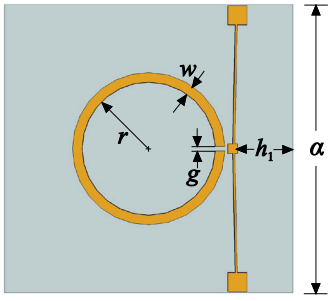

(b)

Figure 4: Geometry and design parameters of (a) the reconfigurable, in terms of V-beam electrothermal actuators, metamaterial and (b) the unit cell.

2.2. Electrothermally controlled metamaterial

A tunable complex medium can be designed by using the V-beam electrothermal actuator, as in Fig. 4, along with its corresponding unit cell. When a certain voltage is applied, the resulting thermal expansion moves the tip of the structure and the gap is modified. Thus, any variation in the actuation voltage level introduces a reconfigurable gap and as a consequence a controllable SRR. The cell period is set to 30.4 μm, $h_1 = 5.9$ μm, $r = 7$ μm, $w = 1$ μm, $g = 0.5$ μm, and the thickness of the Si_3N_4 substrate is 2 μm. The SRR consists of gold with 1 μm thickness, whereas a gold coating is placed over the upper side of the actuator as well as on its tip to sustain any resonances. Taking into account these data all numerical simulations are conducted through a properly tailored FEM, whereas a parallel-plate waveguide approach is adopted to extract the *S*-parameters. This technique involving PEC and PMC boundary conditions constitutes an excellent approximation to model the array of the unit cells in comparison with Floquet boundary conditions. Specifically, the unit cell is divided into 28115 tetrahedral elements with 182304 degrees of freedom. A robust homogenization method [15] is also exploited to retrieve the constitutive effective parameters of the proposed complex media.

3. Numerical results and discussion

The properties of the reconfigurable metamaterial are assessed through a large number of comprehensive numerical investigations in the THz frequency region. Several polarization topologies are examined to reveal the characteristics of the associated resonances.

3.1. Initial orientation

The first topology is denoted by an impinging wave parallel to the plane of the resonators. In particular, the magnetic field is perpendicular to the loops of the unit cells, whereas the electric field is parallel to the V-beam electrothermal actuators, as depicted in Fig. 4(a). The magnitude of the S_{21}-parameter is calculated for different values of the actuation voltage and presented in Fig. 5, revealing the existence of two discrete resonances. Furthermore, the real part of the ef-

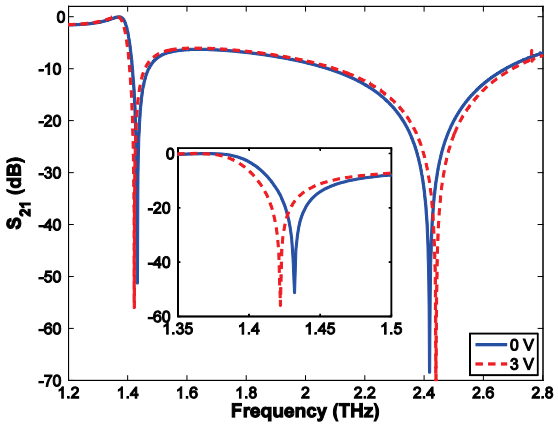

Figure 5: Tunable behavior at several actuation voltages in terms of S_{21}-parameter.

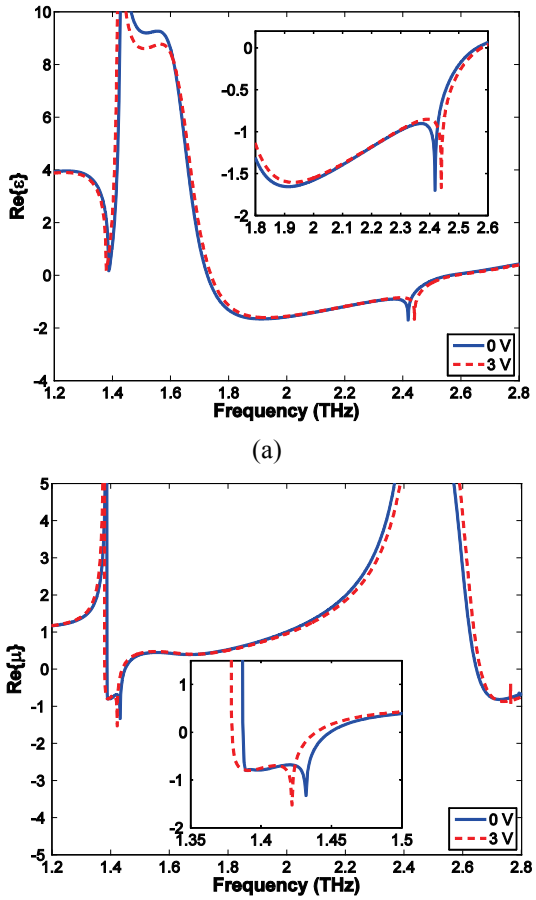

(a)

(b)

Figure 6: Tunable performance at several actuation voltages in terms of (a) effective electric permittivity and (b) effective magnetic permeability.

Table 1: Spectral characteristics of the resonances.

Actuation Voltage (V)	Frequency Regions		
	Start (THz)	End (THz)	BW (GHz)
0	1.4256	1.4397	14.1
	2.3289	2.5003	171.4
3	1.4161	1.4293	13.2
	2.3508	2.5224	171.6

fective electric permittivity and effective magnetic permeability is illustrated in Fig. 6. These results present the MNG THz resonance together with an ENG THz resonance of the complex medium as well as the ability for enlarged bandwidth. The frequency regions of interest are denoted in Table 1, when the actuation voltage increases from 0 V to 3 V. Considering the first resonance, an enhanced tunability is attained, since the narrow bandwidth of 14.1 GHz, is artificially extended to 1.4397 THz – 1.4161 THz = 23.6 GHz, offering a magnification of 61%. Furthermore, the second resonance presents an initial bandwidth of 171.4 GHz, which is further enhanced to 2.5224 THz – 2.3289 THz = 193.5 GHz, offering an improvement of 13%.

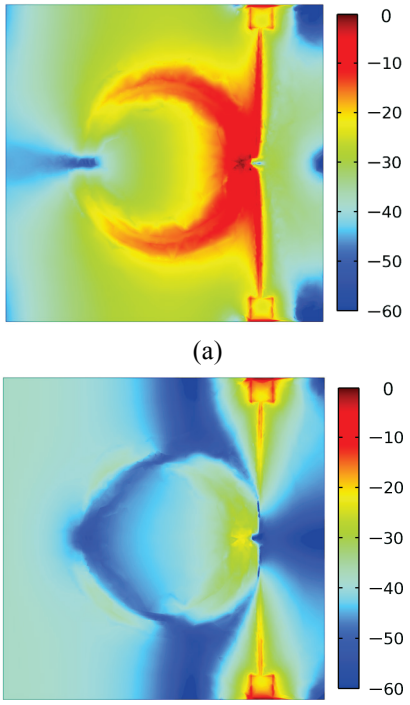

(a)

(b)

Figure 7: Electric field snapshots of the electrothermally controlled metamaterial unit cell, when the actuation voltage is (a) 0 V at 1.432 THz and (b) 0 V at 2.418 THz.

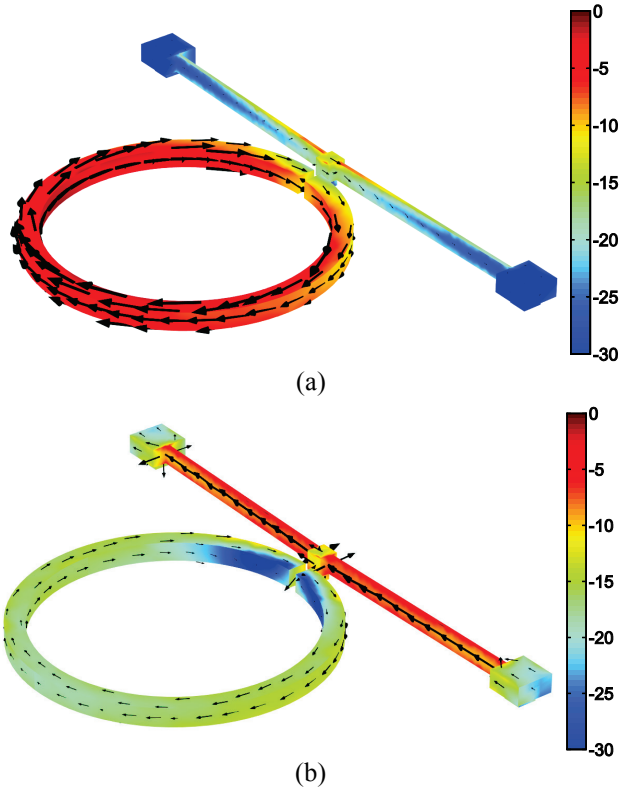

(a)

(b)

Figure 8: Surface current density snapshots of the electrothermally controlled metamaterial unit cell, when the actuation voltage is (a) 0 V at 1.432 THz and (b) 0 V at 2.418 THz (The arrows depict the direction and intensity of the surface current flow).

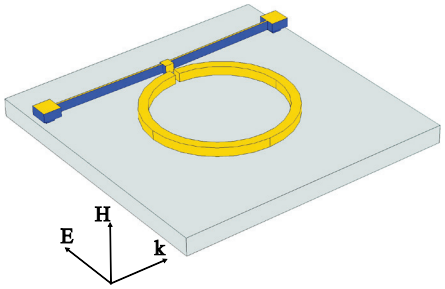

Figure 9: Topology for a different polarization of the reconfigurable, in terms of V-beam electrothermal actuator, unit cell.

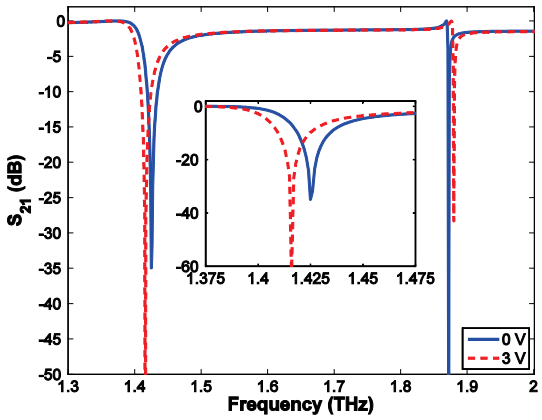

(a)

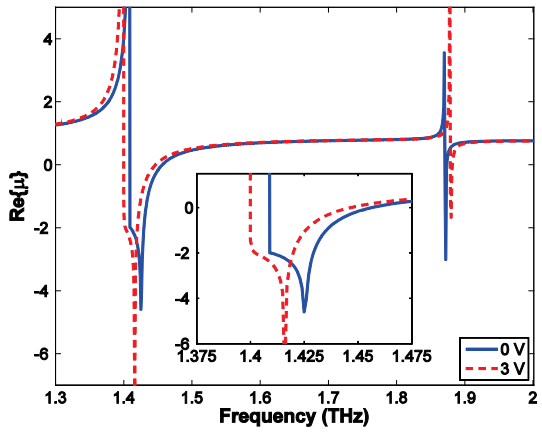

(b)

Figure 10: Tunable performance for different polarization at several actuation voltages in terms of (a) S_{21}-parameter and (b) effective magnetic permeability.

Additionally, two snapshots of the electric field intensity are given in Fig. 7, when the actuation voltage is 0 V and the frequency is 1.432 THz and 2.418 THz, respectively. In the first case, the maximum value is observed in the vicinity of the gap, displaying the MNG performance. The second case presents the ENG behavior of the device, since the maximum values are revealed at the regions of the anchors. Finally, two snapshots of the surface current distribution are depicted in Fig. 8, associated with the aforementioned actuation conditions. It is obvious, in the first case, that the maximum value is revealed upon the surface of the SRR, denoting the presence of an MNG resonance. On the other hand, the second resonance is considered as an ENG, due to the presence of a maximum surface current upon the V-beam electrothermal actuator. Therefore, it is deduced that the prior SRR can be advantageous in several high-frequency arrangements.

Table 2: Spectral characteristics of the resonances for the other polarization.

Actuation Voltage (V)	Frequency Regions		
	Start (THz)	End (THz)	BW (GHz)
0	1.4232	1.4278	4.6
	1.8713	1.8727	1.4
3	1.4138	1.4184	4.6
	1.8796	1.8804	0.8

3.2. Rotated orientation

The second topology is also described by an impinging wave parallel to the plane of the resonators. However, this wave is rotated 90° in comparison to the initial orientation. Thus, in this case the electric field is perpendicular to the V-beam electrothermal actuators, while the magnetic field is perpendicular to the loops, as illustrated in Fig. 9. The magnitude of the S_{21}-parameter is extracted for different values of the actuation voltage and depicted in Fig. 10(a), presenting the existence of two discrete resonances. Moreover, the real part of the effective magnetic permeability is illustrated in Fig. 10(b). These data denote the presence of two MNG THz resonances of the metamaterial as well as the capability for improved bandwidth. The corresponding frequency regions are presented in Table 2, when the actuation voltage increases from 0 V to 3 V. By inspecting the first resonance, an enhanced tunability is attained, since the narrow bandwidth of 4.6 GHz, is artificially extended to 1.4278 THz – 1.4138 THz = 14 GHz, providing an improvement of 204%. In addition, the second resonance presents an initial bandwidth of 1.4 GHz, which is further improved to 1.8804 THz – 1.8713 THz = 9.1 GHz, offering a magnification of 550%.

Also, two snapshots of the electric field intensity are illustrated in Fig. 11, when the actuation voltage is 0 V and the

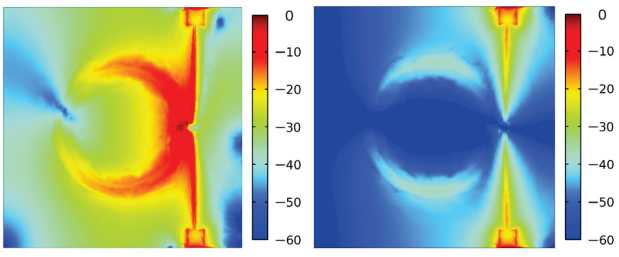

(a) (b)

Figure 11: Electric field snapshots for the other polarization of the electrothermally controlled metamaterial unit cell, when the actuation voltage is (a) 0 V at 1.425 THz and (b) 0 V at 1.872 THz.

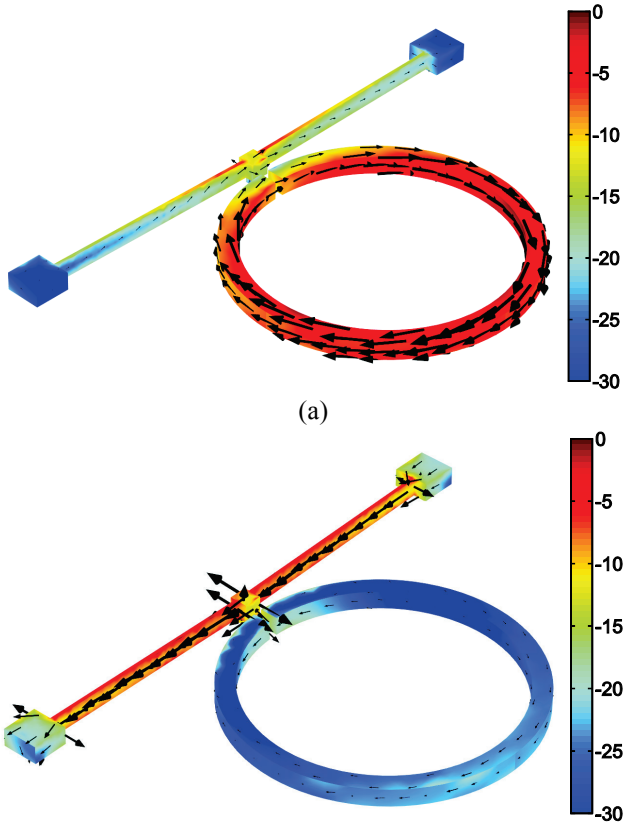

Figure 12: Surface current density snapshots for the other polarization of the electrothermally controlled metamaterial unit cell, when the actuation voltage is (a) 0 V at 1.425 THz and (b) 0 V at 1.872 THz (The arrows depict the direction and intensity of the surface current flow).

frequency is 1.425 THz and 1.872 THz, respectively. In the first case, the maximum value is obtained in the vicinity of the gap, revealing the MNG performance. The second case is moreover associated to an MNG behavior of the structure, however the maximum values are located at the regions of the anchors. Finally, two snapshots of the surface current distribution are presented in Fig. 12, corresponding to the previous actuation conditions. It is apparent, in the first case, that the maximum value is unveiled upon the surface of the SRR, illustrating an MNG resonance. Conversely, the second MNG resonance is less obvious, since the maximum surface current is located upon the V-beam electrothermal actuator. Thus, it is deduced that the SRR under investigation can be profitable in an assortment of high-frequency setups.

3.3. Anisotropic performance

The numerical assessment of the tunable complex medium denotes a different behavior, when the polarization of the impinging wave is altered. Specifically, the central frequency of the resonances is shifted, whereas the corresponding quality factor is modified. Furthermore, in some cases, the essence of each resonance is reconfigured between MNG and ENG performance. Such an observation regarding anisotropy is deemed critical in designing programmable complex media and associated applications.

4. Conclusions

The employment of V-beam MEMS electrothermal actuators for the design of a novel programmable metamaterial is introduced in this paper. Advanced bandwidth tunability at two discrete resonances is verified through several FEM simulations, while different polarization arrangements are also examined indicating its benefits and applicability. The promising properties of the proposed device enable its potential application in a variety of contemporary THz implementations and wireless power transfer systems.

Acknowledgements

This research has been financed by the National Scholarships Foundation of Greece (IKY) through IKY Fellowships of Excellence for Postgraduate Studies in Greece – Siemens Program, under Grant No. SR 22103/13.

References

[1] R. Marqués, F. Martín, M. Sorolla, *Metamaterials with Negative Parameters: Theory, Design and Microwave Applications*, Wiley-Interscience, New Jersey, NY, 2008.

[2] J. M. Manceau, N. H. Shen, M. Kafesaki, C. M. Soukoulis, S. Tzortzakis, Dynamic response of metamaterials in the terahertz regime: Blueshift tunability and broadband phase modulation, *Appl. Phys. Lett.* 96: 021111(1–3), 2010.

[3] D. Wang, C. Qiu, M. Hong, Coupling effect of spiral-shaped terahertz metamaterials for tunable electromagnetic response, *Appl. Phys. A*, 2013.

[4] Y. Urzhumov, D. R. Smith, Metamaterial-enhanced coupling between magnetic dipoles for efficient wireless power transfer, *Phys. Rev. B* 83: 205114, 2011.

[5] B. Wang, K. H. Teo, Metamaterials for wireless power transfer, *IEEE International Workshop on Antenna Technology (iWAT)*, pp. 161–164, 2012.

[6] G. Lipworth, J. Ensworth, K. Seetharam, D. Huang, J. S. Lee, P. Schmalenberg, T. Nomura, M. S. Reynolds, D. R. Smith, Y. Urzhumov, Magnetic metamaterial superlens for increased range wireless power transfer, *Sci. Rep.* 4: 3642(1–6), 2014.

[7] A.-Q. Liu, *RF MEMS Switches and Integrated Switching Circuits*, Springer, New York, 2010.

[8] X. Li, Y. Li, W. Guo, F. Peng, H. Zhang, T. Yang, Wireless magnetic resonant energy transfer system based on micro 3D flexible MEMS Litz coils, *Microsyst. Technol.* 20: pp 477–483, 2014.

[9] H. Tao, A. C. Strikwerda, K. Fan, W. Padilla, X. Zhang, R. D. Averitt, MEMS based structurally tunable metamaterials at terahertz frequencies, *J. Infrared Milli. Terahz Waves* 32: pp. 580–595, 2010.

[10] D. Bouyge, D. Mardivirin, J. Bonache, A. Crunteanu, A. Pothier, M. Duran-Sindreu, P. Blondy, F. Martin, Split ring resonators (SRRs) based on micro-electro-mechanical deflectable cantilever-type rings: Application to tunable stopband filters, *IEEE Microw. Wireless Compon. Lett.* 21: pp. 243–245, 2011.

[11] W. Zhang, A. Q. Liu, W. M. Zhu, E. P. Li, H. Tanoto, Q. Y. Wu, J. H. Teng, X. H. Zhang, M. L. J. Tsai, G. Q. Lo, D. L. Kwong, Micromachined switchable metamaterial with dual resonance, *Appl. Phys. Lett.* 101: 151902(1–5), 2012.

[12] W. M. Zhu, A. Q. Liu, T. Bourouina, D. P. Tsai, J. H. Teng, X. H. Zhang, G. Q. Lo, D. L. Kwong, N. I. Zheludev, Microelectromechanical Maltese-cross metamaterial with tunable terahertz anisotropy, *Nature Commun.* 3: 1274(1–6), 2012.

[13] A. X. Lalas, N. V. Kantartzis, T. D. Tsiboukis, Controllable essence of complex materials exploiting two-hot-arm electrothermal actuators, *Proc. MEMSWAVE13*, Potsdam, Germany, pp. 1–4, 2013.

[14] L. Que, J. S. Park, Y. B. Gianchandani, Bent-beam electrothermal actuators: part I. Single beam and cascaded devices, *J. Microelectromech. Syst.* 10: pp. 247–254, 2001.

[15] X. Chen, T. M. Grzegorczyk, B. I. Wu, J. Pacheco, J. A. Kong, Robust method to retrieve the constitutive effective parameters of metamaterials, *Phys. Rev. E* 70: 016608(1–7), 2004.

Transformation Electromagnetics concepts and applications

Antipodal Radiation Pattern of a Patch Antenna Combined with Superstrate Using Transformation Electromagnetics

Mark Clemente Arenas, Anne Claire Lepage and Xavier Begaud

Institut Mines Telecom, Telecom ParisTech - LTCI CNRS UMR 5141, 46 rue Barrault, 75634 Paris Cedex 13, France.
*corresponding author, E-mail: mark.clemente@telecom-paristech.fr

Abstract

This paper aims to show the design and performances of a flat superstrate placed above an L-band patch antenna. Obtained from the Transformation Electromagnetics (TE) technique, this superstrate enables to produce an antipodal radiation with a quasi-null radiation in the broadside direction. From the analytical transformations used for the calculation of the constitutive parameters, material permittivity and permeability profiles of the superstrate are deduced. Then, the field distribution and radiation patterns of the whole structure confirm the antipodal radiation behavior.

1. Introduction

Since 2006, the work of Pendry about Transformation Electromagnetics (TE) inspired several groups to design exotic devices for many fields as electromagnetism, optics, acoustics, etc. The flexibility in the control of wave propagation allows designing enigmatic devices such as invisibility cloak [1], [2] but also to modify the farfield of a patch antenna combined with a TE based device as in [3-6].
In this article, the proposed device enables the fields to propagate towards the sides ($\theta = \pm 90°$ direction) instead of broadside ($\theta = 0°$ direction) as a classical patch antenna does. Usually when a planar antenna is placed or conformed on a structure, a broadside radiation pattern is obtained. However, in many applications, like airborne systems, it will be interesting to have an exotic radiation pattern where two opposite main beams are generated close to the structure. This last peculiar behavior can be very interesting for applications where protuberate antennas are not allowed because of mechanical constraints. To achieve this kind of radiation, we propose to design a flat superstrate based on TE and to put it above an L-band patch antenna.
First, the principle of the design of the superstrate and the analytical transformations are shown. Then, the description of the 2D and 3D designs and the corresponding simulations results are presented for discussion and analysis. Finally conclusions are drawn.

2. TE Device description

In this section, the analytical transformations are presented on a 2D structure to simplify the design process. Then, this 2D structure is rotated around x axis to create the complete structure, which is described in the next section.

2.1. Analytical Transformations

The design principle for the 2D superstrate is presented in Fig. 1. Two spaces are described. We notice that the virtual space is divided in two symmetrical parts.

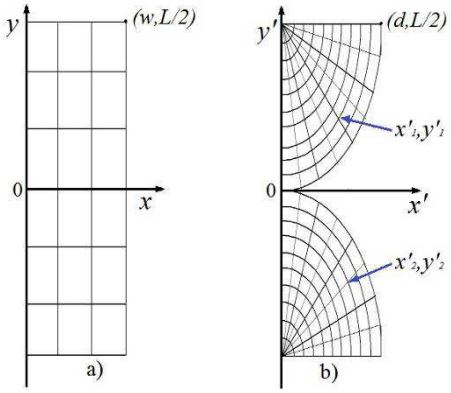

Figure 1: L = 200 mm, d = 37.5 mm, w = 37.5 mm, a = 2 (compression factor). a) Real space. b) Virtual space.

Equation 1 describes the transformation, both x and y coordinates are transformed.

$$x'_{1,2} = \frac{w}{d}\sqrt{(ax)^2 + \left(y \mp \frac{L}{2}\right)^2}\ ,\quad y'_{1,2} = \frac{L}{\pi}\tan^{-1}\left(\frac{y \mp \frac{L}{2}}{ax}\right) \qquad (1)$$

Then, the calculations for the constitutive parameters are performed using Transformation Electromagnetics [1][2]. It is also needed to simplify the permittivity and the permeability tensors in order to achieve a realistic material profile [3][6]. The reduced set of components of the permittivity and permeability tensors is shown in Equation 2.

$$\varepsilon_{zz}^{1,2} = 4\left(\frac{d^2\pi}{w^2 L}x'_{1,2}\right)^2,\ \mu_{yy}^{1,2} = \left(\frac{L}{\pi.x'_{1,2}}\right)^2 \qquad (2)$$

There are two symmetrical substructures for the proposed superstrate, each one has an identical equation, and only the sign is changed. This transformation aims to guide the fields towards the sides of the structure; this is the reason to use a shifted semi elliptical transformation.

2.2. 2D structure

As previously mentioned, the components of the tensors of constitutive parameters are reduced and ε_{zz} and μ_{yy} are the only non-zero values, their values are shown in Fig. 2.

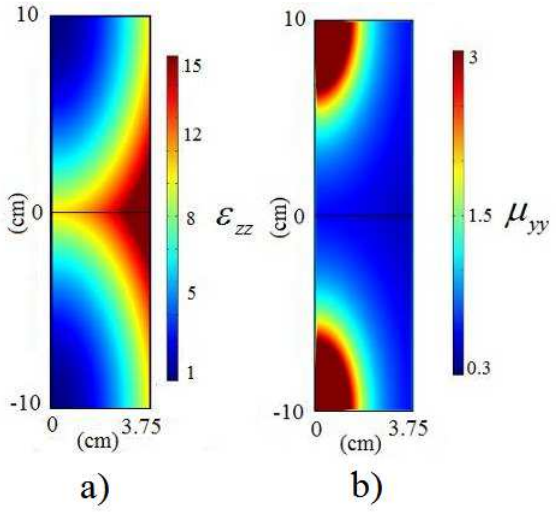

Figure 2: Component ε_{zz} from permittivity tensor. b) Component μ_{yy} from permeability tensor.

In order to evaluate the electromagnetic behavior of the device, the electric near field is analyzed at 1.2 GHz. Comsol Multiphysics is used to perform simulations where an anisotropic and inhomogeneous material is needed.
The antenna is modeled by a surface current, a PEC ground plane and a dielectric. Then, the normalized electric field distribution *Ez* for the 2D structure, respectively the antenna model without and with TE based superstrate, is presented in Fig. 3.a and 3.b.

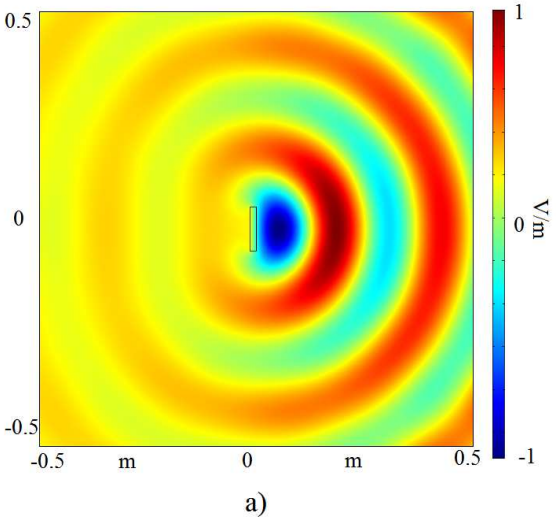

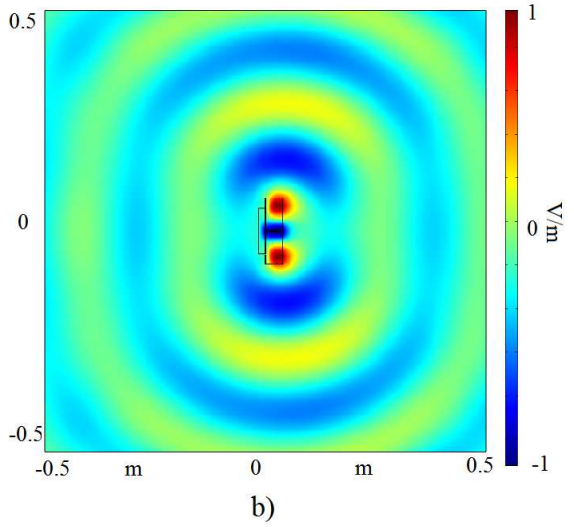

Figure 3: 2D Simulation of *Ez* field distribution at 1.2 GHz for: a) Antenna model only and b) Antenna model with TE based superstrate.

It is observed that the patch antenna, modeled with a surface current, has a directive radiation as expected. After, when the TE based superstrate is placed over the antenna, the electric field is split in two and propagates towards the sides of the antenna.

3. Complete Structure and Results

In order to confirm the performances of the superstrate, the antenna radiation pattern obtained with or without it, has been calculated with CST Microwave Studio. A probe fed patch antenna has been designed in order to work in the L band with the superstrate. The antenna substrate is a 100*100 mm² square with 15.5 mm of thickness and the size of the patch is 65.5*65.5 mm². The substrate is Arlon AD 250 (ε_r = 2.5), and the ground plane has the same size as the substrate.
The 3D TE based structure with the patch antenna is simulated using the discretized values of constitutive parameters ε_{zz} and μ_{yy} shown in Fig. 4. It means that these profiles for both, permittivity and permeability are divided into blocks of constant value (the average value of ε_{zz} and μ_{yy}), and then these 2D blocks are converted into 3D concentric rings. Therefore, three multi-annular layers constitute the superstrate.

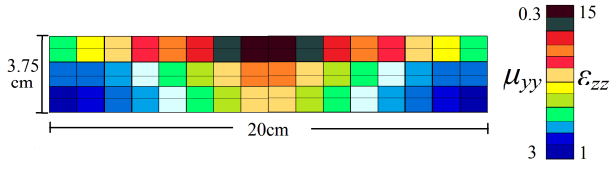

Figure 4: Discretized profile for permittivity and permeability.

Different configurations are explored in order to obtain the patch antenna with the superstrate matched in the desired

frequency band [1.16 GHz-1.2 GHz]. In Fig. 5, the magnitude of the input reflection coefficient of the complete structure is presented for these cases.

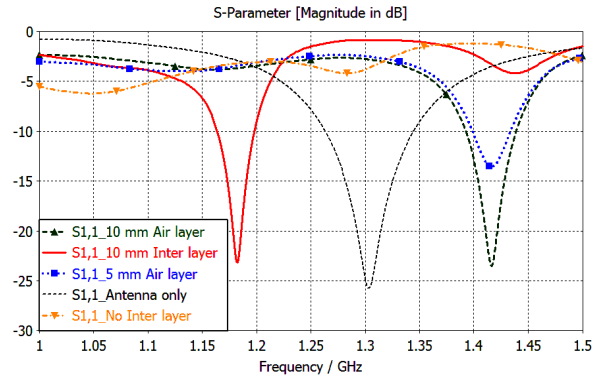

Figure 5: Magnitude of input reflection coefficient of the complete structure with different configurations.

First, we observe that the antenna without superstrate is matched around 1.3 GHz. Then, the impedance matching of the complete structure without any inter layer is clearly affected in the operating band by two major causes. The first one is that there are high values of permittivity and low values of permeability in direct contact with the radiating surface. The second is the discretization of the continuous values of the constitutive parameters (ε and μ), which introduces reflections between each layer.

Adding an air layer between the antenna and the superstrate enables to recover one operating bandwidth but at higher frequencies than the targeted one. Finally, a transition layer of 10 mm thickness and $\varepsilon_r = 4$ is placed between the patch antenna and the superstrate to obtain the desired frequency band. This layer increases the thickness of the whole device from 53 mm to 63 mm for the final structure.

In Fig. 6, the *Ez*-Field distributions of the patch alone and of the complete structure are presented in their operating frequency band. It is observed how the electric field travels towards the side of the structure thanks to the superstrate, instead of traveling in axial direction.

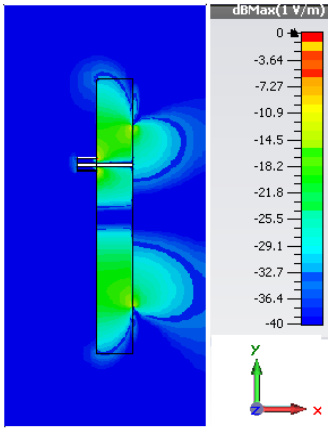

a)

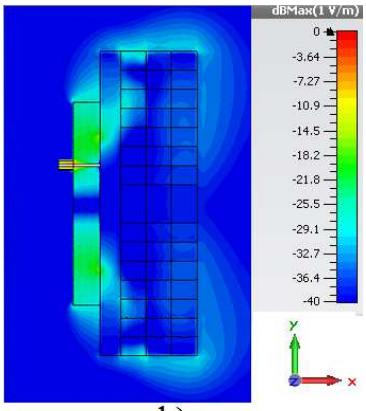

b)

Figure 6: a) *Ez* Field Distribution at 1.3 GHz for the patch only and b) *Ez* Field Distribution at 1.2 GHz for the complete structure.

In order to highlight the performances of the complete structure, the 3D radiation patterns are presented in Fig. 7 with and without superstrate. In Fig. 7.a, the radiation pattern of the patch antenna only calculated at 1.3 GHz shows that the radiation is maximum at 0° (broadside) with a realized gain of 4.2 dB and -8.5 dB at ± 90°.

Therefore, in Fig. 7.b, the antenna and the TE device produce at 1.2 GHz an antipodal radiation pattern with two main beams along the sides with maximum realized gain of 3.5 dB at ± 89° and -14.9 dB in the broadside direction.

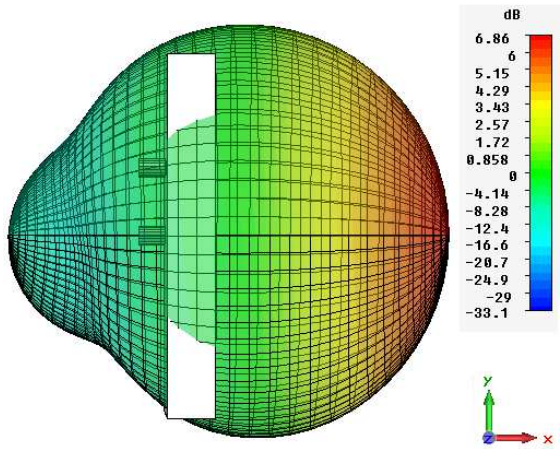

a)

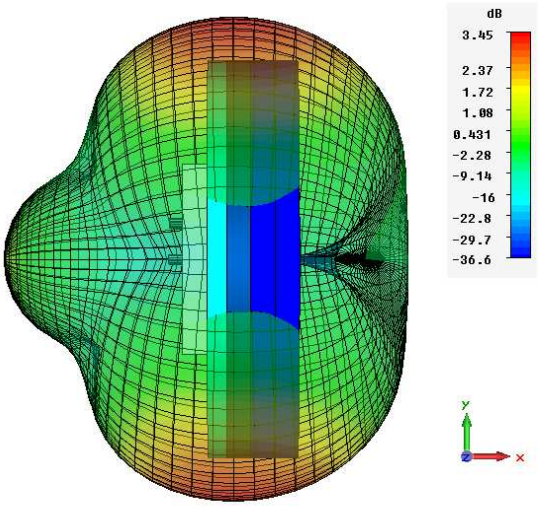

b)

Figure 7: Magnitude of the realized gain for: a) Patch only at 1.3 GHz and b) Patch with TE based superstrate at 1.2 GHz.

The co-polar and cross-polar components of the realized gain in the two main planes of antenna (*phi*=0° and *theta*=90°) are presented in Fig. 8. In the plane *theta*=90°, the two main lobes are close to the antipodes and a third lobe in the *phi*=180° direction is also present with a lower level (-2.2 dB compared to the main lobes). The level of cross-polar component is low.

In the other plane *phi*=0°, the radiation pattern is strongly backwards directed. It presents 1.3 dB of realized gain in the main direction (*theta* =274°). Two other lobes are directed to 12° and 133°. They are quite asymmetrical compared to the ones in the other plane. The level of cross-polar component is very low.

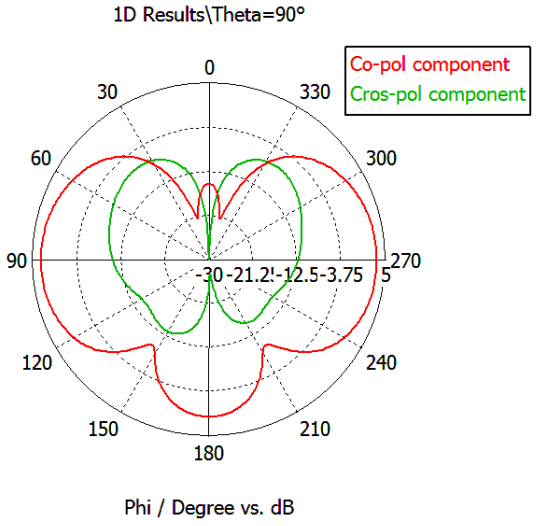

a)

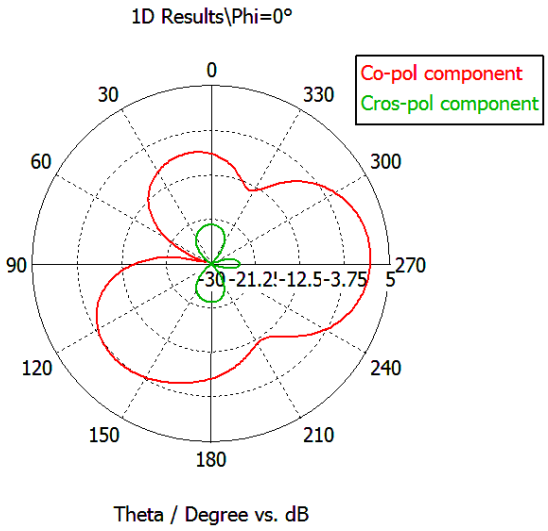

b)

Figure 8: Co-polar and cross-polar components of the realized gain in the two main planes of antenna at 1.2 GHz. a) *theta=90°*. b) *phi=0°*.

4. Conclusion

This paper demonstrates the performances of a superstrate based on TE technique. This flat device produces an interesting electromagnetic behavior with a L-band patch antenna, as there is an antipodal radiation with a realized gain equal to 3.5 dB at ± 89 °, then dropping off to the minimum in the broadside direction which is slightly similar to a dipole pattern. Using the designed TE device decreases the maximum realized gain of the patch antenna which results of the creation of the two lobes.
In addition, as this superstrate is flat, it can be used for some applications, where shape and conformability are highly important. Thickness of the superstrate is equal to 37.5 mm, which corresponds to 0.15 wavelength at 1.2 GHz.

Acknowledgements

The research leading to these results has received funding by British and French Ministries of Defence (DSTL and DGA), through the European Defence Agency (EDA) contract MIMiCRA (Metamaterial Inspired Microwave Conformal Radar Antennas).

References

[1] J. B. Pendry, D. Schurig, D. R. Smith, Controlling electromagnetic fields, *Science*, vol. 312, pp. 1780–1782, 2006.

[2] D. Schurig, J. J. Mock, B. J. Justice, S. A. Cummer, J. B. Pendry, A. F. Starr, D. R. Smith, Metamaterial Electromagnetic Cloak at Microwave Frequencies, *Science*, 314, November 2006, pp. 977-980.

[3] P. H. Tichit, S. N. Burokur, D. Germain, A. De Lustrac, Design and experimental demonstration of a high-

directive emission with transformation optics, *Phys. Rev. B*, vol. 83,n°. 15, pp. 155108, 2011.

[4] D. H. Kwon, D. H. Werner, Transformation Electromagnetics: An Overview of the Theory and Applications, *Antennas and Propagation Magazine, IEEE*, vol.52, no.1, pp.24-46, 2010.

[5] P. H. Tichit, S. N. Burokur, A. De Lustrac, Ultra-directive antenna via transformation optics, *Journal of Applied Physics*, vol.105, no.10, pp.104912-104912-6, May 2009.

[6] M. Clemente Arenas, A. C. Lepage, X. Begaud, P. H. Tichit, A. De Lustrac, All standard materials flat reflector made by transformation electromagnetics, *International Journal of Microwave and Wireless Technologies*, 2014. doi:10.1017/S1759078714000026.

Metamaterial-based radiating and absorbing structures

On-metal UHF-RFID tags based on non-bianisotropic complementary split ring resonators

Simone Zuffanelli, Gerard Zamora, Ferran Paredes, Pau Aguilà, Ferran Martín* and Jordi Bonache

GEMMA/CIMITEC, Departament d'Enginyeria Electrònica, Universitat Autònoma de Barcelona, 08193 Bellaterra, Spain
*corresponding author, E-mail: Ferran.Martin@uab.es

Abstract

The use of non-bianisotropic complementary split ring resonators (NB-CSRRs) as radiating elements in low-profile on-metal UHF-RFID tags is explored in this work. The radiation properties of the particle, along with the impedance matching strategy, are discussed. Based on the electromagnetic simulation, a final device with dimensions $45\times45\times1.27$ mm^3 is proposed. The simulated results exhibit excellent linear polarization of the radiated fields (axial ratio > 40 dB), good impedance matching (-16 dB) at 914 MHz and a maximum read range of 7.6 m.

1. Introduction

RADIO frequency identification (RFID) is a widespread technology that allows tagging of objects by using electromagnetic waves. In the last years, the use of such technology has experienced a rapid increase, whereas the cost of the tags has dropped down, and further penetration into the market is expected for the next years. Typical applications of this technology are smart inventory and item tracking, among others. Passive tags operating at the UHF-RFID frequency bands (860-960 MHz [1]) are especially employed for this kind of applications due to the significant achievable read ranges, low cost, small dimensions, and because such tags do not need batteries. A passive UHF-RFID tag consists of an antenna matched to an application specific integrated circuit (ASIC), which contains the information about the tagged item. A passive tag is capable of using the electromagnetic energy from the reader to activate the chip, which generates a modulated backscattered signal to the reader. Typical peak read ranges of UHF-RFID tags are in the order of 5-10 m, depending on the country regulations (i.e. maximum allowed EIRP value), tag characteristics (i.e. antenna performance and chip sensitivity) and orientation, item material, and environmental conditions. Recently, metamaterials have been applied to the design of RFID devices, in order to control dimensions, impedance matching and radiation properties of the reader antennas [2-4]. Moreover, split ring resonators (SRRs) have been used as radiating elements for UHF-RFID tags [5], or as matching elements capable of providing dual-band functionality to the tag [6]. However, the use of complementary resonators as radiating element for UHF-RFID tags has not been explored. Due to the dipolar moments generated at resonance, which are compatible with the boundary conditions imposed by a metallic surface, this kind of particle is especially interesting for low-profile on-metal applications. Among these particles, the non-bianisotropic complementary split ring resonator (NB-CSRR) (Fig. 1) is especially interesting due to the absence of cross-polarization effects. This property allows the linear polarization of the radiated fields to present a very high axial ratio, which is convenient in UHF-RFID tags.

First of all, electric and magnetic polarizability of the NB-CSRR particle are discussed in section 2. Then, in section 3 the tag design strategy is presented, and the final tag layout and the simulation results are shown in section 4. Finally, a comparison of the radiation properties of the presented particle with respect to the more commonly used complementary split ring resonator (CSRR) is provided in the last section.

2. Polarizability and radiation properties of NB-CSRRs

Given the polarizability tensor of a resonant planar particle, it is possible to deduce the polarizability tensor of its complementary screen by applying the Babinet principle [7], obtaining:

$$m_x = \beta_{xx}^{mm} B_x + \beta_{xy}^{mm} B_y + \beta_{xz}^{me} E_z \quad (1a)$$

$$m_y = \beta_{yx}^{mm} B_x + \beta_{yy}^{mm} B_y + \beta_{yz}^{me} E_z \quad (1b)$$

$$p_z = \beta_{zx}^{em} B_x + \beta_{zy}^{em} B_y + \beta_{zz}^{ee} E_z \quad (1c)$$

where the polarizabilities β can be related to the polarizabilities α of the original particle by using the relations:

$$\beta^{mm} = -c^2 \alpha^{ee}, \beta^{em} = -\alpha^{em}, \beta^{ee} = -\frac{1}{c^2}\alpha^{mm} \quad (2)$$

where c is the speed of light in vacuum. It is important to note that, according to the Babinet principle, if expressions (1a)-(1c) are defined for $z>0$ (where $z=0$ is the plane of the particle), the induced moments for $z<0$ are the same in magnitude but opposite in sign. However, since an infinite metal plate is located at $z<0$ close to the particle, we only are interested in the radiation properties of the particle in the half-space $z>0$.

The non-bianisotropy of the NB-SRR leads all the cross-polarization terms to vanish, allowing simplifying the expression of the polarizability tensor as follows:

$$m_x = \beta_{xx}^{mm} H_x + \beta_{xy}^{mm} H_y \tag{3a}$$

$$m_y = \beta_{yx}^{mm} H_x + \beta_{yy}^{mm} H_y \tag{3b}$$

$$p_z = \beta_{zz}^{ee} E_z \tag{3c}$$

By applying duality to the considerations over the nature of the first and second resonances of the NB-SRR [8], it follows that, for the NB-CSRR, only a normal electric moment p_z is generated at the first resonance by a magnetic current loop, while only a tangential magnetic moment (m_x,m_y) is generated at the second resonance by a magnetic current linear dipole. Now, since the particle is electrically small at the first resonance, and radiation resistance of a small current loop depends upon $(r/\lambda)^4$, this resonance will not provide an acceptable radiation efficiency. On the other hand, at the second resonance, the particle has a larger size and behaves as a linear magnetic current dipole, resulting interesting as a relatively efficient radiator.

3. Tag design strategy

Let us now introduce some design concepts that have been used in order to determine the final tag layout. First of all, impedance matching between the ASIC and the antenna is critical when designing an efficient passive UHF-RFID tag. The input impedance of an UHF-RFID ASIC is typically capacitive, ranging from –100 to –400 Ω, and its real part is about one order of magnitude smaller [9]. Thus, the antenna impedance is required to be highly inductive in order to obtain good impedance matching. The matching strategy adopted in this work takes advantage of the very high reactance slope and values of the NB-SRR input impedance near one of its resonances. In fact, since the first and second resonances can be approximated by a shunt LC model in terms of impedance [10], before the resonance the particle presents an inductive behavior, with a high frequency slope. Since the real part of such impedance also presents a great variation around the resonance, by simply changing the port position P along the slot (i.e. varying the value of the angle ϕ_p (see Fig. 1)) it is possible to obtain the required antenna impedance without the need of a matching network. The resonant nature of the proposed matching strategy, along with the typically small dimensions of the radiating particle, limits the bandwidth of the tag to few MHz, which excludes the possibility of a worldwide functionality of the tag, though it is fully sufficient for the correct operation in one region. However, narrowband impedance matching is typical for low-profile on-metal UHF-RFID tags [11].

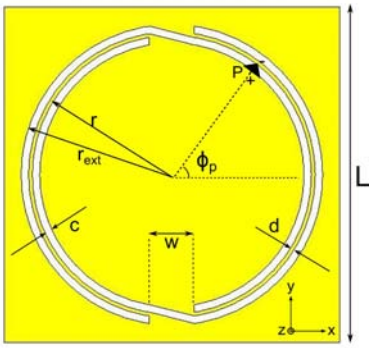

Fig. 1 Non-bianisotropic complementary split ring resonator (NB-CSRR). Metal is depicted in yellow, slot in white.

In order to shift the second resonance of the particle to the desired frequency, there are mainly three parameters to take into account. The first is, obviously, the particle average radius r, which can be evaluated as $r_{ext}-c-d/2$. Then, the separation d of the slots, which controls the coupling between the resonators, can be used as a design parameter since it offers an additional degree of freedom on the tag dimensions. It is well known that increasing the coupling between the resonators the frequency split of the first and second resonance increases, that is, the first resonance is lowered and the second is raised in frequency. Lastly, the thickness t of the dielectric plays an active role in the position of the resonances, since it is the distance between the particle and the metal plane. It is verified by simulation (Fig. 2) that the presence of the metal lowers the electric resonance (first resonance) and raises the magnetic resonance (second resonance), thus increasing the splitting between the first and second resonances.

Other basic considerations about the tag design concern the antenna gain. While the presence of the metal increases the directivity of the radiated fields, the radiation efficiency of a slot antenna rapidly decreases when the substrate thickness decreases to extremely small values in terms of wavelength. As a consequence, a tradeoff between tag thickness and read range must be chosen.

In the next section the proposed tag layout, which has been designed to work at 915 MHz (at the center of the North America UHF-RFID band), is presented.

4. Proposed tag layout and simulation results

The electromagnetic simulations have been carried out by means of the commercial software *CST Microwave Studio*, using the time domain and the frequency domain solvers.

The simulated layout presents the geometry shown in Fig. 1, where the boundaries of the metal plate (of dimensions $L\times L$) which contains the particle have been short-circuited to ground, in order to avoid the presence of a parasitic patch antenna. The substrate used is the *Rogers RO3010*, with relative permittivity $\varepsilon_r = 10.2$ and thickness $h = 1.27$ mm

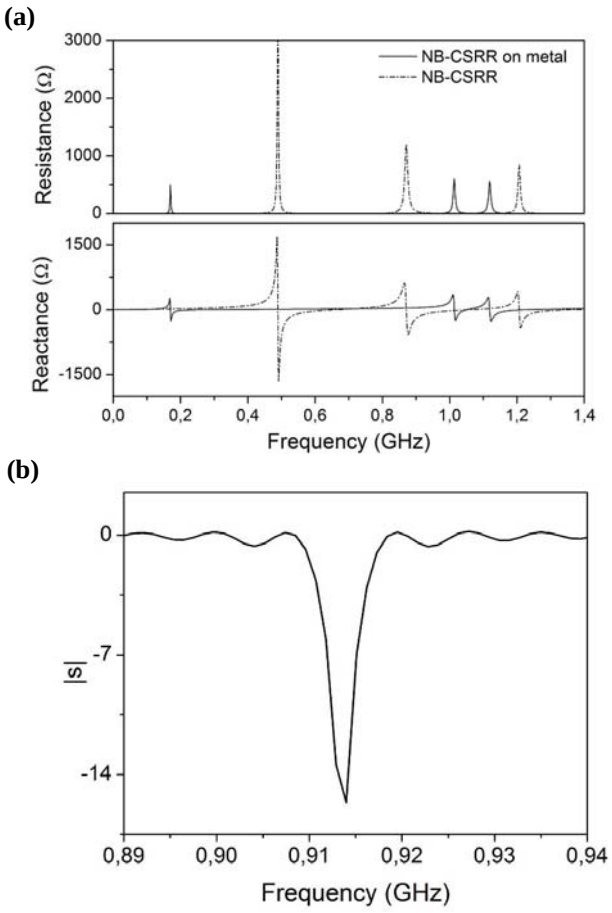

Fig. 2 (a) Simulated input impedance of the proposed structure, (b) power reflection coefficient.

(≈ λ/260). The ASIC used for the design is the *Alien Higgs 3*, which presents an input impedance of $Z_c = 25 - j190\ \Omega$ at 915 MHz, and a read sensitivity of −18 dBm [12]. The dimensions of the proposed tag are 45x45x1.27 mm^3. The values of the geometrical parameters are $L = 45$ mm, $r_{ext} = 20.2$ mm, $c = 1$ mm, $d = 0.5$ mm, $w = 6$ mm. The port position which provided optimal matching impedance was found to be $\phi_p = 60°$.

The simulated input impedance of the structure, as seen from the port position, is depicted in Fig. 2(a). For comparison, the simulated impedance of a NB-CSRR with the same dimensions and substrate, without the presence of the metal plane, is also shown in Fig. 2(a). The input impedance reveals clearly the first three resonances of the particle in both cases, and besides, the effect of the metal plane on the resonance splitting is evident. In our layout, the second resonance is raised from 0.87 GHz to 1.01 GHz due to the proximity to the metal surface. The simulated power reflection coefficient is depicted at Fig. 2(b). A very good matching level (−16 dB) is obtained at 914 MHz, with a half-power bandwidth of 5 MHz.

Let us now focus on the antenna parameters of the tag. As expected, the radiation pattern (Fig. 3(a)) at 915 MHz agrees very well with the pattern produced by the tangential magnetic dipolar moment of the NB-CSRR. The axis of the dipole is oriented at $\phi = 17°$ *(H*-plane*)*, where a null in the

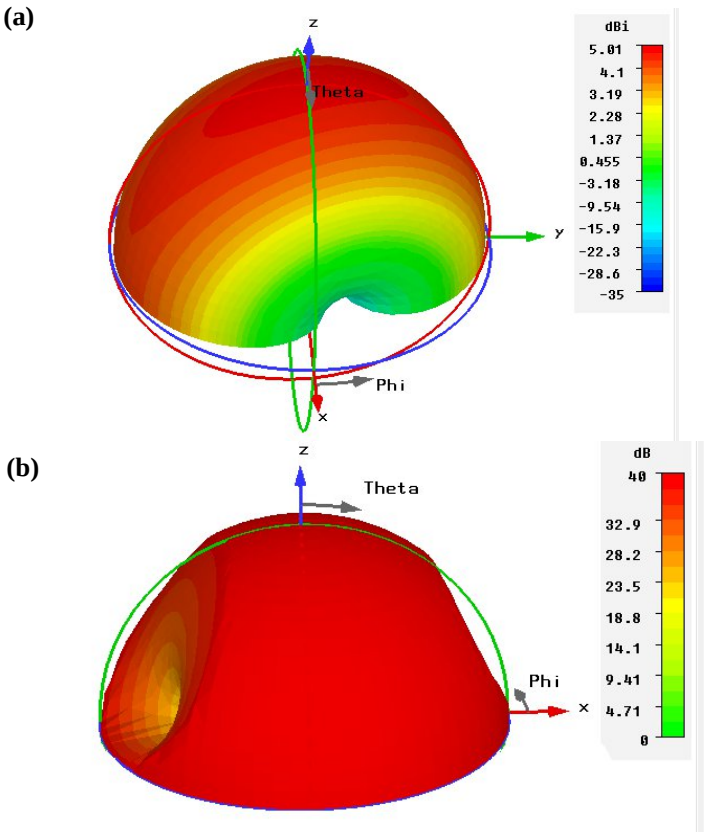

Fig. 3 Far-field radiation pattern (a) and axial ratio (b) of the NB-CSRR-based tag at 915 MHz.

far-field radiation occurs. The directivity of the antenna is 5 dBi (for an infinitely extended metallic plane), and radiation efficiency is 10%, resulting in a gain of −4.7 dB. Therefore, considering $EIRP = 4$ W (which is the maximum allowed value in many countries [1]), the read range reaches 7.6 m, according to the well-known equation [13]

$$r = \frac{\lambda}{4\pi}\sqrt{\frac{EIRP \cdot G_r \cdot \tau}{P_{th}}} \tag{4}$$

where *EIRP* is the equivalent isotropic radiated power, λ is the free-space wavelength at the working frequency, G_r is the gain of the tag antenna, P_{th} is the ASIC read sensitivity and $\tau = (1 - |s|^2)$ is the power transmission coefficient.

Let us now examine the polarization of the radiated fields. The simulated axial ratio is depicted at Fig. 3(b). As expected, the radiated wave is linearly polarized, with an excellent axial ratio (> 40 dB) over the whole half-space (z>0). The degradation of the axial ratio is limited to two very small regions, which are located in the proximity of the radiation minimums. These results suggest that the presence of the port, which formally introduces an asymmetry in the current distribution of the particle, generating a parasitic normal electrical moment p_z, has small effect on the degradation of the axial ratio of the radiated fields.

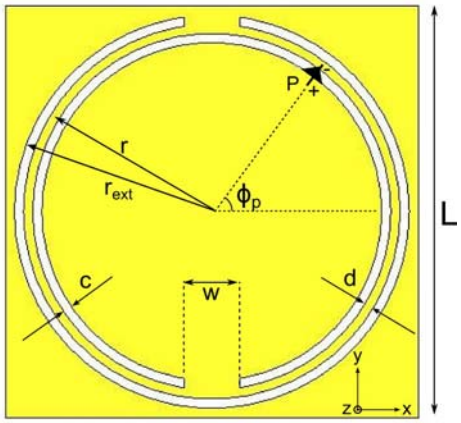

Fig. 4 CSRR-based tag layout. Metal is depicted in yellow, slot in white.

5. CSRR based tag

Let us now present an alternative new tag layout () based on the complementary split ring resonator (CSRR) working near its second resonance. The tag has been designed providing that dimensions of the particle in terms of radii, slot width and separation between rings are the same as in the previous case, in order to compare the radiation properties of the two particles. Due to the analogy of the second resonance properties of the NB-CSRR and the CSRR in terms of dimensions and tangential magnetic polarizability, the radiation pattern and efficiency are expected to be very similar. However, a comparison of the axial ratio is especially interesting because the CSRR presents cross-polarization terms, and therefore it is expected to exhibit a higher level of circular polarization.

The simulation results of the CSRR-based tag in terms of power reflection coefficient are presented at Fig. 5(a). It can be noted that the resonance notch shifted to 0.942 GHz, exhibiting similar values of bandwidth (5 MHz) and impedance matching (−11 dB) with respect to NB-CSRR based tag. The simulated radiation pattern is depicted at Fig. 5(b). As expected, the directivity and the shape of the pattern are the same as in the previous case. However, due to the symmetry of the CSRR with respect to the *yz* plane, the radiation nulls are oriented at ϕ =0º. The radiation efficiency at second resonance (13%) is also very similar that of the NB-CSRR, with a slight increase due to the larger dimension of the particle in terms of wavelength. The most significant difference between the two cases is, as expected, the linear axial ratio values (depicted at Fig. 5(c)) over the whole radiation half-space. Due to the radiation associated to the non-vanishing normal electric moment p_z at second resonance, the degradation of the axial ratio involves a considerable region of space around the radiation zeros of the pattern.

6. Conclusions

The radiation properties of a NB-CSRR placed at very small distance (≈ λ/260) from a metallic plane have been studied

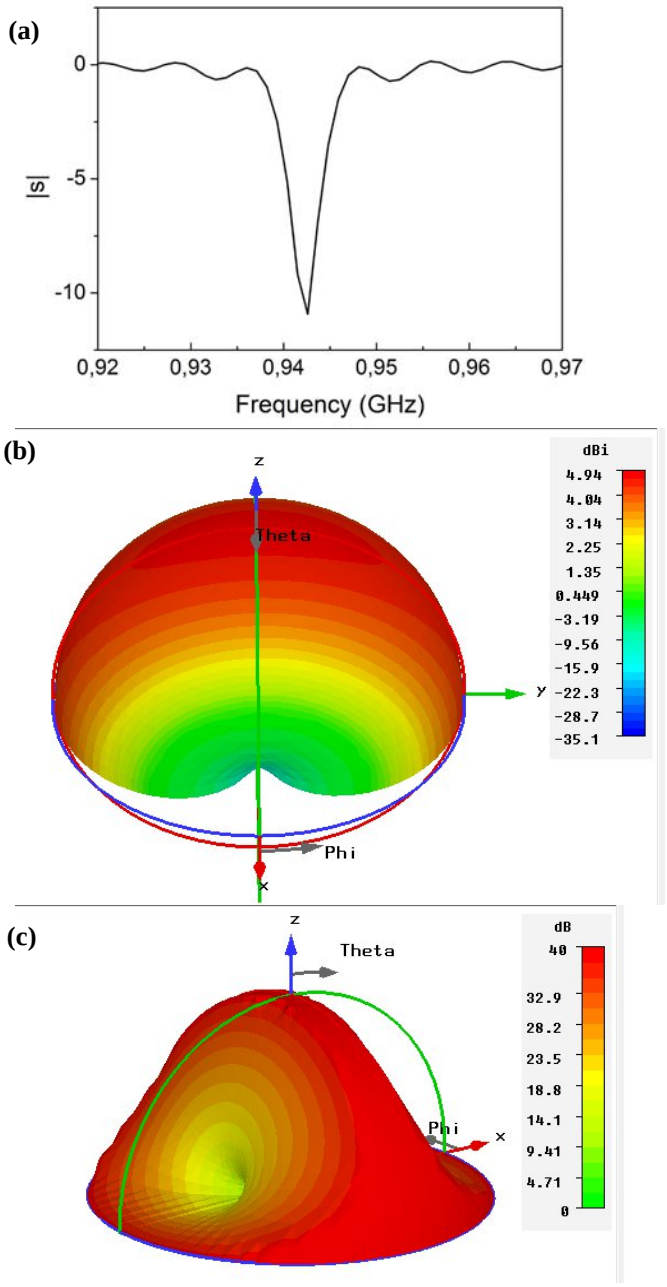

Fig. 5 Simulated power reflection coefficient (a), far-field radiation pattern (b) and axial ratio (c) of the CSRR-based tag at 942 MHz.

in this work. Due to the configuration of its intrinsic dipolar moments, the particle has been found to present an acceptable radiation efficiency (10% with *RO3010* substrate) at its second resonance frequency, which has been adjusted at 914 MHz. Due to the non-bianisotropy of the NB-CSRR, the far-field polarization is highly linear with an excellent axial ratio value (> 40 dB). This property is emphasized when comparing the radiation of the presented particle and a complementary split ring resonator (CSRR) of the same dimensions. The overall antenna gain (−4.7 dB) obtained at 914 MHz, along with the very good impedance matching level (−16 dB) when coupled to the UHF-RFID *Alien Higgs 3* ASIC, makes the proposed structure

(dimensions are 45×45×1.27 mm^3) interesting as on-metal low-profile UHF-RFID tag. The theoretical maximum read range reaches 7.6 m.

Acknowledgements

This work has been supported by MICIIN-Spain (projects TEC2010-17512 METATRANSFER and CONSOLIDER EMET CSD2008-00066), and *Generalitat de Catalunya* (project 2009SGR-421).

References

[1] GS1 EPCglobal, "Regulatory status for using RFID in the EPC Gen 2 band (860 to 960 MHz) of the UHF spectrum", 31 May 2013.

[2] B. D. Braaten, S. Roy, S. Nariyal, M. A. Aziz, B. Ijaz and M. M. Masud, "A metamaterial-based series connected rectangular patch antenna array for UHF RFID Readers," *6th European Conference on Antennas and Propagation (EUCAP)*," Prague, 26-30 March 2012, pp.3164-3167.

[3] M. Smierzchalski, S. Collardey, K. Mahdjoubi," A novel metamaterial-based RFID antenna with efficient of operating distance", *6th European Conference on Antennas and Propagation (EUCAP)*," Prague, 26-30 March 2012, pp.3038-3041.

[4] Y.-K. Jung and B. Lee, "Dual-Band Circularly Polarized Microstrip RFID Reader Antenna Using Metamaterial Branch-Line Coupler," *IEEE Transactions on Antennas and Propagation*, vol. 60 (2), pp. 786-791, Feb. 2012.

[5] S.-H. Lim , Y.-C. Oh, H. Lim, Y.-S. Lee, and N.-H. Myung, "Analysis and design of a UHF RFID tag antenna with a Split Ring Resonator," *International Workshop on Antenna Technology: Small Antennas and Novel Metamaterials*, Chiba, 4-6 March 2008, pp. 446 - 449.

[6] F. Paredes, G. Zamora, F. J. Herraiz-Martínez, F. Martín, and J. Bonache, "Dual-Band UHF-RFID Tags Based on Meander-Line Antennas Loaded With Spiral Resonators," IEE *Antennas and Wireless Propagation Letters,* Vol. 10, pp.768-771, July 2011.

[7] J.D. Jackson, *Classical Electrodynamics*, Wiley, New York, 1999 (3rd. ed.).

[8] J. Garcia, F. Martin, J.D. Baena, R. Marqués and L. Jelinek, "On the resonances and polarizabilities of split ring resonators," *Journal of Applied Physics*, vol. 98 (3), pp. 033103 - 033103-9, Aug. 2005.

[9] G. Marrocco, "The art of UHF RFID antenna design: impedance-matching and size-reduction techniques," *IEEE Antennas and Propagation Magazine*, vol. 50 (1), pp. 66-79, Feb. 2008.

[10] J.-S. Hong, M. J. Lancaster, *Microstrip Filters for RF/Microwave Applications*, John Wiley & Sons, Inc, 2001.

[11] M. Lai, R. Li, and M. M. Tentzeris, "Low-Profile Broadband RFID Tag antennas mountable on metallic objects," *IEEE Antennas and Propagation Society International Symposium (APSURSI)*, Toronto, July 2010, pp. 1-4.

[12] Alien Higgs™-3 datasheet, *Available online at* www.alientechnology.com.

[13] K. V. S. Rao, P. V. Nikitin, S. F. Lam, "Antenna Design for UHF RFID Tags: A Review and a Practical Application," *IEEE Transactions on Antennas and Propagation*, vol. 53, (12), pp. 3870-3876, December 2005.

Resistive High-Impedance Surfaces (RHIS) as Absorbers for Oblique Incidence Electromagnetic Waves

Yenny Pinto[1], Julien Sarrazin[2], Anne-Claire Lepage[1], Xavier Begaud[1], and Nicolas Capet[3]

[1]Institut Mines-Télécom, Télécom ParisTech, Paris, France
[2]Sorbonne Universités, UPMC Univ Paris 06, UR2, L2E, F-75005, Paris, France
[3]Centre National d'Etudes Spatiales, Toulouse, France
*corresponding author, E-mail: pintobal@telecom-paristech.fr

Abstract

This paper presents a lightweight microwave absorber suitable for space applications. The absorber is based on Resistive High Impedance Surface (RHIS) optimized to achieve reflection under -15dB in the band [2-2.3GHz] at normal and oblique incidences for Transverse Electric (TE) and Transverse Magnetic (TM) polarizations. A first classical isotropic RHIS structure is shown to be limited to angles of incidence up to 40° for TE polarized waves and up to 35° for TM polarized waves. So the objective of this contribution is to present a second solution based on an anisotropic RHIS structure which presents good absorption of incident waves in TE and TM polarization for larger angles of incidence. An example is presented for an incidence angle of 65°.

1. Introduction

Microwave absorbers can drastically decrease the reflection of incident electromagnetic waves within a certain frequency range. This property may be used to solve some electromagnetic compatibility problems. For space applications, the potential of absorbers covering satellite's sides in order to reduce antenna interferences and thus improving performances of some radar systems has been investigated. To do so, ultra-light absorbers able to handle extreme space conditions (wide range of temperatures, resistance to corrosion and UV…) are required.

One popular approach to design an absorber is the Salisbury screen [1]. It consists of a resistive sheet located above a ground plane at a distance of a quarter wavelength. This structure is simple but has an inherently narrow band. To increase the operational bandwidth, Jaumann absorbers use several stacked dielectric layers with resistive sheets at their interface [2]. However, this technique leads to a thick and heavy structure which is not appropriate for being embedded on satellites, mainly because of its weight.
Recently, Artificial Impedance Surfaces (AIS) or High Impedance Surfaces (HIS) have been used as absorbers. An HIS consists of a Frequency Selective Surface (FSS) over a grounded dielectric slab. The FSS is usually a periodic array of printed patterns loaded with resistors or resistive sheets in order to achieve absorption. The structure is known as a Resistive High Impedance Surface (RHIS) [3]-[6]. RHIS are usually thinner since no quarter wavelength resonances are involved. Consequently, RHIS appear to be a good candidate to achieve a low profile and light absorber, mandatory for space applications. However, two major limitations exist. Being a resonant structure, RHIS are intrinsically narrow-band. This can be overcome by increasing the distance between the FSS and the ground plane [7], of course at the expense of the thickness. The second limitation is that absorption performance depends on the incoming wave's angle of incidence. Usually, absorber designs are optimized for incident waves at normal incidence. Some research groups developed some oblique optimizations for Jaumann and Circuit Analog absorbers [8]-[10] or other thick structures [11][12], but there are relatively few works regarding the oblique incidence issue for HIS-based absorbers.

Among these few studies, some of them investigate a way to make absorbers insensitive to the angular dispersion. For example in [13], the authors use an analytical model to clearly show that increasing the permittivity of the substrate separating the ground plane from the FSS decreases the incidence angle sensitivity. This approach can be applied when the space between the FSS and the ground plane is fully (or mostly) filled by dielectric. However, achieving a light absorber involves the use of light spacer structures such as honeycomb or foam, commonly found in the space field. These materials have intrinsically a low permittivity (typically less than 1.2) and are therefore not suitable for this approach. Another way is to use ultra-thin RHIS. In fact, a short distance between the FSS and the ground plane decreases the angular dispersion. For example in [14], an absorption defined by a reflection coefficient less than -10 dB is achieved for angles ranging up to 45°, both in TE and TM cases. However, the extremely low profile of the structure ($0.017\lambda_0$) leads to a narrow bandwidth (2.7%). For the targeted application, absorption bandwidths of about 14% are expected, so this technique is not suitable.
So to the authors' knowledge, no wideband and light HIS-based structure capable of an absorption at large incident

angles (greater than 50-60°) for simultaneously TE and TM polarizations has been reported in the literature so far. Since achieving lightweight absorbers insensitive to angle dispersion appears to be a difficult task, we therefore propose a different approach to overcome this problem. In some particular applications, the angle of incidence of the incident interfering wave can be known. This is the case in some radar systems embedded on satellites for example. Thus, in respect to a given system, optimizing the absorber for a particular oblique incidence rather than achieving an angle insensitive absorber is an acceptable option.

Consequently, in this paper, we demonstrate the feasibility of a lightweight microwave absorber suitable for space applications optimized for oblique incidence. First of all, Section 2 describes the design of a light RHIS classically optimized for normal incidence and the absorber's limitations in terms of angular dispersion are highlighted. Section 3 presents the proposed solution. It consists of an anisotropic RHIS optimized simultaneously for TE *and* TM oblique polarizations. Finally, a conclusion is drawn in Section 4.

2. Classical RHIS Design

A typical RHIS consists of an array of square patches interconnected by resistors above a grounded dielectric slab. The analytical model of this structure is explained in [3]. The equivalent RHIS circuit consists of a RLC parallel circuit, where the surface impedance (Z_s) is calculated as indicated in (1) and (2). The real part of Z_s corresponds to the resistance (R) and the imaginary part is set by the patch dimensions (capacitive response Z_C) and metal-backed substrate (inductive response Z_L). Circuit losses are mainly induced by the resistors, the resonance conditions are reached when the imaginary part is zero.

$$Z_S^{-1} = R^{-1} + Z_L^{-1} + Z_C^{-1} \qquad (1)$$

$$Z_S = \frac{R}{1 - jR\left(\frac{1-\omega^2 LC}{L\omega}\right)} \qquad (2)$$

In order to calculate the absorption, this circuit is considered as the load of a transmission line model with free space characteristic impedance (Z_0). The reflection coefficients Γ^{TE} and Γ^{TM} for TE and TM polarizations respectively are obtained as indicated in (3) and (4). Z_s^{TE} and Z_s^{TM} are the surface impedance for TE and TM polarization, and θ is the angle of incidence.

$$\Gamma^{TE} = \frac{Z_s^{TE}\cos\theta - Z_0}{Z_s^{TE}\cos\theta + Z_0} \qquad (3)$$

$$\Gamma^{TM} = \frac{Z_s^{TM} - Z_0.\cos\theta}{Z_s^{TM} + Z_0.\cos\theta} \qquad (4)$$

The maximal absorption is obtained at the resonance, when the reflection coefficient approaches to zero, in that case Z_s equals to (5) or (6) for TE and TM polarization respectively. Thus the imaginary part of Z_s is equal to zero, and the impedance value is equal to the real part that corresponds to the resistance (R).

$$Z_S^{TE} = \frac{Z_0}{\cos\theta} \qquad (5)$$

$$Z_s^{TM} = Z_0.\cos\theta \qquad (6)$$

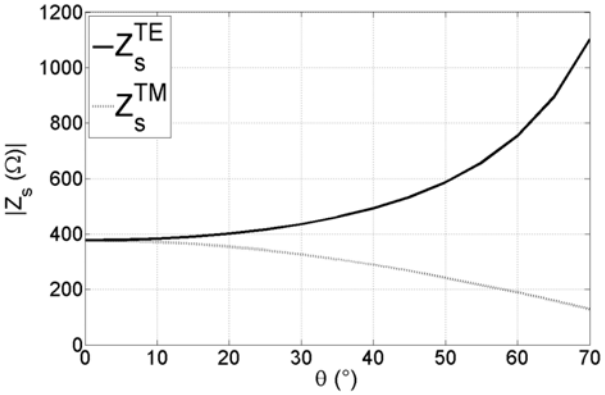

Figure 1: RHIS surface impedance at the resonance for two polarizations (TE and TM) as a function of incidence angle

In Figure 1, it appears that the surface impedance at the resonance depends on the angle of incidence for two polarizations (TE and TM). In the case of TE polarization, the optimal resistance value for maximal absorption increases as the incidence angle rises, whereas for TM polarization, the optimal resistance decreases as the incidence angle increases. So it appears that with isotropic structure, a straightforward simultaneous optimization for both TE and TM polarizations is not possible. In [15], we proposed a lightweight solution to fabricate wideband RHIS for normal incidence. It consists of an array of square patches etched on Rogers® RO4003 substrate (ε_r = 3.38 ± 0.05) on the top of a honeycomb layer (ε_r = 1.08 ± 0.05) with the ground plane (copper film) at the bottom. The resistors are implemented in a TICER® sheet with resistivity R_S = 100 Ω/square and thickness t = 0.1 μm. Figure 2 shows the unit cell of the RHIS structure. This structure, optimized at normal incidence (θ = 0°), presents a reflection coefficient magnitude lower than -15 dB from 2 to 2.3 GHz, for TE and TM polarizations. Simulation and measurement results showed that the RHIS performs well in the required band, at normal incidence, for both TE and TM polarizations. But when the angle of incidence increases, the absorption level decreases and the frequency band shifts towards higher frequencies. Therefore, the absorption in the 2-2.3 GHz band is limited to incidence angles up to 40° for waves in TE polarization, and 35° for waves in TM polarization.

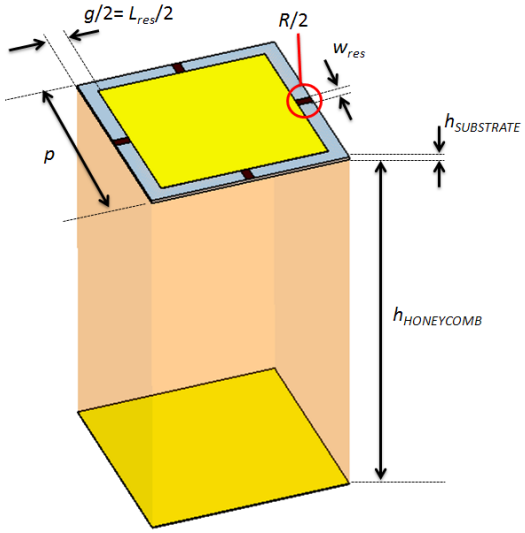

Figure 2: RHIS unit-cell ($h_{HONEYCOMB}$ = 25 mm, $h_{SUBSTRATE}$= 0.203 mm, p = 13 mm, g = 2 mm, W_{res} = 0.53 mm, L_{res} = 2 mm, R = 377 Ω)

3. Anisotropic RHIS

In this section, an optimization strategy based on a hybrid structure is proposed. The design consists in the combination of two classical RHIS structures, one optimized for TE polarization and the other one for TM polarization (Figure 3), leading then to anisotropic RHIS.

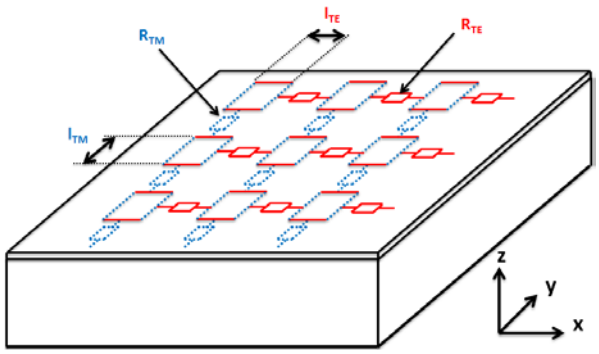

Figure 3: Configuration of the RHIS with anisotropic geometry

Thus, the structure is formed by rectangular patches instead of square patches and the patch's interconnection is made using different resistance values on each rectangle side. The RHIS anisotropic unit-cell is shown in Figure 4. Dimension p_{TM} (p_{TM} = g + l_{TM}) and resistance R_{TM} are optimized for TM polarization and p_{TE} (p_{TE} = g + l_{TE}) and R_{TE} for TE polarization.

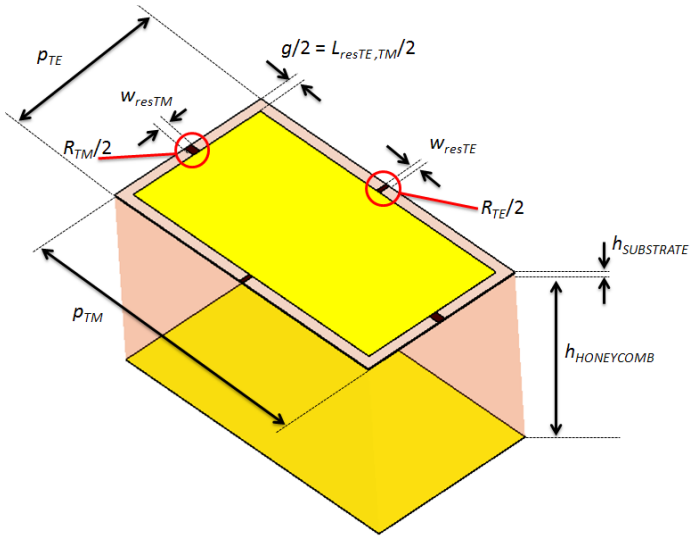

Figure 4: Anisotropic RHIS unit-cell ($h_{HONEYCOMB}$ = 25 mm, $h_{SUBSTRATE}$ = 0.203 mm, p_{TE} = 22.8 mm, p_{TM} = 42.5 mm, g = 3 mm, W_{resTE} = 0.55 mm, W_{resTM} = 1 mm, R_{TE}= 444Ω and R_{TM} = 333Ω)

This RHIS is then optimized to achieve a reflection lower than -15 dB in the band [2-2.3GHz] for TE and TM polarization at 65° angle of incidence. The structure is made of the same materials with same characteristics as the classical isotropic RHIS presented in the previous section.
The RHIS anisotropic unit-cell is simulated using CST Microwave Studio©. The simulated results are plotted in Figures 5 and 6; the required performance is obtained for 65° angle of incidence in both TE and TM polarization.

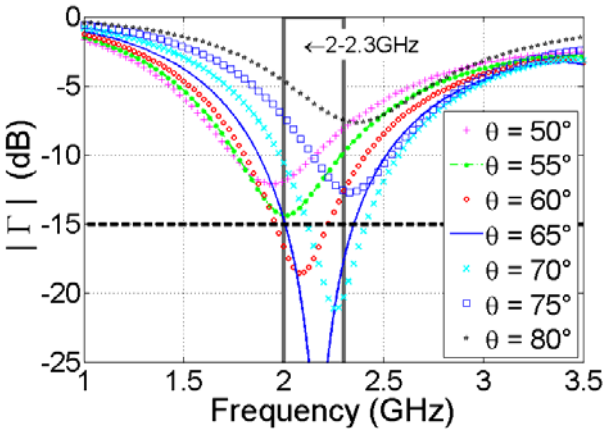

Figure 5: Reflection coefficient for different angles of incidence for TE polarization

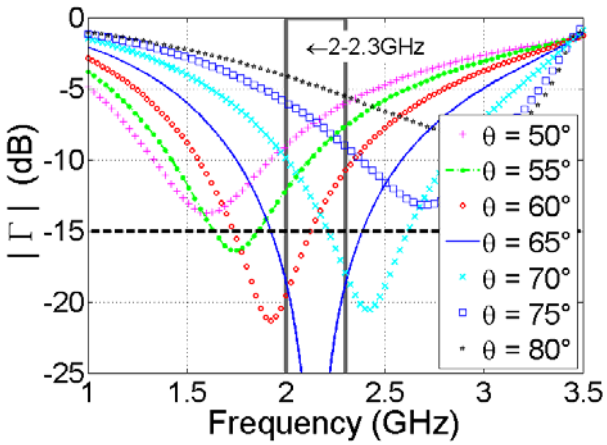

Figure 6: Reflection coefficient for different angles of incidence for TM polarization

These results show that to absorb incident waves in a particular oblique incidence and working at the same time for TE and TM polarizations is feasible using an RHIS structure with anisotropic geometry. However, the angular dispersion is restricted to +/- 5° around the optimal angle of incidence, with a -15 dB reflection criteria in both TE and TM polarizations, but the frequency band is shifted. The frequency shift is more significant in TM polarization.
In order to validate the concept, simulation results have been compared to measurements. The anisotropic RHIS prototype is realized using the same materials and method as those of the isotropic RHIS prototype described in [15]. The patches with resistors are implemented over Rogers® RO4003 substrate with the TICER® resistive film, on top of a honeycomb slab with a copper film at the bottom. Figure 7 shows the prototype.

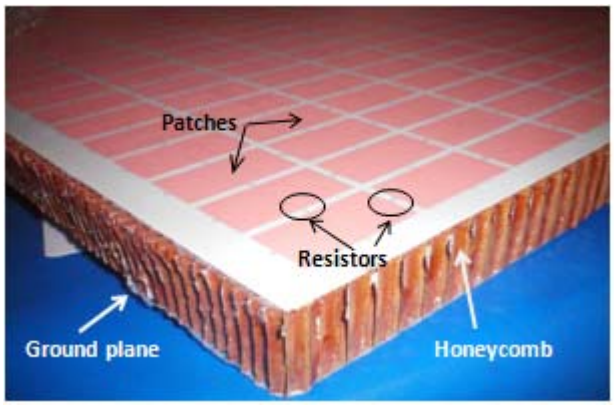

Figure 7: Anisotropic RHIS prototype

The measurement of the reflection coefficient is carried out as detailed in [15]. The reflection coefficient is measured using two horn antennas. The two horn antennas are connected to a network analyzer E5071C Agilent. The Figure 8 illustrates the measurement setup at oblique incidence. The distance between the antenna and anisotropic RHIS prototype is d_{am} = 107 cm. The anisotropic RHIS prototype is fixed and the antennas are placed according to incidence angle ($\theta_i = \theta_r$).

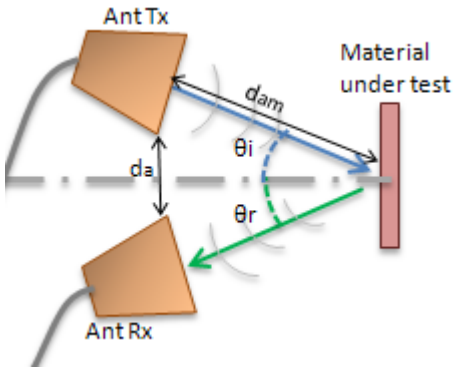

Figure 8: Measurement setup at oblique incidence

The measurements are performed for oblique incidence (60 °). The results are plotted in Figure 9 for TE polarization and measurements for TM polarization are presented in Figure 10.

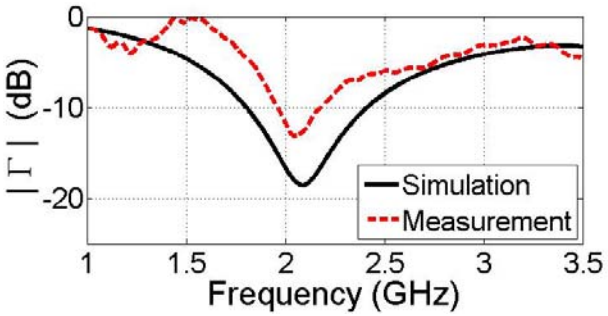

Figure 9: Comparison between simulation and measurement results at oblique incidence (60 °). TE polarization

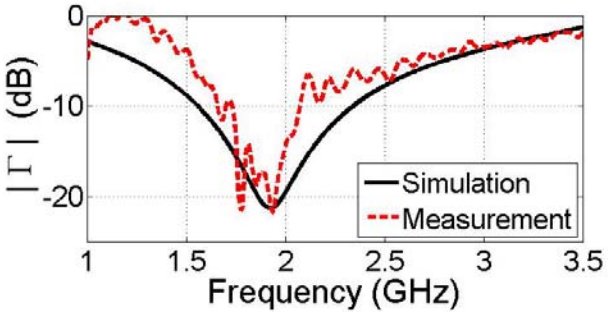

Figure 10: Comparison between simulation and measurement results at oblique incidence (60°). TM polarization

A good agreement between results is obtained however differences in frequency and level are observed.
Shifts in frequency and level can be explained by different ways:

- The imperfections of realisation.

- The simulation does not take into account the presence of the double-sided adhesive film.
- The resistance value is not accurate and has a tolerance of + / - 10 %.
- The permittivity value of honeycomb is not accurate.

4. Conclusions

The design of a lightweight absorbing material for larger angles of incidence based on a Resistive High Impedance Surface (RHIS) has been described. It has been firstly highlighted that the classic isotropic RHIS can meet the required specifications at normal incidence but only up to a 40° incidence for waves in TE polarization, and 35° for waves in TM polarization. Hence a second solution based on an anisotropic RHIS structure has been proposed. This solution performs well for a given angle of incidence in both TE and TM polarization. The final design has been optimized to absorb 65° incident waves on both TE and TM polarization simultaneously. Simulations have been validated by measurements.

References

[1] W.W. Salisbury, "Absorbent, body for electromagnetic waves", U.S. Patent 2599944, June, 1952.

[2] L. J. Du Toit, "The Design of Jaumann Absorbers", *IEEE Antennas and Propagation Magazine*, vol. 36, no. 6, pp. 17-25, Dec. 1994

[3] F. Linot , X. Begaud , M. Soiron, C. Renard and M. Labeyrie, "Characterization of a loaded high impedance surface", *International Journal of Microwave and Wireless Technologies,* 1, pp 483-487, 2009

[4] F. Costa , A. Monorchio, and G. Manara, "Analysis and Design of Ultra Thin Electromagnetic Absorbers Comprising Resistively Loaded High Impedance Surfaces", *IEEE Transactions on Antennas and Propagation*, Vol. 58, No.5, pp.1551-1558, May 2010

[5] Y. Tsuda, T. Yasuzumi and O. Hashimoto, "A ThinWave Absorber Using Closely Placed Divided Conductive Film and Resistive Film", *IEEE Antennas and Wireless Propagation Letters,* Vol. 10, pp. 892-895, 2011

[6] M. Li, S.Q. Xiao, Y. Y. Bai and B.Z. Wang, "An Ultrathin and Broadband Radar Absorber Using Resistive FSS", *IEEE Antennas and Wireless Propagation Letters,* Vol. 11, pp. 748-751, 2012

[7] Y. Pang, H. Cheng, Y. Zhou and J. Wang, "Upper Bound for the Bandwidth of Ultrathin Absorbers Comprising High Impedance Surfaces", *IEEE Antennas and Wireless Propagation Letters,* Vol. 11, pp. 224-227, 2012

[8] B.A. Munk, P. Munk and J. Pryor, "On Designing Jaumann and Circuit Analog Absorbers (CA Absorbers) for Oblique Angle of Incidence", *IEEE Transactions on Antennas and Propagation*, Vol. 55, No.1, pp.186-193, Jan. 2007

[9] A. Kazemzadeh and A. Karlsson, "Multilayered Wideband Absorbers for Oblique Angle of Incidence", *IEEE Transactions on Antennas and Propagation*, Vol. 58, No.11, pp.3637-3646, Nov. 2010

[10] B. Chambers and A. Tennant, "Design of wideband Jaumann radar absorbers with optimum oblique incidence performance", *Electronics Letters*, Vol. 30, No.18, pp. 1530-1532, Sep. 1994

[11] R. Janaswamy, "Oblique Scattering from Lossy Periodic surfaces with Application to Anechoic Chamber Absorbers", *IEEE Transactions on Antennas and Propagation*, Vol. 40, No.2, pp.162-169, Feb. 1992

[12] H. Cho, H. Ling and C.H. Liang, "Design of Corrugated Absorbers for Oblique Incidence Using Genetic Algorithm", *IEEE Antennas and Propagation Society International Symposium*, Vol. 4, pp.708-711, 2001

[13] O. Luukkonen, F. Costa, C.R. Simovski, A. Monorchio, and Tretyakov S.A., "A Thin Electromagnetic Absorber for Wide Incidence Angles and Both Polarizations", *IEEE Transactions on Antennas and Propagation*, Vol. 57, No.10, pp.3119-3125, Oct. 2009

[14] B.Q. Lin, C.M. Tong, W. Li, H.B. Niu and H. Zhou, "An Ultra-thin Electromagnetic Absorber Comprising Resistive Resonance Loops", *IEEE Antennas and Wireless Propagation Letters*, 2012

[15] Y. Pinto, J. Sarrazin, A.C. Lepage, X. Begaud and N. Capet, "Design and measurement of a thin and light absorbing material for space applications", *Applied Physics A*, 2013, 10.1007/s00339-013-8077-5.

Design and Model of Wideband Absorber made of Ultrathin Metamaterial Structures

Alexandre Sellier,[1] Tatiana V. Teperik,[1] Shah Nawaz Burokur,[1,2] Guy Sabanowski,[3] Gérard-Pascal Piau[3] and André de Lustrac[1,2,*]

[1]IEF, Univ. Paris-Sud, CNRS, UMR 8622, 91405 Orsay Cedex, France
[2]Univ. Paris-Ouest, 92410 Ville d'Avray, France
[3]Airbus Group Innovations, 92000 Suresnes, France
*corresponding author, E-mail: andre.de-lustrac@u-psud.fr

Abstract

A planar microwave ultrathin broadband absorber is proposed. It is composed of metallic patterns arranged on a dielectric material which is backed by a copper plate. The patterns of different dimensions allow to judiciously design absorption peaks at specific frequencies of interest. These peaks are due to the mode resonances of the cavities formed by the metallic patches, the dielectric substrate and the copper plate. In order to widen the absorption bandwidth, patterns of different dimensions are used, together with the different modes of these cavities. Numerical and experimental results are presented to validate the proposed method at microwave frequencies. It is also shown that the use of a composite air-dielectric substrate supporting the metallic patterns helps to increase the absorption level.

1. Introduction

Radar absorption materials (RAM) and radar absorbing structures (RAS) are used to absorb electromagnetic waves and to reduce the radar cross section (RCS) in commercial activities such as electromagnetic compatibility (EMC) and defence applications. Dällenbach absorbers, Salisbury screens and Jaumann layers, the first classical structures of electromagnetic absorbers are resonant and constitute the base of today's developments [1,2]. In Dällenbach absorbers, the incident power is dissipated in a homogeneous dielectric layer over a ground plane. In Salisbury screens, a resistive sheet with tuned impedance is placed over a ground plane at a distance of $\lambda/4$ (where λ is the working wavelength) in order to generate destructive interference in a narrow frequency band. To generate a wider absorption band, several Salisbury screens are stacked over each other to form the Jaumann configuration. Possibilities to enhance the performance of these absorbers have been widely studied and common absorbers are issued from these studies especially ferrite electromagnetic wave absorbers [3] and pyramidal RAM [4].

Recent developments in absorbers are mostly oriented toward the use of frequency selective surfaces (FSS) [5-7]. Most investigations around FSS are based on adding high impedance surfaces (HIS) on thin Salisbury electromagnetic absorbers to minimize reflectivity over a wide frequency band [8,9]. An interesting way consists in designing a material which presents impedance close to the impedance of free space by using genetic algorithms [10,11]. A recently proposed optimization consists in employing metamaterials (MMs) to increase losses. To create an efficient absorber from metamaterials, the imaginary parts of the electromagnetic parameters are manipulated to enhance the tangent losses [12,13]. Therefore, radiative and dissipative damping are tuned, as in a cavity, to trap the incident wave. Single-layered metamaterial absorbers have been designed to operate at different frequencies simultaneously [14-16]. However, they are not able to cover a wide frequency range due to strong coupling between each pattern on the same layer. Multilayer metamaterial absorbers have then been designed to overcome the coupling problem and to create wideband frequency operation [17-19]. Such multilayer structures are thick and complicated to fabricate. Very recently, a metamaterial absorber has been applied to a waveguide slot antenna in order to reduce its radar cross section [20]. MM absorbers are the keys for future development in various applications including camouflaging, non-invasive probing and sensing in medical and biological applications. Several studies have been made on these new kinds of absorbers, mainly in the THz and visible domains [21-29]. However, these studies deal with the realization of multi-band absorbers using different resonances.

In this paper, we present a new type of ultrathin wideband metamaterial absorbers for microwave and optical applications. These ultrathin materials, without lossy dielectric substrate of thickness of $\lambda/50$, are able to absorb an electromagnetic wave with nearly 100% efficiency, as well as a much thicker classical absorber. Classical absorbers generally use lossy dielectric and/or magnetic substrates to obtain wide absorption frequency band and metamaterials absorbers use complex multilayer structures. Conversely, we demonstrate that using only plasmonic effect in metallic structures on a low-loss dielectric substrate, absorption can be realized using resonance in ultrathin cavities. Furthermore, we achieve wide band

operation using an engineering of different electromagnetic modes of different metallic cavities. We describe also the strategy to obtain an adjustable wideband frequency operation from such configuration. Comparison between simulation and experimental result demonstrates the validity of this approach. Finally a theoretical model is presented to analyze the physical behavior of these ultrathin absorbers and to allow their optimization.

2. Design methodology

We consider a periodic lattice of metallic patches etched on a perfect electric conductor (PEC) backed commonly used 17.5 µm copper clad epoxy-FR4 material (ε_r = 4.4 and tan δ = 0.0197) of thickness h = 0.3 mm. The basic structure of a single unit cell is shown in Fig. 1(a). For an electromagnetic

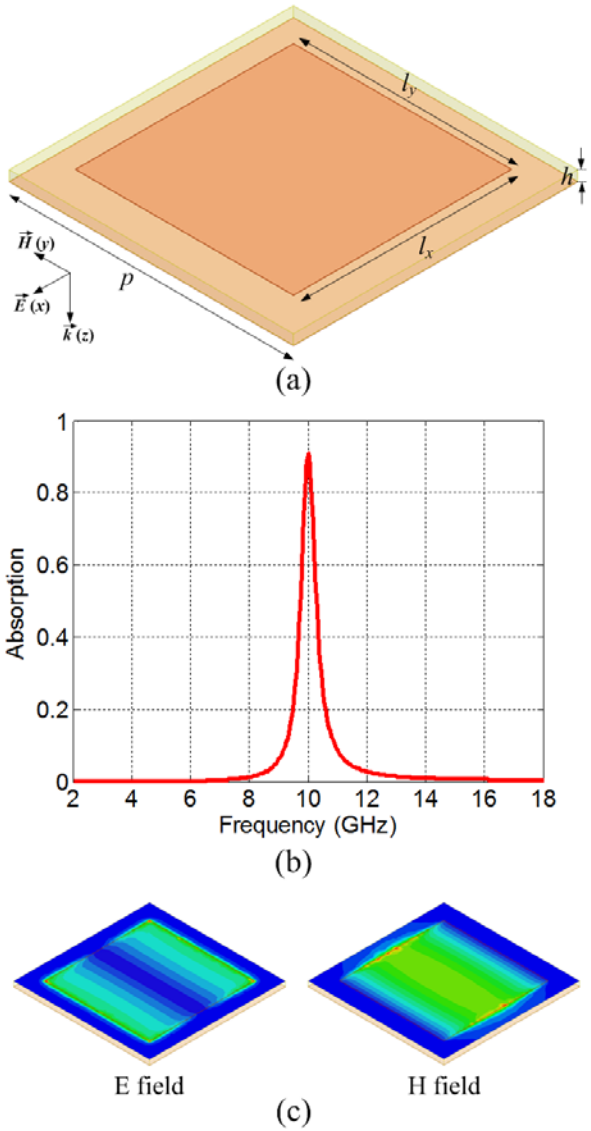

Figure 1: (a) Unit cell of the metamaterial absorber composed of a copper patch patterned on a dielectric material backed by a copper plate. (b) Absorption performance of the absorber. (c) E and H field distributions at the maximum absorption frequency on the surface of dielectric substrate where the patch is printed.

wave incident with a wave vector normal to the surface of the patch and field polarization of Fig. 1(a), electromagnetic resonances are excited at specific frequencies.

The first resonance occurs at a frequency corresponding to roughly below half the guided wavelength. The different dimensions of the patches are as follows: p = 8.6 mm and l_x = l_y = 6.6 mm. The electromagnetic behaviour of the structure is analyzed through the use of the commercial software Ansys HFSS [30] based on the finite element method. The elementary cell is simulated using appropriate periodic boundaries. Since there is no transmission due to the metallic ground plane of the structure, the absorption is calculated using the simple formula $A = 1\text{-}R^2$, where R is the magnitude of the reflection of the structure. The transmission factor is null due to the metallic ground plane of the structure. Fig. 1(b) and 1(c) respectively shows the absorption peak at the first resonance of the patch and the E and H field distributions at resonance on the surface of the dielectric substrate. Microwave cavity TE or TM model is well suited to approximate the resonant frequencies of the structure, though the lattice effect and inter-element capacitance is not taken into account in such model. Rectangular cavity TE_{mnp} or TM_{mnp} modes are defined by [5,31-33]:

$$f_{mnp} = \frac{c}{2\sqrt{\varepsilon_r \mu_r}} \sqrt{\left(\frac{m}{h}\right)^2 + \left(\frac{n}{l_x}\right)^2 + \left(\frac{p}{l_y}\right)^2}, \quad (1)$$

where m, n and p being the mode numbers and h, l_x and l_y the corresponding dimensions of the cavity as defined above. ε_r and μ_r are respectively the relative permittivity and permeability of the substrate. The calculated f_{010} is 10.8 GHz which is close to the simulated value of 10 GHz of Fig. 1(b). Fig 1(c) shows that indeed the electromagnetic energy is confined in the cavity at 10 GHz to achieve the 90% absorption.

The bandwidth $\Delta\omega$ of the resonance is determined by the quality factor Q of the cavity formed by the metallic patch, the dielectric substrate and the ground plane:

$$Q = \omega W / P_{loss} \quad \text{and} \quad \Delta\omega = P_{loss} / W, \quad (2)$$

where W is the stored energy in the cavity and P_{loss} is the power losses in this cavity. Here the relative bandwidth $\Delta\omega/\omega$ of the resonance is around 6% and the quality factor Q is around 16. These values are determined by the losses in the dielectric substrate and also by the radiating losses.

In such metallic patch structure, the absorption is limited to a very narrow frequency band around the resonance. To extend the useful bandwidth, a recently proposed possibility consists in stacking several metallic structures with different sizes separated by dielectric layers [19]. Such a configuration can be very thick. We propose here another strategy, which consists in juxtaposing several metallic structures with different sizes in order to remain in a planar configuration. The unit cell presented in Fig. 2(a) illustrates an example of such a design. The dimensions of the different patches composing the unit cell are given in Table 1. The E-

field of the incident wave is oriented along the *x*-axis. Fig. 2(b) shows the different absorption peaks located in the 2-18 GHz frequency band. Each peak corresponds to a specific resonant patch of the cell. As illustrated in Fig. 2(c), the absorption peak at 4.65 GHz corresponds to the 010 mode of the patch B, whereas the one located at 9.1 GHz corresponds to the 010 mode of the patch E. The absorption peak at 10 GHz on the counterpart corresponds to the 010 resonance mode of the patches A and C simultaneously since they both have the same dimensions l_x along the direction of the E-field. We can also note the resonance of the 030 mode of the patch B at 13.5 GHz.

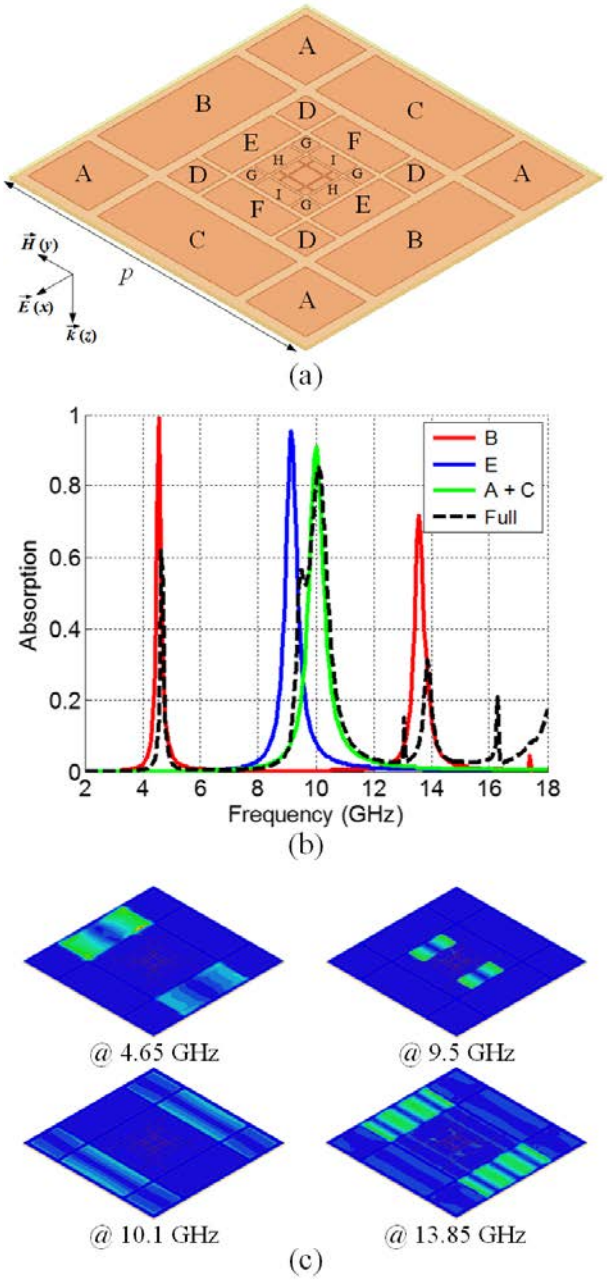

Figure 2: (a) Unit cell of the proposed broadband absorber. (b) Absorption peaks created by the patches of different dimensions and the whole structure associating the patches. (c) Field distributions at the different absorption peaks.

Table 1: Dimensions of the different patches of the broadband absorber unit cell of periodic lattice p = 32.4 mm

Patch	l_x (mm)	l_y (mm)
A	6.6	6.6
B	15.2	6.6
C	6.6	15.2
D	3.3	3.3
E	7.6	3.3
F	3.3	7.6
G	1.65	1.65
H	3.8	1.65
I	1.65	3.8

This configuration is interesting as it shows several features that we can use to increase the absorption band of this type of structure. For instance, Fig. 2(b) shows that the resonance of the patches A and C is close to that of E and indicates that they can be merged to constitute a wider absorption band. Higher resonance modes can also be used to create absorption peaks at high frequencies, as illustrated by the 030 resonance mode of the patch B.

The calculated absorption response of the whole structure is also given by the dashed black trace in Fig. 2(b). The absorption peaks are consistent with those when the patches were simulated separately. Associating the patches of different dimensions together in a single structure has an impact on the level of absorption. As it can be clearly observed, the absorption level is reduced. We can also note that a wider absorption band is obtained around 10 GHz resulting from two close resonances. Two other low absorption peaks at 13.05 GHz and 16.3 GHz are observed from the response of the whole structure. The one at 13.05 GHz corresponds to the 012 resonant mode of the patch C and the other one at 16.3 GHz corresponds to the 010 mode of the patch H.

3. Experimental validation

A prototype of the structure associating the patches of different dimensions shown in Fig. 2(a) has been fabricated and the photography is shown in Fig. 3(a). The prototype has been experimentally measured using an Agilent 8722ES network analyzer and two 2-18 GHz wideband horn antennas. In this prototype, the patterns are printed on one of the face of the epoxy-FR4 material. A copper plate is applied on the back of the dielectric substrate. To increase the level of absorption when associating the patches of different dimensions on a single structure, a thin air layer of 0.2 mm is left between the dielectric substrate and the copper plate. The consequences of this thin air layer are important on the results. The air layer reduces the apparent permittivity of the dielectric substrate, which causes the resonances to shift towards higher frequencies. The addition of the thin air layer also widens bandwidth due to the increase in thickness of the dielectric support. And, finally the absorption level is higher than without the air layer, approaching value close to unity support by a better agreement between radiative and dissipative damping for each resonant mode [Fig. 3(b)].

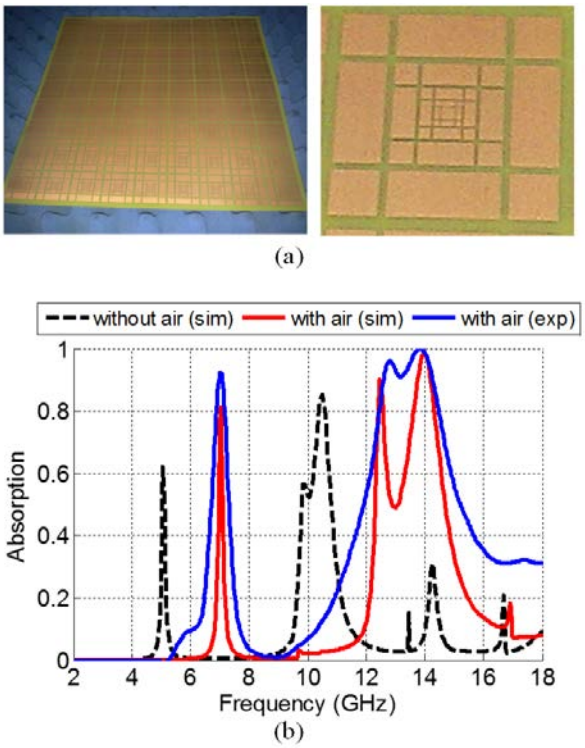

Figure 3: (a) Photography of the fabricated prototype of the metamaterial absorber. (b) Realized performances of the proposed metamaterial absorber.

4. Enhancing the absorption bandwidth

As stated earlier, the absorption bandwidth can be broadened by designing close resonances from judiciously calculated dimensions of the metallic patches. As illustrated in Figs. 2(b) and 3(b), the successful merging of two close resonances has led to a simulated 50% absorption frequency band of 1 GHz. To further justify such design methodology and to enhance even more the absorption frequency band, the metamaterial cell has been recalculated to produce four close resonances. The new design is illustrated in Fig. 4(a) and the dimensions of the different patches are given in Table 2.

Table 2: Dimensions of the different patches of the optimized broadband absorber unit cell of periodic lattice p = 36.4 mm and h = 0.4 mm

Patch	l_x (mm)	l_y (mm)
A	6.6	6.6
B	11.2	6.6
C	6.6	11.2
D	6.4	6.4
E	3.8	6.4
F	6.4	3.8
G	3.8	3.8

This optimized configuration shows the merging of four close resonances in order to widen the absorption bandwidth [Fig. 4(b)]. The 50% absorption bandwidth of the optimized broadband cell is 2 GHz that is 2 times wider than the cell merging two resonances. We observe that the absorption is

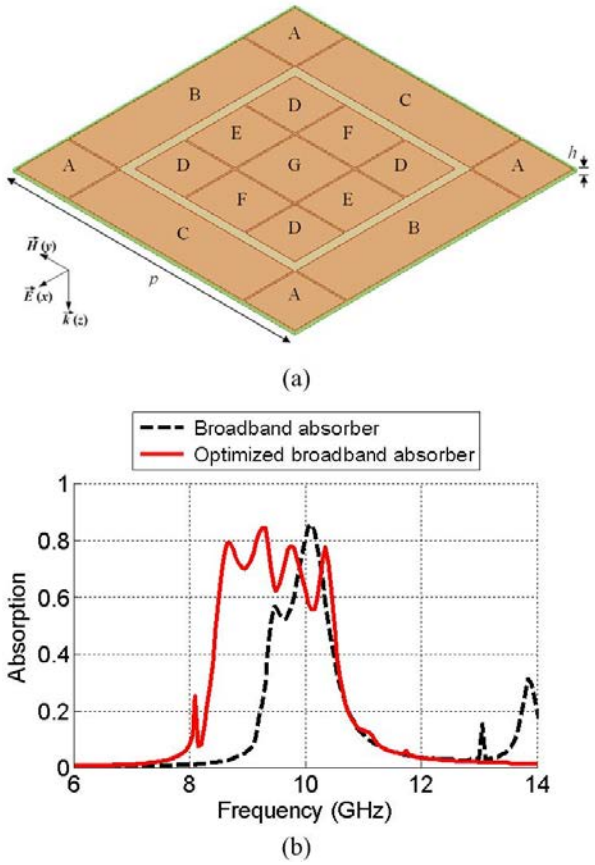

Figure 4: (a) Unit cell of the optimized broadband absorber composed of four resonances. (b) Simulated absorption response of the optimized design.

lower than 100% in this configuration. This indicates that a further optimization is needed to increase the absorption level of this structure.

5. Theoretical model

After these first experimental results we present here a simple physical model describing the properties of planar metallic metamaterial in terms of equivalent oscillating-current resonant circuit. In this analytical approach we describe the absorptive layer squeezed between the periodic arrangement of metallic patches and ground plane by effective load impedance. This allows us to go beyond the geometry and to find the universal ruler for total absorbing effect to be achieved.

In Fig. 5 we present the structure under consideration. It is a periodic arrangement of square metallic patches of length l located above a ground plane at a distance $s << \lambda$ (λ is the wavelength). Between the patch and the ground plane we include an absorptive layer with a weak loss tangent ($\tan\delta = \varepsilon''/\varepsilon' << 1$, where ε' and ε'' are respectively the real and imaginary part of the dielectric permittivity). We assume at the beginning that the ground plane as well as the patch is made of perfect metal.

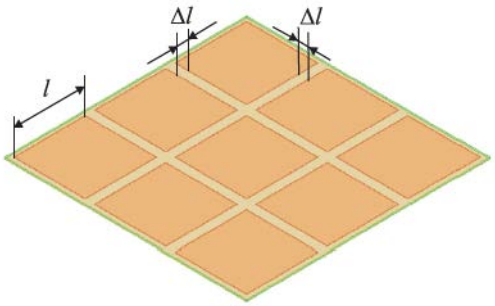

(a)

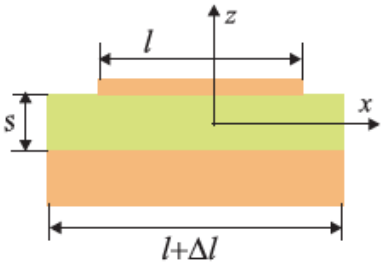

(b)

Figure 5: (a) Schematic of planar metamaterials with lattice of metallic patches separated from the ground plane by absorptive layer. (b) Dimensions of a patch.

In general this structure poorly absorbs the electromagnetic energy. However, if one could match the free-space impedance (purely resistive), $Z_0 = 120\pi\Omega$, to the impedance of the metasurface, the incident energy would be completely transformed into Ohmic losses inside the absorptive layer and the total absorption effect would be achieved. If we consider that the electric current induced in absorptive layer by an incident plane wave is oscillating along the patch side, the electronic resistance R of the absorptive layer is inversely proportional to the layer thickness s and, therefore, extremely large compared to the free-space impedance Z_0. Using an intrinsic resonance may solve the problem of the impedance matching. At resonance, the real part of the effective impedance (i.e. the effective electric resistance) can be drastically decreased, while the inductive reactance inherent to the resonance may be canceled by a capacitive one, thus leaving the effective impedance purely resistive. The absorptive layer squeezed between the patches and ground plane supports a transverse magnetic (TM) mode with a dispersion that can be easily obtained by imposing the zero electric field conditions above and below the absorptive layer:

$$k = \omega\sqrt{\varepsilon}/c\,, \qquad (3)$$

Here ω is the frequency, $\varepsilon = \varepsilon'(1 + i\tan\delta)$ is the complex dielectric function of the absorptive layer, and c is the speed of light. The resonance frequencies of the structure in Fig. 5 can be obtained by quantization of the TM mode (Eq. (3)) by the patch. The metallic patches play the role of a Fabry-Perot resonator for the guided TM mode squeezed between the patch and ground plane, propagating along the absorptive layer and reflected at the terminations of the patch. Assuming that the modes are strongly localized under the patch and the field does not undergo the fringing at the patch edges, we obtain that:

$$k_{nm} = \frac{\omega_{nm}\sqrt{\varepsilon}}{c} = \frac{\pi}{l}\sqrt{n^2 + m^2}\,, \qquad (4)$$

where

$$f_{mn} = \frac{\omega_{mn}}{2\pi} = c\sqrt{n^2 + m^2}\,/\,2l\sqrt{\varepsilon}\,, \qquad (5)$$

are actually the resonant frequencies of a classical square patch antenna [5,31-33]. n, m = 0;1;2;… are integer and $n^2+m^2 \neq 0$.

In Fig. 6a we present the absorption spectra of the metamaterial absorber for a patch-to-patch separation Δl = 2 mm and different patch lengths l. The calculations have been performed for normal incidence with use of the commercial software COMSOL Multiphysics [34] based on the finite element method. We can observe a series of resonances associated with the excitations of the first (n = 1, m = 0) and the next (n = 3, m = 0) patch antenna's modes. One can notice nearly total absorption of electromagnetic radiation at the resonance of the first TM mode.

In order to provide a general view on the effect of total absorption regardless the particular geometry of the patch, we apply a RLC circuit model (Fig.7). In this RLC model a structured surface is considered as load impedance at the end of the transmission line modeling the free space. Let us first introduce the effective surface impedance Z_{eff} of the metasurface. In this case the reflection from metasurface can be described on a common basis independently of type of structuring. We describe the resonance of the TM mode excited by a normally incident plane wave and squeezed between the patch and ground plane in terms of its equivalent resonant RLC circuit. In Fig. 7b we present the equivalent RLC circuit of the TM mode for the metasurface of Fig. 7a. This circuit describes the main physical features of the resonant structures and contains (i) the total resistance R that determines the amount of power absorbed due to Ohmic losses, (ii) the total inductance L created by the finite electric currents oscillating in metallic patch and ground plane, and (iii) the total capacitance C that describes the

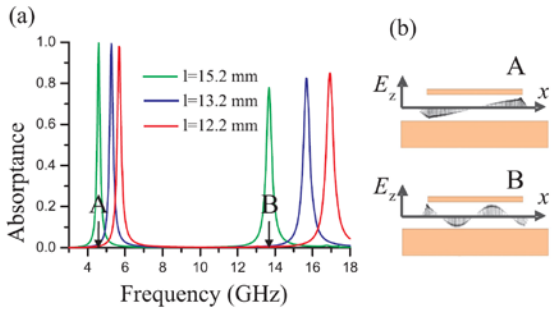

Figure 6: (a) Absorption spectra for different patch length l: 12.2 mm (red curve), 13.2 mm (blue curve), and 15.2 mm (green curve). The period of the structure is l +Δl with patch to-patch separation Δl = 2 mm and absorptive layer thickness s = 0.3 mm. (b) Near-field distribution Ez in the first and third resonant modes calculated along the line z = 0 and x = 0.

charge accumulation induced by the external field.

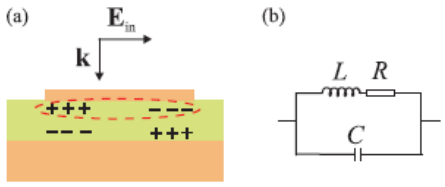

Fig.7: (a) Schematically charge distribution in TM mode induced by normally incident plane wave. (b) Resonant RLC equivalent circuit

The equivalent impedance of the circuit can be written as

$$Z = \frac{R + i\omega L}{1 - \omega^2 LC + i\omega RC^2}, \tag{6}$$

Equivalently, Eq. (6) can be cast in the form

$$Z = \frac{1}{C}\frac{2\nu + i\omega}{\omega_0^2 - \omega^2 + 2i\omega\nu}, \tag{7}$$

where the dissipative mode damping $\nu=R/2L$ and $\omega_0 = 1/\sqrt{LC}$. The resonant frequency can be derived by $Im(Z)=0$ as $\omega_{res}^2 = \omega^2 - \left(\frac{R}{L}\right)^2 = \omega^2 - 4\nu^2 \approx \omega_0^2$. In the vicinity of the resonance $\omega \approx \omega_0$ assuming that $2\nu << \omega_0$ (i.e. high quality resonance) we obtain:

$$Z = \frac{1}{C}\frac{i}{\omega_0 - \omega + i\nu}, \tag{8}$$

The total frequency-dependent equivalent impedance of the metasurface can be expressed as

$$Z = \frac{|\beta|^2}{C}\frac{i}{\omega_0 - \omega + i\nu}, \tag{9}$$

where we introduce the coefficient $|\beta|^2 < 1$ responsible for the coupling of the incident field with the resonant mode. The coupling coefficient $|\beta|^2$ depends both: on the mode number and geometry of the structure (namely patch-to-patch distance).

Now let us calculate the absorption by a thin layer characterized by effective impedance Z_{eff}. Since there is no transmission through the structure we apply the impedance boundary condition [34] and obtain a complex-valued reflection coefficient for the normal incidence in the form

$$r = \frac{Z_{eff} - Z_0}{Z_{eff} + Z_0}, \tag{9}$$

Then, the reflectance and absorbance of the electromagnetic energy in the vicinity of a given trapped mode resonance can be expressed as

$$R = |r|^2 = \frac{(\omega_0 - \omega)^2 + (\nu - \gamma)^2}{(\omega_0 - \omega)^2 + (\nu + \gamma)^2}, \tag{10}$$

$$A = 1 - |r|^2 = \frac{4\nu\gamma}{(\omega_0 - \omega)^2 + (\nu + \gamma)^2}, \tag{11}$$

γ is defined by

$$\gamma = |\beta|^2 / 2CZ_0, \tag{12}$$

γ is the radiative damping of the mode that depends through the capacitance C on the geometry of the structure and the dielectric function of the absorptive layer.

Having introduced the radiative and dissipative damping of the resonant TM modes, we now discuss their contribution to the shape of absorption spectra. From Eqs. (11) and (12) one finds at resonance ($\omega = \omega_0$)

$$R = |r|^2 = \frac{(\nu - \gamma)^2}{(\nu + \gamma)^2}, \tag{13}$$

and

$$A = \frac{4\nu\gamma}{(\nu + \gamma)^2}, \tag{14}$$

from where one can readily see that resonant total absorption ($A_{res} = 1$) occurs when

$$\nu = \gamma, \tag{15}$$

or

$$\frac{R}{2L} = \frac{|\beta|^2}{2CZ_0}, \tag{16}$$

This is the condition to obtain a total absorption in these structures.

6. Conclusion

To summarize, a new type of ultrathin wideband metamaterial absorber has been proposed for microwave and optical applications. The design method to extend at will the absorption band of this absorber has been presented. The absorber is made of a set of cavities of different dimensions showing different resonant frequencies. The cavities are formed by metallic patches placed over a dielectric substrate backed by a metallic plate. The absorption phenomenon due to the cavity effect in metallic structure is strong even with low-loss dielectric substrate. The absorption level and bandwidth can be judiciously enhanced by using a composite air-dielectric substrate. Along with rigorous electromagnetic calculations and characterization of prototypes we present a simple resonant circuit model that describes the resonant absorption in terms of impedance matching and radiative/dissipative damping of the resonant mode. We show that in spite of evident simplicity of the model it fully reproduces the rigorous calculations. We distinguished the radiative and dissipative contributions to

the resonance linewidth and discussed the role of radiative and dissipative trapped mode decay rates in formation of the absorption spectra. In particular, we found that the square patch based metasurface can exhibit the effect of total absorption once the radiative and dissipative damping of modes are equal. This concept can be transposed to any frequency domain, even in infrared and could be used in photovoltaic applications where it can allow increasing the efficiency of such devices [35].

Acknowledgements

The authors are grateful to the Direction Générale de l'Armement (DGA) for the financial support of the REI project "Novel Metamaterial-based Radar Absorbing Structures" under Contract No. 2009-34-0030. The authors also thank S. Gransart for fruitful discussions.

References

[1] W. Dällenbach and W. Kleinsteuber, Hochfreq. u Elektroak **51**, 152 (1938).
[2] W. W. Salisbury, United States Patent, no. 2599944 (1952).
[3] Y. Naito and K. Suetake, IEEE Trans. Microwave Theory Tech. **19**, 65 (1971).
[4] H. A. Tanner, United States Patent, no. 2977591 (1961).
[5] B. A. Munk, Frequency Selective Surfaces: Theory and Design (John Wiley & Sons, Inc., NJ, USA, 2000).
[6] D. Sievenpiper, L. Zhang, R. Broas, N. Alexopolous, and E. Yablonovitch, IEEE Trans. Microwave Theory Tech. **47**, 2059 (1999).
[7] A. Alù and N. Engheta, IEEE Antennas Wireless Propag. Lett. **4**, 417 (2005).
[8] O. Luukkonen, F. Costa, A. Monorchio, and S. A. Tretyakov, IEEE Trans. Antennas Propag. **57**, 3119 (2009).
[9] F. Costa, A. Monorchio, and G. Manara, IEEE Trans. Antennas Propag. **58**, 1551 (2010).
[10] S. Cui, D. S. Weile, and J. L. Volakis, IEEE Trans. Antennas Propag. **54**, 1811 (2006).
[11] A. Fallahi, A. Yahaghi, H.-R. Benedickter, H. Abiri, M. U. Shahabadi, and C. V. Hafner, IEEE Trans. Antennas Propag. **58**, 4051 (2010).
[12] N. I. Landy, S. Sajuyigbe, J. J. Mock, D. R. Smith, and W. J. Padilla, Phys. Rev. Lett. **100**, 207402 (2008).
[13] B. Zhu, C. Huang, Y. Feng, J. Zhao, and T. Jiang, PIER B **24**, 121 (2010).
[14] H. Li, L. H. Yuan, B. Zhou, X. P. Shen, Q. Cheng, and T. J. Cui, J. Appl. Phys. **110**, 014909 (2011).
[15] P. K. Singh, K. A. Korolev, M. N. Afsar, and S. Sonkusale, Appl. Phys. Lett. **99**, 264101 (2011).
[16] X. Shen, T. Cui, J. Zhao, H. Ma, W. Jiang, and H. Li, Opt. Express **19**, 9401 (2011).
[17] J. Sun, L. Liu, G. Dong, and J. Zhou, Opt. Express **19**, 21155 (2011).
[18] Y. Ye, Y. Jin, and S. He, J. Opt. Soc. Am. B **27**, 498 (2010).
[19] F. Ding, Y. Cui, X. Ge, Y. Jin, and S. He, Appl. Phys. Lett. **100**, 103506 (2012).
[20] T. Liu, X. Cao, Q. Zheng, W. Li, and H. Yang, IEEE Trans. Antennas Propag. **61**, 1479 (2013).
[21] B. Zhang, J. Hendrickson, and J. Guo, J. Opt. Soc. Am. B **30**, 656 (2013).
[22] M. G. Nielsen, A. Pors, O. Albrektsen, S. I. Bozhevolnyi, Opt. Express **20**, 13311 (2012).
[23] T. Hu, C. M. Bingham, D. Pilon, F. Kebin, A. C. Strikwerda, D. Shrekenhamer, W. J. Padilla, Z. Xin, R. D. Averitt, J. Phys. D: Appl. Phys. **43**, 225102 (2010).
[24] J. W. Park, P. V. Tuong, J. Y. Rhee, K. W. Kim, W. H. Jang, E. H. Choi, L. Y. Chen, Y. Lee, Opt. Express **21**, 9691 (2013).
[25] Q.-Y. Wen, H.-W. Zhang, Y.-S. Xie, Q.-H. Yang, Y.-L. Liu, Appl. Phys. Lett. **95**, 241111 (2009).
[26] H.-X. Xu, G.-M. Wang, M.-Q. Qi, J.-G. Liang, J.-Q. Gong, Z.-M. Xu, Phys. Rev. B **86**, 205104 (2012).
[27] Y. Yuan, C. Bingham, T. Tyler, S. Palit, T. H. Hand, W. J. Padilla, N. M. Jokerst, S. A. Cummer, Appl. Phys. Lett. **93**, 191110 (2008).
[28] Y. Q. Ye, Y. Jin & S. He, J. Opt. Soc. Am. B **27**, 498 (2010).
[29] L. Meng, D. Zhao, Q. Li & M. Qiu, Opt. Express **21**, A111 (2013)
[30] http://www.ansys.com/fr_fr/Produits/Flagship+Technology/ANSYS+HFSS
[31] C. A. Balanis, Modern Antenna Handbook (John Wiley & Sons, Inc., NJ, USA, 2007).
[32] R. E. Collin, Foundations for microwave engineering (John Wiley & Sons, Inc., NJ, USA, 2007).
[33] D. M. Pozar, Microwave engineering (John Wiley & Sons, Inc., NJ, USA, 2009).
[34] http://www.comsol.com
[35] H. A. Atwater and A. Polman, Nat. Mater. **9**, 205 (2010).

Hyperbolic metamaterials

Tailoring Radiation Patterns in Planar RF Metamaterials

Polina Kapitanova[1]*, Alena Shchelokova[1], Dmitry Filonov[1], Alexander Poddubny[1,2], Pavel Ginzburg[3], Anatoly Zayats[3], Pavel Belov[1], and Yuri Kivshar[1,4]

[1] ITMO University, St. Petersburg 197101, Russia
[2] Ioffe Physical-Technical Institute of the Russian Academy of Science, St. Petersburg 194021, Russia
[3] Department of Physics, King's College London, Strand, London WC2R 2LS, United Kingdom
[4] Nonlinear Physics Centre, Australian National University, Canberra ACT 0200, Australia
*corresponding author, E-mail: kapitanova.poli@phoi.ifmo.ru

Abstract

We realize an indefinite media with hyperbolic isofrequency curve in wave vector space by employing two-dimensional metamaterial transmission lines in radio-frequency range. We classify different types of such media, and visualize the peculiar character of wave propagation by study of the cross-like emission pattern of a linearly polarized emitter placed in the lattice center. We also demonstrate an excitation of extraordinary waves propagating in a prescribed direction controlled by the polarization handedness of localized circularly polarized emitter. Our results are supported by a solution of the Kirchhoff equations and experimental data.

1. Introduction

Hyperbolic metamaterials, being a particular class of indefinite media [1], are described by the electric or/and magnetic tensors with the components of the opposite sign. Due to the hyperbolic isofrequency contours in the wave-vector space, such structures exhibit a number of unusual properties. First, waves at their boundaries may exhibit negative refraction, similarly to the case of double-negative metamaterials. Second, they have a diverging density of photonic states that allows enhancing the strength of light-matter coupling [2]-[4]. This makes a concept of hyperbolic media very promising for tailoring broad-band light-matter interaction, nanophotonics applications, including single-photon generation, sensing, and photovoltaic [5]-[7].

Here, we consider an uniaxial anisotropic hyperbolic medium characterized by the scalar permittivity ε and longitudinal and transverse permeabilities μ_{xx} and μ_{yy}. In the radio-frequency (RF) regime we mimic such a medium by artificial two-dimensional transmission lines based on lumped elements [8]. We demonstrate that a circularly polarized emitter near an anisotropic hyperbolic metamaterial unidirectionally emits in extraordinary modes of the metamaterial with the directionality of energy propagation controlled by the circular dipole handedness [9]. The effect is numerically demonstrated and confirmed by the experimental investigation of the hyperbolic metamaterial prototype operating at 36 MHz frequency.

2. Planar Hyperbolic Metamaterial

We mimic an uniaxial anisotropic hyperbolic medium characterized by permeabilities ±0.33 at the operational frequency f_0= 36 MHz by artificial two-dimensional transmission lines (Fig. 1 (a)) whit the values of lumped elements C_y=3.2 nF, L_x=3.2 nH and L_z=9.5 nH [8]. For the grid consisting of 21×21 unit cells, we analytically solve the Kirchhoff equations and obtain the voltage distribution along the grid. A radiating dipole is mimicked by small current filaments, while nearly harmonic regime of weak coupling between the dipole and the metamaterial is assumed. To mimic the linearly polarized dipole, two sources with the same amplitude and opposite phases in two diagonal nodes of the structure (marked in Fig. 1 (a) as +1 and -1, respectively) are used. A circular dipole is implemented using four sources connected to neighboring four nodes at the centre of the array. The sources share the same amplitude but are 90^o phase-shifted with respect to each other (marked in Figs.1 (b) and (c)). The modeled magnetic field distribution in the RF hyperbolic metamaterial excited by the linearly polarized dipole (Fig.

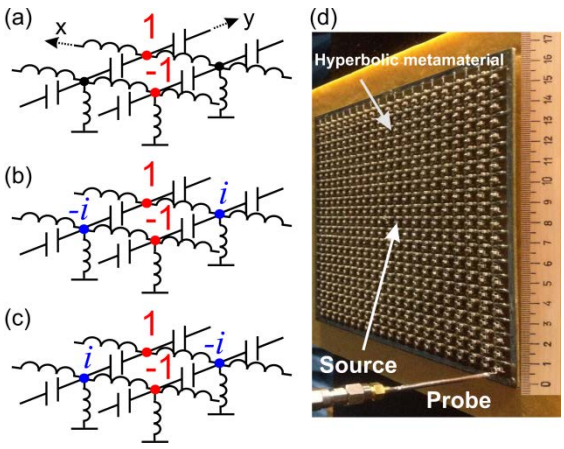

Figure 1: The unit cell of the two dimensional transmission line metamaterial composed of lumped elements excited by (a) a linearly polarized and (b,c) circularly polarized dipoles. (d) Photograph of the two-dimensional hyperbolic metamaterial prototype composed of 21 × 21 unit cells.

2(a)) placed at the centre of metamaterials shows a symmetric radiation pattern, where the energy propagates equally along the direction of the extraordinary axes. Strongly directional, not symmetric magnetic field intensity distributions are excited by either left-hand or right-hand polarized dipoles (Fig. 2 (b, c)). The contrast ratio of the intensity in orthogonal directions corresponds to about 10 dB, with the width of the excited mode being λ/300 (full width at half maximum). Fig. 2 (d-f) represents the modeled magnetic field distribution with Ohmic loss in all components and 10% tolerance of component nominal values taken in to account.

3. Experimental Investigation

The photograph of the two-dimensional hyperbolic metamaterial prototype composed of commercially available RF components for the operating frequency f_0=36 MHz is depicted in Fig. 1(d) [8], [9]. We have experimentally studied the emission of a dipole of different polarizations placed inside of this two-dimensional hyperbolic metamaterials using a two-port VNA Agilent E8362C PNA. One port of the VNA has been used to excite the prototype, while the second one has been used to measure the response. To achieve the dipoles with different polarizations, we have used the commercially available splitters (SBTCJ-1W+, JSPQ-65W+) from Mini-Circuits®. The components have been mounted on an additional circuit board (FR4, ε_r = 4.4) connected between the first port of the VNA and the nodes of the metamaterial prototype. The second port of the VNA has been used to measure the signal collected by a magnetic probe at a distance of 1 mm above the top surface of the prototype using an automatic, mechanical, near-field scanner. The field has been measured along the metamaterial surface with a 4 mm step (λ/2500). The measured field distribution has a pronounced cross-like shape for the linearly polarized dipole (Fig. 2 (g)) in agreement with the simulations. For the circularly polarized dipoles, the measured field exhibits unidirectional energy propagation depending on the dipole polarization handedness (Fig. 2 (h and i)).

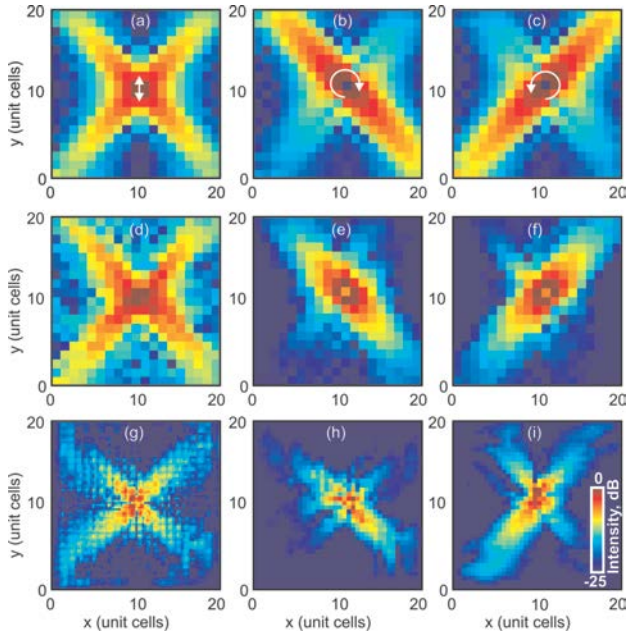

Figure 2: The intensity distributions of the waveguided modes in the metamaterial excited by linear polarised (left column) and circular polarised dipole of different handedness (middle and right columns). (a-c) Simulated intensity maps in the case of ideal lossless metamaterial, (d-f) simulated intensity maps in the case of metamaterial with random imperfections, and (g-l) experimentally measured intensity maps. The excitation dipole polarization is indicated in the figures.

4. Conclusions

We have analytically and experimentally demonstrated that the circularly polarized emitter near the RF anisotropic hyperbolic metamaterial unidirectionally emits in extraordinary modes of the metamaterial with the directionality of energy propagation controlled by the circular dipole handedness.

Acknowledgements

This work has been supported, in part, by EPSRC (UK), the Ministry of Education and Science of Russian Fed. (Projects 11.G34.31.0020, 14.B37.21.1941), Scholarship of the President of Russian Federation, and by the Australian Research Council (CUDOS Centre of Excellence CE110001018).

References

[1] D. R. Smith and D. Schurig, Electromagnetic wave propagation in media with indefinite permittivity and permeability tensors, *Phys. Rev. Lett.* 9: 077405, 2003.

[2] I. Iorsh, A. Poddubny, A. Orlov, P. Belov, and Yu. S. Kivshar, Spontaneous emission enhancement in metal-dielectric metamaterials, *Phys. Lett. A* 376: 18587, 2012.

[3] H. N. S. Krishnamoorthy, Z. Jacob, E. Narimanov, I. Kretzschmar, and V.M. Menon, Topological Transitions in Metamaterials, *Science* 336: 205-209, 2012.

[4] O. Kidwai, S. V. Zhukovsky, and J. E. Sipe, Physical nature of volume plasmon polaritons in hyperbolic metamaterials, *Opt. Lett.* 36: 2530, 2011.

[5] A. V. Kabashin, P. Evans, S. Pastkovsky, W. Hendren, G. A. Wurtz, R. Atkinson, R. Pollard, V. A. Podolskiy, and A. V. Zayats, Plasmonic nanorod metamaterials for biosensing, *Nature Materials* 8: 867 – 871,2009.

[6] Z. Jacob, L.V. Alekseyev, and E. Narimanov, Optical Hyperlens: Far-field imaging beyond the diffraction limit, *Opt. Express* 14: 8247-8256, 2006.

[7] F.J. Rodríguez-Fortuño, G. Marino, P. Ginzburg, D. O'Connor, A. Martínez, G. A. Wurtz, and A. V. Zayats, Near-Field Interference for the Unidirectional Excitation of Electromagnetic Guided Modes, *Science* 340: 328-330, 2013.

[8] A. V. Chshelokova, P. V. Kapitanova, A. N. Poddubny, D. S. Filonov, A. P. Slobozhanyuk, Y. S. Kivshar, and

P. A. Belov, Hyperbolic transmission-line metamaterials, *J. Appl. Phys.* 112: 073116, 2012.

[9] P. V. Kapitanova, P. Ginzburg, F. J. Rodríguez-Fortuño, D. S. Filonov, P. M. Voroshilov, P. A. Belov, A. N. Poddubny, Y. S. Kivshar, G. A. Wurtz, and A. V. Zayats, Photonic spin Hall effect in hyperbolic metamaterials for polarization-controlled routing of subwavelength modes, *Nature Communications* 5: 3226, 2014.

New Materials for Plasmonics and Photonic Metamaterials

Design of Ultracompact Electroabsorption Based on Novel CMOS-Compatible Plasmonic Materials

Shiyang Zhu*, G. Q. Lo, and D. L. Kwong

Institute of Microelectronics, A*STAR, 11 Science Park Road, 117685, Singapore
*corresponding author, E-mail: zhusy@ime.a-star.edu.sg

Abstract

We propose an ultra-compact electro-absorption (EA) modulator operating around 1550-nm telecom wavelengths. The modulator is composed of a stack of Cu/ITO/HfO_2/TiN deposited on a dielectric waveguide to form a hybrid plasmonic waveguide (HPW). The thin ITO layer behaves as a semiconductor whose electron concentration (N_{ITO}) can be modified by a voltage applied between the Cu and TiN electrodes, which in turn modulate the permittivity of ITO (ε_{ITO}) as well as the real and imaginary parts of effective mode index (n_{eff}) of the HPW. For a Cu/3-nm ITO/5-nm HfO_2/5-nm TiN/220-nm a-Si hybrid plasmonic waveguide, the propagation loss at 1550 nm increases from ~1.4 dB/μm to ~27 dB/μm when N_{ITO} in the thin ITO layer increases from ~3×10^{20} cm^{-3} to ~7.1×10^{20} cm^{-3}. Electrical simulation shows that such a N_{ITO} modulation can be obtained by a 4-V voltage applied between the Cu and TiN electrodes and the modulation speed is ~56 GHz. Finite-difference time-domain (FDTD) simulation shows that a 2-μm-long EA modulator, which is composed of one 1-μm-long Cu/ITO/HfO_2/TiN/a-Si HPW and two 0.5-μm-long Cu/ITO/HfO_2/a-Si couplers to link with the conventional a-Si wire waveguides, exhibits insertion loss of ~5.2 dB and modulation depth of ~7.5 dB. Numerical simulation indicates that the performance can be further improved after optimization of ITO's properties and the device's geometry.

1. Introduction

As a key device in silicon integrated photonic circuits, Si modulators have been well developed, commonly based on the Si plasma dispersion effect, in which the concentration of free charges in Si changes the real and imaginary parts of the Si refractive index [1]. Electrical manipulation of the charge density interacting with the propagating light is achievable through mechanisms such as carrier injection, accumulation or depletion in either a PN diode or a MOS capacitor. The phase variation is converted into the optical intensity modulation through a Mach-Zehnder interferometer (MZI) or a ring resonator [2]. Due to the weakness of the Si plasma dispersion effect and the diffraction limit, the Si MZI modulators suffer from a large footprint of ~10^3–10^4 μm^2. The ring modulators have a reduced footprint of ~10^2–10^3 μm^2, but with a price of a higher temperature sensitivity and lower optical bandwidth.

Moreover, the Si modulators are only applicable for single-crystalline Si, which limit the optical devices to a single layer. Recently, optical circuits based on deposited waveguide materials are emerging for three-dimension integration of multiple photonic layers as well as for flexible network on chip [3]. The device for modulation of optical signals propagating in these dielectric waveguides is still lack.

A potential method to miniaturize optical devices is by utilizing nanoplasmonis owing to its capability of tight optical mode confinement [4]. Ultra-compact nanoplasmonic electro-absorption (EA) and phase modulators using Si as the active material have been demonstrated [5,6]. The working mechanism still relies on the Si plasma dispersion effect. Due to the large high-frequency permittivity (ε_∞) of Si (~11.7), a very high carrier concentration is required for sufficient EO modulation in these Si-based plasmonic modulators.

Recently, transparent oxide conductor (TOC) materials such as ITO are introduced as an active material for novel plasmonic modulators. Feigenbaum et al. [7] reported a phase modulation in Au/SiO_2/ITO/Au plasmonic waveguide. Melikyan et al [8] and Sorger et al [9] reported plasmonic EA modulators based on Ag/SiO_2/ITO/Ag and Au/SiO_2/ITO/Si plasmonic waveguides, respectively. The modulation relies on free-carrier induced permittivity modification of ITO. Because ITO behaviors as a semiconductor and has a relatively small ε_∞ (~3.9), its real part of permittivity crosses zero at a relatively low free carrier concentration based on the Drude model, which in turn modulate the effective mode index of the ITO-based plasmonic waveguides significantly. These ITO-based EA modulators, as well as that reported by Z. Lu et al [10] are only applicable for the single-crystal Si waveguides because the Si is used as one of the electrodes. Moreover, the relationship between the ITO properties and the modulator performance is still unclear.

In this paper, a novel ITO-based plasmonic modulator is proposed, which is comprised of a stack of Cu/ITO/HfO_2/TiN deposited on a dielectric waveguide. The stack itself forms a MOS capacitor in which the ITO behaves as a semiconductor, the HfO2 behavior as high-κ dielectric, and the top Cu and the bottom ultrathin TiN behave as electrodes. As a result, the modulator is applicable for any kind of dielectric waveguides, including single-crystal Si, amorphous Si, SiN, AlN, and TiO_2. The

effect of the ITO properties and the device geometry on the modulator's performance is investigated thoroughly.

2. Device structure

The proposed modulator is shown in Fig. 1 schematically. For simplification, the waveguide is conventional single-mode Si waveguide with height of 220 nm and width of 400 nm. The whole device is embedded in thick SiO_2 cladding layer. The main body of the modulator is a Cu/ITO/HfO_2/TiN/Si hybrid plasmonic waveguide with the structural parameters as follows: the thicknesses of TiN, HfO_2, ITO are 5 nm, 5 nm, and 3 nm respectively, while the Cu cap is optically thick. The width of HfO_2, ITO and Cu is the same as the beneath Si waveguide, while the width is TiN layer is infinite large.

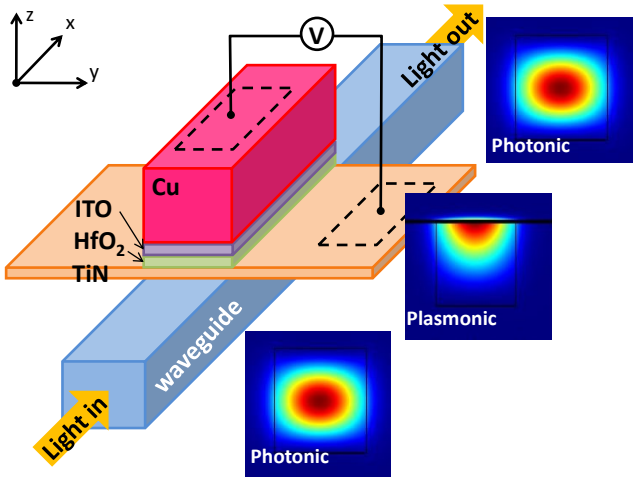

Figure 1: Schematic structure of the proposed plasmonic EA modulator.

The refractive indices of Si, SiO_2, HfO_2, TiN, and Cu at 1550 nm are 3.445, 1.444, 1.87, 2.03+*j*3.70, and 0.282+*j*11.048, respectively. The permittivity of ITO is modeled by the Drude mode as: $\varepsilon = \varepsilon_\infty - \frac{\omega_P^2}{\omega^2 + i\omega\Gamma}$, $\omega_P^2 = \frac{N_{ITO}e^2}{\varepsilon_0 m^*}$. $\varepsilon_\infty = 3.9$, Γ = 1.8×10^{14} s^{-1}, and $m^*=0.35m_e$. Fig.2 plots real and imaginary parts of permittivity of ITO as a function of N_{ITO} at different wavelengths of 1.45, 1.55, and 1.65 μm. Re(ε_{ITO}) crosses zero at N_{ITO} of ~6.5×10^{20} cm^{-3} at 1.55 μm.

3. Electrical simulations

The stack forms a MOS capacitor in which a voltage is applied between the TiN and Cu electrodes, as shown in Fig. 3(a). 2-D MEDICI simulation shows that the electron distribution $N_{ITO}(x, y)$ in the ITO layer is almost independent on x, thus the 2-D distribution may reduce to the 1-D distribution as $N_{ITO}(y)$. Fig. 3(b) plots $N_{ITO}(y)$ in the 3-nm-thick ITO layer at different voltages. The initial electron density (N_0) is assumed to $3.5\times10^{20}cm^{-3}$.

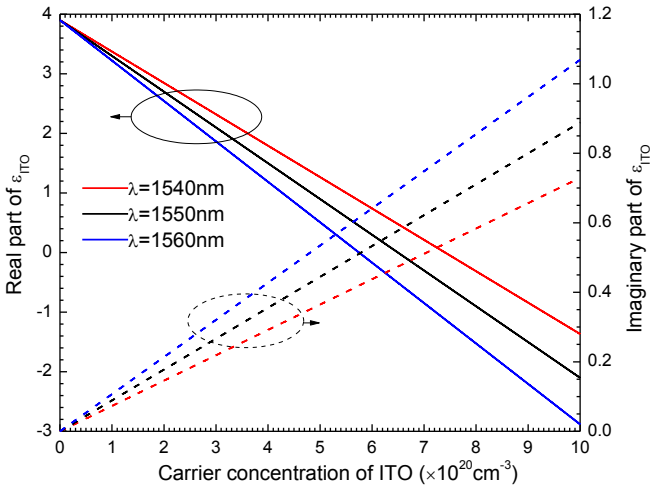

Figure 2: Schematic structure of the proposed plasmonic EA modulator.

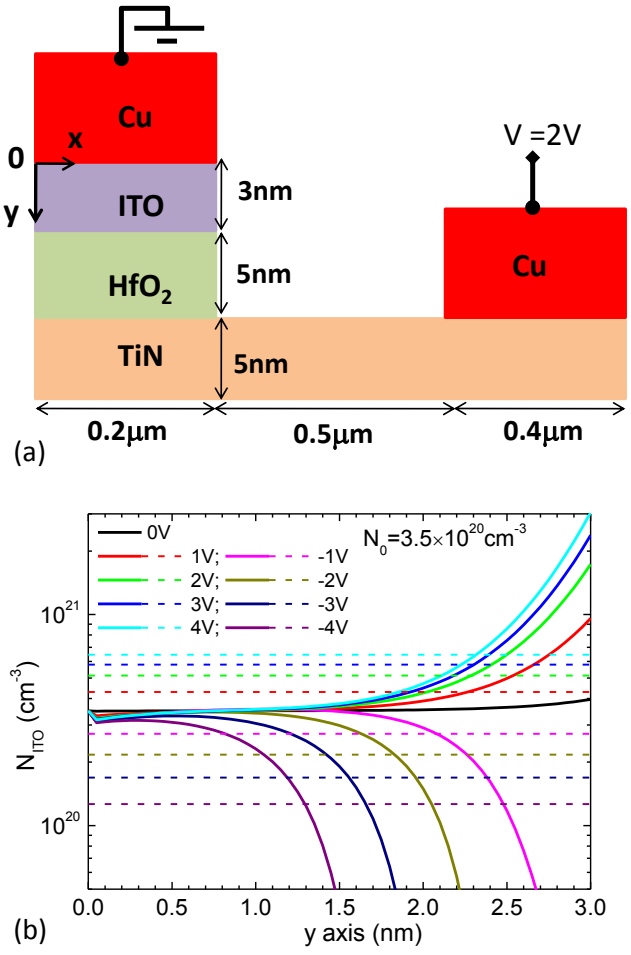

Figure 3: (a) 2-D structure of the modulator for electrical simulation, and (b) Electron concentration in the 3-nm ITO at different voltages.

As expected, $N_{ITO}(y)$ can be modified from depletion to accumulation with voltage increasing from negative to positive. In order to calculate the effect of this carrier density changes on the optical property it is more practical

to use the average carrier density across the 3-nm-thick ITO layer. The average N_{ITO} in the ITO layer is also plotted in Fig. 3(b) as the dash lines. The average N_{ITO} modification can also estimated by: $\Delta N_{ITO} = \frac{\varepsilon_0 \cdot \varepsilon_{HfO2}}{e \cdot t_{HfO2} \cdot t_{ITO}} (V - V_{FB})$.

For the transient state simulation, the gate voltage was increased from -1 to 3V with the ramp time of 10 fs. Fig. 4 plots variation of the average N_{ITO} in the 3-nm ITO layer with time. The sum of the rise and fall times is read to ~17.8 ps, which corresponds to a modulation speed of ~56 GHz. The modulation speed can be improved by increasing TiN thickness and/or shorting the distance between two electrodes but with the price of degradation of the optical performance. A method to improve the modulation speed without sacrificing optical performance is to improve the mobility of the TiN layer.

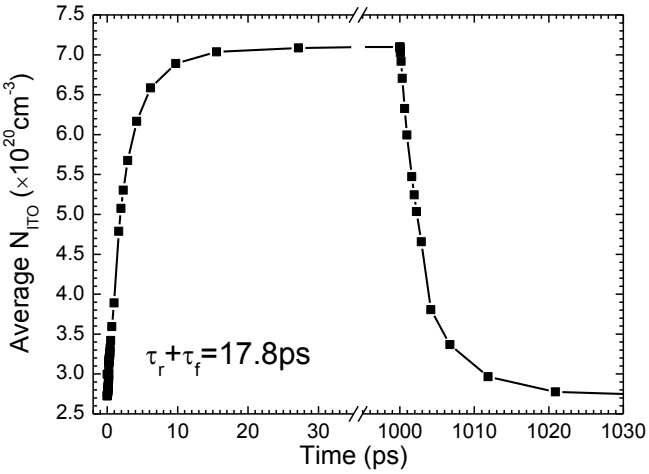

Figure 4: Temporal response of the Cu/5-nm HfO_2/3-nm ITO/TiN capacitor under -1-3 voltage pulse. The modulation speed is estimated to be ~56 GHz from the rise and fall times.

4. Optical simulations

The mode properties of the Cu/ITO/HfO_2/TiN/a-Si and Cu/ITO/HfO_2/TiN/SiN hybrid plasmonic waveguides are calculated using the eigen-mode expansion (EME) method. Fig. 5 plots the ratio of electric field intensity in the 3-nm ITO layer, the real part of effective modal index (n_{eff}), and the propagation loss as a function of average electron concentration in the ITO layer. All these curves show a peak around N_{ITO} at which Re(ε_{ITO}) is zero, which we can defined as the critical concentration N_C. N_C is almost independent on the beneath waveguide. However, the modulation depth depends on the beneath waveguide. When N_{ITO} increases from ~3×10^{20} cm^{-3} to 7.1×10^{20} cm^{-3}, the propagation loss of he Cu/ITO/HfO_2/TiN/a-Si HPW increases from ~1.4 dB/μm to ~27 dB/μm and that of the Cu/ITO/HfO_2/TiN/SiN HPW increases from ~0.9 dB/μm to ~4.2 dB/μm. This is because the a-Si can provides tight lateral mode confinement than the SiN as a-Si has much larger index than SiN. Nevertheless, the device proposed here provides a solution for the first time to modulate light propagation in the SiN waveguide.

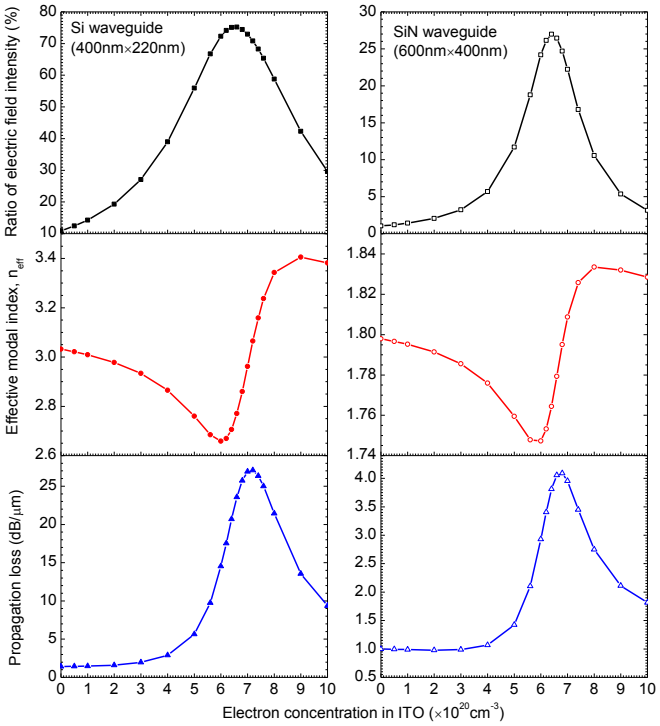

Figure 5: The mode properties of the Cu/ITO/HfO_2/TiN/Si (left) and Cu/ITO/HfO_2/TiN/SiN (right) hybrid plasmonic waveguides as a function of electron concentration in the 3-nm ITO layer: (top) ratio of electric field in the 3-nm ITO layer, (middle) real part of effective modal index, n_{eff}, and (bottom) propagation loss.

The 400-nm×220-nm a-Si strip waveguide has effective index of 1.714 for the 1550-nm fundamental TM mode, while the effective index for the Cu/ITO/HfO_2/TiN/Si HPW (with N_{ITO} =0) is 3.037. Therefore, couplers are required to link the conventional a-Si wire waveguide and the Cu/ITO/HfO_2/TiN/Si HPW. Here, the TiN layer length is set to be shorter than the other layers of the Cu/ITO/HfO_2/TiN/Si HPW, i.e., we use the Cu/ITO/HfO_2 stack at both sides as the couplers, as shown in Fig. 6.

Fig. 7 shows the FDTD simulation results where N_{ITO} = 0 is defined as on state and N_{ITO} = 7.1×10^{20} cm^{-3} is defined as off state. For this 2-μm-long EA modulator, insertion loss (IL) is ~5.2 dB and extinction ratio (ER) is ~7.5 dB.

5. ITO properties and tolerance analysis

The performance of the proposed EA modulator depends strongly on the material property of ITO. It has been experimentally demonstrated that the permittivity of ITO can be modeled by the Drude model very well at the near infrared wavelengths [11]. The parameters in the Drude model, i.e., ε_∞, Γ, and N_0, depend on the fabrication condition. In other words, one may tune the values of ε_∞, Γ, and N_0 by modifying the deposition condition. From Fig. 5, we can see that the preferred initial electron concentration in ITO is ~3.5×10^{20}cm^{-3}, which is about half of N_C, so that NITO may be modulated between 0 to N_C effectively. Fig. 8 shows the effect of ε_∞ and Γ on the performance of the

proposed EA modulator. One sees that with ε_∞ decreasing, N_C decreases, the propagation loss at the on state decreases, and the propagation loss at the off state increases. It indicates that the EA modulator will have large ER, small IL, and low voltage when ε_∞ is decreased. In other words, ε_∞ is as small as better for the plasmonic modulator applications. This result also explains that Si is not a good active material for the plasmonic modulator because it has a relatively large ε_∞ of ~11.7. Γ of ITO is also as smaller as better, as shown in Fig. 8(b).

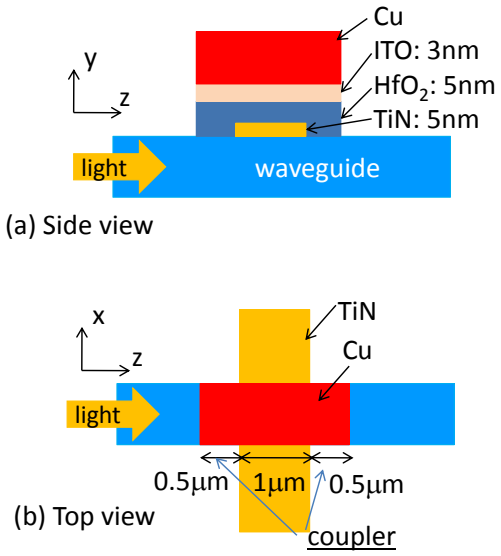

Figure 6: (a) Side view and (b) top view of Cu/ITO/HfO_2/TiN stack deposited on a Si strip waveguide, the Cu/ITO/HfO2 stack on both sides are regarded as coupler, which can reduce the coupling loss between the Si strip waveguide and the Cu/ITO/HfO_2/TiN/Si HPW.

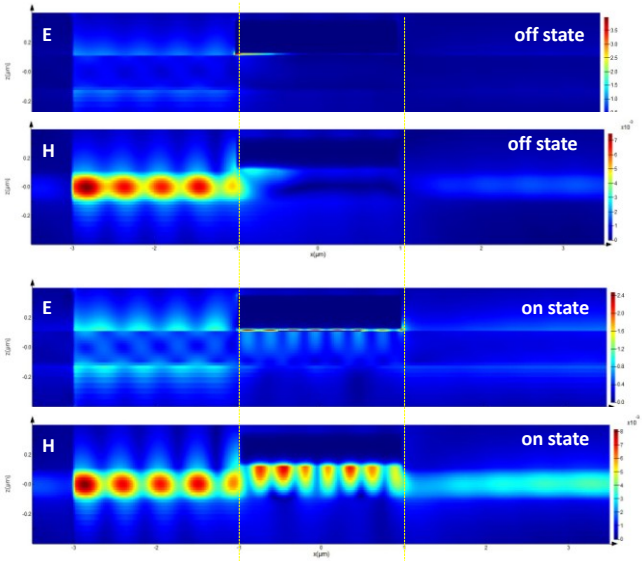

Figure 7: FDTD simulation results of an EA modulator with 1-μm-long Cu/ITO/HfO_2/TiN stack and 0.5-μm-long Cu/ITO/HfO_2 at both sides (thus the total length is 2 μm), the transmission power at on-state is -5.2 dB and that in the off-state is -12.7 dB.

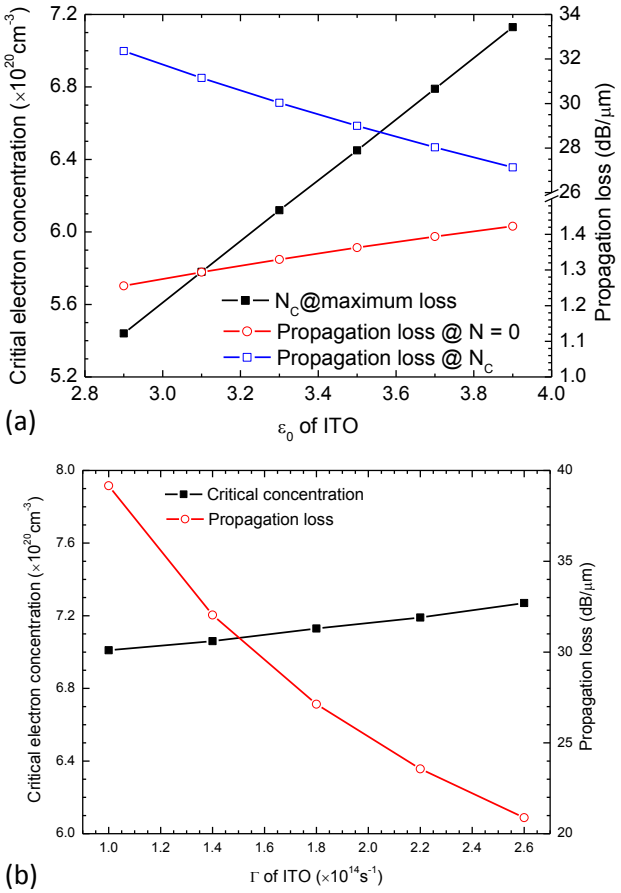

Figure 8: The effect of (a) ε_∞ and (b) Γ of ITO on the performance of EA modulator.

The proposed EA modulator offers a large fabrication tolerance. Fig. 9 shows the effect of the width of Cu/ITO/HfO_2 stack on the performance of the proposed EA modulator. One can see that the performance depends on the width weakly in the width range of 200 nm (narrower than the beneath Si waveguide) to 800 nm (larger than the beneath Si waveguide).

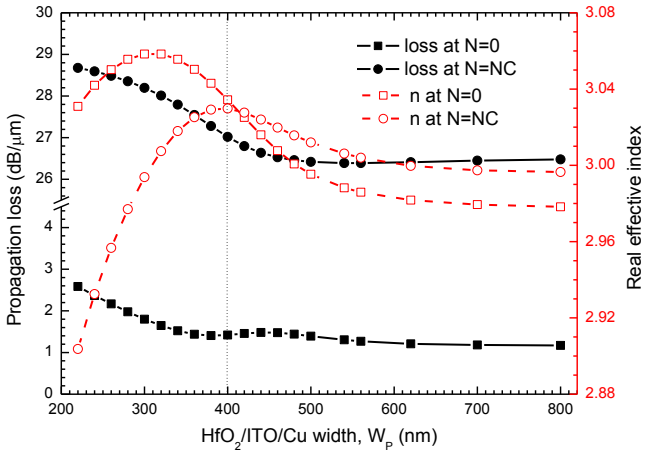

Figure 9: The effect the width of Cu/ITO/HfO_2 stack on the performance of EA modulator.

6. Suggested processing flow

The proposed modulator can be fabricated using standard CMOS technology. Fig. 10 shows the fabrication flow. The key technology is the atomic layer deposition of ultrathin TiN, HfO_2, and ITO layers. The fabrication has low thermal budget, thus is compatible to the backend CMOS technology.

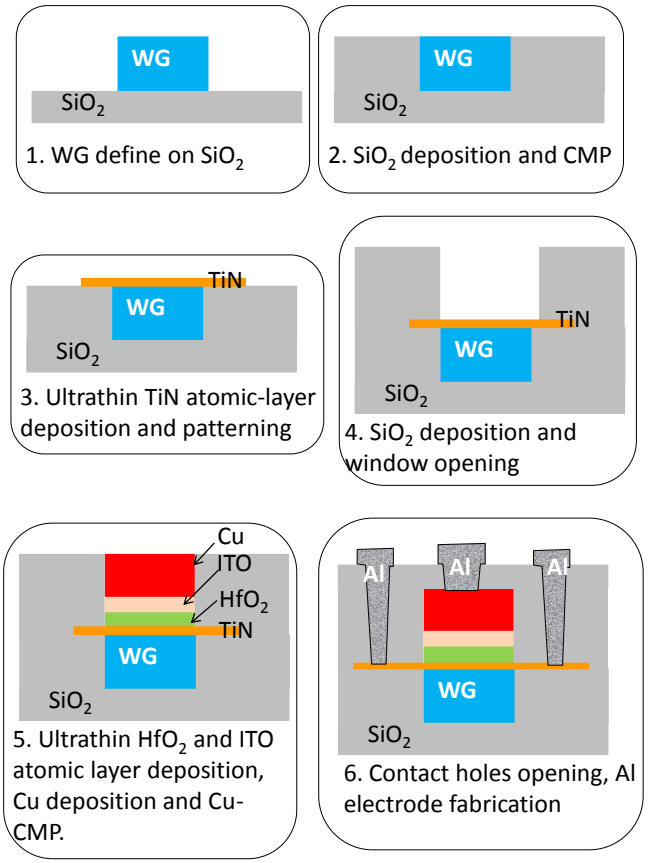

Figure 10: The fabrication flow of the proposed EA modulator, it is compatible to the backend CMOS technology.

7. Conclusions

An ultracompact plasmonic EA modulator is proposed and investigated theoretically, which offers advantages of (1) ultra-compact footprint (~2 μm^2), (2) high speed (> 50 GHz), (3) broad optical bandwidth (>100 nm), (4) low power consumption , (5) compatible to the back-end CMOS process, (6) large fabrication tolerance, and (7) applicable for all kinds of waveguides besides the Si waveguide. A key technology to realize this modulator is the optimization of atomic layer deposition of ultrathin ITO layer. The relationship between the ITO material parameters and the performance of EA modulator is revealed, which can be used to guide the optimization of ALD condition.

Acknowledgements

This work was supported by Singapore A*STAR-MINDEF Joint Grant 122-331-0074.

References

[1] G. T. Reed, G. Mashanovich, F. Y. Gardes, and D. J. Thomson, "Silicon optical modulators," *Nat. Photon. 4*: pp. 518-526, 2010.

[2] D. Marris-Morini, L. Vivien, et al. "Recent progress in high-speed silicon-based optical modulators," *Proc. of the IEEE 97(7)*: pp. 1199-1215, 2009.

[3] A. Biberman, K. Preston, et al, "Photonic network-on-chip architectures using multilayer deposited silicon materials for high-performance chip multiprocessors," *ACM J. on Emerging Techn. in Computing Sys. 7(2)*: art. 7, 2011.

[4] D. K. Gramotnev and S. I. Bozhevolnyi, "Plasmonics beyond the diffraction limit," *Nat. Photon. 4*: pp. 83-91, 2010.

[5] S. Zhu, G. Q. Lo, and D. L. Kwong, "Electro-absorption modulation in horizontal metal-insulator-silicon-insulator-metal nanoplasmonic slot waveguides," *Appl. Phys. Lett. 99*: art. 151114, 2011.

[6] S. Zhu, G. Q. Lo, and D. L. Kwong, "Phase modulation in horizontal metal-insulator-silicon-insulator-metal plasmonic waveguides," *Optics Express 21(7)*: pp. 8320-8330, 2013.

[7] E. Feigenbaum, K. Diest, and H. A. Atwater, "Unity-order index change in transparent conducting oxides at visible frequencies," *Nano Lett., 10*: pp. 2111-2116, 2010.

[8] A. Melikyan, N. Lindenmann, S. Walheim, P. M. Leufke, S. Ulrish, J. Ye, P. Vincze, H. Hahn, Th. Schimmel, C. Koos, W. Freude, and J. Leuthold, "Surface plasmon polariton absorption modulator," *Optic Express 19(9)*: pp. 8855-8869, 2011.

[9] V. J. Sorger, N. D. Lanzillotti-Kimura, R. M. Ma, and X. Zhang, "Ultra-compact silicon nanophotonic modulator with broadband response," *Nanophotonic 1*: pp. 17-22, 2012.

[10] Z. Lu, W. Zhao, and K. Shi, "Ultracompact electroabsorption modulators based on tunable epsilon-near-zero-slot waveguides," *IEEE Photonics Journal 4(3)*: pp. 735-740, 2012.

[11] M. A. Noginov, L. Gu, J. Livenere, G. Zhu, A. K. Pradhan, R. Mundle, M. Bahoura, Y. A. Barnakov, and V. A. Podolskiy, "Transparent conductive oxides: plasmonic materails for telecom wavelengths," *Appl. Phys. Lett. 99*: art. 021101, 2011.

PT-symmetry in photonics, metamaterials and plasmonic systems

Practical Limitation on Operation of Nonlinear Parity-Time Bragg Gratings

Sendy Phang[1,*], Ana Vukovic[1], Hadi Susanto[2], Trevor M. Benson[1], and Phillip Sewell[1]

[1]The George Green Institute for Electromagnetics Research, Faculty of Engineering, University of Nottingham, Nottingham NG7 2RD UK
[2]Department of Mathematical Sciences, University of Essex, Colchester CO4 3SQ, UK
*corresponding author, E-mail: sendy.phang@nottingham.ac.uk

Abstract

The paper analyses the operation of PT Bragg gratings when the dielectric material is considered to be both dispersive and nonlinear and gain and loss are saturable. The paper demonstrates the application of the nonlinear PT Bragg Grating as an optical logic gate and an optical switch.

1. Introduction

A Parity-Time (PT) structure is formed by balancing inherent loss in a medium by an equal gain in a certain design. The PT-symmetric structures mimic the PT-symmetric potential system in quantum physics which, under certain conditions, operates in a stable regime. As optical waveguides have inherent material loss, it is desirable to balance the loss with gain for optimal performance. This is one of the reasons why PT structures have become the subject of increased interest in photonics. Several kinds of PT-symmetric structures have been reported so far based on either grating [1–4], coupler [5–9], or lattice [10–12] structures with a range of applications including lasing and absorber cavities [2], switches [4,13] and memory [14]. PT-structures have been extensively modelled using coupled-mode theory [3,7], the transfer-matrix (T-matrix) method [1,14–16], Floquet-Bloch theory [11] and Fourier modal analysis [17,18]. The inclusion of material nonlinearity has also been reported with a speculation that nonlinearity combined with a PT structure will open a new range of functionalities [1,19–21]. However, all the reported models have assumed that gain and loss are frequency and intensity independent. The important question arises on how a nonlinear PT-symmetric device will perform in a practical situation where gain and loss are both dispersive and saturable, especially when medium nonlinearity is also taken into account.

To consider such a scenario we use a time-domain numerical technique, namely the Transmission Line Modelling (TLM) method [22,23]. The TLM method is based upon the analogy between the propagating electromagnetic field and voltage impulses travelling on an interconnected mesh of transmission lines. Successive repetitions of a scatter-propagate procedure provide an explicit and stable time-stepping-algorithm that mimics electromagnetic field behaviour to second order accuracy in both time and space [24,25]. It is important to note that the TLM method has been successfully implemented to model a dispersive and nonlinear dielectric material [22,23]. In principle any time-domain numerical method, including the Finite Difference Time Domain (FDTD) method could be used as a basis for the simulation undertaken.

In our previous work, we have validated the TLM method to model a linear PT Bragg Grating (PTBG) with non-dispersive gain and loss [4,26]. The impact of gain/loss saturation on the switching performance of a linear PTBG, has also been demonstrated [4]. In this paper we extend our model to include nonlinear and dispersive materials with saturable gain and loss. The Kerr nonlinearity is assumed in this paper and is controlled by a strong pump beam away from the Bragg frequency of the grating. The performance of the grating for different pump beam intensities and different saturation intensities is analysed. This is followed by studies of the applications of a nonlinear PTBG as an optical logic gate and a switch.

This paper is structured as follows; in the next section the model of the PTBG structure as implemented in the TLM method is given. Section 3 analyses the performance of the nonlinear PTBG for different input intensities and different intensity saturation levels. Section 4 demonstrates practical applications of the nonlinear PTBG and Section 5 outlines the main conclusions of the paper.

2. Structure and model

A Parity-Time symmetric material in optics requires a complex refractive index profile that satisfies $\hat{n}(-z) = \hat{n}^*(z)$, where z denotes the spatial position of the grating and * denotes the complex conjugate. The schematic of a PT grating is shown in Fig. 1. The grating is embedded in a medium of background refractive index n_B as shown in Fig. 1(a), and is made of N periods. A single period, Λ, of the PTBG is shown in Fig. 1(b) representing equal amounts of loss and gain per period and with the real refractive index varying in a piecewise constant manner between n_L and n_H (dashed line in Fig. 1(b)). The Bragg frequency f_B is related to the average refractive index $\bar{n}$ of the structure by $f_B = \frac{c}{2\bar{n}\Lambda}$, where c is the speed of light in free space.

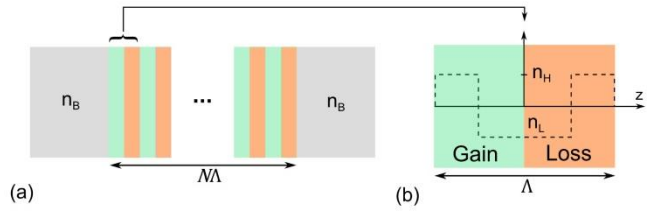

Fig. 1(a) Schematic of the PTBG within a background material n_B; (b) A single period of PTBG showing gain and loss half-periods and (dashed line) modulation of the real refractive index.

The refractive index profile of the nonlinear PT Bragg grating for one period n_G can be expressed as:

$$n_G(z,\omega,t,I) = \begin{cases} n(\omega) \pm \Delta n(z) + n_2 I(z,t) + j\frac{c}{\omega}\alpha(\omega,I), & z < \frac{\Lambda}{2} \\ n(\omega) \mp \Delta n(z) + n_2 I(z,t) - j\frac{c}{\omega}\alpha(\omega,I), & z > \frac{\Lambda}{2} \end{cases} \quad (1)$$

Here, $n(\omega)$ is the base refractive index as a frequency dependent material, $\Delta n(x)$ is the modulation of the real refractive index as a spatially dependent function, n_2 is the Kerr nonlinearity constant, I is the input intensity of the field and $\alpha(\omega, I)$ denotes gain or loss in the grating which is dispersive and saturable. Equation (1) shows that Kerr nonlinearity also contributes to the overall real part of the refractive index.

The frequency and intensity dependent dielectric material is modelled in the TLM model using the Duffing equation of polarisation [27],

$$\frac{\partial^2 P_D}{\partial t^2} + 2\delta\frac{\partial P_D}{\partial t} + \omega_{0D}^2 P_D f_D = \epsilon_0 \chi_{e0}\omega_{0D}^2 E \quad (2)$$

where P_D and E denote the electric polarisation and field, δ and ω_{0D} denote the damping and dielectric resonant angular-frequency parameters of the medium respectively, and χ_{e0} denotes the dielectric susceptibility at DC. The nonlinearity is implemented with the function f_D as [28],

$$f_D = e^{\zeta P_D^2}, \quad (3)$$

where $\zeta = -\frac{n_2\sqrt{\chi_{e0}+\chi_{e\infty}+1}}{\epsilon_0^2(\chi_{e0}+\chi_{e\infty})^3\eta_0}$, n_2 is the Kerr nonlinear constant, $\chi_{e\infty}$ denotes the constant susceptibility at infinite frequency and η_0 is the free-space impedance. It is emphasised that when $f_D = 1$ the Duffing equation reduces to the linear model of optical material based on simple harmonic oscillator with a Lorentzian profile. In this case the refractive index at a given angular frequency ω is calculated as,

$$\hat{n}^2 = (1+\chi_{e\infty}) + \frac{\chi_{e0}\omega_{0D}^2}{2j\delta\omega+(\omega_{0D}^2-\omega^2)}. \quad (4)$$

The implementation and validation of the Duffing equation to model a realistic dispersive and nonlinear optical dielectric has been reported in [28].

On the other hand, a dispersive and saturable gain/loss model with a Lorentzian profile is implemented as [29],

$$|\alpha|(\omega,I) = \Omega(I)\left(\frac{\alpha_0}{1+j(\omega-\omega_{0\sigma})\tau} + \frac{\alpha_0}{1+j(\omega+\omega_{0\sigma})\tau}\right), \quad (5)$$

where the gain/loss parameter $|\alpha|$ is related with the imaginary part of refractive index n_I by $|\alpha| = \frac{\omega}{c}n_I$, $\omega_{0\sigma}$ denotes the atomic transition angular-frequency, τ is the dipole relaxation time parameter and α_0 is the peak value of the gain or loss at $\omega_{0\sigma}$. In order to quantify the saturation level, it is useful to introduce the saturation factor Ω defined as,

$$\Omega = \frac{1}{1+\frac{I}{I_S}}, \quad (6)$$

where I is the input beam intensity and I_S is the saturation intensity. For a fixed I_S, the saturation factor Ω varies over the interval $0 < \Omega < 1$, with $\Omega = 0$ denoting a highly saturated state ($\frac{I}{I_S} \to \infty$) and $\Omega = 1$ denoting negligible saturation ($\frac{I}{I_S} \to 0$). It is emphasised that the model described in (2)-(6) satisfies the Kramers-Kronigs conditions which relates the real and imaginary part of a refractive index.

3. Results and Discussion

In this section, the performance of 200 periods of nonlinear PTBG based on GaAs material is analysed using the TLM method. The following material parameters are used throughout this paper, $\chi_{e0} = 7.5$, $\omega_{0D} = 4614.4\ \text{rad/ps}$, and $\delta = 0.0923\ \text{rad/ps}$ [30], with the high and low refractive index, i.e. n_H and n_L obtained respectively from the high and low dielectric susceptibilities, $\chi_{e\infty} = 2.8$ and 2.5, which form the grating. The Kerr nonlinearity constant is $n_2 = 2\times10^{-17}\ \text{m}^2\text{W}^{-1}$ [31,32] throughout the structure. The gain and loss parameters are $\tau = 0.1$ ps and $\omega_{0\sigma} = 2116.5\ \text{rad/ps}$ [29] while α_0 depends on the gain/loss given. The periodicity of the PTBG is designed so that the Bragg frequency is at the atomic-transitional frequency, i.e. $f_B = \frac{\omega_{0\sigma}}{2\pi}$, hence $\Lambda = 122.7$ nm. The background material is GaAs with $n_B = 3.626$ at the Bragg frequency f_B. The unidirectional (U) operation of the PTBG occurs when the gain/loss in the PTBG satisfies $|\alpha_0| = \frac{1\omega}{2c}(n_H - n_L)$ [4] which for the chosen material parameters, happens when the gain/loss coefficient $|\alpha_0| = 1460.24\ \text{cm}^{-1}$.

The main characteristic of the linear PT Bragg grating is that transmission is the same regardless of whether the grating is excited from the left or right of the grating but the reflectances are different. The amount of gain/loss of the system also influences the operation of the grating in that above a certain threshold point the operation of grating is in an unstable regime. Another characteristic of a linear PTBG is that the grating exhibits unidirectional invisibility – commonly referred to as the U point.

In the light of the refractive index profile given in (1), for the nonlinear PT Bragg grating, we consider a scenario where an input beam is comprised of two beams, namely a strong pump beam and a probe beam. The pump beam is a CW beam and is used to activate the Kerr nonlinearity. The frequency of the pump beam f_{pump} is set to be far from the Bragg frequency, i.e. $f_{pump} = 200$ THz. The probe signal is a Gaussian pulse modulated at the Bragg frequency f_B and is low in intensity, with its maximum intensity being 1% of

the pump beam intensity. Since the intensity of probe beam is very low compared to the strong pump beam, its effect can be seen as a perturbation of the pump beam and hence the pump beam can be considered as the input beam.

In order to investigate the effect of different saturation levels on the performance of a nonlinear PTBG the saturation intensity I_S is fixed to a certain level and the saturation factor Ω is changed by changing the intensity of the pump beam.

Fig. 2 shows the frequency response of the nonlinear PTBG for a saturation intensity $I_S = 5 \times 10^{10}$ Wm^{-2} at the U-point. For a given level of saturation intensity, the effect of the Kerr nonlinearity is low since $n_2 I_S = 1 \times 10^{-6}$. Four different intensities of the input beam I are considered so that the saturation factor Ω varies from low to high saturation, i.e. $\Omega = 0.99,\ 0.8,\ 0.01$ and 2×10^{-6}. Fig. 2 compares results together with the analytical solution obtained using the T-matrix method [34]. It is emphasised here, that the T-matrix method models a linear and dispersive structure, i.e. no Kerr nonlinearity and no gain/loss saturation. With that in mind, the T-matrix method results are presented more as a reference than for a direct comparison. The response of the linear PTBG using the idealised model of gain/loss [1] is also included in Fig. 2 for comparison. The ideal gain/loss model here is implied to be frequency and intensity independent.

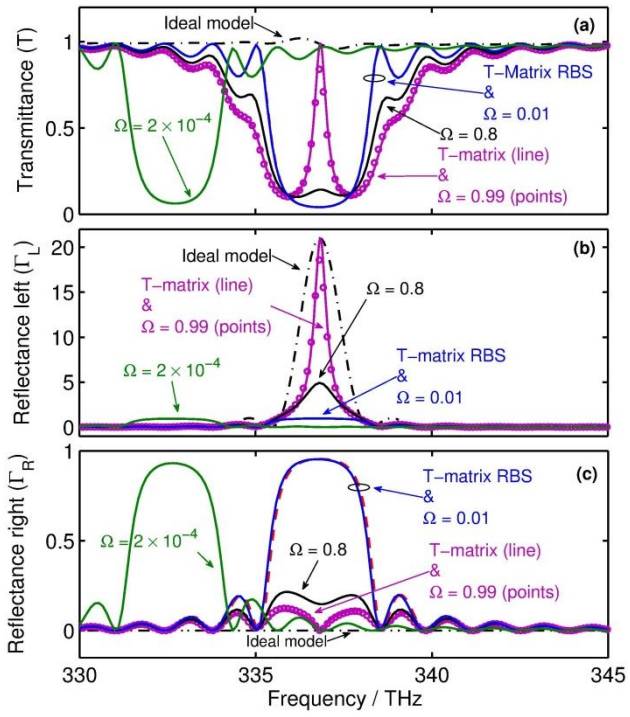

Fig. 2(a)Transmittance (b) reflectance for left, Γ_L , and (c) right, Γ_R, incident for different saturation levels Ω

Fig. 2(a) shows that transmittance of the ideal PTBG model has almost-total transmission $T \approx 1$ at all frequencies. At low saturation level ($\Omega = 0.99$), the transmittance calculated using the TLM method agrees with one calculated with the T-matrix method, due to the fact that in this case the change of refractive index and gain/loss in the PTBG induced by the Kerr nonlinearity and saturation respectively are negligible. It is noticeable that compared to the idealised case, the total transmission $T = 1$ occurs only at the Bragg frequency f_B. This result confirms that material dispersion prohibits unidirectional behaviour at all frequencies as shown in the case of an ideal PTBG [4]. Furthermore, as the saturation factor Ω decreases the transmittance becomes similar to that of the regular Bragg grating (RBG), i.e. it loses PT behaviour. This is shown in Fig. 2(a) where the response for $\Omega = 0.01$ overlaps with that of the RBG. By increasing the input beam intensity even further, $\Omega = 2 \times 10^{-4}$, the band-gap is shifted to the lower frequency due to the fact that the dominant modulation mechanism becomes the Kerr nonlinearity.

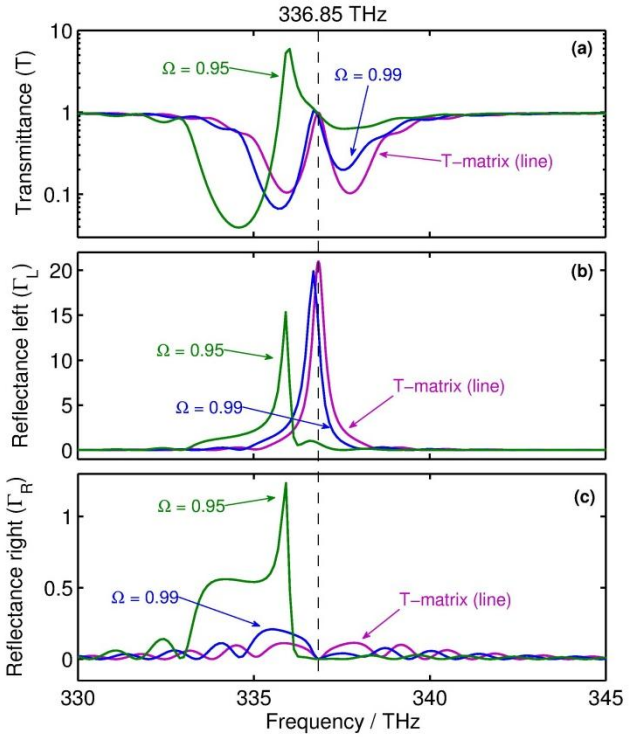

Fig. 3(a)Transmittance (b) reflectance for left Γ_L and (c) right Γ_R incident beam for high saturation intensity and different saturation factors Ω

Fig. 2(b) and Fig. 2(d) show the reflectance for beams incident from the left, Γ_L, and right, Γ_R, side of the PTBG respectively. For the ideal linear PTBG the reflectance Γ_R is zero and Γ_L is amplified, showing the unidirectional behaviour at all frequencies. At low saturation levels ($\Omega = 0.99$) the reflectance Γ_L has narrower bandwidth and the PTBG maintains the unidirectional behaviour around f_B. Furthermore, at low saturation, $\Omega = 0.99$, the TLM results for Γ_L and Γ_R agree very well with results obtained using the T-matrix method due to the negligible effect of nonlinearity. Further increase in saturation level shifts the reflectance spectra to lower frequencies due to the dominant Kerr nonlinearity.

Fig. 3(a) shows the response of the nonlinear PTBG

under the condition of high saturation intensity, which if it was reached, produces high Kerr nonlinearity of $n_2 I_S = 0.5$. The grating is operated at the U point with $|\alpha_0| = 1460.24$ cm^{-1}. Two different input intensities are considered so that gain/loss saturation is $\Omega = 0.99$ and 0.95, corresponding to low saturation. The induced Kerr modulation for given intensities is $n_2 I = 0.0051$ and 0.0263 respectively. The response of the linear structure (no Kerr nonlinearity and no gain/loss saturation) calculated using the T-matrix method is included for comparison. Fig. 3 shows that as the intensity and saturation increase the overall responses for T, Γ_R and Γ_L shift towards lower frequencies as the Kerr nonlinearity increases overall refractive index. It is observed that at the f_B the unidirectional invisibility is preserved, $T \approx 1$ and $\Gamma_R \to 0$, whilst transmittance higher than 1 is observed for $f < f_B$. The reflectance for the left incident case, Γ_L, decreases and is shifted to a lower frequency. On the other hand, the Γ_R increases as the input beam increases and negligible reflectance is observed for $f > f_B$.

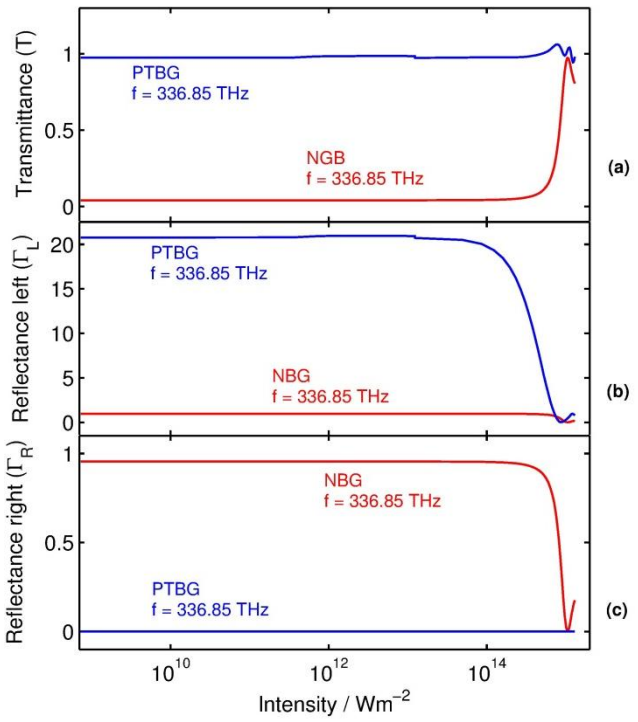

Fig. 4 (a) Transmittance, (b) reflectance for left and (c) reflectance for right of PTBG at the U operation as a function of input intensity at $f = 336.85$ THz. The gain/loss has high saturation intensity $n_2 I_S = 0.5$. Results for the NBG($\alpha_0 = 0$) at the Bragg frequency $f_B = 336.85$ THz are included for reference.

Fig. 4 shows the response of the nonlinear PTBG as a function of input beam intensity, when the gain/loss intensity saturation is high $(n_2 I_S = 0.5)$. The grating is operated at the U point with $f = 336.85$ THz. The frequency $f = 336.85$ THz is the Bragg frequency of the linear grating. The response for the nonlinear Bragg grating (NBG) at $f = 336.85$ THz , with no gain and loss $(\alpha_0 = 0)$ is also included in Fig. 4(a) and shows that at low intensities the transmittance is very low but then switches to total transmittance at high intensity. This can be explained that by the fact that at high input intensity the band-gap of the nonlinear Bragg grating is shifted to the lower frequency so that $f = 336.85$ THz lies outside the band-gap. For the case of the nonlinear PTBG operating at $f = 336.85$ THz, the total transmission $T = 1$ is achieved regardless of the input beam intensity.

Since the NBG is orthogonal (reciprocal and lossless), i.e. $T + \Gamma = 1$, Fig. 4(b,c) show that at low input intensity the reflectance is close to 1, and it is very small at high input intensity. For the case of a nonlinear PTBG the reflectance, $\Gamma_L \neq \Gamma_R$ with $\Gamma_L > \Gamma_R$ at low input intensity, i.e. small Kerr effect, but as the input intensity increases the Γ_L decreases to almost zero and fits with the response of the NBG. Fig. 4(a,b) show that at high input intensity and for high saturation intensity, total transmittance with both $\Gamma_L, \Gamma_R \to 0$ is observed corresponding to a bidirectionally transparent grating for frequencies $f > f_B$.

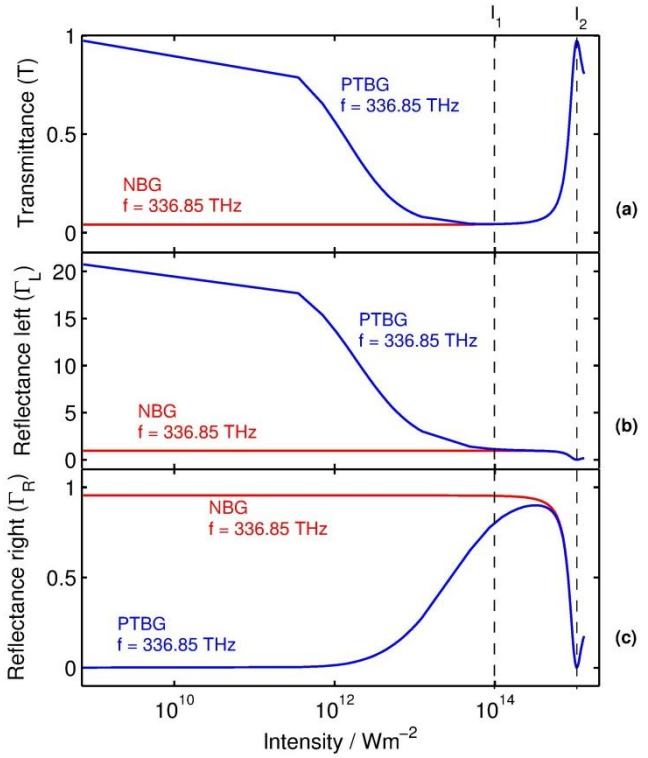

Fig. 5 (a) Transmittance, (b) reflectance for left and (c) reflectance for right incidence of PTBG at the U operation as a function of input intensity at $f = 336.85$ THz. The gain/loss has low saturation intensity $n_2 I_S = 0.0005$. Results for the NBG $(\alpha_0 = 0)$ at the Bragg frequency $f_B = 336.85$ THz are included for reference.

The impact of gain/loss saturation on the performance of the nonlinear PTBG as a function of input beam intensity is shown in Fig. 5. The grating is operated at $f = 336.85$ THz, similarly as in Fig. 4. The saturation intensity is low and set to $I_S = 2.5 \times 10^{13}$ Wm^{-2}, corresponding to a low Kerr nonlinearity of $n_2 I_S = 0.0005$. The PTBG operates at

the U point with $|\alpha_0| = 1460.24\ \mathrm{cm}^{-1}$. Fig. 5(a) shows almost total transmittance at low input intensity but it gradually decreases and fits with the response of the NBG as the input intensity is increased.

Fig. 5(b) and (c) depict the reflectance for the left Γ_L and right Γ_R incidence respectively. At low input intensity $\Gamma_L > \Gamma_R$, but it gradually decreases and fits with the response of the NBG as the input intensity is increased. Fig. 5(a-c) show the impact of the gain/loss saturation, that it effectively reduces the gain/loss in the system to a negligible level at high input intensity, and hence inhibits the interplay of Kerr nonlinearity and PT behaviour as is observed in Fig. 4.

4. Applications

In this section two potential applications of a nonlinear PTBG based on GaAs are investigated, namely an optical logic gate and a switch. The input beam comprises of a probe beam and a strong pump beam. The probe beam is a CW operated at the Bragg frequency $f_{probe} = 336.85$ THz and has a low intensity which is kept constant throughout the simulation with $I = 1 \times 10^6\ \mathrm{Wm}^{-2}$. The pump beam is a CW signal operated far from the Bragg frequency at $f_{pump} = 200$ THz. The intensities of the pump beam are switched between two different values, i.e. $I_1 = 1 \times 10^{14}\ \mathrm{Wm}^{-2}$ and $I_2 = 1 \times 10^{15}\mathrm{Wm}^{-2}$ as marked in Fig. 5, where the pump beam intensity is shown against time. The pump beam is initially turned off and then turned on to intensity I_1 for a duration of 10 ps, followed by an increase to intensity I_2 for another 10 ps. The pattern is then repeated as seen in Fig. 6(a).

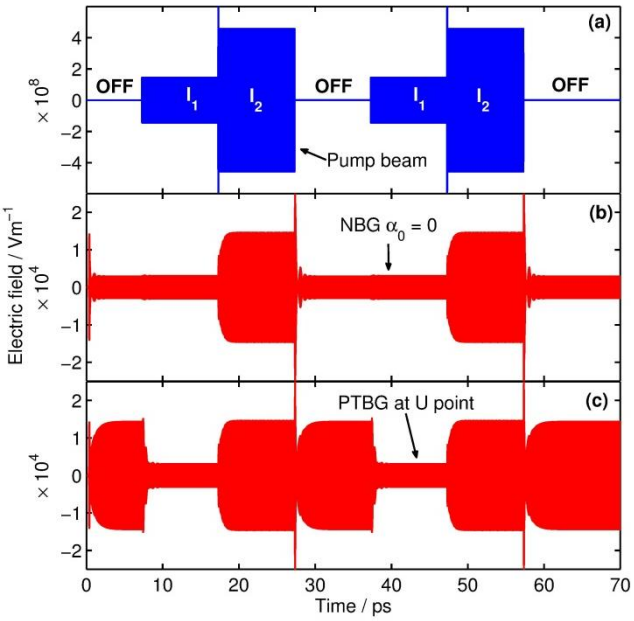

Fig. 6 Comparison of switching operation between the (b) NBG and (c) PTBG for the pump beam intensity profile shown in (a).

Fig. 6 compares the performance of the NBG and PTBG where Fig. 6(b) shows the transmitted probe beam of a NBG structure ($\alpha_0 = 0$) when excited from the left side. The transmitted probe beam of the NBG is very low when the pump beam is turned off or operated at $I = I_1$. However, when the pump beam is switched to operate at I_2 total transmitted power is observed. On the other hand, Fig. 6(c) shows the output of the PTBG when the grating is excited from the left. It can be seen that when the pump beam is off the probe beam is totally transmitted $T = 1$. Increase in the pump beam intensity to I_1 reduces the transmitted probe beam intensity. A subsequent further increase of the pump beam to I_2 increases the transmitted probe beam to total transmittance. Although Fig. 6(b) and Fig. 6(c) show that NBG and PTBG have similar switching operation, the PTBG achieves switching at lower pump intensity with the default ON state for $I = 0$ and OFF state at $I = I_1$.

5. Conclusion

The performance of a nonlinear PT Bragg grating that has dispersive material and a saturable gain/loss model is analysed and compared with the performance of an idealised PT Bragg grating and a nonlinear Bragg grating with no gain/loss. It is shown that material dispersion limits the unidirectional behaviour of the PTBG to a narrowband region around the Bragg frequency. The interplay of saturation and nonlinearity is important as low saturation intensity can prohibit the impact of Kerr nonlinearity in a nonlinear PTBG. At high saturation intensity the impact of nonlinearity contributes to bidirectional invisibility for frequencies above the Bragg frequency. The operation of the PTBG as an optical switch and logic gate confirms that the switching operation can be achieved at lower pump intensities than is the case for the nonlinear Bragg grating with no gain and loss.

References

1. Z. Lin, H. Ramezani, T. Eichelkraut, T. Kottos, H. Cao, and D. N. Christodoulides, "Unidirectional Invisibility Induced by PT-Symmetric Periodic Structures," Physical Review Letters 106, 213901 (2011).
2. Y. D. Chong, L. Ge, and a. D. Stone, "PT-symmetry breaking and laser-absorber modes in optical scattering systems," Physical Review Letters 106, 093902 (2011).
3. M. Kulishov, J. M. Laniel, N. Bélanger, J. Azaña, and D. V Plant, "Nonreciprocal waveguide Bragg gratings," Optics Express 13, 3068–78 (2005).
4. S. Phang, A. Vukovic, H. Susanto, T. M. Benson, and P. Sewell, "Ultrafast optical switching using parity–time symmetric Bragg gratings," Journal of the Optical Society of America B 30, 2984 (2013).
5. M. Greenberg and M. Orenstein, "Unidirectional complex grating assisted couplers.," Optics Express 12, 4013–8 (2004).
6. T. Kottos, "Optical physics: Broken symmetry makes light work," Nature Physics 6, 166–167 (2010).

7. R. El-Ganainy, K. G. Makris, D. N. Christodoulides, and Z. H. Musslimani, "Theory of coupled optical PT-symmetric structures," Optics Letters 32, 2632 (2007).
8. L. Chen, R. Li, N. Yang, D. Chen, and L. Li, "Optical modes in PT-Symmetric double-Channel waveguides," arXiv preprint arXiv: 1202.2956 (2012).
9. C. E. Rüter, K. G. Makris, R. El-Ganainy, D. N. Christodoulides, M. Segev, and D. Kip, "Observation of parity–time symmetry in optics," Nature Physics 6, 192–195 (2010).
10. A. Regensburger, C. Bersch, M.-A. Miri, G. Onishchukov, D. N. Christodoulides, and U. Peschel, "Parity-time synthetic photonic lattices - Supplementary method.," Nature 488, 167–71 (2012).
11. K. G. Makris, R. El-Ganainy, and D. N. Christodoulides, "Beam dynamics in PT symmetric optical lattices," Physical Review Letters 100, 103904 (2008).
12. S. Nixon, L. Ge, and J. Yang, "Stability analysis for solitons in PT-symmetric optical lattices," Physical Review A 85, 023822 (2012).
13. F. Nazari, M. Nazari, and M. K. Moravvej-Farshi, "A 2×2 spatial optical switch based on PT-symmetry.," Optics Letters 36, 4368–70 (2011).
14. M. Kulishov, B. Kress, and R. Slavík, "Resonant cavities based on Parity-Time-symmetric diffractive gratings," Optics Express 21, 68–70 (2013).
15. A. Mostafazadeh, "Invisibility and PT symmetry," Physical Review **A** 11 (2013).
16. A. Mostafazadeh, "Spectral singularities of complex scattering potentials and infinite reflection and transmission coefficients at real energies," Physical Review Letters 102, 220402 (2009).
17. J. Čtyroký, V. Kuzmiak, and S. Eyderman, "Waveguide structures with antisymmetric gain/loss profile," Optics Express 18, 21585–21593 (2010).
18. J. Čtyroký, "Dispersion properties of coupled waveguides with loss and gain: a full-vectorial analysis," Optical and Quantum Electronics (2014).
19. H. Ramezani, T. Kottos, R. El-Ganainy, and D. N. Christodoulides, "Unidirectional nonlinear PT-symmetric optical structures," Physical Review **A** 82, 043803 (2010).
20. Z. Musslimani, K. Makris, R. El-Ganainy, and D. N. Christodoulides, "Optical solitons in PT periodic potentials," Physical Review Letters 100, 030402 (2008).
21. V. Achilleos, P. G. Kevrekidis, D. J. Frantzeskakis, and R. Carretero-González, "Dark solitons and vortices in PT-symmetric nonlinear media: From spontaneous symmetry breaking to nonlinear PT phase transitions," Physical Review A 86, 013808 (2012).
22. J. Paul, C. Christopoulos, and D. W. P. Thomas, "Generalized material models in TLM .I. Materials with frequency-dependent properties," IEEE Transactions on Antennas and Propagation 47, 1528–1534 (1999).
23. J. Paul, C. Christopoulos, and D. W. P. Thomas, "Generalized material models in TLM - part 3: materials with nonlinear properties," IEEE Transactions on Antennas and Propagation 50, 997–1004 (2002).
24. W. J. R. Hoefer, "The Transmission-Line Matrix Method--Theory and Applications," IEEE Transactions on Microwave Theory and Techniques 33, 882–893 (1985).
25. C. Christopoulos, The Transmission-Line Modeling Method TLM (IEEE Press, 1995).
26. S. Phang, A. Vukovic, H. Susanto, T. Benson, and P. Sewell, "Time domain modeling of all-optical switch based on PT-symmetric Bragg grating," in 29th Annual Review of Progress in Applied Computational Electromagnetics (Applied Computational Electromagnetics Society, 2013), pp. 693–698.
27. V. Janyani, A. Vukovic, and J. Paul, "The development of TLM models for nonlinear optics," Microwave review 10, 35–42 (2004).
28. V. Janyani, A. Vukovic, J. D. Paul, P. Sewell, and T. M. Benson, "Time domain simulation in photonics: A comparison of nonlinear dispersive polarisation models," Optical and Quantum Electronics 37, 3–24 (2005).
29. S. C. Hagness, R. M. Joseph, and A. Taflove, "Subpicosecond electrodynamics of distributed Bragg reflector microlasers: Results from finite difference time domain simulations," Radio Science 31, 931–941 (1996).
30. M. Bass, G. Li, and E. van Stryland, Handbook of Optics Vol. 4, 3rd ed. (McGraw Hill, 2010).
31. J. S. Aitchison, D. C. Hutchings, J. U. Kang, G. I. Stegeman, and a. Villeneuve, "The nonlinear optical properties of AlGaAs at the half band gap," IEEE Journal of Quantum Electronics 33, 341–348 (1997).
32. S. Lan, A. V. Gopal, K. Kanamoto, and H. Ishikawa, "Ultrafast response of photonic crystal atoms with Kerr nonlinearity to ultrashort optical pulses," Applied Physics Letters 84, 5124 (2004).

Parity-time symmetric cloak with one-way invisibility

Xue-Feng Zhu,[1,2] Liang Feng,[1] Peng Zhang,[1] Xiaobo Yin,[1,3] and Xiang Zhang[1,3],*

1 NSF Nanoscale Science and Engineering Center, 3112 Etcheverry Hall, University of California, Berkeley, CA 94720, USA
2Huazhong University of Science and Technology, Wuhan, Hubei 430074, China
3Materials Science Division, Lawrence Berkeley National Laboratory, 1 Cyclotron Road, Berkeley, CA 94720, USA
*Corresponding author: xiang@berkeley.edu

Abstract

A one-way invisible cloak is proposed by transforming the parity-time (PT) symmetric optical materials. At the PT-symmetry breaking threshold, incident light is scattered only along one direction but not the other by satisfying the phase matching condition, making the cloak one-way invisible. In addition, optical scattering from the one-way cloak can be further engineered to create a unidirectional optical illusion of the concealed object.

1. Introduction

In recent years, transformation optics has attracted considerable research attention in the development various devices with unprecedented performances not found in nature [1-8]. Myriad novel effects such as invisibility cloaking have been theoretically and experimentally demonstrated by using the coordinate transformation [3-5]. The previous studies were mainly focused on the realization of perfect cloaks, *viz*. making the concealed object omnidirectionally invisible to the outside observers [1-2]. In many cases, however, it might be important to have the cloak selectively visible for only a specific direction, *i.e.*, a one-way invisible cloak. Some researchers have proposed a coordinate-transformed nonreciprocal photonic crystal cloak, where an external magnetic field is used to create an asymmetric permeability tensor, thus breaking the reciprocity of light [9]. Nevertheless, it is more desirable for optical devices and applications to realize a one-way cloak without applying a static magnetic field. In the past few years, the PT symmetric materials have been studied intensely, which is shown to be able to provide a unidirectional light transport with the complex dielectric permittivity plane engineered in its entirety. As an example, one-way invisible medium has been demonstrated at the spontaneous PT symmetry breaking threshold, which is also the exceptional point [10]. Even though the unidirectional invisibility breaks down for the PT symmetric materials with a large number of unit cells [11], the unidirectional invisibility from the PT symmetric materials at short lengths can provide an efficient approach to achieving one-way invisible cloaks, complementing the so far explored omnidirectional invisible cloaks.

2. Parity-time symmetric cloak

In this paper, we propose a new scheme to realize the PT symmetric cloak by introducing the PT symmetric optical materials into the transformation optics. The transformed PT symmetric materials provide a unidirectional wave vector. Therefore, the light scattering is expected to occur when the phase matching condition is satisfied in one direction, while no scattering can be observed with light incident from other directions. For the outside observers, the concealed object is cloaked depending on incident directions of light. Moreover, we show that the enhanced scattering from the transformed PT symmetric materials can be engineered to provide a one-way optical illusion of the concealed object.

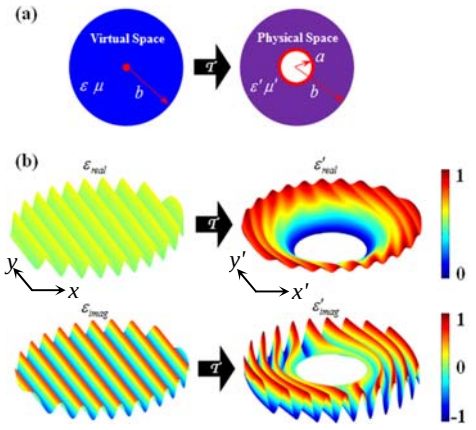

Figure 1: (a) Coordinate transformation to expand a point (r=0) in the virtual space ($r \le b$) into a hole ($r' \le a$) in the physical space ($a \le r' \le b$). (b) Complex permittivities of the PT symmetric materials in the virtual and physical spaces, respectively.

In Fig. 1(a), a point is expanded into a circular hole by the pushing-forward coordinate mapping, where $r = f(r') = b(r'-a)/(b-a)$ and $\theta=\theta'$ in polar coordinates [1]. It needs to be mentioned that even though PT symmetric materials have a broadband unidirectional response, the singularity at the boundary of the circular hole limits the operating bandwidth of the transformed PT symmetric cloak. In the

virtual space ($r \le b$), the PT symmetric material is built up by a periodic complex modulation in its permittivity: $\varepsilon = 1 + \zeta \exp(i\boldsymbol{\beta}\cdot\boldsymbol{x})$, where ζ is the modulation amplitude and β the modulation vector, respectively, and $\boldsymbol{\beta}\cdot\boldsymbol{x} = \beta r\cos\theta$. In Fig. 1(b), ε' and μ' in the physical space ($a \le r' \le b$) after transformation is written as $\varepsilon'_{z} = f(r')f'(r')\,\varepsilon/r'$, $\mu'_{r'} = f(r')\mu/[r'f'(r')]$, and $\mu'_{\theta} = f'(r')r'\mu/f(r')$ for transverse electric (TE) polarized light, where the permeability tensor is anisotropic and inhomogeneous.

According to transformation optics, the wave dynamics in virtual space should be equivalent to that in physical space. For simplicity, we only investigate the propagation behavior of TE polarized light in the virtual space, where the scalar Helmholtz equation can be written in the form

$$\frac{\partial^2 E_z}{\partial x^2} + \frac{\partial^2 E_z}{\partial y^2} + \frac{\omega^2}{c^2}\varepsilon E_z = 0, \tag{1}$$

where c is the speed of light in vacuum. Applying the coupled mode theory, we decompose the total electric field in terms of incident and scattered components into

$$E_z = E_{in}(\boldsymbol{x})\exp(i\boldsymbol{k}_1\cdot\boldsymbol{x}) + E_{sc}(\boldsymbol{x})\exp(i\boldsymbol{k}_2\cdot\boldsymbol{x}). \tag{2}$$

Assuming slowly varying amplitudes of the incident and scattered waves and substituting Equation (2) into the Equation (1), one can obtain

$$\begin{aligned} &i2\boldsymbol{k}_1\cdot\nabla E_{in}(\boldsymbol{x})\exp(i\boldsymbol{k}_1\cdot\boldsymbol{x}) + i2\boldsymbol{k}_2\cdot\nabla E_{sc}(\boldsymbol{x})\exp(i\boldsymbol{k}_2\cdot\boldsymbol{x}) \\ &+\omega^2\zeta E_{in}(\boldsymbol{x})\exp[i(\boldsymbol{\beta}+\boldsymbol{k}_1)\cdot\boldsymbol{x}]/c^2 \\ &+\omega^2\zeta E_{sc}(\boldsymbol{x})\exp[i(\boldsymbol{\beta}+\boldsymbol{k}_2)\cdot\boldsymbol{x}]/c^2 = 0 \end{aligned}. \tag{3}$$

Define a detuning factor $\boldsymbol{\delta} = \boldsymbol{\beta} + \boldsymbol{k}_1 - \boldsymbol{k}_2$. Equation (3) can be formalized into the coupled mode equation

$$i\begin{bmatrix} \dfrac{\boldsymbol{k}_1}{|\boldsymbol{k}_1|^2} \\ \dfrac{\boldsymbol{k}_2}{|\boldsymbol{k}_2|^2} \end{bmatrix}^T \cdot\nabla\begin{bmatrix} E_{in}(\boldsymbol{x}) \\ E_{sc}(\boldsymbol{x}) \end{bmatrix} = \begin{bmatrix} -\dfrac{\omega^2\zeta}{2c^2|\boldsymbol{k}_1|^2}\exp(i\boldsymbol{\beta}\cdot\boldsymbol{x}) \\ -\dfrac{\omega^2\zeta}{2c^2|\boldsymbol{k}_2|^2}\exp(i\boldsymbol{\delta}\cdot\boldsymbol{x}) \end{bmatrix}, \tag{4}$$

$$\begin{bmatrix} -\dfrac{\omega^2\zeta}{2c^2|\boldsymbol{k}_1|^2}\exp[i(2\boldsymbol{\beta}-\boldsymbol{\delta})\cdot\boldsymbol{x}] \\ -\dfrac{\omega^2\zeta}{2c^2|\boldsymbol{k}_2|^2}\exp(i\boldsymbol{\beta}\cdot\boldsymbol{x}) \end{bmatrix}\begin{bmatrix} E_{in}(\boldsymbol{x}) \\ E_{sc}(\boldsymbol{x}) \end{bmatrix}$$

where $|\boldsymbol{k}_1| = |\boldsymbol{k}_2| = \omega/c$ since the incident and scattered lights are both propagating in the free space. In our study, the initial condition of incident and scattered waves are $E_{in} \neq 0$ and $E_{sc} = 0$, respectively. Therefore, for a specific incident beam with $\boldsymbol{k}_1$ that satisfies $\boldsymbol{\delta} = 0$, the momentum of the scattered waves is determined by $\boldsymbol{k}_2 = \boldsymbol{\beta} + \boldsymbol{k}_1$. And the value of E_{sc} increases linearly with the propagation distance inside the PT symmetric materials while E_{in} remains unchanged under the constraint of reciprocity. On the other hand, for the incident waves with momentum that always leads to $\boldsymbol{\delta} \neq 0$, the overall energy transfer to the scattered components is negligible due to the phase mismatch, which leads to a near-zero scattering cross-section.

In the following, we carry out full-wave simulations using a finite element solver (COMSOL Multiphysics) to demonstrate the one-way invisibility effect of transformed PT symmetric materials. In the numerical simulations, the TE-polarized plane wave is incoming from the left (Figs. 2(a) and 2(c)) and right (Figs. 2(b) and 2(d)) directions, respectively. The wavelength of light is set to be $\lambda = 0.1$ unit. In order to form the distinctive Bragg scattering, the modulation vector of the PT material in the virtual space is $\beta = 4\pi/\lambda$. The parameters in the circular region ($|x| \le 2.5\lambda$) (see Figs. 2(a) and 2(b)) are then expressed as $\varepsilon = 1 + 0.1\exp(i125.66x)$ and $\mu = 1$. In Fig. 2(a), strong Bragg reflection is visualized for left incidence due to the satisfied phase matching condition $k_2 \approx \beta + k_1$, shown by the inset vector diagram. For the right incidence in Fig. 2(b), the scattered light is barely observed due to the very fact that the corresponding vector diagram reveals that k_2 will be much larger than k_1 and thus fall into the evanescent regime.

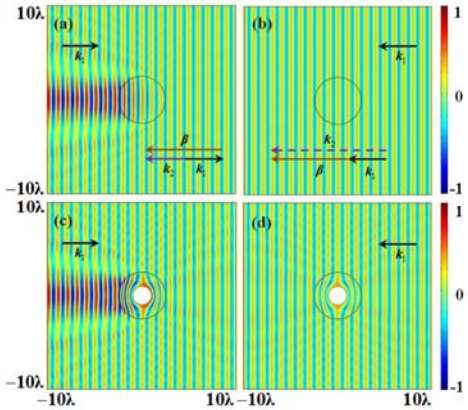

Figure 2: The total electric field distribution in the virtual space [(a), (b)] and the physical space [(c), (d)].

The results in our simulations are consistent with the previously reported unidirectional invisibility [10]. In Figs. 2(c) and 2(d), the unidirectional wave scattering of the PT symmetric cloak is demonstrated in the physical space, where a perfect electric conductor (PEC) cylinder with a radius of λ is concealed and one-way cloaked. Basically, the field distributions in both directions are in good agreement with the results in the virtual space (Figs. 2(a) and 2(b)) despite of a small amount of scattering caused by the singularity at the boundary of the PEC cylinder $|x'| = \lambda$. In addition, the total power in the whole simulation domain increases as wave propagates though the PT symmetric material, which does not violate the energy conservation law, since the optical gain is introduced to balance out the loss inside and provide the additional power.

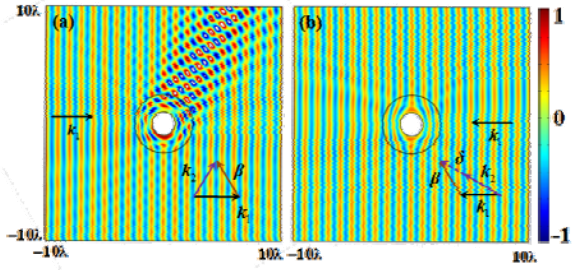

Figure 3: The total electric field distribution with TE-polarized plane waves coming from (a) the left and (b) the right, respectively. Here the modulation vector β is not in parallel with the incident wave vector k_1.

We also consider the case when the modulation vector β is not in parallel with the incident wave vector k_1. The parameters in the virtual space ($|x|\leq 2.5\lambda$) are instead expressed as $\varepsilon=1+0.1\exp(-i31.42x+i54.41y)$ and $\mu=1$. In Fig. 3(a), inset vector diagram shows that the incident wave vector $\boldsymbol{k}_1$, scattered wave vector $\boldsymbol{k}_2$, and modulation vector $\boldsymbol{\beta}$ form an equilateral triangle, which indicates a strong forward scattering, and the phase mismatch $\delta\neq 0$ enables nearly no reflection for the backward propagation as shown in Fig. 3(b).

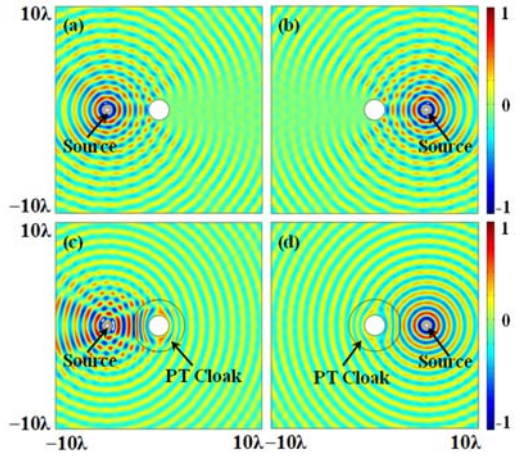

Figure 4: The total electric field distribution with a TE-polarized point source impinging on a PEC cylinder ($r'\leq\lambda$) without [(a)-(b)] and with the PT cloak ($\lambda\leq r'\leq 2.5\lambda$) [(c)-(d)]. The point source is located at (-5λ, 0) [(a), (c)] and (5λ, 0) [(b), (d)], respectively.

Figures 4(a) and 4(b) show the scattering pattern of a PEC cylinder for a point source located at (-5λ, 0) and (5λ, 0), respectively. In Figs. 4(c) and 4(d), when the PEC cylinder is shielded by the PT symmetric cloak, the one-way invisibility effect can also be clearly observed. In Fig. 4(d), an undisturbed cylindrical wave pattern is presented in the far-field on both sides of the cloak where the point source is located right to the cloak, showing an excellent cloaking effect since the phase mismatch forbids the energy transfer from incident waves to the scattered waves. In Fig. 4(c), the point source is located left to the cloak, and the reflection is induced by the phase matching. However, the concealed PEC cylinder in Fig. 4(c) still remains invisible to the observer standing right to the PT cloak, due to the fact that the unidirectional phase matching is only valid for reflection rather than transmission. Therefore, the total electric field distribution after the PT cloak remains the same as that from the point source with no contribution from scattering in light transmission. Different from the observer behind the PT symmetric cloak that sees unperturbed light propagation, the one in front may have an illusion that light is reflected back from a concave mirror.

3. Unidirectional optical illusion

In Fig. 5, we have compared the electric field distributions from the cloaked PEC cylinder with the one from a PEC concave mirror. The normalized scattering field distributions of the cloaked PEC cylinder are plotted, under the different illumination conditions of TE-polarized cylindrical light, where the point source is located at (-3λ, 0), (-5λ, 0), and (-7λ, 0), respectively, as shown in Fig. 5(a). The results clearly show that the backward scattering angle becomes narrower as the source is moved away from the concealed object.

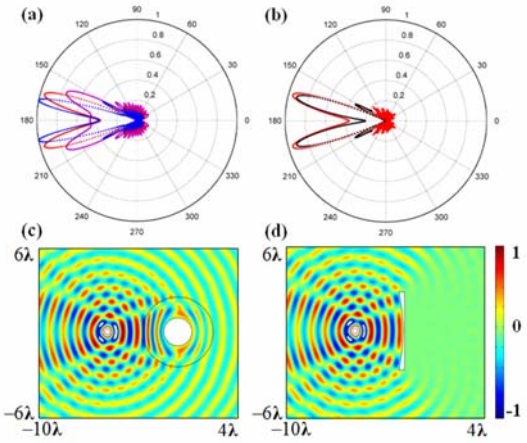

Figure 5: (a) For the point source located at (-3λ, 0), (-5λ, 0), and (-7λ, 0), the normalized scattering fields of the cloaked PEC cylinder are represented by the purple, red, and blue curves, respectively. (b) The normalized scattering fields from the cloaked PEC cylinder (red) is compared with that of a concave PEC mirror (black), where the point source is located at (-5λ, 0). (c) and (d) are the total electric field distributions for the cloaked PEC cylinder and the concave PEC mirror, respectively.

In Fig. 5(b), the backscattering patterns from the PT symmetric cloak are nearly equivalent to those from a PEC concave mirror, thus providing an illusion in reflection as if there is a PEC concave mirror instead of the concealed PEC cylinder. Moreover, the simulated field distributions in Figs. 5(c) and 5(d) further confirm the resemblance of scattered fields between two cases. It is shown that great consistence in both amplitude and phase of backscattering has been achieved around the point source. Such an optical illusion is also unidirectional, similar to the demonstrated one-way invisibility for the PT symmetric cloak.

4. Conclusions

We theoretically demonstrated a new type of one-way invisible cloak by transforming PT symmetric materials at the spontaneous PT symmetry threshold. Light is strongly reflected for one direction that the phase matching condition is satisfied, while being unperturbed in the other direction. The results show that the scattering from the PT symmetric cloak can be employed to provide a specific detectable route to the outside world and even give an optical illusion for the concealed object. Furthermore, it will be necessary to engineer the direction, amplitude, and phase of each scattered component in order to create an arbitrary optical illusion, which is possible by introducing a more generalized PT symmetric potential in the virtual space, *i.e.* $\Delta\varepsilon(x)=\sum_j \zeta_j \exp(i\beta_j\cdot x+i\varphi_j)$. Here, the amplitude, direction,

and phase of the scattered light (j) can be tuned flexibly by the material parameters of ζ_j, β_j, and φ_j, respectively, when the physical size of the illusion device and the wave vector of incident light are given. It needs to be mentioned that the proposed method can also be used to design other transformation optics devices such as PT carpet cloak, PT optical rotator, *etc*. Our scheme offers great material design flexibility and additional freedoms for developing novel photonic devices by investigating the PT symmetric optical materials within the context of transformation optics.

Acknowledgements

This work was supported by the US ARO MURI program (W911NF-09-1-0539). X. F. Z acknowledges the financial support from the Bird Nest Plan of HUST.

References

[1] J. B. Pendry, D. Schurig, D. R. Smith, Controlling electromagnetic fields, *Science* 312: 1780, 2006.

[2] U. Leonhardt, T. Tyc, Broadband invisibility by non-Euclidean cloaking, *Science* 323: 110, 2009.

[3] W. S. Cai, U. K. Chettiar, A. V. Kildishev, V. M. Shalaev, Optical cloaking with metamaterials, *Nature Photon.* 1: 224-227, 2007.

[4] A. V. Kildishev, V. M. Shalaev, Engineering space for light via transformation optics, *Opt. Lett.* 33: 43-45, 2008.

[5] J. Valentine, J. Li, T. Zentgraf, G. Bartal, X. Zhang, An optical cloak made of dielectrics, *Nature Mater.* 8: 568, 2009.

[6] M. Rahm, D. A. Roberts, J. B. Pendry, D. R. Smith, Transformation-optical design of adaptive beam bends and beam expanders, *Opt. Express* 16: 11555-11567, 2008.

[7] N. M. Litchinitser, A. I. Maimistov, I. R. Gabitov, Roald Z. Sagdeev, Vladimir M. Shalaev, Metamaterials: electromagnetic enhancement at zero-index transition, *Opt. Lett.* 33: 2350-2352, 2008.

[8] J. Li, J. B. Pendry, Hiding under the carpet: a new strategy for cloaking, *Phys. Rev. Lett.* 101: 203901, 2008.

[9] C. He, X. L. Zhang, L. Feng, M. H. Lu, Y. F. Chen, One-way cloak based on nonreciprocal photonic crystal, *Appl. Phys. Lett.* 99: 151112, 2011.

[10] Z. Lin, H. Ramezani, T. Eichelkraut, T. Kottos, H. Cao, D. N. Christodoulides, Unidirectional invisibility induced by PT-symmetric periodic structures, *Phys. Rev. Lett.* 106: 213901, 2011.

[11] S. Longhi, Invisibility in PT-symmetric complex crystals, *J. Phys. A: Math. Theor.* 44: 485302, 2011.

Bionanoplasmonics

New SERS-active junction based on cerium dioxide facet dielectric films for biosensing

Ilya Kurochkin[1*], Ilya Ryzhikov[2], Andrey Sarychev[2], Konstantin Afanasiev[2], Igor Budashov[3], Marina Sedova[2], Irina Boginskaya[2], Sergey Amitonov[4] and Andrey Lagarkov[2]

[1]Faculty of Chemistry, Lomonosov Moscow State University, Moscow, Russia
[2]Institute for Theoretical and Applied Electromagnetics, The Russian Academy of Science, Moscow, Russia
[3]Emanuel Institute of Biochemical Physics, The Russian Academy of Science, Moscow, Russia
[4]Faculty of Physics, Lomonosov Moscow State University, Moscow, Russia
*corresponding author, E-mail: ikur@genebee.msu.su

Abstract

Further enhance of the Raman scattering is the priority for the development of the modern molecular diagnostic methods. Expected increasing in detection sensitivity of the biological and chemical agents provides substantial progress in such areas as: proteomics (discovery of new disease markers), pharmacokinetics of drugs, analysis of toxins and infections agents, drug analysis, food safety, and environmental safety.

In this paper we investigated the possibility of the facet structures, based on cerium dioxide for the purpose of increasing the intensity of the SERS signal. During the studies a new metamaterial was developed. The metamaterial is based on the facet cerium dioxide films and plasmonic nanoparticles that are immobilized on its surface. The new metamaterial provides additional SERS signal amplification factor of 211. Thus developed material offers the prospect of increasing the sensitivity and selectivity of biochemical and immunological analysis.

1. Introduction

Over the last decade, many research efforts have been focused on the development the fast, sensitive, and low cost sensors, especially for biological and chemical compounds. Emerging advances in plasmonics, nanotechnology, surface engineering, and optics open an opportunity of using the near-field interactions to significantly increase the optical signal strength.

It is known that the media with random distribution of the refractive index and non-uniform rough surface provide the inhomogeneous distribution of the intensity maxima in transmitted and reflected light [1]. Recently, we have shown that resonant interactions in the special dielectric metamaterials (facet dielectric films) yield significantly enhanced local fields covering large surface areas [2]. In this report we consider the possibility of combining plasmon resonances in metal (gold) nanoparticles with localized electromagnetic resonaces in the facet dielectric films of cerium dioxide for highly sensitive SERS detection of chemical compounds and biological agents.

2. Results

2.1. Preparation of facet cerium dioxide films

A technological route to facet cerium dioxide films consists of the following:

• pretreatment of surface of a polycor substrate by washing in isopropyl alcohol and ion cleaning in vacuum chamber (10^{-2} Torr) by an ion beam (beam current 150 mA, voltage 1.5 kV) for 15 minutes;

• deposition by electron beam evaporation of aluminum sublayer, thickness of 100-150 nm, current in the electron beam was 100 mA, voltage - 8kV;

• cerium dioxide of high purity was placed in a water-cooled copper crucible, electron-beam evaporation was carried out at a beam current of 30 mA and a voltage of 8 kV.

The thickness of the deposited films was controlled by optical inspection of the interference maxima and minima of the transmittance at a wavelength of 900 nm on the control glass samples.

2.2. Preparation and immobilization of Au-nanoparticles on the facet cerium dioxide films

Au-nanoparticles (Au-NP) were prepared by well-known citrate method [3]. Au-Np size was determined by Nanoparticle Tracking Analysis (average size - 56±1 nm). For the preparation of SERS active particles, Au-NPs were modified by 3,3'-dithio-bis(6-nitrobenzoic acid) - (DTNB) in accordance with the scheme shown in Fig. 1.

Au-NPs were adsorbed onto facet cerium dioxide films after deposition of polycation (poly(diallyldimethylammonium chloride)) according to the procedure described in the article [4].

2.3. Morphology and structure of cerium dioxide films

Morphology of cerium dioxide films were studied by scanning electron microscopy (SEM) using a Quanta microscope (FEI) with resolution near 5 nm. Representative

SEM image and cross section of cerium dioxide film are shown in Fig. 2.

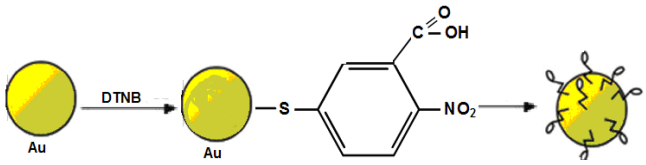

Figure 1: Scheme for preparation of Au-NP - DTNB conjugates.

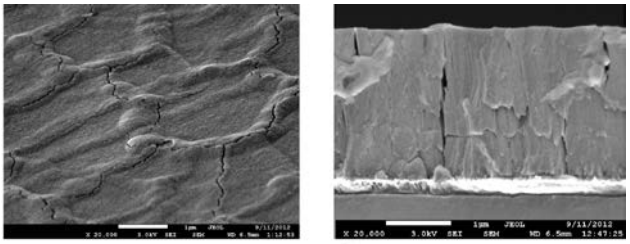

Figure 2: (a) General SEM view of the CeO2 structure; (b)cross section of CeO2 film.

Presented in Fig. 2 images show characteristic faceted structure of the films. A detailed study of the structure facet films was conducted by atomic force microscopy. Dedicated as a result the basic elements of this structure are reflected in the scheme shown in Fig. 3.

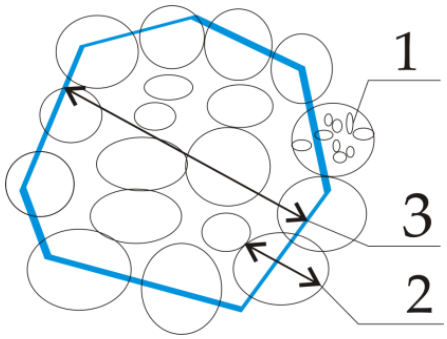

Figure 3: The general scheme of the resulting facet structure.

Nanoscale structures (1) form larger agglomerates (2) with characteristic dimensions of several hundred nanometers. Agglomerates are arranged so that they form a facet (3). Perimeter facet (blue line) forms a kind of curb. The facets are separated from each other by small cracks (several nanometers). Estimated by AFM dimensions for selected structures are shown in Table 1.

Table 1: Dimensions of the elements of the facet structures at various cerium dioxide film thicknesses.

Film thickness, nm	Curb height, nm	Facet size, µm	Agglo-merate size, µm	Nano struct. size, nm
800	29± 4	1,3±0,1	0,32±0,03	28±2
1200	50± 7	1,5±0,1	0,37±0,04	29±4
1600	118±17	2,0±0,1	0,45±0,04	32±4
2000	126±15	2,5±0,3	0,57±0,04	23±3
2400	105±24	2,3±0,3	0,60±0,05	25±4
2800	128±19	2,8±0,2	0,65±0,06	75±7

The Table 1 shows that nanoscale structures size remains constant for all thickness except 2800 nm where average size is higher in 3 times. Increase in film thickness leads to an increase in the size of the agglomerates curb height and facet size. A slight deviation from this rule is observed at 2400 nm film thickness.

Investigation of the optical images and the distribution of Raman signal on the cerium dioxide films was performed using confocal Raman imaging system Alpha 500R (WITec, Germany). Raman scattering system registration was equipped with WITec inverted confocal microscope. It is situated at solid granite plate mounted at active vibration isolation system. Special XY positioner provide accuracy moving of sample table. Microscope objective is EC Epiplan-Neofluar 100x/0,9 DIC ∞/0 Carl Zeizz objective. Objective numerical aperture consists 0,9. Light source is green laser WITec with 532 nm wave length and its maximal power is 60 mW. Measurement was carried out at 5 mW of all laser power. Raman scattering light from sample enters the optical fiber and goes to the spectrometer. Signal registration is performed by Andor CCD camera. WITec Raman scattering system provides 90% delivery of light to the detector.

Fig. 4 show optical image and Raman intensity distribution at 456 cm^{-1} (characteristic Raman shift for cerium dioxide).

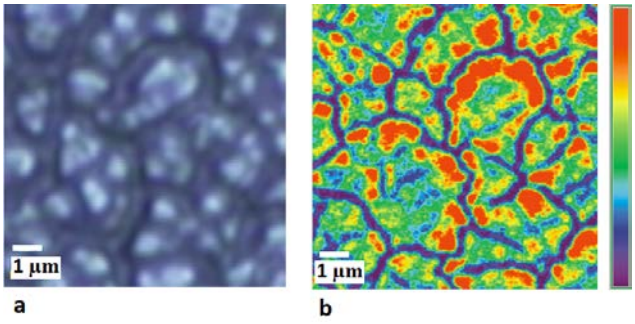

Figure 4: (a) Optical image of 2400 nm CeO2 surface; (b) intensity distribution maps for mainRaman peak of 2400 nm CeO2. Red - 300 CCD counts, violet - 1700 CCD counts.

These images show the irregular distribution of the signal on the film surface. Areas of more intense signal located mainly in the border area of facets.

2.4. Morphology of SERS-active junction of Au-NP and facet cerium dioxide films

Morphology of cerium dioxide films after Au-NP deposition were studied by SEM using a Supra-40 microscope (Carl Zeiss). Representative SEM images are shown in Fig. 5.

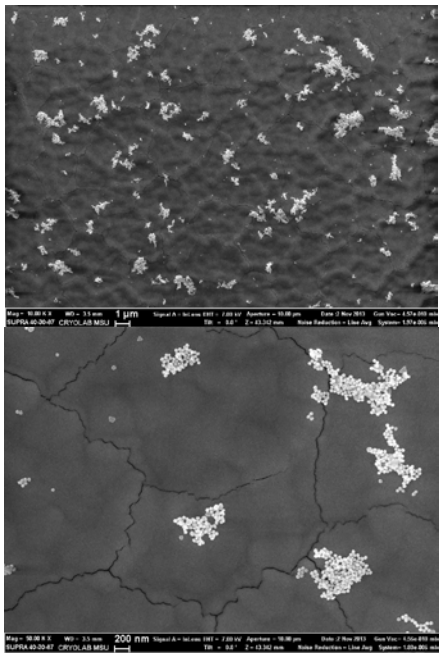

Figure 5: SEM images of facet cerium dioxide films with Au-NP.

The fraction of the surface occupied by the gold nanoparticles after deposition to the cerium dioxide surface was evaluated using software Gwyddion. Data for films with different thickness are given in Table 2.

Table 2: Fraction of surface occupied by the gold nanoparticles after deposition to the cerium dioxide films.

Film thickness, nm	Fraction of surface for gold NP [%]
90	5.7±0.7
200	5.8±0.7
300	4.6±0.7
400	3.8±0.7
500	1.3±0.7
600	3.7±0.8
700	2.3±1.1
800	4.5±1.2
1200	7.7±4.6
1600	6.0±3.7
2000	5.2±0.6
2400	2.3±1.1
2800	2.1±2.7

From Table 2 it follows that immobilization of Au-NPs lead to covering from 1 to 8 percent of the cerium dioxide surface.

2.5. SERS spectra

A Raman spectrometer innoRam, model BWS445(B)-785S (B&W Tek, Inc.) with continuous-wave laser-785 (290 mW) was used for the collection of spectra using an excitation wavelength of 785 nm. The excitation was performed in an epi configuration through a 20X objective (NA= 0.4) on a microscope. The SERS signal was collected through the same objective in 180 degree backscattering geometry. Laser power for all experiments was 29 mW. The acquisition time was 1.5 seconds. 326 cm^{-1}, 1060 cm^{-1}, 1338 cm^{-1} and 1558 cm^{-1} Raman scattering bands of thio 6-nitrobenzoic acid [5] were used to assess the effectiveness of the SERS signal. SERS signal intensity of these bands was calculated as the average of the measurements in the ten points of the sample after subtracting the baseline signal.

3. Discussion

Studies have shown that in the process of formation of cerium dioxide films as a result apparently of relaxation of tensions arising formed facet structure with a characteristic size about 2-3 microns. Irregular distribution of the Raman signal on the film surface (see Fig. 4) indicates the possibility of an additional signal amplification after immobilization SERS active structures on the surface of the facet structures due to the presence of local amplification of the electromagnetic field. Study of SERS signal intensity from DTNB - Au-NP on cerium dioxide films with various thicknesses showed that the magnitude of the signal oscillates with increasing film thickness (see Fig. 6).

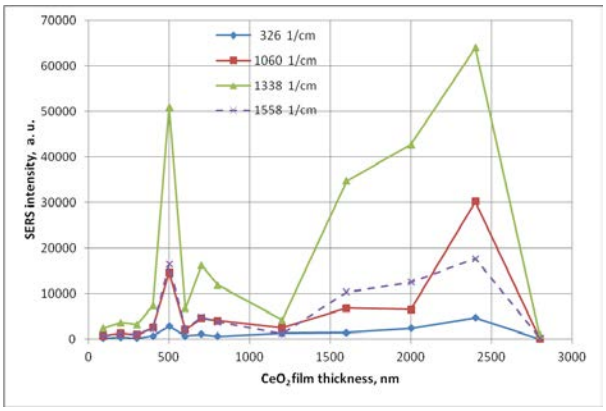

Figure 6: SERS signal at different Raman scattering bands from DTNB - Au-NP on cerium dioxide films with various thicknesses after normalization to the amount of gold nanoparticles.

Normalization of SERS signals on the magnitude of the signal received at a film thickness of 2800 nm (minimal signal), makes it possible to estimate the values of the coefficients of additional enhancing for the SERS signal. The data after the appropriate transformation shown in Fig. 7.

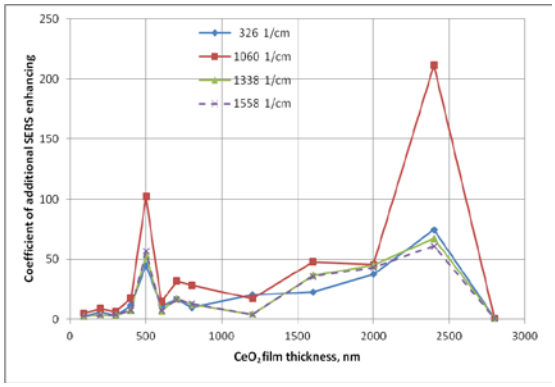

Figure 7: This is the figure caption. Color figures are acceptable.

Maximum, more than 200 times, additional enhancing for the SERS signal is achieved at a film thickness of 2400 nm and Raman shift 1060 cm^{-1}. It should be noted that the signal enhancement depends on the selected SERS shift as well. In other words, the films of different thickness have a different selectivity relative to the vibrations of different frequencies.

4. Conclusions

A new metamaterial based on facet cerium dioxide films and immobilized on its surface plasmonic nanoparticles have been developed. The new material provides additional SERS signal amplification factor of 211. Using the developed material offers the prospect of increasing the sensitivity and selectivity of biochemical and immunological analysis.

Acknowledgements

This research was supported by Lomonosov Moscow State University Programm of Development and Programm №3 of BEMMBCS of RAS and RFFI grant 12-02-01365-a.

References

[1] Ed. By J.C. Dainty, *Laser Specle and Related Phenomena*, Springer-Verlag, Berlin, Heidelberg, New York, 1975.

[2] I.N. Kurochkin, A.K. Sarychev, I.A. Ruzhikov, I.A. Budashov, S.S. Maklakov, S.O. Boyarintsev, A.N. Lagarkov, Surface-enhanced raman scattering–based biosensors // *Portable Biosensing of Food Toxicants and Environmental Pollutants. — Series in Sensors.* — 6000 Broken Sound Parkway NW, STE 300, BOCA RATON, USA, FL, 33487-2742: 2013. — P. 97–123.

[3] J. Turkevich, P.S. Stevenson, J. Hiller, A study of the nucleation and growth processes in the synthesis of colloidal gold, *Discuss. Faraday Soc.* 11: 55-75, 1955.

[4] M.S. Gromova, L.V. Sigolaeva, M.A. Fastovets, E.G. Evtushenko, I.A. Babin, D.V. Pergushov, S.V. Amitonov, A.V. Eremenko, I.N. Kurochkin, Improved adsorption of choline oxidase on a polyelectrolyte LBL film in the presence of iodine anions, *Soft Matter* 7: 7404-7409, 2011.

[5] U. Tamer, I.H. Boyacı, E. Temur, A. Zengin, I. Dincer, Y. Elerman, Fabrication of magnetic gold nanorod particles for immunomagnetic separation and SERS application, *J. Nanopart. Res.*, 13:3167-3176, 2011.

New horizons for NTA: scattering labelling of "soft particles"

Evgeniy Evtushenko[1*]

[1]Faculty of Chemistry, Lomonosov Moscow State University, Moscow, Russia
*corresponding author, E-mail: e.evtoochenko@gmail.com

Abstract

The ability of Nanoparticle Tracking Analysis (NTA) to discriminate between weakly and strongly scattering particles has been tested. Only partial discrimination is possible with standard implementation of NTA. Algorithm based on particle spot shape analysis to limit the upper and lower edges of detection volume has been proposed. These improvements open the possibility for the new type of specific labelling in NTA, scattering labelling of "soft particles", i.e. weakly scattering biological particles, including exosomes, viruses and protein aggregates.

1. Introduction

Exosomes and microvesicles research is the emerging field of molecular biology and medicine. In general, these extracellular vesicles are involved in long-range intercellular communications. Thus they attracted a great attention as possible messengers in different pathological conditions and also as a new class of diagnostic markers [1]. Among many particle sizing techniques Nanoparticle Tracking Analysis (NTA) is one of the most convenient tools for vesicles characterization due to ability to measure both concentration and particle size distribution on particle-by-particle basis [2]. Besides purified exosomes samples, NTA allows to count and size vesicles or any other particles of interest in complex mixtures (e.g. culture medium and body fluids) by selective fluorescent labelling [3]. Although providing a great possibility, this approach has some drawbacks: the requirement of multiple fluorescent molecules per particle for robust detection and fluorophore photobleaching issues.

In this paper we suggest the new type of selective NTA measurements by labelling the particles of interest by strongly scattering gold nanoparticles. The discrimination of labeled and label-free particles could be made by scattering intensity.

2. Experimental section

All NTA experiments were made with Nanosight LM10 HS instrument (Nanosight Ltd, UK) equipped with 405 nm, 65 mW laser and EMCCD Andor Luca camera. Samples were diluted with appropriate buffer or MilliQ water to reach the optimal concentration for NTA according to ASTM E2834–12 [4]. Recorded videos of particles' Brownian motion were processed with standard NTA 2.3 software, build 0033 (Nanosight Ltd, UK).

Gold nanoparticles with nominal diameter of 20 nm from Sigma Aldrich (Art. 753610-25ML, OD 1, stabilized suspension in 0.1 mM PBS) and Thermo Scientific 3000 Series polystyrene particles with nominal diameter of 400±9 nm were used without any further purification.

Platelet-free plasma of healthy men was freshly prepared prior to measurements as described elsewhere. Briefly, 3 ml of blood were collected in BD EDTA Vacutainer. Two aliquots 1.5 ml were centrifuged for 5 minutes at 1000 g to separate most of blood cells. Supernatant was additionally centrifuged for 20 minutes at 15000 g to sediment platelets and cell debris.

3. Discussion

Mean scattering intensity of each tracked particle is an additional measured parameter during any NTA experiment. Instrument and software producer (Nanosight Ltd, UK) claims, that this data could be used for discrimination of particles made of different materials if they strongly differ by their optical properties (refractive index and extinction coefficient). Theoretically according to Rayleigh scattering intensity equation, if the sample contains spherical particles of different size made of same material, the scattering intensity I plotted vs particle size d should show the power-law behavior. If there are two different materials, theoretically such a graph should show two distinct power-law branches.

With real samples of spherical particles $I(d)$ graph looks like prolate cluster of points rather than well-defined power-law curve due to imperfectness of optical setup and inaccuracies of intensity calculation algorithms. That's the reason why this valuable for the first glance information about the particles is rarely used in scientific papers.

To test the ability of standard NTA software to distinguish between weakly and strongly scattering particles two samples have been measured in the same conditions: 20 nm gold nanoparticles (diluted by clean PBS 500 times) as one of the strongest known scatterer and weakly scattering sub-μm particles of blood plasma (diluted by clean PBS 50000 times). Video recording parameters were: "Camera shutter" = 1000, "Camera gain" = 500, video duration 120 s; processing parameters were "Detection threshold" = 10 (multi), "Min track length": Auto, "Min expected size": Auto. Superposition of $I(d)$ graphs for both samples (Fig.1)

shows, that although clusters for different samples are distinguishable from each other, the difference is not strong enough for reliable determination of particles' type, especially for small sizes and low scattering intensities.

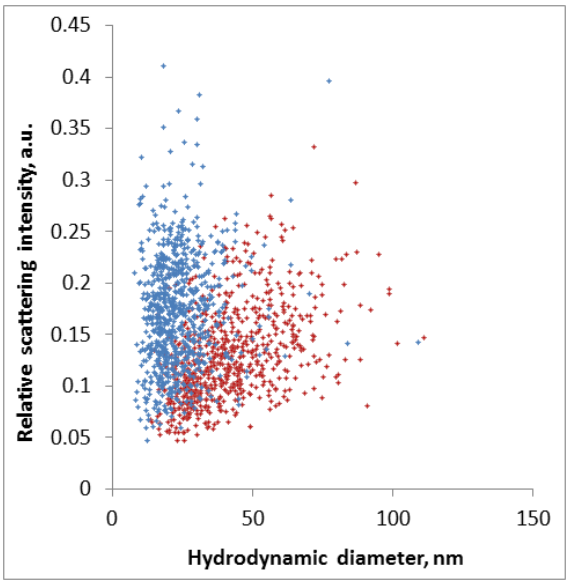

Figure 1: Scattering intensity versus diameter for 20 nm gold nanoparticles (blue dots) and sub-μm blood plasma particles (red dots) measured by standard NTA 2.3 software.

We propose that such a small difference of measured scattering intensity between weakly scattering blood plasma particles and strongly scattering gold nanoparticles is a result of different scattering volumes for these two types of samples. The top and bottom edges of laser beam in Nanosight instrument optical setup are not sharp. With the constant camera sensitivity strongly scattering gold nanoparticles are detected even at the edges of the beam, where the incident beam intensity I_0 is much less, than in the beam intensity in the middle. These particles form the lower part of *I(d)* cluster. Weakly scattering blood plasma particles are visible in the middle of the beam only, where the I_0 is high. So we propose that the crucial step for correct NTA intensity measurements, required for scattering labelling is to fix the upper and lower edge of the detection volume and do not count particles located outside these limits.

This aim could be reached by analysis of the particles' spot shape. It depends on the vertical position of the particle regarding to focal plane of the objective. To get the quantitative information about spot shape vs particle vertical position very diluted sample (20000 times) of 400 nm latex particles was measured. Large size of the particle is required for very slow Brownian motion, around 100 nm per frame. Sphericity is needed to have no intensity fluctuations due to rotation of the particle. The sample was slowly pumped through the beam until only one particle was presented in the scattering volume. Focal plane position has been moved up and down by tweaking wheel of the microscope. Typical images of the same particle with different focal plane positions (Fig. 2) shows that for microscope setup used in Nanosight LM10 instrument spot for particle located above the focal plane is a single wide blob (Fig. 2A), the perfectly focused particle shows Airy disk pattern (Fig. 2B), while the particle under the focal plane shows multiple diffraction rings (Fig. 2C).

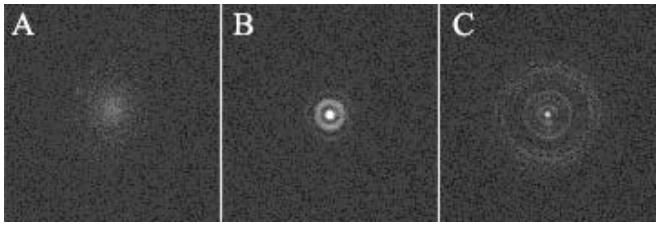

Figure 2: Spot shape for different positions of the particle regarding to focal plane of the objective with Nanosight LM10 microscope setup. A – particle is above the focal plane; B – particle is near the focal plane; C – particle is under the focal plane.

The determination of vertical position of the particle could be done by full spot profile fitting, but to show the principal possibility we used the simple approach of measuring the full width at the half-height (FWHH) of the central maximum of the spot. Measured FWHH shows the monotonous dependence vs vertical position of the particle regarding to focal plane of the objective (Fig. 3). This calibration curve could be used to select the particles in the middle of the laser beam only.

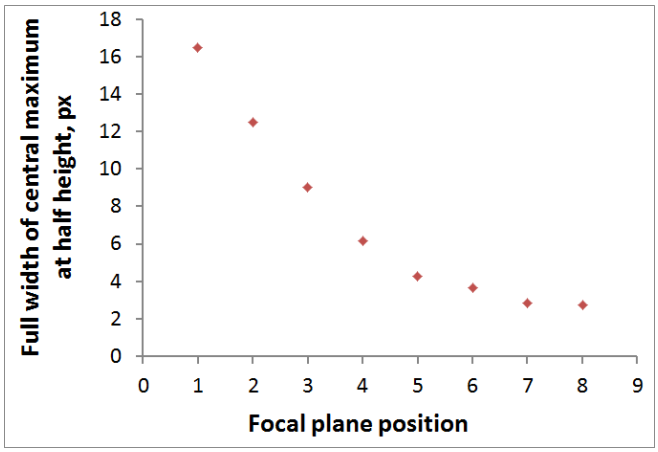

Figure 3: Measured dependence of full width at the half-height (FWHH) of the central maximum of the spot from focal plane position in a.u.

This approach will be tested on real videos of gold and blood plasma particles.

4. Conclusions

New type of particles labelling, scattering labelling is proposed for selective measurements of particles of interest with NTA. Impossibility of strong and weak scatterers discrimination with standard NTA 2.3 software have been shown. The approach for scattering volume correction using analysis of the particles' spot shape has been proposed.

Acknowledgements

The present work is supported by Russian Foundation for Basic Research (RFBR), project # 13-08-01062A.

References

[1] B. Gyorgy, T.G. Szabo, M. Pasztoi, Z. Pal, P. Misjak, B. Aradi, V. Laszlo, E. Pallinger, E. Pap, A. Kittel, G. Nagy, A. Falus, E.I. Buzas, Membrane vesicles, current state-of-the-art: emerging role of extracellular vesicles, *Cell. Mol. Life Sci* 68: 2667−2688, 2011.

[2] C.Y. Soo, Y. Song, Y. Zheng, E.C. Campbell, A.C. Riches, F. Gunn-Moore, S.J. Powis, Nanoparticle tracking analysis monitors microvesicle and exosome secretion from immune cells, *Immunology* 136: 192−197, 2012.

[3] R.A. Dragovic, C. Gardiner, A.S. Brooks, D.S. Tannetta, D.J.P. Ferguson, P. Hole, B. Carr, C.W.G. Redman, A.L. Harris, P.J. Dobson, P. Harrison, I.L. Sargent, Sizing and phenotyping of cellular vesicles using Nanoparticle Tracking Analysis, *Nanomedicine* 7: 780−788, 2011.

[4] ASTM Standard E2834, 2012, "Standard Guide for Measurement of Particle Size Distribution of Nanomaterials in suspension by Nanoparticle Tracking Analysis (NTA)," ASTM International, West Conshohocken, PA, DOI: 10.1520/E2834-12.

Superconducting and Quantum Metamaterials

Wide-Band Tuneability, Nonlinear Transmission, and Dynamic Multistability in SQUID Metamaterials

G. P. Tsironis, N. Lazarides, I. Margaris

Crete Center for Quantum Complexity and Nanotechnology, Department of Physics,
University of Crete, P.O. Box 2208, 71003 Heraklion, Greece
&
Institute of Electronic Structure and Laser,
Foundation for Research and Technology-Hellas, P.O. Box 1527, 71110 Heraklion, Greece
*corresponding author, E-mail: nl@physics.uoc.gr

Abstract

Superconducting metamaterials comprising rf SQUIDs (Superconducting QUantum Interference Devices) have been recently realized and investigated with respect to their tuneability, permeability and dynamic multistability properties. These properties are a consequence of intrinsic nonlinearities due to the sensitivity of the superconducting state to external stimuli. SQUIDs, made of a superconducting ring interrupted by a Josephson junction, possess yet another source of nonlinearity, which makes them widely tuneable with an applied dc dlux. A model SQUID metamaterial, based on electric equivalent circuits, is used in the weak coupling approximation to demonstrate the dc flux tuneability, dynamic multistability, and nonlinear transmission in SQUID metamaterials comprising non-hysteretic SQUIDs. The model equations reproduce the experimentally observed tuneability patterns, and predict tuneability with the power of an applied ac magnetic magnetic field. Moreover, the results indicate the opening of nonlinear frequency bands for energy transmission through SQUID metamaterials, for sufficiently strong ac fields.

1. Introduction

Superconducting metamaterials [1], a particular class of artificial media that rely on the extraordinary properties of superconductors at sufficiently low temperatures, have been recently attracted great attention (see e.g., reference [2]). Conventional metamaterials, that comprise highly conducting metallic elements [3, 4, 5], typically exhibit high losses in the frequency range where their unusual and sought properties are manifested. The key element for the construction of conventional (metallic) metamaterials has customarily been the split-ring resonator (SRR), typically a highly conducting metallic ring with a slit, that can be regarded as an inductive-capacitive ($L\,C$) resonant oscillator. Nonlinearity, provided by combination of SRRs with electronic components (e.g., diodes [6]), adds a new degree of freedom for the design of tuneable metamaterials. Superconductors, on the other hand, are intrinsically nonlinear materials, due to the extreme sensitivity of the superconducting state in external stimuli [7, 8], which moreover exhibit significantly reduced Ohmic losses. They thus provide unique opportunities to the researchers in the field for the fabrication of superconducting metamaterials with highly controllable effective electromagnetic properties including wideband tuneability [9, 10, 11, 12, 13, 14, 15, 16, 17, 18, 19, 20].

The direct superconducting analogue of a nonlinear SRR is the rf SQUID (rf Superconducting QUantum Interference Device), a long-known device in community of superconductivity. It consists of a superconducting ring interrupted by a Josephson junction (JJ) Josephson junction (JJ) [21], as shown schematically in figure 1(a). The SQUID is a strongly nonlinear resonator [22, 23], that is tuneable over a wide frequency range by applying either a flux bias [18, 24] or by varying the incoming rf power of an applied alternating field [24, 25]. This superconducting device has found up to date numerous applications [26, 27, 28, 29], and it is known to be the worlds most sensitive detector of magnetic signals. The replacement of metallic SRRs with rf SQUIDs, which have no direct electrical conduct but instead they are coupled magnetically through their mutual inductances, has been suggested theoretically a few years ago [30, 31]. Such SQUID metamaterials have been recently realized in the lab [18, 19, 32, 24, 25], that exhibit strong nonlinearities and wide-band tuneability with unusual magnetic properties due to macroscopic quantum effects. Nonlinearity and discreteness in SQUID metamaterials, along with low Ohmic losses (at least at microwave frequencies) may also lead in the generation of discrete breathers [33, 34, 35], i.e., time-periodic and spatially localized modes that change locally the magnetic response. Recent advances that led to nano-SQUIDs makes possible the fabrication of SQUID metamaterials at the nanoscale [36] (and references therein).

Superconducting metamaterials, resulting either from bare replacement of the metallic parts employed in conventional metamaterials by superconducting ones [37, 12, 11, 38, 39, 40, 41, 42], or by constructing hybrid structures comprising superconducting components [43, 44, 45, 46, 47, 48, 14, 49], or even by incoprorating the Josephson effect as in arrays of SQUIDs [50, 18, 19, 32, 24], have been already proposed and/or demonstrated experimentally. Their operation frequency spans a huge range, from zero

[51, 52, 53, 54] to microwaves [55, 18, 56, 19, 32] and to Terahertz [11, 12, 37, 57, 38, 39, 40, 15, 58, 59, 41, 42] and visible [45] frequencies. Moreover, researchers rely on particular superconducting devices to access the trully quantum metamaterial regime [30, 60, 61, 62, 63].

In the present work, numerical calculations that rely on a model SQUID metamaterial in the weak coupling approximation are shown to reproduce fairly well the experimentally observed tuneability patterns with an applied constant (dc) flux bias. Specifically, it is demonstrated that the frequency band of linear flux waves of a SQUID metamaterial can be tuned periodically with the dc flux, with a period of one flux quantum. These results in a sense validate the discrete model. Quantitative differences in the tuneability patterns are attributed to the system size, dimensionality, nonlinearity strength (equivalently the amplitude of an applied rf alternating magnetic field), and coupling strength between neighboring SQUIDs. The transmission properties of SQUID metamaterials are investigated in the weakly nonlinear regime for a one-dimensional (1D) SQUID metamaterial with respect to the loss coefficient of the SQUIDs, for coupling strength which is in accordance with the weak coupling approximation (and in the range of values achieved in the experiments). For low losses and substantial nonlinearity, the transmission of flux waves through the metamaterial is also possible for frequencies outside the linear band, though the opening of one or more "channels" (i.e., nonlinear bands), whose effectiveness in transmitting energy depends on the nonlinearity strength.

2. SQUID Metamaterial Equations

Consider a two-dimensional (2D) rectangular lattice of identical SQUIDs in an ac and/or dc magnetic field, $\mathbf{H}(t)$, which is spatially uniform, as in figure 1(c). In the following we adopt the description (and notation) in references [35, 64], thus summarizing the essential building blocks of the model in a self-contained manner, yet omitting unnecessary details. The dynamic equations for the fluxes, $\phi_{n,m}$, in the (n,m) SQUID ring are given by [33, 34, 64]

$$\begin{aligned} \ddot{\phi}_{n,m} + \gamma\dot{\phi}_{n,m} + \phi_{n,m} + \beta\,\sin(2\pi\phi_{n,m}) \\ -\lambda_x(\phi_{n-1,m} + \phi_{n+1,m}) - \lambda_y(\phi_{n,m-1} + \phi_{n,m+1}) \\ = [1 - 2(\lambda_x + \lambda_y)]\phi_{ext}, \end{aligned} \quad (1)$$

where the overdots denote differentiation with respect to the normalized time τ, λ_x and λ_y are the coupling coefficients in the x and y direction, respectively, $\beta = LI_c/\Phi_0 = \beta_L/2\pi$ is the rescaled SQUID parameter, and γ is a dimensionless coefficient representing all of the dissipation in each SQUID. The frequency and time in equation (1) are normalized to the corresponding LC SQUID frequency $\omega_0 = 1/\sqrt{LC}$ and its inverse ω_0^{-1}, respectively, while all fluxes are normalized to the flux quantum, Φ_0. The external flux ϕ_{ext} is of the form

$$\phi_{ext} = \phi_{dc} + \phi_{ac}\cos(\Omega\tau), \quad (2)$$

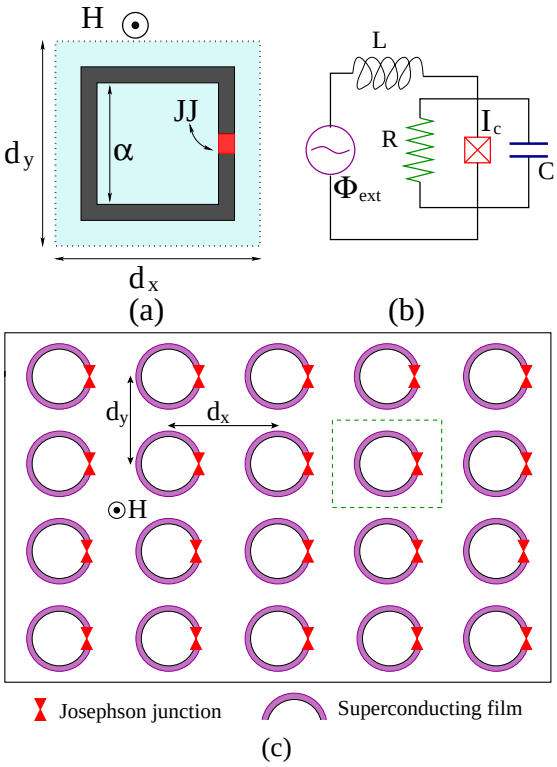

Figure 1: (color online) (a) Schematic drawing of an rf SQUID in a perpendicular time-dependent magnetic field $\mathbf{H}(t)$. (b) Equivalent electrical circuit (RCSJ model) for a single rf SQUID driven by a flux source Φ_{ext}. (c) Schematic drawing of a two-dimensional rf SQUID metamaterial, where the unit cell is indicated by the green-dashed line.

where Ω is the driving frequency, ϕ_{dc} is the flux bias, and ϕ_{ac} is the amplitude of the ac field. The current, $i_{n,m}$, flowing in the (n,m) SQUID, normalized to the critical current of the junction, I_c, is given by

$$\begin{aligned} i_{n,m} = \frac{1}{\beta}\{\phi_{n,m} - \phi_{eff} - \lambda_x(\phi_{n-1,m} + \phi_{n+1,m}) \\ -\lambda_y(\phi_{n,m-1} + \phi_{n,m+1})\}. \end{aligned} \quad (3)$$

For later use, the total maximum current per SQUID of the SQUID metamaterial is defined as

$$i_{max} = max\left\{\frac{1}{N_x N_y}\sum_{n,m=1}^{N_x,N_y} i_{n,m}\right\}_T, \quad (4)$$

i.e., the maximum value of the total current (given by the expression in the curly brackets) in one driving period $T = 2\pi/\Omega$. The SQUID metamaterial supports linear flux waves which frequency dispersion is

$$\Omega \equiv \Omega_\kappa = \sqrt{1 + \beta_L - 2(\lambda_x\,\cos\kappa_x + \lambda_y\,\cos\kappa_y)}, \quad (5)$$

where $\kappa = (\kappa_x, \kappa_y)$ is the normalized wavevector.

The dynamic behavior of rf SQUIDs has has been investigated extensively for more than two decades, both in

the hysteretic ($\beta_L > 1$) and the non-hysteretic ($\beta_L < 1$) regimes. Just as conventional metamaterials acquire their properties from their individual elements, SQUID metamaterials acquire their resonance properties from individual SQUIDs. For very low amplitude of the ac driving field (linear regime), an rf SQUID exhibits a resonant magnetic response at a particular frequency

$$\omega_{SQ} = \omega_0 \sqrt{1+\beta_L}, \tag{6}$$

which is always larger than its corresponding LC frequency, ω_0. Tuneability of an rf SQUID can be achieved either with the amplitude of the ac field, ϕ_{ac}, or with the flux bias, ϕ_{dc}, which generate the flux threading its loop [35]. The resonance shift due to a dc flux bias has been actually observed in low$-T_c$, single rf SQUIDs in the linear regime [18], as well as in 1D SQUID metamaterials [19, 32, 56]. Assuming isotropic coupling, i.e., $\lambda_x = \lambda_y = \lambda$, the maximum and minimum values of the linear frequency band are then obtained by substituting $\kappa = (\kappa_x, \kappa_y) = (0,0)$ and (π,π), respectively, into equation (5). Thus we get

$$\omega_{max} = \sqrt{1+\beta_L+4|\lambda|}, \quad \omega_{min} = \sqrt{1+\beta_L-4|\lambda|}, \tag{7}$$

that give an approximate bandwidth $\Delta\Omega \simeq 4|\lambda|/\Omega_{SQ}$, where

$$\Omega_{SQ} = \frac{\omega_{SQ}}{\omega_0} = \sqrt{1+\beta_L}. \tag{8}$$

The dynamic equations (1) are integrated with a fourth-order Runge-Kutta algorithm with fixed time-stepping, and the total energy of the SQUID metamaterial, in units of the Josephson energy E_J, is calculated from the expression

$$\begin{aligned} E_{tot} = \sum_{n,m} \Big\{ & \frac{\pi}{\beta}\left[\dot{\phi}_{n,m}^2 + (\phi_{n,m}-\phi_{ext})^2\right] \\ & +[1-\cos(2\pi\phi_{n,m})] \\ & -\frac{\pi}{\beta}\left[\lambda_x(\phi_{n,m}-\phi_{ext})(\phi_{n-1,m}-\phi_{ext})\right. \\ & +\lambda_x(\phi_{n+1,m}-\phi_{ext})(\phi_{n,m}-\phi_{ext}) \\ & +\lambda_y(\phi_{n,m-1}-\phi_{ext})(\phi_{n,m}-\phi_{ext}) \\ & \left.+\lambda_y(\phi_{n,m}-\phi_{ext})(\phi_{n,m+1}-\phi_{ext})\right]\Big\}. \end{aligned} \tag{9}$$

The averaged energy in one driving period $T = 2\pi/\omega$ of evolution then reads

$$< E_{tot} >_T = \frac{1}{T}\int_0^T d\tau E_{tot}(\tau), \tag{10}$$

where $\omega = \omega_0\Omega$ is the frequency of the applied ac flux.

3. dc flux tuneability

At frequencies within a narrow band, the metamaterial absorbs a large amount of energy. For dc flux bias equal to integer multiples of Φ_0 (including zero), that band coincides with the linear flux-wave band given in equation (5). However, for any other value of the dc flux, that band shifts downwards, down to a minimum attained for dc flux bias equal to odd semi-integer multiples of Φ_0. This procedure results in a very clear pattern of periodic shifting of the linear band with the dc flux bias, which has been observed in experiments [19, 32, 24]. Here the basic features of the dc flux tuneability patterns are reproduced by integrating equations (1) and using the calculated fluxes $\phi_{n,m}$ and voltages $\dot{\phi}_{n,m}$ to obtain the averaged energy per period of the ac field $< E_{tot} >_T =< E_{tot} >_T (\Omega = 2\pi/T, \phi_{dc})$ from equations (9) and (10) as a function of the frequency of the ac field Ω and the dc flux ϕ_{dc}. The quantity $< E_{tot} >_T (\Omega =, \phi_{dc})$ is then presented in density plots on the $\Omega - \phi_{dc}$ plane in figure 2, fo several combinations of ac flux amplitudes ϕ_{ac} and coupling coefficients λ. In these plots, the regions of resonant absorption correspond to maxima in the averaged energy, which appear as minima in the corresponding plots obtained from experiments, where the measured quantity is the frequency-dependent complex transmission amplitude $|S_{21}(\Omega)|$. In figure 2, while the dc flux is measured in units of Φ_0, the frequencies has been transformed in natural units (GHz); the single-SQUID resonance frequency is chosen to be $f_{SQ} = 15\ GHz$. The frequency f_{SQ} can be either calculated from the SQUID parameters or measured experimentally. The chosen value for f_{SQ} is slightly higher than the one measured in reference [25] for similar SQUID parameters; no attempt for an accurate fitting of the experimental data was made in this work. In figure 2, the ac amplitude ϕ_{ac} increases from left to right, while the coupling λ increases from top to bottom. Apparently, the resonant energy absorption, indicated by the dark regions, become stronger as one moves from left to right (increasing ϕ_{ac}), since the nonlinear effects become more and more important. When going from top to bottom panels, a smearing of the resonance is observed with increasing $|\lambda|$, along with the appearence of secondary resonances. The latter manifest themselves as thin dark curves that are located close to the main shifting pattern, and they are better seen around half-intefger values of the applied dc flux. The thickness of the low-transmission (dark) region in the close-to-linear regime, roughly corresponds to the width of the linear band, i.e., $\Delta\Omega \simeq 4|\lambda|/\Omega_{SQ}$.

These tuneability patterns can be understood within an approximate treatment valid for $\phi_{ac} \ll 1$. First assume that $\phi_{n,m} \simeq \phi$ for any n, m, i.e., that the SQUIDs are synchronized [64]; small deviations from complete synchronization arise due to the finite size of the metamaterial. We also assume that $\gamma \simeq 0$. Substitution into equations (1) and using equation (2), we get

$$\ddot{\phi} + (1-4\lambda)\phi + \beta\,\sin(2\pi\phi) = (1-4\lambda)[\phi_{dc} + \phi_{ac}\cos(\Omega\tau)]. \tag{11}$$

In the earlier equation we further make the approximation

$$\beta\sin(2\pi\phi) \simeq \beta_L\phi - \frac{2\pi^2}{3}\beta_L\phi^3, \tag{12}$$

and the ansatz

$$\phi = \phi_0 + \phi_1\cos(\Omega\tau), \tag{13}$$

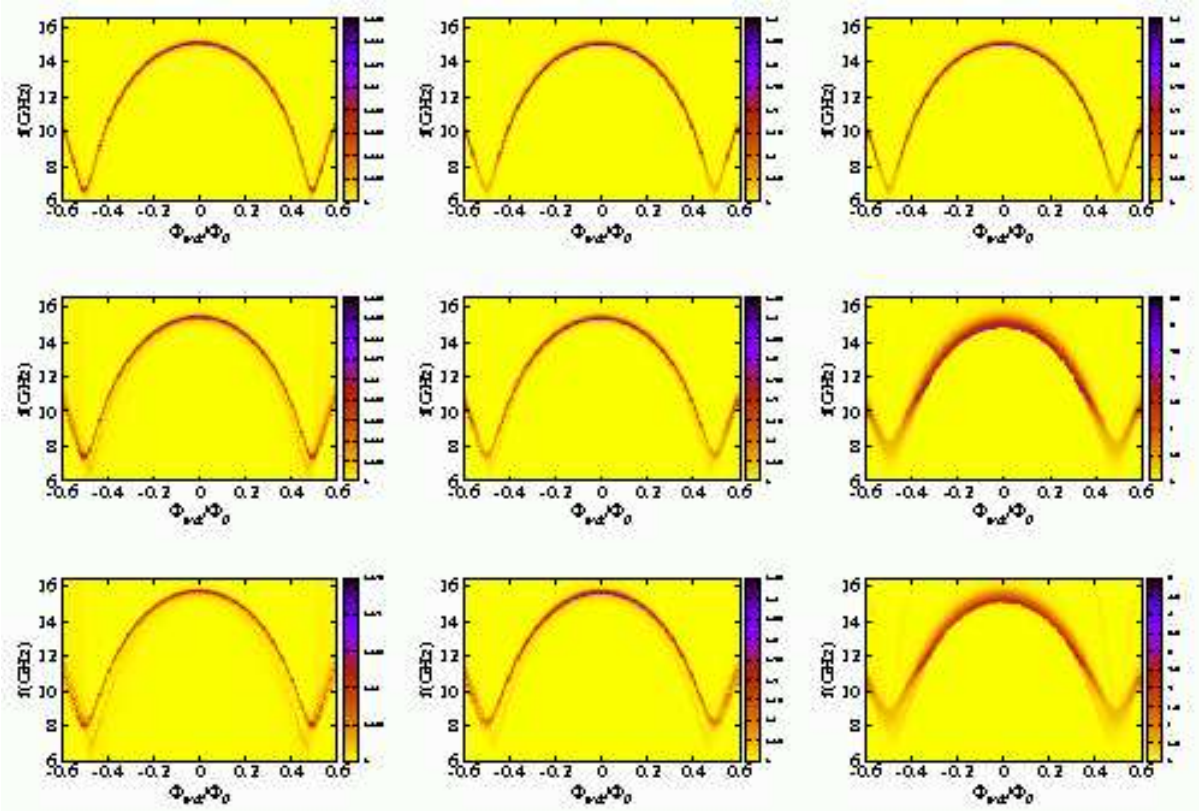

Figure 2: (color online) Density plot of the averaged total energy, $< E_{tot} >_T$ as a function of the dc flux bias $\phi_{dc} = \Phi_{dc}/\Phi_0$ and the ac frequency f, for $N_x = N_y = 11$, $\beta_L \simeq 0.7$, $\gamma = 0.009$, and several combinations of ac amplitude $\phi_{ac} = \Phi_{ac}/\Phi_0$ and coupling coefficients λ. The driving ac amplitude increases from left to right, while the coupling increases from top to bottom. First column: $\lambda_x = \lambda_y = -0.01$, and $\phi_{ac} = 1/5000$ (left); $1/1000$ (middle); $1/200$ (right). Second column: $\lambda_x = \lambda_y = -0.03$, and $\phi_{ac} = 1/5000$ (left); $1/1000$ (middle); $1/200$ (right). Third column: $\lambda_x = \lambda_y = -0.05$, and $\phi_{ac} = 1/5000$ (left); $1/1000$ (middle); $1/200$ (right). The single-SQUID resonance frequency f_{SQ} used in the calculations is $15\ GHz$.

Substituting equations (12) and (13) into equation (11), using the rotating wave approximation (RWA), and separating constant from time-dependent terms, we get

$$\frac{2\pi^2}{3}\beta_L\phi_0^3 - (1-4\lambda+\beta_L)\phi_0 - \frac{3}{2}\phi_0\phi_1^2 + (1-4\lambda)\phi_{dc} = 0, \quad (14)$$

$$\frac{\pi^2}{2}\beta_L\phi_1^3 - \left\{(1-4\lambda+\beta_L-\Omega^2) - 2\pi^2\beta_L\phi_0^2\right\}\phi_1 + (1-4\lambda)\phi_{ac} = 0. \quad (15)$$

Limiting ourselves in the case $\phi_1 < \phi_0 << 1$, we may simplify equations (14) and (15), by neglecting terms proportional to ϕ_1^3, ϕ_0^3, and $\phi_0\phi_1^1$. Note that we keep the term $\propto \phi_0^2\phi_1$, i.e., the lowest order coupling term between the two equations. Then, the resulting equations can be easily solved to give

$$\phi_0 = \frac{(1-4\lambda)\phi_{dc}}{(\Omega_{SQ}^2 - 4\lambda)}; \quad (16)$$

$$\phi_1 = \frac{(1-4\lambda)\phi_{ac}}{\left\{(\Omega_{SQ}^2 - 4\lambda - \Omega^2) - 2\pi^2\beta_L\phi_0^2\right\}}. \quad (17)$$

Obviously, the ac flux amplitude in the SQUIDs, ϕ_1, attains its maximum value when the expression in the curly brackets in the denominator of equation (17) is zero. Solving for Ω, we get

$$\Omega = \sqrt{(\Omega_{SQ}^2 - 4\lambda) - (2\pi^2\beta_L)\frac{(1-4\lambda)^2\phi_{dc}^2}{(\Omega_{SQ}^2-4\lambda)^2}}, \quad (18)$$

or, in natural units

$$f = \frac{f_{SQ}}{\Omega_{SQ}}\sqrt{(\Omega_{SQ}^2 - 4\lambda) - (2\pi^2\beta_L)\frac{(1-4\lambda)^2\phi_{dc}^2}{(\Omega_{SQ}^2-4\lambda)^2}}, \quad (19)$$

which corresponds to the "resonance frequency" of the SQUID metamaterial itself, with f_{SQ} is the single-SQUID resonance frequency. From the data of the tuneability patterns presented in the left column of figure 2 (weak driving amplitude), that correspond to increasing coulping from top to bottom, we have extracted the frequency of maximum response by simply identifying the frequency where the total energy is maximum. A typical curve of this kind is shown in figure 3, along with the corresponding one calculated from equation (18). This is the case of low-amplitude ac driving,

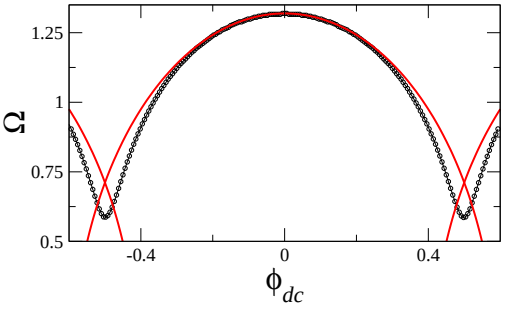

Figure 3: (color online) Normalized frequency at maximum response of the SQUID metamaterial, Ω, as a function of the dc applied (normalized) flux, ϕ_{dc}, in the presence of a low-amplitude alternating signal. The black circles are obtained from the numerical simulations through model equations (1) (see text), while the red solid lines are plotted from the approximate equation (18). Parameters: $\lambda_x = \lambda_y = -0.01$, $N_x = N_y = 11$, $\phi_{ac} = 1/5000$, $\gamma = 0.009$, and $\beta_L \simeq 0.7$.

that is the closest to the assumptions made for the derivation of expression (18). It is remarkable that this simple expression, which contains only two parameters, λ and β_L, fairly agrees with the simulations in a rather wide region of dc fluxes, i.e., from $\phi_{dc} \sim -0.3$ to $\sim +0.3$. Within this interval, the normalized frequency in figure 3 changes from $\Omega = 1.12$ to 1.32, that makes a tuneability range of 15%. This is approximatelly the "useful" tuneability range [19, 32], since at these frequencies the energy absorption remains at high levels (i.e., the resonance is strong). For larger ϕ_{dc}, the importance of the term $\propto \phi_0^3$ increases and it cannot be neglected for the solutions of equations (14) and (15). The approximate expression (18) also captures another experimentally observed feature, namely the increase of the metamaterial resonance frequency at zero dc flux, $f(\phi_{dc} = 0)$. By setting $\phi_{dc} = 0$ in equation (18) we get that $f = \frac{f_{SQ}}{\Omega_{SQ}}\sqrt{(\Omega_{SQ}^2 - 4\lambda)}$, which, for $f_{SQ} = 15\ GHz$, $\Omega_{SQ} = 1.304$ ($\beta_L = 0.7$), $\lambda = -0.01,\ -0.03,\ -0.05$ gives respectively, $f = 15.2,\ 15.5, 15.9\ GHz$ in agreement with the numerical results. The $\lambda-$dependence of the SQUID metamaterial resonance frequency is weaker in the corresponding one-dimensional case. This effect does not however result directly from the nonlinearity; the ac field is very week to induce significant nonlinear effects. Instead, it comes from the assumed uniformity of the SQUID metamaterial state, i.e., the assumption $\phi_{n,m} = \phi$ for any n, m. From that, and neglecting the dissipation and driving terms, we get the single eigenfrequency of the metamaterial in that state as $\Omega = \sqrt{\Omega_{SQ} - 4\lambda}$, so that deviations of the resonance frequency from that of a single SQUID are approximatelly proportional to λ ($|\lambda| \ll 1$).

4. Energy Transmission through SQUID Metamaterial Lines.-

SQUID metamaterials support flux waves that are capable of transmitting energy, in much the same way as in nonlinear magnetoinductive transmission lines made of conventional (metallic) metamaterials [65], which may function as a frequency-selective communication channel for devices. For simplicity and clarity we use a one-dimensional SQUID metamaterial comprising $N = 54$ identical elements with $\beta_L = 0.7$ ($\beta = 0.1114$) weakly coupled to their nearest neighbors. In order to investigate the transfer of energy through the array, the SQUID that is located at the left end (i.e., that for $n = 1$) is excited by an ac flux field at a particular frequency. The system of equations (1) and equation (9) in the present case read

$$\ddot{\phi}_n + \gamma\dot{\phi}_n + \phi_n + \beta\,\sin(2\pi\phi_n) - \lambda(\phi_{n-1} + \phi_{n+1}) = (1 - 2\lambda)\phi_{ext}\,\delta_{n,1}, \quad (20)$$

where the coupling coefficient is now denoted by λ and the Kroneckers' delta $\delta_{n,1}$ indicates that only the SQUID with $n = 1$ is driven by the ac field, and

$$E_{tot} = \sum_n \left\{ \frac{\pi}{\beta}\left[\dot{\phi}_n^2 + (\phi_n - \phi_{ext})^2\right] + 1 - \cos(2\pi\phi_n) - \frac{\pi}{\beta}\left[\lambda(\phi_n - \phi_{ext})(\phi_{n-1} - \phi_{ext}) + \lambda(\phi_{n+1} - \phi_{ext})(\phi_n - \phi_{ext})\right]\right\} \quad (21)$$

Equations (20) implemented with the boundary conditions $\phi_0 = \phi_{N+1}$ are integrated in time for $12000\,T$ time units, where $T = 2\pi/\Omega$ is the driving period, so that transient effects are eliminated and the system has reached a stationary state. The energy density in the metamaterial is then calculated from (21) as the average over the next $2000\,T$ time units. The decimal logarithm of the averaged energy density is mapped on the frequency Ω - site number n plane (figure 4), where high transmission regions are indicated with darker colors. In figure 4, the changes in the energy transmission with respect to the dissipation coefficient γ are shown for fixed coupling coefficient $\lambda = -0.01$ and ac field $\phi ac = 0.1$. Note that for that value of ϕac, significant nonlinearity is already present.

The energy transmission map for relatively strong dissipation ($\gamma = 0.009$) is shown in the upper panel of figure 4. Significant energy transmission occurs in a narrow band, of the order $\sim 2\lambda$ around the single SQUID resonance frequency $\Omega_{SQ} \simeq 1.3$ (for $\beta_L = 0.7$). This band almost coincides with the linear band for the one-dimensional SQUID metamaterial. Note that energy transmission also occurs at other frequencies; e.g., at $\Omega \sim 0.43$ that corresponds to a subharmonic resonance. Subharmonic resonances result from nonlinearity; in this case, nonlinear effects are already significant due to the relatively high ac field amplitude ($\phi_{ac} = 0.1$). However, with decreasing losses (middle panel), more energy is transmitted both at frequencies in the linear band and the subharmonic resonance band. In

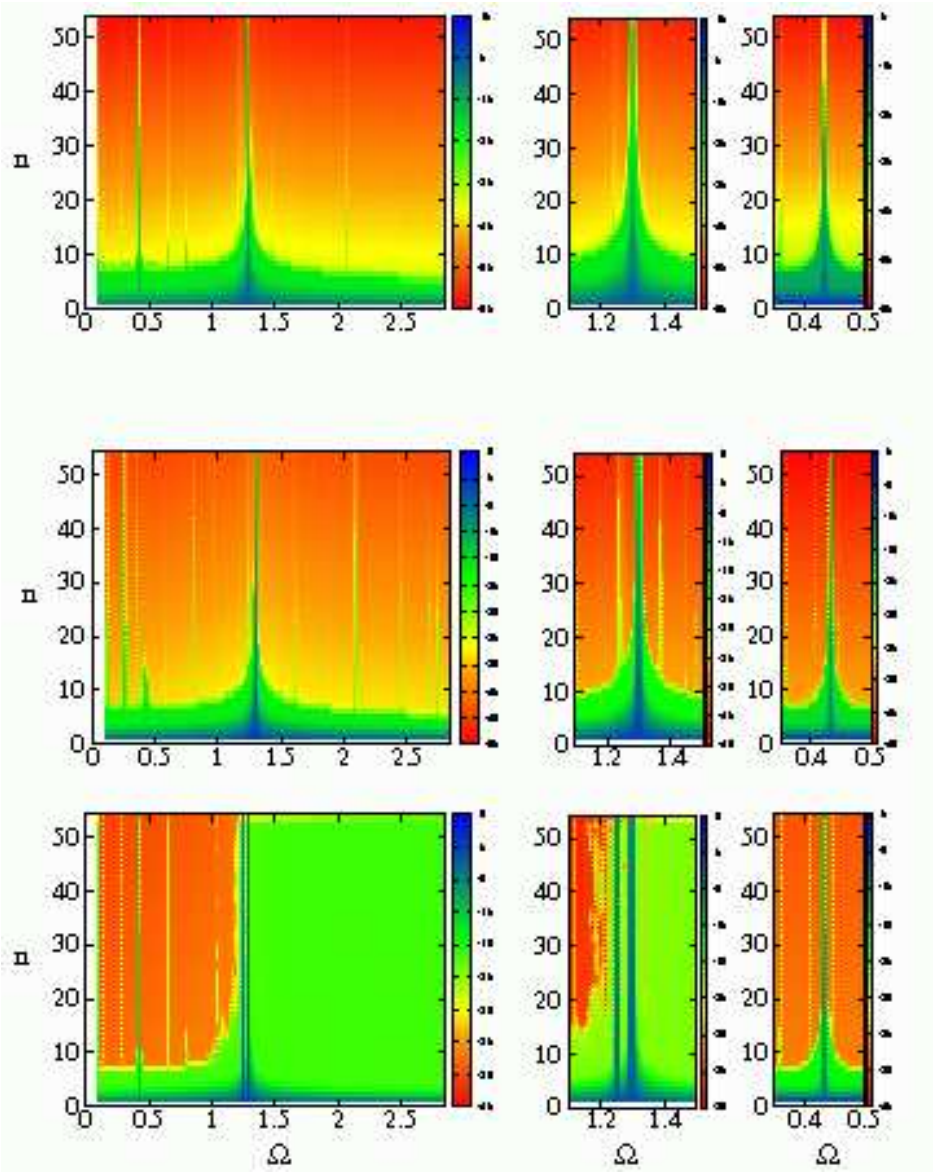

Figure 4: (color online) Energy transmission through a one-dimensional SQUID metamaterial line with $N = 54$ SQUIDs. The logarithm of the energy density averaged over $2000\,T$ time units, $\log_{10}[< E_n >_T]$, is plotted on the site number n - driving frequency Ω plane for $\beta_L = 0.7$ ($\beta = 0.1114$), $\lambda = -0.01$, and $\gamma = 0.009$ (upper); $\gamma = 0.004$ (middle); $\gamma = 0.001$ (lower). The middle and left columns are enlargements in frequency ranges around the fundamental and the subharmonic resonance, respectively, at $\Omega \simeq 1.302$ and 0.43.

the following we refer to the latter as the nonlinear band, since it results from purely nonlinear effects. With further decrease of losses (lower panel), the transmitted energy in these two bands becomes more significant. The comparison can be made more clearly by looking at the panels in the middle and right columns, which show enlarged regions of the corresponding panels shown in the left column. The enlargement around the linear band shown in the middle column shows clearly the increase of the transmitted energy with decreasing losses. Moreover, in the case of very low losses ($\gamma = 0.001$) the linear band splits into two bands, where significant energy transmission occurs. The energy transmission in the nonlinear band increases with decreasing losses, accordingly (left column, losses decrease from top to bottom).

Thus, for sufficiently strong ac field, energy can be transmitted not only for frequencies in the linear band, but also in otherwise forbidden frequency regions. The metamaterial thus becomes transparent in energy transmission at frequency intervals around nonlinear resonances (subharmonic, in the present case) of single rf SQUIDs. That type of self-induced transparency due to nonlinearity is a robust effect as can be seen in figure 4, where the loss coefficient has been varied by almost an order of magnitude. In the density plots above, the right boundary was actually a reflecting one, that allows the formation of stationary states in

the array. However, the same calculations performed with a totally absorbing boundary give practically identical results.

For very low amplitude of the applied ac field ϕ_{ac} and $\phi_{dc} = 0$, equations (20) can be linearized to give

$$\ddot{\phi}_n + \gamma\dot{\phi}_n + \Omega_{SQ}^2\phi_n - \lambda(\phi_{n-1} + \phi_{n+1}) = \bar{\phi}_{ac}\cos(\Omega\tau)\,\delta_{n,1}, \qquad (22)$$

where $\bar{\phi}_{ac} = (1 - 2\lambda)\phi_{ac}$. If we further neglect the loss term, equations (22) can be solved exactly in closed form for any driving frequency Ω and for any finite N, the total number of SQUIDs in the one-dimensional array. By substitution of the trial solution $\phi_n = q_n\cos(\Omega\tau)$ into equations (22) and after some rearrangement we get

$$sq_{n-1} + q_n + sq_{n+1} = \kappa_0\,\delta_{n,1}, \qquad (23)$$

where

$$s = -\frac{\lambda}{\Omega_{SQ}^2 - \Omega^2}, \qquad \kappa_0 = \frac{\bar{\phi}_{ac}}{\Omega_{SQ}^2 - \Omega^2}, \qquad (24)$$

or, in matrix form

$$\mathbf{q} = \kappa_0\,\hat{\mathbf{S}}^{-1}\mathbf{E}_1, \qquad (25)$$

where $\mathbf{q}$ and $\mathbf{E}_1$ are $N-$dimensional vectors with componets q_n and $\delta_{n,1}$, respectively, and $\hat{\mathbf{S}}^{-1}$ is the inverse of the $N \times N$ coupling matrix $\hat{\mathbf{S}}$. The latter is a real, symmetric, tridiagonal matrix that has its diagonal elements equal to unity, while all the other non-zero elements are equal to s. The elements of the matrix $\hat{\mathbf{S}}^{-1}$ can be obtained in closed analytical form [66] using known results for the inversion of more general tridiagonal matrices [67]. Then, the components of the $\mathbf{q}$ vector can be written as

$$q_n = \kappa_0\left(\hat{\mathbf{S}}^{-1}\right)_{n,1}, \qquad (26)$$

where $\left(\hat{\mathbf{S}}^{-1}\right)_{n,1}$ is the $(n,1)-$element of $\hat{\mathbf{S}}^{-1}$, whose explicit form is given in reference [66]. Then, the solution of the linear system (22) with $\gamma = 0$ is

$$\phi_n(\tau) = \kappa_0\mu\frac{\sin[(N-n+1)\theta']}{\sin[(N+1)\theta']}\cos(\Omega\tau), \qquad \theta' = \cos^{-1}\left(\frac{1}{2|s|}\right), \qquad (27)$$

for $s > +1/2$ and $s < -1/2$ (in the linear flux-wave band), and

$$\phi_n(\tau) = \kappa_\mu\frac{\sinh[(N-n+1)\theta]}{\sinh[(N+1)\theta]}\cos(\Omega\tau), \qquad \theta = \ln\frac{1+\sqrt{1-(2s)^2}}{2|s|}, \qquad (28)$$

for $-1/2 < s < +1/2$ (outside the linear flux-wave band), where

$$\mu = \frac{1}{|s|}\left(-\frac{|s|}{s}\right)^{n-1}. \qquad (29)$$

The above expressions actually provide the asymptotic solutions, i.e., after the transients due to dissipation, etc., have died out. Thus, these driven linear modes correspond to the stationary state of the linearized system; the dissipation however may alter somewhat their amplitude, without affecting very much their form. Note also that the q_ns are uniquely determined by the parameters of the system, and they vanish with vanishing ϕ_{ac}.

From the analytical solution at frequencies within the linear flux-wave band, equation (27) which corresponds to either $s > +1/2$ or $s < -1/2$, the resonance frequencies of the array can be obtained by setting $\sin[(N+1)\theta'] = 0$. Thus we get

$$s \equiv s_m = \frac{1}{2\cos\left[\frac{m\pi}{(N+1)}\right]}, \qquad (30)$$

where m is an integer ($m = 1, ..., N$). By solving the first of equations (24) with respect to Ω, and substituting the values of $s \equiv s_m$ from equation (30) we get

$$\Omega \equiv \Omega_m = \sqrt{\Omega_{SQ}^2 + 2\,\lambda\,\cos\left(\frac{m\pi}{N+1}\right)}, \qquad (31)$$

which is the discrete frequency dispersion for linear flux-waves in a one-dimensional SQUID metamaterial, with m being the mode number ($m = 1, ..., N$).

5. Dynamic Multistability and Power-Dependent Tuneability.-

The dc flux tuneability of SQUID metamaterials is a truly nonlinear effect, which appears also in the "linear regime", where the very low ac power levels allow for the treatment of a Josephson junction as a quasi-linear inductance. In figure 2 we have observed that with increasing ϕ_{ac} (increasing thus the significance of nonlinearity), the complexity of the tuneability patterns increases as well, while they exhibit high power absorption in a frequency range that exceeds the boundaries of the linear band. Thus, with increasing power, new dynamic effects are expected to appear; with resonance frequency shifts and multistability being the most prominent. The latter, in particular, is a purely dynamic phenomenon that is not related to the multistability known from hysteretic SQUIDs. For a particular choise of parameters, dynamic multistability manifests itself as a small number of simultaneously stable states. As it has been shown in recent experiments [18], each of these states corresponds to a different value of the SQUID magnetic flux susceptibility at the driving frequency, that may be either possitive or negative. This implies that, depending on the state of individual SQUIDs, the metamaterial can either be magnetically almost transparent or not.

While in figure 2 the amplitude of the ac field was kept to low values (0.005 the highest), in the present section we use higher values. Due to the resonant nature of the SQUIDs, the current may attain values that are higher than the critival current of the Josephson junctions. In this case,

the standard RCSJ model gives unphysically high current values, because it does not take into account the change in the conductance of the junctions [23] (p. 48). In order to incorporate that change, we replace the dissipation coefficient γ in equations (1) with the following current dependent function

$$\gamma_{n,m} = \gamma_0 + c\left[1 + \tanh\left(\frac{i_{n,m} - 1}{d}\right)\right], \qquad (32)$$

where $c = 0.12$, $d = 0.02$, and $\gamma_0 = 0.009$, the value of γ used for obtaining the results of figure 2. That function allows for an abrupt but continuous change of the dissipation coefficient from low values $\gamma_{n,m} \simeq \gamma_0$ (low current, less than I_c) to high values $\gamma_{n,m} \simeq 28\gamma_0$ (high current, greater than I_c). We have calculated several curves of the total current maximum i_{max} as a function of the driving frequency Ω, which are shown in figure 5. In this figure, the amplitude of the applied ac field increases from the bottom to the upper panel [from (f) to (a)]. In all subfigures, the frequency is varied between $\Omega \simeq 0.8 - 6.28$ in both increasing from the lowest frequency or decreasing from the highest frequency (only part of this range is shown). In this way we may identify two different branches of the $i_{max} - \Omega$ at a particular frequency range for relatively high ac powers. For low power of the ac field [figures 5(f)-5d] no hysteresis and thus multistability is observed. However, hysteretic effects appears in figure 5(c) for $\phi_{ac} = 0.03$ for a very narrow frequency interval. With further increasing ϕ_{ac} we see that the hysteretic lobe, and thus the frequency region of multistability, significantly increases [figures 5(b)-5(a)]. Besides the multistability effects, in figure 5 we also observe strong resonance red-shift with increasing ac power level. For low power levels [figure 5(f)] the curve exhibits a strong resonant response at $\sim \Omega_{SQ}$, the single SQUID (linear) resonance frequency. With increasing ac power, however, the resonance frequency, determined by the maximum of each curve, moves to lower frequencies. Note that in figures 5(b) and 5(a), there are frequency regions where the SQUID metamaterial jumps intermittently from the low to the high current state (or vice versa). In comparison with the standard RCSJ model, that nonlinear resistive Josephson junction model severely limits total maximum currents which are greater than the critical one; it also exhibit much less hysteretic effects, that are visible at relatively high powers only.

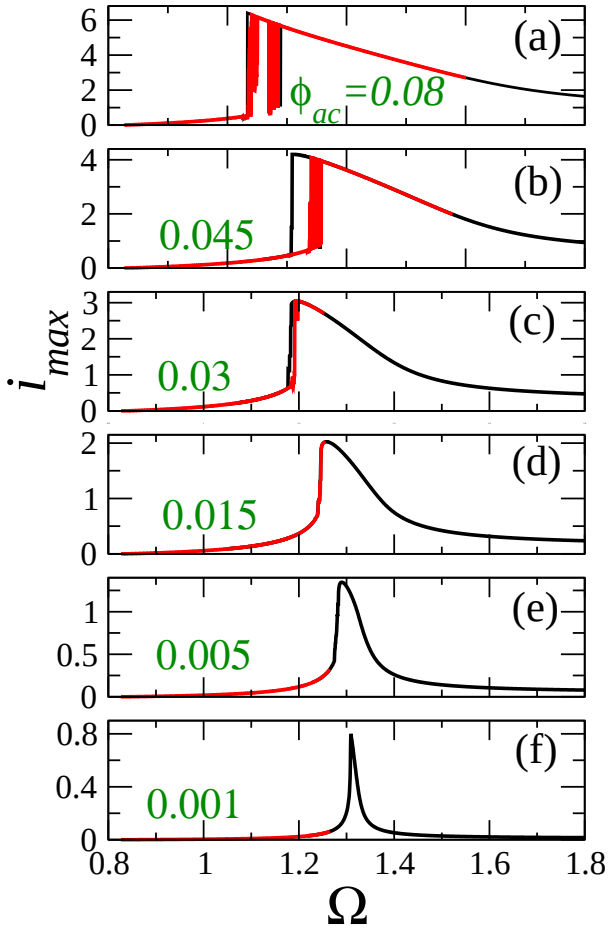

Figure 5: (color online) The maximum total current i_{max} in the SQUID metamaterial as a function of the normalized frequency Ω, for $N_x = N_y = 11$, $\lambda_x = \lambda_y = -0.01$, $\beta_L \simeq 0.7$, $\gamma_0 = 0.009$ (see text), $\phi dc = 0$, and (a) $\phi_{ac} = 0.08$; (b) $\phi_{ac} = 0.045$; (c) $\phi_{ac} = 0.03$; (d) $\phi_{ac} = 0.015$; (e) $\phi_{ac} = 0.005$; (f) $\phi_{ac} = 0.001$.

6. Conclusions.-

We have used a SQUID metamaterial model in the weak coupling approximation, in order to explore the tuneability, nonlinear transmission, and dynamic multistability properties of SQUID metamaterials. The numerical results reproduce very well the experimentally observed dc flux tuneability patterns, whose form remains qualitatively unaffected from the details of the particular SQUID metamaterial. System parameters such as the size of the system, its dimensionality, the SQUID parameter, and the coupling between SQUIDs, mainly affect the tuenability range (i.e., the minimum and maximum value of resonance frequency of the metamaterial).

In the linear regime, a simple approximate expression which gives the dependence of the resonance frequency on the dc flux bias and the coupling strength can be obtained. Although it has been obtained under several simplifying assumptions, it agrees fairly well with the numerically obtained tuneability patterns within a significant tuneability range. This expression also explains the increase of the zero dc flux resonance frequency with increasing coupling strength, which comes from the excitation of a mode where all the SQUIDs are synchronized.

Simulations of one-dimensional SQUID metamaterials which are driven at one end, reveal their energy transmission properties. For low amplitude of the ac applied field, energy transmission is limited at frequencies within the linear band. In that case, the linearized equations can be solved exactly, and the amount of transmitted energy in each SQUID could be calculated (with a correction for slight reduction of energy due to dissipation which has been

neglected in the analytical calculations). For stronger ac fields, the nonlinear effects become significant, and significant amounts of energy can be transmitted through nonlinear frequency bands which appear due to secondary SQUID resonances.

The resonance of the maximum total current as a function of the driving frequency shifts to lower frequencies with increasing ac field amplitude. For relatively strong ac fields, dynamic bistability appears. For a more realistic description of the Josephson junctions in the SQUID metamaterial, the nonlinear variation of their resistance with current in each SQUID has been taken into account.

Acknowledgement

This work was partially supported by the European Union's Seventh Framework Programme (FP7-REGPOT-2012-2013-1) under grant agreement n^o 316165, and by the Thales Project MACOMSYS, cofinanced by the European Union (European Social Fund ESF) and Greek national funds through the Operational Program "Education and Lifelong Learning" of the National Strategic Reference Framework (NSRF) Research Funding Program: THALES. Investing in knowledge society through the European Social Fund.

References

[1] S.M. Anlage, J. Opt. **13**, 024001 (2011)

[2] in *Special Issue: Focus on Superconducting Metamaterials*, vol. 26, ed. by A.V. Ustinov, S. Anlage, A. Sanchez (Supercond. Sci. Technol., 2013)

[3] D.R. Smith, J.B. Pendry, Wiltshire, Science **Vol. 305 no. 5685**, 788 (2004)

[4] V.M. Shalaev, Nature Photonics **1**, 41 (2007)

[5] C.M. Soukoulis, M. Wegener, Nature Photonics **5**, 523 (2011)

[6] I.V. Shadrivov, A.B. Kozyrev, D.W. van der Weide, Y.S. Kivshar, Appl. Phys. Lett. **93**, 161903 (2008)

[7] N.I. Zheludev, Science **328**, 582 (2010)

[8] N.I. Zheludev, Optics and Photonics News **22**, 31 (2011)

[9] M.C. Ricci, N. Orloff, S.M. Anlage, Appl. Phys. Lett. **87**, 034102 (2005)

[10] M.C. Ricci, H. Xu, R. Prozorov, A.P. Zhuravel, A.V. Ustinov, S.M. Anlage, IEEE Trans. Appl. Supercond. **17**, 918 (2007)

[11] H.T. Chen, H. Yang, R. Singh, J.F. OHara, A.K. Azad, A. Stuart, S.A. Trugman, Q.X. Jia, A.J. Taylor, Phys. Rev. Lett. **105**, 247402 (2010)

[12] B. Jin, C. Zhang, S. Engelbrecht, A. Pimenov, J. Wu, Q. Xu, C. Cao, J. Chen, W. Xu, Opt. Express **18**, 17504 (2010)

[13] V.A. Fedotov, A. Tsiatmas, J.H. Shi, R. Buckingham, P. de Groot, Y. Chen, S. Wang, N.I. Zheludev, Opt. Express **18**, 9015 (2010)

[14] C. Kurter, P. Tassin, A.P. Zhuravel, L. Zhang, T. Koschny, A.V. Ustinov, C.M. Soukoulis, S.M. Anlage, Appl. Phys. Lett. **100**, 121906 (2012)

[15] R. Singh, J. Xiong, A.K. Azad, H. Yang, S.A. Trugman, Q.X. Jia, A.J. Taylor, H.T. Chen, Nanophotonics **1**, 117123 (2012)

[16] R. Singh, J. Xiong, D.R. Chowdhury, H. Yang, A.K. Azad, S.A. Trugman, Q.X. Jia, A.J. Taylor, H.T. Chen, Proc. SPIE **8423**, 84230Y (2012)

[17] V. Savinov, V.A. Fedotov, S.M. Anlage, P.A.J. de Groot, N.I. Zheludev, Phys. Rev. Lett. **109**, 243904 (2012)

[18] P. Jung, S. Butz, S.V. Shitov, A.V. Ustinov, Appl. Phys. Lett. **102**, 062601 (2013)

[19] S. Butz, P. Jung, L.V. Filippenko, V.P. Koshelets, A.V. Ustinov, Opt. Express **29 (19)**, 22540 (2013)

[20] D. Zueco, C. Fernández-Juez, J. Yago, U. Naether, B. Peropadre, J.J. García-Ripoll, J.J. Mazo, Supercond. Sci. Technol. **26**, 074006 (8pp) (2013)

[21] B. Josephson, Phys. Lett. A **1**, 251 (1962)

[22] A. Barone, G. Patternó, *Physics and Applications of the Josephson Effect.* (Wiley, New York, 1982)

[23] K.K. Likharev., *Dynamics of Josephson Junctions and Circuits.* (Gordon and Breach, Philadelphia, 1986)

[24] M. Trepanier, D. Zhang, O. Mukhanov, S.M. Anlage, arXiv:1308.1410 (2013)

[25] P. Jung, S. Butz, M. Marthaler, M.V. Fistul, J. Leppäkangas, V.P. Koshelets, A.V. Ustinov, arXiv:1312.2937 (2013)

[26] W.G. Jenks, S.S.H. Sadeghi, J.P.W. Jr, J. Phys. D: Appl. Phys. **30**, 293 (1997)

[27] D. Koelle, R. Kleiner, F. Ludwig, E. Dantsker, J. Clarke, Rev. Mod. Phys. **71**, 631 (1999)

[28] R. Kleiner, D. Koelle, F. Ludwig, J. Clarke, Proceedings of the IEEE **92**, 1534 (2004)

[29] R.L. Fagaly, Review of Scientific Instruments **77**, 101101 (2006)

[30] C. Du, H. Chen, S. Li, Phys. Rev. B **74**, 113105 (2006)

[31] N. Lazarides, G.P. Tsironis, Appl. Phys. Lett. **16**, 163501 (2007)

[32] S. Butz, P. Jung, L.V. Filippenko, V.P. Koshelets, A.V. Ustinov, Supercond. Sci. Technol. **26**, 094003 (2013)

[33] N. Lazarides, G.P. Tsironis, M. Eleftheriou, Nonlinear Phenom. Complex Syst. **11**, 250 (2008)

[34] G.P. Tsironis, N. Lazarides, M. Eleftheriou, PIERS Online **5**, 26 (2009)

[35] N. Lazarides, G.P. Tsironis, Proc. SPIE **8423**, 84231K (2012)

[36] W. Wernsdorfer, Supercond. Sci. Technol. **22**, 064013 (2009)

[37] J. Gu, R. Singh, Z. Tian, W. Cao, Q. Xing, M.X. He, J.W. Zhang, J. Han, H. Chen, W. Zhang, Appl. Phys. Lett. **97**, 071102 (2010)

[38] C.H. Zhang, J.B. Wu, B.B. Jin, Z.M. Ji, L. Kang, W.W. Xu, J. Chen, M. Tonouchi, P.H. Wu, Opt. Express **20 (1)**, 42 (2011)

[39] J.B. Wu, B.B. Jin, J. Wan, L. Liang, Y.G. Zhang, T. Jia, C.H. Cao, L. Kang, W.W. Xu, J. Chen, P.H. Wu, Appl. Phys. Lett. **99**, 161113 (2011)

[40] C.H. Zhang, J.B. Wu, B.B. Jin, Z.M. Ji, L. Kang, W.W. Xu, J. Chen, M. Tonouchi, P.H. Wu, Opt. Express **20 (1)**, 42 (2012)

[41] C.H. Zhang, J.H. B. B. Jin, I. Kawayama, H. Murakami, X. Jia, L. Liang, L. Kang, J. Chen, P. Wu, M. Tonouchi, New Journal of Physics **15**, 055017 (2013)

[42] B.B.Jin, C. H. Zhang, J. Han, I. Kawayama, H. Murakami, J.B. Wu, L. Kang, J. Chen, P.H. Wu, M. Tonouchi, Appl. Phys. Lett. **102**, 081121 (2013)

[43] A. Pimenov, A. Loidl, P. Przyslupski, B. Dabrowski, Phys. Rev. Lett. **95**, 247009 (2005)

[44] A.G. Kussow, A. Akyurtlu, A. Semichaevsky, N. Angkawisittpan, Phys. Rev. B **76**, 195123 (2007)

[45] N. Limberopoulos, A. Akyurtlu, K. Higginson, A.G. Kussow, C.D. Merritt, Appl. Phys. Lett. **95**, 023306 (2009)

[46] A.L. Rakhmanov, V.A. Yampolskii, J.A. Fan, F. Capasso, F. Nori, Phys. Rev. B **81 (7)**, 075101 (2010)

[47] V.A. Golick, D.V. Kadygrob, V.A. Yampolskii, A.L. Rakhmanov, B.A. Ivanov, F. Nori, Phys. Rev. Lett. **104**, 187003 (2010)

[48] C. Kurter, P. Tassin, L. Zhang, T. Koschny, A.P. Zhuravel, A.V. Ustinov, S.M. Anlage, C.M. Soukoulis, Phys. Rev. Lett. **107**, 043901 (2011)

[49] J. Prat-Camps, A. Sanchez, C. Navau, Supercond. Sci. Technol. **26**, 074001 (2013)

[50] M.A. Castellanos-Beltran, K.D. Irwin, G.C. Hilton, L.R. Vale, K.W. Lehnert, Nature Physics **4**, 928 (2008)

[51] F. Magnus, B. Wood, J. Moore, K. Morrison, G. Perkins, J. Fyson, M.C.K. Wiltshire, D. Caplini, L.F. Cohen, J.B. Pendry, Nature Mater. **7**, 295 (2008)

[52] C. Navau, D.X. Chen, A. Sanchez, N. Del-Valle, Appl. Phys. Lett. **94 (24)**, 242501 (2009)

[53] Y. Mawatari, C. Navau, A. Sanchez, Phys. Rev. B **85**, 134524 (2012)

[54] Y. Mawatari, Supercond. Sci. Technol. **26**, 074005 (2013)

[55] C. Kurter, J. Abrahams, S.M. Anlage, Appl. Phys. Lett. **96**, 253504 (2010)

[56] B.G. Ghamsari, J. Abrahams, S. Remillard, S.M. Anlage, Appl. Phys. Lett. **102 (1)**, 013503 (2013)

[57] J. Wu, B. Jin, Y. Xue, C. Zhang, H. Dai, L. Zhang, C. Cao, L. Kang, W. Xu, J. Chen, P. Wu, Opt. Express **19**, 12021 (2011)

[58] A. Tsiatmas, V.A. Fedotov, F.J.G. de Abajo, N.I. Zheludev, New Journal of Physics **14**, 115006 (2012)

[59] J. Zuo, R. Liu, Y. Zhou, Y. Li, Y. Wang, Science China Physics, Mechanics and Astronomy **55 (2)**, 224 (2012)

[60] A.M. Zagoskin, J. Opt. **14**, 114011 (2012)

[61] S.I. Mukhin, M.V. Fistul, arXiv:1302.5558v1 (2013)

[62] R.D. Wilson, M.J. Everitt, S. Savelev, A.M. Zagoskin, Supercond. Sci. Technol. **26**, 084005 (2013)

[63] P. Macha, G. Oelsner, J.M. Reiner, M. Marthaler, S. André, G. Schön, U. Hübner, H.G. Meyer, E. Il'ichev, A.V. Ustinov, arXiv:1309.5268v1 (2013)

[64] N. Lazarides, G.P. Tsironis, Supercond. Sci. Technol. **26**, 084006 (2013)

[65] N. Lazarides, V. Paltoglou, G.P. Tsironis, Int. J. Bifurcation Chaos **21**, 2147 (2011)

[66] N. Lazarides, G.P. Tsironis, Phys. Lett. A **374**, 2179 (2010)

[67] Y. Huang, W.F. McColl, J. Phys. A: Math. Gen. **30**, 7919 (1997)

Numerical Modeling Techniques for Metamaterials

Approximation of Transformation Media-based Reshaping Action by Genetic Optimization

Ozlem Ozgun[1*], and Mustafa Kuzuoglu[2]

[1]TED University, Dept. of Electrical and Electronics Engineering, Ankara, Turkey
[2]Middle East Technical University, Dept. of Electrical and Electronics Engineering, Ankara, Turkey
*corresponding author, e-mail: ozgunozlem@gmail.com

Abstract

The reshaping technique that is based on Transformation Optics renders an object to be perceived as if it has a different shape irrespective of the location of the observer. This is achieved by coating the object with an anisotropic and spatially-varying metamaterial layer by employing the concept of coordinate transformation. This paper presents a design approach for numerical approximation of reshaper medium by means of concentric layers coated over the object, each of which has simpler and easily-realizable material parameters that are determined by the Genetic Optimization algorithm. The results of various finite element simulations are presented .

1. Introduction

Transformation Optics (TO) is an intuitive approach to the design of application-oriented transformation media that can flexibly tune electromagnetic waves in a desired manner by employing coordinate transformations. The invisibility cloak as a transformation medium led to the widespread use of the TO approach [1]. However, the range of applications of this approach is comprehensive and some of which are listed in [2]-[11]. In 2007, the authors proposed the concept of 'reshaping', which is based on the idea that if an object of an arbitrary shape is coated by transformation medium layer, an observer at an arbitrary location perceives this object as if it has a different shape [2]. In other words, an object that is coated by a properly-designed transformation medium is transformed to a new object of different shape. At the extreme case, if the object is transformed to a point, the object becomes invisible, as in the case of invisibility cloaking. The main difficulty in transformation optics is the realization of the transformation medium through physical experiments because material parameters are inherently anisotropic and spatially varying, which make their realizations challenging. Although some promising developments have been proposed for the practical realization of transformation media, such as in [10-11], it is almost impractical to design anisotropic material parameters at each point within the medium, and some approximations to the material parameters are needed to make the physical realization feasible. In this study, the reshaping action is achieved by concentric layers, each of which has simpler constitutive parameters, designed over the object to be reshaped. The material parameters are determined by the Genetic Optimization algorithm in such a way that the concentric layers coated over the object mimic the behavior of the reshaping medium designed by the transformation optics. In this way, the reshaping action can approximately be realized by simpler and natural media (such as isotropic, uniaxial or biaxial) having relative permittivity and permeability values *not* smaller than unity.

The paper is organized as follows: Sec. 2 summarizes the design principles of the reshaping approach that is based on transformation optics. Sec. 3 presents the reshaper design that is based on the genetic algorithm. In Sec. 4, the results of several finite element simulations are presented in the context of two-dimensional Helmholtz-type scattering problems.

2. Reshaper Design via Transformation Optics

This section briefly summarizes the design procedure of the electromagnetic reshaper medium by using the principles of transformation optics. When an object of certain shape is coated by a transformation medium layer that is characterized by suitably-determined material parameters as shown in Fig. 1(a), an observer located at an arbitrary point perceives this object as if it has a different shape. That is, the transformation medium transforms an object to another object with reference to an observer. Note that the transformation medium can be of arbitrary convex shape. In designing the transformation medium layer (Ω_T), each point P inside Ω_T is mapped to $\tilde{P}$ inside the transformed region $\tilde{\Omega} = \Omega \cup \Omega_T$. This mapping is defined as a coordinate transformation $T : \Omega_T \to \tilde{\Omega}$ as follows [2]:

$$\tilde{\mathbf{r}} = \frac{\|\mathbf{r}_A - \mathbf{r}_C\|}{\|\mathbf{r}_A - \mathbf{r}_B\|}(\mathbf{r} - \mathbf{r}_B) + \mathbf{r}_C \qquad (1)$$

where $\mathbf{r}$ and $\tilde{\mathbf{r}}$ are the position vectors of the points P and $\tilde{P}$ in the original and transformed coordinates, respectively; and $\|\cdot\|$ represents the Euclidean norm. Moreover, $\mathbf{r}_A$, $\mathbf{r}_B$ and $\mathbf{r}_C$ are the position vectors of the respective points through the unit vector $\hat{\boldsymbol{a}}$, which is emanated from a point inside the innermost domain (such as the center-of-mass point) in the direction of the point P in the transformation medium layer.

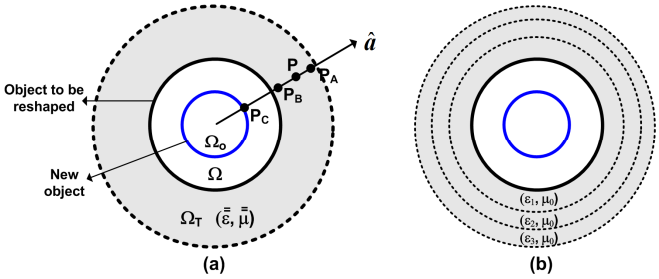

Figure 1: Reshaper design: (a) Object coated by transformation medium (Sec. 2); (b) Object coated by multiple simple medium layers (Sec. 3).

The coordinate transformation in (1) creates spatially-varying anisotropic materials where the original forms of Maxwell's equations are still preserved in the transformed space. That is, Maxwell's equations are form-invariant under space transformations, and a coordinate transformation leads to the following permittivity and permeability tensors:

$$\bar{\bar{\varepsilon}} = \varepsilon \bar{\bar{\Lambda}} \quad \text{and} \quad \bar{\bar{\mu}} = \mu \bar{\bar{\Lambda}}, \tag{2}$$

where ε and μ are the constitutive parameters of the original medium, and

$$\bar{\bar{\Lambda}} = (\det \bar{\bar{J}}) \left(\bar{\bar{J}}^{T} \cdot \bar{\bar{J}} \right)^{-1}, \tag{3}$$

where $\bar{\bar{J}}$ is the Jacobian tensor that is given as $\bar{\bar{J}} = \partial(\tilde{x}, \tilde{y}, \tilde{z}) / \partial(x, y, z)$ in Cartesian coordinates.

3. Reshaper Design via Genetic Algorithm

Being motivated to overcome the difficulties in the realization of anisotropic and spatially-varying transformation medium, this section proposes an approach for the numerical approximation of reshaper medium by coating the object with a number of concentric layers that have simpler material parameters (see Fig. 1(b)). The constitutive parameters of the layers are optimized by using the genetic algorithm to mimic the behavior of the transformation medium-based reshaper.

Genetic algorithm is based on the principles of natural selection. It manipulates strings of binary digits, called chromosomes, and carries out simulated evolution on populations of such chromosomes. Genetic algorithm, like nature, finds good chromosomes by evaluating each chromosome through evaluation (cost) function. A cost function takes a chromosome as input and returns a number that is a measure of the performance (fitness) of the chromosome. Thus, it biases the selection of chromosomes such that those with the best evaluations tend to be more reproductive than those with the worst evaluations.

For the model problem in Fig. 1(b), three cases are considered depending on the type of media. These are isotropic (dielectric constant ε is a constant), uniaxial and biaxial media. Note that the layers are assumed to be non-magnetic. An axial medium is characterized by the following dielectric tensor:

$$\bar{\bar{\varepsilon}} = \begin{bmatrix} \varepsilon_{xx} & 0 & 0 \\ 0 & \varepsilon_{yy} & 0 \\ 0 & 0 & \varepsilon_{zz} \end{bmatrix} \tag{4}$$

For the uniaxial medium, $\varepsilon_{xx} = \varepsilon_{yy} \neq \varepsilon_{zz}$; whereas for the biaxial medium, $\varepsilon_{xx} \neq \varepsilon_{yy} \neq \varepsilon_{zz}$.

In the genetic algorithm, the number of layers is assumed to be fixed, and the dielectric constant of each layer is optimized. Therefore, for the isotropic case, each layer has a single dielectric constant parameter. For the uniaxial and biaxial cases, each layer is assigned to two ($\varepsilon_{xx} = \varepsilon_{yy}$ and ε_{zz}) and three (ε_{xx}, ε_{yy} and ε_{zz}) dielectric constant parameters, respectively. These dielectric constant parameters are optimized through genetic algorithm by minimizing the following cost function:

$$f_{cost} = \sum_{i=1}^{N} \int_{0}^{2\pi} \left| RCS_i - RCS_{i,TO} \right|^2 d\phi \tag{5}$$

where N is the number of incidence angles illuminating the object; and ϕ refers to observation angles for each incidence angle. This cost function compares the radar cross-section (RCS) values that are obtained by the genetic algorithm and the transformation optics (target) based on the least-square approximation. Depending on the shape of the object, some of the incidence angles might be skipped if there is a sort of symmetry in the geometry. For example, for a circular object, a single incidence angle is sufficient because the object is symmetrical for all angles.

4. Numerical Results

This section presents the results of some numerical simulations based on the finite element solution of TM_z (transverse magnetic) electromagnetic scattering problems. In all cases, the free-space wavelength λ is 1 m, and the element size is $\lambda/40$.

First, the performance of the transformation medium-based reshaper is demonstrated, as described in Sec. 2. In Fig. 2, the results are given for a circular object with radius of 0.5λ to be reshaped as an object with radius of 0.3λ by means of a transformation medium layer whose thickness is 0.5λ. The object is illuminated by a plane wave whose angle of incidence is 90° with respect to the x-axis. Fig. 2(a) shows the field distribution that is obtained by the conventional finite element solution of the new object with radius of 0.3λ. Fig. 2(b) shows the field distribution of the equivalent model that is based on the transformation medium layer. It is expected that the fields outside the transformation layer should be the same in both cases so that the two problems become equivalent. In Fig. 2(c), RCS profiles are plotted. A perfect agreement is observed between the two results. Similar simulations are performed for a square object with half-edge length of 0.5λ to be reshaped as an object with half-edge length of 0.3λ. Assuming that the angle of incidence is 45°, the results are shown in Fig. 3.

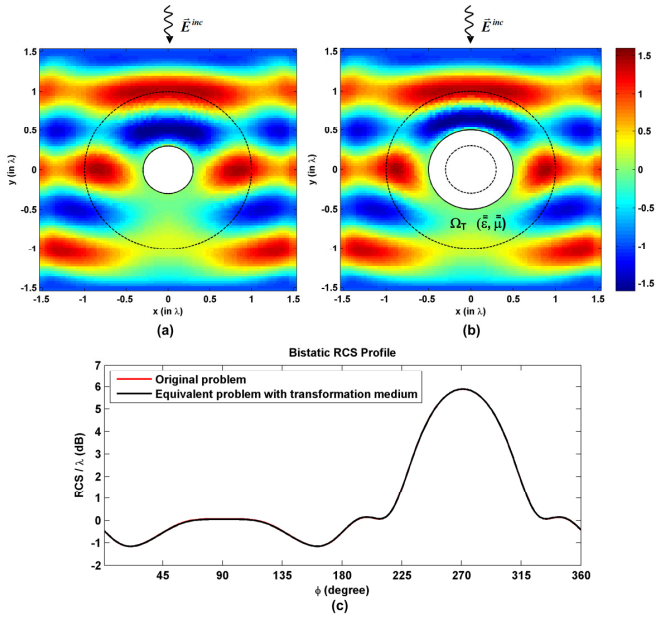

Figure 2: [Transformation medium-based design] Circular object with radius of 0.5λ to be reshaped as an object with radius of 0.3λ: (a) Real part of electric field for the original problem involving an object with radius of 0.3λ; (b) Real part of electric field for the equivalent problem involving an object with radius of 0.5λ and coated by a transformation medium layer; (c) RCS profiles comparing two cases.

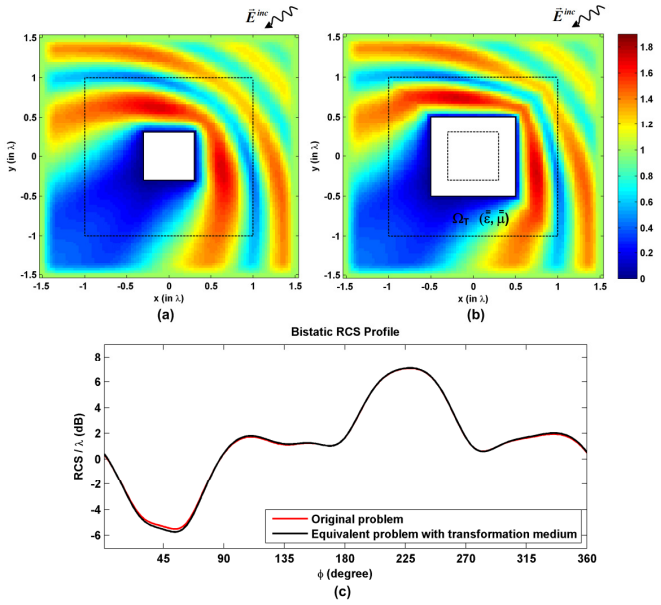

Figure 3: [Transformation medium-based design] Square object with half-edge length of 0.5λ to be reshaped as an object with half-edge length of 0.3λ: (a) Magnitude of electric field for the original problem involving an object with radius of 0.3λ; (b) Magnitude of electric field for the equivalent problem involving an object with radius of 0.5λ and coated by a transformation medium layer; (c) RCS profiles comparing two cases.

Table 1: Input parameters for the genetic optimization.

Parameters	Values
Population size	1500
Max number of generation	20
Crossover probability	0.65
Mutation probability	0.03
Range of each parameter (isotropic)	[1, 10]
Range of each parameter (uniaxial, biaxial)	[1, 5]
Crossover technique	One-point
Selection technique	Roulette Wheel

Second, the results for the multiple layers that are designed by the genetic algorithm are presented, as described in Sec. 3. The input parameters that are used in the genetic algorithm are listed in Table 1. For the circular object with radius of 0.5λ, the results are shown in Fig. 4 and Fig. 5 for different types and number of layers. The total thickness of the layers is 0.5λ, and the layers have equal thicknesses. The optimized material parameters are tabulated in Table 2 and Table 3.

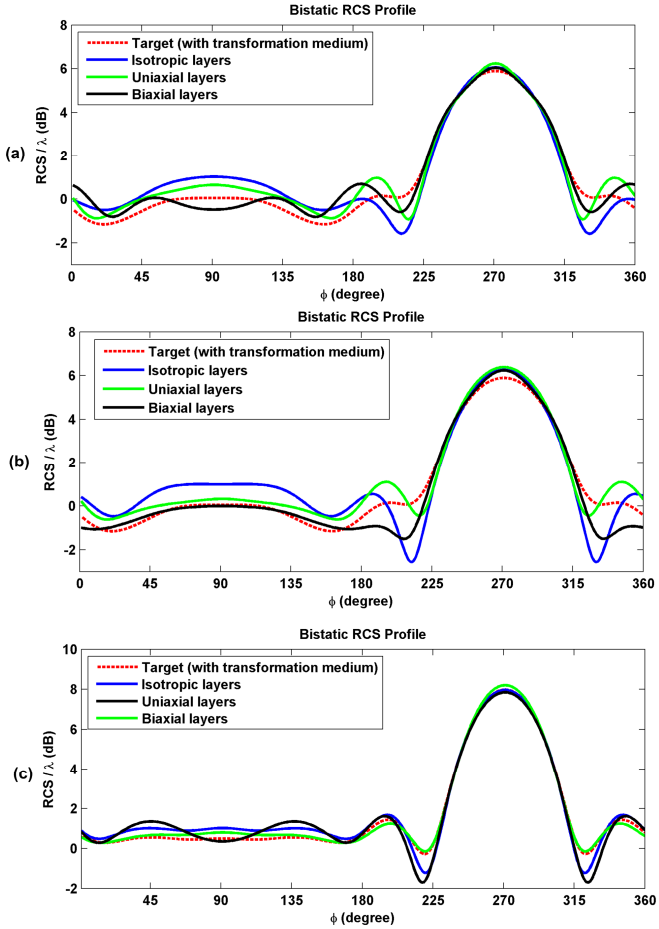

Figure 4: [Genetic optimization design] RCS profiles for circular object with radius of 0.5λ: (a) The new radius is 0.3λ and the number of layers is 5; (b) The new radius is 0.3λ and the number of layers is 8; (c) The new radius is 0.4λ and the number of layers is 5.

Table 2: Optimized material parameters for circular object with radius of 0.5λ. The new radius is 0.3λ and the number of layers around the object is 5.

	Isotropic layers	Uniaxial layers	Biaxial layers
Layer 1	$\varepsilon = 9.68$	$\varepsilon_{xx} = \varepsilon_{yy} = 3.12$ $\varepsilon_{zz} = 4.84$	$\varepsilon_{xx} = 1.05$ $\varepsilon_{yy} = 2.69$ $\varepsilon_{zz} = 4.15$
Layer 2	$\varepsilon = 2.38$	$\varepsilon_{xx} = \varepsilon_{yy} = 4.98$ $\varepsilon_{zz} = 3.69$	$\varepsilon_{xx} = 3.23$ $\varepsilon_{yy} = 4.65$ $\varepsilon_{zz} = 2.99$
Layer 3	$\varepsilon = 9.29$	$\varepsilon_{xx} = \varepsilon_{yy} = 4.98$ $\varepsilon_{zz} = 4.94$	$\varepsilon_{xx} = 4.79$ $\varepsilon_{yy} = 2.47$ $\varepsilon_{zz} = 1.77$
Layer 4	$\varepsilon = 1.78$	$\varepsilon_{xx} = \varepsilon_{yy} = 1.11$ $\varepsilon_{zz} = 1.91$	$\varepsilon_{xx} = 1.29$ $\varepsilon_{yy} = 1.41$ $\varepsilon_{zz} = 1.80$
Layer 5	$\varepsilon = 1.56$	$\varepsilon_{xx} = \varepsilon_{yy} = 1.24$ $\varepsilon_{zz} = 1.89$	$\varepsilon_{xx} = 4.65$ $\varepsilon_{yy} = 1.13$ $\varepsilon_{zz} = 1.98$

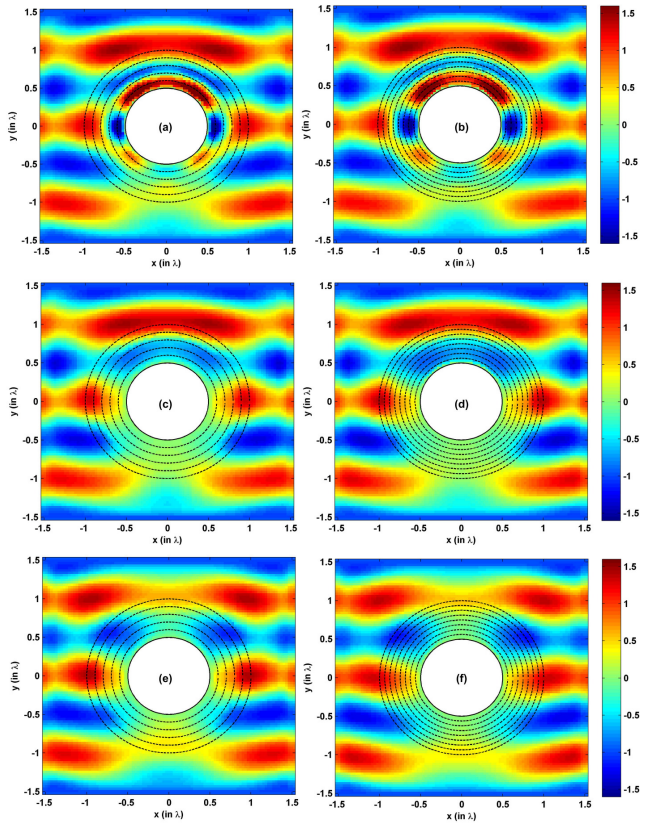

Figure 5: [Genetic optimization design] Real part of electric field for circular object with radius of 0.5λ to be reshaped as an object with radius of 0.3λ: (a) Isotropic layers (the number of layers is 5); (b) Isotropic layers (the number of layers is 8); (c) Uniaxial layers (the number of layers is 5); (d) Uniaxial layers (the number of layers is 8); (e) Biaxial layers (the number of layers is 5); (f) Biaxial layers (the number of layers is 8).

Table 3: Optimized material parameters for circular object with radius of 0.5λ. The new radius is 0.3λ and the number of layers around the object is 8.

	Isotropic layers	Uniaxial layers	Biaxial layers
Layer 1	$\varepsilon = 7.46$	$\varepsilon_{xx} = \varepsilon_{yy} = 1.08$ $\varepsilon_{zz} = 1.86$	$\varepsilon_{xx} = 1.02$ $\varepsilon_{yy} = 4.03$ $\varepsilon_{zz} = 2.25$
Layer 2	$\varepsilon = 5.45$	$\varepsilon_{xx} = \varepsilon_{yy} = 4.56$ $\varepsilon_{zz} = 3.02$	$\varepsilon_{xx} = 2.87$ $\varepsilon_{yy} = 4.72$ $\varepsilon_{zz} = 4.97$
Layer 3	$\varepsilon = 2.55$	$\varepsilon_{xx} = \varepsilon_{yy} = 3.37$ $\varepsilon_{zz} = 4.75$	$\varepsilon_{xx} = 4.07$ $\varepsilon_{yy} = 3.69$ $\varepsilon_{zz} = 3.90$
Layer 4	$\varepsilon = 1.46$	$\varepsilon_{xx} = \varepsilon_{yy} = 3.99$ $\varepsilon_{zz} = 3.69$	$\varepsilon_{xx} = 3.09$ $\varepsilon_{yy} = 3.23$ $\varepsilon_{zz} = 1.19$
Layer 5	$\varepsilon = 8.27$	$\varepsilon_{xx} = \varepsilon_{yy} = 3.95$ $\varepsilon_{zz} = 1.03$	$\varepsilon_{xx} = 4.11$ $\varepsilon_{yy} = 2.32$ $\varepsilon_{zz} = 2.16$
Layer 6	$\varepsilon = 8.59$	$\varepsilon_{xx} = \varepsilon_{yy} = 1.29$ $\varepsilon_{zz} = 1.31$	$\varepsilon_{xx} = 3.56$ $\varepsilon_{yy} = 2.09$ $\varepsilon_{zz} = 1.97$
Layer 7	$\varepsilon = 1.14$	$\varepsilon_{xx} = \varepsilon_{yy} = 1.71$ $\varepsilon_{zz} = 1.97$	$\varepsilon_{xx} = 2.41$ $\varepsilon_{yy} = 1.09$ $\varepsilon_{zz} = 1.36$
Layer 8	$\varepsilon = 3.19$	$\varepsilon_{xx} = \varepsilon_{yy} = 1.17$ $\varepsilon_{zz} = 2.57$	$\varepsilon_{xx} = 1.55$ $\varepsilon_{yy} = 1.19$ $\varepsilon_{zz} = 2.44$

Simulations are also performed for a square object with half-edge length of 0.5λ to be reshaped as an object with half-edge length of 0.3λ, assuming that the number of layers is 5. The results are shown in Fig. 6 and Fig. 7 for two different incidence angles. The optimized material parameters are listed in Table 4.

From the results, it is observed that the biaxial and uniaxial layers provide better results compared to the isotropic layers because of higher degrees of freedom. It is also observed that as the radius of the new object decreases relative to the radius of the original object, it becomes difficult to find optimum values for the material parameters. Increasing the number of layers does not give rise to considerable differences, but the computational load increases because of increase in the number of parameters to be optimized.

5. Conclusions

This paper presented a numerical design approach for the approximation of reshaper medium by means of a number of concentric layers that are coated around the object to be reshaped. The main purpose is to achieve the reshaping action by using simpler and easily-realizable material parameters that are optimized by the genetic algorithm. It has been observed that the results are promising and the reshaping action can approximately be achieved to some extent by means of concentric layers of natural media.

Table 4: Optimized material parameters for square object with half-edge length of 0.5λ. The half-edge length is 0.3λ and the number of layers around the object is 5.

	Uniaxial layers	Biaxial layers
Layer 1	$\varepsilon_{xx} = \varepsilon_{yy} = 1.52$ $\varepsilon_{zz} = 4.76$	$\varepsilon_{xx} = 1.67$ $\varepsilon_{yy} = 2.57$ $\varepsilon_{zz} = 1.73$
Layer 2	$\varepsilon_{xx} = \varepsilon_{yy} = 2.63$ $\varepsilon_{zz} = 4.95$	$\varepsilon_{xx} = 4.48$ $\varepsilon_{yy} = 2.27$ $\varepsilon_{zz} = 4.09$
Layer 3	$\varepsilon_{xx} = \varepsilon_{yy} = 4.79$ $\varepsilon_{zz} = 1.11$	$\varepsilon_{xx} = 4.55$ $\varepsilon_{yy} = 3.48$ $\varepsilon_{zz} = 2.98$
Layer 4	$\varepsilon_{xx} = \varepsilon_{yy} = 1.06$ $\varepsilon_{zz} = 1.11$	$\varepsilon_{xx} = 1.28$ $\varepsilon_{yy} = 1.85$ $\varepsilon_{zz} = 1.22$
Layer 5	$\varepsilon_{xx} = \varepsilon_{yy} = 1.45$ $\varepsilon_{zz} = 2.13$	$\varepsilon_{xx} = 1.34$ $\varepsilon_{yy} = 1.20$ $\varepsilon_{zz} = 2.07$

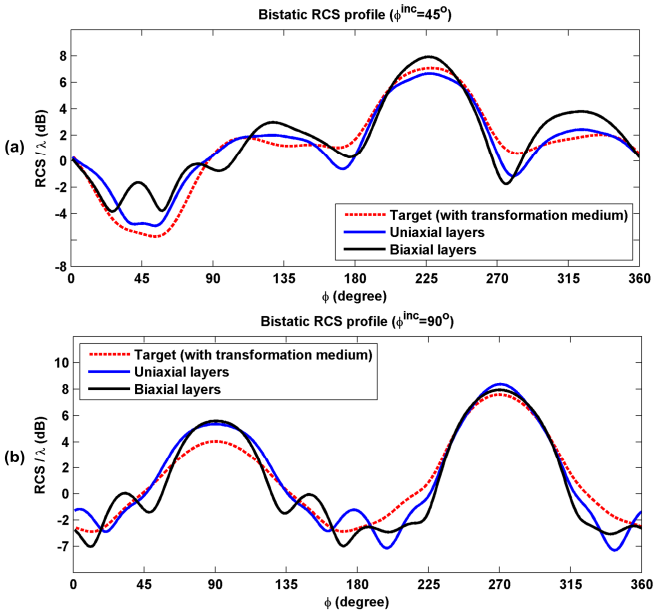

Figure 6: [Genetic optimization design] RCS profiles for square object with half-edge length of 0.5λ to be reshaped as an object with half-edge length of 0.3λ. The number of layers is 5.: (a) $\phi^{inc} = 45°$; (b) $\phi^{inc} = 90°$

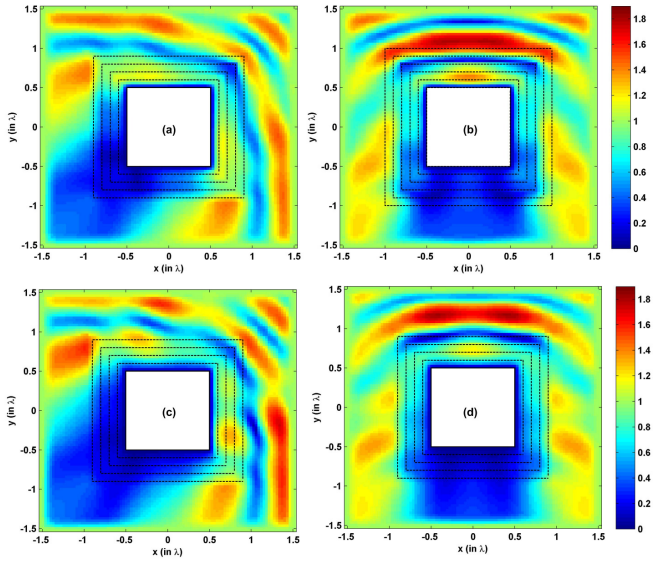

Figure 7: [Genetic optimization design] Magnitude of electric field for square object with half-edge length of 0.5λ to be reshaped as an object with half-edge length of 0.3λ. The number of layers is 5.: (a) Uniaxial layers ($\phi^{inc} = 45°$); (b) Uniaxial layers ($\phi^{inc} = 90°$); (c) Biaxial layers ($\phi^{inc} = 45°$); (d) Biaxial layers ($\phi^{inc} = 90°$).

References

[1] J.B. Pendry, D. Schurig, D.R. Smith, Controlling electromagnetic fields, *Science* 312: 1780-1782, 2006.

[2] O. Ozgun, M. Kuzuoglu, Electromagnetic metamorphosis: Reshaping scatterers via conformal anisotropic metamaterial coatings, *Microwave Opt. Technol. Lett.* 49: 2386-2392, 2007.

[3] O. Ozgun, M. Kuzuoglu, Utilization of anisotropic metamaterial layers in waveguide miniaturization and transitions, *IEEE Microwave and Wireless Components Letters* 17: 754-756, 2007.

[4] F. Kong, B.I. Wu, J.A. Kong, J. Huangfu, S. Xi, H. Chen, Planar focusing antenna design by using coordinate transformation technology, *Applied Physics Letters* 91: 253509, 2007.

[5] B. Donderici, F.L. Teixeira, Metamaterial blueprints for reflectionless waveguide bends, *IEEE Microwave and Wireless Components Letters* 18: 233-235, 2008.

[6] R. Mittra, Y. Zhou, Designing Cloaks and Absorbing Blankets for Scattering Reduction Using Field and Impedance Transformation Techniques, Chapter 14 of *Computational Electromagnetics, Recent Advances and Engineering Applications*, Springer, 2014.

[7] O. Ozgun, M. Kuzuoglu, Form Invariance of Maxwell's Equations: The Pathway to Novel Metamaterial Specifications for Electromagnetic Reshaping, *IEEE Antennas and Propagation Magazine* 52: 51-65, 2010.

[8] O. Ozgun, M. Kuzuoglu, Domain Compression via Anisotropic Metamaterials designed by Coordinate Transformations, *Journal of Computational Physics* 229: 921-932, 2010.

[9] O. Ozgun, M. Kuzuoglu, Software Metamaterials: Transformation Media Based Multiscale Techniques for Computational Electromagnetics, *Journal of Computational Physics* 236: 203-219, 2013.

[10] Q. Cheng, T. J. Cui, W. X. Jiang, B. G. Cai, An omnidirectional electromagnetic absorber made of metamaterials, *New J. Phys.* 12: 063006, 2010.

[11] X.-Y. He, C. Yang, B. Li, Q. Chen, B.-H. Zhou, C.-X. Tang, Experimental verification of the bending of electromagnetic waves using metamaterials, *Appl. Phys. Lett.* 98: 204105, 2011.

Automated Synthesis of Transmission Lines Loaded with Complementary Split Ring Resonators (CSRRs) and Open Complementary Split Ring Resonators (OCSRRs) through Aggressive Space Mapping (ASM)

Jordi Selga[1], Ana Rodríguez[2], Marco Orellana[1], Vicente Boria[2], Ferran Martín*[1]

[1]GEMMA/CIMITEC, Departament d'Enginyeria Electrònica, Universitat Autònoma de Barcelona, 08193 Bellaterra, Spain
[2]Departamento de Comunicaciones-iTEAM, Universidad Politécnica de Valencia, 46022 Valencia, Spain
*corresponding author, E-mail: Ferran.Martin@uab.es

Abstract

This paper is focused on the application of space mapping optimization to the automated synthesis of transmission lines loaded with complementary split ring resonators (CSRRs) and open complementary split ring resonators (OCSRRs). These structures are of interest for the implementation of resonant-type metamaterial transmission lines, and for the design of planar microwave circuits based on such complementary resonators. The paper presents a method to generate the layouts of CSRR- and OCSRR-loaded microstrip lines from the elements of their equivalent circuit models. Using the so-called aggressive space mapping (ASM), a specific implementation that uses quasi-Newton type iteration, we have developed synthesis algorithms that are able to provide the topology of these CSRR- and OCSRR-loaded lines in few steps. The most relevant aspect, however, is that this synthesis process is completely automatic, i.e., it does not require any action from the designers, other than initiate the algorithm. Moreover, this technique can be translated to other electrically small planar elements described by lumped element equivalent circuit models.

1. Introduction

Metamaterial transmission lines have attracted the attention of RF/microwave engineers in the last years due to their enhanced design flexibility as compared to ordinary lines [1-4]. Such lines are implemented by loading a host line with reactive elements (inductors, capacitors, resonators, or a combination of them). Thanks to the presence of such additional elements, metamaterial transmission lines exhibit functionalities not easily achievable in conventional lines, mostly related to the fact that their dispersion can be engineered or tailored to satisfy certain requirements. This extra controllability of the dispersion diagram (and characteristic impedance as well) has open the door to the design and implementation of enhanced bandwidth components [5-7], multiband and multifunctional devices [8-10], compact filters and diplexers [11,12], backfire-to-endfire leaky wave antennas [13,14], etc.

One of the drawbacks in the design of microwave circuits based on metamaterial transmission lines is related to their synthesis. This is due to the presence of the loading elements and their interaction with the host line. There are two main approaches for the implementation of metamaterial transmission lines: (i) the CL-loaded approach, where a host line is loaded with series capacitances and shunt inductances [15-17], and (ii) the resonant-type approach, where the host line is loaded with electrically small resonant elements, typically (although not exclusively) split ring resonators (SRRs) or complementary split ring resonators (CSRRs), and additional reactive elements [18,19]. This work is focused on the second approach, specifically on the automated synthesis of metamaterial transmission lines based on CSRRs. Moreover, we will also consider the synthesis of microstrip lines loaded with open complementary split ring resonators (OCSRRs), of interest for the implementation of metamaterial transmission lines (in combination with OSRRs [20]) and bandpass filters [21].

2. CSRR- and OCSRR-loaded microstrip lines

The considered structures are microstrip lines loaded with CSRRs etched in the ground plane (Fig. 1a), and microstrip lines loaded with OCSRRs connected to ground through via holes (Fig. 2a). CSRR-loaded lines are described by the lumped element circuit depicted in Fig. 1(b), where the CSRR is modeled by the L_c-C_c resonant tank, C models the coupling between the line and the resonator, and L accounts for the line inductance [22]. According to the circuit model, CSRR-loaded lines exhibit a stopband behavior (there is a transmission zero at the frequency where the shunt branch shorts to ground). This behavior can also be attributed (in a line loaded with an array of CSRRs) to the negative effective permittivity and large positive effective permittivity above and below, respectively, the resonance frequency of the CSRRs. It is also well-known that by adding series capacitive gaps to CSRR-loaded lines, the line exhibits also a negative effective permeability in a certain band, and the structure presents a composite right/left handed (CRLH) behavior [23]. Both types of lines CSRR-

and CSRR/gap-loaded lines have been applied to the design of many circuits, being the synthesis, in general, a complex task. This has motivated our research activity towards obtaining algorithms able to help the designers in finding the appropriate topologies to satisfy the requirements or specifications.

OCSRR-loaded microstrip lines are described by the circuit model depicted in Fig. 2(b), where the effect of the access lines has been ignored. It has been demonstrated that the structure of Fig. 2(a) is accurately described by this model [20,24], where the inductance L_{sh} is included to account for the strip (of width e) present between the inner metallic region of the OCSRR and the access lines (or ports). In combination with OSRR (described by a series resonator in a first order approximation [20]), OCSRR are of interest for the implementation of CRLH lines and filters. It is also possible to implement bandpass filters by coupling OCSRRs through admittance inverters in microstrip technology [25].

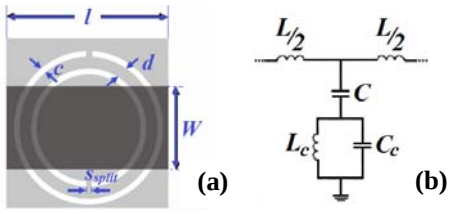

Figure 1: Typical topology (a) and circuit model (b) of a CSRR-loaded microstrip line (the ground plane is indicated in light grey).

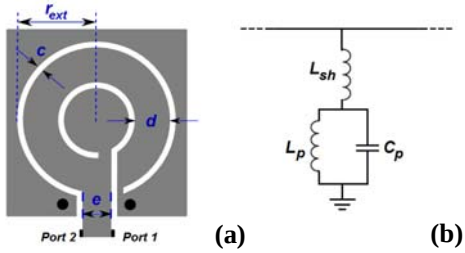

Figure 2: Typical topology (a) and circuit model (b) of a OCSRR-loaded microstrip line. Vias are indicated with black dots.

In the next section, it is briefly explained how CSRR- and OCSRR-loaded microstrip lines can be synthesized with the use of the so-called aggressive space mapping (ASM) algorithm.

3. Synthesis of CSRR and OCSRR loaded lines by means of ASM

In this section, a general formulation of ASM is first given, and then it is applied to obtain the automated synthesis of the considered structures.

3.1. Aggressive space mapping (ASM)

Space mapping is a technique extensively used for the synthesis of microwave devices [26-28]. It makes use of two simulation spaces: in the optimization space, $\mathbf{X}_c$, the variables are linked to a coarse model, which is simple and computationally efficient, although not accurate; in the validation space, $\mathbf{X}_f$, the variables are linked to a fine model, typically more complex and CPU intensive, but significantly more precise. In each space, a vector containing the different model parameters is defined. Such vectors are designated as $\mathbf{x}_f$ and $\mathbf{x}_c$ for the fine and coarse model parameters, respectively, and their responses are denoted as $\mathbf{R}_f(\mathbf{x}_f)$ and $\mathbf{R}_c(\mathbf{x}_c)$. In planar microwave circuits, the vectors $\mathbf{x}_f$ and $\mathbf{x}_c$ typically contain a set of geometric and circuit parameters, respectively, whereas the model responses are related to the evaluation of the device behaviour, e.g., a scattering parameter, such as S_{11} or S_{21}, computed in a certain frequency range.

ASM [27] is an advanced space mapping optimization technique that uses a quasi-Newton type iteration to find the target solution. The goal in ASM is to solve the following set of non-linear equations

$$\mathbf{f}(\mathbf{x}_f) = \mathbf{P}(\mathbf{x}_f) - \mathbf{x}_c^* = 0 \tag{1}$$

where $\mathbf{x}_c^*$ is the vector that contains the target circuit elements and $\mathbf{P}(\mathbf{x}_f)$ is a function that gives the extracted circuit parameters from the electromagnetic response of the layout. For a better understanding of the iterative optimization process, a superscript is added to the notation that actually indicates the iteration number. Hence, let us assume that $\mathbf{x}_f^{(j)}$ is the j-th approximation to the solution of (1) and $\mathbf{f}^{(j)}$ the error function corresponding to $\mathbf{f}(\mathbf{x}_f^{(j)})$. The next vector of the iterative process $\mathbf{x}_f^{(j+1)}$ is obtained by a quasi-Newton iteration according to

$$\mathbf{x}_f^{(j+1)} = \mathbf{x}_f^{(j)} + \mathbf{h}^{(j)} \tag{2}$$

where $\mathbf{h}^{(j)}$ is given by:

$$\mathbf{h}^{(j)} = -\left(\mathbf{B}^{(j)}\right)^{-1}\mathbf{f}^{(j)} \tag{3}$$

and $\mathbf{B}^{(j)}$ is an approach to the Broyden matrix [29]:

$$\mathbf{B}^{(j+1)} = \mathbf{B}^{(j)} + \frac{\mathbf{f}^{(j+1)}\mathbf{h}^{(j)T}}{\mathbf{h}^{(j)T}\mathbf{h}^{(j)}} \tag{4}$$

which is also updated at each iterative step. In (4), $\mathbf{f}^{(j+1)}$ is obtained by evaluating (1) using a certain parameter extraction method providing the coarse model parameters from the fine model parameters, and the super-index T stands for transpose.

3.2. Application of ASM to the synthesis of CSRR- and OCSRR-loaded lines.

To start the ASM, we first need an initial geometry for the structure. Then, the circuit parameters are extracted from the electromagnetic simulation of the initial layout, we compute the error function, and initiate the Broyden matrix. Then the process is iterated until convergence is achieved. For the CSRR-loaded lines, the parameter extraction method, generation of the first layout, and initiation of the Broyden matrix has been explained in detail in [30]. To illustrate the possibilities of the approach, we report the synthesis of a CSRR loaded line with the circuit elements indicated in table 1. Application of the developed ASM algorithm has lead to the geometry given in table 2, and convergence (the error is indicated in the table) has been

achieved after a single iteration (the reason is that we have applied a pre-optimization, also described in [30], so that the initial layout is already very close to the target).

Table 1. Circuit elements of the CSRR-loaded line

L (nH)	C (pF)	L_c (nH)	C_c (pF)
4.860	1.880	2.417	3.053

Table 2. Geometry of the synthesized structure

l (mm)	W (mm)	c (mm)	d (mm)	Error
8.47	2.22	0.36	0.17	<1%

Figure 3 depicts the target frequency response, i.e., the one resulting from the circuit simulation of the circuit of Fig. 1(b) with the elements of table 1, compared to the electromagnetic simulation of the initial and final layout. As can be seen the initial layout EM simulation is already very close to the target, and the difference between the target response and that of the final layout is roughly undistinguishable.

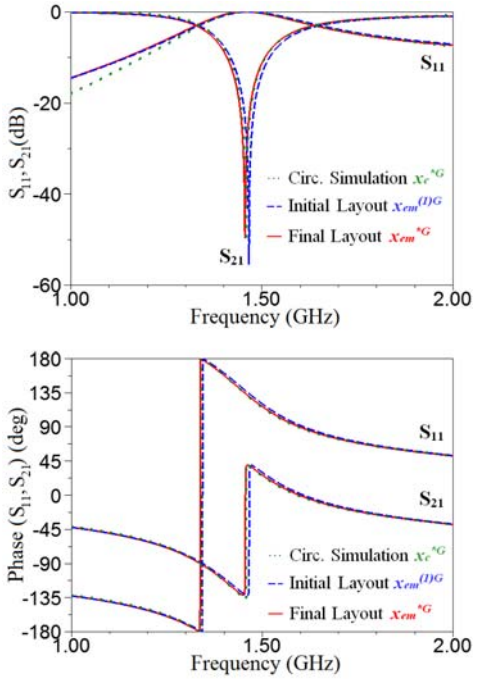

Figure 3: Magnitude (a) and phase (b) of the scattering parameters S_{21} and S_{11} at initial solution $\boldsymbol{x}_{em}^{(1)}$, final solution $\boldsymbol{x}_{em}^{*}$, and circuit simulation of $\boldsymbol{x}_c^{*}$ (the parameters of table 1). The considered substrate in the (lossless) EM simulation is the *Rogers RO3010* with thickness h = 1.27 mm and dielectric constant ε_r = 10.2.

For the OCSRR-loaded microstrip lines, the procedure to determine the layout is similar, but there are some differences that must be explained in detail (we dedicate further effort to the synthesis of this particle since the details of the CSRR-loaded line where provided in [30]). First of all, the geometrical variables in the OCSRR-loaded structure of Fig. 2(a) are not the same ones than in Fig. 1(a). Notice that, as mentioned before, the access lines are not considered. However, there is a strip connecting the ports with the inner metallic region of the OCSRR. Thus we have 4 geometrical parameters in the OCSRR (c, d, r_{ext} and e), indicated in Fig. 2(a). Since the number of electrical parameters of the circuit model (Fig. 2b) is 3, and it is convenient to deal with the same number of parameters in both spaces (optimization and validation spaces), one of the geometrical parameters is set to a fixed value in this paper. Specifically, the slot width is set to c = 0.25 mm.

To determine the initial OCSRR geometry, necessary to initiate the Broyden matrix, the model of the CSRR reported in [22] is considered. The use of this model is justified since, to a first order approximation, the capacitance of the OCSRR (C_p) coincides with the capacitance of the CSRR (C_c), and the inductance of the OCSRR (L_p) is four times larger than the inductance of the CSRR (L_c). This is true as far as c, d and r_{ext} are identical for both particles and they are etched on the same substrate [31]. On the other hand, to estimate e, well-known formulas providing the inductance of an electrically small and narrow strip section are used. Once the initial layout is known, the Broyden matrix is obtained by slightly perturbing OCSRR dimensions (d, r_{ext} and e) and obtaining the values of C_p, L_p and L_{sh} from parameter extraction. This allows us to compute the initial Broyden matrix as follows:

$$\mathbf{B}^{(1)} = \begin{pmatrix} \frac{\delta L_p}{\delta r_{ext}} & \frac{\delta L_p}{\delta d} & \frac{\delta L_p}{\delta e} \\ \frac{\delta C_p}{\delta r_{ext}} & \frac{\delta C_p}{\delta d} & \frac{\delta C_p}{\delta e} \\ \frac{\delta L_{sh}}{\delta r_{ext}} & \frac{\delta L_{sh}}{\delta d} & \frac{\delta L_{sh}}{\delta e} \end{pmatrix} \tag{5}$$

Once the Broyden matrix is initiated, the algorithm can be iterated using (2), where the first error function in (3) is inferred from the extracted parameters of the first layout.

Concerning parameter extraction from the electromagnetic simulation results of a given layout, the three conditions considered are: (i) the position of the transmission zero frequency:

$$f_z = \frac{1}{2\pi}\sqrt{\frac{1}{C_p}\left(\frac{1}{L_p}+\frac{1}{L_{sh}}\right)} \tag{6}$$

(ii) the position of the reflection zero frequency (or intrinsic resonance of the OCSRR):

$$f_o = \frac{1}{2\pi}\sqrt{\frac{1}{L_p C_p}} \tag{7}$$

and (iii) the susceptance slope at f_o. All these parameters can be easily inferred from the electromagnetic simulation.

As a synthesis example, we report here the automated layout generation of an OCSRR with target values indicated in table 3.

Table 3. Circuit elements of the OCSRR-loaded line

L_{sh} (nH)	L_p (nH)	C_p (pF)
0.5	3.8	4.1

The considered substrate is the *Rogers RO3010* with thickness h = 0.254 mm and dielectric constant ε_r = 10.2. The error function (1) is obtained as follows

$$\left\|\mathbf{f}(x_f)\right\| = \sqrt{\left(1-\frac{L_p}{L_p^*}\right)^2 + \left(1-\frac{C_p}{C_p^*}\right)^2 \left(1-\frac{L_{sh}}{L_{sh}^*}\right)^2} \qquad (8)$$

and the algorithm ends when (8) is smaller than a certain predefined value. In our case, it has been found that eight iterations suffice to obtain an error function smaller than 1%. The evolution of the error function is depicted in Fig. 4.

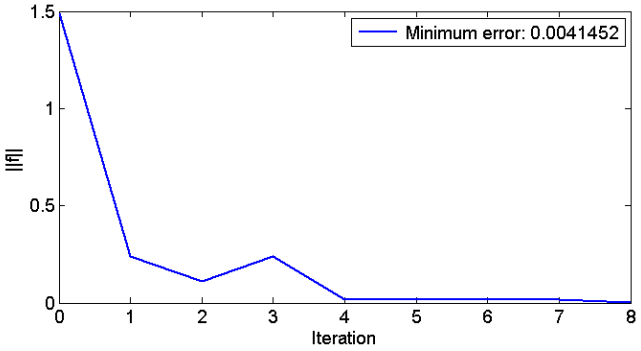

Figure 4: Evolution of the error function with the number of iterations.

The synthesis process has provided the layout depicted in Fig. 5. The geometrical variables are indicated in table 4. The target response, namely, the one that results by circuit simulation of the circuit of Fig. 2(b) with the target values, and the response obtained from (lossless) electromagnetic simulation of the generated layout, are depicted in Fig. 6. As can be seen, the agreement between the circuit (target) and electromagnetic simulation after optimization is excellent in the frequency range shown, covering a span up to twice the OCSRR intrinsic resonance frequency. However, notice that the electromagnetic simulation of the first (initial) layout, also depicted in Fig. 6, is very different, pointing out the need for the proposed synthesis algorithm.

Table 4. Geometry of the synthesized OCSRR

e (mm)	r_{ext} (mm)	c (mm)	d (mm)	Error
0.52	2.25	0.25	0.35	<1%

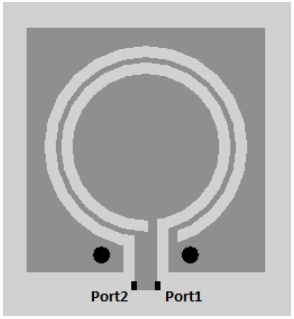

Figure 5: Final layout of the synthesized OCSRR. Dimensions are those indicated in table 4 (the ground plane is indicated in light grey).

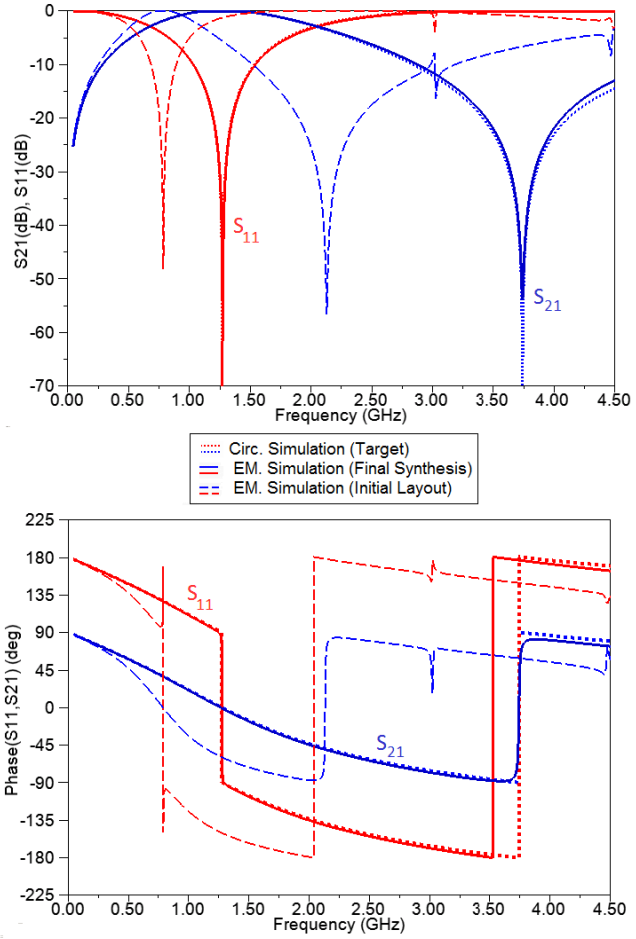

Figure 6: Comparison of the target response and electromagnetic simulation of the generated layout. (a) Magnitude; (b) Phase. The electromagnetic simulation of the initial geometry is also included for comparison purposes.

4. Discussion on the synthesis of OCSRRs

In the preceding section, the synthesis of OCSRRs has been realized by setting the value of the slot distance to c = 0.25mm. In this way, the number of geometrical and electrical variables involved in the synthesis algorithm is the same. Nevertheless, with this approach the range of implementable values of L_p, C_p and L_{sh} may be limited. Therefore, another potential approach, where none of the geometrical variables (c, d, r_{ext} and e) is set to a fixed value, is discussed next.

The idea consists on determining regions in the L_p-C_p space corresponding to implementable values of these variables for different values of the external radius r_{ext}, and considering the target value of L_{sh}. The procedure is as follows. First of all, we set r_{ext} to a certain reasonable value, and c and d to the minimum value of the available technology (c_{min}, d_{min}), and we optimize e (by means of a specific one-variable aggressive space mapping algorithm) in order to recover the target value of L_{sh}. From the resulting layout, we obtain through parameter extraction the values of L_p and C_p, corresponding to a point in the L_p-C_p space. We repeat this procedure by maintaining r_{ext} to the same value,

and setting $c = c_{min}$ and $d = d_{max}$ (the maximum allowed inter-slot distance). This gives another point in the L_p-C_p space. Next, we repeat the process for $c = c_{max}$ and $d = d_{min}$, and for $c = c_{max}$ and $d = d_{max}$, giving two additional points in the L_p-C_p space. The four points define thus a polygon in the plane L_p-C_p. It is expected that if the target value of L_p and C_p corresponds to a point within that polygon, then there exists a solution for c and d (with the considered value of r_{ext}) satisfying $c_{min} < c < c_{max}$ and $d_{min} < d < d_{max}$, and providing the required (target) values of L_p and C_p. Notice that with this procedure, we obtain a polygon in the plane L_p-C_p for a certain value of r_{ext}. The next step is to repeat this process for a different value of r_{ext}. Obviously, the larger the external radius r_{ext}, the larger the values of L_p and C_p at the four vertexes of the polygon. Thus, the criterion to determine the external radius r_{ext} is simply to choose the smallest value that provides a polygon enclosing the target value of L_p and C_p (optimum polygon). This procedure optimizes the size of the OCSRR. If the ratio between the target L_p and C_p values is too extreme, it is possible that none of the polygons contains the point associated to such pair of element values. In that case, the resonator is not synthesizable with an OCSRR.

Assuming that the target values L_p^*, C_p^* and L_{sh}^* can be physically implemented, r_{ext} is determined through the procedure detailed in the previous paragraph. A further step is required to obtain the initial values of c, d and e necessary to initiate the ASM algorithm, unless L_p^*, C_p^* coincide with any of the vertices of the smaller polygon enclosing the L_p^*-C_p^* point (in this case, the layout is already known, and, hence, no further optimization is necessary). A similar procedure to that reported in [30] for CSRR-loaded lines can be applied to determine the initial values of c, d and e (rather than determining them from existing, but not accurate enough, models, as reported in the preceding section). It is expected that the dimensions of the OCSRR after ASM optimization depend on the position of the point L_p^*, C_p^* in the optimum polygon. Namely, if the point L_p^*, C_p^* is close to a vertex, it is expected that c, d and e are similar to the values corresponding to that vertex.

The specific procedure to determine the initial layout (c, d and e) is as follows [30]: we assume that c, d and e have a linear dependence on L_p and C_p. In particular, for c we can write (identical expressions are used for the other variables):

$$c = f(L_p, C_p) = (A + BL_p)(C + DC_p) \tag{9}$$

The previous expression can be alternatively written as

$$c = f(L_p, C_p) = a_0 + a_1 L_p + a_2 C_p + a_3 L_p C_p \tag{10}$$

where the constants a_i determine the functional dependence of the initial value of c with L_p and C_p. To determine the constants, four conditions are needed. Let us consider the following error function:

$$f_{error} = \sum_{j=1}^{N_v} \left(c_j - f(L_{p_j}, C_{p_j}) \right)^2 \tag{11}$$

where the subscript j is used to differentiate between the different vertices, and hence c_j is the value of c in the vertex j, and L_{pj} and C_{pj} are the corresponding values of L_p and C_p for that vertex. We have considered a number of vertices equal to $N_v = 4$ (as mentioned before), but the formulation can be extended to a higher number of vertices. The previous error function can be written as

$$f_{error} = \sum_{j=1}^{4} c_j^2 - 2\sum_{j=1}^{4} c_j \cdot (a_0 + a_1 L_{p_j} + a_2 C_{p_j} + a_3 L_{p_j} C_{p_j}) + \\ + \sum_{j=1}^{4} (a_0 + a_1 L_{p_j} + a_2 C_{p_j} + a_3 L_{p_j} C_{p_j})^2 \tag{12}$$

To find the values of the constants a_i, we obtain the partial derivatives of the previous error function with regard to a_i and force them to be equal to zero [32] as

$$\frac{\partial f_{error}}{\partial a_i} = -2\sum_{j=1}^{4} c_j \frac{\partial f(L_{p_j}, C_{p_j})}{\partial a_i} + \\ + 2\sum_{j=1}^{4} \left[f(L_{p_j}, C_{p_j}) \frac{\partial f(L_{p_j}, C_{p_j})}{\partial a_i} \right] = 0 \tag{13}$$

for i = 1,2,3,4. Following this least-squares approach, four independent equations for the constants a_i are obtained. Such equations can be written in matrix form as:

$$\begin{pmatrix} 4 & \sum_{j=1}^{4} L_{p_j} & \sum_{j=1}^{4} C_{p_j} & \sum_{j=1}^{4} L_{p_j} C_{p_j} \\ \sum_{j=1}^{4} L_{p_j} & \sum_{j=1}^{4} L_{p_j}^2 & \sum_{j=1}^{4} L_{p_j} C_{p_j} & \sum_{j=1}^{4} L_{p_j}^2 C_{p_j} \\ \sum_{j=1}^{4} C_{p_j} & \sum_{j=1}^{4} L_{p_j} C_{p_j} & \sum_{j=1}^{4} C_{p_j}^2 & \sum_{j=1}^{4} C_{p_j}^2 L_{p_j} \\ \sum_{j=1}^{4} L_{p_j} C_{p_j} & \sum_{j=1}^{4} L_{p_j}^2 C_{p_j} & \sum_{j=1}^{4} C_{p_j}^2 L_{p_j} & \sum_{j=1}^{4} C_{p_j}^2 L_{p_j}^2 \end{pmatrix} \begin{pmatrix} a_o \\ a_1 \\ a_2 \\ a_3 \end{pmatrix} = \\ \begin{pmatrix} \sum_{j=1}^{4} c_j \\ \sum_{j=1}^{4} c_j L_{p_j} \\ \sum_{j=1}^{4} c_j C_{p_j} \\ \sum_{j=1}^{4} c_j L_{p_j} C_{p_j} \end{pmatrix} \tag{14}$$

Once the constants are obtained (solving the previous equations), the initial value of c is inferred from (10). The process is repeated for d and e, and the initial geometry necessary for the initiation of the ASM algorithm is thus obtained.

To gain insight on the previous procedure to determine the initial layout of the OCSRR, where none of the geometrical variables is a priori fixed, various polygons in the L_p-C_p plane (for different radius) have been calculated. Namely, we have set e to 0.5 mm (this gives approximately the same value L_{sh}), and we have extracted the pair of values L_p and C_p for the extreme combinations of c and d considering different external radius, r_{ext}. The results are depicted in Fig. 7. As expected the polygons roughly scale

with r_{ext}, since L_p and C_p are approximately proportional to r_{ext} for a fixed value of c and d. Notice that the polygons define a pair of roughly diagonal envelopes in the L_p-C_p plane. The region contained between both envelopes is the region of implementable values of L_p and C_p for the considered value of L_{sh}. The results also confirm that there is an optimum external radius for the OCSRR, i.e., the smaller one whose corresponding polygon encloses the target values of L_p and C_p.

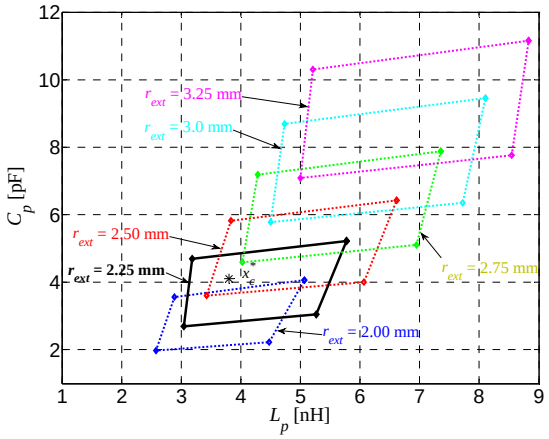

Figure 7: Polygons in the L_p-C_p space corresponding to the indicated values of the external radius. The four combinations for each polygon correspond to extreme values of c and d, that is, $c = c_{min}$, $d = d_{min}$; $c = c_{min}$, $d = d_{max}$; $c = c_{max}$, $d = d_{min}$; $c = c_{max}$, $d = d_{max}$, with $c_{min} = d_{min} = 0.15$ mm and $c_{max} = d_{max} = 0.45$ mm. In all the cases $e = 0.5$ mm corresponding to an inductance of $L_{sh} = 0.5$ nH. The optimum radius for the considered target value of L_p and C_p (indicated by the symbol *) is $r_{ext} = 2.25$ mm, and the corresponding polygon is highlighted.

Thus, the alternative approach for the determination of the initial layout of the OCSRR, rather than forcing one of the geometrical variables to have a certain value, it determines the optimum radius, and then gives the initial values of c, d and e (to be optimized in the ASM process) from a least squares approach (rather than from existing, but inaccurate, models). The application of this strategy for the synthesis of OCSRR is left for a future work.

5. Conclusions

In conclusion, we have applied ASM optimization to the synthesis of CSRR- and OCSRR-loaded microstrip lines, with special emphasis in OCSRR loaded lines. The model of a shunt connected OCSRR in microstrip technology, including the series inductance, has been considered. With this model, the OCSRR is accurately described up to frequencies much beyond its resonance frequency, and the transmission zero, typical of these particles in shunt connection, can be predicted. In the considered optimization scheme of the OCSRRs, the optimization variables have been considered to be the external radius, the distance between the slots, and the width of the metallic strip connecting the host line and the inner metallic region of the OCSRR. The width of the slots has been forced to a certain reasonable value. With this strategy, the number of geometrical variables is the same than the number of electrical variables of the circuit model, this being very convenient in ASM optimization. Concerning the initial layout, necessary to initiate the ASM synthesis process, existing models linking electrical variables and geometry for both the OCSRR and the inductive strip have been considered. We have applied this optimization approach to the synthesis of an OCSRR with certain electrical parameters. The generated layout has been simulated, and the electromagnetic response has been found to be in very good agreement with the circuit simulation of the electrical model, thus validating the model and the synthesis method.

In the last part of the paper, an alternative approach to avoid setting one geometrical variable of the OCSRR to a certain value has been discussed. With this approach, the optimum external radius that minimizes particle size can be determined, and the synthesis process involves the other three geometrical variables. Moreover, a method to determine the initial layout has been pointed out.

In summary, the results of this paper confirm that the proposed ASM techniques are efficient and useful for the synthesis of CSRRs and their open counterparts, OCSRRs.

Acknowledgements

This work has been partially supported by MICIIN-Spain (projects TEC2010-17512 METATRANSFER, TEC2010-21520-C04-01 AVANSAT, CONSOLIDER EMET CSD2008-00066, and grant AP2008-04707), *Generalitat de Catalunya* (project 2009SGR-421), and MITyC-Spain (project TSI-020100-2010-169 METASINTESIS).

References

[1] G.V. Eleftheriades and K.G. Balmain, *Negative refraction metamaterials: fundamental principles and applications*, John Wiley & Sons, Inc, New Jersey 2005.

[2] C. Caloz and T. Itoh, *Electromagnetic Metamaterials: Transmission Line Theory and Microwave Applications*, John Wiley & Sons, 2006.

[3] R. Marqués, F. Martín and M. Sorolla, *Metamaterials with negative parameters: theory, design and microwave applications*, John Wiley & Sons, Inc, New Jersey 2008.

[4] F. Martín, *Artificial Transmission Lines for RF and Microwave applications*, John Wiley & Sons, Inc, New Jersey, to be published.

[5] M.A. Antoniades and G.V. Eleftheriades, "A broadband series power divider using zero-degree metamaterial phase shifting lines", *IEEE Microwave and Wireless Components Letters*, vol. 15, pp. 808-810, Nov. 2005.

[6] H. Okabe, C. Caloz and T. Itoh, "A compact enhanced bandwidth hybrid ring using an artificial lumped element left handed transmission line section", *IEEE Trans. Microwave Theory and Techniques*, vol. 52, pp. 798-804, March 2004.

[7] G. Sisó, J. Bonache, M. Gil and F. Martín, "Application of resonant-type metamaterial transmission lines to the design of enhanced bandwidth components with compact dimensions", *Microwave and Optical Technology Letters*, vol. 50, pp. 127-134, January 2008.

[8] I.H. Lin, M. De Vincentis, C. Caloz and T. Itoh, "Arbitrary dual-band components using composite right/left handed transmission lines", *IEEE Trans. Microwave Theory and Techniques*, vol. 52, pp. 1142-1149, April 2004.

[9] A. C. Papanastasiou, G. E. Georghiou, and G. V. Eleftheriades, "A quad-band wilkinson power divider using generalized NRI transmission lines", *IEEE Microwave and Wireless Components Letters*, vol. 18, pp. 521-523, August 2008.

[10] M. Durán-Sindreu, G. Sisó, J. Bonache and F. Martín, "Planar multi-band microwave components based on the generalized composite right/left handed transmission line concept", *IEEE Transactions on Microwave Theory and Techniques*, vol. 58, no 12, pp. 3882-3891, Dec. 2010.

[11] J. Bonache, I. Gil, J. García-García, F. Martín, "Novel microstrip band pass filters based on complementary split ring resonators", *IEEE Transactions on Microwave Theory and Techniques*, vol. 54, pp. 265-271, January 2006.

[12] M. Gil, J. Bonache, J. García-García, J. Martel and F. Martín, "Composite right/left handed (CRLH) metamaterial transmission lines based on complementary split rings resonators (CSRRs) and their applications to very wide band and compact filter design", *IEEE Transactions on Microwave Theory and Techniques*, vol. 55, pp. 1296-1304, June 2007.

[13] S. Lim, C. Caloz, and T. Itoh, "Metamaterial-based electronically-controlled transmission line structure as a novel leaky-wave antenna with tunable angle and beamwidth," *IEEE Trans. Microwave Theory Techniques*, vol. 52, No. 12, pp. 2678-2690, December 2004.

[14] G. Zamora, S. Zuffanelli, F. Paredes, F. Javier Herraiz-Martínez, F. Martín, and J. Bonache, "Fundamental mode leaky-wave-antenna (LWA) using slot line and split-ring-resonator (SRR) based metamaterials", *IEEE Antennas and Wireless Propagation Letters*, accepted.

[15] A. K. Iyer and G. V. Eleftheriades. "Negative refractive index metamaterials supporting 2-D waves," in *IEEE-MTT Int'l Microwave Symp.*, vol. 2, Seattle, WA, pp. 412– 415, June 2002.

[16] A.A. Oliner, "A periodic-structure negative-refractive-index medium without resonant elements," in *URSI Digest, IEEE-AP-S USNC/URSI National Radio Science Meeting*, San Antonio, TX, pp. 41, June 2002.

[17] C. Caloz and T. Itoh. "Application of the transmission line theory of left-handed (LH) materials to the realization of a microstrip LH transmission line," *in Proc. IEEE-AP-S USNC/URSI National Radio Science Meeting*, vol. 2, San Antonio, TX, pp. 412–415, June 2002.

[18] F. Martín, F. Falcone, J. Bonache, R. Marqués and M. Sorolla, "Split ring resonator based left handed coplanar waveguide", *Appl. Phys. Lett*., vol. 83, pp. 4652-4654, December 2003.

[19] F. Falcone, T. Lopetegi, M.A.G. Laso, J.D. Baena, J. Bonache, R. Marqués, F. Martín, M. Sorolla, "Babinet principle applied to the design of metasurfaces and metamaterials", *Phys. Rev. Lett*., vol. 93, paper 197401, November 2004.

[20] M. Durán-Sindreu, A. Vélez, F. Aznar, G. Sisó, J. Bonache and F. Martín, "Application of Open Split Ring Resonators and Open Complementary Split Ring Resonators to the Synthesis of Artificial Transmission Lines and Microwave Passive Components", *IEEE Trans. Microwave Theory and Techniques*, vol. 57, pp. 3395-3403, Dec. 2009.

[21] A. Vélez, F. Aznar, M. Durán-Sindreu, J. Bonache and F. Martín, "Stop-Band and Band-Pass Filters in Coplanar Waveguide Technology Implemented by Means of Electrically Small Metamaterial-Inspired Open Resonators", *IET Microwaves, Antennas and Propagation*, vol. 4, pp. 712-716, Jun. 2010.

[22] J.D. Baena, J. Bonache, F. Martín, R. Marqués, F. Falcone, T. Lopetegi, M.A.G. Laso, J. García, I Gil, M. Flores-Portillo and M. Sorolla, "Equivalent circuit models for split ring resonators and complementary split rings resonators coupled to planar transmission lines", *IEEE Transactions on Microwave Theory and Techniques*, vol. 53, pp. 1451-1461, April 2005.

[23] M. Gil, J. Bonache, J. Selga, J. García-García, F. Martín, "Broadband resonant type metamaterial transmission lines", *IEEE Microwave and Wireless Components Letters*, vol. 17, pp. 97-99, February 2007.

[24] M. Durán-Sindreu, P. Vélez, J. Bonache and F. Martín, "Broadband Microwave Filters Based on Open Split Ring Resonators (OSRRs) and Open Complementary Split Ring Resonators (OCSRRs): improved models and design optimization", *Radioengineering*, vol. 20, pp. 775-783, Dec. 2011.

[25] P. Vélez, J. Naqui, M. Durán-Sindreu, J. Bonache, and F. Martín, "Broadband Microstrip Bandpass Filter Based on Open Complementary Split Ring Resonators", *International Journal of Antennas and Propagation*, vol. 2012, 6 pages, 2012

[26] J.W. Bandler, R.M. Biernacki, S.H. Chen, P.A. Grobelny and R.H. Hemmers, "Space mapping technique for electromagnetic optimization", *IEEE Trans. Microw. Theory Techn.*, vol. 42, pp. 2536-2544, Dec. 1994.

[27] J.W. Bandler, R.M. Biernacki, S.H. Chen, R.H. Hemmers, and K. Madsen, "Electromagnetic optimization exploiting aggressive space mapping", *IEEE Trans. Microw. Theory Techn.*, vol. 43, pp. 2874-25442882, Dec. 1995.

[28] J. W. Bandler, Q. S. Cheng, S. A. Dakroury, A. S. Mohamed, M. H. Bakr, K. Madsen, and J. Søndergaard, "Space mapping: the state of the art," *IEEE Trans. Microw. Theory Tech.*, vol. 52, pp. 337-361, Jan. 2004.

[29] C. G. Broyden, "A Class of Methods for Solving Nonlinear Simultaneous Equations", *Mathematics of Computation*, vol. 19, no. 92, pp. 577-593, Oct. 1965.

[30] J. Selga, A. Rodríguez, V.E. Boria, and F. Martín, "Synthesis of Split Rings based Artificial Transmission Lines through a New Two-Step, Fast Converging, and Robust Aggressive Space Mapping (ASM) Algorithm", *IEEE Transactions on Microwave Theory and Techniques*, vol. 61(6), pp. 2295-2308, June 2013.

[31] A. Velez, F. Aznar, J. Bonache, M.C. Velázquez-Ahumada, J. Martel and F. Martín, "Open complementary split ring resonators (OCSRRs) and their Application to Wideband CPW Band Pass Filters", *IEEE Microwave and Wireless Components Letters*, vol. 19, pp. 197-199, April 2009.

[32] D. M. Bates and D. G. Watts, Nonlinear Regression Analysis and Its Applications. New York, NY, USA: Wiley, 1998.

Design of 2D and 3D isotropic transformation media for light management

Carlos García-Meca* **and Alejandro Martínez**

Nanophotonics Technology Center,
Universitat Politècnica de València, 46022 Valencia, Spain
*corresponding author, E-mail: cargarm2@ntc.upv.es

Abstract

We present a method for designing isotropic transformation media in two and three dimensions (2D and 3D). It relies on a special kind of shape-preserving mappings based on the so-called Green Coordinates (GC). In 2D, GC-based mappings present several advantages over standard quasi-conformal mapping algorithms, such as the possibility of working with holey domains or performing multivalued transformations. In 3D, the combination of this method with a subsequent optimization algorithm enables the implementation of completely 3D transformation media with minimized anisotropy, which can be neglected for sufficiently smooth transformations. This way, the need for magnetic materials in eliminated in many situations. We illustrate the potential of the proposed method with several numerical examples.

1. Introduction

Transformation optics is currently becoming a mainstay in the design of photonic devices with advanced functionalities. Essentially, this technique provides a link between a coordinate transformation and the optical medium that would force light to follow the distortion encoded by such a transformation [1, 2]. Its use has enabled the achievement of unprecedented effects such as invisibility and other optical illusions [3, 4, 5, 6, 7]. Inspired by transformation optics, the transformational paradigm has been gradually unfolding in other areas of physics, e.g., acoustics [8, 9, 10, 11, 12], elasticity [13], quantum mechanics [14], or thermodynamics [15]. However, the price to pay for the wave-manipulation flexibility offered by this method is that general transformations are usually associated with complex media. Specifically, any distribution of inhomogeneous and anisotropic medium properties may arise from an arbitrary transformation. Even with the advent of metamaterials, it is extremely difficult to control independently all components of a certain tensorial property. For instance, constructing inhomogeneous devices with arbitrary anisotropic optical parameters that do not display undesired couplings between different polarizations is a challenging task. This fact is further complicated by the need for magnetic materials not available in nature, especially at high frequencies [16]. Although magnetic permeabilities can be artificially synthesized, their realization requires the use of resonant elements exhibiting a narrow-band response and, usually, high losses.

If we restrict ourselves to 2D transformations and propagation directions parallel to the transformation plane (say XY plane), a possible solution relies on using conformal mappings (CM), which preserve the isotropy of the original space in the XY plane [1]. Although the resulting off-plane and in-plane parameters are different, it can be shown that isotropic non-magnetic materials provide exact implementations of CM for transverse-electric waves (E-field along the z-direction) [7]. In the ray optics approximation, this is also valid for any polarization as long as the wave propagates parallel to the XY plane. When a CM mapping the original region of interest to the desired one does not exist, we can resort to quasi-conformal mappings (QCM), which restrict anisotropy to small negligible values [17]. However, quasi-conformal mappings are calculated numerically, e.g., by minimizing some functional or by solving Beltrami or inverse Laplace equations [17, 18, 19]. Apart from being numerical techniques, these methods present several disadvantages. For instance, the original domain must be simply connected and often have a rectangular shape. Moreover, multivalued mappings are not allowed.

In 3D the situation dramatically worsens. In this case, the implementation of the magnetic response associated with general anisotropic transformations cannot be avoided if the device is to work for any direction and polarization (this holds in the geometrical approximation). Even if the transformation is conformal in 2D, it cannot be implemented with all-dielectric parameters for off-plane propagation directions. The ideal solution would be to use 3D CM giving rise to isotropic media, since the synthesis of highly anisotropic 3D materials is significantly more difficult than that of isotropic materials [20, 21]. Moreover, in the optical case we can omit the magnetic properties of isotropic materials without affecting the dynamics of rays.

Nonetheless, the only existing CM in 3D are Möbius transformations (similarities and inversions on spheres), which extremely limits the range of implementable functionalities [22]. Some approaches have been proposed to simplify the medium parameters associated to 3D transformations. In [20], 2D QCM are mapped to 3D ones with revolution symmetry. Although the resulting parameters are still anisotropic, the device can be implemented with dielectric isotropic media for wavevectors without azimuthal component. However, an additional magnetic component is necessary for other directions. In [16], it was shown that wave propagation in spherically symmetric anisotropic di-

electric media can be independently engineered for each polarization, although with different functionalities. Finally, feasible realizations of different devices have been demonstrated for situations in which only propagation in specific directions is of interest [21, 23, 24]. Therefore, existing solutions still impose strong restrictions, while the anisotropy requirement remains in the general 3D case, rendering the implementation of 3D transformation media technologically challenging.

In this work, we propose the use of a special class of transformations based on GC to lift some of the above-mentioned limitations. We illustrate the potential of our proposal with several theoretical examples, including illusion-optics devices [6] and light squeezers [25, 26, 27, 28, 29]. The functionality of the studied devices is verified via numerical simulations performed with the commercial software COMSOL Multiphysics.

2. Green coordinate transformations

GC use a cage-based representation in which each point within a simplicial surface (polygon in 2D and mesh made up of triangles in 3D) is expressed as a linear combination of its vertices and faces normals [30]

$$\boldsymbol{x} = \sum_{i \in I_{\mathbb{V}}} \phi_i(\boldsymbol{x}) \boldsymbol{v}_i + \sum_{j \in I_{\mathbb{T}}} \psi_j(\boldsymbol{x}) s_j \boldsymbol{n}_j \ , \qquad (1)$$

where $\boldsymbol{v}_i$ is the i-th vertex, $\boldsymbol{n}_j$ is the outward normal to the j-th face, $s_j = 1$, and $I_{\mathbb{V}}$ and $I_{\mathbb{T}}$ are the sets of all vertices and faces, respectively (see Figure 1). A point $\boldsymbol{x}$ is univocally specified by the functions $\phi_i(\boldsymbol{x})$ and $\psi_j(\boldsymbol{x})$, known as GC (the derivation of these functions is based on Green's third identity [30]). A certain transformation $\bar{\boldsymbol{x}} = f(\boldsymbol{x})$ is achieved just by deforming the cage, that is, Eq. (1) gives the transformed points $\bar{\boldsymbol{x}}$ if we replace $\boldsymbol{v}_i$ and $\boldsymbol{n}_j$ by the vertices $\bar{\boldsymbol{v}}_i$ and normals $\bar{\boldsymbol{n}}_j$ of the deformed cage. This way, the change $\boldsymbol{v}_i \to \bar{\boldsymbol{v}}_i$ defines a mapping f for all points enclosed by the cage. The most interesting property of GC transformations is that they are least-distorting (minimize anisotropy) when the scalars s_j are also a proper function of the j-th face dimensions [30]. Thus, they are good candidates to attain quasi-isotropic transformation media. One just needs to enclose the region to be transformed by a cage and deform it as desired. All points inside the cage will follow this transformation in a low-distorting way. An additional advantage of GC is that they are based on closed analytical expressions so no meshing or numerical approximations are required [30]. Moreover, any transformation can be simply calculated as a linear combination of the precalculated coordinates as shown by Eq. (1).

3. 2D isotropic transformation media

In 2D, the transformational method based on green coordinates always produces conformal mappings at the expense of a slight deformation of the final domain. Thus, in contrast with other quasi-conformal mapping algorithms, we do not have to worry about the degree of anisotropy of the resulting optical medium, which will always be isotropic. Therefore, the application of GC-based transformations to the design of isotropic transformation media is straightforward in the 2D case. Moreover, this method has two additional advantages. First, multivalued mappings and inversions are allowed. Second, the initial domain can have any shape and even contain holes.

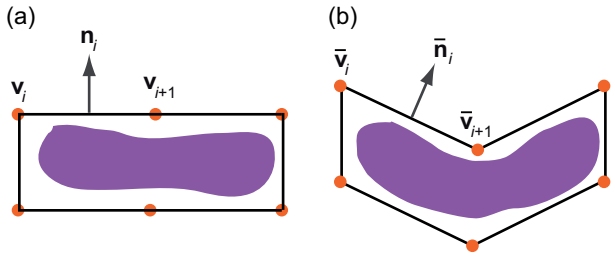

Figure 1: 2D green coordinate transformation. (a) The region to be transformed (purple) is enclosed by a cage (polygon). (b) A cage deformation ($\boldsymbol{v}_i \to \bar{\boldsymbol{v}}_i$) defines a smooth mapping for all points inside it, which follow the cage deformation in a low-distorting way.

As an example, we will illustrate this last possibility by changing the way in which the shape of a metallic scatterer affects the propagation of light. To this end, let us consider a square region containing a hole with the shape of the scatterer, e.g. a rectangle, as in Fig. 2(a). For the sake of visual clarity, we have filled this region with a chessboard pattern. It is possible to construct a polygon surrounding this region if some of its sides and vertices overlap [see Fig. 2(a)]. Now, by changing only the position of vertices $\boldsymbol{v}_7$ to $\boldsymbol{v}_{10}$, we can modify the shape of the hole without altering the outer square shape. The GC-based transformation method associates a conformal mapping with this polygon deformation for all points inside the polygon [see in Fig. 2(b)].

Using the rules of optical conformal mapping [1], we can obtain the refractive index of the isotropic device that implements this transformation, which is depicted in Fig. 2(c). A metallic object with the shape of the transformed hole surrounded by a medium with this refractive index distribution produces the same scattering (outside the medium) as the original metallic object (with the shape of the initial hole). As a result, we are producing an optical illusion; a metallic horizontal rectangle appears as a vertical one. The numerical simulations shown in Fig. 3 verify this behavior.

It is worth mentioning that the outer sides of the transformed region have been slightly curved by the transformation. However, this deformation is so small that it does not influence the performance of the device.

4. 3D isotropic transformation media

With the exception of Möbius transformations, CM are found exclusively in 2D spaces. QCM are sometimes thought of as existing only in 2D for this reason and, so far, they have been overlooked as a tool to achieve quasi-

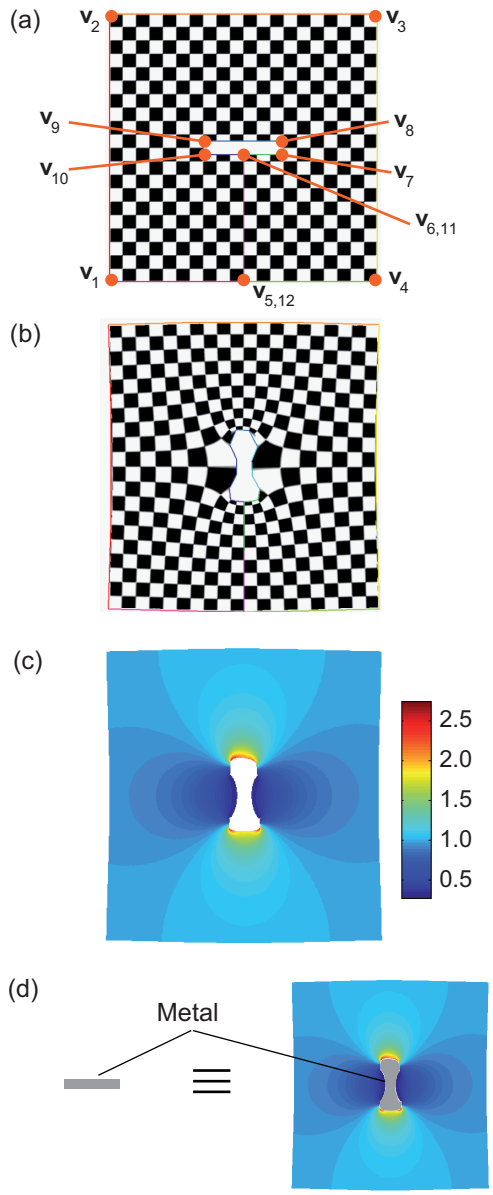

Figure 2: Application of 2D GC transformations to produce an optical illusion. (a) The region to be transformed (filled with a chessboard pattern) contains a hole an is enclosed by a polygon with some overlapping sides and vertices. (b) Transformed region, defined by the modification of the position of vertices $\boldsymbol{v}_7$ to $\boldsymbol{v}_{10}$. (c) Refractive index that implements this transformation. (d) To an external observer, a metallic object with the shape of the initial rectangular hole is equivalent to a different metallic object with the shape of the transformed hole surrounded by a medium with the previous refractive index distribution.

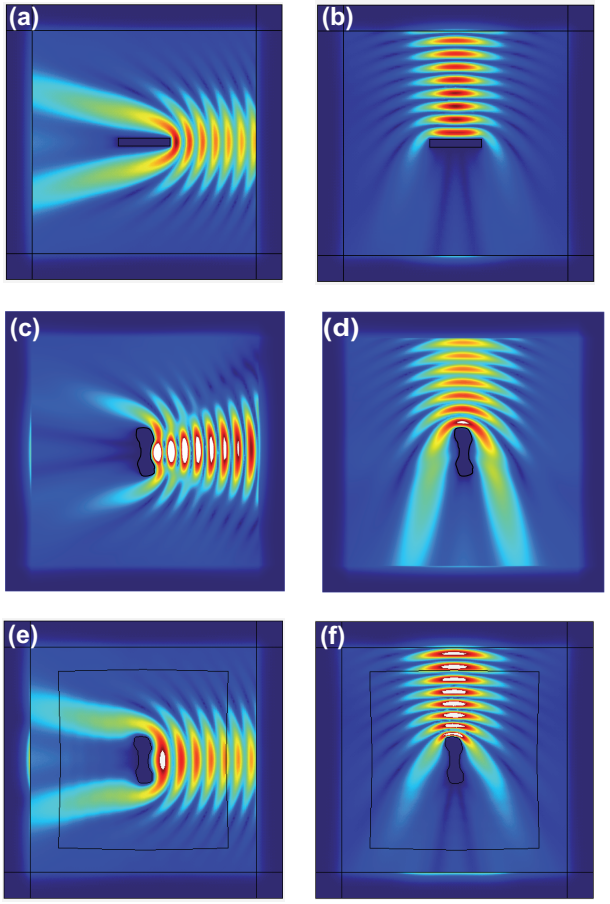

Figure 3: Simulated electric field resulting from the diffraction produced by different scatterers under the incidence of a gaussian beam impinging from the right (left column) and from the top (right column). (a,b) The scatterer is a bare metallic horizontal rectangle. (c,d) The scatterer is a vertically-oriented bare metallic object (transformed horizontal rectangle). The scattering properties of this object are clearly different from those of the metallic horizontal rectangle. (e,f) Same scatterer as in (c,d) but surrounded by the designed device. We can observe that, outside the device, the electric field is very similar to that in (a,b).

isotropic 3D transformation media. However, QCM exist in any number of dimensions and form a much larger set than conformal ones [31]. This is because, while CM transform infinitesimal spheres into (scaled and rotated) infinitesimal spheres, QCM transform spheres into ellipsoids of bounded eccentricity. The question is whether we can find 3D QCM that introduce a degree of anisotropy sufficiently low so as to be negligible in practice. Unfortunately, although GC transformations provide 3D QCM, we found that in most cases the resulting anisotropy is not low enough to be negligible. In this section, we review how this drawback was overcome in [32]. The main idea is to exploit the fact that a certain functionality can be implemented by a wide range of transformations. Thus, we can find the transformation that is closest to a conformal one through optimization and use it to implement the desired functionality. In order to measure the degree of anisotropy introduced by a certain 3D transformation, we define in analogy with the 2D case an anisotropy factor $\alpha = \max_{\forall \boldsymbol{x}}\{n_1/n_2, n_1/n_3, n_2/n_3\}$, which varies between 1 (no anisotropy) and grows with the anisotropy. Here, n_i are the principal components

of the refractive index tensor in a local Cartesian system ($n_1 > n_2 > n_3$). The refractive index tensor can be obtained from the permittivity $\epsilon^{\bar{i}\bar{j}}$ and permeability $\mu^{\bar{i}\bar{j}}$ associated with a certain transformation, which are given by $\epsilon^{\bar{i}\bar{j}} = \mu^{\bar{i}\bar{j}} = \Lambda_i^{\bar{i}}\Lambda_j^{\bar{j}}\delta^{ij}/\det(\Lambda_i^{\bar{i}})$, where $\Lambda_i^{\bar{i}}$ is the transformation Jacobian matrix (we assume that the original medium is vacuum) [2, 7].

Next, we illustrate the proposed method by describing the design of a 3D isotropic squeezer. TO-based squeezers have been extensively studied due to their simplicity and potential applications. Isotropic 2D squeezers can be easily achieved by using standard QCM algorithms [28, 29]. Unfortunately, existing 3D designs are highly anisotropic. For instance, imagine that we want to gradually compress the gray square prism shown in Figure 4, from zero compression at $z = 0$ to a compression factor F at $z = l$ (the results are independent of the length scale so we work in arbitrary units).

If we employ a linear transformation such as $\bar{x} = x(1 + az); \bar{y} = y(1 + az); \bar{z} = z$, with $a = (F - 1)/l$, a strong anisotropy is introduced. As an example, for $F = 0.57$ (reduction of the output face to one third of its initial area), $l = 2$ and $w = 1$ we obtain $\alpha = 1.81$. The corresponding values of n_i in a 3D grid covering the whole transformed volume are shown in Figure 5(d). Clearly, there is a marked discrepancy between the different components. A nice way to visualize the degree of anisotropy is to see how some small spheres within the original prism are transformed [Figure 5(a)].

As seen, the spherical shape is not preserved when using the previous linear transformation [Figure 5(b)]. Now we apply the proposed method. To do so, we surround the prism by a cage consisting of 30 vertices and 56 triangles [Figure 4(a)]. Note that the cage has a width $w_c = 1.6$, larger than w. The reason is that we found that a high distortion usually appears near the cage boundaries. Initially, we transformed the vertices using the above-mentioned linear mapping. GC are not interpolatory and it is not guaranteed that compressing the cage by a certain factor will yield a prism compression of the same factor. Actually, in this case the side of the cage output face must be compressed by a factor around 0.5 to achieve the desired value of 0.57. This GC transformation automatically reduces anisotropy to $\alpha = 1.31$. However, this is not a value low enough to be negligible. Fortunately, we can use the fact that we are only interested in having a compressed version of the field at the squeezer output, and we do not care about how the fields are transformed inside the squeezer. Thus, the only restrictions are that the shape of the input surface should not be changed by the transformation and that the transformed output surface must be a compressed version of the original one. Hence, the position of all the vertices that do not belong to these faces, as well as the squeezer height, can be optimized to minimize anisotropy. This is done through a standard Nelder-Mead algorithm [33]. It is worth mentioning that another advantage of GC is that optimizing a transformation only requires the tuning of a few variables

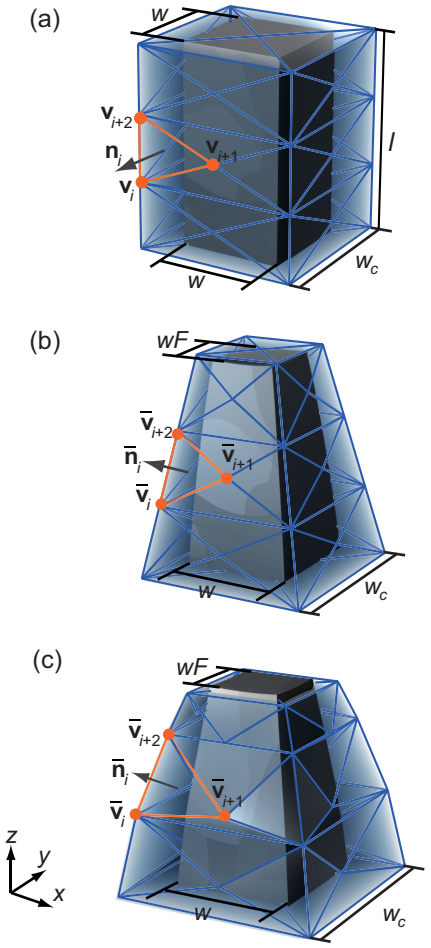

Figure 4: 3D GC transformations. (a) The region to be transformed (gray square prism in this case) is enclosed by a cage made up of triangles. A cage deformation ($\boldsymbol{v}_i \rightarrow \bar{\boldsymbol{v}}_i$) defines a smooth mapping for all prism points, which follows the cage deformation in a low-distorting way. (b) Result of a transformation in which the cage is linearly compressed. (c) Optimized cage that minimizes anisotropy and corresponding transformed prism.

(vertices positions), which completely define the mapping. Taking advantage of the symmetries, we only need to optimize 11 variables to obtain a suitable transformation of the prism [see Figure 4(c)]. The corresponding index eigenvalues are shown in Figure 5(e). They are remarkably close to each other, indicating a low anisotropy. This agrees with the fact that this mapping hardly distorts the shape of small spheres [Figure 5(c)]. In fact, a very low anisotropy factor of 1.08 is obtained after optimization. This is of the order of the values obtained in 2D QCM [17] and allows us to neglect the anisotropy. We do this by approximating the anisotropic index by an isotropic one n_{m} equal to the mean of its principal components $n_{\mathrm{m}} = (n_1 + n_2 + n_3)/3$, i.e., we take $\epsilon^{\bar{i}\bar{j}} = \mu^{\bar{i}\bar{j}} = n_{\mathrm{m}}\delta^{\bar{i}\bar{j}}$.

To verify its functionality, the designed 3D squeezer is simulated in COMSOL Multiphysics. A Gaussian beam is used as the source. Figure 6(a) shows the power flow in the

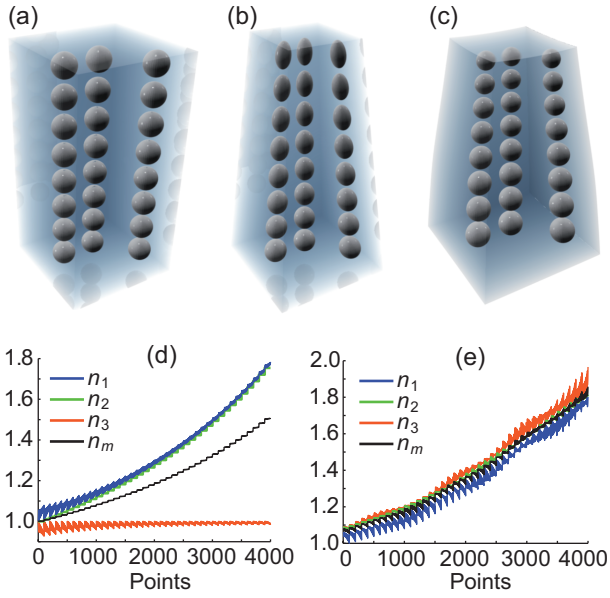

Figure 5: 3D squeezing transformations. (a) Original prism and some spherical regions within it. (b,c) Prism and spheres transformations associated with a linear mapping and the proposed 3D QCM, which preserves spherical shapes. (d,e) Refractive index corresponding to the linear and 3D QCM.

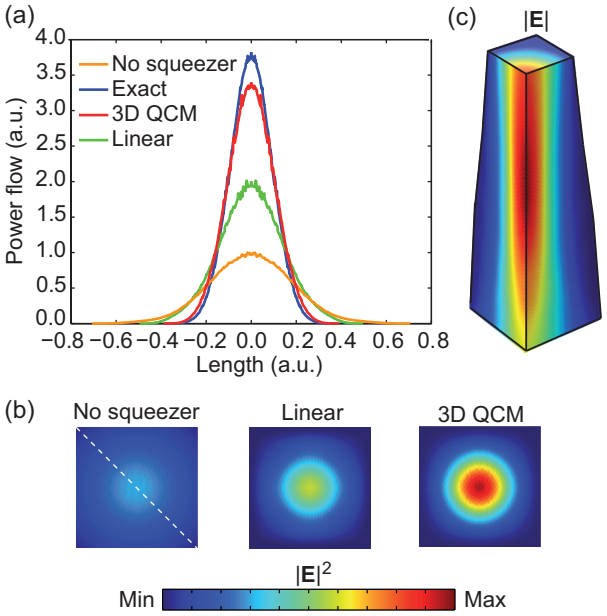

Figure 6: Squeezers performance. (a) Power flow in the propagation direction along a diagonal (dashed line in b) of the output face for the different squeezer versions and power flow of the beam after propagating a distance l in free space. (b) $|\boldsymbol{E}|^2$ distributions at the output face. (c) Beam $|\boldsymbol{E}|$-field cuts in its propagation through the GC isotropic squeezer. The wavelength is taken to be 0.15.

propagation direction along a diagonal of the output face for different cases. The power at the output of the exact anisotropic squeezer (blue) is a perfect compressed version of the beam power flow after propagating a distance l in free space (orange). Very similar results are obtained for the isotropic GC-based squeezer, confirming that neglecting the anisotropy hardly affects the squeezer performance. Moreover, almost the same results are obtained by dropping the magnetic permeability, i.e, taking $\epsilon^{\bar{i}\bar{j}} = n_{\rm m}^2 \delta^{\bar{i}\bar{j}}$ and $\mu^{\bar{i}\bar{j}} = \delta^{\bar{i}\bar{j}}$ (red). However, if we approximate the index of the linear-transformed squeezer by the mean of its eigenvalues, its performance is significantly deteriorated (green). The field profiles at the output face for the free-space case and the GC and linear isotropic squeezers are shown in Figure 6(b). Different cuts of the $|\boldsymbol{E}|$-field along its propagation through the GC isotropic squeezer are depicted in Figure 6(c).

5. Conclusions

In conclusion, we have shown that transformations based on Green coordinates are a powerful tool for designing isotropic transformation media. In 2D, this kind of transformations presents several advantages over standard quasi-conformal mapping algorithms, such as the possibility of performing multivalued transformations or working with holey domains. As an example, we have designed an illusion-optics device that changes the way in which the shape of a metallic scatterer affects the propagation of light. In 3D, the combination of GC transformations and a suitable optimization process leads to a significant reduction of the typical anisotropy associated with 3D transformation media. In the case of sufficiently smooth transformations the anisotropy can be minimized to negligible values. Full 3D isotropy has an important implication for electromagnetic transformation media, whose magnetic properties can be dropped without affecting the dynamics of rays. It is worth mentioning that the anisotropy arising from abrupt transformations might not be negligible. In those situations, and depending on the specific transformation, other kind of mappings not based on GC [34], as well as more advanced optimization algorithms, could provide even better results. In any case, we can conclude that the use of special 3D QCM techniques could become a key enabling methodology to achieve practically realizable 3D transformation media.

Acknowledgement

The authors acknowledge support from projects Consolider EMET (CSD2008-00066), TEC2011-28664-C02-02, and GVA ACOMP/2013/013.

References

[1] U. Leonhardt, Optical conformal mapping, *Science* 312: 1777–1780, 2006.

[2] J. B. Pendry, D. Schurig, D. R. Smith, Controlling electromagnetic fields, *Science* 312: 1780–1782, 2006.

[3] D. Schurig, J. J. Mock, B. J. Justice, S. A. Cummer, J. B. Pendry, A. F. Starr, D. R. Smith, Optical conformal mapping, *Science* 314: 977–980, 2006.

[4] A. Greenleaf, Y. Kurylev, M. Lassas, G. Uhlmann, Electromagnetic Wormholes and Virtual Magnetic Monopoles from Metamaterials, *Phys. Rev. Lett.* 99: 183901, 2007.

[5] V. M. Shalaev, Transforming Light, *Science* 322: 384–386, 2008.

[6] H. Chen, C. T. Chan, P. Sheng, Transformation optics and metamaterials *Nature Mater.* 9: 387–396, 2010.

[7] U. Leonhardt, T. Philbin, *Geometry and light. The science of invisibility*, Dover Publications, Mineola, New York, 2010.

[8] S. A. Cummer, D. Schurig, One path to acoustic cloaking, *New J. Phys.* 9: 45, 2007.

[9] H. Chen, C. T. Chan, Acoustic cloaking in three dimensions using acoustic metamaterials, *Appl. Phys. Lett.* 91: 183518, 2007.

[10] A. N. Norris, Acoustic metafluids, *J. Acoust. Soc. Am.* 125: 839, 2009.

[11] H. Chen, C. T., Chan Acoustic cloaking and transformation acoustics, *J. Phys. D: Appl. Phys.* 43: 113001, 2010.

[12] C. García-Meca, S. Carloni, C. Barceló, G. Jannes, J. Sánchez-Dehesa, A. & Martínez, Analogue transformations in physics and their application to acoustics, *Sci. Rep.* 3: 2009, 2013.

[13] A. N. Norris, A. L. Shuvalov, Elastic cloaking theory, *Wave Motion* 48: 525 (2011).

[14] S. Zhang, D. A. Genov, C. Sun, X. Zhang, Cloaking of Matter Waves., *Phys. Rev. Lett.* 100: 123002, 2008.

[15] S. Guenneau, C. Amra, D. Veynante, Transformation thermodynamics: cloaking and concentrating heat flux, *Opt. Express* 20: 8207, 2012.

[16] A. J. Danner, T. Tyc, U. Leonhardt, Controlling birefringence in dielectrics, *Nature Photon.* 5: 357, 2011.

[17] J. Li, J. B. Pendry, Hiding under the Carpet: A New Strategy for Cloaking, *Phys. Rev. Lett.* 101: 203901, 2008.

[18] N. I. Landy, W. J. Padilla, Guiding light with conformal transformations, *Opt. Express* 17: 14872–14879, 2009.

[19] Z. Chang, X. Zhou, J. Hu, G. Hu, Design method for quasi-isotropic transformation materials based on inverse Laplaces equation with sliding boundaries, *Opt. Express* 18: 6089–6096, 2010.

[20] N. I. Landy, N. Kundtz, D. R. Smith, Designing Three-Dimensional Transformation Optical Media Using Quasiconformal Coordinate Transformations, *Phys. Rev. Lett.* 105: 193902, 2010.

[21] Y. Urzhumov, N. Landy, D. R. Smith, Isotropic-medium three-dimensional cloaks for acoustic and electromagnetic waves, *J. Appl. Phys.* 111: 053105, 2012.

[22] D. E. Blair, *Inversion theory and conformal mapping*, American Mathematical Society, Providence, RI, 2000.

[23] H. Chen, B. Zheng, Broadband polygonal invisibility cloak for visible light, *Sci. Rep.* 2: 255, 2012.

[24] N. Landy, D. R. Smith, A full-parameter unidirectional metamaterial cloak for microwaves, *Nature Mater.* 12: 25, 2013.

[25] M. Rahm, D. Schurig, D. A. Roberts, S. A. Cummer, D. R. Smith, J. B. Pendry, Design of electromagnetic cloaks and concentrators using form-invariant coordinate transformations of Maxwell's equations, *Photon. Nanostruct. Fundam. Appl.* 6: 87, 2008.

[26] M. Rahm, D. A. Roberts, J. B. Pendry, D. R. Smith, Transformation-optical design of adaptive beam bends and beam expanders, *Opt. Express* 16: 11555–11567, 2008.

[27] M. Schmiele, V. S. Varma, C. Rockstuhl, F. Lederer, Designing optical elements from isotropic materials by using transformation optics, *Phys. Rev. A* 81: 033837, 2010.

[28] C. García-Meca, M. M. Tung, J. V. Galán, R. Ortuño, F. J. Rodríguez-Fortuño, J. Martí, A. & Martínez, Squeezing and expanding light without reflections via transformation optics, *Opt. Express* 19: 3562, 2011.

[29] D. Liu, L. H. Gabrielli, M. Lipson, S. G. Johnson, Transformation inverse design, *Opt. Express* 21: 14223, 2013.

[30] Y. Lipman, D. Levin, D. Cohen-Or, Green Coordinates, *ACM Trans. Graph.* 27: 78, 2008.

[31] J. Heinonen, What is a quasiconformal mapping, *Notices Amer. Math. Soc.* 53: 1334, 2006.

[32] C. García-Meca, R. Ortuño, J. Martí, A. & Martínez, Full three-dimensional isotropic transformation media, *New J. Phys.* 16: 023030, 2014.

[33] J. A. Nelder, R. A. Mead, Simplex Method for Function Minimization, *Comput. J.* 7: 308, 1965.

[34] G.-P. Paill, P. Poulin, As-conformal-as-possible discrete volumetric mapping, *Comput. Graph.* 36: 427–433, 2012.

Photonic Crystals (Theory and Applications)

A Band Structure Calculation Method for One-Dimensional Photonic Crystals Based on Time Integration and Matrix-Exponential Decomposition

Xiao-Xing Su[1]*, Chuanzeng Zhang[2] and Yue-Sheng Wang[3]

[1]School of Electronic and Information Engineering, Beijing Jiaotong University, Beijing 100044, China
[2]Department of Civil Engineering, University of Siegen, D-57068 Siegen, Germany
[3] Institute of Engineering Mechanics, Beijing Jiaotong University, Beijing 100044, China
*Corresponding author, E-mail: xxsu@bjtu.edu.cn

Abstract

By incorporating the Floquet-Bloch boundary conditions of the periodic media into a time integration scheme and matrix-exponential decomposition technique, a time-domain method for calculating the band structure of one-dimensional (1D) photonic crystals is proposed in this paper. The mathematical details are given, and the numerical examples, which are used to verify the correctness of the proposed method and to explore the time-stability properties of this method, are presented. The numerical results show that, although the proposed method is still conditionally stable, it is more stable than the conventional finite difference time-domain (FDTD) method. The minimal time-step with which the proposed method runs stably can be much smaller than the Courant-Friedrichs-Lewy lower bound in 1D case.

1. Introduction

Photonic crystals (PCs) [1] are a kind of composite materials with periodic spatial modulation of the refractive index. The most attractive property of PCs is the possibility of having complete band gaps, within the wavelength regions of which the lights are totally forbidden in all directions. The band structure calculation is therefore an important aspect of the theoretical studies of PCs, and the finite difference time-domain (FDTD) method [2-4] is widely used. Since the pioneer work of Yee [5] in 1966, the FDTD method has gained general popularity not only in electromagnetics and optics, but also in many other disciplines, such as acoustics and quantum mechanics. However, a notable disadvantage of the conventional FDTD method is the conditional stability, which requires the time-step used in the method should not be bigger than the lower bound predicted by the Courant-Friedrichs-Lewy (CFL) stability condition [6].

A variety of new time-domain methods trying to overcome the stability difficulty of the conventional FDTD method had been proposed in recent decades, such as the alternating-direction implicit (ADI) FDTD method [7] and some kinds of operator or time-step splitting methods [8-12]. In one typical kind of operator splitting methods [8-11], based on the time-domain integration, the transfer operator of the field evolution is written as an operator- (or matrix-) exponential. And to expedite the computational efficiency, the exponential may be approximated by splitting the operator (or matrix) acting as the index into several sub-ones. Kole et al [8,9] had proposed an operator splitting method which is unconditionally stable under perfect conductor boundary conditions. In this method, the matrix-exponential characterizing the field evolution is efficiently approximated by using Suzuki's matrix-exponential decomposition theory [13,14]. Based on Kole's time integration formulations, Faragó et al [15] established a uniform theoretical framework of several existing time-domain methods under perfect conductor boundary conditions.

Although Kole's method had been applied to the photonic band gap calculations [8,9], a big-sized super-cell should be chosen as the modeled domain to avoid the negative influence of perfect conductor boundary conditions. Hence, the calculation will not be as efficient as a single-cell-based method developed through the application of the Floquet-Bloch boundary conditions [1] for the periodic media. In this paper, by incorporating the Floquet-Bloch boundary conditions into the basic procedures of Kole's method (time integration and Suzuki's matrix-exponential decomposition), a time-domain method for calculating the band structure of one-dimensional (1D) PCs is proposed. The numerical results show that, although the proposed method is still conditionally stable, the time-step with which the method runs stably can be much smaller than the CFL lower bound. The rest of this paper is organized as follows. To make our presentation more clear and self-contained, the time integration formulations under perfect conductor boundary conditions and the matrix-exponential decomposition technique are introduced in Secs. 2 and 3, respectively. Then, the idea of our method is detailed in Sec. 4, which includes the derivations demonstrating how the Floquet-Bloch boundary conditions are incorporated into the time integration and matrix-exponential decomposition procedures. In Sec. 5, the numerical examples showing the correctness and time stability

properties of the proposed method are presented. And at last, Sec. 6 concludes the present paper.

2. Time integration formulations under perfect conductor boundary conditions

Assume that a 1D electromagnetic wave propagates along the *x* axis. The wave is in fact transverse-electric-magnetic (TEM) and can be decoupled into two independent and equivalent linearly polarized modes. We only consider the mode with the wave equations written as:

$$\frac{\partial H_y}{\partial t}=\frac{1}{\mu}\frac{\partial E_z}{\partial x}, \tag{1a}$$

$$\frac{\partial E_z}{\partial t}=\frac{1}{\varepsilon}\frac{\partial H_y}{\partial x}, \tag{1b}$$

where E and H denote the electric and magnetic fields, respectively; ε and μ are the electric permittivity and magnetic permeability of the material, respectively.

Substituting $X_y=\sqrt{\mu}H_y$ and $Y_z=\sqrt{\varepsilon}E_z$ into Eqs. (1a) and (1b) yields:

$$\frac{\partial X_y}{\partial t}=\frac{1}{\sqrt{\mu}}\frac{\partial}{\partial x}\left(\frac{Y_z}{\sqrt{\varepsilon}}\right), \tag{2a}$$

$$\frac{\partial Y_z}{\partial t}=\frac{1}{\sqrt{\varepsilon}}\frac{\partial}{\partial x}\left(\frac{X_y}{\sqrt{\mu}}\right). \tag{2b}$$

Fig. 1 shows the spatial sampling pattern of the field components within the modeled domain (with the length T), at both ends of which perfect conductor boundary conditions satisfies (i.e. the field vanishes on the boundaries). The whole length is equally divided into N spatial intervals, where N is an even number; δ is the spatial interval satisfying $(N/2)\delta=\mathrm{T}$; and X_y, Y_z are sampled at the even- and odd-numbered points, respectively.

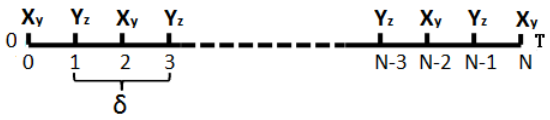

Fig. 1 Spatial sampling pattern within the modeled domain

Applying the second-ordered central difference to the right part of Eqs. (2a) and (2b), we obtain:

$$\frac{\partial X_y^i(t)}{\partial t}=\frac{1}{\delta\sqrt{\mu^i}}\frac{\partial}{\partial x}\left[\frac{Y_z^{i+1}(t)}{\sqrt{\varepsilon^{i+1}}}-\frac{Y_z^{i-1}(t)}{\sqrt{\varepsilon^{i-1}}}\right],\ i=2,\ldots,N\text{-}2, \tag{3a}$$

$$\frac{\partial Y_z^j(t)}{\partial t}=\frac{1}{\delta\sqrt{\varepsilon^j}}\frac{\partial}{\partial x}\left[\frac{X_y^{j+1}(t)}{\sqrt{\mu^{j+1}}}-\frac{X_y^{j-1}(t)}{\sqrt{\mu^{j-1}}}\right],\ j=1,3,\ldots,N\text{-}1, \tag{3b}$$

where the superscripts denote the sampling positions (e.g. $i\to i(\delta/2)$). By combining Eq. (3) with the perfect conductor boundary conditions $X_y^0(t)=0$ and $X_y^N(t)=0$, we obtain the following differential equation with a compact matrix form:

$$\frac{d\boldsymbol{\Psi}}{dt}=\mathbf{H}\boldsymbol{\Psi}\cdot \tag{4}$$

Here, the column vector $\boldsymbol{\Psi}$ is defined as:

$$\boldsymbol{\Psi}(t)=\begin{bmatrix}X_y^0(t)\\ Y_z^1(t)\\ \vdots\\ \vdots\\ Y_z^{N-1}(t)\\ X_y^N(t)\end{bmatrix}, \tag{5}$$

and $\mathbf{H}$ is a sparse matrix with the following form:

$$\mathbf{H}=\begin{bmatrix}
0 & \beta_{0,1} & 0 & \cdots & \cdots & \cdots & \cdots & 0 & 0\\
-\beta_{0,1} & 0 & \beta_{2,1} & 0 & \cdots & \cdots & \cdots & \cdots & \cdots\\
0 & -\beta_{2,1} & 0 & \beta_{2,3} & 0 & \cdots & \cdots & \cdots & \cdots\\
\cdots & \cdots & \cdots & \cdots & \cdots & \cdots & \cdots & \cdots & \cdots\\
\cdots & \cdots & 0 & -\beta_{i-1,i} & 0 & \beta_{i+1,i} & 0 & \cdots & \cdots\\
\cdots & \cdots & \cdots & 0 & -\beta_{i+1,i} & 0 & \beta_{i+1,i+2} & 0 & \cdots\\
\cdots & \cdots & \cdots & \cdots & \cdots & \cdots & \cdots & \cdots & \cdots\\
\cdots & \cdots & \cdots & \cdots & \cdots & \cdots & -\beta_{N-2,N-1} & 0 & \beta_{N,N-1}\\
0 & 0 & \cdots & \cdots & \cdots & \cdots & 0 & -\beta_{N,N-1} & 0
\end{bmatrix}, \tag{6}$$

where $\beta_{i,j}=1/\left(\delta\sqrt{\mu_i\varepsilon_j}\right)$. The non-zero elements of $\mathbf{H}$ appear only near the diagonal. The exact time-integration solution of Eq. (4) is

$$\boldsymbol{\Psi}(t)=e^{\int_{t_0}^{t}\mathbf{H}dt}\,(t_0)=e^{(t-t_0)\mathbf{H}}\,(t_0), \tag{7}$$

implying a time-stepping scheme for solving the field evolution within the modeled domain: $\boldsymbol{\Psi}(0)\to(\tau)\to(n\tau)\to\boldsymbol{\Psi}((n+1)\tau)\to\cdots$.

$\mathbf{H}$ is a skew-symmetric matrix satisfying $\mathbf{H}^{\mathrm{T}}=-\mathbf{H}$ with T denoting the transposition operation. It is therefore not difficult to prove that $|\boldsymbol{\Psi}(t)|^2$ remains constant with the time evolution. Hence, the time-stepping scheme is unconditionally stable. Despite the sparsity of $\mathbf{H}$, $e^{\tau\mathbf{H}}$ may be a full matrix due to the exponentiation computation involved. The matrix-vector multiplication $e^{\tau\mathbf{H}}\boldsymbol{\Psi}$ performed in each time-step may be very time-consuming, if the multiplication is performed directly and the spatial sampling is dense enough.

3. Matrix-Exponential Decomposition

To expedite the efficiency of the matrix-vector multiplication in each time-step, an approximation method for calculating the matrix-exponential $e^{\tau\mathbf{H}}$ was adopted by Kole et al, based on Suzuki's matrix-exponential decomposition theory [13,14]. First, the matrix H is split into the sum of a number of other matrixes:

$$\mathbf{H}=\mathbf{H}_1+\mathbf{H}_2+\cdots+\mathbf{H}_p\cdot \tag{8}$$

Then, with different-ordered accuracy of τ, $e^{\tau\mathbf{H}}$ is approximated in the following recursive manner:

first order: $$\mathbf{U}_1(\tau)=e^{\tau\mathbf{H}_1}\cdot e^{\tau\mathbf{H}_2}\cdots\cdot e^{\tau\mathbf{H}_p}\ , \tag{9a}$$

second order:

$$\mathbf{U}_2(\tau)=e^{\tau\mathbf{H}_1/2}\cdot e^{\tau\mathbf{H}_2/2}\cdots\cdot e^{\tau\mathbf{H}_p}\cdots\cdot e^{\tau\mathbf{H}_2/2}\cdot e^{\tau\mathbf{H}_1/2}, \tag{9b}$$

fourth order:

$$\mathbf{U}_4(\tau)=\mathbf{U}_2(a\tau)\cdot\mathbf{U}_2(a\tau)\cdot\mathbf{U}_2[(1-4a)\tau]\cdot\mathbf{U}_2(a\tau)\cdot\mathbf{U}_2(a\tau), \tag{9c}$$

……

where $a = \dfrac{1}{4-\sqrt[3]{4}}$. The matrix **H** defined in Eq. (6) can be split as $\mathbf{H}=\mathbf{H}_1+\mathbf{H}_2$, where

$$\mathbf{H}_1 = \begin{bmatrix} 0 & \beta_{0,1} & \cdots & \cdots & \cdots & \cdots & \cdots & \cdots & \cdots \\ -\beta_{0,1} & 0 & \cdots & \cdots & \cdots & \cdots & \cdots & \cdots & \cdots \\ 0 & 0 & 0 & \beta_{2,3} & \cdots & \cdots & \cdots & \cdots & \cdots \\ \cdots & \cdots & -\beta_{2,3} & 0 & \cdots & \cdots & \cdots & \cdots & \cdots \\ \cdots & \cdots & \cdots & \cdots & \cdots & \cdots & \cdots & \cdots & \cdots \\ \cdots & \cdots & \cdots & \cdots & \cdots & \cdots & \cdots & \cdots & \cdots \\ \cdots & \cdots & \cdots & \cdots & \cdots & \cdots & 0 & \beta_{N-2,N-1} & \cdots \\ \cdots & \cdots & \cdots & \cdots & \cdots & \cdots & -\beta_{N-2,N-1} & 0 & 0 \\ \cdots & \cdots & \cdots & \cdots & \cdots & \cdots & \cdots & 0 & 0 \end{bmatrix}, \tag{10a}$$

and

$$\mathbf{H}_2 = \begin{bmatrix} 0 & 0 & \cdots & \cdots & \cdots & \cdots & \cdots & \cdots & \cdots \\ 0 & 0 & \beta_{2,1} & \cdots & \cdots & \cdots & \cdots & \cdots & \cdots \\ 0 & -\beta_{2,1} & 0 & 0 & \cdots & \cdots & \cdots & \cdots & \cdots \\ \cdots & \cdots & 0 & 0 & \beta_{4,3} & \cdots & \cdots & \cdots & \cdots \\ \cdots & \cdots & \cdots & -\beta_{4,3} & 0 & \cdots & \cdots & \cdots & \cdots \\ \cdots & \cdots & \cdots & \cdots & \cdots & \cdots & \cdots & \cdots & \cdots \\ \cdots & \cdots & \cdots & \cdots & \cdots & \cdots & \cdots & \cdots & \cdots \\ \cdots & \cdots & \cdots & \cdots & \cdots & \cdots & \cdots & 0 & \beta_{N,N-1} \\ \cdots & \cdots & \cdots & \cdots & \cdots & \cdots & \cdots & -\beta_{N,N-1} & 0 \end{bmatrix}. \tag{10b}$$

$\mathbf{H}_1$ and $\mathbf{H}_2$ are both formed by cascading the 2×2 matrixes with the form $\begin{bmatrix} 0 & \alpha \\ -\alpha & 0 \end{bmatrix}$ along the diagonal. Therefore, according to the matrix-exponential theory [16], $e^{r\mathbf{H}_1}$ and $e^{r\mathbf{H}_2}$ are both sparse matrixes formed by diagonally cascading the exponentials of these 2×2 matrixes calculated exactly as:

$$e^{\begin{bmatrix} 0 & \alpha \\ -\alpha & 0 \end{bmatrix}} = \begin{bmatrix} \cos\alpha & \sin\alpha \\ -\sin\alpha & \cos\alpha \end{bmatrix}. \tag{11}$$

The multiplication between a sparse matrix of this kind and a column vector can be reduced to a series of multiplications between a 2×2 matrix and a 2×1 sub-vector.

By using the decompositions shown in Eq. (9), the multiplication between a non-sparse matrix and a column vector is reduced to a series of multiplications between a sparse matrix and a column vector. The total efficiency can therefore be improved. Because the matrixes $\mathbf{H}_1$ and $\mathbf{H}_2$ are both skew-symmetric, the stepping scheme with the matrix-exponential decomposition approximation still remains unconditionally stable.

4. Incorporation of Floquet-Bloch Boundary Conditions

Let's consider the case of an 1D periodic medium. The modeled domain shown in Fig. 1 now represents one repeating periodicity of the medium. For the sampling points inside the domain, Eqs. (3a) or (3b) still hold; and at the two boundaries, the equations with the same form of Eq. (3a) hold, if the spatial sampling is extended outside the modeled domain. We therefore obtain:

$$\frac{\partial X_y^i(t)}{\partial t} = \frac{1}{\delta\sqrt{\mu^i}}\frac{\partial}{\partial x}\left[\frac{Y_z^{i+1}(t)}{\sqrt{\varepsilon^{i+1}}} - \frac{Y_z^{i-1}(t)}{\sqrt{\varepsilon^{i-1}}}\right], \quad i=0,2,\ldots,N, \tag{12a}$$

$$\frac{\partial Y_z^j(t)}{\partial t} = \frac{1}{\delta\sqrt{\varepsilon^j}}\frac{\partial}{\partial x}\left[\frac{X_y^{j+1}(t)}{\sqrt{\mu^{j+1}}} - \frac{X_y^{j-1}(t)}{\sqrt{\mu^{j-1}}}\right], \quad j=1,3,\ldots,N\text{-}1. \tag{12b}$$

$Y_z^{-1}(t)$ and $Y_z^{N+1}(t)$, which appear on the right side of Eq. (12a) when i=0 and i=N+1, respectively, are sampled outside the modeled domain. In terms of the Floquet-Bloch theorem, they can be evaluated as

$$Y_z^{-1}(t) = Y_z^{N-1}(t)e^{-jk_xT} \tag{13a}$$

$$Y_z^{N+1}(t) = Y_z^1(t)e^{jk_xT} \tag{13b}$$

where $j=\sqrt{-1}$; and k_x is the Bloch wave number.

Eqs. (12) and (13) can also be rewritten together as a compact matrix form of Eq. (4). But now the matrix **H** is defined as:

$$\mathbf{H} = \begin{bmatrix} 0 & \beta_{0,1} & 0 & \cdots & \cdots & \cdots & 0 & -e^{-jk_xT}\beta_{0,N-1} & 0 \\ -\beta_{0,1} & 0 & \beta_{2,1} & 0 & \cdots & \cdots & \cdots & \cdots & \cdots \\ 0 & -\beta_{2,1} & 0 & \beta_{2,3} & 0 & \cdots & \cdots & \cdots & \cdots \\ \cdots & \cdots & \cdots & \cdots & \cdots & \cdots & \cdots & \cdots & \cdots \\ \cdots & \cdots & 0 & -\beta_{i-1,i} & 0 & \beta_{i+1,i} & 0 & \cdots & \cdots \\ \cdots & \cdots & \cdots & 0 & -\beta_{i+1,i} & 0 & \beta_{i+1,i+2} & 0 & \cdots \\ \cdots & \cdots & \cdots & \cdots & \cdots & \cdots & \cdots & \cdots & \cdots \\ \cdots & \cdots & \cdots & \cdots & \cdots & \cdots & -\beta_{N-2,N-1} & 0 & \beta_{N,N-1} \\ 0 & e^{jk_xT}\beta_{N,1} & 0 & \cdots & \cdots & \cdots & 0 & -\beta_{N,N-1} & 0 \end{bmatrix}, \tag{14}$$

Therefore, with the exact time integration, the field evolution can also be solved with a time-stepping scheme under Floquet-Bloch boundary conditions. However, now the matrix **H** is not skew-symmetric, so the new method may not be unconditionally stable.

Let's explore the feasibility of an matrix-exponential decomposition scheme to improve the calculation efficiency. It is noticed that the matrix **H** defined by Eq. (14) can be decomposed into the sum of three sparse matrixes:

$$\mathbf{H} = \mathbf{H}_1 + \mathbf{H}_2 + \mathbf{H}_3, \tag{15}$$

where $\mathbf{H}_1$ and $\mathbf{H}_2$ are the same as the ones defined by Eqs. (10a) and (10b), respectively; and $\mathbf{H}_3$ is defined as:

$$\mathbf{H}_3 = \begin{bmatrix} 0 & 0 & \cdots & \cdots & \cdots & \cdots & 0 & -e^{-jk_xT}\beta_{0,N-1} & 0 \\ 0 & 0 & \cdots & \cdots & \cdots & \cdots & \cdots & \cdots & \cdots \\ \cdots & \cdots & \cdots & \cdots & \cdots & \cdots & \cdots & \cdots & \cdots \\ \cdots & \cdots & \cdots & \cdots & \cdots & \cdots & \cdots & \cdots & \cdots \\ \cdots & \cdots & \cdots & \cdots & \cdots & \cdots & \cdots & \cdots & \cdots \\ \cdots & \cdots & \cdots & \cdots & \cdots & \cdots & \cdots & \cdots & \cdots \\ \cdots & \cdots & \cdots & \cdots & \cdots & \cdots & \cdots & \cdots & \cdots \\ \cdots & \cdots & \cdots & \cdots & \cdots & \cdots & \cdots & \cdots & \cdots \\ 0 & e^{jk_xT}\beta_{N,1} & 0 & \cdots & \cdots & \cdots & 0 & \cdots & 0 \end{bmatrix}. \tag{16}$$

The matrix $\mathbf{H}_3$ in fact embodies the introduction of the Floquet-Bloch boundary conditions. There are only two non-zero elements in $\mathbf{H}_3$ ($\mathbf{H}_3(0,N\text{-}1)$ and $\mathbf{H}_3(N,1)$). It is not difficult to prove that $\mathbf{H}_3^n = \mathbf{0}$ when $n \geq 2$. Then, using the Taylor's series definition of the matrix exponentials [16]:

$$e^{\boldsymbol{A}} = \mathbf{I} + \sum_{n=1}^{\infty}\frac{\boldsymbol{A}^n}{n!}, \tag{17}$$

where $\boldsymbol{A}$ is an arbitrary square matrix and **I** the unit matrix, we arrive at an exact expression of the matrix $e^{r\mathbf{H}_3}$:

$$e^{\tau \mathbf{H}_3} = \mathbf{I} + \tau \mathbf{H}_3 . \tag{18}$$

Therefore, $e^{\tau \mathbf{H}_3}$ is also a sparse matrix, and has a very simple form. The product of this matrix and a column vector $\boldsymbol{\Psi}$ is simply:

$$e^{\tau \mathbf{H}_3}\boldsymbol{\Psi} = \begin{bmatrix} \Psi_0 - \tau e^{-jk_x T}\beta_{0,N-1}\Psi_{N-1} \\ \Psi_1 \\ \vdots \\ \vdots \\ \Psi_{N-1} \\ \tau e^{jk_x T}\beta_{N,1}\Psi_1 + \Psi_N \end{bmatrix}. \tag{19}$$

The calculations are only needed for the first and last vector elements, so the computational complexity is obviously trivial.

Therefore, by splitting the matrix **H** into three components shown in Eq. (15), the Floquet-Bloch boundary conditions can be incorporated into Suzuki's matrix-exponential decomposition schemes of Eq. (9), which are used to expedite the efficiency of the matrix-vector multiplication during the time-stepping process. And moreover, no evident increase of the total computational complexity is brought about by introducing the matrix $\mathbf{H}_3$.

5. Numerical results and discussion

We give the following numerical examples to verify the correctness of the proposed method, and to explore the time-stability properties of this method as well. The fourth-ordered approximation (Eq. (9c)) is used in the proposed method. Fig. 2 shows the 1D PC model formed by alternating layers of materials A and B and the modeled one repeating periodicity delimited by the dashed lines. Without loss of generality, we assume that $\varepsilon_B = 1$, $\mu_B = 1$ and the repeating periodicity T=1. The filling fraction is defined as the ratio between the length of the layer A and the whole periodicity T.

To characterize the time stability of the proposed method, we define a dimensionless parameter γ relating the time-step Δt and the spatial interval δ:

$$\Delta t = \frac{\delta}{\gamma c_{\max}}, \tag{20}$$

where $c_{\max}=\max\{c_A, c_B\}$ ($c_A = 1/\left(\sqrt{\varepsilon_A \mu_A}\right)$ and $c_B = 1/\left(\sqrt{\varepsilon_B \mu_B}\right)$ are the wave speeds of the two component materials, respectively). In the following calculations, the spatial interval δ=1/30T.

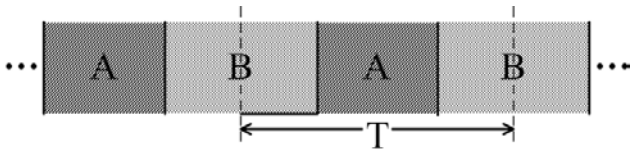

Fig. 2 The 1D PC model adopted in the present work

The upper subfigures of Figs. 3 (a)-(d) show the calculated band diagrams of the 1D PCs with different material parameters, where the dots and circles denote the results obtained with the proposed method and the conventional FDTD method, respectively; and $\Omega = fT/c_B$ is the normalized frequency with f being the real frequency. Here, for the material A, the values of the magnetic permeability (μ_A) are all set to be 1.0 and the filling fractions are all 0.5; and ε_A takes different values in the four cases. For both the two methods, the time-step parameters (γ) are all set to be 1.0, which is the CFL lower bound in 1D case. The eigenfrequencies of the PC system are calculated by applying the fast Fourier transform (FFT) to the time series of the field components generated during the time-stepping process. Good agreement of the two methods can be found and the correctness of the proposed method is therefore verified.

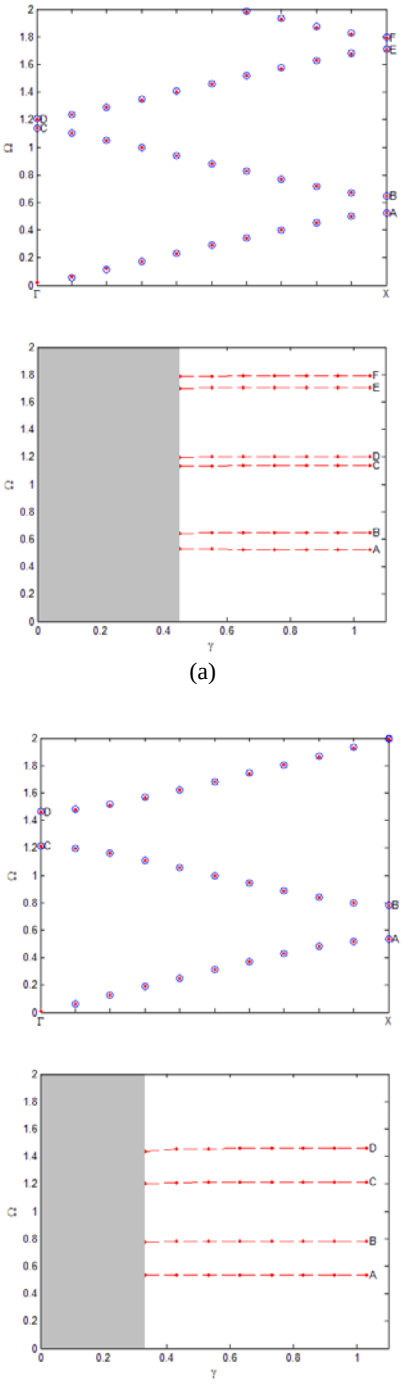

(a)

(b)

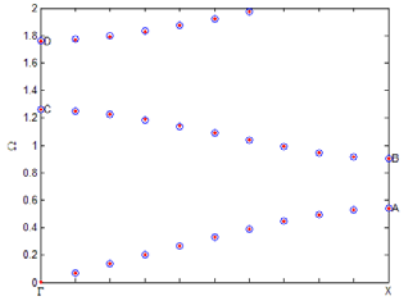

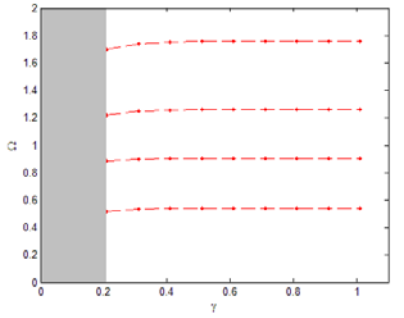

(c)

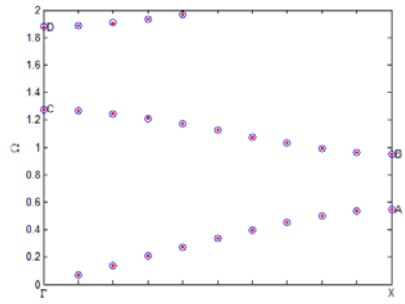

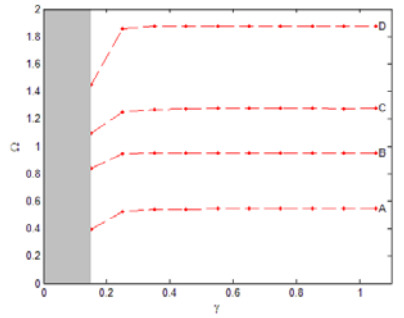

(d)

Fig. 3 Band diagrams of the 1D PC calculated by the proposed method and the conventional FDTD method (upper) and variations of the band gap boundaries calculated by using the proposed method with the time-step parameter γ (lower) in the cases of $\varepsilon_A = 0.5$ (a), $\varepsilon_A = 0.25$ (b), $\varepsilon_A = 0.1$ (c) and $\varepsilon_A = 0.05$ (d). In each case, $\mu_A = 1.0$ and the filling fraction of the material A is 0.5. The dots and circles in the upper subfigures represent the results obtained with the proposed method and the FDTD method, respectively. "A" and "B", "C" and "D", and "E" and "F" are used for denoting the boundaries of the first, second and third band gaps, respectively.

To explore the time stability of the proposed method, we find out the minimal time-step parameters (γ_{min}) just enough to make the method run stably under various conditions. γ_{min} is determined in the following way. For a given numerical example, γ is assigned from the CFL lower bound 1.0, and it is reduced gradually by a small step $\Delta\gamma$ (0.01 in the present work), until the stopping value making the proposed method diverge within the predefined number of time-steps (10000 in the present work). γ_{min} is thus defined as the value just bigger than this stopping value by $\Delta\gamma$. Tab. 1 show the values of γ_{min} for different values of ε_A, where the filling fractions are all set to be 0.5. Here, the material parameters are grouped in terms of the wave speed of material A. It can be found that γ_{min} are smaller than 1.0 in all cases. Hence, the proposed method, although it is not unconditionally stable, is more stable than the conventional FDTD method. The values of γ_{min} are mainly dependent on the wave speeds of material A (or more exactly the ratio between the wave speeds of the two component materials), and they only depend slightly on the specific values of ε_A and μ_A under certain conditions (except the case of $c_A = 2$, γ_{min} remains invariant once the wave speed of material A is determined). It can also be found that γ_{min} decreases with the increase of the ratio between the wave speeds of the two component materials. In other words, the stability of the proposed method improves with the increase of this ratio. In the case of $c_A = \sqrt{20}$, γ_{min} is as small as 0.15.

To make clear the influence of the filling fraction of the material A, we also find out the values of γ_{min} for different filling fractions in the cases of different combinations of the material parameters, as shown in Tab. 2. It can be found that γ_{min} depends slightly on the filling fractions. Therefore it is further proved that γ_{min} is mainly dependent on the wave speed ratio between the component materials.

Although the proposed method shows better stability than the conventional FDTD method, the accuracy of the proposed method may deteriorate with the decrease of the time-step parameter γ. The lower sub-figures of Figs. 3(a)-(d) show the variations of the band gap boundaries calculated by the proposed method with the parameter γ. The shadowed regions in the figures show the range of γ where the proposed method becomes unstable. With the decrease of γ, the calculated band gap boundaries become deviated from the stable values and become smaller, especially for the high-ordered ones. However, when γ is bigger than 0.4, no noticeable accuracy deterioration is observed among obtained results.

Tab. 1 The values of γ_{min} for different material parameters of the layer A (with the filling fraction of the material A being 0.5)

c_A $(=\frac{1}{\sqrt{\varepsilon_A \mu_A}})$					
	$\sqrt{2}$	ε_A	$\sqrt{1/2}$	0.5	0.25
		μ_A	$\sqrt{1/2}$	1	2
		γ_{min}	0.45	0.45	0.45
	2	ε_A	0.5	0.25	0.125
		μ_A	0.5	1	2
		γ_{min}	0.33	0.32	0.33
	$\sqrt{10}$	ε_A	$\sqrt{1/10}$	0.1	0.05
		μ_A	$\sqrt{1/10}$	1	2
		γ_{min}	0.21	0.21	0.21
	$\sqrt{20}$	ε_A	$\sqrt{1/20}$	0.05	0.025
		μ_A	$\sqrt{1/20}$	1	2
		γ_{min}	0.15	0.15	0.15

Tab. 2 The values of γ_{min} for different filling fractions in the cases of different combinations of the material parameters

(ε_A, μ_A)	Filling fractions		
	0.2	0.5	0.8
(0.5, 1)	0.46	0.45	0.43
(0.25, 1)	0.33	0.32	0.34
(0.1,1)	0.21	0.21	0.21
(0.05, 1)	0.15	0.15	0.15

6. Conclusions

By incorporating the Floquet-Bloch boundary conditions of periodic media into a time integration scheme and matrix-exponential decomposition technique, we propose a time-domain method for calculating the band structures of 1D PCs. The matrix-exponential decomposition approximation with the fourth-ordered accuracy is used. The numerical results show that,

(1) The proposed method is more stable than the conventional FDTD method, although it is still conditionally stable. The minimal time-step with which the method runs stably can be much smaller than the CFL lower bound.

(2) The minimal value of the time-step parameter (γ, defined in Eq. (20)), is mainly dependent on the ratio between the wave speeds of the two component materials, and decreases with the increase of this ratio.

(3) The accuracy of the proposed method may deteriorate with the decrease of the time-step parameter γ. However, the accuracy deterioration is noticeable only when γ is significantly smaller than 1.0.

In the future work, we plan to extend the proposed method to the band structure calculations of 2D or 3D PCs.

Acknowledgements

This work is supported by the National Natural Science Foundation of China under Grant No. 11372031.

References

[1] J. D. Joannopoulos, S. G. Johnson, J. N. Winn and R. D. Meade, *Photonic crystals: Molding the Flow of Light (Second Edition)*, Princeton University Press, New Jersey, 2008.

[2] M. Qin, S. L. He, A nonorthogonal finite-difference time-domain method for computing the band structure of a two-dimensional photonic crystal with dielectric and metallic inclusions, *J. App. Phy.* 87 (12): 8268 - 8275, 2000.

[3] G. W. Burr and A. Farjadpour, Balancing accuracy against computation time: 3-D FDTD for nanophotonics device optimization, *Proc. SPIE* 5733: 336-347, 2005.

[4] Z. T. Ma and K. Ogusu, FDTD analysis of 2D triangular-lattice photonic crystals with arbitrary-shape inclusions based on unit cell transformation, *Opt. Commun.* 282 (7): 1322-1325, 2009.

[5] K. S. Yee, Numerical solution of initial boundary value problems involving Maxwell's equations in isotropic media, *IEEE Trans. Ant. Prop.* ,14 (3): 302-307, 1966.

[6] D. M. Sullivan, *Electromagnetic Simulation Using the FDTD Method*, IEEE Press, New York, 2000.

[7] T. Namiki, A new FDTD algorithm based on alternating-direction implicit method, *IEEE Trans. Micro. Theory. Tech.* 47 (10): 2003-2007, 1999.

[8] J. S. Kole, M. T. Figge and H. D. Raedt, Unconditionally stable algorithms to solve the time-dependent Maxwell equations, *Phy. Rev. E* 64 (6): 066705, 2001.

[9] J. S. Kole, *New methods for the numerical solution of Maxwell's Equations (Ph. D. thesis)*, University of Groningen, Netherlands, 2003.

[10] M. A. Botchev, I. Faragó and R. Horváth, Application of operator splitting to the Maxwell equations including a source term, *App. Num. Math.* 59 (3): 522-541, 2009.

[11] H. Bauke and C. H. Keitel, Accelerating the Fourier split operator method via graphics processing units, *Com. Phy. Com.*, 182 (7) : 2454-2463, 2011.

[12] Y.-D. Kong and Q.-X. Chu, High-order split-step unconditionally-stable FDTD methods and numerical analysis, *IEEE Trans. Ant. Prop.* 59 (9): 3280-3289, 2011.

[13] M. Suzuki, Fractal decomposition of exponential operators with applications to many-body theories and Monte Carlo simulations, *Phys. Lett. A* 146 (6): 319-323, 1990.

[14] M. Suzuki, General theory of higher-order decomposition of exponential operators and symplectic integrators, *Phys. Lett. A*165 (6): 387-395, 1992.

[15] I. Faragó, R. Horváth and W. H. A. Schilders, Investigation of numerical time-integrations of Maxwell's equations using the staggered grid spatial discretization, *Int. J. Numer. Model.* 18 (1):149-169, 2005.

[16] C. Moler, C. V. Loan, Nineteen Dubious Ways to Compute the Exponential of a Matrix, Twenty-Five Years Later, *SIAM Rev.* 45 (1): 1-46, 2003.

Flexible Ag electrode for quantum dot light-emitting diode

Jing Chen[1], Zhi Li[1], Jiangyong Pan[1], Du Qingguo[2], Wei Lei[1*], Qing Li, Jun Xia, Yan Tu

[1]School of Electronic Science and Engineering, Southeast University, Nanjing, China, 210096
[2]Institute of High Performance Computing, 1 Fusionopolis Way, #16-16 Connexis North, Singapore 138632
*corresponding author, E-mail: lw@seu.edu.cn

Abstract

In this paper, we have fabricated quantum dot light emitting diode (QD-LED) based on silver (Ag) electrode. The QD-LED with Ag electrode is demonstrated with decreased leakage current, improved luminous efficiency, low turn-on voltages, and saturated emission exhibiting the Commission Internationale de l'Enclairage (CIE) coordinates of (0.59, 0.40). Meanwhile, compared to the QD-LED with ITO coated PET electrode, the EL intensity was enhanced twice for QD-LED based on Ag electrode, and turn on voltage was reduced to 4.7 V, which was attributed to the higher conductivity and better transmission of Ag electrode.

1. Introduction

Quantum dot LEDs (QD-LEDs) have been attracting much attention in the past few years since they possess unique properties of the tunable emission wavelengths by controlling the size of QDs, highly saturated emission, narrow emission with small full width at half maxima (FWHM), solution process, and compatible with flexible substrates[1]. Flexible quantum dot light-emitting diodes (QD-LEDs) have been a promising candidate for high-efficiency and color-saturated displays[2].

Various types of transparent and conductive oxides (TCO) have been widely used in optoelectronics, such as indium tin oxide (ITO), which is traditionally used for organic solar cells and light emitting diodes due to the high transparency and conductivity. However, the significant disadvantages still existed for the flexible ITO electrode. For example, the performance of QD-LED is low, the process of ITO film requires a vacuum deposition and is expensive due to the high indium costs[3]. Therefore, a candidate for replacing of ITO is urgently needed.

Here, we shall report a simply solution-processed QD-LED using Ag nanoparticles coated on polyethylene terephthalate (PET) substrate as the flexible electrode replaced of indium-tin-oxide (ITO) coated on PET substrate. The performance of QD-LED is also investigated

2. Experiment

Patterned Ag flexible substrate (Cima Nanotech) was exposed to the UV ozone treatment for 30 min in air. The Poly (ethylenedioxythiophene): polystyrene sulphonate (PEDOT:PSS) as hole injection layer (HIL) was spin coated on ITO glass at 5000 rpm, and backed at 180°C for 15 min. Thereafter, poly [(9, 9-dioctylfluorenyl-2,7-diyl)-co-(4,4'-(N-(4-sec-butylphenyl))diphenylamine)] (TFB) as hole transport layer (HTL) was coated at 2000 rpm followed by annealing at 120 °C for 10 min. The thickness of HTL is fixed at 30 nm. The emissive layer of colloidal quantum dots CdSe/ZnS (QDs) were spin coated on HTL at different spin-coating conditions and various concentrations with annealing at 120°C for 15 min and ZnO NPs layer as ETL was deposited at 2000 rpm on QDs layer and annealed at 120 °C for 30 min. Thereafter, aluminum (Al) as electrode was thermally evaporated , followed by a post annealing on whole devices at 120 °C for 10 min. The devices were fabricated with ITO and Ag electrodes were named as sample A and B, respectively.

The current density-voltage (J-V) characteristics were measured with Keithley-2400 source-meter and electroluminescence (EL) spectra were recorded with an Ocean Optics Maya 2000-PRO spectrometer. The morphologies were investigated using a field-emission scanning electron microscope (FESEM) and a field-emission gun transmission electron microscope (Tecnai G2 F30).

3. Discussion

Figure 1(a) and (b) show the FESEM image and magnified image of Ag electrode. It can be seen that the Ag network can be formed by cross linking of Ag nanowires. It is also worth noting that the use of Ag network electrode results in an increased spectral transmission due to this novel nanostructure, ensuring increased light emission in the QD-LED. Fig. 1(b) shows the magnified SEM image of single Ag nanowire deposited on substrate, which composed of nanoparticles with the average diameter of 50 nm. It is predicted that the deformation of Ag electrode is small attributed to the densely-packed nanoparticles. The conductivity of this flexible Ag electrode can be reached as high as 3.5 ohms/sq, and transmittance is higher than 80% due to the formation of Ag network nanostructure. Compared to the commercial flexible ITO electrode (higher than 50 ohms/sq), the conductivity of this flexible Ag electrode is much higher.

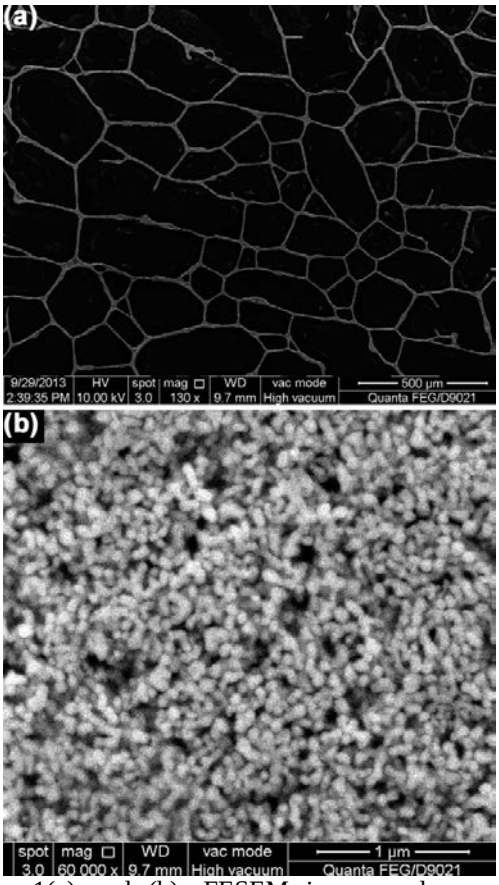

Figure 1(a) and (b): FESEM image and magnified image of flexible Ag electrode

The schematic of our device structure is shown in Fig. 2. The device consists of Ag network electrode as the anode, a 50 nm poly(ethylenedioxythiophene): polystyrene sulphonate (PEDOT:PSS) as the hole injection layer (HIL), a variable (10~40 nm) poly[(9,9-dioctylfluorenyl-2,7-diyl)-co-(4,4-(N-(4-sec-butylpheny -l)) diphenylamine)] (TFB) layer as the HTL, a 30 nm QD layer as the emissive layer with 3 to 4 closely packed QD monolayers, a 40 nm ZnO layer as the ETL, and a 100 nm aluminum (Al) layer as the cathode.

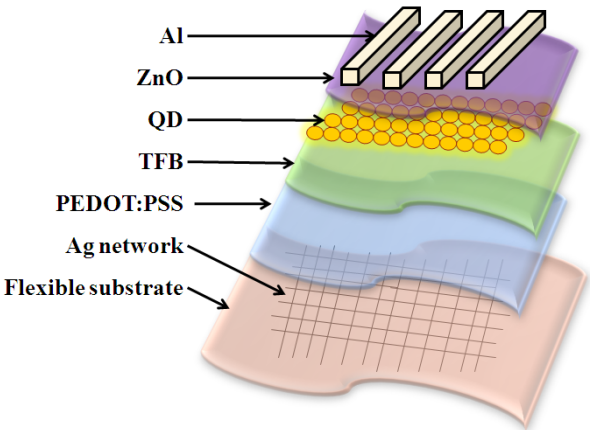

Figure 2: A schematic of the device structure of flexible QD-LED based on Ag electrode

Figure 3(a) shows the absorption and PL spectra of ZnCdSeS QDs used in this study. The absorption spectrum clearly displays the first excitonic transition peak at 572 nm, estimating the sizes of these QDs to be 3.3 nm without the ligand length, calculated as reported[4]. The PL spectrum shows a Gaussian-shaped peak located at 586 nm with a narrow FWHM of 30 nm, indicating the yellow emission of QD solution.

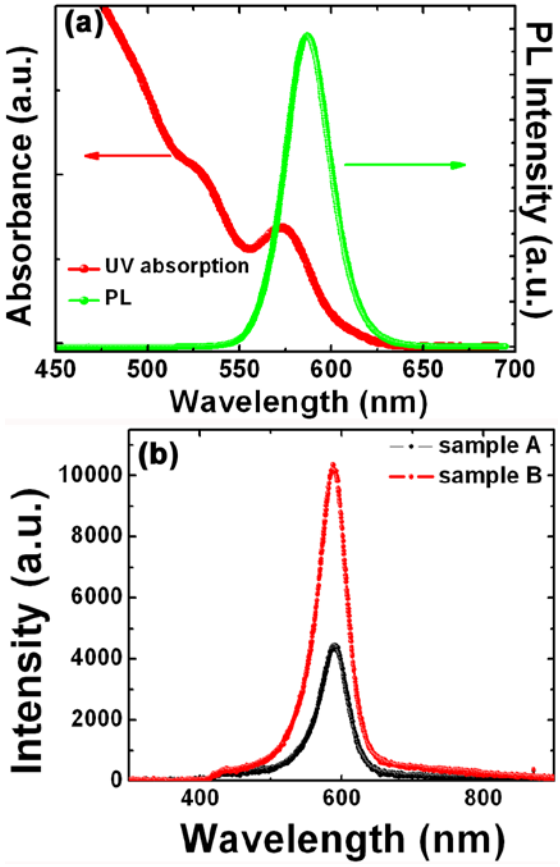

Figure 3(a): UV-Vis absorption and PL spectra of ZnCdSeS QDs dispersed in toluene (b): The EL spectra of sample A and B at the operation voltage varying from 8 V.

The EL spectra of sample A and B at the driving voltage of 8 V are shown in Fig. 3 (b). It can be seen that the EL intensity of 588 nm emission for sample A and B, which is consistent with the result of PL spectra in Fig. 3(a). Compared to sample A, the intensity of sample B has more than twice enhancement. The reason is possibly due to the better conductivity and higher transmittance of sample B than those of sample A.

Both of the QD-LEDs were tested as-made in air for several days, without encapsulation, and stored at atmosphere between tests. Fig. 4 shows the current density-voltage (J–V) of sample A and B under forward bias. The devices exhibit low turn-on voltage of 4.7 V for sample B and 7.3 V for sample A, respectively, primarily attributed to the increased conductivity of sample B. The current density of sample B in the ohmic conduction region is lower than that of sample A, indicating that the leakage current of sample B decreases remarkably. The slope of the J-V curve for sample B is steeper than that of sample A in the trap-limited conduction region. This is attributed to improved

charge transport in sample B beyond the threshold voltage causing higher conductivity of sample B.

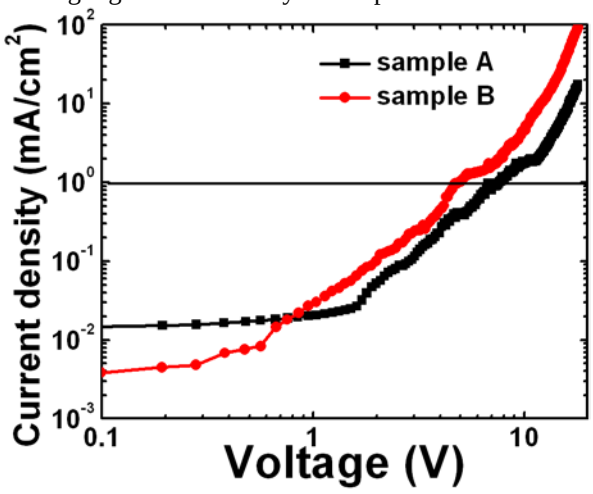

Figure 4: current density-voltage (J–V) of sample A and B under forward bias.

Figure 5(a) show the real photo of flexible QD-LED without applying voltage after bending to a radius of 5 mm. Fig. 5(b) show the orange light is emitted, showing the Commission Internationale de l'Enclairage (CIE) coordinates of (0.59, 0.40) at voltage of 5.5 V and the luminance of 50 cd/m^2.

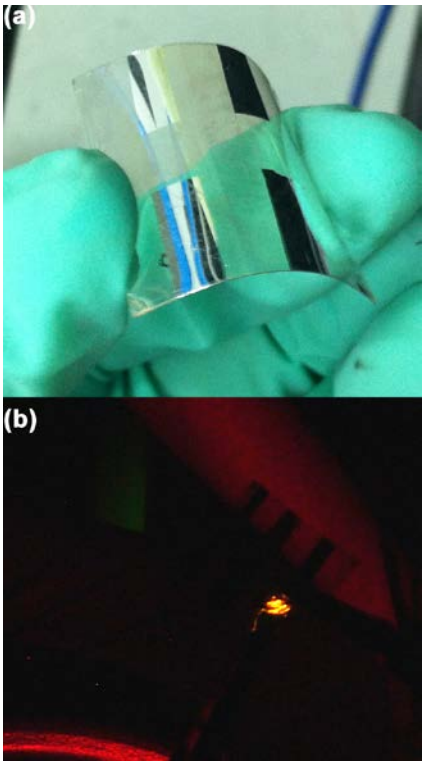

Figure 5(a) and (b): real photos of flexible QD-LED before and after applying voltage

4. Conclusions

In summary, we have demonstrated the flexible QD-LED can be fabricated by Ag electrode. The nanostructure of Ag network, which is composed of 50 nm Ag nanoparticles, is benefit for the increase of conductivity and transmission of electrode. The EL intensity was enhanced twice for QD-LED based on Ag electrode, and turn on voltage was reduced to 4.7 V, which was attributed to the higher conductivity and better transmission of Ag electrode. It is demonstrated that Ag nanoparticle electrode will be promising for the use in practical flexible flat panel displays (FPDs).

Acknowledgements

This work was supported partially by the National Key Basic Research Program 973 (2013CB328804, 2013CB328803, and 2010CB327705), the National High-Tech R&D Program 863 of China (2012AA03A302, 2013AA011004) National Natural Science Foundation Project (51002031, 61007036, 61101023, 51202028, 61106055, 51372039, and 61271053), Foundation of Doctoral Program of Ministry of Education under Grant (20120092120025), and the Chinese 111 Project (B07027).

References

1 Kim, T.H., Cho, K.-S., Lee, E.K., Lee, S.J., Chae, J., Kim, J.W., Kim, D.H., Kwon, J.-Y., Amaratunga, G., Lee, S.Y., Choi, B.L., Kuk, Y., Kim, J.M., and Kim, K.: 'Full-colour quantum dot displays fabricated by transfer printing', Nat Photon, 2011, 5, (3), pp. 176-182

2 White, M.S., Kaltenbrunner, M., Glowacki, E.D., Gutnichenko, K., Kettlgruber, G., Graz, I., Aazou, S., Ulbricht, C., Egbe, D.A.M., Miron, M.C., Major, Z., Scharber, M.C., Sekitani, T., Someya, T., Bauer, S., and Sariciftci, N.S.: 'Ultrathin, highly flexible and stretchable PLEDs', Nat Photon, 2013, 7, (10), pp. 811-816

3 Krantz, J., Richter, M., Spallek, S., Spiecker, E., and Brabec, C.J.: 'Solution-Processed Metallic Nanowire Electrodes as Indium Tin Oxide Replacement for Thin-Film Solar Cells', Advanced Functional Materials, 21, (24), pp. 4784-4787

4 Yu, W.W., Qu, L.H., Guo, W.Z., and Peng, X.G.: 'Experimental determination of the extinction coefficient of CdTe, CdSe, and CdS nanocrystals', Chem. Mater., 2003, 15, (14), pp. 2854-2860

Active and Tunable Metamaterials

Tunable Terahertz Metamaterials by means of Piezoelectric MEMS Actuators

Antonios X. Lalas, Nikolaos V. Kantartzis, and Theodoros D. Tsiboukis

Department of Electrical and Computer Engineering, Aristotle University of Thessaloniki, Thessaloniki, Greece
*corresponding author, E-mail: tsibukis@auth.gr

Abstract

A programmable THz metamaterial, derived from the utilization of a piezoelectric controlled microgripper as a split-ring resonator (SRR), is introduced in this paper. By applying the appropriate actuation voltage on the piezoelectric microelectromechanical systems (MEMS), a reconfigurable complex medium, offering enhanced bandwidth tunability, is attained. Several polarization topologies are examined to clarify the interesting attributes of the metamaterial. Thorough numerical investigations, via a robust finite element method (FEM), support the efficiency and reveal the advantages of the proposed device.

1. Introduction

An inspiring feature of concurrent RF technology is related to artificially synthesized complex media, like metamaterials [1], [2], which offer unique electromagnetic properties not available in nature. This extraordinary behavior is employed in many contemporary applications, especially in the THz frequencies [3]-[7]. Nonetheless, their inherent lack of wide spectral bandwidths is deemed prohibitive to real-life configurations. To tackle this shortcoming, various mechanisms have been proposed, such as magnetically or thermally controlled liquid crystals, and optically reconfigurable silicon apparatuses. However, radio-frequency microelectromechanical systems (RF-MEMS) [8] are considered as the most competent devices to accomplish advanced bandwidth tunability. Amid them, thermal and electrostatic RF-MEMS, such as curved membranes, comb drives and cantilevers, have been exploited for the required response controllability [9]-[13]. Alternatively, a reconfigurable metamaterial, that associates the double two-hot arm electrothermal actuator with a split-ring resonator (SRR), has been proposed [14]. These arrangements yield a tunable mu-negative (MNG) behavior, while the MEMS device is only a part of the resonator.

In this paper, piezoelectric MEMS actuators are utilized to develop a microgripper, i.e. a device capable of handling objects at the scale of micrometers. This new structure is exploited to implement the SRR and sustain the MNG resonances. The proposed resonator's functionality is modified in terms of its operability. Instead of gripping objects, the microgripper acts as a resonator, whereas the movement of its arms provides the required frequency shifting and bandwidth enhancement. The new configuration successfully exhibits this attribute, as verified by numerical simulations.

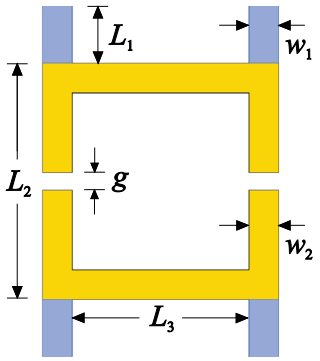

Figure 1: Geometry and design parameters of the piezoelectric microgripper (cyan: actuator, yellow: arms).

2. The reconfigurable THz metamaterial

2.1. Features of the piezoelectric MEMS actuators

The piezoelectric actuator exhibits a simple, yet rather effective, geometry in terms of displacement generation. Furthermore, this device involves low temperature operation as well as insensitivity to ambient electromagnetic fields. A small fragment of a piezoelectric material shaped in a rectangle form can be considered as a voltage-driven actuator. The actuator's principal operation is summarized in the development of piezoelectric expansion and thus displacement of the associated tip, when excited by a potential difference. An actuator of this kind is depicted in Fig. 1, while four actuators are employed, together with metal strips, in order to design the proposed microgripper (also shown in Fig. 1). Specifically, an electrostatic field, which generates a strain due to the piezoelectric effect, is created in each actuator. Therefore, an expansion occurs, whereas the arms are deflected towards each other, resulting in gripping procedure. On the other hand, when the bias voltage is decreased or reversed, the contraction of the MEMS devices moves away the associated arms and thus releases an object.

The design parameters of the proposed structure are selected as: $L_1 = 2$ μm, $L_2 = 8$ μm, $L_3 = 6$ μm, $w_1 = w_2 = 1$ μm, and $g = 0.6$ μm. Its metal section comprises a 0.4 μm thick gold layer, while the piezoelectric modules consist of lead

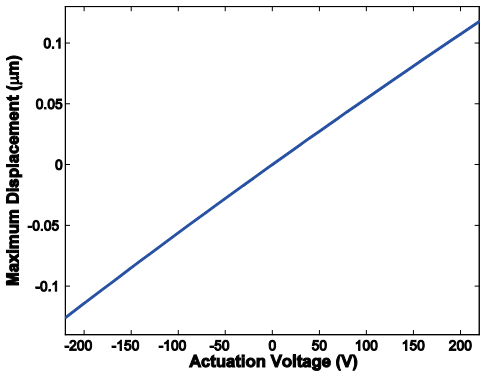

Figure 2: Maximum tip displacement for different values of the actuation voltage.

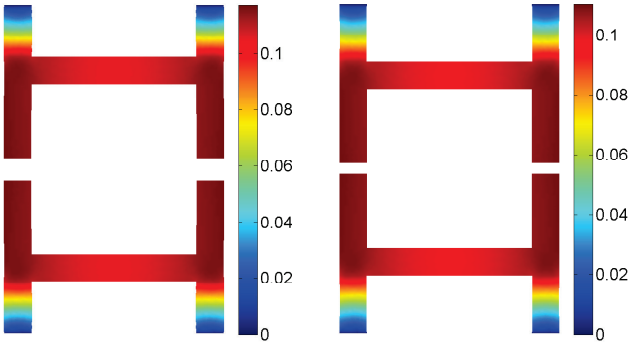

(a) (b)

Figure 3: Total displacement distribution (in μm) at the actuation voltage of (a) -200 V and (b) 200 V.

zirconate titanate (PZT-5H). Based on the above aspects, a coupled electric/structural analysis is performed via the FEM approach, while the resonator is discretized into 1216 prismatic elements with 22954 degrees of freedom. The maximum tip displacement is calculated for different values of the actuation voltage, as shown in Fig. 2. Also, its corresponding total displacement distribution at two distinct actuation voltages, namely -200 V and 200V, is presented in Fig. 3.

2.2. Piezoelectric controlled complex medium

A reconfigurable metamaterial can be designed by exploiting the aforementioned microgripper, as illustrated in Fig. 4, along with its corresponding unit cell. When a certain voltage is applied, the resulting piezoelectric expansion or contraction, moves the metal parts of the structure and the gaps are shortened or enlarged, respectively. Thus, variations in actuation voltage levels introduce tunable gaps and as a consequence a programmable SRR. The cell period is set to 18 μm, $h_1 = 5$ μm, $h_2 = 3$ μm, and the thickness of the Si_3N_4 substrate is 2 μm. Taking into account these data, all numerical simulations are conducted through a properly tailored FEM, whereas a parallel-plate waveguide approach is adopted to extract the *S*-parameters. This technique involving PEC and PMC boundary conditions constitutes an excellent approximation to model the array of the unit cells in comparison with Floquet boundary conditions. In particular, the unit cell is divided into 23412 tetrahedral elements with

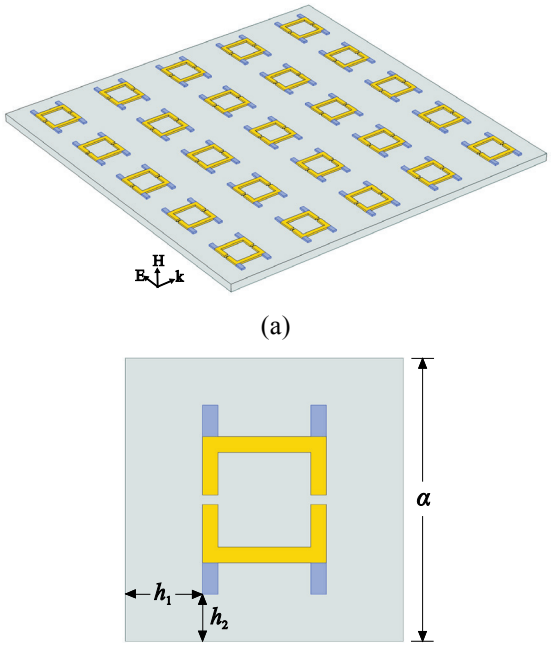

(a)

(b)

Figure 4: Geometry and design parameters of (a) the reconfigurable, in terms of piezoelectric MEMS actuators, metamaterial and (b) the unit cell.

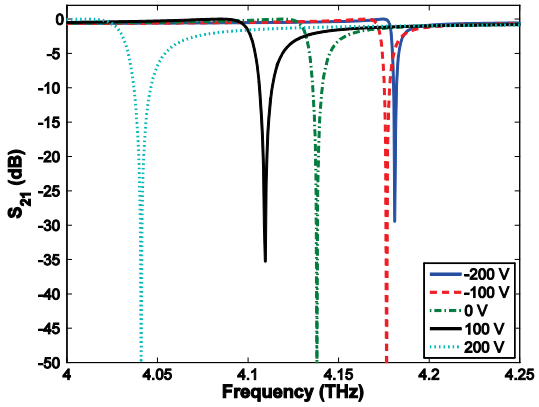

(a)

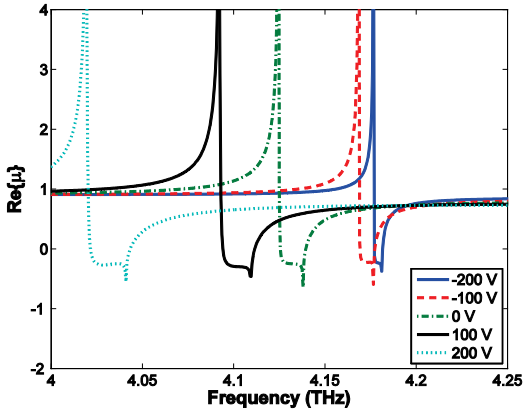

(b)

Figure 5: Tunable behavior at several actuation voltages in terms of (a) S_{21}-parameter and (b) effective magnetic permeability.

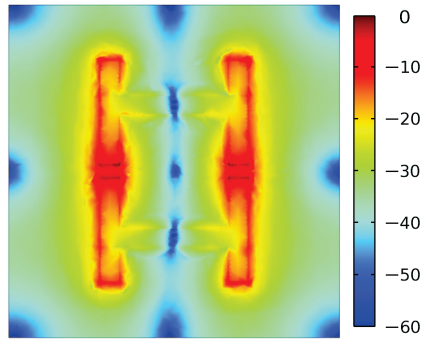

(a)

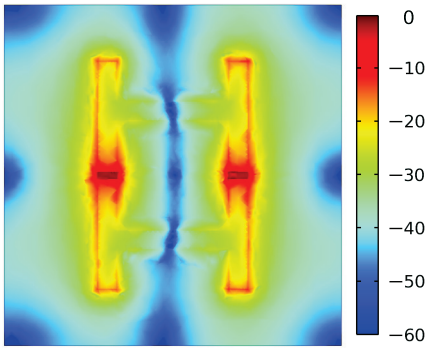

(b)

Figure 6: Electric field snapshots of the piezoelectric controlled metamaterial unit cell, when the actuation voltage is (a) -200 V at 4.181 THz and (b) 200 V at 4.041 THz.

152416 degrees of freedom. Furthermore, a robust homogenization method [15] is exploited to retrieve the constitutive effective parameters of the proposed complex materials.

3. Numerical results and discussion

A detailed assessment regarding the properties of the novel controllable metamaterial in the THz frequency region is performed. Several polarization topologies are examined to reveal the characteristics of the associated resonances.

3.1. Initial orientation

The first topology is denoted by an impinging wave parallel to the plane of the resonators. Specifically, the magnetic field is perpendicular to the loops of the unit cells, whereas the electric field is parallel to the piezoelectric actuators, as depicted in Fig. 4. The magnitude of the S_{21}-parameter along with the real part of the effective magnetic permeability are calculated and presented in Fig. 5, both for different values of the actuation voltage. These results reveal the MNG THz resonance of the complex medium as well as the ability for improved bandwidth. The frequency regions of interest are denoted in Table 1, when the actuation voltage increases from -200 V to 200 V. An enhanced tunability is accomplished, since the narrow bandwidth of 1.7 GHz, is artificially extended to 4.1813 THz – 4.0396 THz = 141.7 GHz, offering an improvement of 83 times magnification. Furthermore, two snapshots of the electric field intensity are given in Fig. 6, when the actuation voltage is -200 V and 200 V, respectively. The maximum values are observed at the

Table 1: Spectral characteristics of the MNG resonances.

Actuation Voltage (V)	Frequency Regions		
	Start (THz)	End (THz)	BW (GHz)
-200	4.1807	4.1813	0.6
-100	4.1760	4.1770	1.0
0	4.1372	4.1389	1.7
100	4.1083	4.1104	2.1
200	4.0396	4.0424	2.8

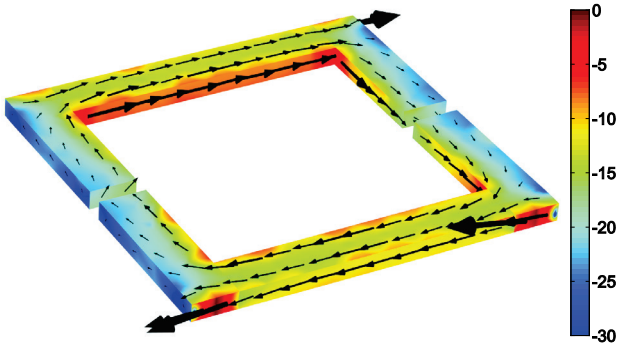

Figure 7: Surface current density snapshot of the piezoelectric controlled metamaterial unit cell, when the actuation voltage is 200 V at 4.041 THz (The arrows depict the direction and intensity of the surface current flow).

gap regions, displaying the MNG performance. Finally, a snapshot of the surface current distribution is depicted in Fig. 7, when the device is actuated by 200 V. Apparently, the maximum value is obtained upon the surface of the SRR and especially the inner part of the resonator, denoting the presence of an MNG resonance. So, it is deduced that the prior SRR can be useful in several high-frequency arrangements.

3.2. Rotated orientation

The second topology is also described by an impinging wave parallel to the plane of the resonators. However, this wave is rotated of 90° in comparison to the initial orientation. Thus, in this case the electric field is perpendicular to the piezoelectric actuators, while the magnetic field is perpendicular to the loops, as illustrated in Fig. 8.

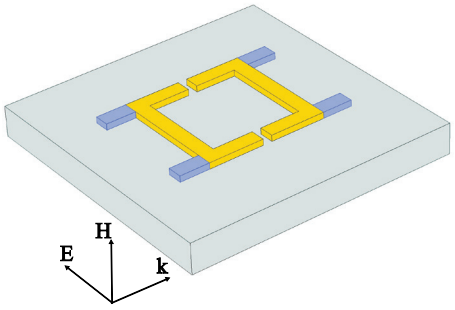

Figure 8: Topology for an alternative polarization of the reconfigurable, in terms of piezoelectric MEMS actuators, unit cell.

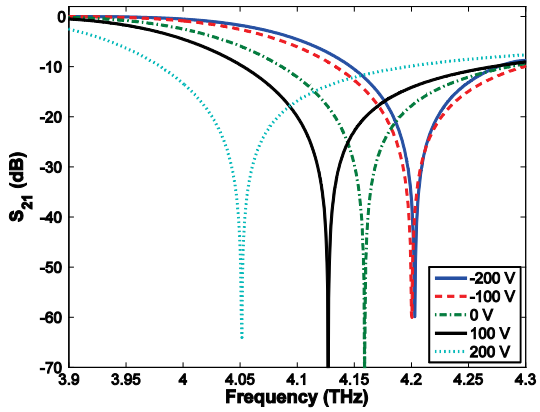

(a)

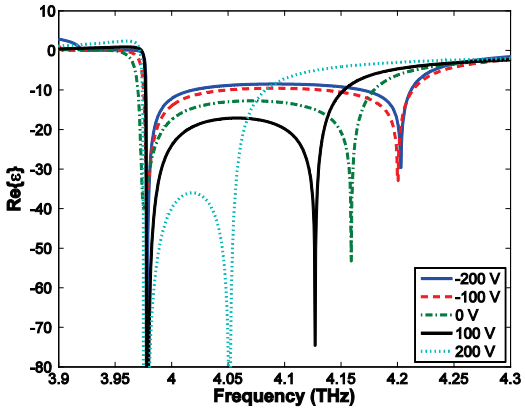

(b)

Figure 9: Tunable behavior for different polarization at several actuation voltages in terms of (a) S_{21}-parameter and (b) effective electric permittivity.

Table 2: Spectral characteristics of the ENG resonances for the other polarization.

Actuation Voltage (V)	Frequency Regions		
	Start (THz)	End (THz)	BW (GHz)
-200	4.1842	4.2229	38.7
-100	4.1772	4.2263	49.1
0	4.1331	4.1899	56.8
100	4.1001	4.1598	59.7
200	4.0253	4.0832	57.9

The magnitude of the S_{21}-parameter along with the real part of the effective electric permittivity are extracted and depicted in Fig. 9, both for different values of the actuation voltage. These data denote the presence of an ENG THz resonance of the complex medium as well as the capability for enhanced bandwidth. The corresponding frequency regions are presented in Table 2, when the actuation voltage increases from -200 V to 200 V. An improved tunability is attained, since the narrow bandwidth of 56.8 GHz, is artificially extended to 4.2263 THz – 4.0253 THz = 201 GHz, offering an improvement of 253.9%.

Moreover, two snapshots of the electric field intensity are

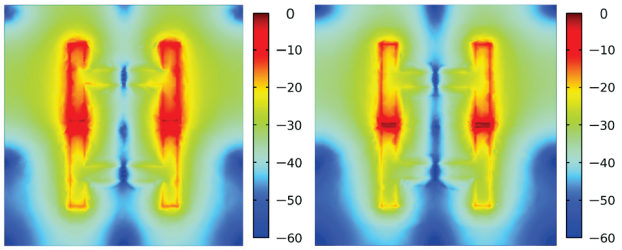

(a) (b)

Figure 10: Electric field snapshots for the other polarization of the piezoelectric controlled metamaterial unit cell, when the actuation voltage is (a) -200 V at 4.203 THz and (b) 200 V at 4.051 THz.

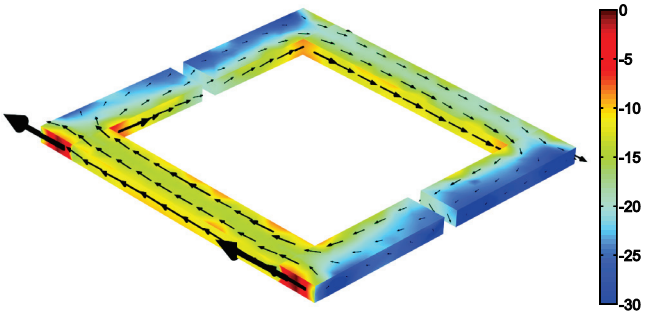

Figure 11: Electric field snapshots for the other polarization of the piezoelectric controlled metamaterial unit cell, when the actuation voltage is 200 V at 4.051 THz (The arrows depict the direction and intensity of the surface current flow).

are depicted in Fig. 10, when the actuation voltage is -200 V and 200 V, respectively. The maximum values are located at the regions of the gaps and especially at the half part of the resonator, thus displaying the ENG behavior. Additional evidence of this performance is drawn from a snapshot of the surface current distribution, presented in Fig. 11, when the device is actuated by 200 V. It is clear, that the maximum value is observed only upon the half portion of the SRR. In this manner, the unit cell acts as a metal wire, sustaining an ENG resonance. Therefore, it is concluded that the above SRR can be beneficial in diverse high-frequency setups.

3.3. Anisotropic behavior

The controllable metamaterial exhibits a different performance, when the polarization of the impinging wave is modified. The numerical assessment of the device denotes that the central frequency of the resonances is shifted, while the corresponding quality factor is altered. Moreover, in some topologies, the essence of each resonance is reconfigured between ENG and MNG performance. This observation regarding anisotropy is deemed crucial in designing programmable metamaterials and associated apparatuses.

4. Conclusions

The exploitation of piezoelectric MEMS actuators for the design of a novel microgripper, which behaves as a recon-

figurable metamaterial, is presented in this paper. Different polarization arrangements are also investigated revealing the possibilities of the structure. Several FEM simulations identify the properties of the proposed device, which enables advanced bandwidth tunability and potential application in various THz implementations.

Acknowledgements

This research has been cofinanced by the European Union (European Social Fund − ESF) and Greek national funds through the Operational Program "Education and Lifelong Learning" of the National Strategic Reference Framework (NSRF) − Research Funding Program: Aristeia I. Investing in knowledge society through the European Social Fund.

References

[1] R. Marqués, F. Martín, M. Sorolla, *Metamaterials with Negative Parameters: Theory, Design and Microwave Applications*, Wiley-Interscience, New Jersey, NY, 2008.

[2] F. L. Zhang, L. Kang, Q. Zhao, J. Zhou, X. Zhao, D. Lippens, Magnetically tunable left handed metamaterials by liquid crystal orientation, *Opt. Express* 17: pp. 4360–4366, 2009.

[3] J. M. Manceau, N. H. Shen, M. Kafesaki, C. M. Soukoulis, S. Tzortzakis, Dynamic response of metamaterials in the terahertz regime: Blueshift tunability and broadband phase modulation, *Appl. Phys. Lett.* 96: 021111(1–3), 2010.

[4] R. Singh, I. A. I. Al-Naib, M. Koch, W. Zhang, Asymmetric planar terahertz metamaterials, *Opt. Express* 18: pp. 13044–13050, 2010.

[5] D. Wang, C. Qiu, M. Hong, Coupling effect of spiral-shaped terahertz metamaterials for tunable electromagnetic response, *Appl. Phys. A*, 2013.

[6] F. Kebin, Z. Xiaoguang, Z. Jingdi, G. Kun, G. R. Keiser, H. R. Seren, G. D. Metcalfe, M. Wraback, Z. Xin, R. D. Averitt, Optically Tunable Terahertz Metamaterials on Highly Flexible Substrates, *IEEE Transactions on Terahertz Science and Technology* 3: pp.702–708, 2013.

[7] B.-X. Wang, L.-L. Wang, G.-Zhen Wang, W.-Q. Huang, X.-F. Li, X. Zhai, Frequency continuous tunable terahertz metamaterial absorber, *J. Lightwave Technology* 32: pp.1183–1189, 2014.

[8] A.-Q. Liu, *RF MEMS Switches and Integrated Switching Circuits*, Springer, New York, 2010.

[9] H. Tao, A. C. Strikwerda, K. Fan, W. Padilla, X. Zhang, R. D. Averitt, MEMS based structurally tunable metamaterials at terahertz frequencies, *J. Infrared Milli. Terahz Waves* 32: pp. 580–595, 2010.

[10] X. He, Z. Lu, B. Liu, Z. Li, Tunable magnetic metamaterial based multi-split-ring resonator (MSRR) using MEMS switch components, *Microsystem Technol.* 17: pp. 1263–1269, 2011.

[11] D. Bouyge, D. Mardivirin, J. Bonache, A. Crunteanu, A. Pothier, M. Duran-Sindreu, P. Blondy, F. Martin, Split ring resonators (SRRs) based on microelectromechanical deflectable cantilever-type rings: Application to tunable stopband filters, *IEEE Microw. Wireless Compon. Lett.* 21: 243–245, 2011.

[12] W. Zhang, A. Q. Liu, W. M. Zhu, E. P. Li, H. Tanoto, Q. Y. Wu, J. H. Teng, X. H. Zhang, M. L. J. Tsai, G. Q. Lo, D. L. Kwong, Micromachined switchable metamaterial with dual resonance, *Appl. Phys. Lett.* 101: 151902(1–5), 2012.

[13] W. M. Zhu, A. Q. Liu, T. Bourouina, D. P. Tsai, J. H. Teng, X. H. Zhang, G. Q. Lo, D. L. Kwong, N. I. Zheludev, Microelectromechanical Maltese-cross metamaterial with tunable terahertz anisotropy, *Nature Commun.* 3: 1274(1–6), 2012.

[14] A. X. Lalas, N. V. Kantartzis, T. D. Tsiboukis, Controllable essence of complex materials exploiting two-hot-arm electrothermal actuators, *Proc. MEMSWAVE13*, Potsdam, Germany, pp. 1–4, 2013.

[15] X. Chen, T. M. Grzegorczyk, B. I. Wu, J. Pacheco, J. A. Kong, Robust method to retrieve the constitutive effective parameters of metamaterials, *Phys. Rev. E* 70: 016608(1–7), 2004.

Graphene-based electrically reconfigurable deep-subwavelength metamaterials for active control of THz light propagation

Sara Arezoomandan[1], Kai Yang[1], and Berardi Sensale-Rodriguez[1,*]

[1]Department of Electrical and Computer Engineering, The University of Utah, Salt Lake City 84112, USA
*corresponding author, E-mail: berardi.sensale@utah.edu

Abstract

This work studies the terahertz light propagation through graphene-based reconfigurable metasurfaces where the unit cell dimensions are much smaller than the terahertz wavelength. The proposed devices, which poses deep-subwavelength unit-cell and active-region dimensions can operate as amplitude and/or phase modulators in certain specific frequency bands determined by the device geometry. Reconfigurability is attained via electrostatically tuning the optical conductivity of patterned graphene layers, which are strategically located in each unit cell. The ultra-small unit-cell dimensions can be advantageous for beam shaping applications.

1. Introduction

Future compact low-cost terahertz systems, such as beam steerers for MIMO communications approaches, tunable flat lenses for IR/THz cameras, and so on, will demand components capable of achieving some degree of beam shaping. Currently there are only a small number of studies proposing or demonstrating devices achieving terahertz beam steering (e.g. [1-4]). Although these devices represent a significant technological advance, most of them are bulky in size (e.g. either require mechanical actuation or external lasers for optical excitations) and, therefore, unsuitable for compact integration [1-3]. From this point of view, there is a need for compact devices enabling active terahertz beam shaping.

In this context, active semiconductor-based metamaterials were shown capable -at certain frequencies- of producing phase modulation of an arbitrary terahertz beam, whereas not affecting the amplitude of the transmitted wave [5]. This is of special interest in order to construct arbitrary phase gradients, which in turn can shape a beam in accordance to the generalized laws of reflection and refraction [6]. Since in order to achieve maximum control over the properties of the transmitted terahertz beam, the phase gradient should be maximized, is of interest to develop metamaterials capable of simultaneously: i) achieving the largest phase modulation -per unit cell-, and ii) having the smallest unit cell dimensions.

This work presents a planar deep-subwavelength active metamaterial (i.e. a metamaterial with unit-cell dimensions $<< \lambda/10$). By independently biasing each of the unit-cells (meta-atoms), reconfigurable planar phase gradients might be constructed, which can in turn be employed for terahertz beam shaping. The ultra-scaled dimensions of the proposed meta-atoms can allow for construction of more abrupt phase gradients than conventional (i.e. no ultra-scaled) metasurfaces, which consequently can lead to larger degrees of reconfigurability. Owed to its intrinsic two-dimensional nature, low-cost, and ease of integration [7], graphene is proposed as the active terahertz material in these devices. The active area of the device –area covered by graphene- is just a 0.5% of the total unit cell area. Therefore the proposed devices might also enable very fast switching.

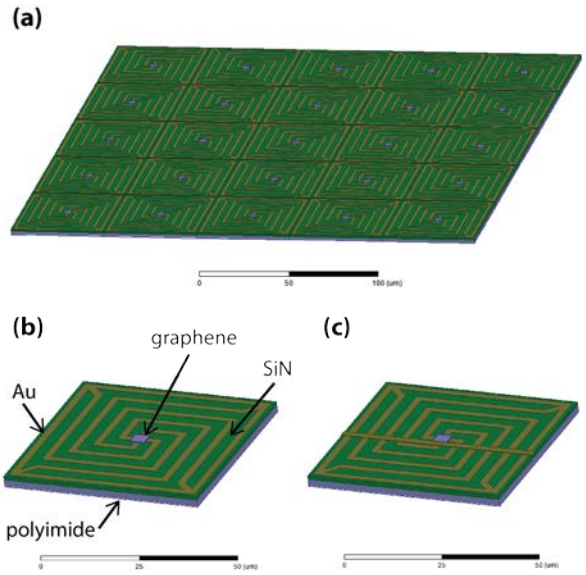

Figure 1: (a) Sketch of the device structure. (b) Detail of one element of the array (meta-cell). (c) Gating structure (electrode configuration) for electrically controlling the graphene conductivity.

2. Device structure

Shown in Fig. 1(a-b) are the structure of the proposed device -which consists of an array of spiral resonators- and the detail of one unit-cell -single spiral resonator-, respectively. An active graphene layer is placed in the center of each unit-cell; its electromagnetic properties and therefore the effective properties of the device can be

controlled via controlling the Fermi level of graphene thus its density of states available for intra-band transitions [8-11]. Although graphene metamaterials have been widely employed in devices modulating the amplitude of a transmitted terahertz beam (e.g. [12-14]), graphene-based structures controlling phase have not yet been proposed in the literature.

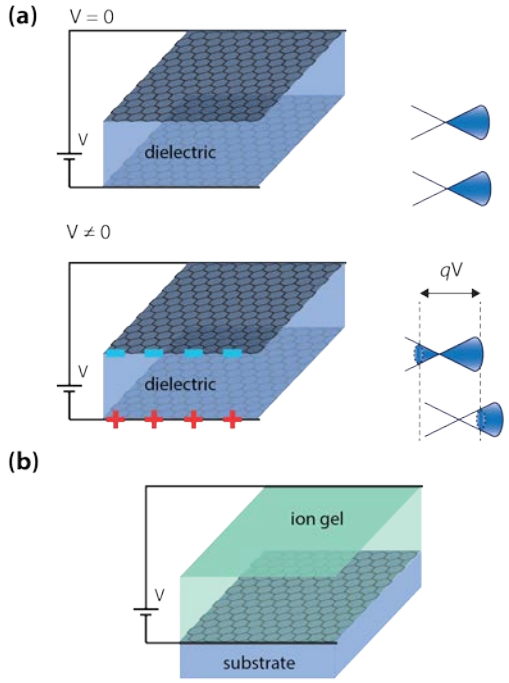

Figure 2: (a) Sketch of a self-gated graphene pair, at zero voltage both the top and bottom graphene layers are assumed to be at Dirac point thus the total free charge density and the effective conductivity approaches zero. When a finite voltage is applied carriers of opposite type accumulate in the graphene layers. (b) Sketch of an ion-gel gated graphene layer.

Actuation over the graphene optical conductivity can be achieved electrostatically via either gating graphene with another graphene layer (self-gated structure) [15-17] or via employing ion-gel as the gating element [18]. Since the optical conductivity of graphene at terahertz frequencies follows a Drude-like dispersion:

$$\sigma(\omega) = \frac{\sigma_{DC}}{1 - j\omega\tau}, \tag{1}$$

where τ is the momentum relaxation time for carriers, $\omega=2\pi f$ is angular frequency, and:

$$\sigma_{DC} = q\mu n_s, \tag{2}$$

is its DC electrical conductivity, it can be easily understood that controlling the charge density -n_s- in graphene allows us to control its optical conductivity -$\sigma(\omega)$-. In Eqn. (2) q represents electron charge, μ is carrier mobility, and n_s is carrier density. Details of the self-gated and ion-gel gating structures are sketched in Fig. 2(a-b), respectively. As shown in Fig. 2(a) by applying a finite voltage between the two capacitively coupled graphene layers, carriers of the opposite type accumulate in each layer, therefore the overall carrier density thus optical conductivity can be controlled. For the situation represented in the lower sketch of Fig. 2(a) the total terahertz optical conductivity of the structure is given by the sum of the hole conductivity of the bottom layer and the electron conductivity of the top layer.

For a given linear THz polarization metal stripes perpendicular to the polarization direction can be employed as electrodes without altering the transmission properties of the structure, as illustrated in Fig. 1(c).

3. Discussion

Numerical simulations were performed employing HFFS; graphene was modeled as a 1-nm conductive layer with variable conductivity in the range from 0.1 to 4mS (conductivity can be modified in practice via gating the structure as discussed in the previous section). Polyimide was employed as substrate, SiN as spacer, and the metal was chosen as 100-nm thick gold. The unit cell dimension is 54-µm, the spacing between metal stripes is 3-µm, and the width of the metal stripes is 2-µm. The thickness of the SiN layer is 1-µm, whereas the thickness of the substrate was set to 2-µm.

Figure 3(a) shows the simulated transmission amplitude versus frequency for different graphene conductivities. Three resonant features are observed, one at around 0.30-040THz, other at around 0.70THz, and the third one at around 1.05THz. At these frequencies the device can operate as an amplitude modulator.

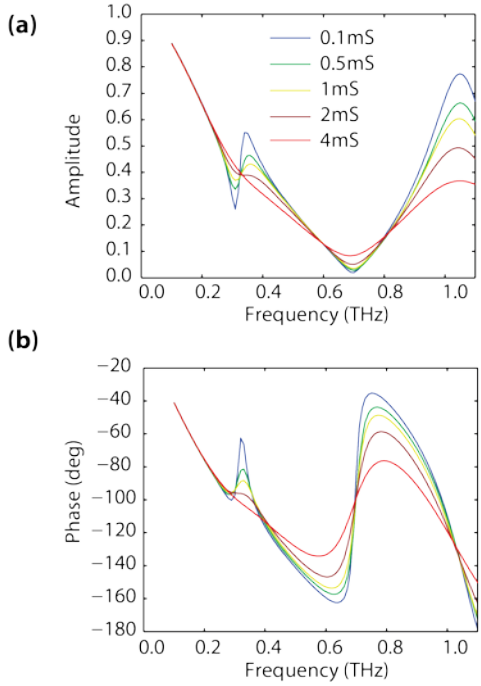

Figure 3: (a) Amplitude and (b) phase transmission vs. frequency, for different graphene conductivities. Graphene conductivity is varied from 0.1mS to 4mS.

As discussed by Chen *et al*, the terahertz transmission amplitude and phase are not independent of each other, but are related by Kramers-Kronig (KK) relations [5]. Near frequencies where the amplitude has no strong dependence on the applied voltage bias (has not dependence on graphene conductivity), the phase experiences a maximum shift. In contrast at the frequencies where maximum phase modulation is achieved no amplitude modulation takes place. Shown in Fig. 3(b) is phase versus frequency for different graphene conductivities. It is observed that at 0.32 THz, 0.65 THz, and 0.75 THz maximum phase modulation can be achieved. It is worth observing that at these frequencies the amplitude modulation is negligible (see Fig. 2(a)), in accordance with the observation by *Chen et al* [5]. The phase modulation, when tuning graphene conductivity from 0.1 mS to 4 mS, at 0.32 THz, 0.65 THz, and 0.75 THz is 42°, 40°, and 46°, respectively.

Table 1: Phase modulation in reconfigurable metamaterials.

	Chen *et al* [5]	Kafesaki *et al* [19]	This work
Unit cell dimension (μm^2)	50	50	54
Frequency (THz)	0.88	1.20	0.32
Phase modulation	32°	45°	42°
Transmission amplitude	60%	40%	40%
Unit cell to wavelength ratio	0.15	0.20	**0.06**

Shown in Table 1 are the unit cell parameters for several reconfigurable metamaterials proposed in the literature ([5], [19]). The frequency reported for this work is 0.32 THz, at which a phase modulation of 42° was obtained. It can be observed that the devices here discussed can achieve similar phase modulation than those previously reported in the literature, but with unit-cell size over wavelength ratio much smaller than that of these prior works. The unit cell to wavelength ratio here reported is just 0.06, which is 2.5 times and 3.33 smaller than those reported by Chen *et al* and Kafesaki *et al*, respectively [5, 19]. Moreover, the transmission amplitude at this frequency -40%- is similar to that reported by Kafesaki *et al* -also 40%- [19] but smaller than that reported by Chen *et al* -60%- [5]. The transmission amplitude in these cases indicates the loss introduced by the structure. From these points of view, due to the smallest unit cell to wavelength ratio and comparable phase modulation at resonance, the spiral-resonator graphene-based metamaterials here proposed can promise more abrupt phase gradients than the other two geometries previously analyzed in the literature therefore provide advantages for terahertz beam steering applications.

The active area dimension -in each unit cell- is 4-μm x 4-μm, thus active area to unit cell area ratio is just 0.5%. Since the speed of these devices is constrained by *RC* time constant limitations, switching speed becomes proportional to the active area, thus the smaller the active area the fastest the switching speed (see Ref. [10]). For comparison, the active area to unit cell area ratio of previously proposed graphene active terahertz metamaterials lies between 50% and 100% (e.g. [12-15, 18]) with reported switching in the order of 10-kHz (e.g. Ref. [10, 20]); via reducing the active area switching speeds associated with GHz frequencies can be attained.

4. Conclusions

We have proposed graphene-based electrically reconfigurable metasurfaces, which poses deep-subwavelength unit-cell/active-region dimensions. The devices here proposed can achieve similar phase modulation than other devices previously proposed in the literature, but with 2.5X smaller unit-cell to wavelength ratio. These ultra-small unit-cell dimensions can be advantageous for beam shaping applications.

Acknowledgements

The authors acknowledge the support from the NSF MRSEC program at the University of Utah under grant # DMR 1121252 and from the NSF CAREER award # 1351389 (monitored by Dimitris Pavlidis).

References

[1] Y. Monnai, C. Jansen, H. Hillmer, M. Koch, and H. Shinod, "Terahertz beam steering and variable focusing using programmable diffraction gratings," *Optics Express* 21(2): 2347-2354, 2013.

[2] S. Busch, B. Scherger, M. Scheller, and M. Koch, "Optically controlled terahertz beam steering and imaging," *Opt. Lett.* 37(8): 1391–1393, 2012.

[3] H. Fuser and M. Bieler, "Terahertz beam steering by optical coherent control," *Appl. Phys. Lett.* 102: 251109, 2013.

[4] B. Scherger, M. Reuter, M. Scheller, K. Altmann, N. Vieweg, R. Dabrowski, J. A. Deibel, and M. Koch, "Discrete terahertz beam steering with an electrically controlled liquid crystal device," *J. Infrared Milli. Terahz Waves* 33(11): 1117–1122, 2012.

[5] H. T. Chen, W. J. Padilla, M. J. Cich, A. K. Azad, R. D. Averitt, and A. J. Taylor, "A metamaterial solid-state terahertz phase modulator," *Nature Photon.* 3(3): 141–151, 2009.

[6] N. Yu, P. Genevet, M. A. Kats, F. Aieta, J. P. Tatienne, F. Capasso, and Z. Gaburro, "Light Propagation with Phase Discontinuities: Generalized Laws of Reflection and Refraction," *Science* 334: 333, 2011.

[7] B. Sensale-Rodriguez, R. Yan, L. Liu, D. Jena, and H. G. Xing, "Graphene for Reconfigurable Terahertz

Optoelectronics," *Proceedings of the IEEE* 101(7): 1705-1706, 2013.

[8] J. Horng, C.-F. Chen, B. Geng, C. Girit, Y. Zhang, Z. Hao, H. A. Bechtel, M. Martin, A. Zettl, M. F. Crommie, Y. R. Shen, and F. Wang, "Drude conductivity of Dirac fermions in graphene," *Phys. Rev. B* 83: 165113, 2011.

[9] B. Sensale-Rodriguez et al., "Unique prospects for graphene-based terahertz Modulators," *Appl. Phys. Lett.* 99: 113104, 2011.

[10] B. Sensale-Rodriguez, R. Yan, M. M. Kelly, T. Fang, K. Tahy, W. S. Hwang, D. Jena, L. Liu, and H. G. Xing, "Broadband graphene terahertz modulators enabled by intraband transitions," *Nat. Commun*. 3: 780, 2012.

[11] L. Ren, Q. Zhang, J. Yao, Z. Sun, R. Kaneko, Z. Yan, S. Nanot, Z. Jin, I. Kawayama, M. Tonouchi, J. M. Tour, and J. Kono, "Terahertz and Infrared Spectroscopy of Gated Large-Area Graphene," *Nano Letters* 12: 3711, 2012.

[12] S. H. Lee, M. Choi, T.-T. Kim, S. Lee, M. Liu, X. Yin, H. K. Choi, S. S. Lee, C.-G. Choi, S.-Y. Choi, X. Zhang, and B. Min "Switching terahertz waves with gate-controlled active graphene metamaterials." *Nature Mater.* 11: 936-941, 2012.

[13] S. H. Lee, J. Choi, H. D. Kim, H. Choi, and B. Min "Ultrafast refractive index control of a terahertz graphene metamaterial," *Scientific Reports* 3: 2135, 2013.

[14] W. Gao, J. Shu, K. Reichel, D. V. Nickel, X. He, G. Shi, R. Vajtai, P. M. Ajayan, J. Kono, D. M. Mittleman, and Q. Xu, "High-Contrast Terahertz Wave Modulation by Gated Graphene Enhanced by Extraordinary Transmission through Ring Apertures," *Nano Letters* 14(3) : 1242-1248, 2014.

[15] R. Yan, B. Sensale-Rodriguez, L. Liu, D. Jena, and H. G. Xing "A new class of tunable metamaterial terahertz modulators", *Optics Express* 20(27): 28664-28671, 2012.

[16] S. J. Koester, and M. Li "High-speed waveguide-coupled graphene-on-graphene optical modulators", *Appl. Phys. Lett.* 100: 171107, 2012.

[17] M. Liu, X. Yin, and X. Zhang "Double-layer graphene optical modulator," *Nano Letters* 12: 1482–1485, 2012.

[18] L. Ju, B. Geng, J. Horng, C. Girit, M. Martin, Z. Hao, H. A. Bechtel, X. Liang, A. Zettl, Y. R. Shen, and F. Wang "Graphene plasmonics for tunable terahertz metamaterials." *Nat. Nanotechnol.* 6: 630–634, 2011.

[19] M. Kafesaki, N. H. Shen, S. Tzortzakis, and C. M. Soukoulis, "Optically switchable and tunable terahertz metamaterials through photoconductivity," *J. Opt.* 14: 114008, 2012.

[20] B. Sensale-Rodriguez, R. Yan, S. Rafique, M. Zhu, W. Li, X. Liang, D. Gundlach, V. Protasenko, M. M. Kelly, D. Jena, L. Liu, and H. G. Xing "Extraordinary control of terahertz beam reflectance in graphene electro-absorption modulators", *Nano Letters* 12: 4518–4522, 2012.

Resonant dielectric nanostructures and metamaterials

A Sensitive Sensor with a Double U-shaped Rings-based Metamaterial

An Yang[1], Chang-Chun Yan[1*], Jie-Bing Tian[1], Cheng Wang[1], Ying Han[1], Dao Hua Zhang[2], Dong-Dong Li[2], and Zheng-Ji Xu[2]

[1]School of Physics and Electronic Engineering, Jiangsu Normal University, Xuzhou, 221116, China
[2]School of Electrical and Electronic Engineering, Nanyang Technological University, 639798, Singapore
*corresponding author, E-mail: *yhchangchun@163.com

Abstract

We design a double U-shaped rings-based metamaterial which has a good capability of the realization of sense of refractive indexes. The metamaterial consists of two regularly spaced parallel arrays of U-shaped rings with 90 degree rotation embedded in a medium, in the top of which an array of holes are dug for sensing unknown materials. Our simulations demonstrate that the structure can recognize subtle changes in refractive indexes of the unknown materials by special resonance frequencies, and it can thus be regarded as a highly sensitive sensor. Furthermore, it could also be integrated into other electronic devices because of its tiny size.

1. Introduction

Metamaterials are artificially engineered materials which are usually much smaller than the wavelengths of external stimuli in size and exhibit infusive properties and applications, including electromagnetic cloaking [1,2], supper-resolution imaging [3-5], filters [6], and absorbers [7].

Metamaterial-based sensors [8-13] also attract great attention to researchers. It was demonstrated that resonance frequencies of the metamaterial-based structures are sensitive to the changes in capacitance and inductance produced in the metamaterials. Utilizing this characteristic, many types of sensors have been reported, such as pressure sensors [8], temperature sensors [9], bio-sensors [10], optical sensors [11], refractive index sensors [12,13] and so on.

In this paper, we propose a refractive index sensor based on a metamaterial which consists of two regularly spaced parallel arrays of U-shaped rings with 90 degree rotation embedded in a silicon medium. Periodic holes for sensing unknown materials are dug in the top of each unit cell of the metamaterial. Simulations show that the resonance frequency is greatly sensitive to the refractive indexes of the unknown materials, and the precision of the refractive indexes can be higher than 0.01, which is almost the highest precision utilizing metamaterials so far.

2. Structure

Figure 1 shows one unit cell of the metamaterial made up of two-layered arrays of U-shaped rings embedded in a silicon medium, where the lower layer is rotated by 90 degrees relative to the upper one. A hole is dug in the top of the silicon medium for sensing an unknown material. The silicon medium is surrounded by air. The detailed dimensions of the unit cell are described in the figure caption. A light wave is supposed to be incident perpendicularly onto the structure, with its ***E*** polarization and ***H*** polarization along the *x* and *y* directions, respectively. In the following simulations, only one unit cell is considered due to the periodicity of the structure. Concretely, the two-paired surfaces of the unit cell in the two periodic arrangement directions (namely, the *x* and *y* directions) are set to periodic boundary conditions. The material of the U-shaped rings in the unit cell is supposed to be a perfect conductor, which is the same as that used in Ref. [14]. As described in this reference, this assumption is acceptable for most metals in the middle-infrared region. The permittivity of the silicon medium is 11.7, extracted from Ref. [15].

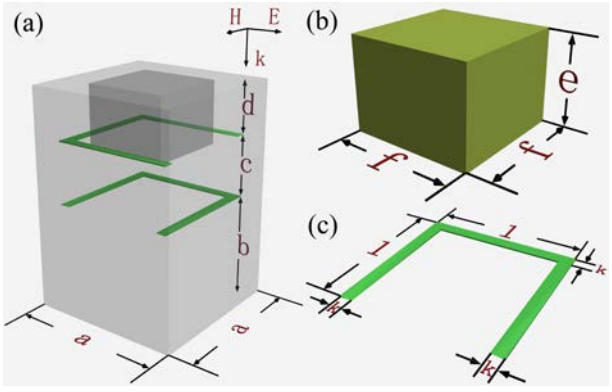

Figure 1: (a) Schematic of one unit cell of the asymmetric metamaterial consisting of two regularly spaced parallel arrays of U-shaped rings, with the two-layered arrays embedded in a silicon medium. The geometric dimensions are a = 1500 nm, b = 1015 nm, c = 600 nm, and d = 465 nm, respectively. (b) Schematic of the hole which is in the top of the silicon medium for sensing an unknown material

with geometric dimensions of e = 600 nm and f = 800 nm. (c) Schematic of one of the U-shaped rings in the unit cell with geometric dimensions of l = 1200 nm and k = 100 nm. The thickness of each U-shaped ring is h = 10 nm. The thickness of the silicon medium is $D=b+c+d+2h$.

3. Simulation results and discussion

Based on the above structure, the simulated transmittance as a function of frequency is plotted in Fig. 2 when refractive index of an unknown material in the hole is set to 1.3. It is found that the transmittance is almost zero with a higher Q factor of 331 at a frequency of 43.06 THz (the Q factor refers to the ratio of the center frequency to the full width at half maximum (FWHM) of a resonance [16]). The higher Q factor indicates more sensitive to sensing.

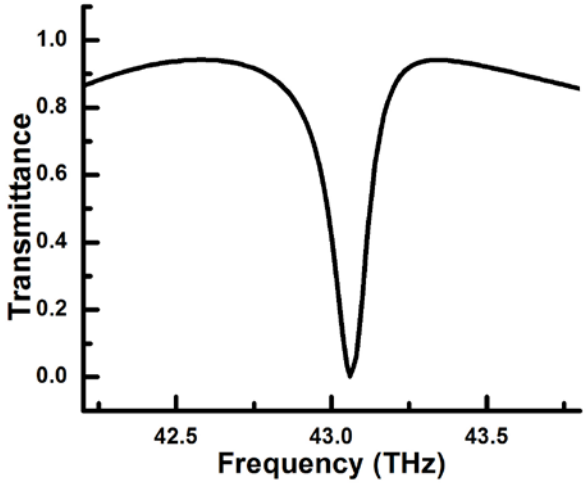

Figure 2: Transmittance as a function of frequency.

Next, influence of the U-shaped ring numbers in the unit cell on transmittance and resonance positions is investigated. We simulated transmittance for additional two cases, namely, the lower ring removed, and the upper ring removed. The corresponding results are shown in Figs. 3 (a) and 3(b). It can be seen that their resonances are obviously weaker than that of the structure with the two U-shaped rings, and therefore the later is more applicable to sensing.

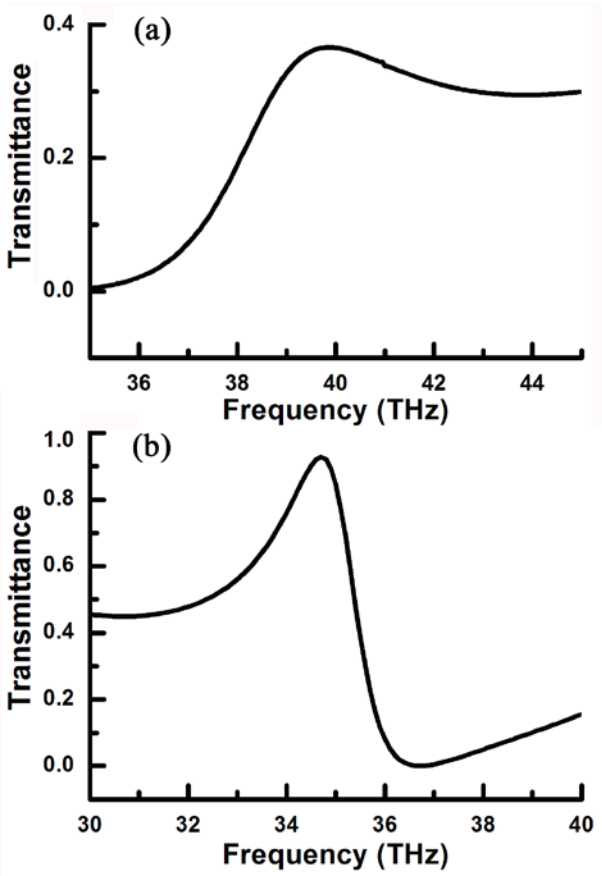

Figure 3: (a) Transmittance as a function of frequency when the lower U-shaped ring is removed. (b) Transmittance as a function of frequency when the upper U-shaped ring is removed.

Then, the refractive index of the unknown material shown in Fig. 1 (b) is changed. It increases from 1.3 to 1.33, 2.3 to 2.33, and 3.3 to 3.33, with a same step of 0.01, respectively. The corresponding transmittance as a function of frequency is shown in Figs. 4, 5, and 6, respectively. Obviously, the resonance positions corresponding to different refractive indexes can be clearly distinguished, and the resonance frequencies move towards the lower frequency with increasing refractive index. As a result, the structure can be used as a sensor. From the three figures, it can also be seen that the transmittance at resonances is almost zero, indicating strong resonance. Meanwhile, the transmittance spectra at resonance are narrow, which means more sensitive to sensing.

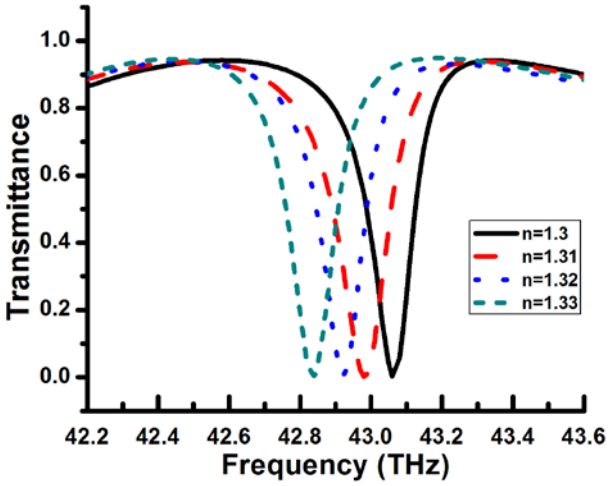

Figure 4: Transmittance as a function of frequency when the refractive index increases from 1.3 to 1.33. The black solid shows the case for a refractive index of 1.3. The red dash shows the case for a refractive index of 1.31. The blue dot shows the case for a refractive index of 1.32. The green short dash shows the case for a refractive index of 1.3.

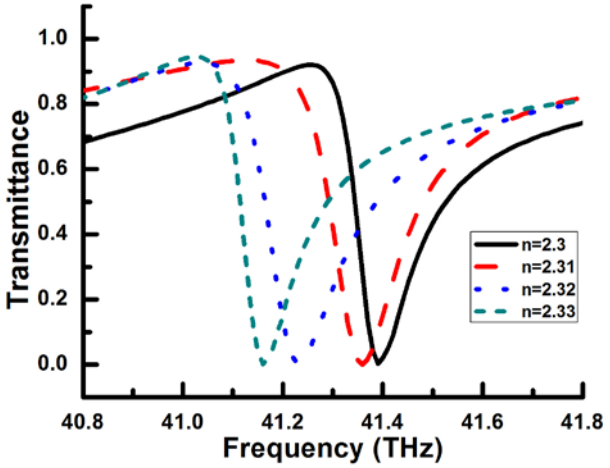

Figure 5: Transmittance as a function of frequency when the refractive index increases from 2.3 to 2.33. The black solid shows the case for a refractive index of 2.3. The red dash shows the case for a refractive index of 2.31. The blue dot shows the case for a refractive index of 2.32. The green short dash shows the case for a refractive index of 2.33.

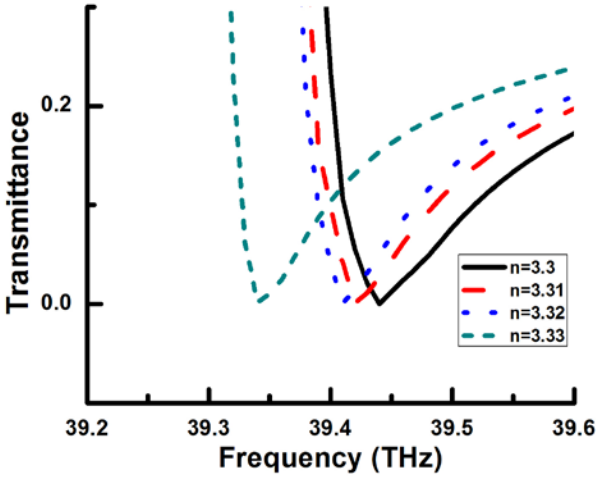

Figure 6: Transmittance as a function of frequency when the refractive index increases from 3.3 to 3.33. The black solid shows the case for a refractive index of 3.3. The red dash shows the case for a refractive index of 3.31. The blue dot shows the case for a refractive index of 3.32. The green short dash shows the case for a refractive index of 3.33.

To exhibit better the sensing property, the refractive index as a function of resonance frequency is plotted in Fig. 7. It is obviously observed that the resonance frequency gradually becomes lower with the increase of refractive index. Each refractive index corresponds to a special resonance frequency. Consequently, once the resonance frequency for an unknown material is measured, its refractive index can be obtained following the curve in Fig. 7.

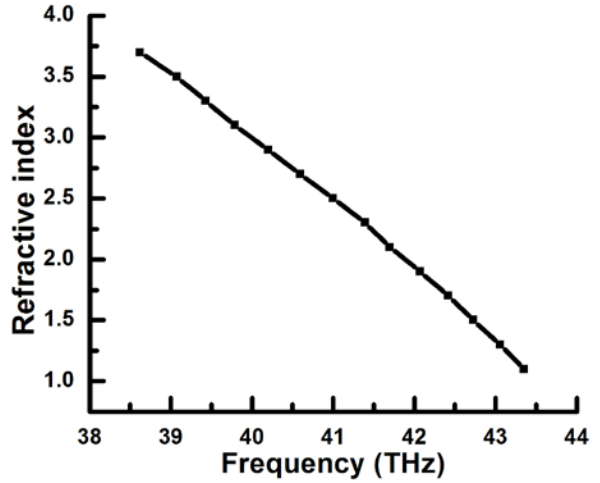

Figure 7: Refractive index as a function of resonance frequency. The refractive index of the unknown material increases from 1.1 to 3.7.

4. Analysis of physical mechanism

To investigate physical mechanism for the production of the transmittance, we discussed the current distributions in the U-shaped rings at the resonance when the refractive index of the unknown material is 1.3. The results are shown in Fig. 8. It can be observed that currents distribute in the upper ring

as well as the lower one. That is to say, the currents in two rings, accompanying with coupling each other, simultaneously contribute to the resonances. Any current distribution may be taken as consisting of different electric dipoles excited by the incident electromagnetic field. At the resonance, a part of electromagnetic energy can be confined in the space between the two U-shaped rings, which engenders a narrow resonance.

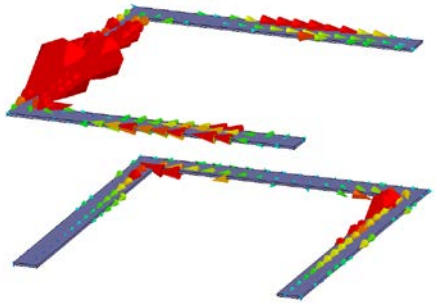

Figure 8: Surface current distributions in the two U-shaped rings at the resonance frequency when the refractive index is equal to 1.3.

When the refractive index of the unknown material increases, the average refractive index of the medium in the unit cell consequently also increases. The conduction currents produced in the two U-shaped rings induce the polarization of the medium around the two rings. The polarization charges reversely impede the conduction currents. The resonance position hence shifts to the lower frequency with the increasing refractive index of the unknown material, which explains the phenomenon shown in Fig. 7.

5. Conclusions

In summary, we proposed an asymmetric metamaterial based on two regularly spaced parallel arrays of U-shaped rings. The simulation results show that the structure can be regarded as a greatly sensitive refractive-index sensor. The precision of the refractive index can be higher than 0.01. Another advantage lies in that it is easily integrated into other devices because of its tiny size, compared with traditional methods.

Acknowledgements

The project is supported by the Natural Science Foundation (BK2011203) of Jiangsu Province, the National Natural Science Foundation of China (61372057), and the Priority Academic Program Development of Jiangsu Higher Education Institutions (PAPD), China.

References

[1] D. Schurig, J. J. Mock, B. J. Justice, S. A. Cummer, J. B. Pendry, A. F. Starr, D. R. Smith, Metamaterial electromagnetic cloak at microwave frequencies, Science 314: 977−980, 2006.

[2] J. B. Pendry, D. Schurig, D. R. Smith, Controlling electromagnetic fields, Science 312: 1780−1782, 2006.

[3] N. Fang, H. Lee, C. Sun, X. Zhang, Sub–diffraction-limited optical imaging with a silver superlens, Science 308: 534−537, 2005.

[4] Z. Liu, H. Lee, Y. Xiong, C. Sun, X. Zhang, Far-field optical hyperlens magnifying sub-diffraction-limited objects, Science 315: 1686, 2007.

[5] I. I. Smolyaninov, Y. J. Hung, C. C. Davis, Magnifying superlens in the visible frequency range, Science 315: 1699−1701, 2007.

[6] G. Jang, E. C. Shin, C. H. Lee, C. M. Shin, S. Kahng, Design of dualband metamaterial bandpass filter using zeroth order resonance, IEEE Microw. Conf. Singapore, pp. 492−495, 2009.

[7] R. Melik, E. Unal, N. Perkgoz, C. Puttlitz, H. Demir. Metamaterial-based wireless strain sensors, Appl. Phys. Lett. 95: 011106, 2009.

[8] E. Ekmekci, G. Turhan-Sayan, Metamaterial sensor applications based on broadside-coupled SRR and V-shaped resonator structures, IEEE Inter. Symp. Ante. and Prop. pp. 1170−1172, 2011.

[9] V.A. Fedotov, A. Tsiatmas, J. H. Shi1, R. Buckingham, P. de Groot, Y. Chen, S. Wang, N.I. Zheludev, Temperature control of Fano resonances and transmission in superconducting metamaterials, Opt. Express 18: 9015−9019, 2010.

[10] A. V. Kabashin, P. Evans, S. Pastkovsky,W. Hendren, G. A.Wurtz, R. Atkinson, R. Pollard, V. A. Podolskiy, A. V. Zayats, Plasmonic nanorod metamaterials for biosensing, Nat. Mater. 8: 867−871, 2009.

[11] N. Papasimakis, Z. Luo, Z. X. Shen, F. D. Angelis, E. D. Fabrizio, A. E. Nikolaenko, N. I. Zheludev, Graphene in a photonic metamaterial, Opt. Express 18: 8353−8359, 2010.

[12] N. Liu, M. Mesch, T. Weiss, M. Hentschel, H. Giessen, Infrared perfect absorber and its application as plasmonic sensor, Nano Lett. 10: 2342−2348, 2010.

[13] G. Nemova1, R. Kashyap, Theoretical model of a planar integrated refractive index sensor based on surface plasmon–polaritonexcitation with a long period grating, J. Opt. Soc. Am. B. 24: 2696−2701, 2007.

[14] N. I. Zheludev, S. L. Prosvirnin, N. Papasimakis, V. A. Fedotov. Lasing spaser, Nat. Photon. 2: 351−354, 2008.

[15] E. D. Palik, Handbook of Optical Constants of Solids, Academic Press, New York, 1985.

[16] I. A. I. Al-Naib, C. Jansen, N. Born, M. Koch, Polarization and angle independent terahertz metamaterials with high Q-factors, Appl. Phys. Lett. 98: 091107, 2011.